Discrete Element Method Investigation of Stainless Steel 316l Powder Flow in Vacuum Conditions during Additive Manufacturing

Andrew Joseph Burgess

A thesis submitted in partial fulfilment of the requirements of Liverpool John Moores University for the degree of Doctor of Philosophy

May 2024

Abstract

Additive Manufacturing is an increasingly popular approach for manufacturers to generate complex components more efficiently. As a flagship process of Industry 4.0, researchers are leveraging digital modelling to optimise the process without incurring the costs of practical trial and error experiments. This project pursues methods to optimise the powder spreading process and deliver novel solutions for commercial practices, using Discrete Element Methods to investigate how the spreading parameters and powder characteristics influence the quality of the formed powder bed. Three discrete metrics were identified to determine the powder bed quality: the packing density, surface roughness, and dispersion of polydisperse powder elements within the spread layer.

A key knowledge gap exists in the current research landscape. The majority of contemporary simulations insert powder in a user-defined volume which then falls to the substrate under gravity, a process referred to as the “rainfall” method. This misrepresents powder deposition in commercial Additive Manufacturing systems, where the powder is inserted using various techniques such as by a moving funnel, or a piston-operated supply table. This project addresses this knowledge gap by inserting Stainless Steel 316l powder with a moving funnel to provide a more realistic deposition approach than existing methods in the literature. Stainless Steel 316l is a metallic material, widely used in Powder Bed Fusion applications for its processability in generating high-quality and dense parts with complex geometries, excellent corrosion resistance, and mechanical properties such as strength, ductility, and toughness.

The novel simulation approach has been benchmarked against values set by the rainfall approach, with multiple powder sets inserted for comparison. These sets included uniform powder consisting of same-sized particles, and polydisperse sets with varying fractions of relatively coarse, fine, and intermediately sized particles within the size range in commercial Additive Manufacturing. The veracity of the digital model was ascertained by comparison to practical powder experiments, and confirmed the fidelity of the model to physical powder flow analysis.

Research highlighted that depositing the powder with the moving funnel engenders a significant difference in the spread layer. The funnel generally lowered the packing density by between 1-2% for all inserted sets and incurred a rougher surface in the spread layer ranging from 4.77% rougher to 72.34% rougher depending on the inserted particle size ranges. These results were significant to the existing research landscape, as they imply that rainfall models may artificially increase the quality of the formed powder beds. The results showed a suitable powder size range for Stainless Steel 316l, delivered by the moving funnel in the spreading conditions tested, would be a 60% population of 15-25 µm particles, 25% of the population between 25-40 µm, and no more than 15% of the particles ≥ 40 µm in diameter.

The key outcomes of the thesis, specifically that existing deposition methods currently misrepresent the techniques observed in industrial Powder Bed Fusion machinery, lay the foundation for future research. This work provides the basis for the realistic deposition of powder, advancing existing knowledge by increasing

the accuracy of the Discrete Element Methods for Additive Manufacturing investigations, and more accurately reflecting commercial methods. Thus, giving a foundation for researchers in the industrial and academic spheres to adapt parameters and engender conditions which serve to optimise the powder bed. This contribution is further reinforced by the suggested size distribution of particles that optimise spreading conditions. For contemporaries in the simulation and modelling of Additive Manufacturing processes, a significant contribution has been made by establishing a direct conversion between properties known as the Surface Energy and Cohesion Energy Density. To the best of the author's knowledge this relationship, although explored in literature and within the wider Discrete Element Method community, had not previously been numerically established.

Acknowledgements

To perform a PhD project is a tremendous undertaking, and I would like to place on record my sincere gratitude to a number of key people who have supported me in delivering successful project conclusions. Without whom, the PhD would not have been possible.

Firstly, my supervisory team. As my director of study, Dr Sean Malkeson has been nothing short of an excellent supervisor. Dr Malkeson has provided me with an array of interesting research areas to explore whilst also affording me the freedom to investigate my own ideas. His commitment to helping me deliver my best work has not gone unnoticed.

Immense thanks for the tireless work and support of Prof. Peter Falkingham, who has fundamentally built my skills in the digital modelling of engineering processes from the first principles. His patience has been a cornerstone of the PhD success as I have often asked what to him must have been the most rudimentary of questions. It is impossible to overstate how important Prof. Falkingham's contributions have been to both the PhD and my personal and professional development.

I give thanks too to Dr Martin Sharp, not only for sharing his expertise in Additive Manufacturing processes but also for his unwavering commitment to making me a better researcher and a better engineer, by encouraging me to move out of my comfort zone whenever possible and diversify my skill set to explore new and exciting opportunities that have enriched the PhD experience.

Many thanks also to Dr Rob Darlington. Dr Darlington's relentless positivity and enthusiasm for the PhD work, even during challenging times, has been vital to maintaining my morale and commitment to achieving the best possible solutions in the PhD project.

Special thanks are afforded to Dr Sam Tammas-Williams for sharing his expertise in Additive Manufacturing and his commitment to helping me deliver only the very best research possible. Dr Tammas-Williams has been a vitally important person for aiding my writing skills and helping me to publish multiple publications during the course of the project. A very special mention is made is for Dr Sam Tammas-Williams, Dr Martin Sharp, and Prof. Falkingham for their conceptualisation of the PhD project and for seeing in me a potential to complete the PhD that I would not, without their encouragement, have seen in myself.

I would like to thank Dr Tahsin Opoz for agreeing to act as my independent assessor during my confirmation of registration, and for the valuable contribution his time and input made to building on the PhD work at that time.

I would also like to take this opportunity to acknowledge and give thanks for the work of the people who have supported my project and my development. Namely: Dr Juan Ahuir-Torres, for aiding me in developing new skills and inviting me to engage with his research, the technical team on campus, the team in the Faculty of Engineering Research Administration, the Doctoral Academy, and the IT support technicians. A special thank you to Harvey Thompson and Alec Robinson, for their assistance in practical analysis to inform the work of the thesis. Although a PhD is an independent and self-driven project, I would like to afford the courtesy to thank all who contributed in any way to the success of this project.

Many firms in industry have taken an interest in the project, and thanks is given for their attention and the professional expertise provided in the development of the PhD solutions. Including, but not limited to, Wayland Additive Ltd, Croft Filters Ltd, DONAA, Granutools, Carpenter Additive Ltd, and Fort Wayne Metals Ltd.

As this PhD has been performed with financial support in the form of a scholarship from Liverpool John Moores University, the awarding body has my sincere gratitude, along with the people who supported the application. Once again, Dr Tammas-Willaims, Dr Sharp, Prof. Falkingham, Dr Chris Smith at Wayland Additive Ltd and Mr Eddy Stocker are thanked for their contributions in formulating the application. For their references which endorsed the application, special thanks are given to Mr Neil Burns, Mr John Carrier, and Prof. Xun Chen. Finally, a very special thanks to Prof. Keith George and the assessment panel for choosing my scholarship application in what was no doubt an extremely competitive pool.

I would also like to acknowledge my friends and colleagues in the General Engineering Research Institute for their help and support during the PhD. A special mention is reserved for Dr Tom Cottage for all the laughs we have shared in the office and to commend his work as the pinnacle of professionalism. I will miss the coffees.

To my sister Katie, a massive thank you for the support and help you have provided before, during, and no doubt after the PhD. Big thanks also go to “the boys”, and all my friends for their support and all the laughs we have shared, and for providing me with a sounding board during the course of my PhD. A special mention also for Dr David Hitchmough, thanks is given for the many lifts and laughs on the way to the campus.

Thanks to Marlon Burgess, Carl, Denise, Mabel, and Millie van Breemen, and Pamela and Poppy Hall for their accommodations and emotional support throughout the PhD.

Last, but most definitely not least, a very special thanks to Emma van Breemen, who colours everything I do, for the love and support throughout the PhD. You are the best.

SARS-CoV-2 Statement

The global Coronavirus pandemic of the respiratory disease SARS-CoV-2, which began in 2019 and is often referred to as ‘Covid-19’, had a significant effect on the project. In response to the pandemic, the government of the United Kingdom (UK) implemented numerous restrictions in an effort to prevent the spread of the disease, including constraints on the number of people congregating within a given proximity. This extended to the closure of certain educational and business premises including the facilities within Liverpool John Moores University (LJMU) which remained inaccessible for the first six months of the PhD project, and the resulting ramifications disrupted progress throughout the first year of research. In response to these adverse circumstances, all possible measures have been implemented where appropriate and deemed reasonably practicable in line with government and institutional guidance. Furthermore, all necessary actions have been taken to mitigate the influence on the project outcomes by the parties involved in the project.

Table of Contents

List of Acronyms

The following list records all of the acronyms used in the written text with their associated expansion. Note that the acronyms are recorded alphabetically and then numerically, and not in the order in which they appear chronologically with the written text.

Acronym	***Expansion***
ABS	Acrylonitrile Butadiene Styrene
AlSi12	Aluminium Silicon Alloy.
AM	Additive Manufacturing.
AoR	Angle of Repose.
ASTM	American Society for Testing and Materials.
BS	British Standards.
CAD	Computer Aided Design.
CFD	Computational Fluid Dynamics.
CFD-DEM	Computational Fluid Dynamics coupled with Discrete/Distinct Element Method/ Modelling.
CGS	Centimetres-Grams-Seconds.
CI	Carr Index.
CNC	Computer Numerical Control.
CoCr	Cobalt-Chromium.
CRIQ	Quebec International Research Centre.

CT	Computed Tomography.
DED	Directed Energy Deposition.
DEM	Discrete/Distinct Element Method/Modelling.
DEM-AM	Discrete/Distinct Element Method/Modelling for Additive Manufacturing.
DfAM	Design for Additive Manufacturing.
DMLS	Direct Metal Laser Sintering.
DMT	Derjaguin-Muller-Toporov.
EBM	Electron Beam Melting.
FEA	Finite Element Analysis.
FDM	Fused Deposition Modelling.
GE	General Electric.
GPU	Graphical Processing Unit.
HFM	Hall Flow Meter.
HFR	Hall Flow Rate.
HIP	Hot Isostatic Pressing.
HPC	High-Performance Computing.
ISO	International Organisation for Standardisation.

JKR	Johnson-Kendall-Roberts.
JPEG	Joint Photographic Experts Group.
LAMMPS	Large-scale Atomic/Molecular Massively Parallel Simulator.
LIGGGHTS®.	LAMMPS Improved for General Granular and Granular Heat Transfer Simulations.
LPBF	Laser Powder Bed Fusion.
MPI	Message Passing Interface.
PBF	Powder Bed Fusion.
PEEK	Polyetheretherketone.
PEI	Polyetherimide.
PLA	Polylactic Acid.
PNG	Portable Network Graphic.
PPE	Personal Protective Equipment.
PSD	Particle-size Distribution.
RCST	Ring Cell Shear Tester.
RMS	Root Mean Square.
RPA	Revolution Powder Analyser.
SEM	Scanning Electron Microscopy.

S.I	Système International – International System of Units.
SJKR	Simplified Johnson-Kendall-Roberts.
SLM	Selective Laser Melting.
SLS	Selective Laser Sintering.
SS316l	Stainless Steel 316l.
STL	Stereolithographic.
Ti-6Al-4V	Titanium/Aluminium/Vanadium.
™ (Superscript)	Trademarked.
UK	United Kingdom.
VER	Volume Expansion Ratio.
2D	Two-Dimensional.
3D	Three-Dimensional.

List of Figures

List of Equations

List of Tables

Nomenclature

The nomenclature provided below records each symbol used within the written text, in conjunction with a description pertaining to said symbol, and the associated unit of measurement from the metric International System of Units (S.I) where applicable. The nomenclature is provided in the conventional order of Upper Case, Lower Case, Greek, and miscellaneous, and each symbol is listed alphabetically or numerically within the associated section:

Upper Case

Symbol	***Description***	***S.I Unit/Expansion***
A	The contact point at an equal distance between points A_d and A_w.	N.A.
A_d	The point on the outside edge of disc **X**, on the horizontal axis running through the centre of the disc.	N.A.
Al_2O_3	Aluminium Oxide Ceramic Powder.	N.A.
A_w	The wall point on the horizontal axis running through the centre of disc **X**. Both A_d and A_w are drawn on the line perpendicular to the walls compressing the discs.	N.A.
A_0	Cross Sectional Area.	Square Metres.
B	The contact point between disc **X** and disc **Y**.	N.A.
C	The contact point halfway between points C_d and C_w.	N.A.

C	Coulombs.	N.A.
C_d	The point on the outside edge of disc **Y**, on the horizontal axis running through the centre of the disc.	N.A.
C_w	The wall point on the horizontal axis running through the centre of disc **Y**. Both C_d and C_w are drawn on the line perpendicular to the walls compressing the discs, as is also the case with disc **X**.	N.A.
$\mathrm{C}_{\mathbf{X}}$	Centre of Disc **X**.	N.A.
$\mathrm{C}_{\mathbf{Y}}$	Centre of Disc **Y**.	N.A.
D	Diameter.	Metres.
D	Distance between the centre points of discs.	Metres.
$D_{Geometric}$	Geometric Mean Diameter.	Metres.
D_{Min}	Minimum Diameter.	Metres.
D_{Max}	Maximum Diameter.	Metres.
D_{Nozzle}	Diameter of the nozzle in the moving funnel model.	Metres.
Dyne	The force required to accelerate a mass of one gram at a rate of one centimetre per second squared.	N.A.

E_1	Young's Modulus of Elasticity of Material 1.	Gigapascals.
E_2	Young's Modulus of Elasticity of Material 2.	Gigapascals.
F	Force.	Newtons.
F_i^g	Forces due to gravity acting on Particle i.	Newtons.
F_{ij}^n	Normal contact force acting on Particle i by Particle j or wall effects.	Newtons.
F_{ij}^s	Tangential contact force acting on Particle i by Particle j or wall effects.	Newtons.
F_{JKR}	Separation force applied in Johnson-Kendall-Roberts contact modelling theory.	Newtons.
G	Shear Modulus.	Gigapascals.
GPa	Gigapascals.	N.A.
G_{SS316l}	Shear modulus of Stainless Steel 316l powder.	Gigapascals.
$G_{Two\ Orders\ of\ Magnitude\ Smaller}$	Shear modulus of Stainless Steel 316l powder at two orders of magnitude below reality.	Pascals.
$G_{Three\ Orders\ of\ Magnitude\ Smaller}$	Shear modulus of Stainless Steel 316l powder at three orders of magnitude below reality.	Pascals.

I_i	Moment of Inertia of Particle i	Kilogram-Metres Squared.
J	Joules.	N.A.
L	Length in Dimensional Analysis.	Metres.
L	Length estimate used in surface fractal powder analysis.	Metres.
M	Moment.	Newton-Metres.
MJ	Megajoules.	N.A.
MPa	Megapascals.	N.A.
N (subscript)	Instantaneous Timestamp.	Seconds.
$\mathbf{N}_{Maximum}$	The maximum number of particles in the powder bed.	N.A
$\mathbf{N}_{Realistic}$	The realistic number of particles in the powder bed.	N.A
P	Contact region of Disc **X** and Disc **Y**.	N.A.
Pa	Pascals.	N.A.
$P_{\mathbf{X}}$	Intersecting point of Disc **X** on the line connecting the centre of Disc **X** to Disc **Y**.	N.A.
$P_{\mathbf{Y}}$	Intersecting point of Disc **Y** on the line connecting the centre of Disc **X** to Disc **Y**.	N.A.
Q	A positive value.	N.A.

R_a	Arithmetic mean surface roughness.	Micrometres.
R_q	Root Mean Square value as denoted in the ImageJ software.	Micrometres.
R_{q1}	The first tested Root Mean Square value in Surface Roughness analysis.	Micrometres.
R_{q2}	The second tested Root Mean Square value in Surface Roughness analysis.	Micrometres.
T	Time in Dimensional Analysis.	Seconds.
T_{ij}^{r}	Torque acting on Particle i due to rolling friction.	Newton-Metres.
T_{ij}^{s}	Torque acting on Particle i due to tangential forces.	Newton-Metres.
$V_{Deposition}$	Deposition speed of moving funnel.	Metres per Second.
$\mathbf{V}_{Impact}$	Impact velocity.	Metres per Second.
$V_{Particle}$	Volume of a particle.	Metres Cubed.
$V_{Powder\ Bed}$	Volume of a powder bed.	Metres Cubed.
V_{Solids}	Volume of solids within the powder bed.	Metres Cubed.
V_{Sphere}	Volume of a sphere.	Metres Cubed.
V_{Voids}	Volume of voids within the powder bed.	Metres Cubed.

X	Disc.	N.A.
$\dot{\mathbf{X}}_\iota$	Velocity vector of Disc **X**.	Metres per Second.
Y	Disc.	N.A.
$\dot{\mathbf{Y}}_\iota$.	Velocity vector of Disc **Y**.	Metres per Second.

Lower Case

Symbol	***Description***	***S.I Unit/Expansion***
a	Acceleration.	Metres per Second Squared.
$\mathrm{a_P}$	The area of particle contact in the Simplified Johnson-Kendall-Roberts contact modelling theory.	Metres Squared.
$\mathbf{cd}$	Chord.	Metres.
$\mathbf{cd}_{\boldsymbol{min}}$	Minimum chord.	Metres.
cm	Measurement of distance.	Centimetres.
cm^3	Measurement of volume.	Centimetres Cubed.
d	Darcy.	N.A.
d	Derivative.	N.A.
$\boldsymbol{d_{Feret}}$	Feret Diameter.	Metres.
$\boldsymbol{d_{Feret_{max}}}$	Maximum Feret Diameter.	Metres.
d_{Impact}	Impact distance of indentation.	Metres.
$\boldsymbol{d_{Martin}}$	Martin Diameter.	Metres.

$\boldsymbol{d_{Martin_{max}}}$	Maximum Martin Diameter.	Metres.
$\boldsymbol{d_{Pile}}$	Diameter of the pile.	Metres.
d_{10}	Percentile value used when measuring the constituents of a cumulative PSD, suggesting 10% of the particles fall in this size range.	Dimensionless.
d_{50}	Percentile value used when measuring the constituents of a cumulative PSD, suggesting 50% of the particles fall in this size range.	Dimensionless.
d_{90}	Percentile value used when measuring the constituents of a cumulative PSD, suggesting 90% of the particles fall in this size range.	Dimensionless.
$\boldsymbol{e}$	Coefficient of Restitution.	Dimensionless.
e_i	The unit vector pointing from the centre of Disc **X** to the centre of Disc **Y**.	Metres.
$ergs$	Unit of energy used in the LIGGGHTS® run script.	N.A.
g	Acceleration due to gravity.	Metres per Second Squared.
h	Height at which a space ray intersects the powder bed in surface roughness analysis.	Millimetres.

$\boldsymbol{h_{Pile}}$	The height of the pile formed in discharging powder experiments.	Millimetres.
k	Stiffness.	Newtons per Metre.
kg	S.I base unit of mass.	Kilogram.
$l_{Dynamic}$	Length of the dynamic powder during rotation in spatial fluctuation analysis.	Centimetres.
$l_{Stationary}$	Length of the stationary powder in spatial fluctuation analysis.	Centimetres.
m	Mass.	Kilogram.
m	S.I base unit of length and distance.	Metres.
mbar	Millibar.	N.A.
m_{Error}	Error between the expected and the actual mass values in the powder insertion process.	Dimensionless.
$m_{Fraction}$	Intended insertion fraction of powder.	Kilogram.
m_i	Mass of Particle i.	Kilogram.
mm	Reflective of one millionth of the base unit ‘Metre’.	Millimetres.
$m_{Particle}$	Mass of one particle.	Kilogram.
$m_{Particle\ Set}$	Mass of a given particle set.	Kilogram.

$m_{Particle\ Set\ 1}$	Total mass of the first set of measured particles in a polydisperse mix.	Kilogram.
$m_{Particle\ Set\ 2}$	Total mass of the second set of measured particles in a polydisperse mix.	Kilogram.
$m_{Particle\ Set\ 3}$	Total mass of the third set of measured particles in a polydisperse mix.	Kilogram.
$\dot{m}_{Powder}$	Mass Flow Rate of Powder.	Kilogram per Second.
n	Number of surface points analysed.	Dimensionless.
$\dot{\boldsymbol{n}}$	Normal component of the relative velocities.	Metres per Second.
n (subscript)	Normal.	N.A.
nm	Nanometres.	N.A.
pg	Picogram.	N.A.
r	Radius.	Metres.
r^*	Effective radius.	Metres.
$\boldsymbol{rad}$	Radians.	N.A.
$r_{Particle}$	Radius of a particle.	Metres.
r_{Sphere}	Radius of a sphere.	Metres.
$\mathrm{r}_{\mathbf{X}}$	Radius of Disc **X**.	Metres.

$\mathrm{r}_{\mathbf{Y}}$	Radius of Disc **Y**.	Metres.
s	S.I base unit of time.	Seconds.
$\dot{s}$	Tangential component of the relative velocities.	Metres.
s (subscript)	Denotes shear.	Pascals.
t	Time or Timestep.	Seconds.
t_c	Critical timestep.	Seconds.
t_i	The unit vector found with the clockwise rotation of e_i through 90°.	N.A.
t_0	Timestep zero.	Seconds.
t_1	First timestep.	Seconds.
t_2	Second timestep.	Seconds.
$\mathbf{v}$	Velocity acting on discs.	Metres per Second.
$\mathbf{v}_i$	Translational Velocity of Particle i.	Metres per Second.
$\mathbf{v}_{w\mathbf{X}}$	Velocity of the wall in contact with disc **X**.	Metres per Second.
$\mathbf{v}_{w\mathbf{Y}}$	Velocity of the wall in contact with disc **Y**.	Metres per Second.
x	Horizontal axis within a Cartesian coordinate system.	Millimetres.

x_h	The axis in the length of the formed powder heap in line with the recoater trajectory.	Millimetres.
x_{h-}	The first one-third in the length of the heap.	Millimetres.
x_{h0}	The middle segment of the heap.	Millimetres.
x_{h+}	The final one-third segment of the heap at the “far” end of the bed.	Millimetres.
xz	The projection of the horizontal axis onto the vertical axis in a Cartesian coordinate system.	Centimetres.
x_-	The initial segment measured in the x plane relative to recoater velocity at x = 0.3cm to x = 0.5cm.	Centimetres.
x_0	The middle segment measured in the x plane relative to recoater velocity at x = 0.5cm to x = 0.7cm.	Centimetres.
x_+	The last segment measured in the x plane relative to recoater velocity at x = 0.7cm to x = 0.9cm.	Millimetres.
y	The perpendicular axis to the x and z planes of a Cartesian coordinate system.	Millimetres.

y_h	The plane measured as the width of the formed powder heap in line with the funnel trajectory.	Millimetres.
y_{h-}	The first 1/3rd of the heap width nearest to the funnel starting point (early pouring).	Millimetres.
y_{h0}	The middle segment of the heap width between the start and end of the funnel trajectory (mid pouring).	Millimetres.
y_{h+}	The far end of the heap width relative to the funnel trajectory (late pouring).	Millimetres.
y_-	The first 1/3rd of the bed width nearest to the funnel starting point (early pouring).	Millimetres.
y_{-_1}	The first average roughness taken in the y_- segment line profile, respectively.	Micrometres.
y_{-_2}	The second average roughness taken in the y_- segment line profile, respectively.	Micrometres.
y_0	The middle segment of the bed width between the start and end of the funnel trajectory (mid pouring).	Millimetres.
$y_{0.5\text{mm}}R_{q_{\text{A}_1}}$	The first tested RMS surface roughness in Model A for the slab at $y = 0.5\text{mm}$.	Micrometres.

$y_{0.5\mathrm{mm}}R_{q_{\mathrm{A}_2}}$	The second tested RMS surface roughness in Model A for the slab at $y = 0.5\mathrm{mm}$.	Micrometres.
$y_{0.5\mathrm{mm}}R_{q_{B_1}}$	The first tested RMS surface roughness in Model B for the slab at $y = 0.5\mathrm{mm}$.	Micrometres.
$y_{0.5\mathrm{mm}}R_{q_{B_2}}$	The second tested RMS surface roughness in Model B for the slab at $y = 0.5\mathrm{mm}$.	Micrometres.
$y_{0.5\mathrm{mm}}R_{q_{c_1}}$	The first tested RMS surface roughness in Model C for the slab at $y = 0.5\mathrm{mm}$.	Micrometres.
$y_{0.5\mathrm{mm}}R_{q_{c_2}}$	The second tested RMS surface roughness in Model C for the slab at $y = 0.5\mathrm{mm}$.	Micrometres.
$y_{1\mathrm{mm}}R_{q_{\mathrm{A}_1}}$	The first tested RMS surface roughness in Model A for the slab at $y = 1\mathrm{mm}$.	Micrometres.
$y_{1\mathrm{mm}}R_{q_{\mathrm{A}_2}}$	The second tested RMS surface roughness in Model A for the slab at $y = 1\mathrm{mm}$.	Micrometres.
$y_{1\mathrm{mm}}R_{q_{B_1}}$	The first tested RMS surface roughness in Model B for the slab at $y = 1\mathrm{mm}$.	Micrometres.
$y_{1\mathrm{mm}}R_{q_{B_2}}$	The second tested RMS surface roughness in Model B for the slab at $y = 1\mathrm{mm}$.	Micrometres.

$y_{1\text{mm}}R_{q_{C_1}}$	The first tested RMS surface roughness in Model C for the slab at $y = 1\text{mm}$.	Micrometres.
$y_{1\text{mm}}R_{q_{C_2}}$	The second tested RMS surface roughness in Model C for the slab at $y = 1\text{mm}$.	Micrometres.
$y_{1.5\text{mm}}R_{q_{A_1}}$	The first tested RMS surface roughness in Model A for the slab at $y = 1.5\text{mm}$.	Micrometres.
$y_{1.5\text{mm}}R_{q_{A_2}}$	The second tested RMS surface roughness in Model A for the slab at $y = 1.5\text{mm}$.	Micrometres.
$y_{1.5\text{mm}}R_{q_{B_1}}$	The first tested RMS surface roughness in Model B for the slab at $y = 1.5\text{mm}$.	Micrometres.
$y_{1.5\text{mm}}R_{q_{B_2}}$	The second tested RMS surface roughness in Model B for the slab at $y = 1.5\text{mm}$.	Micrometres.
$y_{1.5\text{mm}}R_{q_{C_1}}$	The first tested RMS surface roughness in Model C for the slab at $y = 1.5\text{mm}$.	Micrometres.
$y_{1.5\text{mm}}R_{q_{C_2}}$	The second tested RMS surface roughness in Model C for the slab at $y = 1.5\text{mm}$.	Micrometres.
z	Vertical axis within a Cartesian coordinate system.	Millimetres.
$\bar{z}$	Average position of the surface point group data.	Micrometres.

z_i	Height of the best-fit plane in the z axis.	Micrometres.
z_h	The axis representing the depth and therefore vertical measurements of the formed powder heap.	Micrometres.
z_{h-}	The bottom 50 µm in the depth of the heap.	Micrometres.
z_{h0}	The 50 µm segment in the vertical middle of the heap.	Micrometres.
z_{h+}	The top 50 µm of the heap.	Micrometres.
z_-	The bottom 50 µm in the depth of the powder bed (z = 0 µm to z = 50 µm).	Micrometres.
z_0	The 50 µm segment in the vertical middle of the powder bed (z = 50 µm to z = 100 µm).	Micrometres.
z_+	The top 50 µm in the height of the bed (z = 100 µm to z = 150 µm).	Micrometres.

Greek – Upper Case

Symbol	***Description***	***S.I Unit/Expansion***
$\mathbf{\Gamma}$	A constant at least equal to unity.	Dimensionless.
$\varDelta_{Frame}$	Number of frames in which powder flow occurs in powder testing.	Dimensionless.

Δn	Magnitude of disc overlaps.	Meters.
$\Delta n_{\mathbf{X}}$	Relative displacement of disc **X**.	Meters.
$\Delta n_{\mathbf{Y}}$	Relative displacement of disc **Y**.	Meters.
Δs	Tangential displacements.	Meters.
Δ_t	Timestep increment.	Seconds.
Σ	Sum of.	Dimensionless.
$\Sigma_{m_{System}}$	Total mass of particles into the system.	Kilogram.
Φ	Solid Volume Fraction.	Dimensionless.
Φ_{cr}	Critical Solid Volume Fraction.	Dimensionless.
ψ^*	The effective elastic constant between the two particles.	Pascals.

<u>Greek – Lower Case</u>

α	The angle between the unit vector e_i and the horizontal.	Degrees (°).
β	Segregation.	Dimensionless.
$\gamma_{Surface}$	The surface energy between the particles.	Joules per Cubic Metres.
δ	Penetration length between the radius of the contact area and the surface.	Metres.

$\delta_{Spreader-Funnel}$	Horizontal distance between the recoater face and the moving funnel.	Metres.
$\delta_{Stand\ Off}$	Vertical distance between the nozzle of the moving funnel and the substrate.	Metres.
ϵ	Surface Roughness.	Micrometres.
$\boldsymbol{\zeta}$	The scale of measurement used in a Revolution Powder Analyser.	N.A.
$\boldsymbol{\kappa}$	Cohesion Energy Density.	Joules per Cubic Metres.
$\bar{\lambda}$	The average particle size or PSD in the total bed.	Micrometres.
λ_{Front}	The average particle size or PSD in the front segment of the bed.	Micrometres.
λ_{Rear}	The average particle size or PSD in the rear segment of the bed.	Micrometres.
μm	Reflective of one millionth of the base unit 'Metre'.	Micrometre.
$\mu_{Rolling}$	Rolling Friction Coefficient.	Dimensionless.
μs	Reflective of one millionth of the base unit 'Second'.	Microsecond.
$\mu_{Sliding}$	Sliding Friction Coefficient.	Dimensionless.
ν_1	Poisson's Ratio of Material 1.	Dimensionless.
ν_2	Poisson's Ratio of Material 2.	Dimensionless.

ρ_{Free}	The freely settled bulk density of the powder.	Kilograms per Cubic Metres.
$\rho_{Particle}$	Density of a single particle.	Kilograms per Cubic Metres.
ρ_{SS316l}	Density of Stainless Steel 316l sample.	Kilograms per Cubic Metres.
ρ_{Tapped}	The tapped bulk density of the powder.	Kilograms per Cubic Metres.
ω_i	Rotational Velocity of Particle i.	Radians.

Miscellaneous

Symbol	***Description***	***S.I Unit/Expansion***
1	Horizontal direction of disc travel.	Metres.
2	Vertical direction of disc travel.	Metres.
®	Registered trademark.	N.A.
°	Degree Symbol.	N.A.

1. Introduction

This section introduces the primary research areas that the project work is categorised into. ***Subsection 1.1*** provides an introduction to the manufacturing technology in which the project is situated, the dynamics of metal powder particle flow, and the computational methods which are used. The aims and objectives established to guide the project to completion are stated in ***Subsection 1.2***, and the structure of the full thesis is outlined in ***Subsection 1.3***.

1.1 Introduction to Additive Manufacturing, Powder Particle Flow, and the Discrete Element Method

1.1.1 Introduction to Additive Manufacturing

Adopting and integrating modern technology is vital to the continuous evolution of the manufacturing sector. A key element of this transformation is the development and implementation of Additive Manufacturing (AM) solutions in contemporary industrial processes. As recognised by standard-setting bodies such as the International Organisation for Standardisation (ISO), and the American Society for Testing and Materials (ASTM), AM is the official industry standard umbrella term to encompass techniques such as three-dimensional (3D) Printing and Rapid Prototyping [1] and is often heralded as a cornerstone of the ‘4th generation of the Industrial Revolution’ [2], forming one of the nine pillars of Industry 4.0.

Compared to the subtractive methods historically observed in the wider manufacturing landscape, the advent of AM is engendering new possibilities for commercial entities in ventures such as product design, supply chain management, and material efficiency. The ‘complexity for free’ design freedom inherently associated with AM yields many perceived advantages against traditional manufacturing methods. Notably, the proposed ability to generate near net-shaped artefacts exhibiting complex geometrical features [3, 4], and the progress of metal AM has enabled manufacturers to generate components more efficiently than could previously be achieved.

These parts typically begin as fine metallic powders, which are spread in layers, melted, and built up in a layer-upon-layer deposition technique to generate a complete artefact. The trajectory of the build head, and thus the desired dimensions and geometrical features of the part, are controlled by a digital model of the component generated using 3D Computer Aided Design (CAD) software. This unique building operation is advantageous with respect to cost savings, as it obviates the requirement for expensive tooling systems, and creates parts with assembly-free mechanisms through the integrated fabrication of components [5].

Throughout industry, AM is considered a novel approach for the design and generation of high-performance components [6], with the implementation of AM parts observed in an array of applications. For example, AM is widely used in the aerospace sector for the fabrication of complex parts serving integrated functions

[7]. Dimla et al [8] exemplified this and noted that aerofoil cooling channels are often fabricated with straight contours, reducing the rate of cooling across the part. The ability to redesign the model to implement freeform channels with curves and sophisticated shapes, without the use of specialist tooling systems, enables the development of designs with a more homogenous heat transfer through the material structure. Thus, this acts to reduce the risk of thermal damage to the part and minimises the prospect of the part warping.

Further applications of AM can be found in sectors as diverse as in the manufacture of bio-medical implants, such as hip replacements; the inherent surface roughness of the AM part facilitates the osseointegration process between the bone of the patient and the prosthesis [9]. The wide applicability of AM solutions to a range of contemporary engineering problems, and the advantages attained compared to conventional manufacturing techniques (such as the aforementioned design complexity benefits, the ability to integrate components to reduce sub-assemblies, and the elimination and reduction of tooling), have made it an attractive proposition for manufacturers. Thus, the motivations for optimising the AM design build process are severalfold. For example, improving the efficiency of the build process engenders both economic and environmental benefits by reducing the waste of powder and energy resources required in each design build.

In addition to the economic and environmental benefits, optimising the build process will also be advantageous to the quality of the components formed, with respect to their mechanical properties and structural integrity in service.

Although AM is widely considered to be a staple of modern manufacturing technology, it remains a developing process, and the behaviour and flow of the constituent powders during the design build is not well understood [10, 11]. Consequently, this reflects an underexplored area for development in a field of substantial importance. However, many typical manufacturing research centres across industry do not possess the technical expertise or resources to properly analyse this complex physical process. This presents a significant opportunity for further exploration, through a combination of simulation-based studies and practical experiments.

During the course of the project, a significant number of knowledge gaps in both the academic and commercial research spheres have been identified. These areas of exploration can broadly summarised into either powder-centric analyses such as the effect of the powder size range and the morphology of the constituent particles on the quality of the formed layer [12, 13, 14, 15], and process related investigations exploring parametric factors including, but not limited to, the distance between the spreading device and the substrate which controls the height of the spread layer, the melting strategy applied by the laser or electron beam depending on the process characteristics, and the influence of the environment in the build chamber [16, 17, 18, 19].

To address the knowledge gaps described, the current research sphere is populated largely by simulations where the configurations of the build operation are adapted to ascertain the effect on the spread layer quality, such as the effect of the recoater speed and shape used to disperse the powder across the plate [17], the mass of powder dispersed by the recoater and the implications of the layer height on build quality [20, 21], and analysis into the interparticle behaviour observed such as through cohesive modelling [22, 23, 24]. In practical analysis, experiments have been conducted to evaluate the effects of processing factors such as the build orientation on the quality of the formed part [25], the pattern and trajectory of the build head [26], melt pool dynamics and the thermo-mechanical powder behaviour governed by heat source used as the melting medium [27, 28]. Further analysis has also been performed into the effects of post-processing on the mechanical properties of the built component [29, 30].

A distinction is made here that, due to the comprehensive and multi-physics nature of the complete AM process, this project investigates only the phase commencing with the initial powder delivery to the build chamber and concluding at the point immediately prior to when the powder is melted. Hence, a more detailed analysis of the existing areas of research in AM solutions that have informed the work in this project is provided throughout ***Section 3***.

In this project, an original area of research has been pursued into the effect of the deposition method on the quality of the powder bed formed. This reflects a novel exploration that, to the best of the author's knowledge, has not previously been performed using simulation and modelling techniques.

The proposed study has investigated the powder particle physics of a metal AM technique. Research has been performed into quantifying the influence of powder characteristics on the flow behaviour, such as morphology, Particle Size Distribution (PSD), segregation within the powder bed, and particle aspect ratios. Investigations were also performed into the effect of multiple processing parameters, including the deposition technique used to deliver powder to the build platform. Thus, determining the most suitable methods of processing a given powder batch. When evaluating the array of designs generated using an AM approach, the literature suggests that more than 130 different processing parameters can be adapted to induce a change in quality to the component produced [31].

1.1.2 Introduction to Powder Particle Flow

A key consideration of optimising the AM process is in the spreading of the powder used to generate the component, as the powder dynamics are sensitive to the properties of the powder material used. Other influences include environmental factors, such as the atmosphere in the build chamber, and parametric variables such as the speed of spreading and the energy input from the powder melting medium [32].

During the powder processing phase of an AM part build, powder particles are spread across a substrate with a recoating medium, traditionally a roller or rake, over a layer of preheated powder. Subsequently, a laser or electron beam, depending on the characteristics of the process, is directed towards a specific area of the powder bed to generate a melt pool, allowing the powder particles to coalesce together and fabricate the cross section of the geometry being constructed. The build plate is then moved a vertical distance of one layer height by the action of a piston, to realise all of the desired features of the part until the design is complete.

The suitability and effectiveness of the powder spreading method has a significant influence on the quality of the powder bed, which by extension has implications for the material properties and thus quality of the part generated. Powder bed instabilities, caused by unsuitable powder flow techniques, and manifested by undesired effects such as inadequate powder coverage, have a detrimental influence on the performance of a finished component in service. For example, the structural integrity of the part may be compromised by weak bonding between the layers deposited during the design build. The effects of porosity, which causes voids to form and cracks to propagate within the material microstructure, becomes a significant concern when the models generated are used in applications in which part failure could be catastrophic, such as in turbine blades for aircrafts [32].

1.1.3 Introduction to the Discrete Element Method

As alluded to in ***Subsection 1.1.1***, the simulation and modelling of the powder particle physics will be underpinned by the integration of scientific and engineering analysis. To achieve this, the Discrete Element Method (DEM), also referred to interchangeably in literature as the 'Distinct' Element Method, and in other forms with 'Method' substituted for 'Modelling', is used.

The DEM describes a range of numerical approaches for modelling the motion of the constituent particles of granular materials. Thus, the DEM represents the elements of the granular media as discrete particles and models their interactions with one another. Pioneering work in the early stages of the DEM was performed by Cundall & Strack [33], who proposed the method as a numerical technique to model the behaviour and mechanical perturbations of particles, when formed together in an assembly of discrete discs and spheres. Elaborating, the underlying principles of the DEM were described by stating that the contact forces and displacement of the total system of particles is calculated by tracking the movements of the individual elements compromising the bulk. Hence, the motion of each element occurs as a result of the propagation occurring throughout the system, spreading from the origin of the dynamic process at the boundaries. Physical characteristics that are used to evaluate the system, such as the speed of propagation, are functions of the physical properties of the discrete medium [33].

To implement the DEM, conditions must be satisfied which make it possible to accurately model the non-linear interactions and heterogenous particle behaviour with a large number of system elements. A key assumption applied to the dynamic analysis of the system is that the length of each single timestep is small enough to prevent disturbances from particle motion spreading further than the nearest neighbouring particles. Hence, the resultant forces on each element are only determined by the motion of the particles that they are in contact with [33].

To validate the technique, Cundall & Strack compared the DEM results to previous work performed by De Josselin de Jong & Verruijt [33, 34], who used a photoelastic approach to practically evaluate a system of discs. The force vector plots produced experimentally were robust when compared to the corresponding practical vector plots, corroborating the DEM. In contemporary research, the technological advances in computational power and processing capabilities have given rise to the application of the DEM to an array of engineering and scientific problems.

A continuum approach to mechanical analysis homogenises the material or object under evaluation by, for the purposes of the experimental context, modelling the subject as a mass forming a continuum body. Conversely, the DEM simulates the behaviour of individual particles, and models the dynamic interactions that occur between each particle and the environment. The theoretical foundation of the DEM is therefore underpinned by the Lagrangian approach to fluid motion [35], as the particles are considered as discrete elements and the dynamical variables which influence their behaviour within the system are analysed over time. DEM simulations model the detection of particle contacts, calculation of the interparticle forces between each particle, and the resulting particle trajectories for all elements of the system at each timestep [36]. A simple concept illustration of the key differences between continuous and discrete modelling techniques is provided in ***Figure 1*** [37, 38].

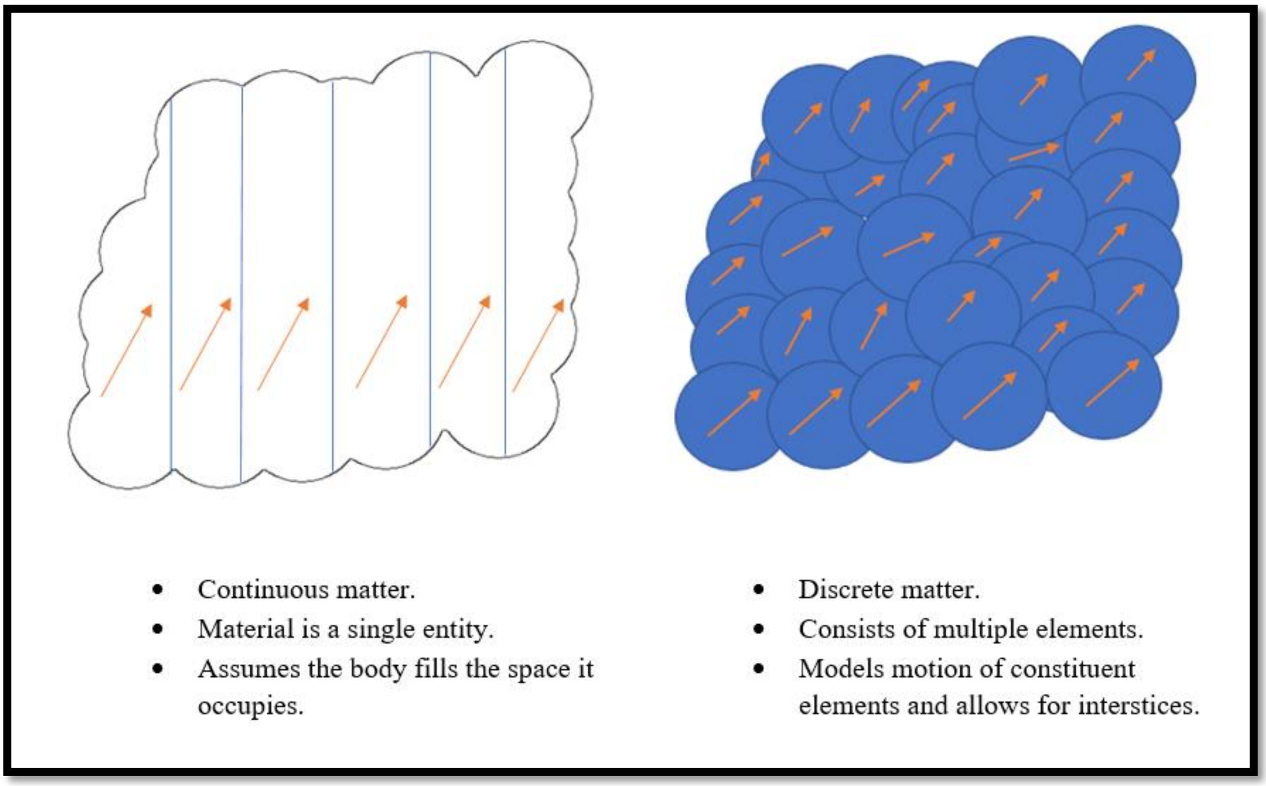

Figure 1 - Comparison Between Continuum Mechanics and the DEM.

The parameters which influence the behaviour of a DEM model include the velocity at which the particles are displaced, the orientation of each element within the assembly if irregular shapes are used, and the resultant reactions manifested by the presence of stresses within the system particles. Associatively, Newton's Second Law of Motion is applied within the DEM to define the movement of the particles due to the forces they are subjected to. Cundall and Strack also defined a Force-Displacement Law, by using the displacements to determine the contact forces between two neighbouring particles [33, 39]. A comprehensive explanation of the equations that govern the DEM is provided in ***Subsection 2.1.1***.

The DEM was chosen to investigate the granular media inherent to a Powder Bed Fusion process due to its superiority to alternative methods. For example, continuum mechanics techniques such as Finite Element Analysis (FEA), model the materials as a continuous mass, which constrains the understanding of the interparticle behaviour such as cohesion and their proclivity to form agglomerations, which has wider impacts on the packing and dispersion in the spread layer. Conversely, the DEM models the contact forces, cohesion, and friction properties directly, providing a more informative insight into powder-centric behaviour such as arching, segregation, and jamming, all of which influence the deposition, spreading, and compaction of the powder and therefore provides a more accurate reflection of powder flow behaviour.

In terms of alternative methods such as Computation Fluid Dynamics (CFD) analysis, CFD packages are more often applied to simulate the flow of gas and liquids, rendering them less accurate than modelling distinct constituents in the flow of particulate systems. Furthermore, in terms of time and computational efficiency, the DEM enables the simulation of local particle interactions with a degree of high degree of precision in demonstrating the powder flow behaviour without incurring the computational costs of a fully resolved CFD or FEA numerical solution.

The DEM is an invaluable tool for modelling the flow characteristics and dynamic behaviour of granular media in scientific and engineering problems. This is of particular significance when micro-dynamic factors are a subject of interest, such as in the analysis of interparticle forces, the force networks that propagate through the granular structure, and the influences that these networks have on the bulk powder system. Applying the DEM to the simulation and modelling of powder flow is an advantageous technique in systems where in-situ monitoring is difficult to achieve in practice, on account of the size and quantity of the particles the study would necessitate, and the difficulty in monitoring extremely fine powder particles.

In the context of this research project, a DEM study presents a viable technique of modelling the phenomena of powder flow in an AM system, without necessitating costly trial and error-based experiments in a commercial environment, and circumnavigating the complexity of practical modelling exercises.

1.1.4 Additive Manufacturing Research with Discrete Element Methods

Various DEM software packages have been used to model powder flow in AM systems. For example, LIGGGHTS®, LAMMPS®, Rocky DEM®, and Ansys Rocky® have all been observed in both academic and commercial Discrete Element Method for Additive Manufacturing (DEM-AM) research ventures. When comparing these applications for their suitability in modelling Powder Bed Fusion processes, each package has distinct advantages and limitations with respect to their functionality and technical capabilities. For example, LIGGGHTS®, an open-source particle simulator, is an extension of the LAMMPS® that is specifically designed for handling complex particle interactions and large-scale granular media simulations.

Although LAMMPS® offers a broader range of multi-scale modelling capabilities and can perform DEM simulations, it was originally developed for molecular dynamics modelling. Thus, research indicates that LAMMPS® is generally more suitable for simulating the behaviour of atomic and nanoscale materials, and is not as optimised for large-scale simulations of micrometre-sized powder flow analysis as LIGGGHTS® [40]. Furthermore, LIGGGHTS® advances LAMMPS® by incorporating granular models for particle-particle and particle-wall interactions [41].

This is further emphasised by the full expansion of the acronyms in these software packages, which are:

LAMMPS Improved for General Granular and Granular Heat Transfer Simulations (LIGGGHTS®).

Large-scale Atomic/Molecular Massively Parallel Simulator. (LAMMPS®).

Rocky DEM® is a commercial software package used for analysing the behaviour of discontinuous material. Like LIGGGHTS®, it is capable of accurately modelling non-spherical particles and has been shown to integrate effectively with FEA and CFD applications, making it an attractive prospect for comprehensive multi-physics modelling exercises. Compared to LIGGGHTS® and LAMMPS®, the software is constrained by being less flexible for customisation, which would impede efforts to examine a wider range of parameters to optimise spreading conditions in this research project. An example of this is in the fixed cohesion models implemented in Rocky DEM®, such as the Johnson-Kendall-Roberts (JKR) and Derjaguin-Muller-Toporov (DMT) theories. Although these contact models are also a feature of LIGGGHTS®, the ability to implement numerical values for cohesion and associated properties enables a more thorough investigation of how adapting such properties influences the behaviour of the particles [42].

Ansys Rocky® is another powerful software with DEM capabilities. As with Rocky DEM®, it can integrate with other modelling techniques such as CFD and FEA and thus excels at exploring the multi-physics phenomena observed in the melt pool dynamics of AM processes. Regarding its flexibility for analysing the behaviour of discrete media, Ansys Rocky® uses built-in tools with predefined settings for the materials within the software database. Thus, constraining the modification of contact laws and proving less customisation for investigating specific powder flow characteristics in PBF modelling exercises. The open-source applications, specifically LIGGGHTS® and LAMMPS®, support the generation of powder spreading models with custom contact conditions and forces, such as cohesion, van der Waals interactions, and electrostatic attractions between the particles. This enables users to more accurately generate models with conditions that are critically reflective of the powder flow and spreading behaviour in PBF systems [43].

Regarding the technical capabilities of the software packages, in terms of large-scale simulations and parallel computing, LIGGGHTS® and LAMMPS® are optimised for Message Passing Interface (MPI) based parallelisation and capable of running on high-performance computing clusters, enabling the performance of large-scale powder bed simulations involving several million particles. Whilst Rocky DEM® and Ansys Rocky® support Graphical Processing Unit (GPU) acceleration, which can significantly reduce run times for certain contact models and particle morphologies, parallelisation can be inhibited by licensing constraints and limitations in hardware compatibility [44].

In alignment with the project scope, multi-physics modelling such as the thermal phenomena observed in the powder melting process is outside of the research interests in this project, which obviates the necessity for some of the key advantages of Ansys Rocky® and Rocky DEM®. Thus, when considering the flexibility and customisability required, there is little evidence to justify further pursuing either of these software applications for the DEM models in this project. Furthermore, the assumption that all particles modelled are spherical in composition nullifies the benefits that would be achieved by the more accurate particle morphology observed in Ansys Rocky® and Rocky DEM®.

Table 1 compares the particle interactions and contact models, and the computational performance and scalability aspects of each DEM method:

Table 1 - Comparison of Each DEM Method.

Feature	Ansys Rocky®	Rocky DEM®.	LIGGGHTS®	LAMMPS®
Cohesion & Adhesion Properties.	JKR, DMT, fixed parameters.	JKR, DMT, fixed parameters.	JKR, Hertz Mindlin, Customisable.	JKR, Hertz Mindlin, Customisable.
Electrostatic Interactions	No (possible with coupling).	No (possible with coupling).	Yes (through customisation of parameters)	Yes (through customisation of parameters).
Capillary Attractions	No (possible with CFD-DEM coupling).	No (possible with CFD-DEM coupling).	Yes (through customisation of parameters, and electrostatic models available)	Yes (through customisation of parameters).
GPU Acceleration	Yes.	Yes.	No.	No.
Scalability	GPU acceleration, but possibly constrained by software and licensing.	GPU acceleration, but possibly constrained by software and licensing.	MPI Parallelisation for High Performance Computing (HPC) operation.	MPI Parallelisation for HPC operation.

Owing to the particle size range observed in PBF processes being at the micrometre scale, and the optimisations of LIGGGHTS® compared to LAMMPS® for granular media, LIGGGHTS® was selected to perform all powder-based simulations in this project.

1.1.5 Discussion of the LIGGGHTS® Software Package

LIGGGHTS® is a classical molecular dynamic simulator used for modelling industrial granular media-based processes. LIGGGHTS® is a C++ based DEM code for simulating applications such as AM processes, powder flow in silos [45], terrain modelling for geomorphology [46], and vibratory mass finishing processes [39]. Creating a simulation in LIGGGHTS® is achieved by firstly generating an input script which defines all of the properties and characteristics of the simulation, thereby establishing all values that govern how the simulation will behave. Due to the wide range of applications of LIGGGHTS®, it is reasonable to suggest there is no "typical" run script. However, almost all models require scripts defining details including, but not limited to:

- The specification of all system variables. For example: the units used in the model, the number of materials present and their material properties, and the timestep size. The early phase of the script also requires the size of the domain in each axis, and the boundary type applied to the domain walls (fixed, periodic, or moving).

- Physical settings which implement the effect of gravity, and the selection of contact models to govern the particle behaviour on collisions between particles, walls, and geometries in the simulation.

- The insertion, scaling and transformation of CAD files to import geometries into the system.

- The insertion and distribution of particles based on their morphology, size distribution, properties, and quantity.

- Specification of the required data values for the post-processing of the model, such as particle positions, velocities, energy in the system, and heat transfer [39, 47].

- The run command used to launch the simulation, and the insertion of checkpoints from which a simulation can be recommenced once the current run has finished.

The ability to parallelise LIGGGHTS® presents a useful opportunity to distribute the model into different processors in each axis of the domain. This is particularly advantageous when the computationally intense modelling processes necessitate the use of HPC systems, as the regions of interest can be afforded more processing power and divided according to the particle population.

Preliminary research shows that the LIGGGHTS® code has been used to accurately model powder flow behaviour in AM systems on numerous occasions [11, 12, 48, 49, 50], and has therefore been selected to further investigate the development of optimised solutions for AM powder beds in this project.

Following the completion of the simulation in LIGGGHTS®. The output files are visualised using a post-processing software, OVITO®, which is short for the "Open Visualisation Tool" and depicts the results of molecular dynamics models and other particle-based simulations. To achieve this, particle and geometry files are imported to the software interface and played as an animation in sequence from the output file chosen at a given timestep.

Selection of the timestep used in all simulations of this project is based on a fraction of the Rayleigh time, testing of simulation stability, and values derived from literature for particles of a similar size distribution. Incorrect selections of the timestep size have been evidenced by model instability such as the effect of particles exploding upon contact with each other and the walls within the simulation, causing the model to fail. The Rayleigh time, and the rationale which underpins the timestep values chosen, is explored later in ***Subsection 5.3.1***.

1.2 Aims & Objectives

In order to guide the project to completion, it is necessary to firstly define the project aims and objectives as in ***Subsection 1.2.1*** and ***Subsection 1.2.2***, respectively.

1.2.1 Project Aims

The project aims to identify a novel method to optimise the spreading process in a PBF system. Preliminary research highlighted that all previous investigations using the DEM-AM deposited powder by a rainfall technique [17, 51, 52, 53, 54, 55], in which powder is inserted in a given volume at a region above the powder bed, and allowed to fall under gravity. Conversations with industry [56], and wider reading of commercial AM practices [57, 58, 59, 60], have elucidated that this is not an accurate reflection of the powder delivery process, and thus presents a significant oversight with respect to the accuracy of current modelling methods. In real PBF processes, the powder supply is delivered by a moving funnel, a piston-operated supply table, or by the action of a hopper or powder reservoir depending on the characteristics of the process.

Based on the above information, the project aim has been more specifically refined to investigate the influence of the deposition mechanism on powder bed quality, and how the influence of powder variables including the PSD (***Section 6***), in conjunction with the novel deposition technique modelled digitally (***Section 7***), impacts the quality of the spread layer formed. The project aims can be succinctly defined as:

- To determine the most suitable processing conditions for the spreading and delivery of an AM powder set, as explored in a digital twin of a commercial PBF set up with as close fidelity to a real powder spreading process as possible.

- To explore the effect of powder characteristics including the PSD and the delivery technique to determine their influence on the quality of the formed powder layer. Thus, suggesting parameters which inform the optimisation of the spreading process.

1.2.2 Project Objectives

Based on the aims specified in ***Subsection 1.2.1***, the following objectives were established to guide the project to successful conclusions:

1. To ensure the correct material and system properties were assigned to the modelling system, digital powder flow experiments were validated against practical testing using industry standard AM powders processed on contemporary powder flow equipment, such as calibrated funnel devices and a practical powder spreading test rig.

2. To model the particle movement during manufacturing, a digital twin of commercial powder spreading systems had to be generated within LIGGGHTS®. To achieve this, various PSD sets ranging from polydisperse digital experiments consisting of relatively fine, median-sized, and relatively coarse particles, along with powder sets consisting of uniform elements, were inserted and spread to determine the effect of the powder characteristics on layer quality.

3. To investigate, using numerical techniques, novel methods and research areas for optimising AM powder bed quality, with a focus on powder deposition.

1.2.3 Project Scope

In terms of the scope of the project: powder spreading is considered to be the processing phase commencing at the delivery of the powder to the substrate, and ending at the conclusion of the recoating process when the spread layer has settled in the bed immediately prior to melting. As such, the distinction is made at this point that thermo-physical processes, such as the coalescence of the powder during melting and the subsequent consolidation into the formed component, and powder preparation such as atomisation techniques, are not considered part of the spreading operation and are thus outside of the project remit.

As described in ***Subsection 1.1***, the dynamic flow behaviour of powder during AM processing remains an area of ongoing research in both the commercial and academic spheres. By generating a digital twin of an industrial AM process, different powder and system variables have been explored to yield the highest quality powder beds. Hence, a novel contribution to knowledge has been made by increasing the fidelity of the digital twin and providing a more accurate reflection of powder deposition than previously observed in DEM-AM investigations. Research showed that modelling all possible parameters that could influence the flow was not feasible due to computational and time constraints. As such, what constituted an optimisation of the spreading process has been determined by the metrics of powder bed quality established in research

(***Section 3***), and configuring the processing to engender an improvement in these quality markers. Hence, the analytical chapters of the thesis comprised the following:

- Powder flow behaviour in the DEM models were validated against practical powder flow conditions (***Section 5*** of the thesis).
- Various particle size distribution sets were modelled to determine the influence on powder flow behaviour (***Section 6*** of the thesis).
- More realistic powder deposition methods were modelled in this project, than have previously been observed in the research landscape, to establish the effect on spread layer quality (***Section 7*** of the thesis).

1.3 Structure of the Thesis

The complete structure of the remaining chapters of the thesis takes the following form:

Firstly, to fully leverage the benefits of the digital twin of a commercial PBF system, the fundamental mathematical principles which govern the modelling system had to be understood and have been examined in detail in ***Section 2***. Thus, providing the complete mathematical background which underpins the computational analysis performed. In ***Subsection 2.1.1***, the mathematical principles of the DEM are outlined and includes an explanation of particle-particle and particle-wall interactions, and illustrates the calculation cycle of the DEM. ***Subsection 2.1.2*** outlines the governing equations which underpin the contact models used within the DEM, and provides an insight as to how the correct models are selected for a given simulation set up.

To identify the current best practice in powder spreading for AM, and what specially constitutes a high-quality powder bed for AM processes, consultation of literature in conjunction with communication with industry has been performed in a comprehensive programme of research collated and reviewed in ***Section 3***. ***Subsection 3.1*** investigates the state of the art and contextualises the research. Then, the powder spreading processes used in the digital modelling of AM powder beds is reviewed in ***Subsection 3.2***. A review of publications pertaining to powder flowability is performed in ***Subsection 3.3***. Later in this section, a literature review of Electron Beam Melting (EBM) processes is performed. As EBM research was significantly constrained by proprietary data at the time of the project commencement, identify the areas of further exploration which underpin elements of the research agenda performed. ***Subsection 3.4*** introduces EBM, with the further avenues of exploration of the technique reviewed in ***Subsection 3.5***. ***Subsection 3.6*** records the review of cohesion and friction parameters for model calibration, with a review of how a concentration of fine particles may serve to optimise the build processes performed in ***Subsection 3.7***. A final executive summary of the literature is included in ***Subsection 3.8***.

From the review of literature and the industrial feedback, a shortlist of proposed areas of further research which may yield a route to optimise the AM powder spreading process has been established, and the most suitable avenue for exploration has been determined against a range of criteria in ***Section 4***. The prospective research subjects are explored in ***Subsection 4.1***. The selection of the research subjects which motivate the investigations of the PhD to optimise the AM powder bed is then performed in ***Subsection 4.2***.

The validation of the simulation and modelling techniques used to generate a digital twin of the real AM powder bed is performed in ***Section 5***. The simulation properties were validated to ensure that accurate flow behaviour was observed in the powder spreading models later on in the thesis. ***Subsection 5.1*** records the simulation method and results of the preliminary tests performed on granular media in the LIGGGHTS® software package. A test of the discharge time of powder processed through a calibrated funnel is performed both practically and digitally in ***Subsection 5.2***. A comparison of the powder pile angle found both experimentally and in the digital twin, to calibrate the input parameters to reality, is performed in ***Subsection 5.3***. The final subsection in this chapter, ***Subsection 5.4***, records the performance of practical powder spreading analysis using a constructed powder test bed system and image analysis techniques.

In ***Section 6***, the investigation of the effect of the particles sizes and insertion fractions is performed. ***Subsection 6.1*** introduces this analysis and records the existing theories in published literature, and the design of the simulation and methods to derive the data which quantifies powder bed quality is recorded in ***Subsection 6.2***. The results of the simulations are recorded in ***Subsection 6.3***, with the discussion of these results and the implications of the findings for powder bed optimisation methods summarised in ***Subsection 6.4*** and ***Subsection 6.5***, respectively.

Section 7 explores the novel contribution to knowledge by comparing the dynamic deposition method applied to digital AM powder beds, to the conventional rainfall approach for a wide range of powder size sets. An introduction to the analysis is provided in ***Section 7.1***, with the set up of the modelling system and the analysis used to derive the data which quantifies the quality of the formed powder beds described in ***Subsection 7.2***. The results for all of the proposed metrics of powder bed quality are recorded in ***Subsection 7.3***, with a comprehensive examination of the results and their implications for the project, and the impact of the project work on the current knowledge in the research landscape, discussed in ***Subsection 7.4***.

Finally, a summary of the research findings and conclusions is presented in ***Subsection 7.5***. Note that, due to the nuances and requirements of each modelling process, an explicit method subsection pertaining to the described simulations is recorded in each chapter. By collating, discussing, and drawing conclusions from all of the powder flow analysis results, a novel approach to powder bed optimisation in PBF processing was established in accordance with the project aims.

A summary of the complete thesis and the final project conclusions are presented in ***Section 8***. A discussion of the proposed further areas of exploration to build on the information established by this project has been recorded in ***Section 9***. A flow diagram demonstrating the thesis structure is in ***Figure 2***.

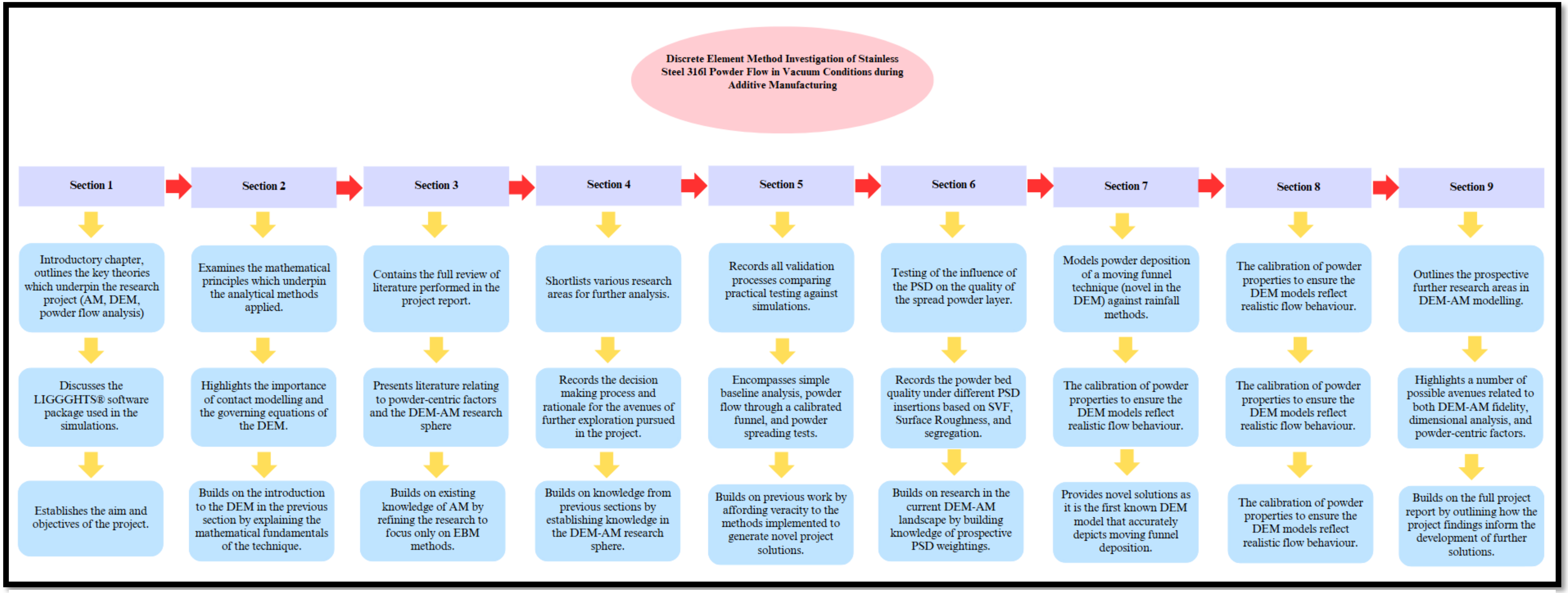

Figure 2 - Flow Diagram showing the Structure of the Thesis.

2. Mathematical Background

Section 2 explains the mathematical background which underpins the numerical implementation of the DEM. In the case of this research project, all investigations of powder in the simulations such as spreading and the flow behaviour are governed by the mathematical theories described. ***Subsection 2.1.1*** demonstrates the mathematical principles used by the DEM to model the movement of each element. The full calculation cycle of the DEM is expressed, in conformance with the seminal work by Cundall & Strack [33], using a system comprising a pair of weightless discs compressed between rigid walls. The contact models which govern the interparticle behaviour, such as the contact area and pressure as a function of the overlap distance between two contacting elements, is explored in ***Subsection 2.1.2***. These models have a significant influence on the observed particle behaviour and thus it is essential to ensure the correct models and parameters are implemented to produce a robust model of the flow and spreading behaviour.

Finally, the computational costs of the DEM approach for AM powder bed modelling, and the ramifications and viability of simulating a full AM powder bed system and how this is accounted for to ensure a robust model is produced in this research, is explained thoroughly in ***Subsection 2.1.3***.

2.1.1 Mathematical Principles of the Discrete Element Method.

An explanation of the general concepts and contextualisation of the DEM for particle-based systems has been provided in ***Subsection 1.1.5***.

The mathematics involved in powder-centric phenomena such as the spreading and flow behaviour involve principles from numerous branches of physics, including kinematics, contact mechanics (see ***Subsection 2.1.2***), and fluid dynamics. LIGGGHTS® implements the key governing equations of the DEM to determine the dynamic particle behaviour. Newton's 2nd Law is applied to calculate the linear and rotational motion of each element due to the forces applied to them, expressed in the simplest form in ***Equation 1***:

$$\mathrm{F} = m \times \mathrm{a} \tag{1}$$

In conjunction with the timestep condition pertaining to neighbouring particle interactions (refer to ***Subsection 1.1.5***), Cundall and Strack outlined a second condition of element analysis in their theory. Namely, the deformation of each particle is minor when compared to the deformation of the full system, with the motion of the whole granular assembly a consequence of the rigid body motion of each discrete element. Thus, a reasonably accurate prediction of the bulk system behaviour can be achieved without precise solutions for each individual particle. For this reason, elements were allowed to overlap each other by a small distance (relative to particle size) at the contact points in lieu of the particles deforming [33, 61].

In their seminal work, Cundall and Strack outlined the mechanical foundations of the DEM by means of example. A pair of weightless discs are compressed between two rigid walls, parallel to one another at the sides of each disc. To maintain consistency with the nomenclature of the source material [33], the discs have been named **X** and **Y**. Note they have been presented in bold to prevent confusion with the coordinate system used in the simulation and modelling techniques later.

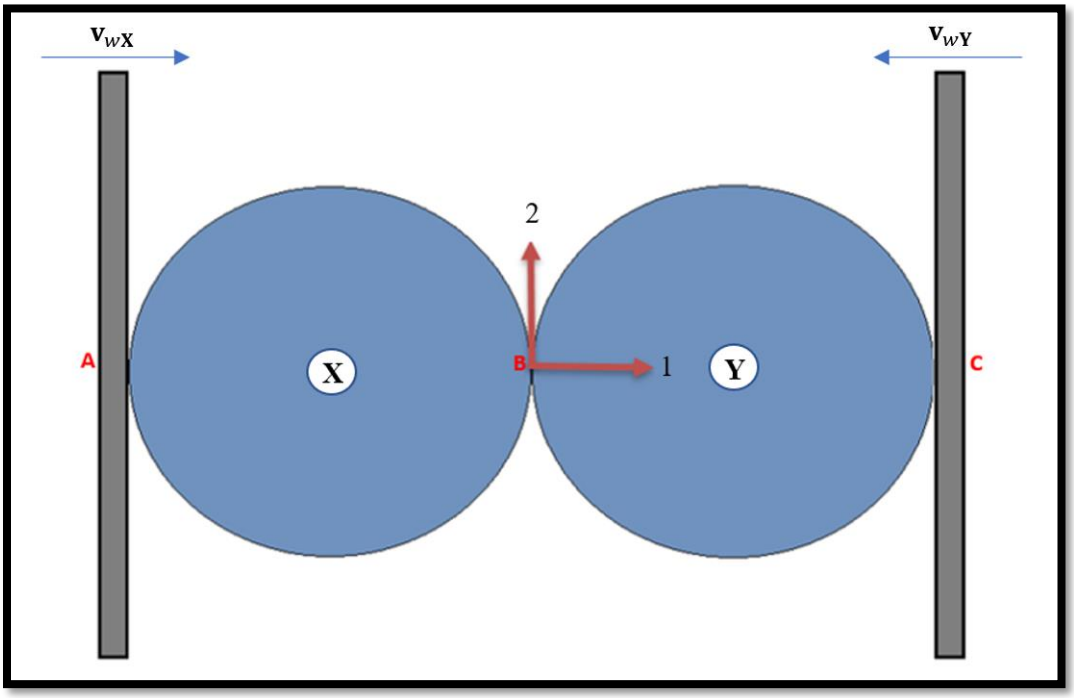

Figure 3 - Two Weightless Discs between Rigid Walls at Timestep t_0. Adapted from *[33]*.

Figure 3 shows all of the components of the system at the timestep t_0. At this point, the system can be considered at rest, as although all components of the system are touching, no contact forces exist.

Applying a constant opposing velocity ($\mathbf{v}_{w\mathbf{X}}$ & $\mathbf{v}_{w\mathbf{Y}}$) to each wall creates an overlap between each wall and disc. Assuming this occurs over the chosen timestep value, Δt, the equation for t_1 can be defined as in ***Equation 2***:

$$\mathrm{t}_1 = \mathrm{t}_0 + \Delta t \tag{2}$$

It is assumed that disturbances cannot propagate beyond a single disc during a single timestep [33]. Hence, an overlap is created between each element and the walls compressing them at t_1, as demonstrated in ***Figure 4***. Note that these overlaps have been exaggerated for illustrative purposes, and that the following contact points are defined:

$A -$ The contact point at an equal distance between points A_d and A_w.

$A_d -$ The point on the outside edge of disc **X**, on the horizontal axis running through the centre of the disc.

$A_w -$ The wall point on the horizontal axis running through the centre of disc **X**. Both A_d and A_w are drawn on the line perpendicular to the walls compressing the discs.

$B -$ The contact point between disc **X** and disc **Y**.

$C -$ The contact point halfway between points C_d and C_w.

$C_d -$ The point on the outside edge of disc **Y**, on the horizontal axis running through the centre of the disc.

C_w − The wall point on the horizontal axis running through the centre of disc **Y**. Both C_d and C_w are drawn on the line perpendicular to the walls compressing the discs, as is also the case with disc **X**.

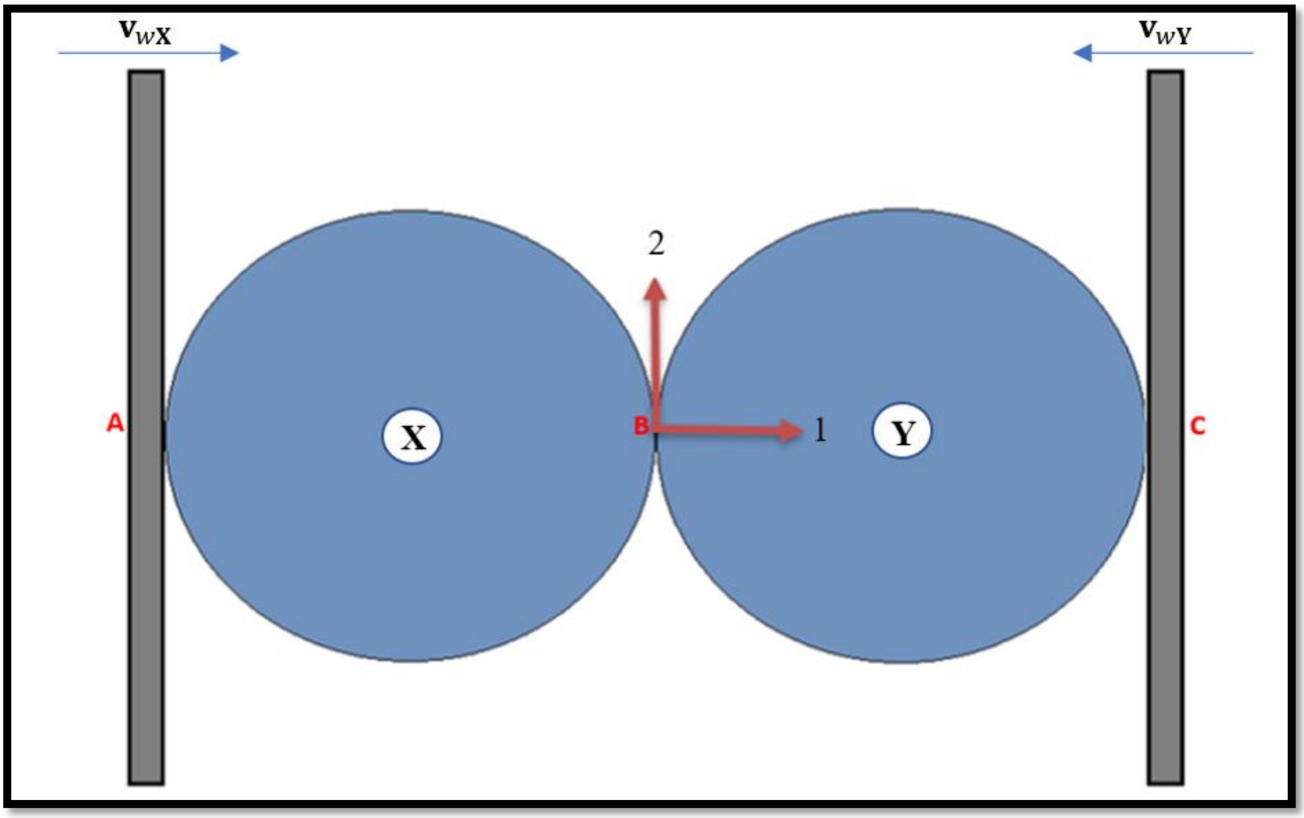

Figure 4 - Two Weightless Discs Compressed between Rigid Walls at Timestep t_1. Adapted from *[33]***.**

The magnitude of the overlaps, Δn, can be found by considering the velocity at which the walls are moving and the current timestep:

$$\Delta n = \mathbf{v} \times \Delta_t \tag{3}$$

Thus, at $t = \mathrm{t}_0 + \Delta_t = \mathrm{t}_1$, the relative displacement of the overlap can be found for each disc when assuming the coordinate system outlined in ***Figure 3*** and ***Figure 4***:

$$\Delta n_{\mathbf{X}} = \mathbf{v}_{w\mathbf{X}} \times \Delta_t \tag{4}$$

&

$$\Delta n_{\mathbf{Y}} = -\mathbf{v}_{w\mathbf{Y}} \times \Delta_t \tag{5}$$

Where $\mathbf{v}_{w\mathbf{X}}$ and $\mathbf{v}_{w\mathbf{Y}}$ are the velocities of the walls in contact with disc **X** and disc **Y**, respectively.

This analysis highlights the second governing equation in the DEM approach (after ***Equation 1***): the Force-Displacement law. In which the displacement of an element is used to calculate the contact forces acting on the discs. Combining ***Equation 3*** and considering the normal stiffness of each disc, k_n, the increment in normal force, ΔF_n, is given by ***Equation 6***:

$$\Delta F_n = k_n \times \Delta n \tag{6}$$

Solving ***Equation 6*** for the incremental contact forces at both discs at $t = \mathrm{t}_1$ yields ***Equation 7*** and ***Equation 8*** for disc **X** and disc **Y**.

$$F_{(\mathbf{X})} = k_n \times (\Delta n)_{\mathrm{t}_1} \tag{7}$$

$$F_{(\mathbf{Y})} = -k_n \times (\Delta n)_{\mathrm{t}_1} \tag{8}$$

By Newtonian Mechanics, combining ***Equation 1*** with ***Equation 7*** and ***Equation 8*** solves for the acceleration in each disc at $t = \mathrm{t}_1$, as in ***Equation 9*** and ***Equation 10***.

$$a_{(\mathbf{X})\mathrm{t}_1} = \frac{F_{(\mathbf{X})}}{m_{(\mathbf{X})}} \tag{9}$$

$$a_{(\mathbf{Y})\mathrm{t}_1} = \frac{F_{(\mathbf{Y})}}{m_{(\mathbf{Y})}} \tag{10}$$

Assuming the acceleration is constant across Δ_t, the velocity of the discs can be found by multiplying the timestep into ***Equation 9*** and ***Equation 10*** as in ***Equation 11*** and ***Equation 12***:

$$\left(v_{(\mathbf{X})}\right)_{\mathrm{t}_2} = \left(\frac{F_{(\mathbf{X})}}{m_{(\mathbf{X})}}\right) \times \Delta_t \tag{11}$$

$$\left(v_{(\mathbf{Y})}\right)_{\mathrm{t}_2} = \left(\frac{F_{(\mathbf{Y})}}{m_{(\mathbf{Y})}}\right) \times \Delta_t \tag{12}$$

Thus, the velocity of the discs over the time $t = \mathrm{t}_1$ to $t = \mathrm{t}_2$ can be determined as in the previous equations, where $\mathrm{t}_2 = \mathrm{t}_0 + 2\Delta_t$. Due to the motion of each disc associated with these velocities, an additional overlap is created between disc **X** and disc **Y** at t_2, as shown in ***Figure 5***.

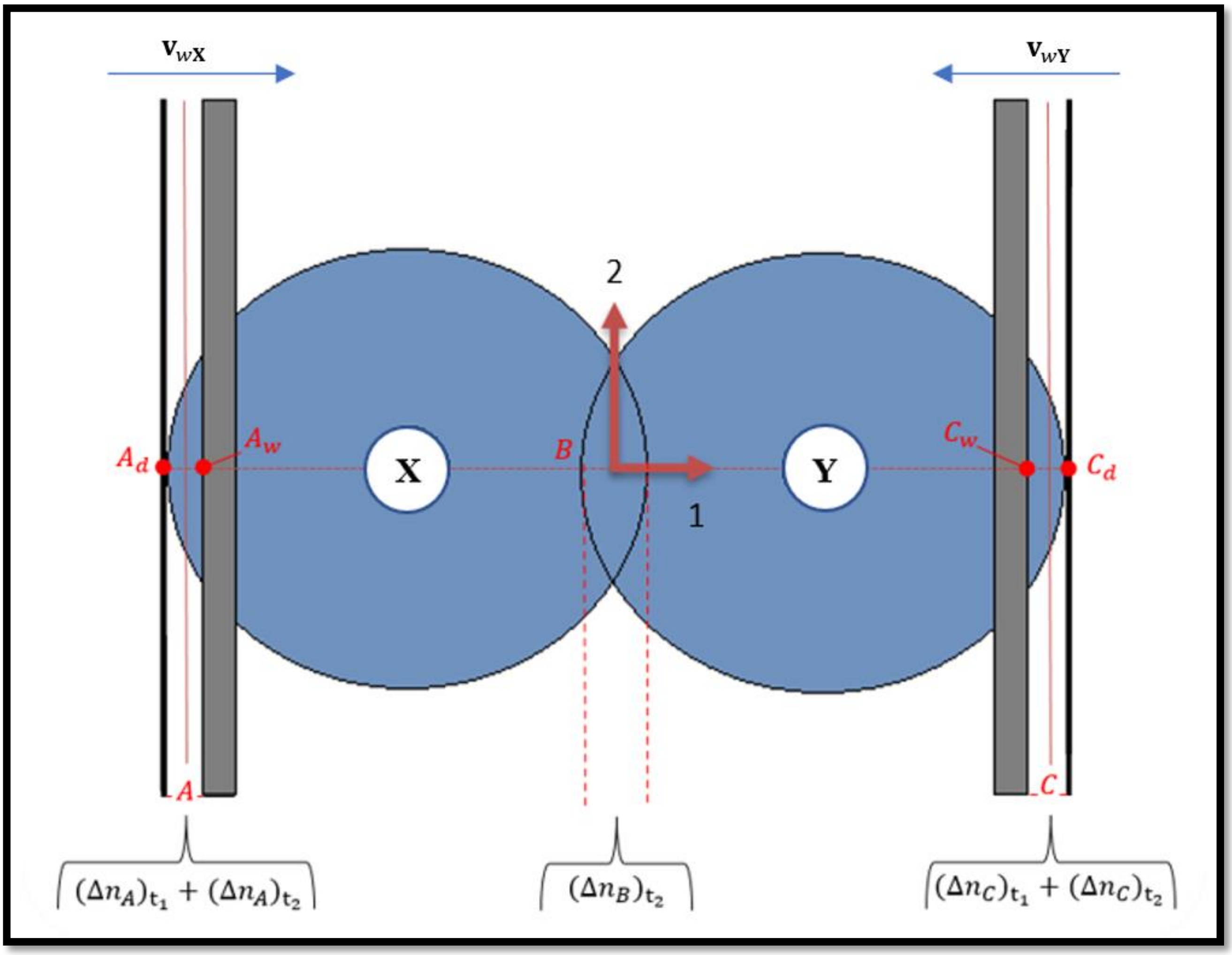

Figure 5 - Discs and Walls System with Overlaps at Points A, B and C at Timestep t_2. Adapted from *[33]*.

The length of all overlaps can be calculated by summing the relative displacement increments at each of the contact points outlined in ***Figure 5***, where each overlap is labelled with the corresponding equation. Hence, at $t = t_2$, the relative displacement increments at contact point A is given by ***Equation 13*** [39]:

$$(\Delta n_A)_{t_2} = \left[\mathbf{v}_{w\mathbf{X}} - \left(\frac{F_{(\mathbf{X})}}{m_{(\mathbf{X})}} \times \Delta_t\right)\right] \times \Delta_t \tag{13}$$

The contact at point B is between the two disc surfaces. Thus, the relative displacement is given by:

$$(\Delta n_B)_{t_2} = \left[\left(\frac{F_{(\mathbf{X})}}{m_{(\mathbf{X})}} \times \Delta_t\right) - \left(\frac{F_{(\mathbf{Y})}}{m_{(\mathbf{Y})}} \times \Delta_t\right)\right] \times \Delta_t \tag{14}$$

Finally, the relative displacement at the disc to wall contact point C is found by ***Equation 15***:

$$(\Delta n_C)_{t_2} = \left[\left(\frac{F_{(\mathbf{Y})}}{m_{(\mathbf{Y})}} \times \Delta_t\right) - (-\mathbf{v}_{w\mathbf{Y}})\right] \times \Delta_t \tag{15}$$

System dynamics behave cyclically with the governing equations of the DEM. The velocity and timestep are used as in ***Equation 3*** to find the displacement of the point of interest, after which the Force-Displacement Law (***Equation 6***) is used to calculate the corresponding forces. In accordance with Newton's Second Law as in ***Equation 9*** and ***Equation 10***, the acceleration of each disc is determined allowing for the velocity and displacements to be identified [39]. ***Figure 6*** shows the dynamic process of the DEM:

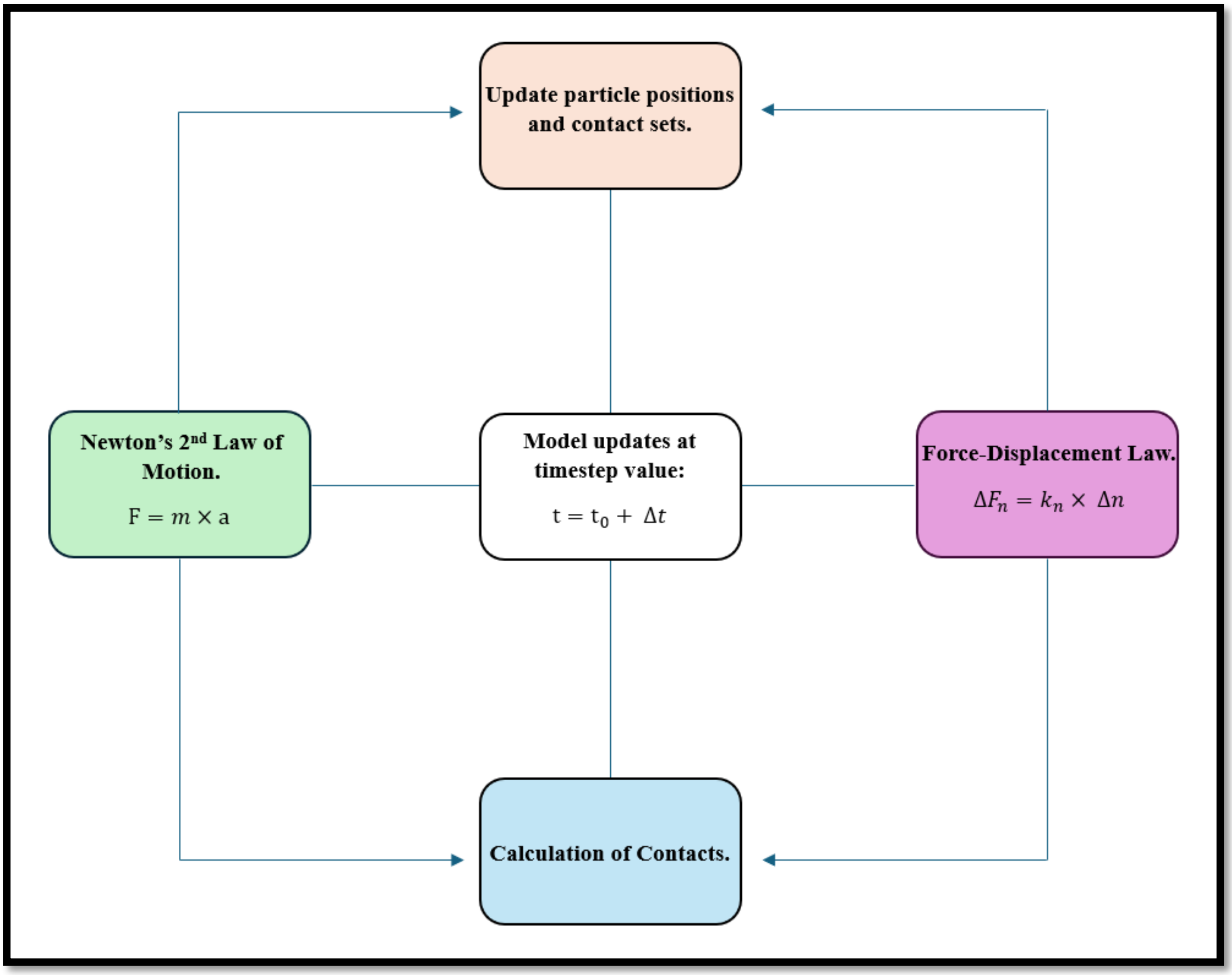

Figure 6 - Calculation Cycle of the DEM. Adapted from *[62]*.

The Force-Displacement Law was illustrated by Cundall and Strack for the case of two overlapping discs [33, 39], and has been amended in ***Figure 7***.

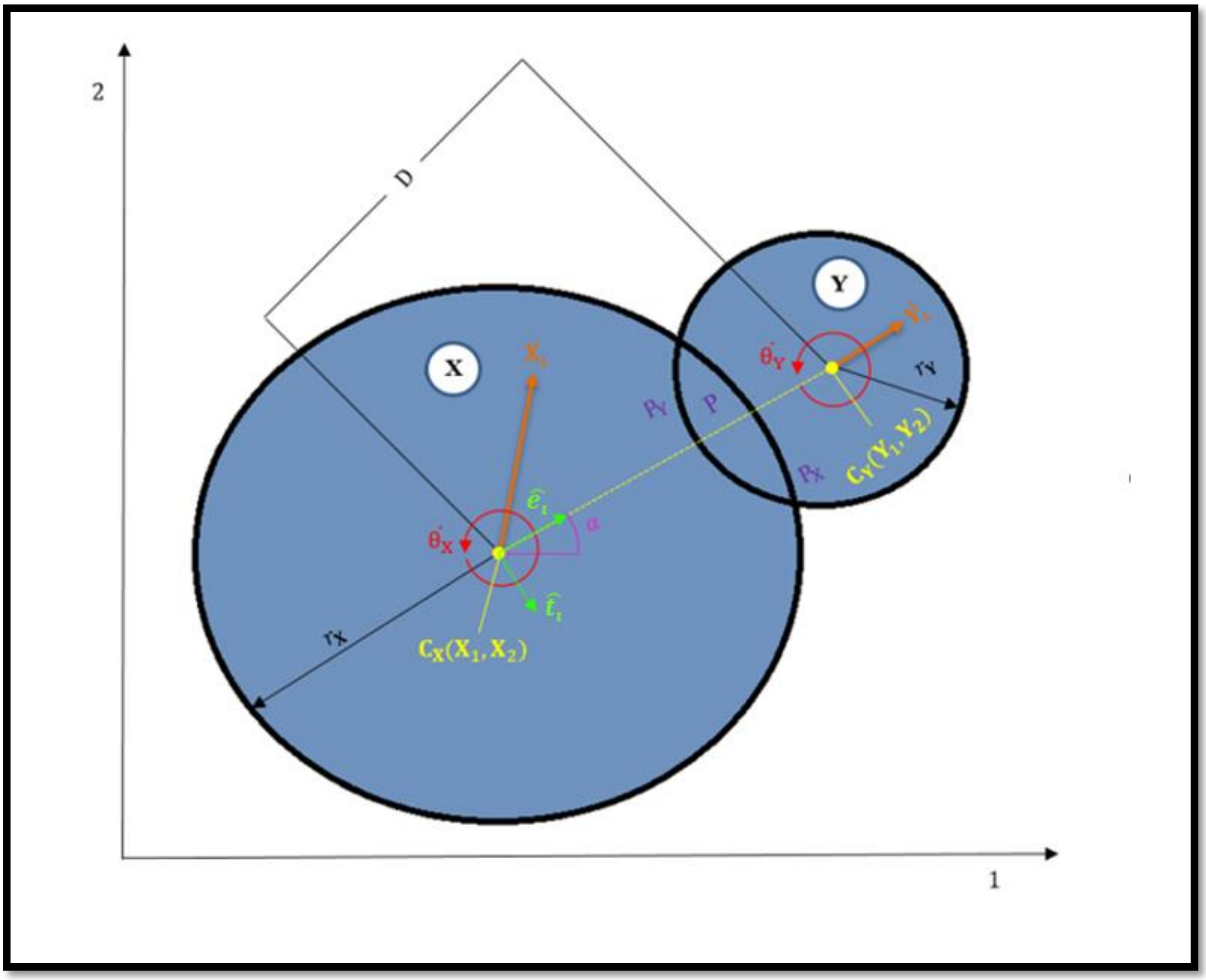

Figure 7 - Force-Displacement Law Applied to Two Contacting Discs. Adapted from *[33, 39]***.**

Where:

D − Distance between the centre points of Disc **X** and Disc **Y**.

C_X − Centre of Disc **X**.

C_Y − Centre of Disc **Y**.

P − Contact region of Disc **X** and Disc **Y**.

P_X − Intersecting point of Disc **X** on the line connecting the centre of Disc **X** to Disc **Y**.

P_Y − Intersecting point of Disc **Y** on the line connecting the centre of Disc **X** to Disc **Y**.

r_X − Radius of Disc **X**.

r_Y − Radius of Disc **Y**.

$\dot{X}_i$ − Velocity vector of Disc **X**.

$\dot{\mathbf{Y}}_i -$ Velocity vector of Disc **Y**.

$\dot{\theta}_{\mathbf{X}} -$ Angular velocity of Disc **X**.

$\dot{\theta}_{\mathbf{Y}} -$ Angular velocity of Disc **Y**.

$\widehat{e_\iota} -$ The unit vector pointing from the centre of Disc **X** to the centre of Disc **Y**.

$\widehat{t_\iota} -$ The unit vector found with the clockwise rotation of e_i through 90°.

$\alpha -$ The angle between the unit vector e_i and the horizontal.

For consistency with the source material, the disc centres are found by the coordinates of the system outlined in ***Figure 7*** so that $\mathrm{C}_{\mathbf{X}} = (\mathbf{X}_1, \mathbf{X}_2)$ and $\mathrm{C}_{\mathbf{Y}} = (\mathbf{Y}_1, \mathbf{Y}_2)$. ***Figure 7*** shows that two discs are only in contact if the following expressions is true:

$$\mathrm{D} < \mathrm{r}_{\mathbf{X}} + \mathrm{r}_{\mathbf{Y}}$$

If the above expression is true, the relative velocity of the contact is defined with respect to the relative velocity between points $\mathrm{P}_{\mathbf{X}}$ and $\mathrm{P}_{\mathbf{Y}}$, which can then be integrated to find the relative displacement of the contact point. Introducing the unit vector $\hat{e}_i$ from the centre points of disc **X** to disc **Y**:

$$\widehat{e_\iota} = \frac{\dot{\mathrm{Y}}_i - \dot{\mathrm{X}}_i}{\mathrm{D}} = (\cos\alpha, \sin\alpha) \tag{16}$$

As in ***Figure 7***, a 90° clockwise rotation of the unit vector $\widehat{e_\iota}$ obtains the unit vector $\widehat{t_\iota}$. From $\widehat{t_\iota}$, the radii of the discs, and the relative angular and linear velocities, the relative velocity of point $\mathrm{P}_{\mathbf{X}}$ with respect to point $\mathrm{P}_{\mathbf{Y}}$ is given by:

$$\mathbf{V}_{(\mathrm{P}_{\mathbf{X}})(\mathrm{P}_{\mathbf{Y}})} = (\dot{\mathbf{X}}_i - \dot{\mathbf{Y}}_i) - \left(\dot{\theta}_{\mathbf{X}}\mathrm{r}_{\mathbf{X}} + \dot{\theta}_{\mathbf{Y}}\mathrm{r}_{\mathbf{Y}}\right)\widehat{t_\iota} \tag{17}$$

Where the expressions $(\dot{\mathbf{X}}_i - \dot{\mathbf{Y}}_i)$ and $\left((\dot{\theta}_{\mathbf{X}}\mathrm{r}_{\mathbf{X}} + \dot{\theta}_{\mathbf{Y}}\mathrm{r}_{\mathbf{Y}})\,\widehat{t_\iota}\right)$ define the relative linear and angular velocities respectively.

The normal ($\dot{\boldsymbol{n}}$) component of the relative velocities is given by:

$$\dot{\boldsymbol{n}} = \mathbf{V}_{(\mathrm{P}_{\mathbf{X}})(\mathrm{P}_{\mathbf{Y}})} \cdot \widehat{e_\iota} = (\dot{\mathbf{X}}_i - \dot{\mathbf{Y}}_i)\,\widehat{e_\iota} - \left[\left(\dot{\theta}_{\mathbf{X}}\mathrm{r}_{\mathbf{X}} + \dot{\theta}_{\mathbf{Y}}\mathrm{r}_{\mathbf{Y}}\right)\widehat{t_\iota} \cdot \widehat{e_\iota}\right] \tag{18}$$

$$\because$$

$$\widehat{t_\iota} \cdot \widehat{e_\iota} = 0$$

$$\therefore$$

$$\dot{\boldsymbol{n}} = \mathbf{V}_{(\mathrm{P}_{\mathbf{X}})(\mathrm{P}_{\mathbf{Y}})} \cdot \widehat{e_\iota} = (\dot{\mathbf{X}}_i - \dot{\mathbf{Y}}_i)\,\widehat{e_\iota} \tag{19}$$

The tangential ($\dot{\boldsymbol{s}}$) component of the relative velocities is given by:

$$\dot{\boldsymbol{s}} = \mathbf{V}_{(\mathrm{P_X})(\mathrm{P_Y})} \cdot \widehat{t_\iota} = (\dot{\mathbf{X}}_i - \dot{\mathbf{Y}}_i) \cdot \widehat{t_\iota} - \left[\left(\dot{\theta}_\mathbf{X}\mathrm{r}_\mathbf{X} + \dot{\theta}_\mathbf{Y}\mathrm{r}_\mathbf{Y}\right) \widehat{t_\iota} \cdot \widehat{t_\iota}\right] \tag{20}$$

$$\because$$

$$\widehat{t_\iota} \cdot \widehat{t_\iota} = 1$$

$$\therefore$$

$$\dot{\boldsymbol{s}} = (\dot{\mathbf{X}}_i - \dot{\mathbf{Y}}_i) \cdot \widehat{t_\iota} - \left(\dot{\theta}_\mathbf{X}\mathrm{r}_\mathbf{X} + \dot{\theta}_\mathbf{Y}\mathrm{r}_\mathbf{Y}\right) \tag{21}$$

Integrating the relative velocity components yields the relative normal and tangential displacements, as in ***Equation 22*** and ***Equation 23*** respectively:

$$\Delta n = \dot{\boldsymbol{n}} \cdot \Delta t \tag{22}$$

$$\therefore$$

$$\Delta n = (\dot{\mathbf{X}}_i - \dot{\mathbf{Y}}_i) \, \widehat{e_\iota} \cdot \Delta t$$

&

$$\Delta s = \dot{\boldsymbol{s}} \cdot \Delta t \tag{23}$$

$$\therefore$$

$$\Delta s = \left[(\dot{\mathbf{X}}_i - \dot{\mathbf{Y}}_i) \cdot \widehat{t_\iota} - \left(\dot{\theta}_\mathbf{X}\mathrm{r}_\mathbf{X} + \dot{\theta}_\mathbf{Y}\mathrm{r}_\mathbf{Y}\right)\right] \Delta t$$

Combining the relative displacements with the Force-Displacement Law allows for the calculation of the incremental normal (ΔF_n) and shear forces (ΔF_s) acting on the disc, by expanding ***Equation 6***:

$$\Delta F_n = k_n \times \Delta n = k_n \times (\dot{\mathbf{X}}_i - \dot{\mathbf{Y}}_i) \, \widehat{e_\iota} \cdot \Delta t \tag{24}$$

Similarly, for the shear force where k_s is the tangential stiffness:

$$\Delta F_s = k_s \times \Delta s = k_s \times \left[(\dot{\mathbf{X}}_i - \dot{\mathbf{Y}}_i) \cdot \widehat{t_\iota} - \left(\dot{\theta}_\mathbf{X}\mathrm{r}_\mathbf{X} + \dot{\theta}_\mathbf{Y}\mathrm{r}_\mathbf{Y}\right)\right] \cdot \Delta t \tag{25}$$

Figure 8 outlines the sign convention on disc **X** for F_n & F_s, which are taken as positive in opposing directions to the unit vectors $\widehat{e_\iota}$ and $\widehat{t_\iota}$.

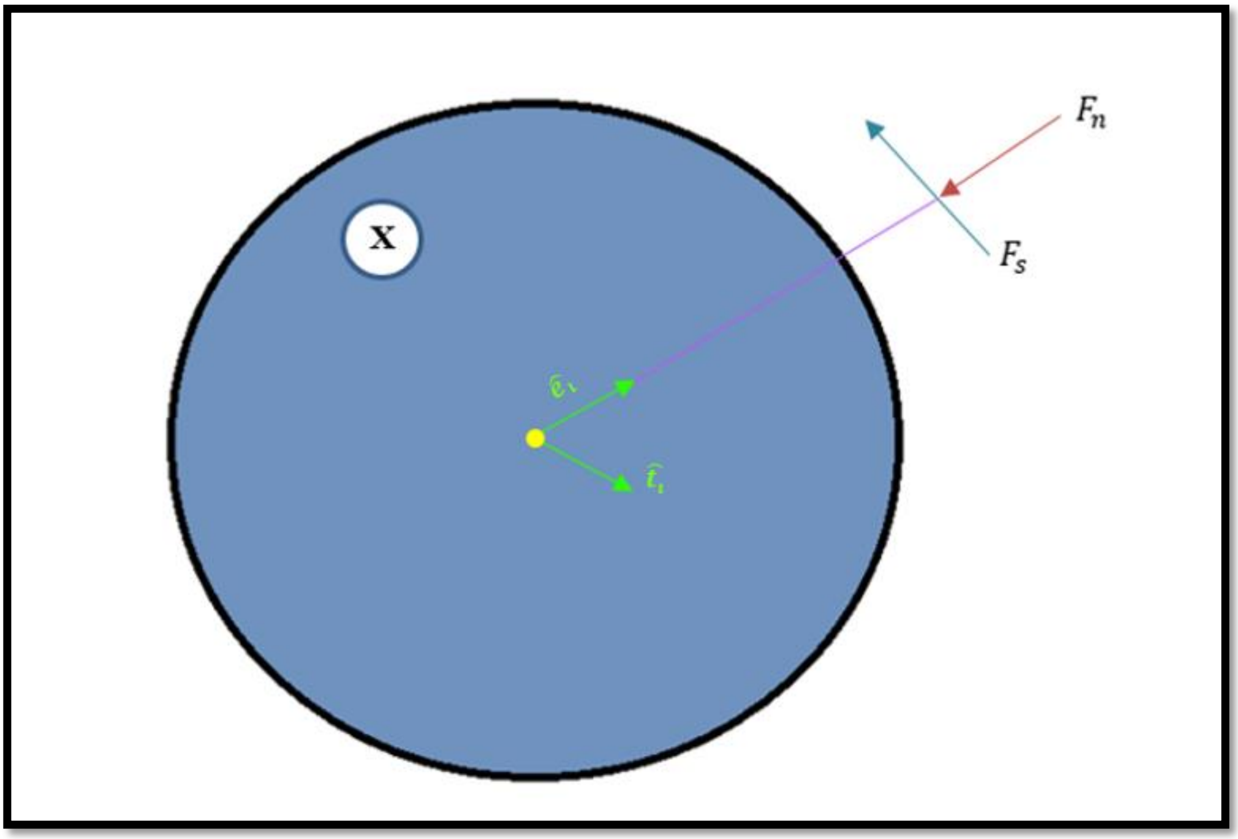

Figure 8 - Sign Convention for Normal and Shear Force Increments. Adapted from *[33]*.

For each timestep of the model, the force increments are added to the summation of all previous increments from each previous timestep. Thus:

$$(F_n)_N = (F_n)_{N-1} + \Delta F_n \tag{26}$$

&

$$(F_s)_N = (F_s)_{N-1} + \Delta F_s \tag{27}$$

Where the subscripts N and $N-1$ denote the time at t_N and t_{N-1}. Thus:

$$t_N - t_{N-1} = \Delta t \tag{28}$$

The normal and shear forces are calculated for each contact between the discs, and the resultant normal and tangential directions are resolved into their direction-dependent components. For example, summing the contact force components of disc **X** generates the resultant forces $\Sigma F_{(\mathbf{X})_1}$ & $\Sigma F_{(\mathbf{X})_2}$. The resultant moment associated with disc **X** is considered positive in the anticlockwise direction and given by:

$$\Sigma M_{(\mathbf{X})} = \Sigma F_s \cdot \mathrm{r}_{\mathbf{X}} \tag{29}$$

The moments and forces are combined with Newton's Second Law to solve the linear and rotational motion of the particles, and the displacements and new element positions are updated in sequence with the model timestep.

2.1.2 Governing Equations of Contact Modelling within the LIGGGHTS® Software Package

As explained in ***Subsection 2.1.1***, the linear and rotational motion of the powder models in this project are governed by Newton's Second Law [63]:

$$m_i \frac{d\mathbf{v}_i}{dt} = \sum_j^i \left(F_{ij}^n + F_{ij}^s\right) + F_i^g \tag{30}$$

$$I_i \frac{d\omega_i}{dt} = \sum_j^i \left(T_{ij}^s + T_{ij}^r\right) \tag{31}$$

Where:

m_i = Mass of Particle i.

I_i = Moment of Inertia of Particle i.

$\mathbf{v}_i$ = Translational Velocity of Particle i.

ω_i = Rotational Velocity of Particle i.

F_{ij}^n = Normal contact force acting on Particle i by Particle j or wall effects.

F_{ij}^s = Tangential contact force acting on Particle i by Particle j or wall effects.

F_i^g = Forces due to gravity acting on Particle i.

T_{ij}^s = Torque acting on Particle i due to tangential forces.

T_{ij}^r = Torque acting on Particle i due to rolling friction.

As described in ***Subsection 2.1.1***, two particles are in contact when the sum of their radii is greater than the distance between their centres. In the LIGGGHTS® software package, specification of the contact models are required in all simulations. It is these models which calculate the contact area and pressure as the surface of two particles interact with one another as a function of the overlap distance, the normal and tangential forces, and the speed of the collision.

Hertzian contact models are one such method to apply these collision parameters. For example, during a particle-wall or particle-particle interaction solids are assumed to deform and a contact area between the elements is calculated. The Hertzian method is underpinned by the assumptions that low strains occur in the material, the bodies are elastic, and friction is neglected between contact areas [64, 65].

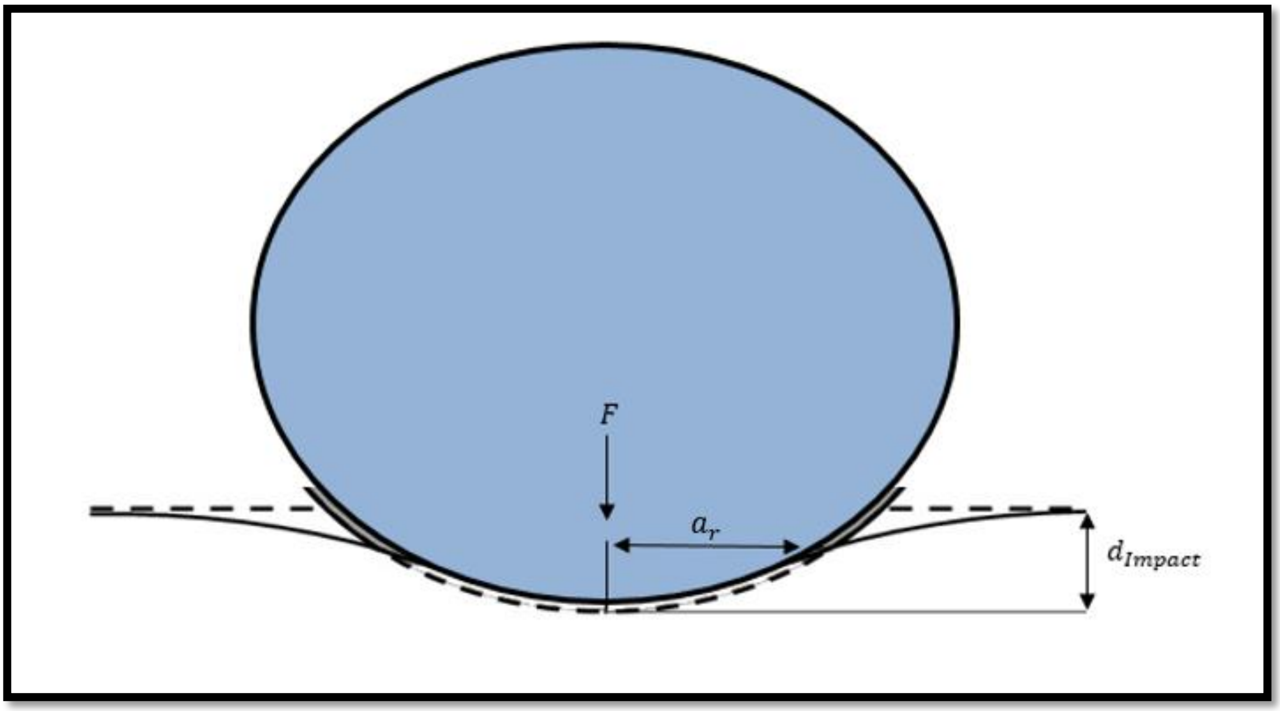

Figure 9 - Elastic Sphere Collision. Adapted from ***[66]*****.**

The calculation of the contact area depends on the shape of each element, and the model assumes that the contact area is considerably smaller than the radius of the body the particle contacts. Hence, as in ***Figure 10*** [67].

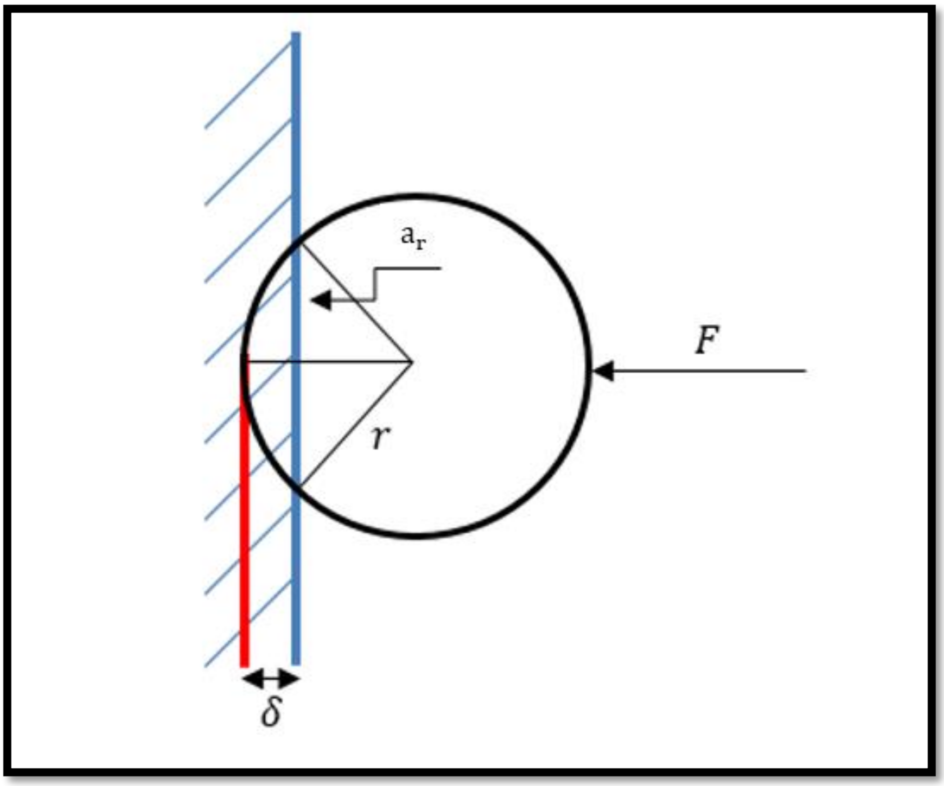

Figure 10 - Contact Area of a Particle Wall Collision. Adapted from ***[67]*****.**

Assuming a particle of radius r collides with a wall at a velocity $\mathbf{V}_{Impact}$, the penetration length between the radius of the contact area and the surface is denoted as δ, and the radius of the contact area is denoted as $\mathrm{a_r}$. Thus [67]:

$$\mathrm{a_r^2} + (r-\delta)^2 = r^2 \tag{32}$$

$$\therefore$$

$$r^2 - (r-\delta)^2 = \mathrm{a_r^2} \tag{33}$$

$$\therefore$$

$$r^2 - (r^2 - 2r\delta + \delta^2) = \mathrm{a_r^2} \tag{34}$$

$$\therefore$$

$$2r\delta - \delta^2 = \mathrm{a_r^2} \tag{35}$$

Assuming δ^2 is of negligible size, the contact area is given by:

$$\mathrm{a_r^2} = 2r\delta \tag{36}$$

From the contact area found in ***Equation 36***, the area of the cross section can be defined as:

$$A_0 = \pi \cdot \mathrm{a_r^2} = 2 \cdot \pi \cdot r \cdot \delta \tag{37}$$

The JKR contact model builds on Hertzian modelling by incorporating the surface energy between the particle contact points and calculating the adhesive forces [68]. To achieve this, the strength of the interfacial attraction is considered in conjunction with the elasticity of the particles and the contact area. The force of adhesion between two particles manifests as the force resisting the separation at the contact unloading.

According to JKR theory, the radius of the contact region between two elements is given by ***Equation 38*** [69]:

$$\mathrm{a_r^3} = \frac{r^*}{\psi^*}\left[F_n + 3 \cdot \gamma_{Surface} \cdot \pi \cdot r^* + \sqrt{6 \cdot \gamma_{Surface} \cdot \pi \cdot r^* \cdot F_n + \left(3 \cdot \gamma_{Surface} \cdot \pi \cdot r^*\right)^2}\right] \tag{38}$$

Where:

r^* = The effective radius between two particles, given by:

$$r^* = \frac{r_i \cdot r_j}{r_i + r_j} \tag{39}$$

ψ^* = The effective elastic constant between the two particles, given by:

$$\psi^* = \frac{4}{3} \cdot \pi \cdot \psi_1 + \psi_2 \tag{40}$$

ψ_1 and ψ_2 are found by ***Equation 41*** and ***Equation 42***:

$$\psi_1 = \frac{1 - \nu_1}{\pi \cdot E_1} \tag{41}$$

$$\psi_2 = \frac{1 - \nu_2}{\pi \cdot E_2} \tag{42}$$

Where:

r_i = The radius of the particle of type i.

r_j = The radius of the particle of type j.

ν_1 & ν_2 = The Poisson's ratio of material 1 and 2, respectively.

E_1 & E_2 = The Young's Modulus of Elasticity of material 1 and 2, respectively.

And:

$\gamma_{Surface}$ = The surface energy between the particles in units of $\frac{J}{m^3}$.

By ***Equation 43***, separation between the two elements will occur independently of the elastic moduli, when [69]:

$$F_{JKR} = -\frac{3}{2} \cdot \pi \cdot \gamma_{Surface} \cdot r^* \tag{43}$$

For a fully elastic contact model incorporating the interparticle adhesive forces, the total normal contact force is given by:

$$F_n = \frac{4 \cdot \mathrm{a}_\mathrm{r}^3 \cdot \psi^*}{3 \cdot r^*} - \sqrt{8 \cdot \gamma_{Surface} \cdot \pi \cdot \psi^* \cdot \mathrm{a}_\mathrm{r}^3} \tag{44}$$

A graphical depiction of the JKR contact model, demonstrating the cohesive tensile forces between two particles in contact is given in ***Figure 11*** [68].

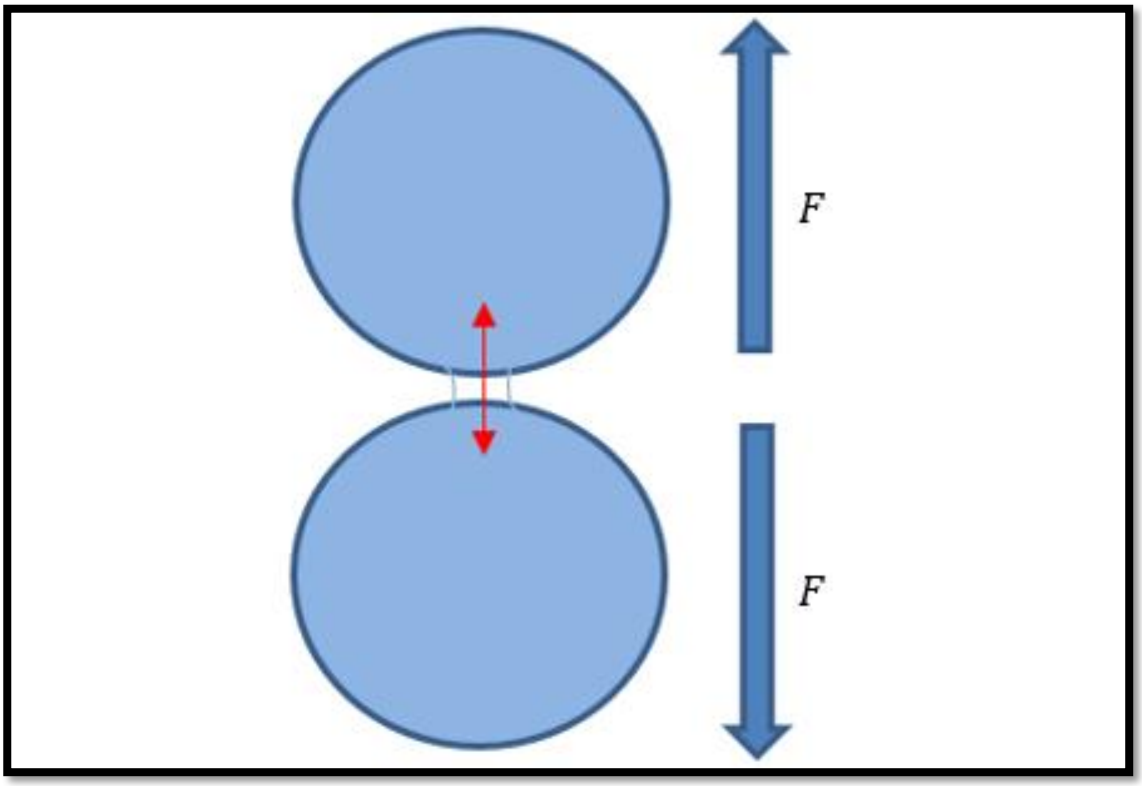

Figure 11 - Tensile Separation of Particles in Cohesive Contact in JKR Modelling. Adapted from *[68]***.**

In this project, a simplified version of the JKR model (SJKR) is used to solve the cohesive interparticle forces. Considering the contact radius as a function of the contact overlap, the SJKR approach approximates the radius of the contact zone as:

$$\mathrm{a}_{\mathrm{r}}^{2} = r^{*} \cdot \delta \tag{45}$$

According to Del Cid [70], simplifying ***Equation 44*** eliminates calculating the radius of the contact zone, yielding the normal force to provide an explicit expression of the force as a function of the overlaps, δ:

$$F_n = \psi^* \cdot \sqrt{r} \cdot \delta_n^{\frac{3}{2}} - \sqrt{6 \cdot \pi \cdot \gamma_{Surface}} \cdot \sqrt{\psi^*} \cdot r^{\frac{3}{4}} \cdot \delta_n^{\frac{3}{4}} \tag{46}$$

To model the SJKR within LIGGGHTS®, an additional normal force is applied by a Cohesion Energy Density (CED) property, which acts to maintain the contact between the elements. Thus, according to the LIGGGHTS® documentation [71]:

$$\mathrm{a_P} \times \boldsymbol{\kappa} = F \tag{47}$$

Where $\mathrm{a_P}$ is the area of particle contact, and $\boldsymbol{\kappa}$ represents the CED. Using this contact model, the contact area between the particles is calculated as in ***Equation 48*** [71, 72]:

$$\mathrm{a_P} = \frac{\pi}{4} \times \frac{\left[(\mathrm{D} - \mathrm{r_i} - \mathrm{r_j}) \cdot (\mathrm{D} + \mathrm{r_i} - \mathrm{r_j}) \cdot (\mathrm{D} - \mathrm{r_i} + \mathrm{r_j}) \cdot (\mathrm{D} + \mathrm{r_i} + \mathrm{r_j})\right]}{D^2} \tag{48}$$

Environmental factors, including the humidity within the build chamber and the presence of moisture in the powder during the spreading operation, will significantly influence the observed flow behaviour. Higher moisture contents and more humid conditions will likely raise the cohesion of the powder and increase the propensity for the material to agglomerate, reducing the ease of dynamic flow behaviour in response to external forces. The mathematics which underpins powder flowability is not easily defined, as the flowability is not an inherent characteristic of a given powder material. Flowability is instead defined relative to the flow requirements of a given process and is influenced by a significant number of variables, ranging from intrinsic material properties determined on the powder used and the atomisation process it is produced from, and the parameters of the spreading operation and the environment of the build chamber. A thorough examination of the variables of powder flowability is provided in ***Subsection 9.2***.

Selection and implementation of the correct contact models was essential to ensure the physics of powder flow in the digital model accurately represented reality. In this research project, failure to implement a model that accurately represented cohesive contacts would have yielded results with deviations from the expected behaviour [22, 73]. The numerical implementation of the DEM, explained thoroughly in ***Subsection 2.1.1*** and ***Subsection 2.1.2***, has been tested against physical powder flow scenarios to afford veracity to the simulations in this project. To achieve this, the properties of SS316l such as cohesion settings, friction parameters, and inherent material characteristics have been calibrated against the observed behaviour of physical SS316l samples processed through practical testing methods. These include the piling behaviour of the powder through an industry-standard calibrated funnel, and investigating the quality of the formed powder bed when SS316l is spread in a physical model reflecting the system produced within the DEM. A thorough explanation recording all of the validation processes performed is provided in ***Section 5*** of the thesis.

The work of ***Section 5*** highlights multiple significant mathematical contributions to the DEM-AM modelling research landscape. This is especially noteworthy in the calibration of the parameters for SS316l samples as implemented in the digital model against flow behaviour observed in practical testing. For example, whilst various authors have demonstrated that reducing the value of Young's Modulus of Elasticity for the particles is a viable means of optimising the simulation and managing the computational costs, there is little exposition as to how this is calibrated correctly with respect to the size of the particles and the timestep implemented to govern the simulation. A thorough mathematical explanation of the value of Young's Modulus for the powder size range in these simulations, with extensive testing at timestep values that ensure model stability has been achieved, has been provided in ***Subsection 5.3.1***.

Another important contribution has been made in the calibration of the rolling friction and sliding friction properties assigned to the SS316l material modelled with the DEM. It is noteworthy that the results showed that, owing to the simplification of using spherical particles, the results of testing the piling behaviour of SS316l conformed to the assumption in the literature that this parameter governs the interlocking of aspherical particles, and could thus be neglected for the powder spreading simulations. A more significant influence was observed by calibrating the sliding friction parameter, and a suitable value was established by the calibration processes in ***Subsection 5.3.1*** for SS316l. This has practical implications for the AM powder spreading operation, as the sliding friction property has a pronounced influence on particle-plane interactions and therefore influences the coverage achieved, packing density, and surface homogeneity of the spread layer.

Arguably the most significant quantitative contribution to using the DEM for PBF investigations was in establishing a conversion factor between the cohesion energy density and surface energy parameters. The research highlighted that, to the best of the author's knowledge, no previous conversion had been recorded in the literature between these properties, which significantly constrained the implementation of suitable contact models in the DEM for AM powder modelling. By numerically defining this relationship, and implementing the conversion factor to the cohesive properties in the simulation script, a more realistic depiction of interparticle behaviour was achieved and verified against the results of practical experimentation. This conversion, in conjunction with the scaling operation applied to the value of Young's Modulus of Elasticity to reduce computational costs, provides a baseline set of values for the optimised modelling of SS316l in powder spreading operations in future DEM-AM investigations. The methods used to derive this relationship is explained fully in ***Subsection 5.3.1***.

2.1.3 Computational Costs of DEM Simulations

One of the key limitations in the DEM modelling of PBF processes is reflected by the number of particles that comprise the powder bed. For example, the Wayland Calibur3™ EBM hardware has a powder bed of dimensions 30cm × 30cm × 10cm [74]. Hence, the number of particles required to produce a 1:1 scale digital twin model can be calculated as follows:

1. **Convert the powder bed volume to micrometres for consistency with the powder material:**

$$\text{As: } 1 \text{ cm} = 10{,}000 \text{ µm}$$

$$\therefore$$

By ***Equation 49***:

$$V_{Powder\ Bed} = (30 \times 10{,}000)\text{µm} \times (30 \times 10{,}000)\text{µm} \times (10 \times 10{,}000)\text{µm} \tag{49}$$

$$\therefore$$

$$V_{Powder\ Bed} = 300{,}00\text{µm} \times 300{,}00\text{µm} \times 100{,}000\text{µm}$$

$$\therefore$$

$$V_{Powder\ Bed} = 9 \times 10^{15}\ \text{µm}^3$$

2. **Estimate the average particle volume:**

Given the size range of the powder in EBM processes of $45 \mu m - 105\ \mu m$, and assuming the powder is inserted under a Gaussian distribution with varying particle sizes, the geometric mean can be calculated to estimate the average particle diameter as in ***Equation 50***:

$$D_{Geometric} = \sqrt{D_{Min} \times D_{Max}} \tag{50}$$

$$\therefore$$

$$D_{Geometric} = \sqrt{45 \times 105} = \sqrt{4725}\ \mu m$$

$$\therefore$$

$$D_{Geometric} = 68.74\ \mu m \approx 69\ \mu m$$

$$\therefore$$

The average particle radius is given by ***Equation 51***:

$$r_{Particle} = \frac{D_{Geometric}}{2} \tag{51}$$

$$\therefore$$

$$r_{Particle} = \frac{D_{Geometric}}{2} = \frac{69}{2} = 34.5\ \mu m$$

Having determined the estimated average particle radius, and assuming the particles comprising the powder bed bulk solid are spherical to neglect irregularities, the average particle volume can be determined from the equation for the volume of a sphere as in ***Equation 52***:

$$V_{Particle} = V_{Sphere} = \frac{4}{3}\pi r^3 \tag{52}$$

$$\therefore$$

$$V_{Particle} = \frac{4}{3}\pi\ ((34.5)^3)\ \mu m^3$$

$$\therefore$$

$$V_{Particle} = 172{,}006.91\ \mu m^3 = 172{,}007\ \mu m^3$$

3. Determine the theoretical maximum particle number.

Assuming a perfect packing of 100% space occupation, the maximum number of particles in the powder bed is given by dividing the total volume of the powder bed by the average particle volume as in ***Equation 53***:

$$\mathbf{N}_{Maxium} = \frac{V_{Powder\ Bed}}{V_{Particle}} \tag{53}$$

$$\therefore$$

$$\mathbf{N}_{Maxium} = \frac{V_{Powder\ Bed}}{V_{Particle}} = \frac{9 \times 10^{15}}{172{,}007} = 5.24\ \times 10^{10}\ Particles$$

As shown, the theoretical maximum particle count is more than 52 billion particles.

4. Determine the realistic maximum particle number.

Due to the random close packing of spheres, a completely dense powder bed populated with 100% of the space occupied by particles is impossible. Assuming a packing density consistent with the critical volume fraction proposed in the literature [17], a more realistic value would be approximately 60% of the theoretical maximum number of particles, as performed in ***Equation 54***:

$$\mathbf{N}_{Realistic} = 0.6 \times\ \mathbf{N}_{Maximum} \tag{54}$$

$$\therefore$$

$$\mathbf{N}_{Realistic} = 0.6 \times\ \mathbf{N}_{Maximum} =\ 0.6 \times 5.24\ \times 10^{10}\ Particles = 3.14 \times 10^{10}\ Particles$$

As shown, an EBM powder bed of dimensions $30\text{cm} \times 30\text{cm} \times 10\text{cm}$ would contain more than 31 billion spherical particles. As the DEM is based on modelling the detection of particle contacts at each timestep, the calculation of the resulting interparticle forces, and the trajectories for all elements of the system at each timestep arising from these contacts [36], the computational costs and the amount of processing power it would take to perform each simulation would be enormous, irrespective of the software program used or the prospect of parallelisation and for optimised running on a HPC cluster. This is further exacerbated by the requirement for a small timestep value as governed by the particle size range, which is typically between $1\ \times\ 10^{-7}$ s and $1\ \times\ 10^{-8}$ s for PBF powders [32, 49, 75].

These calculations are also complicated by the additional force contributions incurred by implementing the cohesive contact models required to reflect realistic powder flow behaviour, and the several weeks or months of clock time required to run each simulation depending on the processing power available. Such timescales are unfeasible within the limitations of this project. In addition to the computational intensity of modelling the movement and interaction of over 31 billion particles, the requirement to store data regarding the positions, velocities, and forces, and to compile neighbour lists makes modelling a full-sized PBF powder bed computationally unviable. To overcome this problem, a method often implemented in DEM-AM research is to model only a smaller segment of the powder bed, with periodic boundaries in a given axis as such that particles leaving one side of the domain re-enter the system at the other side [24]. An explanation as to how this method was used, to ensure robust powder spreading models were generated in the simulations of this project, is provided in ***Section 6*** and ***Section 7***.

3. Literature Review

To accurately model powder flow during AM processing, it was necessary to quantify the metrics that characterised a suitable powder processing technique for a given part or batch. This was in part achieved by analysing the influence of the process variables, such as the recoater geometry and spreading speed, on the quality of the powder bed. Further research was performed into powder characteristics including morphology and flowability. Based on the correlations and relationships identified during the preliminary research, an interest was held into isolating parameters to identify their relative effect on the process. In addition to the review of published literature, further data and the empirical methods used in practice have been established through correspondence with industry.

The preliminary review of literature, and conversations with industry, have highlighted that an insufficient understanding of powder flow constrains the further development of AM technology. This limits the ability to optimise AM processes and inhibits the introduction of new engineering materials. Consequently, work to address such limits in knowledge necessitate costly trial and error calibrations, foster unreliability in the quality and behaviour of the parts in application, and increase the manufacturing process cycle times due to the interrupted builds [12].

3.1 State of the Art and Powder Bed Fusion in Additive Manufacturing

As introduced in ***Subsection 1.1.1***, AM has emerged as a transformative technology in contemporary manufacturing processes. As the building material is deposited and fused layer-by-layer, significant advantages can be achieved with respect to the generation of components exhibiting complex geometries and features that are often unattainable in conventional manufacturing approaches. For example, the additive method enables the incorporation of intricate internal features including lattice structures and conformal cooling channels that would require sophisticated machinery reconfiguration or otherwise impossible-to-achieve methods in traditional material removal procedures such as turning, milling, or forming exercises.

This theorised “complexity for free” design realisation process has revolutionised industry by enabling mass customisation and optimised lead times for an array of products including in the aerospace, medical, and automotive engineering sectors. Whilst originally marketed as a solution for rapid prototyping, advances in AM capabilities have enabled the generation of highly-specialised components with superior mechanical properties fit for application in service.

A variety of case studies have exemplified the benefits of AM solutions. For example, Frazer Nash Consultancy Ltd, a systems, technology and manufacturing engineering company used the Renishaw AM 400 Laser PBF hardware to generate a fastening device for their customer Kwikbolt Ltd. The product was used to align aircraft panels and fuselage during assembly. This leveraged the inherent customisability benefits of AM by reducing the tooling requirements of bespoke machinery processes for each aircraft panel. Thus, improving precision, reducing manufacturing costs, and augmenting production by decreasing the assembly times [76].

Another case study of AM, this time showcasing the benefits of Fused Deposition Modelling (FDM) in the aerospace sector, is presented by BAE Systems PLC. The company have invested in an array of advanced FDM 3D printers, such as the Stratasys F900 and the F3300, to support commercial goals such as reducing costs and achieving a faster time to market for critical components. The precision and reliability of the method has allowed BAE Systems PLC to produce a wide range of aircraft assembly and maintenance equipment, including polymer cockpit floor covers for Typhoon fighter jets. These covers, traditionally made with wood and metal, replaced traditionally manufactured parts with lightweight, robust 3D printed alternatives. Thus, facilitating removal for the crew and optimising the overall maintenance and repair operations [77].

Other applications highlighted in this case study included protective guards for grounded aircraft, and low-volume production tools such as drills and repair kits. BAE Systems also notes the advantages of AM in supply chain management. Specifically, the ability to generate components "in-house", and create temporary representations of required parts in the event of supply issues, helps to mitigate the impact on production by reducing work stoppages [77].

Despite the many advancements that AM has achieved in manufacturing practices, the technology remains constrained by significant limitations. Depending on the specifics of the AM process, only a limited number of materials can be processed compared to subtractive methods. For example, Stoll et al [78] agreed with Bojestig et al [79] by showing that on account of their high reflectivity and thermal conductivity, the laser AM processing of metals such as copper and gold presents significant challenges and can lead to low-density parts with various defects, including porosity and eventual cracking and delamination. Wang et al [80] studied the properties of laser PBF generated Hastelloy X parts and observed micro-cracking issues in their as-built condition, which could only be removed by Hot Isostatic Pressing (HIP).

AM processes that utilise polymeric materials, such as FDM, are also constrained by material limitations, as the thermal requirements of the filament and its curing process inhibit the use of certain polymers. Lee et al [81] studied the crystalline morphology of Polyetherimide (PEI) and Polyether Ether Ketone (PEEK) and found that the high melting temperatures (350-400 °C) require the use of more specialised FDM hardware to ensure successful material extrusion is achieved. Thus, the processing of high-performance thermoplastics as filament material may require more investment, and FDM is generally therefore more limited to thermoplastics with lower melting temperatures such as Polylactic Acid (PLA) and Acrylonitrile Butadiene Styrene (ABS). Wide reading has hence shown that the limitations of AM can engender challenges in achieving uniform material properties, especially in metal AM, and that there is limited availability of multi-material printing capabilities [82].

Another constraint associated with AM processes is the surface finish and accuracy of additively-created parts. The layer-by-layer construction method of each component generally incurs an inferior surface quality compared to traditionally produced counterparts. This increases the lead times and overheads for the design builds by necessitating further machining in the form of post-processing steps [83]. Furthermore, multiple authors note that AM parts are produced with lower dimensional accuracy compared to those created by Computer Numerical Control (CNC) machining methods [84, 85].

One of the key concerns surrounding AM parts, particularly in safety-critical applications, is that the material properties can behave in an anisotropic manner, and deviate depending on the orientation of the component. For example, depending on the direction of the print head during the design-build, properties such as strength and durability can vary due to microstructural heterogeneity incurred by the layer-upon-layer building method. This weakens the mechanical integrity of the part and incurs difficulty in producing fully dense, defect-free components, raising the likelihood of critical failures. Hence, controlling and testing the anisotropic nature of 3D printed parts is a crucial element of Design for Additive Manufacturing (DfAM).

Further limitations are reflected in the size constraints associated with AM components, as the dimensions of the build chamber govern the maximum size of the parts. This further restricts production strategies, as it limits the number of components that can be generated in a single run, making AM less efficient for high-volume manufacturing. Whilst this can be overcome by investing in more AM hardware, the initial costs of the machinery and associated software, and the increased amount of floor space occupied within the manufacturing facility, can make this prohibitive in respect of the organisation's commercial goals. Although the reduction of sub-assemblies is also regarded as a key advantage of AM solutions, the segmentation of sub-assemblies for larger parts can introduce weak points in AM-produced systems [86].

One of the most commercially developed examples of the AM process is PBF. As the name implies, the build material of a PBF process, often comprising a range of fine metallic powders, are dispersed over a substrate to form a powder bed base for additive layer manufacturing. Subsequently, selected regions of the bed melted in the controlled environment with either a laser or electron beam in accordance with the dimensions on an imported CAD drawing. Thus, causing the particles to fuse together and consolidate to generate engineered components. This process is then repeated with a thin layer deposited over the powder bed over the previously fused layer until all the required features of the design build are realised. As noted by Trovato et al [87], the precision of the PBF process leverages the benefits of AM methods by enabling the creation of highly sophisticated topologically optimised components, with complex geometries and intricate structures achievable.

PBF is an umbrella term describing an array of various sub processes, each with unique characteristics, advantages, and limitations depending on defining factors such as the melting medium used to fuse the powder together and the environment of the build chamber. For example, Selective Laser Sintering (SLS), Selective Laser Melting (SLM), Direct Metal Laser Sintering (DMLS) and Electron Beam Melting (EBM) are all commercially practiced PBF techniques. In general, the ability to produce high-resolution, functionally optimised and customisable parts with PBF methods has seen the process gain a significant traction among industrial stakeholders. Including, but not limited to, the Aerospace, Energy, Medical, and Automotive sectors [9, 25].

The Canadian research institute: Centre de Recherche Industrielle du Quebec (CRIQ), leveraged the benefits of EBM for its ability to generate high-strength customised lower jawbone implants for dentistry and orthopaedic patients. This enabled CRIQ to halve lead times from 6 weeks to 3 weeks when compared to traditional manufacturing techniques and produce small batches of mandibles in a cost-effective approach in line with commercial goals. Furthermore, CRIQ noted that the design freedom enabled the generation of patient-specific parts, with enhanced osseointegration properties supported by the surface topology of the produced implants [88, 89].

Another case study, this time highlighting the benefits of PBF in the aerospace sector, is provided by General Electric (GE) Aerospace PLC in the development of the GE9X engine which was designed for the Boeing 777X aircraft. The engine turbine blades, produced using EBM technology, achieved a 30% weight reduction through topological optimisation compared to the blades in its previous model which were traditionally manufactured. This, in turn, contributes to a 10% increase in fuel efficiency, lowering running costs of the aircraft and attaining further environmental benefits by reducing the production of greenhouse gas emissions [90, 91].

The properties and quality of both the build process and the formed components in PBF techniques is governed by a range of interdependent parameters, pertaining to both powder-centric and AM hardware related factors. For example, the power of the melting medium, the spot size of the beam, the depth of the resulting melt pool and line and energy densities, in conjunction with other parameters such as the scan speed, hatch spacing, and thickness of the spread powder layer will significantly affect the efficiency of the process and part quality [92].

Key influences on the quality of the PBF builds are also manifested by powder factors. For example, the shape and size of the constituent powder elements and their proclivity to flow or agglomerate together in response to dynamic processing factors will determine the aptitude of the process for generating parts with the desired mechanical properties. Whilst the rapid solidification of PBF components can culminate in fine microstructures in components to yield superior strength and durability, it can also incur residual stresses, porosity that can propagate into fracture planes and cause critical failures, and the anisotropy discussed previously that can impede predictions of failure modes. Hence, despite the advantages, PBF remains limited by the requirement for part post-processing such as heat treatment and surface finishing methods.

Literature pertaining to both SLM and EBM has been reviewed to ensure that a comparative understanding of the AM techniques has been achieved. Reviewing methods enables a comparative analysis of each to be performed and knowledge to be developed regarding the advantages, limitations, and applications of both techniques in the context of wider PBF technologies. Whilst both processes involve powder spreading and layer wise melting of the components, there are distinct differences in the melting medium and thus thermal properties of the build operations. Nonetheless, owing to the fact that EBM methods have been historically the subject of proprietary information and considered a black-box process, significantly more research exists in the SLM landscape, which has provided useful insights for examining similar phenomena in EBM. Thus, helping to form a baseline of knowledge that builds upon existing advancements in AM.

Many of the factors explored to optimise SLM are common with those that are explored in EBM. Including research areas that inform investigations of powder spreading and flow behaviour such as the effect of particle size and morphology [14], processing parameters such as blade and roller type recoater configurations [17], scanning strategies, pre-heating, and post-processing requirements [29]. As many industries utilise both laser and electron beam PBF technologies, a greater understanding of SLM literature has helped to place the research of this project in a broader context, and enhanced the depth of understanding of EBM processes by leveraging existing knowledge from a closely related, more thoroughly explored field.

The current research landscape is populated by innumerable entries attempting to address PBF constraints such as the process stability and material diversity. One of the primary challenges in PBF is predicting and controlling the multi-physics phenomena which underpin the powder dynamics, which pertain to challenges related to deposition, spreading, and the ability to adapt parameters to engender conditions favourable for AM processing such as high packing densities, a homogenous profile of the spread layer, and even dispersion of the particle elements with respect to their size and morphology. To address this, various studies now implement computational methods to generate numerical solutions for AM powder simulations, by using the DEM introduced in ***Subsection 1.1.3***. A thorough review of literature, on the subject of powder spreading in PBF systems, has been performed subsequently in ***Subsection 3.2***.

3.2 Powder Spreading in Additive Manufacturing

As alluded to in ***Subsection 3.1***, the dispersion of the powder material used to form each cross-section of the component has a significant effect on the quality of the formed powder layer. Uniform, denser layers ensure consistent melting and solidification, which by extension assures the structural integrity of the generated components. A vast number of parameters, both related to the powder elements being spread and the processing factors of the operation, influence the quality of the spread layer. Meier et al [93] studied the behaviour of Ti–6Al–4V powders during the recoating process through DEM simulations. Specifically, their research addressed questions regarding the size of the particles comprising the build material and the influence this has on the propensity for the particles to agglomerate. It was found that at relatively fine particle sizes (with the median particle diameter approximating 17 µm), cohesive forces dominated gravitational forces and culminated in powder beds with less suitable conditions for manufacturing, manifested by more porous regions and a heterogenous surface profile.

Research also shows that powder cohesiveness will also be significantly influenced by environmental factors, including the vacuum pressure, temperature, and humidity [94]. For example, as EBM takes place in a vacuum, the reduced air resistance may support powder spreading by minimising drag effects. Conversely, the lack of air particles between powder elements may increase van der Waals and electrostatic interactions and thus increase cohesion. It is noteworthy, however, that the preheating phase, in which the powder bed is scanned by a diffused beam prior to the spreading and melting, will counteract some of these effects [95]. It is clear that cohesion, relative to both particle size and environmental conditions, significantly affects the quality of the spreading operation.

To determine the correct approach to powder bed optimisation, it is necessary to benchmark the current best practice of powder spreading in AM. During a PBF process, the fresh powder supply is stored in a reservoir known as a 'hopper' near to the powder bed. A key consideration in optimising the spreading process is in the form of the recoater which spreads powder across the print bed, often referred to more specifically in relation to its geometry as a 'roller' or 'blade' [17].

Empirical evidence, in conjunction with the general consensus in published literature, suggests that rollers produce a smoother finish than blades at the same operating conditions [12, 17, 21, 96]. Haeri et al [12] attributes this to the contact dynamics during spreading, suggesting that the greater surface area of the roller gradually rearranges the powder particles, and thus facilitates a greater packing of the powder bed. Conversely, the blade type recoater contacts the powder bed at only a single point along the edge of its profile, culminating in a 'dragging' effect, which produces a rougher layer and degrades the overall bed quality. Despite the proposed superior performance of the roller, a blade mechanism is often used. It is thought that the flexibility of the blade teeth mitigates the compaction of powder, which can cause powder layers to swell during the fusing of each cross section [97].

As the recoater shape has been shown to influence the powder-spreader interactions in the contact area, it follows that adapting the profile of the recoater is one approach to optimise the powder bed, and thus determine the most suitable spreader type to use [17].

A key factor to optimising the PBF process is powder flow. Insufficient flow impedes the operation with an inconsistent powder supply, contributing to the overall bed degradation and causing the weak bonding of layers within the part microstructure. From a commercial standpoint, this increases the build times and prevents the creation of functional parts. Nan et al [32] emphasised how the lack of knowledge regarding powder dynamics, and how to engender free flowing powder rheology, constrains the further development of the powder spreading process. They used the DEM to analyse the effect of the gap height and spreading speed of the recoater on the evolving shear band and the mass flow rate ($\dot{m}_{Powder}$) of powder beneath the spreader. Consideration was afforded to the maximum recoating speed, which is an influential factor in controlling the throughput of production.

Results showed that $\dot{m}_{Powder}$ increased linearly with the gap height and identified two discrete phases of the flow regime. In the first phase, $\dot{m}_{Powder}$ is linearly proportional to the lower blade translational velocities. As the spreading speed is increased, the flow rate eventually becomes asymptomatic of it, implying an upper limit of $\dot{m}_{Powder}$ and that the spreading throughput is limited at higher recoater speeds.

The transition point between the two phases of the regime, where $\dot{m}_{Powder}$ becomes independent of blade speed, is independent of the blade height. However, a critical blade height will exist, below which the mass flow rate is zero. This follows as if the particles jam, or most of the particle diameters are greater than the gap height, there will be a negligible flow.

The effect of particle jamming under the recoater is another area of research that has been observed across practical AM powder beds and the DEM. This phenomenon was the subject of extended reading by Nan et al [98], who observed that powder voids were formed by a jamming effect, degrading the bed quality by creating valleys and heterogeneity in the spread layer. They noted that the frequency and location of jamming was influenced by the particle properties, gap height, and spreading speed.

3.2.1 Quantification and Control of Powder Bed Quality: The Solid Volume Fraction and Surface Roughness

The work of Gibson and Shi [99] states that the behaviour and flow of the powder used to build the AM part has a significant influence on the properties, and by extension the function and quality, of the component in service. Consequently, when evaluating the best current practice in powder spreading for AM, it is essential to firstly identify what constitutes a suitable powder bed for manufacturing, with the suitability of the bed defined by its ability to promote favourable conditions which induce the desired properties for the component to function in application.

Multiple publications by Haeri et al [12, 17], identify the solid volume fraction (SVF) as one quantifiable metric of powder bed quality. In reference to an AM powder bed, the ‘bulk’ refers to the conglomeration of solid granular particles within the structure that forms the bed. Therefore, in the context of the AM system the SVF describes the ratio of the occupied space in the powder bed relative to the overall bed volume, accounting for the presence of interstices between the powder particles. Quantification of the SVF is thus given by:

$$Solid\ Volume\ Fraction = \Phi = \frac{V_{Solids}}{V_{Solids} + V_{Voids}} \tag{55}$$

Thus, the SVF is a value between 0 and 1, where 0 indicates no powder presence at all and 1 would reflect complete population with no interstices between particles. Note that as the units cancel, this is a dimensionless value which is often represented in literature as a percentage [39].

In an AM build, lower SVF bed values culminate in greater porosity in the microstructure of the finished part. Goodridge et al [100] processed ceramics with a SLS process, and indicated that using a wide mixture of particle sizes raises the SVF, and that AM parts made using a mixture of particle sizes demonstrated a greater flexural strength in service.

Conversely, Haeri et al [12] analysed a mixture of particles configured into rod-shaped geometries at different aspect ratios. The aspect ratio is traditionally a metric which provides a measure of width to height.

In an AM context, this term is more accurately defined as the ratio of the greatest dimension of the particle to its smallest due to their often irregular form. They argued that mixing particles with different shapes and size distributions may not be an effective method in controlling the bed quality, due to the potential for defects to arise on account of segregation occurring at different layers within the powder bed. A similar observation was recorded by Mussatto et al [101].

The consensus among academia and industry is that a more densely packed powder bed induces favourable conditions for AM processing, and that the presence of interstitial finer particles fill the voids between larger particles and thereby raise the SVF [12, 17, 49]. Thus, reducing the porosity of the built component through powder coalescence and improving the structural integrity of the part in service.

Closely associated with the inhomogeneity between powder layers is the surface roughness of the powder bed, which is often noted in literature as another key metric of powder bed quality. The consensus holds that increased values of surface roughness at the top layer of the powder bed during the build process can cause weaker bonding between the layers of the part, impeding upon the performance of the component in service. Previous literature has shown a direct correlation between lower values of surface roughness and higher values of volume fraction, and greater quality of the parts in service [102].

Both Haeri et al [12] and Parteli and Pöschel [49] measured the surface roughness topographically as the standard deviation of the powder bed height profile. In the work of Haeri et al [12], a ray-tracing technique was used to analyse 10 rows of equally spaced light sources across the x-plane of the powder surface, in conjunction with a further 500 evenly distributed light sources in the y-axis, generating 5000 data points across the system overall. The surface roughness is quantified by the intersection of each ray to the powder bed at a given height, h, where h is normalised by the diameter of the spheres used to create the rods that formed the constituent particles within their simulation. The surface roughness is thus defined by the standard deviation of h, and can be expressed mathematically as in ***Equation 56*** [12]:

$$\epsilon = \frac{\sqrt{\langle (h - \langle h \rangle)^2}}{D_{Sphere}} \tag{56}$$

Where the averages are calculated across each data point.

Parteli and Pöschel also used the standard deviation of the height profile to measure the surface roughness, but with respect to the projection of the powder bed onto the z-plane parallel to the trajectory of the recoater [49]. Described in the source as the ‘cutout’ of the powder bed, this projection generates a two-dimensional (2D) outline which, when viewed laterally, enables a visual observation of the powder bed surface and thus analysis of the bed quality. A higher surface roughness would therefore be characterised by an undesired heterogenous cutout with an irregular and asymmetrical profile [49].

By reference to the research material, it can be established that the SVF and surface roughness are two influential parameters that can be used to quantitively evaluate the suitability of a powder bed for AM. It has been recorded almost unanimously that lower values of surface roughness and higher values of SVF give rise to the highest bed quality [12, 17, 49, 101, 93]. Therefore, an ideal spreader geometry would induce an inverse relationship between these two metrics [12].

As presented by Parteli and Pöschel [49], a key condition of the spreading process is the homogenous distribution of powder over the component during the design build. In reality, the powder bed is likely to present a highly heterogenous form, characterised by the presence of several undulations which are liable to induce porosity to the material microstructure. Thus, giving rise to the formation of voids and the potential for stress concentrations to propagate into fracture planes when the component is subjected to cyclical loading. A graphical depiction of the aforementioned undulations, which exemplify the surface roughness of the powder bed profile, has been reproduced from the modelling of powder spreading in the Parteli and Pöschel paper in ***Figure 12***.

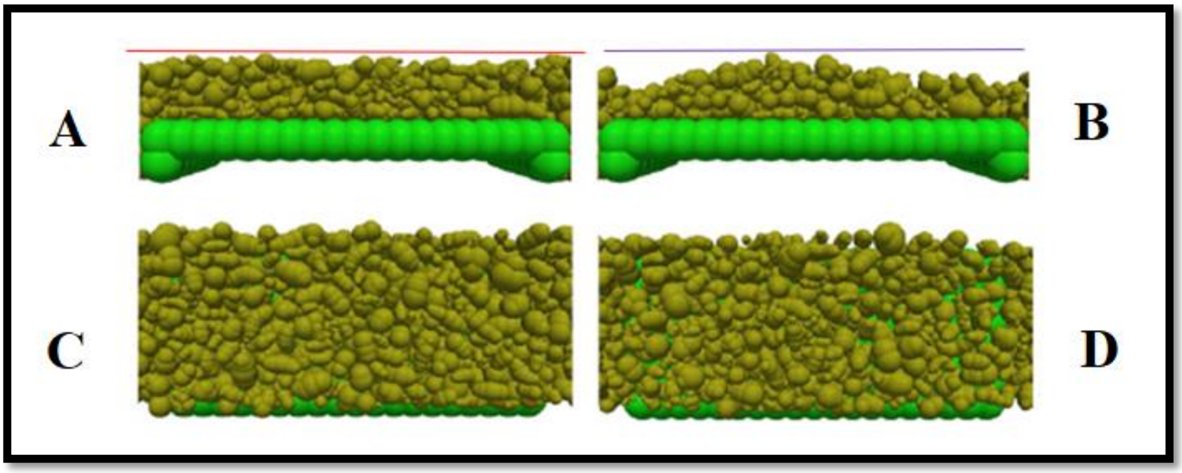

Figure 12 - Deposited Powder Layers during the Simulations of Powder Spreading. Adapted from *[49]***.**

Figure 12 shows a clear difference in the deviations from the horizontal denoted by the red line (Segment A) and the purple line (Segment B). These horizontal markers have been measured at the highest point of the top particle within the powder bed. Segments A and C are corresponding side and top views of the same powder bed respectively, at a recoater translational velocity of 20 $\frac{\mathrm{mm}}{s}$. Segments B and D present corresponding views of the same powder bed, once more in the side and top projections respectively, but at a greater spreader speed of 180 $\frac{\mathrm{mm}}{s}$. As clearly demonstrated, a more homogenous and uniform packing is attained, with respect to the projection of the particle layers against the horizontal, by the slower recoater speed used.

Research to this point has shown that the powder-spreading operation has significant ramifications for the quality of the spread layer formed. Various observable defects, such as a heterogeneous profile of the spread layer, have been recorded in the literature. A clear defect with consequences for the quality of the realised components is asperous regions characterised by voids in the powder bed, as these voids can culminate in incomplete fusing of the powder during the melting operation. Thus, incurring microstructural deficiencies such as porosity in the produced part, and a diminished structural integrity with porosity liable to propagate into fracture planes and engender critical failures.

Ahmed et al [103] prepared a fairly rudimentary experiment by using a blade to manually spread SS316l, in the size range of 15 to 55 µm, over an emery paper substrate with varying recoater gap heights. Thus, evaluating the influence of particle jamming on layer quality. The formed layer was characterised using Scanning Electron Microscopy (SEM). Five different gap heights were used and were multiples of the d_{90} [explain this] value of the powder of 45 µm. These d_{90} describes a percentile value used when measuring the constituents of a cumulative PSD and indicates the size range at which the percentage value in the subscript is found. Hence, the values were:

Table 2 - Multiples of Powder Particle Sizes and Gap Heights used by Ahmed et al in Powder Spreading Analysis. Adapted from *[103]*.

Multiple of d_{90}	Recoater Gap Height (µm)
$1 \times d_{90}$	45
$1.5 \times d_{90}$	67.5
$2 \times d_{90}$	90
$2.5 \times d_{90}$	112.5
$3 \times d_{90}$	135

Thresholding and image enhancement processes confirmed the suitability of the SEM analysis for inspecting the powder bed porosity, as reproduced in ***Figure 13***.

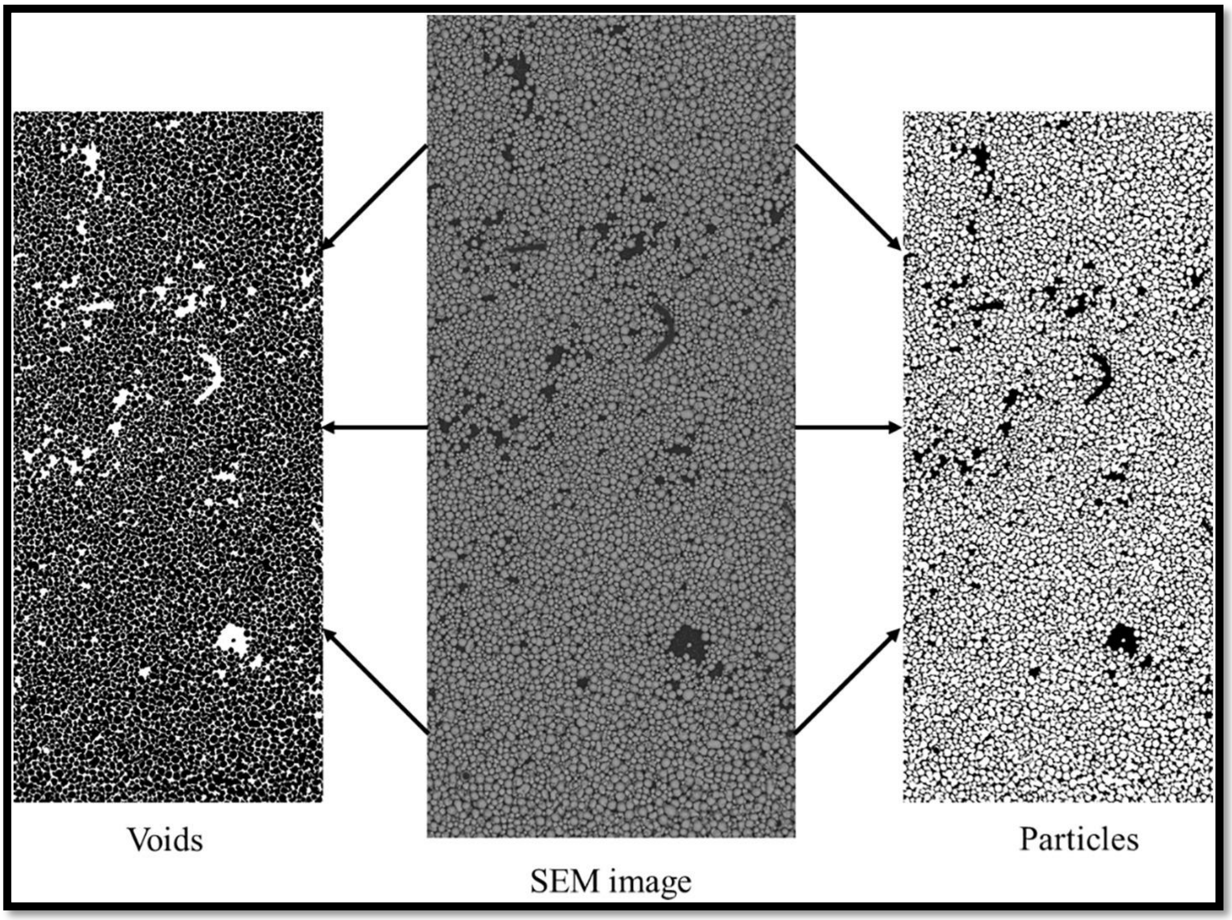

Figure 13 - Refined SEM Images of the Formed Spread Layer, Adapted from *[103]*.

A clear difference was observed in the presence of porosity with the varying gap height. Visual inspections indicated clearly that more voids, manifested by darker regions of the powder bed in ***Figure 14***, were formed when smaller gap heights were used.

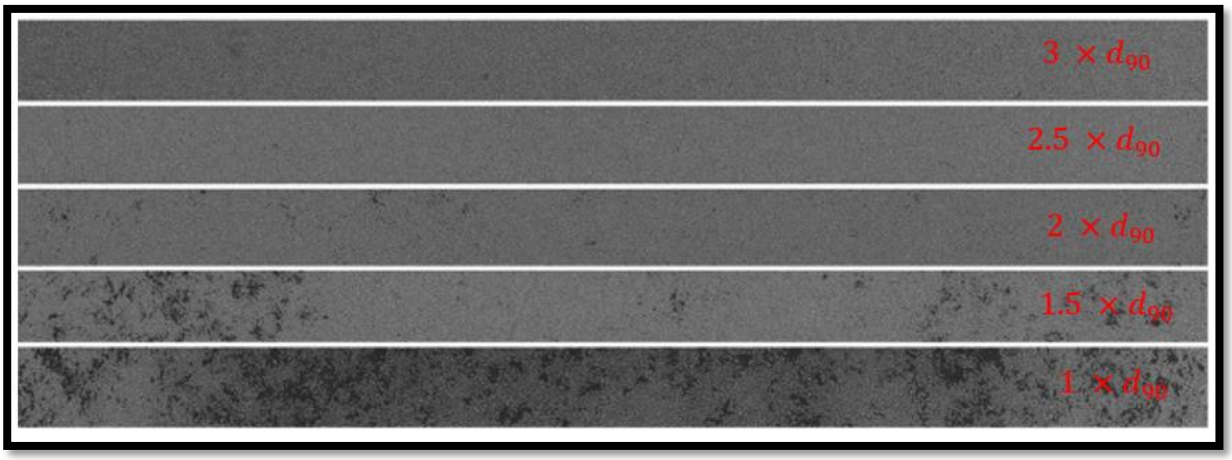

Figure 14 - Powder Bed Porosity at Varying Gap Heights, Adapted from *[103]*.

The authors attempted to replicate the findings with numerical methods, which conformed to the findings found by practical experimentation and showed that areas of porosity increased with narrowing the recoater gaps, as shown in ***Figure 15***.

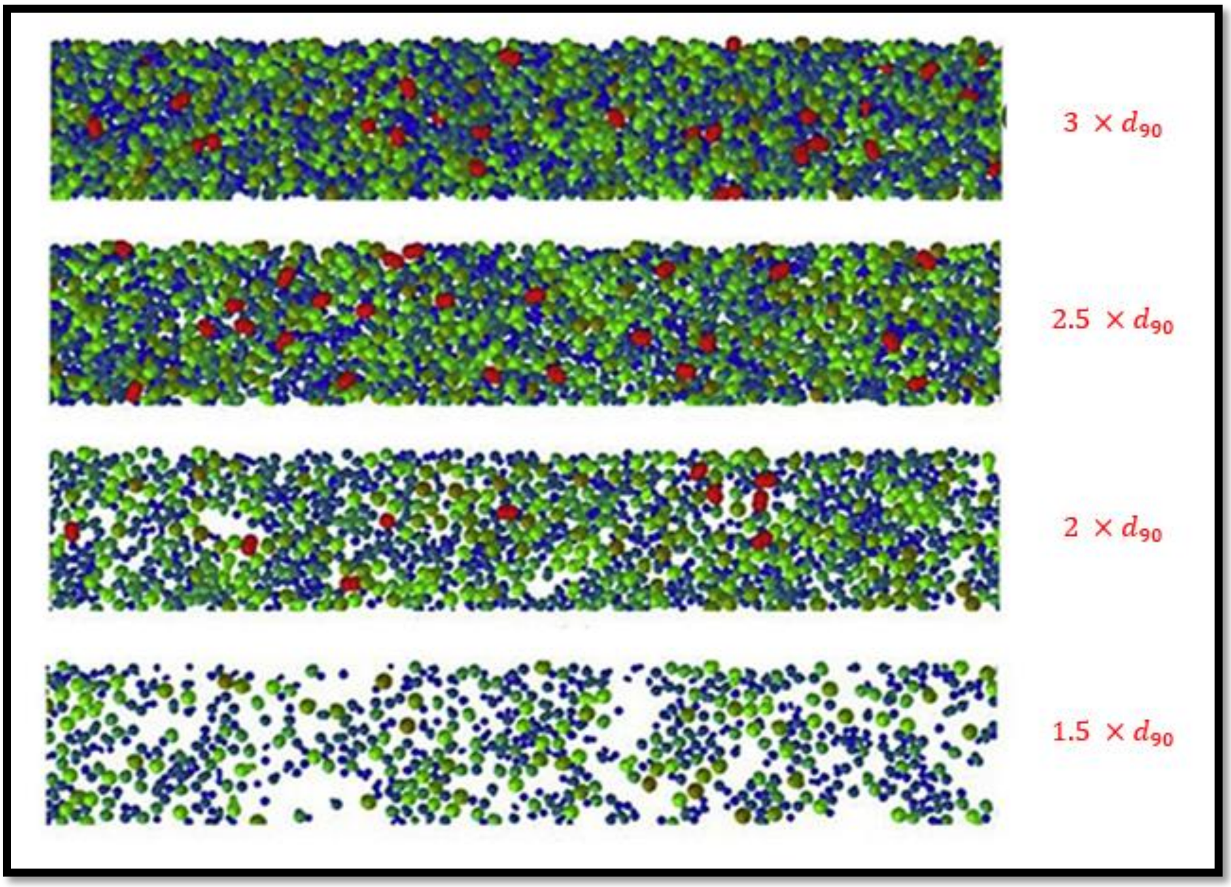

Figure 15 - Powder Bed Porosity at Varying Gap Heights with DEM Analysis. Adapted from *[103]***.**

Boschetto et al [104] performed the in-situ digital image monitoring of powder bed quality of an SLM process in an EOS M290 hardware. To achieve this, a built-in camera detected surface defects incurred by the spreading of AlSi10Mg. By calibrating and enhancing the images of the spreading operation, regions with errors such as layer inhomogeneity were identified. ***Figure 16***, reproduced from the source, shows the image enhancement process applied to the 2870th (top) and 4032nd (bottom) layers

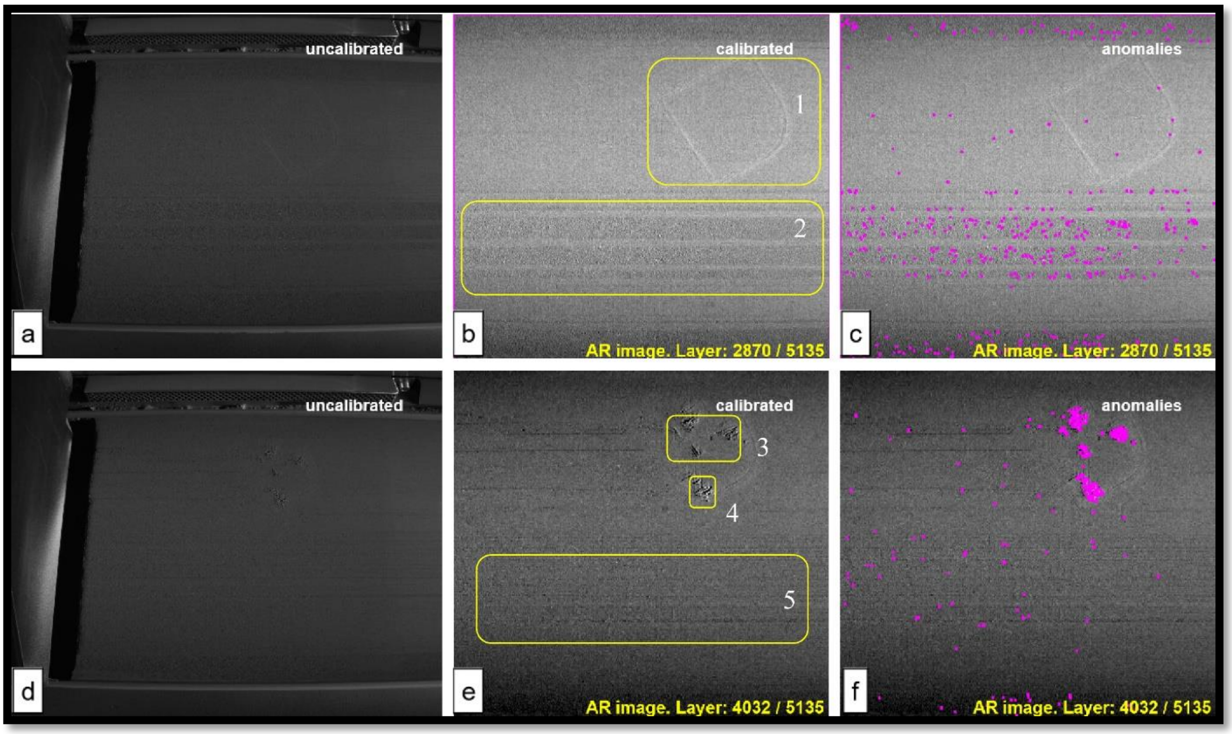

Figure 16 - In-Situ Digital Image Monitoring of Powder Bed Quality. Adapted from *[104]***.**

To ascertain the influence of the defects on the completed part, Computed Tomography (CT) scanning was performed and established internal voids and thickness reductions in the built component. Thus, highlighting the anomalies which matched real defects in the produced component. The defects, labelled 2 and 5 in ***Figure 16*** from the source material, show a dragging effect culminating in a rougher profile with respect to the topography of the spread layer. The defect propagation and detection across subsequent layers on the powder bed is best exemplified by the highlighted line representing dragged particles, labelled "d" in ***Figure 17***.

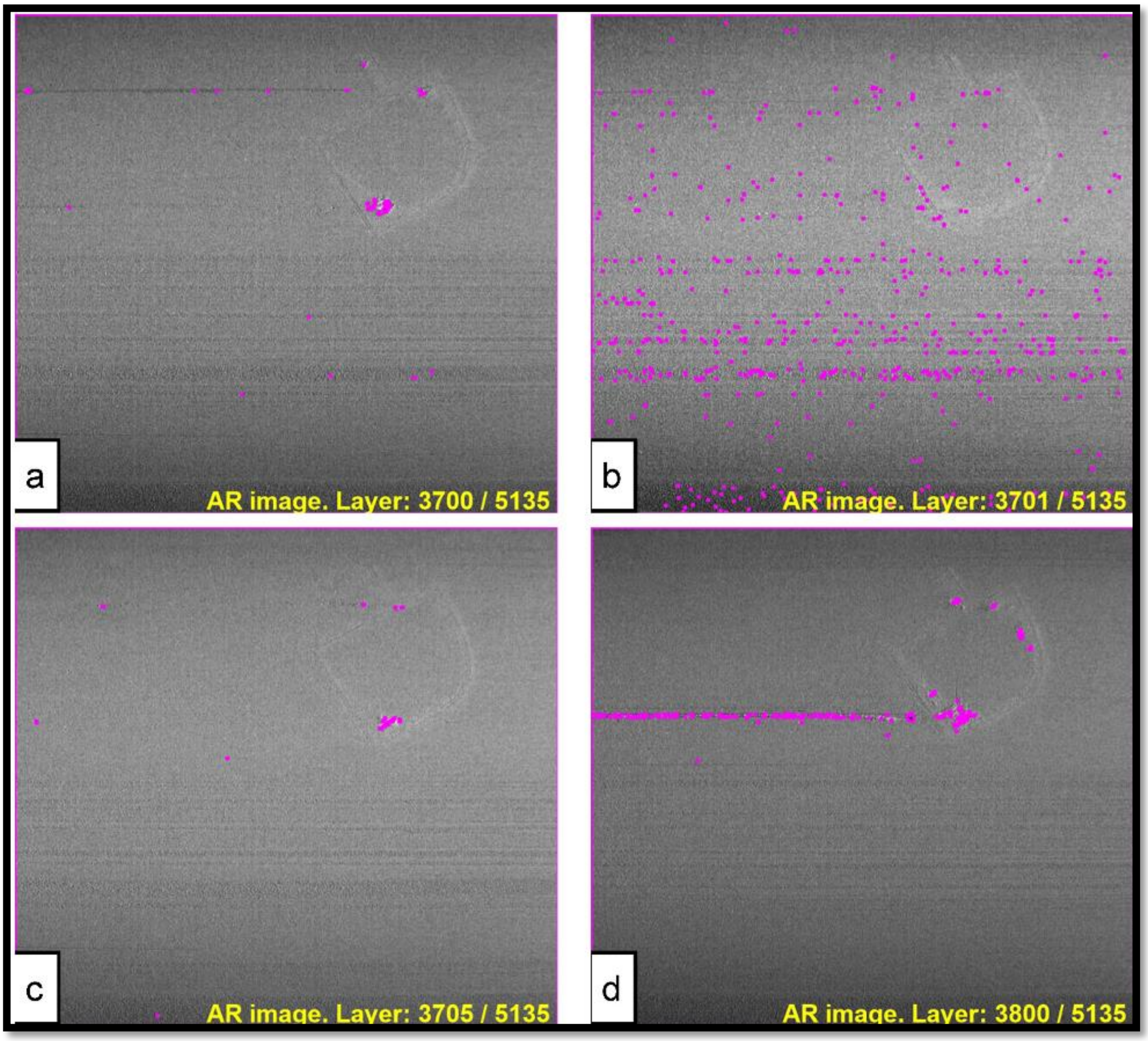

Figure 17 - In-Situ Digital Image Monitoring of Powder Bed Quality Demonstrating Particle Dragging. Adapted from *[104]***.**

The CT examination of the produced component demonstrated that powder bed defects correlate strongly with structural deficiencies in the final part. Notably, areas in which a heterogenous spreading, characterised by rougher topographies in which particle dragging has caused the presence of valleys, were more likely to culminate in a lack of fusion porosity in the component microstructure. ***Figure 18*** highlights the diminished areas of wall thickness that the authors stated were incurred by accumulated layering inconsistencies in the spreading operation [104].

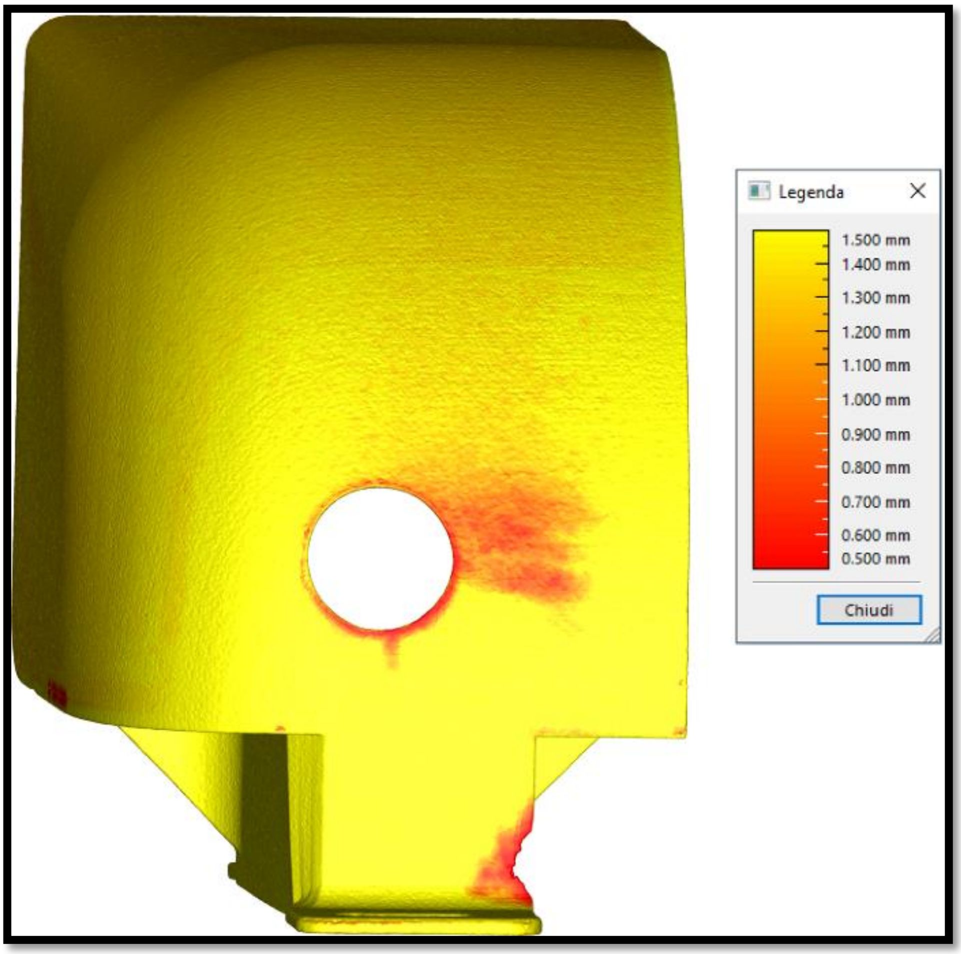

Figure 18 - Structural Deficiencies Manifested by Diminished Areas of Wall Thickness in the Produced Part. Adapted from *[104]***.**

Reflecting on the points in this subsection, the evidence suggests that parameters such as the recoater speed are highly influential on the quality of the AM powder bed. Further reading suggests that local powder agglomerations have significant ramifications on the behaviour of the overall bulk powder bed volume [49]. Thus, providing a justification for further study, and underpinning the motivation for a simulation and modelling-based approach to analysing the behaviour of powder flow, as practical particle analysis on a local scale would be extremely difficult to perform in-situ with AM part builds.

3.2.2 Critical Volume Fraction

One limiting factor identified during the research performed by Haeri [17] is the maximum value of the SVF, when it reaches its 'critical' state (Φ_{cr}). Beyond which, the powder particles begin jamming beneath the spreader, which has a degrading effect on the overall quality of the bed surface. In Haeri's study, Φ_{cr} could be approximated as being between 0.575-0.585, but they noted it would have been extremely computationally intense to converge further, and the value was thus estimated at 0.58 which was sufficiently accurate for their particle modelling [17]. The phenomena of particles jamming was also the focus of the research performed by Nan et al [98], when they used the DEM to identify the conditions at which the particles jam under the recoater, and used the presence of empty patches across the material substrate as the indication of the particle jamming zones.

Nan et al [98] suggested populating the powder bed with a wide Particle Size Distribution (PSD), to allow the finer particles to fill the interstitial voids present. Another possible technique to tend the bed volume toward Φ_{cr} is to reduce the distance between the spreader and the previous layer of deposited powder. However, this also increases the risks of the particles jamming. Furthermore, the simulations performed within Haeri's study suggested that achieving packing values beyond the critical volume fraction would require significant compressive forces not normally observed in AM powder spreading, inducing further steps to the build process and thus increasing cycle times [17]. Hence, any advantages achieved in powder bed optimisation would be offset by the increasing number of steps to other aspects of the powder processing phase, nullifying the commercial benefits attained.

Based on the above, it is reasonable to argue that optimising the powder bed by exceeding the critical SVF cannot be practically achieved without compromising other facets of the powder spreading process. Thus, confirming an upper boundary for the SVF of approximately 58%.

3.2.3 Particle Size Distribution

A key parameter of the AM spreading process is the PSD of the powder. The PSD is a granulometric measure that quantifies the constituent particles within the bulk solid, with respect to the range in the population of particles of different sizes. One of the initial challenges in evaluating the PSD of a given powder is the measuring approach used. Within most powder bulk solid systems, the constituent elements are formed of irregular, non-spherical particles. Resultantly, determining a uniform approach to quantify the constituents is subjective to the nature of the system under analysis. This renders an exact definition of the PSD difficult to ascertain for multidisciplinary applications.

Another factor which complicates measuring the PSD are the different forms of particle agglomerations that occur, most notably manifested by areas of large and small powder element clusters, and the morphology of the powder used. Finer particles are prone to coalescing together during solidification in the gas atomisation process, giving them a propensity to form satellites. Notably, the British Standard (BS) framework for the graphical representation of particle size analysis, BS ISO 9276-1 [105], states that no single definition for the quantification of particle sizes exists.

The approaches used to define the geometric features of the particles vary in relation to their characteristics. For example, BS ISO 9276-1 states that one denotation of particle size is based upon establishing an equivalent dimension, such as the equivalent diameter of an irregular particle that exhibits the same physical properties, and thus behaviour, as a spherical particle [105]. The framework outlines that the measurement of the equivalent diameters is informed by the diameters of the surface areas, or volume of the particles.

The standard also describes other methods for particle size analysis, such as by attributing linear dimensions across the particle geometries with graphical methods, and practical techniques such as sieving, in which the PSD is controlled by the size of the sieve apertures [105].

In an idealised experiment, such as when an assumption that the constituent particles are spherical is made to reduce computational costs, then the particles within the bulk solid can be defined by their average diameter. However, as the morphology of the constituent particles are likely to be highly asymmetrical in nature, alternative methods are needed to characterise the particles in practice.

One such approach, applied by Jacob et al [52], is to use imaging techniques to identify a volumetric aspect ratio of the particles. To achieve this, three sets of dimensional characteristics were taken, the minimum particle diameter as found by the largest chord projections identified, the maximum Feret diameter, which measures the irregular particle dimension across a given direction, and the Martin diameter, which is the linear dimension bisecting the projected area of the particle in a specific measuring direction. A graphical depiction of each of these three measurements is provided in ***Figure 19***.

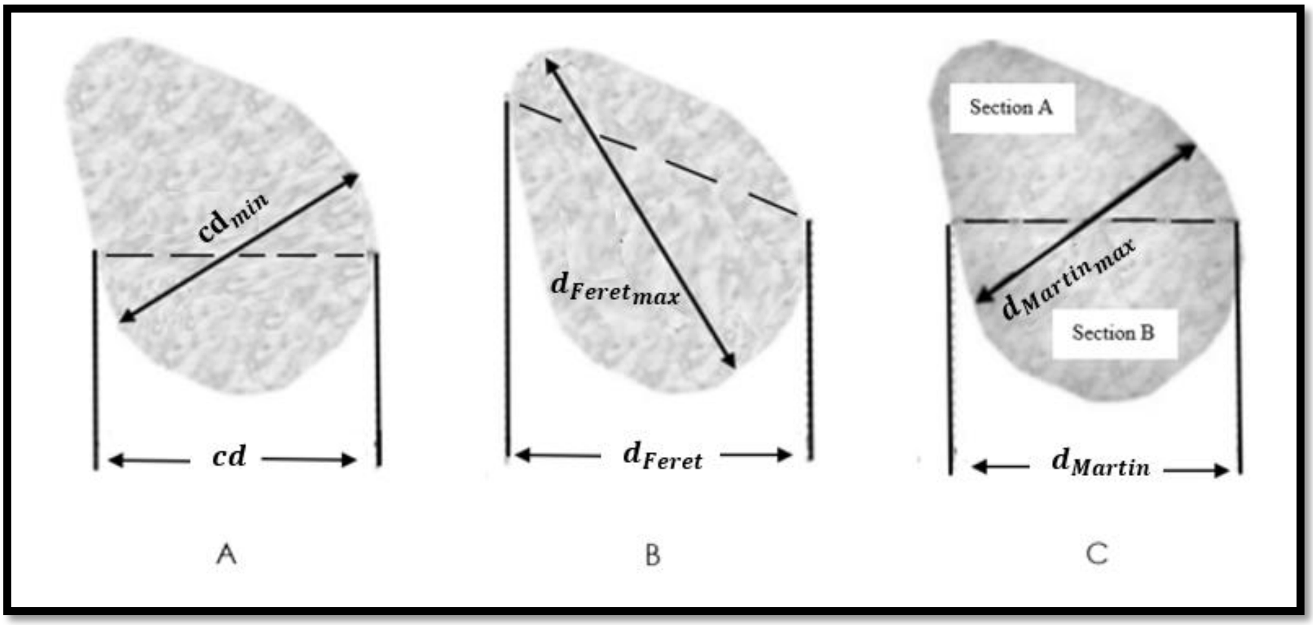

Figure 19 - Particle Element Sizing with a Direct Image Analysis System. Showing Chord Projections (A), Feret Diameters (B), and Martin Diameters which Bisect the Particle (C). Adapted from *[52]***.**

The PSD observed in an AM powder bed is dependent on the deposition process and the melting medium used. Shaji Karapuzha et al [106] and Nguyen et al [107] suggested the range of particle sizes for a PBF approach as being between 15 µm and 105 µm, with the recommended average powder size ranges from 15 µm to 63 µm in a SLM process, and between 45 µm and 105 µm for an EBM technique.

To place the PSD for the different AM processes in context, ***Table 3*** has been adapted from the work of Woodcock & Mason [108], and states the typical size range for bulk solid powders with example materials [39].

Table 3 - Classifications, Size Ranges, and Example Materials for Various Bulk Solids. Adapted from *[39]* **and** *[108]*.

Classification	Approximate Range of Powder Size	Example Material Type
Solid Coarse Materials.	5 mm – 100 mm	Gravels, aggregates and various civil engineering and construction materials such as: Granite and Slate (≈5 mm – 30 mm), and Gabion Stone (≈60 mm – 100 mm).
Solid Granular Materials.	0.3 mm – 5 mm	Quartz sand and smaller aggregates such as pea gravel.
Coarse Powders.	100 µm – 300 µm	Nutraceuticals (≈125 µm – 180 µm) [109] and Table Salt (≈200 µm – 300 µm) [108].
Transitional, Majority Fine, transitioning to Coarser Powder.	45 µm – 105 µm	Recommended range for the powder bed of an EBM System [106].
Fine Powder.	15 µm – 45 µm	Recommended range for the powder bed of an SLM System [106].
Fine Powder.	10 µm – 100 µm	Range of Ti-6Al-4V and Cobalt-Chromium (CoCr) powders for dental applications [110, 111].
Superfine Powder.	1 µm – 10 µm	Aluminium Nitride powders, as electrical insulation for electronic components [112].
Ultrafine Powder.	<1 µm	Encompasses processed powders, such as fine clays for geotechnical engineering [113], and particulates in naturally occurring materials such as asbestos and smoke [114].

Various techniques are used to characterise the powder used for the design build. For example, SEM is a process in which a focused electron beam is projected to scan the surface of a material specimen under vacuum conditions. The electrons then interact with atoms within the sample to produce images which depict the surface topography and composition. SEM is a widely used technique for examining the morphology of AM powder elements due to its typical resolution of between 0.5nm and 4nm [115], enabling it to provide detailed images and depict with clarity micrometre scale satellites and profile irregularities. Hence, SEM has widely been applied in AM powder literature to evaluate both individual particle characteristics and PSD values [22]. An SEM image of plasma-atomised Ti-6Al-4V powder, typically used in EBM processes, is provided to highlight the image clarity achievable in ***Figure 20***.

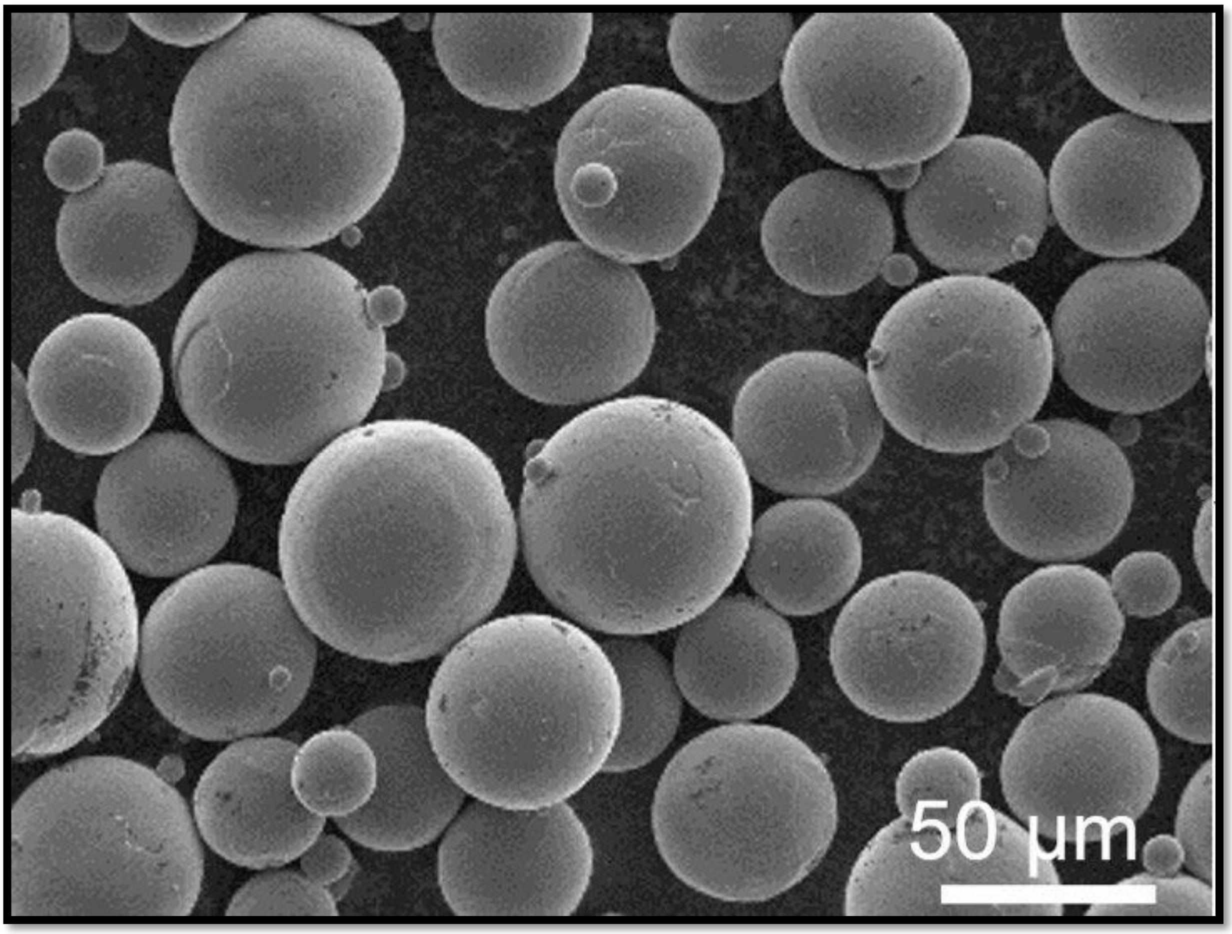

Figure 20 - SEM Image of Plasma-Atomised Ti-6Al-4V Powder. Adapted from *[22]*.

Multiple authors have evaluated the influence of the PSD within AM powder beds, and their findings vary depending on the processing parameters, powder characteristics, and environmental conditions of the build process. For example, Averardi et al [13], sieved steel powders from 10–200 μm and studied the effect of the PSD on the density of a powder bed. They found that a wider PSD generated a greater packing of the powder bed, and thus generated more dense parts with greater structural integrity. Conversely, they showed that a narrower PSD increased the flowability of the powder, improving the dimensional accuracy of the built components and inducing desirable mechanical properties such as a greater hardness.

In contrast, according to Parteli and Pöschel [49], a powder set with a wide PSD is likely to lead to a greater degree of surface roughness, on account of the heterogenous particle distribution at the top layer. The source also remarked that finer particles have a higher propensity to coalesce together and form large, locally concentrated agglomerates, consequently increasing the porosity and lowering the overall SVF.

Similarly, Brika et al [14] analysed three different Titanium-Aluminium-Vanadium (Ti-6Al-4V) powder sets in a laser-based PBF (LPBF) exercise, and the effect of the PSD, morphology, and internal porosity within the powder particles. The performance metrics measured included the surface finish and the mechanical properties of the components, and the smallest geometric features of the part achievable. The relevant data pertaining to each powder type is collated in ***Table 4***.

Table 4 - Powder Types and Data Used by Brika et al. From *[14]*.

Powder Production Method	PSD
Gas Atomisation Procedure.	20–53 μm
Plasma Atomisation Procedure.	20–53 μm
Plasma Atomisation Procedure.	15–45 μm

They concluded that a PSD with a greater quantity of fine particles had a detrimental influence on the SVF, bed profile surface roughness, and the dimensional accuracy of the realised geometries, corroborating the hypotheses of Parteli and Pöschel [49]. The authors theorised this was due to a higher interparticle friction between the finer elements. This has interesting implications for manipulating the PSD as a control method of powder bed quality, particularly when considering the consensus that a wider PSD induces a higher SVF, and the critical volume fraction proposed by Haeri [17]. It suggests an optimum fraction of fine particles in the PSD may exist for populating the powder bed, beyond which particles begin to agglomerate and diminish the packing density. Research to this point indicates that a value or theory of the maximum fine, or coarse, particle fraction for a given PSD has yet to be established.

The research has demonstrated that the PSD has a strong influence on the properties of the bulk powder volume, and on conditions such as powder flowability, the density, and surface roughness of the powder bed. Resultantly, the PSD reflects an area of further exploration in the optimisation of the powder bed and presents one such characterisation approach for the bulk powder of an AM system.

Conflicting information regarding the merits of inducing a wide PSD to the powder bed motivates further study, as the evidence provided so far by the consideration of all sources is inconclusive when critically evaluated. Whilst consensus holds that combining coarser and finer particles is advantageous for improving the solidity of the powder bed, the prospective segregation of polydisperse particles is likely to lead to heterogeneity within the powder layers. Thus, implying that the effect of a broader PSD within the bulk solid is subjective to other parameters of the powder process. To this end, further experimentation is required to determine the effect of the PSD of the powder, and the engendering of desired conditions for the AM process.

3.2.4 Particle Segregation within the Powder Bed

A key influence on the quality of an AM powder bed is particle segregation. In this project, particle segregation refers to the phenomena in which powder elements of different morphologies are prone to segregate within layers after being spread by the recoater. More specifically, it describes the tendency for finer or coarser powders in a PSD to concentrate to a particular area of the powder bed. Although in practice this is nearly impossible to control, and further complicated by the proclivity for finer particles to behave cohesively with one another, the temporal location of these elements has been proposed by multiple authors as to significantly effecting the packing characteristics and quality of the powder bed [101, 116, 117]. In terms of the surface roughness and SVF measurements, a concentration of smaller particles in line with recoater trajectory could viably diminish both of these metrics, by increasing porosity between larger particles. Similarly, saturation of larger particles would also be likely to degrade the bed if fewer fine particles (referred to in DEM-AM literature as simply “fines”) were inserted to occupy the interstices.

The effect of segregation in AM powders was extensively studied by Yao et al [53], who showed that different behaviour between coarse and fine particles during powder spreading culminated in a segregation effect. It is assumed prior to experimentation that as near to an equal dispersion of powders of different morphologies in a polydisperse pack yields the best powder bed for AM, by homogenising the elements in the mixture across the geometry. Powder segregation has previously been analysed using the DEM by various authors and, as previously, the packing density and surface roughness of the spread layer remain two key indicators of powder bed quality with respect to segregation [12, 53].

Previous research shows that segregation is highly influenced by the parameters of both the powder and spreading system. For example, Jacob et al [52] observed that in a wide PSD finer particles are likely to be situated nearer the bottom of the powder layer (lower in the z axis nearer the substrate), with coarser powders migrating toward the top of the layer. This is logical, as it is expected that smaller particles pass through interstices in the layer itself. Experimental analysis [118, 119] has shown that segregation has a significant influence on the melting process of the spread powder, with coarser particles generating a greater variance and therefore more pronounced instability in the formation of the molten pool.

Jacob et al [52] proposed that in SLM powder bed systems, coarser powders had a propensity to segregate at the end of the bed furthest away from the recoater. That is, finer particles were more likely to be deposited at the start of the substrate. Observation of their models showed that the recoater motion had a tendency to push finer particles within the heap formed in front of the spreader down into the powder bed, and thus into powder layers below the top surface. No comment is made as to whether a roller type spreader would induce the same effect, although Wang et al [120], in their work on the adhesion effects in powder spreading, note that a roller type spreader is beneficial for the rearrangement of particles. This improves the bed by overcoming heterogeneity in the initial phases of spreading, and may extend to segregation.

In their study into powder layer formulation, Mindt et al [54] concurred with Jacob et al [52] and noted that finer particles tended to deposit to the powder bed early in the spreading regime, and separate from the pile in front of the spreader during recoating. They elaborated that repeated recoating increases the segregation, and thus reduces the number of fine particles away from the initial spreader position. When a fresh layer of powder is deposited over a spread layer, the dispersion of the new particles depends on the condition of the previous layer. Mindt et al [54] suggested that spreading a new layer over a previously unprocessed layer causes the existing particles to be spread along the recoating direction, exacerbating the segregation effect observed.

When considering the mechanism of segregation, Yao et al [53] commented that the structure of the powder bed causes different mechanical behaviours to occur due to the force chains present. Namely, stronger force networks act upon large particles and sparse, weaker chains act on the finer particles. Hence, different particle velocities arise causing the finer particles to leak through the interstices they populate, manifesting the segregation effect and degrading the overall bed quality. The segregation of smaller particles in the initial region of the powder bed (relative to recoater position) is likely to culminate in higher packing densities compared to further down the spreading regime. Indeed, Mindt et al [54] noted that a discrepancy in packing density is apparent in the recoating direction, so far that higher SVF values were observed in the initial 40% segment of the powder bed substrate length.

Interestingly, practical testing by Muñiz-Lerma et al [121] contradicted the consensus of literature in DEM simulations, that finer particles generally segregate in the initial bed region relative to recoater direction. Instead, they found smaller elements were preferentially deposited toward the end of the bed along with the recoater travel. Mussatto et al [101] practically tested similar sized powders and reached consensus with DEM results: that fine powders situate near the starting point of the recoater travel post-spreading. However, Muñiz-Lerma et al [121] noted that the DEM models often neglect the effect of cohesion and particle-particle interactions, suggesting that the powder cohesion modelling strongly influences segregation results.

Muñiz-Lerma et al [121] postulated that the discrepancy between their findings and consensus is due to the fine particles forming clusters which are spread along with the recoater blade. The source suggested that this cohesive behaviour is not always accurately accounted for in DEM literature. Assuming the shear force between the blade and powder elements exceeds that of the cohesion force later in the spreading regime, the clusters will disintegrate into the powder bed and leave finer deposits at the end of the recoater travel [121].

As briefly alluded to previously, Haeri et al [12] inspected the segregation with respect to the particle morphology. They used polydisperse rod-shaped particles and observed a tendency for elements with greater aspect ratios to accumulate on the upper regions of the powder bed. Their results indicate that the morphology and size of the rods are inexorably linked, complicating powder bed optimisation by manipulation of the particle size and shape, and by extension the PSD. The ramifications are that improvements in the SVF, segregation, and surface homogeneity may not be uniformly observed across each layer of the design build, and improving one of these metrics may adversely affect another.

Multiple approaches are used in literature to quantify the powder bed segregation. Muñiz-Lerma et al [121] sampled various segments across the physical powder bed, and used SEM to find the PSD in each section. Yao et al [53] proposed quantifying segregation based on the average size of the particles, or PSD, in a given region of the powder bed:

$$\beta = \frac{\lambda_{Rear} - \lambda_{Front}}{\bar{\lambda}} \tag{57}$$

Where:

β = Segregation.

λ_{Rear} = The average particle size or PSD in the rear segment of the bed.

λ_{Front} = The average particle size or PSD in the front segment of the bed.

$\bar{\lambda}$ = The average particle size or PSD in the total bed.

Thus, a segregation of 0 would imply no segregation in the powder bed (as would be observed with uniform particles). Positive segregation, where $\beta > 0$, denotes that the average sizes in the front region are finer than those observed in the rear region. Conversely, negative segregation where $\beta < 0$, implies the particles populating the front region are coarser than in the rear region.

In DEM powder beds, there is limited application of ***Equation 57***, as isolating the powder bed into only the front and rear sections fails to make complete use of the model functionality. An alternative approach would be to isolate the particles by their diameter and location in the post-processing software. This would provide a more comprehensive insight into the segregation effect in the powder layers.

Yao et al [53] observed that the segregation effect generally weakens at higher spreader velocities. The authors suggest increasing the recoating speed reduces the time and thus opportunity for fine particles to leak under gravity through the powder layers. However, as stated, increasing the recoater velocity generally degrades the bed quality with respect to the SVF and surface roughness values. This underpins the previous point that improving one metric of bed quality may negatively impact another, and emphasises that the recoater speed is set in accordance with the requirements of the design build.

Research suggests that, despite recent progress in understanding powder bed segregation, the underlying mechanism of segregation and the size and distribution of powders with a proclivity to segregate during spreading remain unanswered questions.

In the context of this project, an original contribution to knowledge is likely to be achieved by inspecting what, if any, effect the deposition method through which particles are supplied to the powder bed has on segregation. To the best of the author's knowledge, all previous numerical investigations have used a stochastic "rainfall" approach to populate the powder bed [52, 53, 54]. A rainfall technique describes the insertion of particles in a given volume to the model, which are then allowed to fall under gravity to populate the area of interest. Hence, numerical modelling of a controlled deposition of powder with a dynamic funnel (as has been sporadically observed in industry for EBM systems [56]) is likely to yield interesting information regarding the propensity of particles to segregate, with implications for both DEM modelling in academia and AM powder bed optimisation in industry.

In addition to modelling the deposition technique, a comprehensive study of various PSDs in the powder bed will reveal the size of the particles that are more prone to segregation. Inspecting the SVF and surface roughness of the built powder beds will also elucidate the viability of manipulating the PSD as a means of controlling bed quality, and in what concentrations the PSD should be to engender favourable building conditions.

The main points from the segregation research in AM powder beds can be summarised as follows:

- The effect of segregation on the packing density and uniformity of the spread layer is not obvious, but likely to be highly subjective to the conditions and properties of the model, necessitating a parametric study.

- The factors which influence the particle segregation in AM powder beds can be broadly outlined as: the PSD, particle morphology, the density of the powder material, the layer thickness of the spread layer, and the velocity at which the recoater spreads the powder [101]. The deposition mechanism of the powder, either by a hopper or directed funnel, is also likely to influence powder segregation. By extension, the deposition speed of a moving funnel is also likely to contribute to the segregation effect.

- The segregation mechanism is theorised to occur because of the force networks between the powder elements, with the strength of the forces increasing with particle size. This, in turn, results in different velocities and trajectories between particles of different morphologies, and eventually segregation.

- Due to the inherent stochasticity of the spreading process, a degree of segregation is almost certainly unavoidable. It is proposed that a reduced segregation can be achieved by properly calibrating system parameters including the recoater velocity, and the properties of the particles used to comprise the powder bed, such as the PSD. Thus, underpinning the motivations for analysing segregation in DEM simulations.

- Particle morphology, in tandem with the PSD, is likely to be influential in the occurrence of segregation in the powder bed. However, due to the lack of uniform behaviour between layers (in terms of both layer depth and span), control of the particle shape and size is not likely to increase deposition homogeneity for all regions of the powder bed. Hence, the segregation analysis should be performed for discrete regions in each axis.

3.2.5 Particle Aspect Ratios

A closely associated parameter to the PSD is the particle aspect ratio. Recapping the definition, the aspect ratio relates the greatest dimension of the particle to its smallest, due to their often-asymmetrical shape. As such, a perfectly spherical particle would be considered to have an aspect ratio of unity, with irregular particles exhibiting aspect ratios greater than 1. As alluded to throughout ***Section 3***, the dimensions of the powder particles used are highly influential on the quality of the formed powder bed.

Many researchers have studied the influence of the aspect ratio on AM powder builds. Haeri et al [12] noted that increasing aspect ratio values at greater translational velocities of the recoater diminished the SVF and exacerbated the surface roughness of the powder bed. They also observed that particles with an aspect ratio of 1.5 gave the highest SVF for all modelling exercises performed. However, they noted that whilst increasing the overall density of the powder bed can be achieved by manipulating the particle morphology, the effect of segregation due to the varied distribution within the powder layers may diminish the advantages achieved.

To aid the understanding of particle morphology, powder elements at aspect ratios of 1.5, 2, and 2.5 have been adapted from the Haeri et al paper in ***Figure 21*** [12].

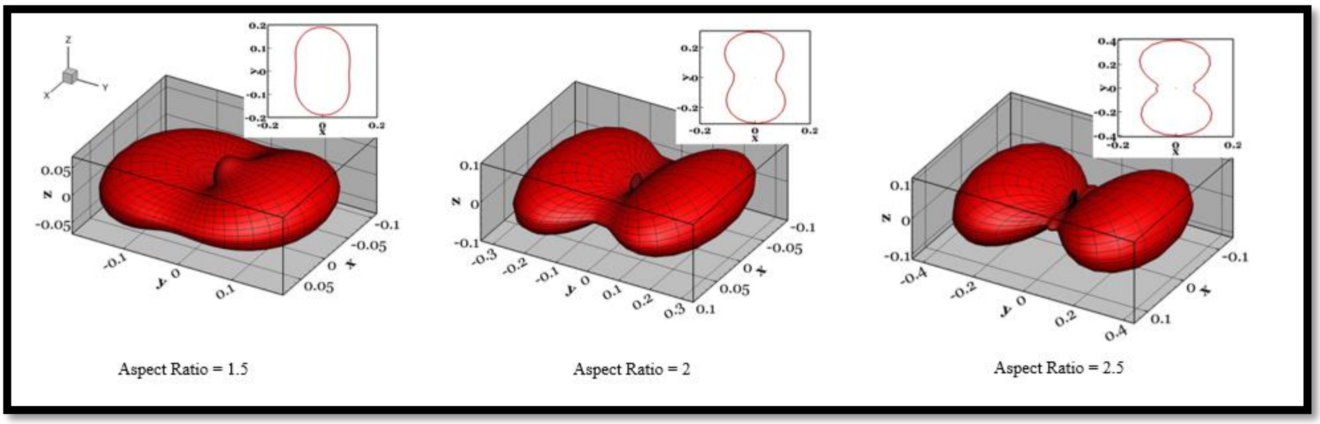

Figure 21 - Illustration of Particle Aspect Ratios. Adapted from *[12]*.

Haeri et al [12] suggested that the optimum aspect ratio is independent of the spreader displacement: which describes the vertical distance between the contact face of the recoater and the surface of the powder bed. However, they remark that the aspect ratio has a more pronounced effect on powder bed quality at lower recoater velocities. This suggests that increasing the SVF to approach Φ_{cr} is likely to only be achievable by adapting both the average particle aspect ratio and the spreader translational velocity.

Haeri et al [12] also found that the surface roughness of the spread layer presents only a weak function of the spreader speed at aspect ratios of unity, but significantly increases at higher aspect ratios. A similar finding is made for the spreader displacement, as the effect of the gap height on the surface roughness also increases with the aspect ratio, reinforcing their findings that higher aspect ratios are detrimental to the quality of the powder bed [12].

Brika et al [14] also investigated the influence of aspect ratio on the rheological behaviour of Ti-6Al-4V powder in the three powder sizes outlined in ***Table 4***, and generally found that the more spherical powders produced with a plasma-atomisation process gave a slightly higher packing density (≈ 5%) when compared to the bed populated with gas-atomised powder.

From their research, Brika et al [14] found that although certain facets of powder processing can be controlled to optimise the built part, adapting powder properties such as morphology, PSD, and atomisation method alone are not enough to improve the overall quality of the components. This is in part accountable to the fact that correlations are difficult to establish between different powder types, part densities, and the mechanical properties. For example, Liu et al [122] observed a correlation between the packing density and the density of the artefact produced, whilst noting that the parts created in a powder bed with a narrow PSD exhibited stronger mechanical properties. Meanwhile, Lutter-Günther et al [15] observed that, in agreement with Averardi et al [13], a wider PSD culminated in a higher SVF of the powder bed. Peculiarly, they noted that this did not translate into relatively high-density parts in their study.

Experimental inconsistencies and contrasting observations, as demonstrated between Liu [122] and Lutter-Günther et al [15], are not uncommon, and results which contradict expectations are also highly prevalent. For example, Seyda et al [123], analysed three sets of Ti-6Al-4V samples, and found a correlation between the powder packing density and the strength of the built part, contrasting the findings of Lutter-Günther et al [15]. Similarly, Baitimerov et al [124] analysed three discrete sets of Aluminium Silicon Alloy (AlSi12) and observed a correlation between the flowability of the powder and the SVF of the powder bed.

The literature review highlights that multiple different processing factors, including the parameters of the build and the powder production method, significantly influence the conditions of the manufacturing operation and by extension the quality of the parts generated. However, for the purpose of this project, it is important to state that, as with all engineering operations, no ‘perfect solutions’ exist, and only trade-offs and compromises that give rise to the best possible conditions for an AM design build are realistically attainable.

Haeri et al noted [12], and Parteli and Pöschel concurred [49], that the recoater speed appeared to be the key parameter in controlling the powder bed quality. Both sources found higher speeds degraded the powder bed. However, a lower recoating speed will increase the build times required and thus raise the processing costs whilst decreasing the production throughput. Hence, it is necessary to consider the relevant commercial constraints when critically evaluating the benefits achieved to the powder bed.

Brika et al [14], in their LPBF studies of the powder sets recorded in ***Table 4***, proposed that a wider PSD achieves a better packing of the powder bed but lowers powder flowability, whilst coarser particles promote overall flow compared to finer elements in the powder bed. They go on to state that particles with aspect ratios nearing unity are more flowable than irregularly shaped particles. A general theory for LPBF processing is that the use of spherical powders with a limited amount of fine particles promotes flowability and generates components with improved mechanical and geometric properties. This hypothesis further motivates the study of AM powder beds with controlled fractions of fine particles, to find the weighting of a PSD that fosters a condition of maximising both flowability and packing density.

In summary, the literature demonstrates that there is a generally a trade-off between increasing the SVF through a wider PSD, and the flowability of the powder in the build chamber when particles are assumed to be spherical in majority. This conclusion seems logical, as if all particles were assumed to be perfectly spherical and of equal diameter, then interstitial spaces would exist between neighbouring particles in the bulk solid. Geometric analysis of random sphere packing indicates a maximum occupancy of approximately 64% of the unit cell volume in three dimensions [125], broadly corroborating the proposed critical volume fraction of Haeri [17]. The implications of these findings for AM processing are significant, as the property requirements of the part in service will govern the build parameters used.

3.3 Powder Flowability

The flowability of the powder used in an AM build has a significant influence on the quality of the powder bed, and by extension the built components.

3.3.1 Definition and Quantification of Powder Flowability

Recent work by Kiani et al [126] noted that, whilst it has been widely documented that the powder flow in the build chamber influences the quality of the built components, the relationships between powder characteristics and the flow behaviour remain underexplored.

Although techniques exist to quantitatively evaluate the flowability of a given powder, such as the Hausner Ratio, Hall Flow Rate (HFR), and the Carr Index, the source suggests that these methods are not reliable and do not present a suitable comparison for the flow in metal AM processes.

Thus, it is necessary to combine existing research into the parameters which optimise the powder bed with a suitable approach to determining flowability in the build chamber. As noted by Brika et al [14], flowability is not an inherent property of a given material such as Young's Modulus of Elasticity or Density. Instead, flowability describes the capability of the powder to exhibit the desired flow characteristics for a given process, making the quantification of the flowability as subjective as the definition itself.

Wider reading establishes that flowability, irrespective of how it is defined and quantified, is highly dependent on several factors. These range from the chemistry of the powder, such as the presence of impurities and surface oxides, and the powder morphology, such as the aspect ratio of the particles and the PSD. Furthermore, flowability is a transient property of the powder.

As the powder is stored in a hopper before being supplied to the build table, it must be capable of overcoming the static condition to initiate the flow. It is then required to maintain the flow dynamics to ensure a homogenous powder supply throughout the build [126]. Intuitively, by considering the chemistry and morphology of the powder sets, it becomes obvious that different powders will behave differently in the same processing conditions, further complicating finding an exact definition of powder flowability.

The powder flow will also depend on the moisture content in the environment which influences the capillary forces. Because of the extremely low pressure within a vacuum chamber, such as that used in the EBM process, moisture can boil at room temperature, making the control of moisture of significant relevance to the flowability analysis. Combining environmental conditions with AM processing parameters and powder variables such as morphology, chemistry, and the PSD illustrates how characterising flowability becomes a complex and multifaceted process [127].

Amado et al [127] used a Revolution Powder Analyser (RPA) device to study powder flow for an SLS process. In this technique, a rotating drum is filled with powder and turned at various speeds to analyse the flow characteristics. The powder in the drum is backlit and thus appears in silhouette when recorded with a camera during each cycle. This, in turn, allows for an inspection of the powder dynamics such as the avalanche angle, surface fractal, and the volume expansion ratio (VER). A brief explanation of each measured characteristic is provided as follows:

Avalanche Angle:

The avalanche angle is the angle formed at the linear profile of the free powder surface, by reference to the horizontal. This is the point of the maximum potential energy before the powder avalanche. Conventionally, the left side of the diameter is evaluated to obtain a higher quality representation of the avalanche angle. It is noted in literature that this is one such approach used to measure the flowability in PBF techniques [128]. However, little evidence has so far been presented to determine the viability of measuring this parameter in a vacuum environment for EBM. Generally, it is regarded that higher values of avalanche angle are indicative of poorer powder flowability, and that lower angles are indicative of a more free-flowing powder.

Surface Fractal:

According to Mercury Scientific [129], the manufacturers of the RPA used by Amado et al [127], the surface fractal of the powder measures the fractal dimension, and thus the irregularity, or jaggedness, of the surface profile. This provides an indicative measure of the cohesiveness between the settling powder after avalanching, and by extension is a parameter for measuring how the powder will settle subsequent to a dynamic flow. Quantification of the surface fractal varies depending on the process and measuring equipment used, but Mercury Scientific state that a “rough” surface fractal, characterised by a jagged powder profile, will exceed unity. In applications requiring a homogenous powder dispersion, a surface fractal nearer one is indicative of a more uniform powder distribution, likely to give rise to a favourable powder flow in a PBF system.

In their system, Mercury Scientific equate the surface fractal with the empirical relationship given by ***Equation 58*** [127]:

$$L(\boldsymbol{\zeta}) = \mathrm{Q} \times \boldsymbol{\zeta}^{(1-\boldsymbol{\Gamma})} \tag{58}$$

Where:

$L =$ Is the length estimate used in powder analysis.

$\boldsymbol{\zeta} =$ The scale of measurement, varied in this approach between a minimum value defined by the resolution of the camera capturing powder flow, and one-third of the drum diameter.

$\mathrm{Q} =$ A positive value.

$\boldsymbol{\Gamma} =$ A constant equal to at least unity.

It is noted in the literature that the particulate properties characterised by the surface fractal have wide ranging implications on PBF processes, as the surface fractal provides an indirect analysis of the interparticle forces, flow rate, and thus flowability of powder [130]. The surface fractal is also a method of determining the sensitivity of the powder flow to changes in the PSD [131]. However, the surface fractal is not a suitable metric of powder flowability in isolation, as a free-flowing powder would be required to also demonstrate a low avalanche angle, and a narrow distribution of the avalanche angle and the surface fractal. Otherwise, agglomerations within the powder would be more likely to give rise to irregular avalanches and higher surface fractal values.

Volume Expansion Ratio:

The VER describes the ratio between the volume of powder as measured within the drum unit, corresponding to the expanded volume considered the bulk density, and the volume of powder in the filling container during the preparation of the experiment, denoted as the tap density. During preparation, Amado et al [127] manually tapped a 25 cm^3 cylinder until filled with compacted powder. Following which, the top surface area of the cylinder was cleaned to ensure an accurate volume reading recorded. The expanded volume of the powder was found by multiplying the sum of each pixel within the image captured by the RPA camera by the width of the drum [127]. A depiction of the avalanche angle, surface fractal, and VER described by Amado et al [127] has been adapted from their work in ***Figure 22***. A simple schematic diagram of the RPA used to characterise the powder dynamics has been provided in ***Figure 23***.

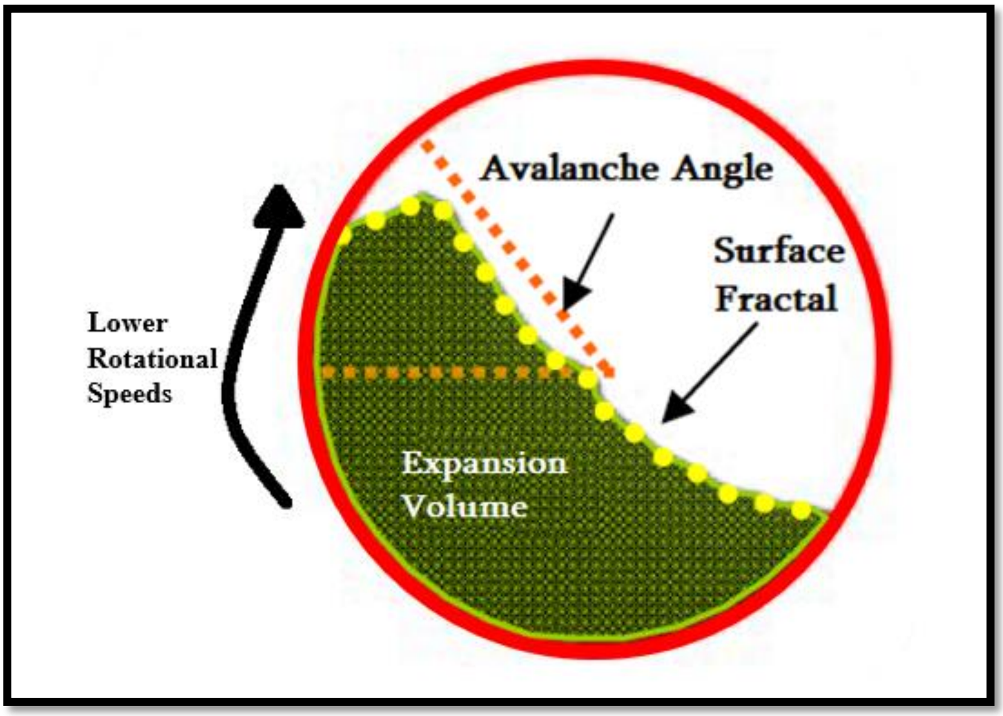

Figure 22 - Visual Demonstration of Avalanche Angle, Surface Fractal, and Expansion Volume Parameters within a Powder Flowability Test. Adapted from *[127]***.**

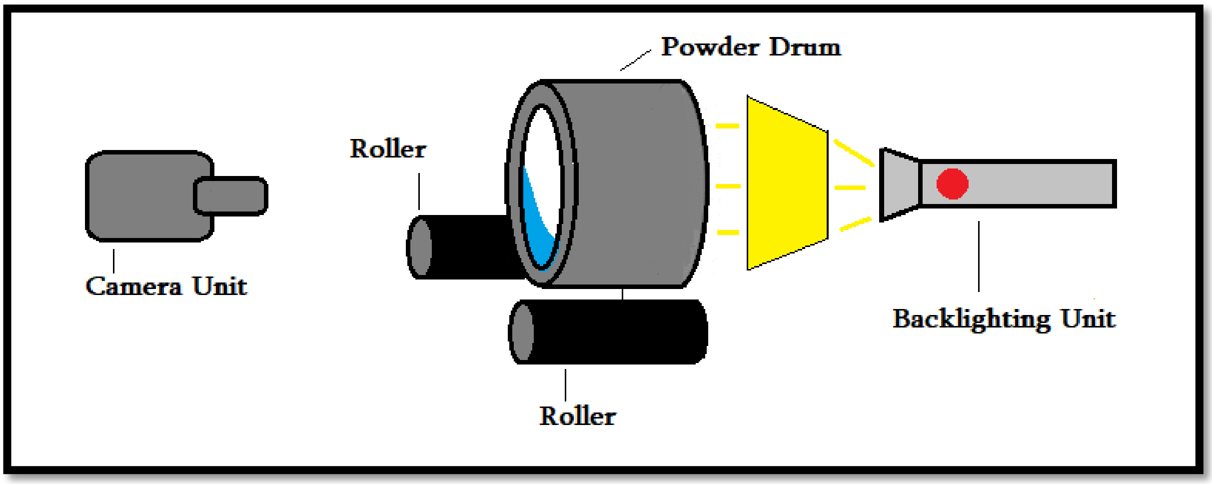

Figure 23 - Schematic Diagram Showing the Components of a Revolution Powder Analyser System.

As shown, various methods exist for analysing the rheological behaviour of powders, and many sources have attempted to find the most suitable method of quantifying metal AM powder flowability. This was most comprehensively reviewed by Spierings et al [128], who compared several techniques with an array of experiments. A description of each approach from their work and wider research is provided subsequently.

Ring Cell Shear Tester:

A device known as a Ring Cell Shear Tester (RCST) has been used to evaluate several powder properties including the flow, consolidation time, compressibility, and internal forces acting on the bulk solid [128]. To achieve this, the normal force acts through a coarsened annular cover at the top of the cell device. Following which, a shear force is applied through the powder by rotating the trough (the bottom half of the cell) relative to the lid, and the torque required to induce the shearing is measured [132].

Spierings et al remarked that the RCST is unsuitable for the evaluation of metal AM powders, as the forces observed during powder spreading in a PBF system are incongruous with the compressive forces present in the RCST [128]. This corroborates Haeri [17], who remarked that the compressive forces required to increase the packing density of their powder bed models were significantly greater than those generally found in commercial AM.

Hausner Ratio and Carr Index:

The Hausner Ratio is another measure of the bulk and tapped densities of a granular material. It describes the ratio of the powder as it has been allowed to settle freely in the vessel, to the density of the sample after it has been subjected to mechanical tapping over a defined period [133]. The value of the Hausner Ratio is indicative of the level of interparticle friction, and a mathematical description of the Hausner Ratio is given in ***Equation 59***.

$$Hausner\ Ratio = \frac{\rho_{Tapped}}{\rho_{Free}} \tag{59}$$

Where:

ρ_{Tapped} = The tapped bulk density of the powder.

ρ_{Free} = The freely settled bulk density of the powder.

As in several approaches to quantifying powder flowability, the Hausner Ratio varies depending on the approach used [134]. As such, the value considered indicative of high flowability tends to vary slightly, but a Hausner Ratio below 1.25 is generally considered to be freely flowing, and powders with a Hausner Ratio above 1.4 are generally found to be more cohesive and thus have poorer flowability [135]. No flow at all is expected to occur at a Hausner Ratio of 1.6 or greater [136].

The use of the Hausner Ratio for powder flow analysis has multiple advantages, namely the ease of the experiment. However, there are some notable limitations. For example, wider reading suggests that achieving a stable powder state is difficult due to number of tapping cycles required. This makes the process time consuming and indicates that the results are also subjective to the number of tapping cycles. Thus, creating a potential disparity in the results between identical powder sets [137].

It is reasonable to argue that a Hausner Ratio approach does not correlate well to the mechanical perturbations of powder in a PBF system, as no compressions nor tapping occur. Additionally, further criticism of the Hausner Ratio in literature states that the approach is relatively crude, and Soh et al [138] note that it compares unfavourably to more sophisticated flow measurement techniques. This source notes that powders with similar Hausner Ratios are likely to behave very differently during the spreading process. Thus, there will likely be difficulty in deriving meaningful data to distinguish between two sets of metal powders, limiting the use of the Hausner Ratio for AM.

Another measure of powder flow is the Carr Index. This method evaluates the compressibility of a powder sample, and thus measures particle interactions through their propensity to agglomerate. ***Equation 60*** shows the similar relationship between this measure and the Hausner Ratio [139].

$$\text{Carr Index} = 100 \times \frac{\rho_{Tapped} - \rho_{Free}}{\rho_{Tapped}} \tag{60}$$

Thus, the Carr Index gives a percentage value of the compressibility index, which is indicative of powder flowability, and is often used in the analysis of powders for pharmaceuticals. As with the Hausner Ratio, the lack of compressive forces in a PBF system limits the use of the Carr Index for AM powders.

Angle of Repose:

The AoR describes the steepest angle formed by a piled granular material, relative to the horizontal plane on which it rests. The AoR presents a simple measurement of flowability, as even a visual inspection can be used to intuitively establish how cohesive or free-flowing the powder sample is. For example, Lumay et al [140] showed that granulated sugar forms a low AoR and thus exhibits a greater flowability. In contrast, a fine powdered sugar sample was more prone to agglomeration, demonstrating a less symmetrical form and higher AoR. A graphical depiction of the AoR for the two different sugar types is provided in ***Figure 24***.

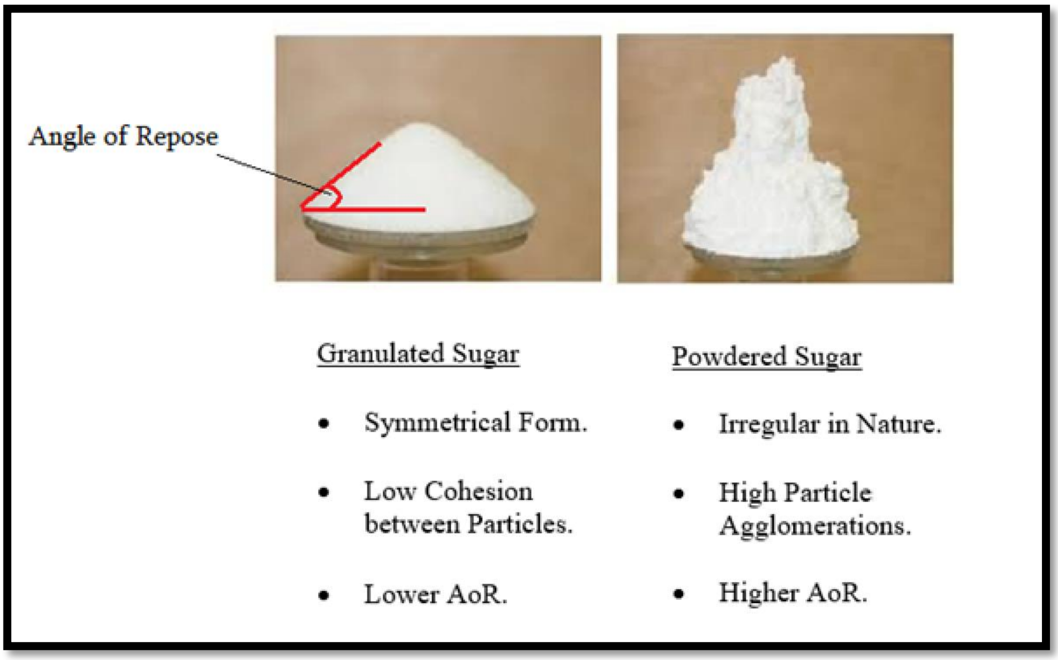

Figure 24 - Practical Comparison between Coarse Granulated Sugar and Fine Powdered Sugar with Respect to the Angle of Repose formed. Adapted from *[140]***.**

As with the Hausner Ratio and Carr Index, different values of the AoR depict a free-flowing powder sample or a cohesive powder agglomeration. These values vary depending on powder characteristics such as the PSD, and experimental factors such as the material and measurement technique used. However, wider reading suggests that the classification of each flow type generally agrees with the values outlined by Ŝimek et al [141], in their analysis of pharmaceutical powders. An interpretation of their work is outlined in ***Table 5***.

Table 5 - Classification of Powder Flow with Respect to the Angle of Repose. Adapted from *[141]*.

Angle of Repose (°)	Powder Characteristics	Flow Classification
25-30	Negligible Cohesion.	Excellent.
31-35	Minimal Cohesion.	Free flowing.
36-40	Mild Cohesion.	Satisfactory – Requires no aid to promote flowability.
41-45	Noticeable Cohesion.	Average or Passable – May require some agitation.
46-55	Substantial Cohesion.	Inadequate – Requires significant vibration/agitation.
56-65	Major Cohesion.	Poor.
≥66	Extreme Cohesion.	Very poor.

Although the AoR is an intuitive measure of powder cohesion, there are some noticeable flaws. For example, whilst the process is more repeatable than the Hausner Ratio and the Carr Index, the assessment of different powders can be limited by the diameter of the funnel nozzle. Furthermore, Schulze [132] concluded that the powder filling stage has implications for the accuracy of results, creating a possible source of experimental error. A further limitation, in terms of its applicability to analysing the behaviour of AM powders, is that the powder is generally measured when static from being poured vertically from a nozzle which, although authors have correlated the AoR formed in this condition to the AoR of the pile in front of the recoater, presents a limited representation of the dynamic flow observed in PBF spreading exercises. It is reasonable to suggest the powder piling behaviour does not directly correlate with the ability of the powder to disperse into a uniform spread layer, which has crucial implications for build quality [142].

Another constraint associated with characterising powder flow behaviour with the AoR is that it provides only a single value to describe the flowability of the tested sample. This contrasts with more sophisticated techniques that can produce a more comprehensive analysis of powder rheology such as the RPA. Despite these limitations of the AoR test, it remains the recommended method for quantifying the flow of metal AM powders by the ASTM [143].

<u>Comparison of Different Powder Flow Characterisation Methods</u>

Research shows that some flow measurement techniques are better suited than others for powder in a metal AM system. It is noted that the compressive forces observed in the Hausner Ratio and Carr Index methods exceed those which are generally found in a PBF system. Furthermore, the stress state of the powder in the AoR analysis is noticeably different to what occurs during PBF spreading. However, the simplicity of the

AoR test gives reasonable grounds to argue for its use as a baseline test for measuring PBF materials. This is supported by multiple examples in literature and industry. Shanbhag and Vlasea [144] used the AoR to characterise Ti-6Al-4V flow for EBM processes, and Carpenter Additive Ltd (a producer and purveyor of metal AM powders) use the AoR to measure flowability in their POWDERFLOW™ device [145].

Considering the similarity of each approach to AM powder flow, an RPA measures three discrete properties in the Avalanche Angle, Surface Fractal, and VER. This theoretically shows the most similar powder dynamics compared to the other methods. However, the current research landscape is almost exclusively populated by the analysis of SLM powder flow, which occurs in an inert atmosphere. This further underpins the motivations of this project, as it emphasises that the powder flow in the vacuum of an EBM building chamber is, as hypothesised, significantly underexplored.

Spierings et al [128] compared the powder flow measurement techniques, and suggested that the RPA provides a relatively accurate measure of differentiating between powders with respect to their suitability for AM processing. They also note that this approach correlates well with optical inspections of power flow, but that the interparticle forces which cannot be observed significantly influence the formed powder layer. This further underlines the need for more sophisticated methods, and that relatively little research exists into quantifying EBM powder flow.

A wide literature review has shown that, from fields as diverse as PBF for aerospace and bio-medical components, to the development and processing of pharmaceutical powders, no single definition of powder flowability exists. Thus, no single technique can quantify powder flow for any arbitrary powder process. Instead, flowability is a product of many different factors inherently connected to powder characteristics, chemistry, and processing parameters. A simple conceptualisation of powder flowability is how prone a sample is to cohesion, so far as more flowable powders show a reduced propensity to agglomerate. Hence, powder cohesion modelling is the first area of interest to quantify powder flowability in a DEM approach.

In this research project, any assessment of flowability for an AM process must firstly define the requirements of the process, and then investigate the influence that the atmosphere in the build chamber has on the mechanical behaviour of powder. Hence, this can be summarised as identifying what constitutes a suitable powder flow in a PBF process, and thus the settings which engender this condition.

3.4 Electron Beam Melting

Until recently, the intricacies of an EBM process were the subject of propriety data belonging to the company who introduced the technique, ARCAM AB, now a subsidiary of GE Additive [56]. Thus, many aspects of EBM have been black-boxed. As the literature review in ***Section 3*** shows, the current research landscape is largely populated with powder analysis for LPBF methods. To develop a benchmark for the best practices of powder processing in PBF systems, a thorough review of EBM is required to address the existing knowledge gaps.

3.4.1 Introduction to Electron Beam Melting

EBM is a PBF process in which a high-powered electron beam is used to create components by selectively melting areas of the powder bed. The bed is then lowered one layer at a time to fuse each cross section of the part until the final design is realised.

To prevent a smoking effect, in which a build-up of charge causes electrons to repel one another and creates a high repulsive force that fills the chamber with powder, the bed of the EBM system is uniformly pre-heated to approximately 40% to 60% of the melting temperature [146]. A diffused beam at speeds in the order of $10\,\frac{m}{s}$ dissipates the charge by bonding the powder particles together and provides a path to ground [147]. All of these steps occur prior to the commencement of the build. Following global preheating a second phase of sintering is performed, this time concentrated locally to the build area.

The two-phase preheating process yields significant advantages, most notably by preventing smoking but also by benefitting the building conditions. As noted by Leung et al [148], and corroborated by Landau et al [149], the local preheating phase reduces the thermal gradient during melting. This nullifies the prospect of the part warping and reduces the residual thermal stresses within the artefact microstructure. Naturally, this improves the mechanical properties of the components, as it raises their strength and increases the thermal and electrical conductivity of the powder. This allows for a lower beam current to be used and achieves a more effective melt between the beam and the powder bed.

Despite the advantages of preheating, there are limitations as to how much it optimises the design build. Leung et al [148] studied the effect of preheating Ti-6Al-4V workpieces and showed that increasing the amount of energy per unit area during preheating adversely effects the building accuracy, raising the error to almost 70μm on some features of the part.

As with all AM builds, the process is governed by the dimensions of the part in the CAD drawing. After importing the model to the AM system, the software slices the component into discrete layers to fabricate each cross section. After the powder supply and preheating, a contour melting pattern defines the perimeter of the component by outlining a 2D layer in the print bed. A hatch melting pattern, characterised by a reciprocating raster trajectory of the beam, creates the internal geometry and cross sections of the model

[150]. The process is then repeated layer-by-layer until the part is complete [151]. A diagram of an EBM system, reproduced from Wang et al [16], is shown in ***Figure 25***.

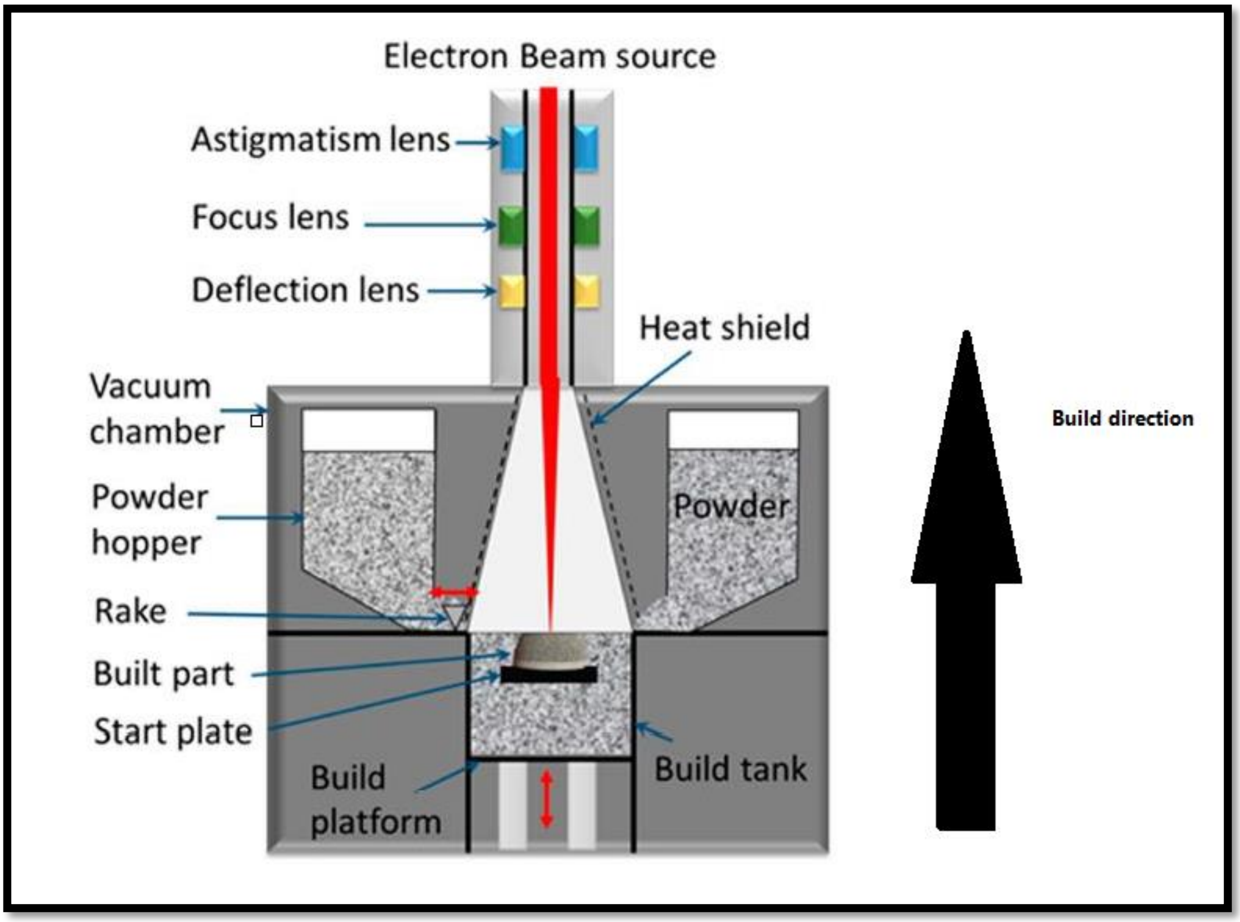

Figure 25 - Diagram of an EBM System. From *[16]*.

Smith et al [150] notes that during the contouring phase a constant beam power and scanning speed is used to formulate the model outline. However, during hatching, these parameters are adapted in response to the powder melting conditions to ensure that steady melt pool properties are maintained. Owing to the number of variables in the EBM build, notably during the preheating stage and considering the contour and hatch melting phases, the parameters used have a significant influence on the interaction between the electron beam and the powder bed.

In this project, a strong interest is held in the powder delivery system used to feed the bed in the build chamber. Specifically, the parameters which characterise the spreading system including the recoater shape and speed and the supply mechanism.

Unlike the other major PBF process, SLM, which takes place under an inert atmosphere, the entire EBM process occurs under a controlled vacuum (2×10^{-3} mbar) [152], as gas atoms within the manufacturing chamber would cause the electrons to scatter. Additionally, the vacuum precludes the inclusion of impurities within the build chamber and thereby strengthens the mechanical properties of the built parts. The vacuum conditions also serve to reduce the prospect of the component oxidising.

Compared to SLM, an EBM process has a slightly lower resolution, which defines the smallest detail of a component geometry that can be captured effectively, and a higher rate of deposition, due to the larger melt pool of the electron beam. Typical spot sizes for an electron beam are about 350 µm, compared to around 50-75µm for the SLM laser [153]. After completing the part, any unfused powder can be recycled back into the process.

A review of the current research landscape indicates that the EBM process is a relatively recent innovation, and that it remains a developing technology of interest to the wider manufacturing community. Galati & Iuliano [154] numerically modelled the EBM process, and found that current optimisation efforts were largely in response to the findings of trial and error investigations. Thus, providing further evidence of an opportunity for a parametric study into EBM manufacturing solutions.

As shown in ***Subsection 3.3.1***, there is no single correct method of analysing powder flow in metal AM. This is particularly noticeable in the review of EBM, as the black box nature of the approach and the lack of research into powder flow in a vacuum limits the ability to establish best powder spreading practices. Furthermore, despite the use of EBM to create parts for applications as diverse as bio-medical implants and the aerospace sector, the further development of the technology remains constrained by the limited number of materials that can be employed in the process. Further analysis of EBM, with respect to considering the advantages and limitations associated with the technique, is provided in ***Appendix A***.

3.5 EBM Areas of Further Exploration

A comprehensive review of the EBM research landscape has highlighted several areas of exploration, which could serve to underpin the approach to optimising the technique in this project.

3.5.1 Powder Flowability in EBM (Vacuum Flow of Powder)

Whilst many authors have sought to optimise EBM parts by modifying the build parameters [57, 155], research has confirmed that the multi-physics nature of powder flowability remains underexplored. However, industrial communication with Wayland Additive Ltd has established that flowability is approximately doubled in an EBM vacuum, when compared to the conditions in an atmosphere. Based on the findings so far, it is evident that control of the flowability could feasibly improve the powder bed formed.

Only one resource can be found to compare AM powder flow in an atmosphere against a vacuum. Espiritu et al [18] characterised powder in argon and the vacuum environment using a rotating drum. They observed that, along with powder properties, the different environments had a pronounced influence on the flow behaviour. Furthermore, they remarked that a controlled presence of finer particles may improve the flowability of coarser elements. Interestingly, they suggested that the quantity of fines may reach a critical point, after which the cohesive forces reduce the particle separation distance and lower the overall flowability. This has implications for another prospective area of further research into the proposed critical value of fine particles in a PSD, as discussed previously.

Espiritu et al [18] did not find a noticeable difference in the dynamic AoR formed by the powder avalanche in each environment. Thus, the spatial fluctuation, a similar concept to the surface fractal of the powder surface in the drum, was used to characterise the flow. The spatial fluctuation measures the powder surface roughness as the ratio of the length of the dynamic powder during rotation, to the length of the stationary powder inside the drum [18], as demonstrated in ***Equation 61*** and ***Figure 26***.

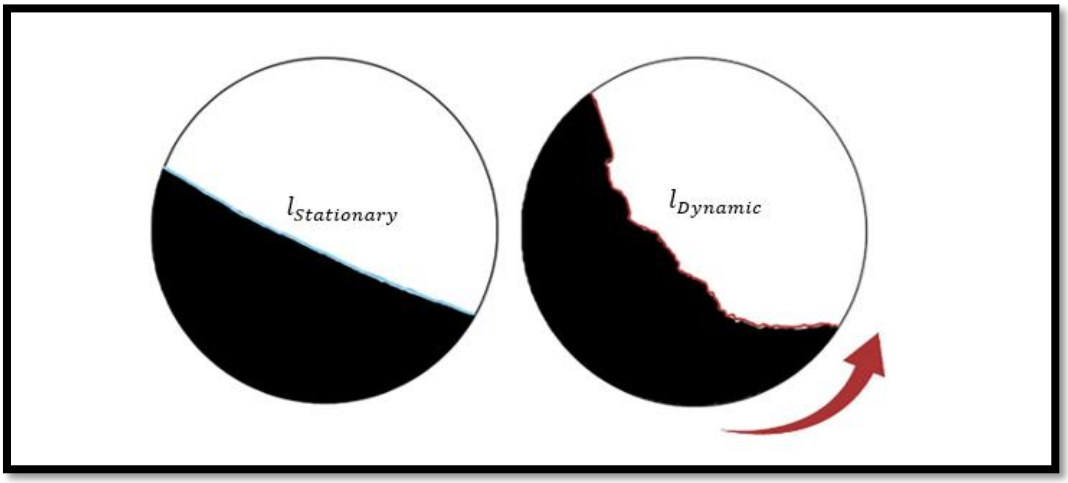

Figure 26 - Stationary and Dynamic Powder Flow to Determine Spatial Fluctuation. Adapted from *[18]*.

$$Spatial\ Fluctuation = \frac{l_{Dynamic}}{l_{Stationary}} \tag{61}$$

A spatial fluctuation approximating unity is indicative of a smoother profile and a freer flowing powder, whereas a spatial fluctuation value exceeding unity suggests a more cohesive powder demonstrating a heterogenous surface profile.

Industrial work suggests that rotating drum speeds can be correlated to linear recoater speeds in AM [156]. However, Espiritu et al [18] remarked that a comparative study of spreading in air versus a vacuum is required to better understand and optimise the process.

One option to model the effect of the build environment on powder spreading was to implement CFD-DEM coupling. As noted by Chen et al [10], the DEM modelling and the CFD-DEM combined approach generally focus on different elements of simulating the PBF process. DEM-only models tend to focus on the powder spreading phase, whereas the CFD-DEM coupled method accounts for thermodynamic processes such as the melt pool formation [157, 158, 159].

As outlined in ***Subsection 1.2.3***, this project concentrates on the spreading of powder which is considered to commence at the delivery of the powder to the substrate and conclude at the point immediately prior to melting. Thus, leveraging CFD-DEM applications to investigate powder melting strategies is both outside of the research interests in the project, and given the computationally intense nature of CFD-DEM coupling, also beyond the capabilities of the time and resources available.

Despite the constraints in evaluating the effect of atmosphere on powder flowability, a concerted effort to investigate the subject further should be made a priority in future research. Understanding and controlling powder flow is a key approach to optimising metal AM builds, and the solutions generated are likely to be of paramount interest to both industry and the wider AM community [18].

As noted many times, flowability is not a single calculable metric and instead depends on the requirements of the AM process. In the context of EBM, defining powder flowability is further complicated by the vacuum environment of the process. To yield meaningful results from this research, it would be necessary to identify the requirements of powder flowability in EBM, and then develop a technique to quantify it mathematically, parametrically, or practically. The overall aim of this approach would therefore be to establish and achieve a value or condition of flowability that serves to optimise the design build.

3.5.2 Powder Recycling and Flowability

Any unfused powder from the build process is recycled for the following layers. A distinction is drawn here between fresh powder from the hopper and the recycled powder which has previously been spread but not melted. The differences in behaviour of the fresh and recycled powder when used together for a given part build would significantly affect the spread layer in terms of PSD, morphology, and flowability. Hence, the proportion of fresh and recycled powder is another relevant parameter in the optimisation of PBF spreading processes.

Concerns arise with the cumulative effect of reprocessing recycled powders. This is predominantly due to the physical and chemical variations over time, which occur due to the inclusion of semi-melted particles. Another concern is presented by impurities, which may contaminate the powder during handling and through exposure to the environment outside of the AM system.

From a commercial standpoint, there is a strong economic motivation for optimising EBM powder processing. Nouri and Sola [160] claimed that 95-97% of the powder in the bed goes unused. This means that most of the powder must be recycled, and that appropriate processing parameters must be used to ensure this is possible. According to Powell et al [161], metal AM powders can cost between £30 and £300 per kg depending on the material used. Assuming a 3-5% yield, a dramatic cost is incurred for the design build. This further underlines the importance of recyclability in the build process [162].

3.5.3 Powder Delivery Systems

Wider reading highlights a significant discrepancy between the modelling of the powder supply in EBM systems with the DEM, and the powder delivery method used in reality. Publications using the DEM almost exclusively deliver powder to the substrate with the rainfall technique [10, 17, 21], where particles are allowed to freefall from a given insertion volume under gravity. In commercial AM systems, the powder is delivered directly to the recoater via a hopper or supplied by the action of a feed piston [163].

Although rare, EBM machines which use a moving funnel to supply powder to the bed have also been observed in industry. In this set up, powder is held in a reservoir and deposited along the front face of the recoater, forming a powder heap which is spread across the substrate after the funnel clears the recoater path. No previous work using the DEM to model a moving funnel approach has been sourced, either from DEM literature or industrial publications. This is proposed as being attributable to the moving funnel being subject to propriety data.

Compared to alternative powder supply methods, such as the use of a hopper or piston-operated supply table, the numerical modelling of the funnel technique is liable to generate highly informative data on powder dynamics and discharging behaviour, particularly with respect to cohesive powder interactions prior to deposition, and the proclivity for size-sorting and segregation during powder delivery. Thus, the author can attest here with some confidence that a DEM study presents a novel approach to optimising powder spreading in AM systems.

3.5.4 Substrate Surface Profile and Influence on Spreadability

In conjunction with the AM build and powder parameters, the powder bed substrate profile is also likely to influence the quality of the spread layer. In literature, the majority of DEM set ups spread powder over a smooth platform modelled with a flat plane [12, 21, 32]. In practice, the spreading surface is likely to be much rougher than the profiles of the digital twin models, as it is the product of powder fused from the previous build layer. Research has shown that the recipient surface layer has implications for the quality of the melt pool and the track formed by the laser in SLM systems [164].

Few researchers have investigated the effect of the substrate geometry on PBF systems. Most notably, Xiang et al [165] modelled a rough surface comparable of that to a laser produced AM part. They used microscopy to characterise the surface of a typical laser generated substrate and noted that it was heterogenous and approximately periodic in form. To recreate this in the DEM, the authors added striations to their model. Surface roughness values for the top layer of SLM parts in the as-built condition generally have arithmetic mean values less than 15µm [165, 166, 167]. Thus, Xiang et al generated roughness values of 0µm (a smooth, flat substrate with no striations), 3µm, 6µm, 9µm, and 12µm to determine how substrate morphology influences the powder layer quality [165].

Using a constant 5 $\frac{\mathrm{cm}}{\mathrm{s}}$ recoater velocity, they observed that the surface homogeneity of the spread layer deteriorated with increasing substrate roughness. A significant increase (≈ 1µm) occurred between the flat substrate and the 6µm rough substrate, with a much smaller increase of 0.1µm between the 6µm rough substrate and the 12µm rough substrate. Interestingly, the SVF increased by approximately 8% at the 9µm rough striated substrate, compared to the flat plane. One theory as to how this occurs is that the undulations require more particles to fill a given volume, and thus finer particles occupy interstices and thereby raise the packing density. This is also suggested by the authors, who assert that the thickness of the spread layer increased with substrate roughness. Thus, indicating more powder in the region of interest and coinciding with the increased SVF measured.

The increase in SVF with substrate roughness is proposed by the authors as being due to the velocity profile of the particles in front of the spreader. It is noted that the range of particle velocities is generally much larger in the smoothest powder bed. This sees the particles flow more continuously during recoating and the velocities can be approximated to the spreading speed. Potent force chains are formed which push the particles along uninhibited, limiting deposition and leaving areas of porosity in the powder bed. Conversely, the rougher substrate caused local particle interceptions which lowered the velocity of the particles in the heap in front of the spreader and increased the powder deposition.

A similar rationale is proposed for the powder layer surface roughness increasing with the substrate roughness, as the strongest force chains between particles were observed in the roughest bed (12µm). This indicated a more pronounced interaction between the elements comprising the powder bed and thus, more stochasticity resulting in a less uniform layer.

A parametric study was performed on the 6µm rough plane and showed consistency with other DEM-AM research publications, indicating that the packing density decreases at higher recoater speed. As previously discussed, this was theorised as being due to the more stochastic velocity regime of the individual particles, resulting in more intensive collisions occurring between elements in the powder bed.

No correlation could be categorically established between the recoater velocity and the uniformity of the spread layer. However, the effect on the spread layer was small relative to the change in recoater speed. Furthermore, it is noted that the inherent anisotropy of the powder layer is likely to be exacerbated by the stochastic flow behaviour.

Xiang et al [165] investigated the influence of the surface roughness orientation relative to the spreading direction, as in an AM design build the laser track direction will differ both between and in the layers. Thus, influencing both the powder deposition to the top layer and the homogeneity between and within the layers of the part. A clear difference was observed when the orientation of the striations was adapted. A 67° rotation of the substrate texture generated striations that were broadly diagonal to the direction of powder flow. According to the author's spreading system, striations at 0° are transverse to the flow direction and 90° striations would be aligned with spreading. Using the 90° substrate, the SVF was approximately 3% lower than in the same experiment but with the striations transverse to the powder flow, which the authors suggested was due to more dynamic spreading pushing the powder along and limiting deposition. No discernible difference was observed in the roughness of the powder surface profile between the transverse striations and the surface rotated through 67°.

No explanation is provided for the 67° angle through which the substrate was rotated. It is assumed this was a baseline test to create striations that were neither fully inline nor fully transverse to the flow. Xiang et al recommended that a consistent angle is maintained between the laser scan track and the powder flow direction [165]. This is thought to minimise the variability and increase the effectiveness of the spreading operation. Regarding melting, Xiang et al practically tested samples with various orientations between the final and penultimately fused layers. The graphic in ***Figure 27*** displays these orientations and has been reproduced directly from the source [165].

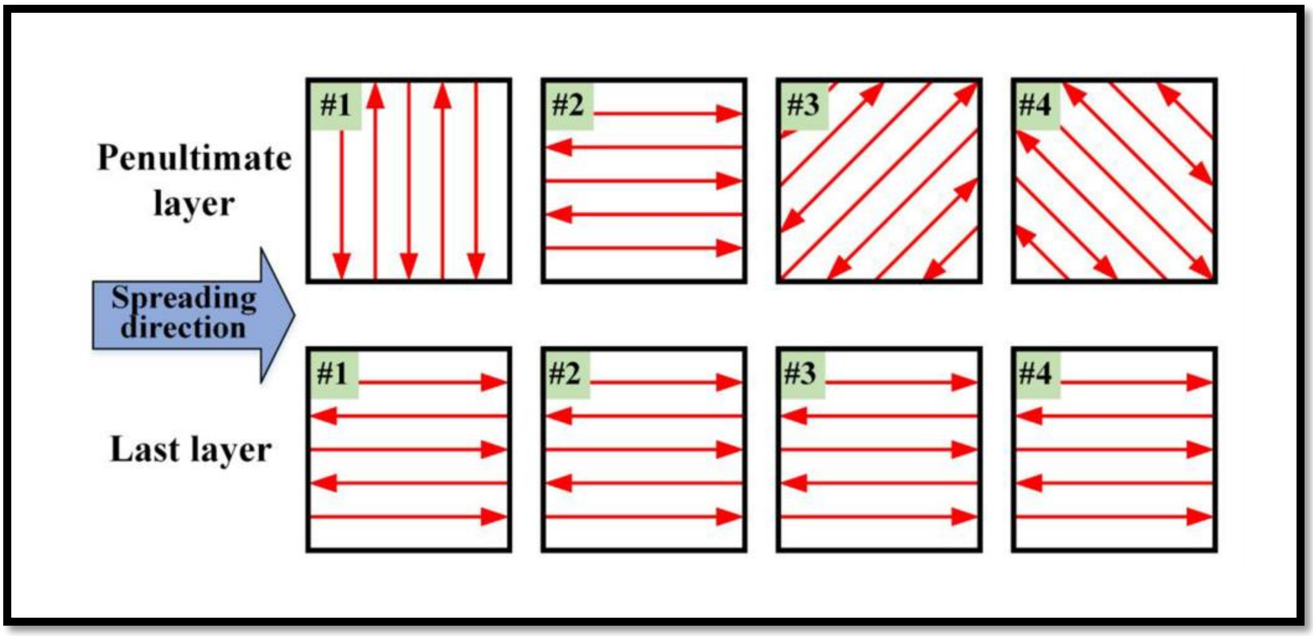

Figure 27 - Different Orientations of Surface Roughness between the Penultimate and Final Layers of an AM Build. From *[165]*.

In agreement with the results found by the DEM, microscopic inspections of the surface indicated greater powder deposition on the penultimate layer of Sample #1, where the substrate roughness is perpendicular to the recoater path. This conforms to the higher packing density observed in digital modelling. No significant difference was observed between Sample #3 and Sample #4 pertaining to the overall layer quality. As expected, this shows little difference in results between the 67° angle and 135° angle of the laser track to the spreading direction.

Based on the results, testing of more incremental roughness orientations would be of interest to determine the point at which the rate of the powder deposition diminishes. Further interest is held into the effect the surface roughness orientation has on the layer thickness. Excessively thick layers inhibit fusing, as the melt pool may not penetrate deep enough into the bed, causing porosity and discontinuity in the component cross section. As with all aspects of PBF, powder deposition and layer thickness must be considered in totality with the rest of the system.

Realistic SLM surfaces were also used by Phua et al [168]. They generated build layer topographies with a CFD software code to model the melting and solidification of Ti-6Al-4V workpieces, and then imported the samples to a pre-loaded layer of powder to accurately reproduce the substrate. In total, six samples were produced to model the different substrates formed in the AM process. Unlike Xiang et al [165], who used a PSD associated with SLM from 15µm to 45µm, Phua et al used wide PSD sets ranging from 20 µm – 63 μm, 45 μm – 106 μm, and 45 μm – 150 μm [168]. The range of PSD sets served to evaluate the influence of the particle sizes on spreading over the rough texture. A blade type recoater spread the powder at a velocity of $11.5\,\frac{\mathrm{cm}}{\mathrm{s}}$. Particle segregation in the spread layer was also investigated by evaluating the PSD in a given region after spreading against the input PSD for the full model.

Phua et al [168] did not investigate the SVF due to the small layer thicknesses used, which measured 1-2 particle diameters thick. Instead, coverage was determined by measuring the volume of deposited powder. Phua et al [168] remarked that more powder was required to adequately recoat the powder bed surface when a realistic substrate is used, compared against a flat plane. This agrees with the hypothesis of Xiang et al that some powder becomes trapped in the striations during the spreading regime [165]. It is found in both publications that the powder coverage increased almost linearly with the degree of surface roughness [165, 168].

Interestingly, the authors observed that the proclivity of finer powders to occupy the asperous regions contributed to them being generally superior at coating the powder bed, despite being inherently more cohesive and thus having a lower flowability. This has wider implications for existing research on flowability, confirming that flowability cannot be used in isolation to control the quality of spreading. Notably, the authors acknowledge that using progressively finer powder sets is not a viable approach to powder bed optimisation, as the interparticle forces would give rise to agglomerations. Thus, giving further credence to the hypothesised existence of a proposed critical fraction of fine powders in a PSD.

Segregation analysis indicated that coarser particles are preferentially deposited later in the spreading regime, which is likely due to the tendency for finer particles to lodge in the valleys of the substrate. It is remarked that in a commercial AM environment, this effect is expected to be even more pronounced as the spreading regime takes place over longer distances than in the DEM set up used by Phua et al [168], and general DEM-AM models.

The gap height between the recoater and the layer is also varied during spreading due to the heterogeneity of the surface profile, limiting the deposition of the coarser particles, and suggesting they are filtered out along the recoater path. The reverse effect was observed at increased gap heights, as larger particles were added to the layer uninhibited. The results showed that the effect of particle size filtration on segregation depends on the layer thickness used, and that substrate roughness has a stronger influence on segregation at lower layer thicknesses [165, 168].

Although the PSD used by Phua et al [168] is more closely associated with EBM, the methodology is still heavily laser based. No sources can be found for modelling the roughness of EBM components during the design realisation process. It is reasonable to suggest there is merit in further pursuing this study, as the range of roughness values for as-built EBM parts are generally recorded as being higher than for SLM components, between 20 μm – 50 μm [169, 170, 171, 172, 173]. Thus, modelling the effect of the substrate roughness on powder spreading is likely to produce results that are of intertest to industrial EBM processes.

The work of Phua et al and Xiang et al disrupt the findings of current DEM methods, as they demonstrate a clear difference in the powder coverage when realistic rough substrates are spread over compared to the more common and idealised flat plane models [165, 168]. It is noted that a striated surface topography retains more of the powder during the spreading regime and that, contrary to the findings of several authors [14, 126, 128, 174], finer powders can sometimes enhance the surface coverage despite their proclivity to coalesce together and thus lower flowability. This reinforces the fact that powder flowability must be considered in conjunction with the powder properties and spreading parameters of the build in efforts to optimise an AM powder bed.

If possible, a combined study of varying substrate roughness profiles, situated in a CFD-DEM model comparing the influence of atmosphere against the vacuum flow of powder, is likely to produce a robust digital twin of a practical EBM process. Literature suggests that no such previous study exists, but that the results of such research would have wide-ranging implications for commercial AM and numerical analysis of PBF systems.

Another recommendation is to ascertain if correlations exist between the roughness of the spread layer and the particle segregation, which may underpin research into the hypothesised critical fraction of fine powders in a PSD, subject to the processing parameters. It would also be interesting to determine what effect, if any, the delivery mechanism has on powder bed quality when realistic substrate surfaces are used. As powder segregation in the delivery chamber, for example from a dynamic deposition process, could theoretically affect the segregation observed in the spread layer.

In summary, a review of EBM processes has highlighted an area of active research, with many avenues ripe for exploration. Key subjects of interest are held in generating realistic substrate surface to model the powder spreading over, the effect of the atmosphere on dynamic powder behaviour in the build chamber, and the influence of the deposition method on powder quality metrics such as the SVF, segregation, and the surface roughness of the spread layer.

3.6 Review of Cohesion and Friction Parameters for Model Calibration

Research highlights the two key parameters that can be adapted to induce a change in the AoR formed: cohesive properties, such as the CED or surface energy depending on the contact model used, and frictional properties such as the rolling and sliding friction coefficients ($\mu_{Rolling}$ and $\mu_{Sliding}$ respectively) [175]. Phua et al [168] noted the friction between the substrate and the powder influences the coverage achieved. They observed that $\mu_{Sliding}$ was the most significant influence, as higher values of particle-plane friction impeded the powder motion to the extent that significantly more material was deposited to the substrate. Thus, it is likely that the coefficient applied to $\mu_{Sliding}$ controls the dispersion of the powder and the diameter of the pile formed in AoR analysis.

As noted, the value of Young's Modulus of Elasticity is often scaled in the modelling of DEM-AM powders to enable computational savings, and multiple authors note that the sensitivity of results is negligible for a large range of Young's Moduli [176, 177, 178]. However, little data exists to clarify by how much the value of E can be reduced. Cleary [179] suggested that the particle behaviour is independent of E when the overlaps are kept beneath 0.5% of the particle radius.

For example, Geer et al [75] modelled SS316l powder with a PSD of 20 µm - 75 µm, and found setting E between 33 MPa and 828 MPa created overlaps of 0.5% and 0.1% of the particle radius respectively. Hence, they suggested an E value of 200 MPa for powder spreading models. This was to ensure that the increasing contact forces from the recoating operation did not create overlaps exceeding the 0.5% threshold. The authors also note that adding a rolling friction property to the simulation code was required to more faithfully reproduce the AoR, which contradicts literature [180, 181]. It is theorised that the influence of rolling friction on the AoR formed was due to the aspherical particles used by Geer et al [75].

To aid the calibration processes in these simulations, reference values of $\gamma_{Surface}$, $\mu_{Sliding}$, and $\mu_{Rolling}$ have been sourced from literature and presented in ***Table 6***.

Table 6 - Reference Values for Adhesive Surface Energy and the Sliding and Rolling Friction Coefficients.

Source	Material and PSD	Value of Adhesive Surface Energy $\frac{\text{mJ}}{\text{m}^2}$	Values of Sliding Friction	Values for the Coefficient of Rolling Friction
Yao et al [182]	SS316l. Various PSDs used.	1	0.6	0.085
Meier et al [22]	Ti-6Al-4V. 20 µm - 44µm.	0.1-1	0.4	Not stated.
Han et al [20]	Hastelloy X [183]. 20 µm - 50 µm.	Range: 0 – 2, optimum 1.6	0.4	0.005
Wu et al [48]	Ti-6Al-4V. 13 µm - 86 µm.	0.75	0.54	0.0033
Chen et al [181]	SS316l. 18 µm -280 µm.	0.097	Range: 0-1, optimum 0.62	0.01 Range: 0.01-0.2
Zhang et al [63]	Aluminium Oxide Ceramic AM powder (Al_2O_3). 20 µm - 80 µm.	0.15	0.34	0.05

3.7 Review of the Concentration of Fines in EBM Powder Size Sets

Numerous researchers have also investigated the influence of particle size on the quality of the formed powder bed in EBM systems. Sullivan et al [184] practically analysed a range of tool-steel grade powder sizes from 15-45 µm (typical of SLM), 45-105 µm (typical of EBM), and a mixture of 50/50% weight mixture of the two. Interestingly, they noted that with respect to the quality of the formed parts, finer powders culminated in mechanically superior, denser components, with lower average surface roughness values. This is noteworthy due to the atypicality of this size range for EBM processing and merits further discussion regarding the motivation of potential numerical investigations.

Similarly, Wang et al [185] investigated relatively fine powders in the range of 20-60 µm in EBM processes in their analysis of how process parameters influenced melt pool stability and defect formation in the formed parts. They found that thinner powder layers (40-60 µm) generally produced better quality melt tracks and that thicker layers (exceeding 100 µm) increased the presence of voids. They also note that layers thinner than 60 µm reduced the incidence of spheroidisation, a phenomena in which molten metal forms into spherical droplets instead of continuous tracks during the melting process. It is highly unlikely, particularly when considering the overlaps between constituent elements in DEM investigations of PBF powder beds, that such thin layers could be modelled at the coarser particle sizes observed in EBM processes, potentially highlighting a research area to investigate a powder bed comprised predominantly of fines below the typical range of EBM powder.

Arguably the most significant research was performed by Karlsson et al [186], who explored the EBM processing of two different Ti–6Al–4V powder fractions: the typical range of 45-105 µm and a finer range of 25-45 µm. Their primary finding, interestingly, was that it was feasible to use the finer range for EBM design builds. They further hypothesised that the use of the finer powder improved the surface resolution of the generated components, suggesting it was advantageous in remedying the topological roughness common in EBM parts. An SEM image of the two powder size samples is provided in ***Figure 28***.

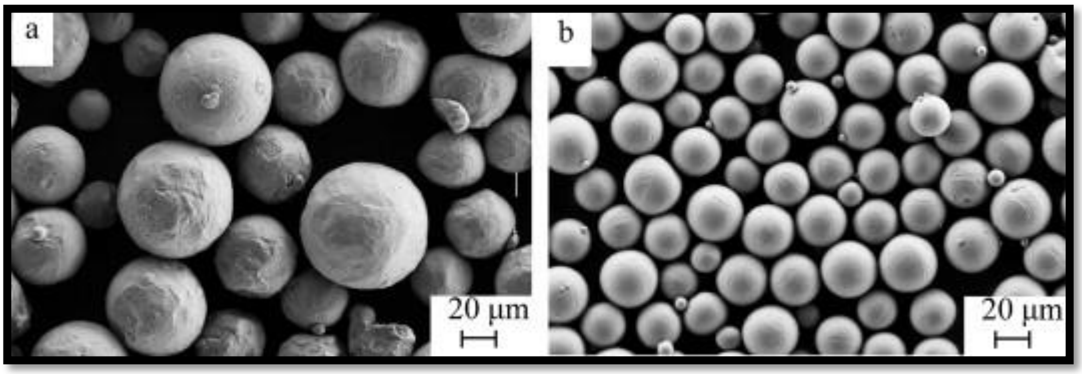

Figure 28 - SEM Images of Two Ti–6Al–4V Powder Size Samples. Adapted from *[186]***.**

Interestingly, the authors analysed the Ti–6Al–4V powder in the range of 45-105 μm and found that a significant percentage of the particles characterised were below the 45 μm size stated. Although it is difficult to ascertain with certainty from the image (***Figure 29***), it appears that at least approximately 30% of the elements tested were below 45 μm. The authors suggested this may be due to the recycling effects of powder during the spreading operation. Thus, it is feasible that finer particles may already populate commercial EBM powder beds than the typical size range quoted.

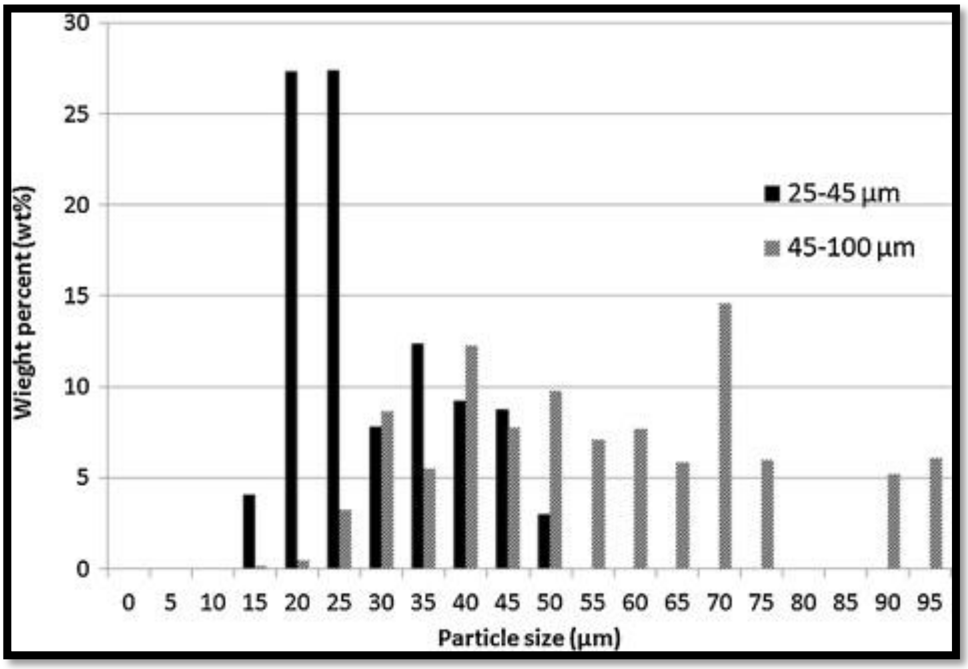

Figure 29 - Size Range of Ti-6Al-4V Powder as Inspected by** [186]**.

The authors concluded that no significant differences, with respect to the mechanical or chemical properties of the built components, were found between varying the range of fine and typical powder sizes, or by varying layer thicknesses using either fraction of powder inserted. They did, however, hypothesise that further refinement of EBM processes to use powder in the size range of 25-45 μm is a viable technique to improve the topological resolution of EBM parts and resolve the differences in SLM and EBM component surface quality.

Strondl et al [187] corroborated the findings of Karlsson et al, noting that the Ti–6Al–4V powder they analysed in EBM processing became progressively finer with powder recycling across multiple reuse cycles.

Furthermore, interparticle attractions such as capillary effects, and van der Waals and electrostatic forces, are significantly more pronounced with decreasing element size. Thus, the focussed modelling of fine particles permits a more detailed study of contact modelling and cohesive powder interactions that are likely to be overshadowed in larger particle distributions. This, in turn, is likely to yield significant insights into powder spreadability and layer uniformity.

The literature reviewed in this section shows that, whilst comprehensive investigations of utilising finer powders than the typical range stated in EBM processes remain limited, further investigations are required to fully comprehend how utilising finer particles influence the quality of the spreading process. Specifically, existing models of EBM systems using the DEM typically do not account for recyclability and thus the proclivity for particles to break down into finer elements during processing, suggesting a possible oversight in modelling methods with respect to the size range inserted to digital models of powder beds.

3.8 Executive Summary of the Existing Research Landscape

The complete review of literature has highlighted a number of active research spheres into DEM solutions for AM processes. Current research into powder spreading can be broadly categorised into two investigative methods: the analysis of powder properties such as the PSD and morphology of constituent elements [14, 188], and the analysis of system processing parameters such as: the recoating speeds and influence of using blade type spreaders against counter-rotating rollers [63, 96], the effect of varying the layer thicknesses of the design build [20, 21], and the study of laser absorption and thermal modelling of the molten pool formed during the melting of the spread layer [24, 189].

In this research, the metrics used to quantify powder bed quality: the surface roughness, SVF, and segregation between polydisperse elements in the powder bulk, have been prioritised for consistency with published literature. As noted, the scope of the project is confined to the delivery and spreading of the powder. Other measurements, such as layer thickness uniformity, are crucial to ensuring successful laser absorption and thus preventing the occurrence of microstructural defects in the part. However, as the melting is not modelled in this project, variations in layer thickness are less meaningful as they are typically analysed concerning how they influence melt pool formation. For similarly obvious reasons, investigations of the powder surface topography after the melting process, and how residual stresses and distortions arise due to thermal expansion and cooling cycles, are also omitted.

Note that the above examples for each investigation method are not exhaustive. As stated previously, more than 130 different processing parameters can be adapted to induce a change in the built component [31], covering many of the complex multi-physics operations too numerous to outline in full. Thus, the emergence of the DEM for powder bed simulations has obviated the need for expensive trial and error calibrations and culminated in the rapid growth of the DEM-AM research sphere.

The existing literature has found many correlations and contradictions in configuring parameters to engender optimised spreading conditions. However, authors unanimously agree that a high SVF and homogeneity in the profile of the spread layer are key quality indicators constituting a suitable powder bed for AM processes [10, 12, 20, 174, 180, 190]. The processing steps required to achieve these conditions is debated, such as by the merits of inducing a wider or narrower PSD to the bed, and the effect of particle sphericity on the flow behaviour and propensity for powder to agglomerate.

Consensus suggests that a powder bed with a deficiency of fines will exhibit a lower SVF, by inducing a higher amount of void space between the neighbouring coarser elements that would otherwise have been filled [101]. Conversely, saturating the powder bed with fines causes the powder to agglomerate into clusters [126, 191]. The adhesive interparticle forces that cause these agglomerations are manifested by several physical phenomena, namely, the influence of a capillary action between neighbouring elements, electrostatic interactions, and van der Waals forces [22]. Multiple sources have also shown that, for the size ranges of powders used in PBF processes, van der Waals forces dominate electrostatic interactions [22, 192]. The work of Haeri et al [12, 17], Nan and Ghadiri [32], and Parteli and Pöschel [49] shows that manipulating the PSD is a key route to optimising the AM powder bed.

With respect to system variables, a consensus has been generally reached that a blade type spreader diminishes the uniformity of the spread layer by inducing a dragging effect to the powder surface [12, 17, 96, 193], and that whilst a roller may benefit the packing density by compaction, it is liable to cause swelling in the melted powder regions to the detriment of the built part [150].

Research has shown a unanimous agreement between authors that a superior powder bed is achieved at lower recoating speeds due to the less stochastic rearrangement of the constituent particles [12, 21, 49, 63, 117, 194], but that this impedes manufacturing operations by reducing the production throughput and incurring economic costs that must be considered from a commercial perspective. These simple examples afford credibility to the statement that, as in all engineering, no ‘perfect solutions’ exist. Only trade-offs and compromises that gave rise to the best possible conditions for a given AM design build were realistically attainable from the project findings. Thus, considering the research to this point holistically, a number of informed assumptions had to be made when developing the digital models of the spreading process, and the number of variables giving rise in causation reduced as much as possible to derive meaningful information for the AM process.

As reviewed at length in ***Subsection 3.7***, interparticle cohesion is a product of many variables relative to both particle size and environmental conditions, and has a pronounced influence on the ability of the spreading operation to engender conditions which promote successful AM builds. Several knowledge gaps exist as highlighted by how humidity, electrostatic interactions, and van der Waal forces behave differently between powder elements in an inert gas and in a vacuum. Along with the effect of the build chamber atmosphere, The previously discussed PSD, and the proclivity of finer powders to coalesce, is another research area in which conflicting literature presents a knowledge gap.

A knowledge gap is presented in the literature, as no evidence has been found to suggest that any digital modelling has ascertained the influence of the powder delivery system on the quality of the spread layer in AM powder beds. It is proposed that, due to the nature of proprietary information regarding machinery configurations, and more specifically, the powder deposition mechanisms used on EBM machines in industry [56], this topic is unlikely to receive any significant research in the short to medium term future. Thus, presenting an opportunity for a study that is likely to yield significant findings for dissemination to both commercial entities and the wider DEM-AM research community.

As stated previously, the powder deposition method in DEM-AM investigations has been performed exclusively via the rainfall technique, in which the powder is allowed to fall under gravity to the substrate in a given insertion volume as commanded by the DEM script [10, 17, 21]. In commercial PBF systems, powder is delivered using a moving funnel, a table that moves vertically to supply powder directly to the recoater, or fed to the substrate via a hopper [59, 60, 163, 195]. This highlights that the idealised rainfall deposition technique does not provide an accurate reflection of the powder delivery process, and thus presents a significant oversight with respect to generating digital twin models with a strong fidelity to commercial AM processes.

The work performed in this thesis, specifically in ***Section 7***, provided a novel contribution to addressing this knowledge gap by delivering the powder more realistically than previously observed in DEM-AM investigations. Thus, improving the fidelity of the digital twin model and demonstrating a more accurate reflection of the powder spreading process. The work is underpinned by the extensive review of previous DEM-AM investigations and the fundamental principles of powder dynamics performed throughout ***Section 3***.

The realistic model of the powder delivery process is likely to provide highly useful information for the wider DEM-AM research sphere, as a basis for increasing the accuracy of powder flow modelling by accounting for the interparticle forces and segregation effects engendered by the deposition process. Prior to the simulation, it was theorised that constraining the flow during deposition, as observed in a moving funnel and in contrast to the free-falling rainfall method, was liable to increase the powder agglomerations prior to spreading and thereby bring about a different initial powder state than previously found in DEM-AM literature. Thus, increasing the fidelity of the digital twin by accounting for how the spreader must overcome cohesive forces in the inserted powder to disperse it across the substrate.

Throughout the research, a number of knowledge gaps pertaining to both powder and AM processing factors have been identified. The literature review has highlighted multiple knowledge gaps that motivate further research in the analytical chapters of the thesis:

- Conflicting research exists regarding how the PSD and morphology influences the cohesive behaviour of powder under different atmospheric and processing conditions, and in relation to the powder characteristics. In DEM-AM investigations, accurate modelling of powder agglomerations is essential to produce robust spreading simulations depicting realistic flow behaviour. Suitable contact models, with parameters calibrated against realistic flow behaviour, are a prerequisite of any digital powder spreading model. A concentrated study, on controlled size insertions and evaluating the effect on the resulting spread layer, would provide beneficial insights.

- In the DEM-AM research landscape, the spreading of the powder in EBM systems is often idealised as occurring over a simple flat plane. This is inaccurate, as it fails to account for undulations and surface morphology incurred by powder spreading over previously melted layers. Modelling of powder spreading over realistic substrate surfaces in EBM would address this knowledge gap.

- Flowability, in the context of AM powder spreading, is not a defined quantifiable metric. It is, instead, a condition or state of powder that is best described by how well the flow of the powder supports conditions for optimising AM design builds.

- Although crucial to the flow of powder and thus the quality of the AM build process, the effect of the vacuum environment on EBM powder spreading is not well understood. There is currently insufficient literature comparing powder spreading in an inert gas atmosphere against vacuum conditions for PBF methods.

A review of all of the identified areas of exploration that may serve to deliver optimised DEM-AM powder beds is provided in ***Section 4***.

4. Outlining Original Areas of Further Research

This section outlines the areas of further research as identified by the thorough literature review performed in the previous section. ***Subsection 4.1*** examines six prospective areas of further research that could viably serve to present novel findings in DEM-AM investigations for PBF methods. An example of required research in terms of validating the simulation method against digital powder flow analysis is also briefly introduced in this section. Subsequently, ***Subsection 4.2*** builds on the previous section by shortlisting each possible research avenue against a range of explained criteria, to ascertain the viability of the chosen solution. Finally, the scoring process as part of a decision matrix operation is performed in ***Subsection 4.2.1*** to determine the selected research area for further investigations.

4.1 Prospective Research Subjects

Research has identified multiple metrics and conditions that measure the quality of an AM powder bed. One of which is the SVF, which relates the space occupied by the powder in the bed to the volume of the voids between the powder elements. The second metric is the surface roughness, characterised by undulations and a heterogenous powder profile at the top of the spread layer. Another measurable property is the segregation in the powder bed, which is characterised by a disproportionate skew of particles of selected sizes to specific regions in the spread layer.

Based on the findings of ***Section 3***, it is evident that PBF provides innovative manufacturing solutions. However, there is strong evidence that numerous factors constrain the development of the process, and that various routes exist to optimise design builds and improve the properties of the built components.

A holistic research approach has comprised: the critical review of literature, empirical investigations of the best practices of PBF processing, assessing the current research landscape within the industrial and academic spheres, communication with industry, and the guidance of project stakeholders. From this research, avenues of further exploration to deliver novel PBF solutions in this project were identified and can be outlined as follows:

Research Option 1 – "Influence of Spherical and Non-Spherical Particle Segregation on Powder Bed Quality"

The investigation of the effect of particle morphology on segregation. In particular, what effect sphericity or an irregular particle form has on segregation relative to the motion of the recoater. Research has shown that particles of various aspect ratios can be inserted to the powder bed by using multisphere approximations within the DEM [12].

Research Option 2 – "Define and Quantify Powder Flowability with Respect to a PBF Process"

The aim of this investigation would be to create an accepted definition of “powder flowability” in the context of a PBF process. Unlike other engineering quantities, such as mass or temperature, no single method to quantify flowability exists. Instead, only properties and the behaviour of the powder during testing give a numerical value indicative of flowability, such as the AoR and cohesive index used by Espiritu et al [18]. Any mathematical definition of flowability would likely comprise a function of numerous variables that effect the mechanical behaviour of powder. Further consideration of this subject is discussed later on in ***Subsection 9.2***.

The concept of “flowability” can be considered as the antonym of “cohesion”. Thus, more cohesive powders are likely to agglomerate and form concentrated clusters in the powder bed, lowering flowability. Several methods have been proposed to quantify flowability, as described in ***Subsection 3.3.1***. Notably, AoR testing is the suggested technique by the ASTM [143]. Thus providing, along with the AoR values of pharmaceutical powders outlined in ***Table 5*** [141], the basis for an initial inspection of flowability in PBF powders.

Further work would identify which processing parameters engender the desired flowability value for the build, the effects of particles jamming under the recoater, and the comparison between the flow over a rough substrate and a flat plane.

Research Option 3 – “Influence of Substrate Surface Characteristics on Powder Bed Optimisation”

This proposed research subject would be to add striations to the substrate model and simulate spreading over a rough profile, which more closely resembles the melted top layer surface of the part during the design build. As this has been done for LBPF [165, 168], this study would be exclusively EBM-based. One way to model the rough substrate would be to add corrugations to the geometry to create an irregular form for the spreading region. Research has also highlighted that the effect of the raster melting pattern during the hatching phase, over a striated digital powder bed model, has yet to be considered in detail.

The aim would be to determine how powder bed quality is influenced by transverse, longitudinal, and combined roughness types relative to the spreading direction. Of particular interest is whether the powder segregates at all, and if so whether particles segregate in line with or against the orientation of the striations. Overall powder bed quality would again be judged on the metrics of packing density, segregation, and the homogeneity of the spread layer.

Research Option 4 – “Identify the Critical Fraction of Fine Particles within a PSD”

The aim of this proposed work would be to determine the fraction of “fine” particles in a PSD, with “fine” describing elements with an aspect ratio below a predetermined value, which benefit the composition of the bulk solid. Research suggests that a deficiency of fines will lead to voids within the powder bed, due to the presence of interstices that would otherwise be filled. Conversely a saturation of fines is also thought to be detrimental, as these particles show a greater proclivity to agglomerate into concentrated clusters.

Based on the information found it can be proposed that, subject to chemical and parametric factors, a critical fraction of fines exists for a given PSD. Beyond which, the inclusion of more fine elements will have a detrimental effect on the powder bed. The requirement for in-situ monitoring of the part build, along with the multi-physics behaviour of powder that cannot be quantified practically, suggests that a numerical study would provide valuable insights into powder bed optimisation.

The theorised critical fraction of fine particles would have significant implications for the PSD used in EBM, as establishing this value would facilitate the manipulation of the PSD to optimise the powder bed.

One way to control the insertion fractions would be through a sieving process. An objective would be to determine the point at which the influence of fines changes the conditions in the powder bed, to enable better control of the optimisation process. This would, however, incur significant processing steps which would offset the advantages gained.

Research Option 5 – "The Effect of the Vacuum on the EBM Building Process"

The findings of ***Section 3*** indicates that, likely owing to the black box nature of the EBM process, very little research has been performed in to how the vacuum environment influences powder flowability. Evidence suggests that the powder is approximately "twice as flowable in a vacuum" (according to industrial communication) when compared to the inert gas build chamber of an SLM process, and the flow of powder in a vacuum is a subject of academic interest [18, 196]. Defining powder flowability mathematically would therefore also provide a basis for researching the effect of the vacuum, as a direct comparison can be made between the flow in a vacuum and under inert gas conditions. Contingent on flowability solutions, scope exists for using CFD-DEM coupling to leverage the capabilities of both techniques and determine the influence of the atmosphere to inform optimising the design builds.

As stated in ***Subsection 3.5.2***, EBM powder beds are never comprised of entirely virgin powder after the first cycle run. Hence, modelling the spreading of recycled powder would be a valuable exercise in any of the proposed research options, and would create models which are more robust to reality. As described previously, the modelling of recycled powder would incorporate multisphere elements to represent powder which has agglomerated and formed satellites during recoating. However, a comprehensive modelling approach, incorporating all of the characteristics of a recycled powder set, would be required to reflect any expected change in rheological behaviour.

Digital modelling of recycled AM powder beds has not been widely researched in literature, so any simulations are would have to be underpinned by empirical evidence and knowledge of powder recyclability from wider-reading [161].

Research Option 6 – "Influence of Deposition Mechanism on Powder Bed Quality"

As discussed in ***Subsection 3.5.3***, a disparity exists between the technique used to provide powder to the substrate in the vast majority of DEM studies, and the supply methods used in industry. DEM models almost exclusively use the rainfall approach [10, 17, 21]. In industry, powder is delivered via a hopper, feed piston, or in rarer cases by the action of a moving funnel. The multi-physics behaviour of the particles in transit will affect the state of the powder delivered to the build chamber and thus, influence the quality of the spread layer in the powder bed.

From research, no evidence can be found of any previous modelling of the powder delivery system. It can be confidently stated that this would provide a novel exploration of optimising the AM powder spreading operation, by determining the effect of different deposition methods on the spread layer with the DEM. To model such a process, a moving funnel consisting of a powder reservoir and deposition nozzle was proposed. The funnel would deposit powder in front of the recoater, which would then be allowed to settle and spread over the build plate.

Similar set ups have been observed in industry but are likely to be the subject of proprietary data. Thus, explaining why no DEM research can be sourced. Analysis of the deposition phase would provide an insight to the mechanical perturbations of powder, and how this influences the quality of the spread layer with respect to the SVF, segregation, and surface profile roughness.

Required Research– "Validation of LIGGGHTS® for Powder Flow Analysis".

Irrespective of the original research pursued in this project, preliminary testing was required to validate applying LIGGGHTS® to powder flow studies. This was achieved by calibrating the properties of the simulation and producing results that were replicated practically. For example, a simple baseline test was to construct a simulation with parameters as near to the physical material sample as possible, and then induce an AoR to the simulated powder. This was then compared to the AoR formed by the physical powder sample through a device such as a Hall Flow Meter (HFM). Thus, also conforming to the recommended framework for characterising AM powder properties as established by the ASTM [143].

In conjunction with the material properties, the DEM was used to investigate the interparticle forces and cohesive behaviours which cause particle agglomeration, and by extension what influence these parameters had on the AoR formed.

Table 7 and **Table *8*** outline the state of the art, identify the research gap, state the hypothesis, and research objective of each of the prospective research subjects.

Table 7 - First Table of Potential Further Research Areas.

Research Option	State of the Art	Identified Research Gap	Hypothesis	Research Objective
1. Influence of Spherical and Non-Spherical Particle Segregation on Powder Bed Quality.	The morphology of constituent AM powder bed particles can be adapted within the DEM.	Particles are often assumed to be spherical, neglecting satellites and the effect of irregular particles on flow behaviour.	Realistic modelling of particle shapes would increase the fidelity of DEM-AM models by accounting more accurately for cohesive interactions.	To characterise AM powder with SEM, and use multi-sphere approximation methods to represent particles in the DEM simulations.
2. Define and Quantify Powder Flowability with Respect to a PBF Process.	Powder flowability is subjective to the requirements of the build process. Various methods to evaluate flow exist, but none provide the complete depiction of flow behaviour for AM processes.	No definitive numerical definition of powder flowability currently exists. It can broadly be considered an antonym of cohesion, but is a consequence of many different variables. A research gap exists to identify a single numerical metric to govern flowability of AM powders.	Establishing a numerical value to quantify flowability would enable any powder to be analysed for its suitability for AM processes.	To mathematically consider all quantities that govern powder flow behaviour and establish non-dimensional values and ranges that accurately quantify flowability.
3. Influence of Substrate Surface Characteristics on Powder Bed Optimisation.	DEM modelling of AM powder beds generally assumes an idealised flat plane as the substrate.	The flat spreading plane is not reflective of the surface topography in PBF, which is liable to be more irregular as a consequence of the previous layer fusing.	Realistic modelling of the substrate will influence powder deposition by trapping particles and thus present a more realistic depiction of powder spreading.	To generate STL models with striated substrate surfaces, and observe the influences in powder layer coverage, segregation, and surface profile. Then, compare against the results of the flat-plane analysis.

Table 8 - Second Table of Potential Further Research Areas.

Research Option	State of the Art	Identified Research Gap	Hypothesis	Research Objective
4. Identify the Critical Fraction of Fine Particles within a PSD.	Various studies have examined the effect of the PSD on powder bed quality, but seldom in controlled insertion fractions.	Conflicting evidence exists as to the merits of inducing a wider or narrower PSD depending on the powder spreading operation.	Refinement of the PSD may elucidate a "critical fraction" of fine particles to insert to a PBF system. Thus, the point at which the insertion of more fines diminishes bed quality by raising agglomerations.	To build DEM simulations with controlled particle size insertion fractions to ascertain the influence on spread layer quality, and identify the point in the PBF process at which optimisation is achieved.
5. The Effect of the Vacuum on the EBM Building Process.	Due to the black box nature of EBM processes, the flow of powder in a vacuum compared to the inert gas atmosphere of SLM is considerably underexplored.	Only one research paper, comparing powder in a vacuum and inert gas processed with a rotating drum, can be sourced. A research gap exists so far as no research can be sourced which directly compares powder flow in a vacuum against an inert gas atmosphere.	Modelling of the powder flow in both environments will elucidate the influence of atmosphere on particle dynamics, and suggest parameters that optimise design builds.	To leverage the DEM and CFD-DEM coupling to compare powder bed quality when the powder is spread in a vacuum and inert gas environments, using digital models.
6. Influence of Deposition Mechanism on Powder Bed Quality.	Virtually all current DEM-AM models researched insert powder using the rainfall method.	The rainfall approach is a clear oversight that decreases the accuracy of the PBF models, by misrepresenting the delivery and initial deposition conditions of the powder.	Digital modelling the powder delivery by a hopper, moving funnel, or piston-operated supply table would present a more accurate reflection of powder delivery.	To produce a modelling system comprising a powder delivery and spreading mechanism, and evaluate the difference in powder quality between realistic and rainfall deposition methods.

4.2 Shortlisting of Research Subjects

As shown in ***Subsection 4.1***, many design build factors could have been investigated further. However, not all research avenues could be explored due to the constraints of time and resources. A shortlist outlined the possible solutions to engender a novel improvement to PBF processing.

To ascertain the most suitable area of investigation to pursue, a decision-making system was required. The following criterions were established based on research and communication with the project stakeholders:

- The viability of achieving successful project conclusions within the time limits of the project.
- The viability of achieving successful project conclusions with the resources available.
- The originality of the research solutions.
- The potential impact of the research solutions.
- The ability to validate the models against practical experimentation.

Each criterion was scored from 1-5 in their suitability for the proposed project, with a higher overall score denoting a more suitable research area. ***Table 9*** outlines the points system for each criterion.

Table 9 - Explanation of Each Criterion Score for Project Shortlisting.

Score.	Project Time Limit	Project Resources	Originality of Solutions	Impact of Solutions	Viability of Practical Validation
1	Cannot be achieved in the project time limit.	Beyond the project resources.	Not novel, commonly held knowledge.	No impact.	Cannot be practically validated.
2	Severe risk of exceeding project time limits.	Only attainable with industrial support.	Incremental to published literature or industrial practice.	Minimal impact, or proposed impact cannot be established.	Practical testing likely to impede the project time and resources.
3	Achievable, but highly dependent on the project running to schedule.	Resources available, but access, use, and training could inhibit project progress.	Novel, but not of great relevance.	Small impact, likely to be confined to the research of project stakeholders.	Can be validated practically, but dependent on access to facilities, training, and provisions.
4	Likely to be achieved within project time limits.	Satisfactory resources existing or attainable.	Novel, and of interest to project stakeholders.	Impactful and likely to contribute to the research landscape.	Can be practically validated with minimal project disruption.
5	Strong probability the project will be completed on time.	Multiple resources and alternatives available to aid project completion.	Novel, and applicable to AM and DEM communities.	Highly impactful and likely to disrupt industrial practice.	Can be practically validated with no adverse effect on project progress.

4.2.1 Research Subject Selection

Based on the criteria outlined in ***Table 9***, a Pugh Matrix has been constructed to select the avenues of further exploration in ***Table 10***.

Table 10 - Pugh Matrix to Select Research Areas to Pursue.

Research Option	Project Time Limit (/5)	Project Resources (/5)	Originality of Solutions (/5)	Impact of Solutions (/5)	Viability of Practical Validation (/5)	Research Option Total Score
Influence of Spherical and Non-Spherical Particle Segregation on Powder Bed Quality.	4	4	2	3	2	15
Define and Quantify Powder Flowability with Respect to a PBF Process.	1	2	5	4	2	14
Influence of Substrate Surface Characteristics on Powder Bed Optimisation.	4	3	2	4	3	16
Identify the Critical Fraction of Fine Particles within a PSD.	4	5	4	3	2	18
The Effect of the Vacuum on the EBM Building Process.	1	2	5	5	2	15
Influence of Deposition Mechanism on Powder Bed Quality.	5	4	4	4	3	20

The scoring system showed that investigating the vacuum flow of powder in EBM processes was unfeasible within the project timeframe. Due to the complexity and multifaceted nature of metal AM, defining powder flowability mathematically also exceeded the constraints of the project. Nevertheless, future research of these topics, potentially by coupling CFD-DEM methods with practical analysis, would be highly informative to optimising powder spreading and likely to impact commercial AM processes.

The majority of numerical AM spreading models overlook realistic surface profiles, despite research documenting their impact on the quality of the layer formed [165, 168]. Whilst this has been explored for SLM models, it is reasonable to suggest that DEM studies with parameters configured to spread powder over realistic EBM processed surfaces would present novel research and significantly contribute to the current academic sphere. Investigating the influence of particle sphericity, and the ramifications this has for segregation, was feasible but not novel [12]. Furthermore, due to the difficulty of in-situ monitoring of AM powder beds, it would have been difficult to ascertain whether the results of digital modelling were replicated practically.

Modelling the effect of the deposition technique emerged as an impactful and novel approach to powder bed optimisation. A study was proposed in which SS316l powder is delivered to the substrate using both the commonly observed rainfall approach, and by the action of a moving funnel mechanism. Parameters were controlled to isolate the effect of the deposition method, and various PSD sets were tested to assess the influence on powder bed quality, based on the identified metrics of powder bed quality: the SVF, segregation, and surface profile roughness. The evaluation of varying PSD sets contributed to presenting original research as, although various PSD sets are widely modelled in DEM literature [13, 14, 168], no evidence has been found to suggest that a proposed critical fraction has been established.

SS316l has been chosen for the analysis as, although the material has been observed in EBM systems, its application in the technology has received considerably less attention than Ti-6Al-4V and Inconel 718 [14, 107, 155, 197]. This is particularly reflected in DEM investigations. Thus, the study of SS316l is likely to be more impactful for powder dynamics research and advance existing knowledge, whilst also yielding further avenues of exploration for alternative material processing methods.

As with any engineering process, no such perfect solution between deposition approaches, the inserted PSD, and the powder bed quality will exist. A successful project conclusion will constitute identifying the best-case scenario, in which the powder bed quality is maximised subject to the processing parameters and conditions of the build. A process map connecting the research areas, hypotheses, and objectives is presented in ***Figure 30***.

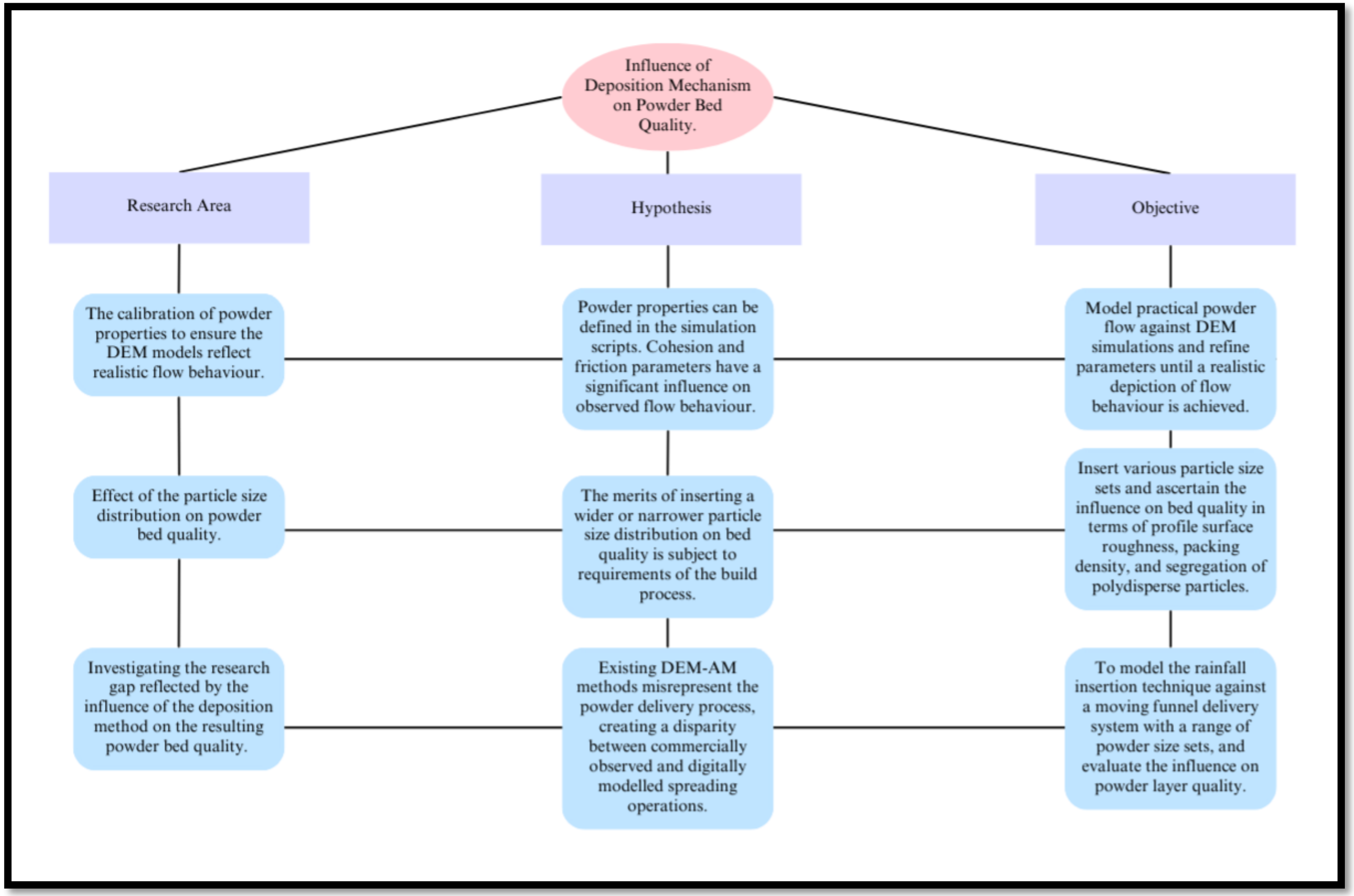

Figure 30 - Process Map Outlining the Research Areas, Hypotheses, and Objectives in DEM-AM Investigations.

5. Validation of LIGGGHTS® Against Practical Experiments using Stainless Steel 316l Powder

As evidenced in ***Section 3***, DEM modelling of AM powder flow has been used in many academic research projects [12, 17, 32, 49, 198]. Conversations with industry throughout this project has identified DEM-AM modelling as being a key area of interest within the commercial sphere, with implications for both current practice and the further development of Industry 4.0. In addition to Wayland Additive Ltd, a commercial interest has been declared by firms including Granutools, Fort Wayne Metals, and DONAA Ltd. Evidence of commercial interest in the technique is provided in ***Appendix B***.

To ensure the fidelity of the DEM models, the results must be authenticated against practical data. To achieve this, three separate tests were proposed. Each of which considered different quantifiable characteristics of powder flow.

Subsection 5.1 describes the first test. A simple baseline simulation of the pile formed by approximately 1000 particles is qualitatively evaluated. This rudimentary inspection will ascertain the viability of LIGGGHTS® for replicating the mechanical behaviour of granular media. Similarity in the form of the piled material will enable progression to more sophisticated analysis.

A powder discharge time test is performed in ***Subsection 5.2***. To achieve this, different quantities of SS316l powder, with a PSD identical to the range used in SLM, is discharged from a HFM under gravity. A digital twin of the experimental setup is then created within LIGGGHTS®, and the discharge duration of the various powder quantities are compared.

The final validation technique is explained in ***Subsection 5.3***. An AoR analysis is performed with the same HFM used in the powder discharge time test. Once more, a given mass of powder is discharged under gravity, with the dimensions of the powder in both the digital model and the practically formed pile compared. This test not only ascertains the fidelity of the LIGGGHTS® simulation, but also investigates the settings that influence the formation of the AoR, such as the cohesion and friction parameters used. This provides an opportunity to determine the most relevant parameters to configure in the powder spreading models.

5.1 Preliminary Testing of Granular Media

5.1.1 Simulation Method

This simulation was loosely based on the principles of a study by Roesller and Katterfeld [199], who calibrated DEM parameters with an AoR test for the flow of sand. In this study, polymer beads were funnelled into a cell, allowed to settle, and the cell was then lifted vertically to create a pile. The aim of the simulation was to compare the shape of the pile formed by the polymer beads to the pile in the digital model. The parameters in LIGGGHTS® were replicated as closely as reasonably practicable to the conditions of the physical experiment. Approximately 1000 polymer beads were used in the simulation and loaded into a cell of volume 7mm by 7mm by 12mm. An arbitrary lifting velocity was used to discharge the particles from the cell.

After applying the required Personal Protective Equipment (PPE), the practical cell was constructed to the required dimensions. These dimensions are provided (not to scale) in ***Figure 31***. Note that the actual dimensions are used to label the cell geometry. Polymer beads were funnelled into the cell and the funnel was agitated to encourage loose polymer beads to occupy the fill volume. The beads are represented by the disc shapes in the centre of the cell in ***Figure 31***. Finally, the beads were discharged by the lifting action and the material was allowed to settle under gravity.

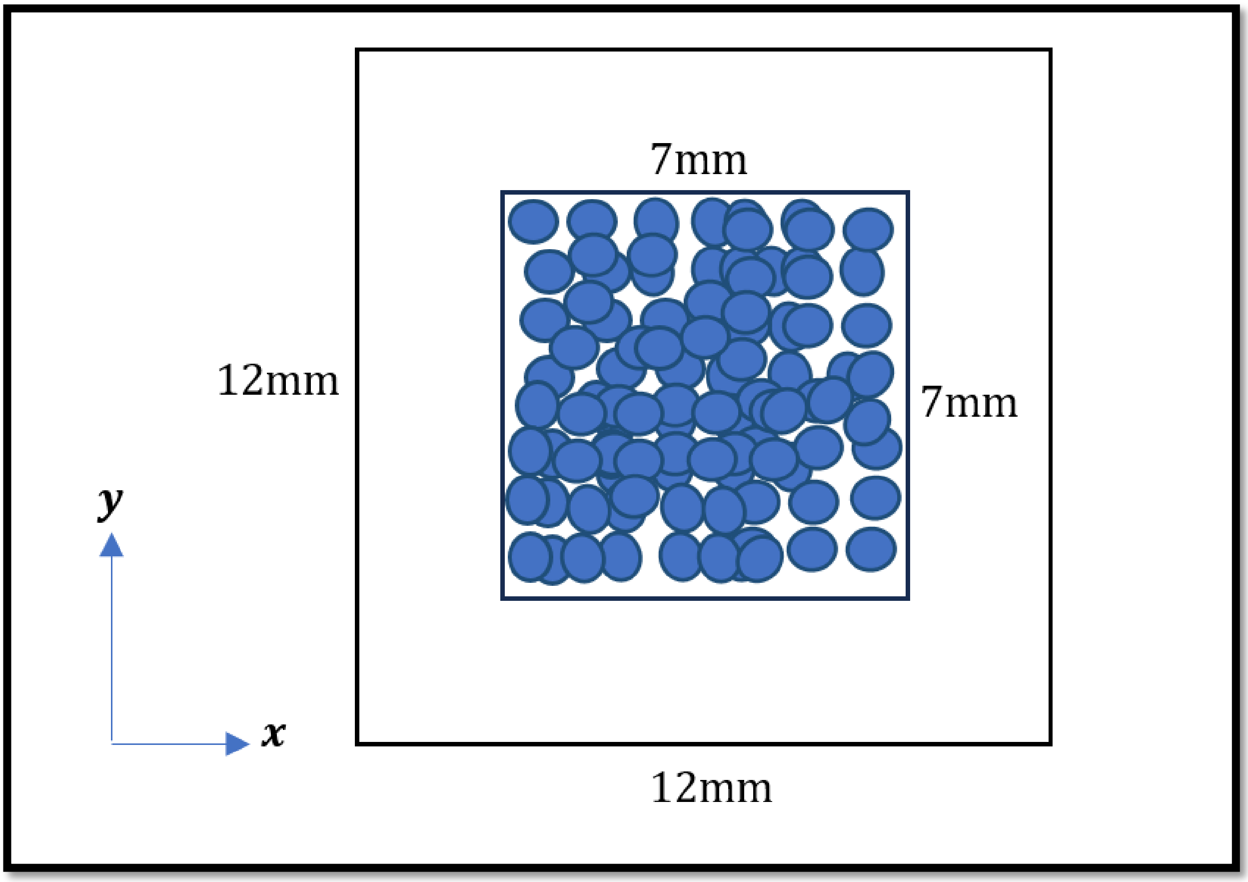

Figure 31 - Dimensions of the Cell for Polymer Bead Analysis (Top View).

Figure 32 shows a diagram of the lifting mechanism of the cell and the discharge of material.

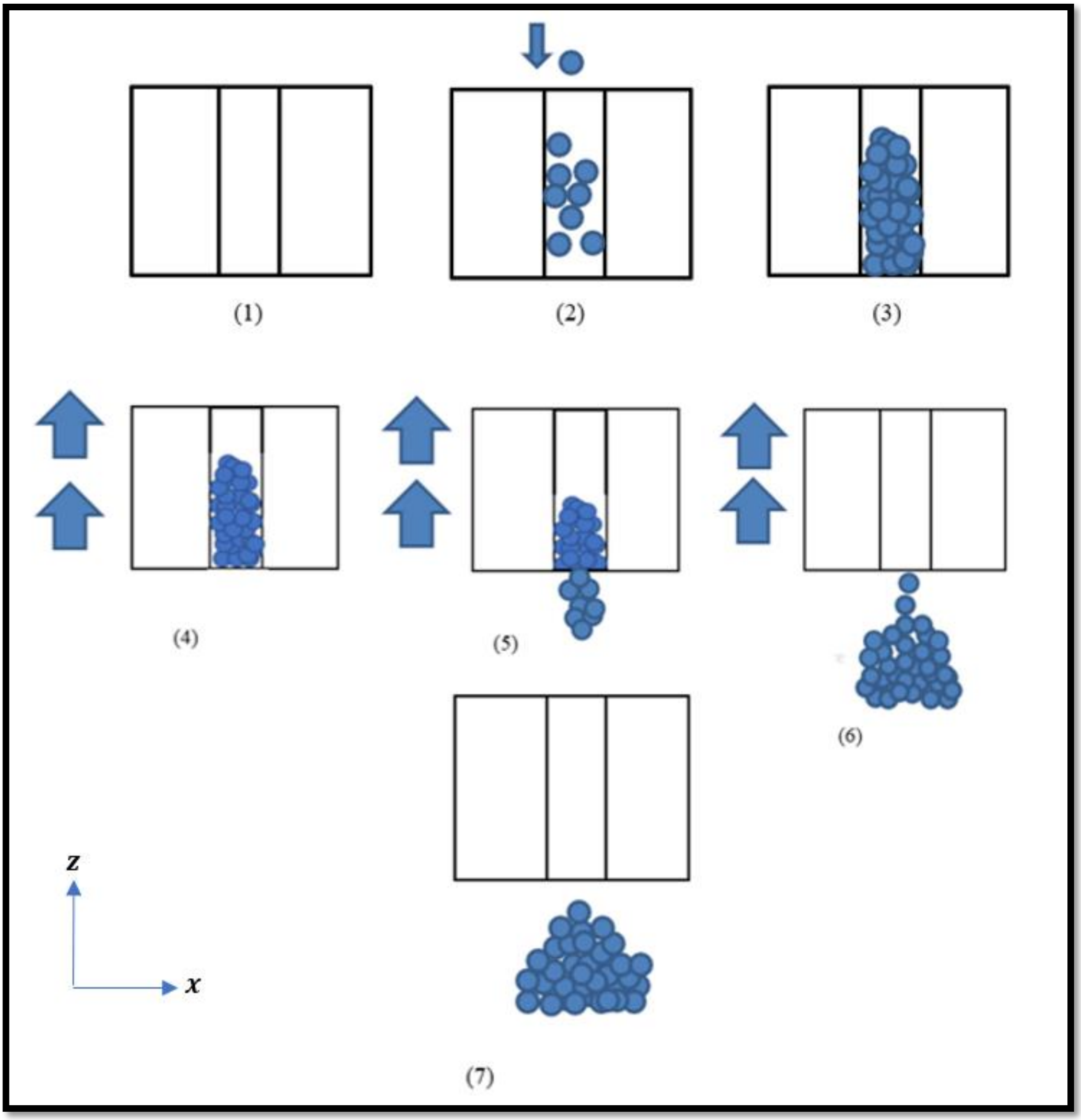

Figure 32 - Diagram of the Cell Discharging Polymer Beads.

Figure 33 shows the pile formed experimentally and in the digital model. A good agreement between the appearance of each pile is observed, justifying the use of LIGGGHTS® for more sophisticated validation tests. Note that, to create the pile in the digital model, the beads have been constrained by boundaries in the computational domain. To further exposit the practical experiment, a still frame of a preliminary test of poppy seeds discharging from the cell is provided in ***Appendix C***.

5.1.2 Results

Figure 33 - Pile Formation of Practical and Digital Polymer Bead Models.

5.2 Powder Discharge Time with Hall Flow Meter

5.2.1 Simulation Method

This simulation aims to validate LIGGGHTS® for SS316l powder flow analysis, and to determine the repeatability and scalability of the flow test. Repeatability, in this context, defines how consistent the time required to discharge a set mass of powder through the HFM is, across multiple tests under identical conditions. The scalability of the simulation describes the change in discharge time when decreasing powder quantities are used. The first test conformed to the guidelines outlined in BS EN ISO 4490:2018 [200], in which 50g of powder is inserted to the HFM, allowed to rest, and discharged by removing a mechanical shutter at the aperture. ***Figure 34*** compares the digital HFM model to the practical device.

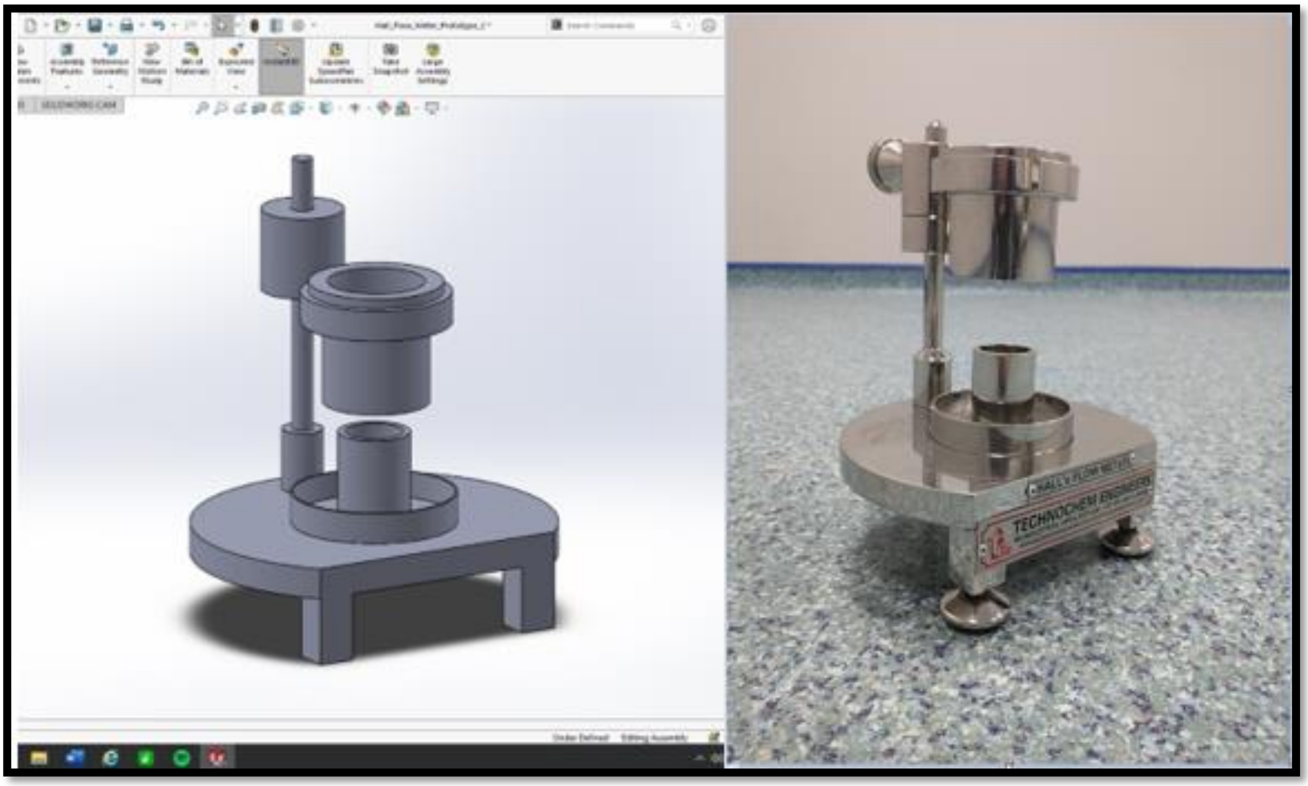

Figure 34 - Digital Hall Flow Meter model and Practical Device.

Prior to commencing the experiment, the following preparatory actions were performed to calibrate the HFM, in accordance with BS EN ISO 4490:2018 [200]:

- The HFM was levelled by adjusting the screws at the bottom of the baseplate.

- The funnel, cup, and overflow plate were aligned along the same vertical axis, to ensure the powder flowed into the cup.

- The distance from the funnel to the cup was set to 25mm. As a 2mm recess is incorporated to the bottom orifice of the funnel, a 23mm spatula is provided to be measure the discharge distance, achieving the 25mm gap required.

To maximise the accuracy of results, the steps outlined below have conformed to BS EN ISO 4490:2018 [200] as closely as reasonably practicable:

- The SS316l powder was tested in the as-received condition, without applying specific drying procedures first.

- In accordance with the framework, a total powder sample of 250g was taken for HFM testing.

- Immediately prior to the test, a 50g portion (±0.1g) was measured with an electronic weighing scale and transferred to the funnel. To prevent powder leakage, the discharge orifice is kept closed by a mechanical shutter during powder loading.

- To increase the accuracy of the results, a high-speed camera (240 frames per second) was used to measure the discharge time instead of a stopwatch. Flow was considered to commence at the frame in which the orifice is opened and conclude at the frame in which the last of the powder has discharged. The number of flow frames is converted to the duration of powder flow through the HFM in seconds, as shown in ***Equation 62***.

$$Powder\ Flow\ Rate = \frac{Final\ Frame\ of\ Flow - Start\ Frame\ of\ Flow}{Number\ of\ Frames\ per\ Second} = \frac{\Delta_{Frame}}{240} \qquad (62)$$

- To ascertain the repeatability of the experiment, each mass of powder was tested five times, and the mean discharge time was found for each sample set.

Initial simulations showed that modelling 50g of actual sized SS316l powder was beyond the computational resources available. Hence, the scalability analysis determined the relationship between total powder mass and discharge time. A linear relationship allowed for the scaling of the digital model. For accurate scaling, the total number of particles in the digital model had to be calculated. Hence, multiple properties of the particles had to firstly be identified. An example model, with the total powder mass of 50g and spherical particles of radius 15 µm, served as the basis for this process.

1. Find the volume of each particle:

$$V_{Particle} = V_{Sphere} = \frac{4}{3}\pi r^3 \tag{63}$$

$$\therefore$$

$$V_{Particle} = V_{Sphere} = \frac{4}{3}\pi\left((15 \times 10^{-6})^3\right) m^3$$

$$\therefore$$

$$V_{Particle} = 1.4137166 \times 10^{-14}\ m^3 = 1.41 \times 10^{-14}\ m^3.$$

2. Find the material density:

From the material datasheet [201], SS316l has a density of 8000 $\frac{kg}{m^3}$ or 8 $\frac{g}{cm^3}$. Thus,

$$\rho_{SS\ 316l} = 8000\ \frac{kg}{m^3} \tag{64}$$

3. Find the mass of each particle:

$$m_{Particle} = V_{Particle} \times \rho_{SS\ 316l} \tag{65}$$

$$\therefore$$

$$m_{Particle} = V_{Particle} \times \rho_{SS\ 316l} = 1.4137166 \times 10^{-14}\ m^3 \times 8000\ \frac{kg}{m^3}$$

$$\therefore$$

$$m_{Particle} = 1.1309734 \times 10^{-10}\ kg = 1.13 \times 10^{-10}\ kg$$

4. Find the total number of particles:

$$Number\ of\ Particles = \frac{m_{Total}}{m_{Particle}} \tag{66}$$

$$\therefore$$

$$Number\ of\ Particles = \frac{m_{Total}}{m_{Particle}} = \frac{50 \times 10^{-3}}{1.1309734 \times 10^{-10}} = 442{,}097{,}046.66 \approx 442{,}097{,}046$$

Equation 66 shows that modelling the full 50g of powder would require over 442 million particles. Initial attempts to perform this simulation culminated in only a single output file of size 7.8 GB, after running for 12 hours on 8000 processors. As the model had only inserted about 25% of the total powder quantity, it showed that modelling the full powder mass was unfeasible. Two options existed to solve this problem. Either scaled particles which showed the same behaviour as unscaled particles had to be used, or fewer particles could be modelled if the scalability analysis demonstrates a linear relationship between the flow rate and the powder mass.

Using ***Equation 66***, the number of particles in each mass inserted to the HFM can be determined.

Mass of 25g:

$$Number\ of\ Particles = \frac{m_{Total}}{m_{Particle}} = \frac{25\times10^{-3}}{1.1309734\ \times10^{-10}} = \ 221{,}048{,}523.33 \approx 221{,}048{,}523$$

Mass of 12.5g:

$$Number\ of\ Particles = \frac{m_{Total}}{m_{Particle}} = \frac{12.5\times10^{-3}}{1.1309734\ \times10^{-10}} = \ 110{,}524{,}261.67 \approx 110{,}524{,}261$$

Mass of 6.25g:

$$Number\ of\ Particles = \frac{m_{Total}}{m_{Particle}} = \frac{6.25\times10^{-3}}{1.1309734\ \times10^{-10}} = \ 55{,}262{,}130.83 \approx 55{,}262{,}130$$

5.2.2 Results

Practical Testing

Four different powder mass sets were practically tested to scale the digital twin model. As stated, this was to determine if the discharge time against the mass of particles behaved linearly. Each sample was tested five times, and the average discharge time was taken from these five samples. The discrepancy from half of the discharge time of the previous sample was taken to evaluate scaling, and the standard deviation of each sample set was taken to measure the repeatability of the tests. The results are provided in ***Table 11*** and the complete data set is provided in ***Appendix D***.

Table 11 - Results of Practical Testing of Powder Discharge Time.

Sample Set (*g*).	Average Discharge Time (s).	Deviation from Half of the Previous Sample (s).	Standard Deviation across Sample Set.
50	19.667	Base Sample	0.363
25	9.495	0.339	0.10
12.5	4.623	0.125	0.07
6.25	2.183	0.129	0.06

Table 11 shows that the discharge time broadly halved between each sample set. Note that tapping was required to initiate flow in two of the tests for the 50g powder set, which may explain the larger deviation in this sample. The results have provided evidence to justify modelling the smallest powder set in LIGGGHTS®, to reduce the computational intensity of the simulations.

Simulation

The practical test set up was replicated as closely as reasonably practicable in the digital model. The top half of the HFM funnel was cut to save computational resources, as the powder occupied only the bottom half of the funnel. 6.25g of spherical particles with a diameter of 30 μm were inserted to the funnel and allowed to settle under gravity. A fixed plane was inserted across the funnel outlet to replicate the mechanical shutter. Due to the time-sensitive nature of the analysis, the particles were only discharged when the energy in the system reached below a very small, predetermined threshold of 50×10^{-6} μJ. Preliminary testing showed that stable particle behaviour was achieved at a timestep of 1×10^{-7} s.

The number of flow steps was found by subtracting the timestep at which flow began from the timestep at which the final particle exited the cone, as in ***Equation 67***:

$$Number\ of\ Discharge\ Steps = Timestep\ at\ Final\ Discharge - Timestep\ at\ Initial\ Discharge \quad (67)$$

To calculate the discharge time, the total number of flow steps was multiplied by the timestep size as in ***Equation 68***.

$$Discharge\ Time = Timestep\ Size \times Number\ of\ Flow\ Steps \quad (68)$$

In the simulation, powder flow commenced at $t = 220{,}000$ and concluded at $t = 21{,}900{,}000$. Thus, combining ***Equation 67*** & ***Equation 68***, the total discharge time for the digital model was found by:

$$Simulation\ Time = (21{,}900{,}000 - 220{,}000) \times (1 \times 10^{-7})\ \text{s} \quad (69)$$

$$\therefore$$

$$Simulation\ Time = 2.168\ \text{s}$$

Thus, the difference between the practical and simulated discharge times is given by ***Equation 70***.

$$Discharge\ Time = Real\ Time - Simulation\ Time \quad (70)$$

$$\therefore$$

$$Discharge\ Time = 2.183 - 2.168 = 0.015\ \text{s}$$

The negligible disparity of 0.015s suggested that comparing the powder discharge times is a viable test of the model validity. Thus, the results justified expanding the validation process to performing an AoR analysis. From which, parameters and material properties could be validated for the powder spreading simulations performed later in ***Section 6*** and ***Section 7*** of the thesis.

5.3 Angle of Repose Analysis to Calibrate Simulation Parameters

5.3.1 Calibration of Powder Parameters

As with the previous powder discharge time analysis, the AoR tests only the flow of SS316l powder. Whilst it is acknowledged that limiting the analysis to only SS316l may reduce the generalisability of results, SS316l is the only material investigated in the subsequent powder spreading simulations. Hence, the calibration of alternative powders was not required for the validation of the models used in this project.

As described previously, the AoR describes the steepest angle formed by a piled granular material relative to the horizontal plane on which it rests. An AoR inspection is a widely used approach for calibrating the DEM model properties against the real behaviours observed in a powder sample set [63, 180, 75].

The AoR formed by a powder depends on several particle characteristics, including the morphology and surface profile. In DEM methods, the AoR has been shown to be influenced by the coefficients of rolling and sliding friction. However, the AoR has not been shown to be sensitive to the inherent material properties such as the Young's Modulus, Poisson's ratio, or Density [75]. Finer aspherical particles generally induce a higher AoR to the pile. In this study, the material properties for the SS316l powder sample were sourced from a material database [201].

A reduced Young's Modulus (E) was implemented to allow for a decreased simulation timestep. Preliminary testing of the Young's Modulus value at two and three orders of magnitude beneath reality (consistent with literature) showed a negligible influence on the powder flow behaviour, justifying assigning these values to E to induce computational savings in these simulations. This finding, in conjunction with the conversion of the surface energy to CED values performed later in this subsection, is likely to yield useful data for the wider DEM research sphere.

For the timestep selection, research has shown that a fraction of the Rayleigh critical timestep, t_c, is often used based on the material properties to ensure model stability [75, 92, 202].

$$t_c = \frac{\pi r}{0.8766 + (0.163\nu)} \times \sqrt{\frac{\rho}{G}} \quad (71)$$

Where, for the SS316l powder in these models:

r = The radius of the smallest particle = 10 µm

ν = Poisson's ratio = 0.27

ρ_{SS316l} = Particle Density = 8 $\frac{g}{cm^3}$ or 8000 $\frac{kg}{m^3}$

G = Shear Modulus in units of Pa.

Equation 71 shows that the value of G will have a significant effect on the selected timestep. Wider reading implies the shear modulus can be scaled as is often the case for E [203, 204]. Marigo [205] used multiple values between $G = 2 \times 10^{4}$ Pa and $G = 2 \times 10^{11}$ Pa, and noted a negligible difference in the discharge rate of oil refining powder through a mixing vessel. For consistency with the scaling factor applied to E, a value for G that is two and three orders of magnitude lower than reality was proposed for setting the timestep in these models.

The actual value of the shear modulus for SS316l is [206]:

G_{SS316l} = 74-82 GPa

Therefore:

$G_{Two\ Orders\ of\ Magnitude\ Smaller}$ = 0.74-0.82 GPa

And:

$G_{Three\ Orders\ of\ Magnitude\ Smaller}$ = 0.074-0.082 GPa

Hence, inserting these values for G into ***Equation 71***:

$$t_c = \frac{\pi \times 10 \times 10^{-6}}{0.8766 + (0.1631 \times 0.27)} \times \sqrt{\frac{8000}{0.74 \times 10^{9}}} = 1.12 \times 10^{-7} \text{ s}$$

Or:

$$t_c = \frac{\pi \times 10 \times 10^{-6}}{0.8766 + (0.1631 \times 0.27)} \times \sqrt{\frac{8000}{0.074 \times 10^{9}}} = 3.55 \times 10^{-7} \text{ s}$$

And thus, multiplying t_c by 0.2 as often observed in literature [75, 207]:

$$0.2\, t_c = 0.2 \times \frac{\pi \times 10 \times 10^{-6}}{0.8766 + (0.1631 \times 0.27)} \times \sqrt{\frac{8000}{0.74 \times 10^{9}}} = 2.24 \times 10^{-8} \text{ s}$$

Or:

$$0.2\, t_c = 0.2 \times \frac{\pi \times 10 \times 10^{-6}}{0.8766 + (0.1631 \times 0.27)} \times \sqrt{\frac{8000}{0.074 \times 10^{9}}} = 7.096 \times 10^{-8} \text{ s}$$

Thus, considering the values found for t_c, the baseline timestep used in the AoR tests have been tested between $t = 2.24 \times 10^{-8}$ s and 7.096×10^{-8} s. It was found that by reconfiguring the input script in LIGGGHTS® to use units of "Centimetres-Grams-Seconds" (CGS) instead of "S.I" [208], model stability could be achieved when the timestep was further reduced to the implemented value of 1×10^{-7} seconds. It is theorised that changing the units makes the calculations of the DEM cycle more precise, as there are fewer digits to process for each particle-particle and particle-wall interaction, thus enabling the lower timestep.

Preliminary testing showed that the pile formed was independent of the rolling friction coefficient. This finding, along with literature suggesting that rolling friction mainly governs the interlocking behaviour of aspherical particles [180], provided grounds for omitting a detailed investigation of the parameter in this study. Instead, the coefficient of $\mu_{Rolling}$ was set in accordance with literature so that particles do not travel more than 15-20 times their own radius [180, 209].

Cohesion, in the AoR tests, was governed by the CED parameter used in SJKR contact modelling. A mathematical description of the cohesion parameter, $\boldsymbol{\kappa}$, is given in ***Subsection 2.1.2***. In DEM-AM literature, little data exists to give a benchmark for the values of $\boldsymbol{\kappa}$ to use for AM powders [49, 210]. In fact, the majority of models use surface energy instead, and consultation of the DEM sphere shows that a direct conversion between the two parameters is not straightforward. Wider reading also highlights that reference values for $\boldsymbol{\kappa}$ for given materials are not easily obtained, and depend on environmental and system properties such as humidity [211, 212]. For this reason, it was assumed a lower value of $\boldsymbol{\kappa}$ could be assigned to powder in vacuum-based systems. Research indicated that the cohesion parameter could only be correctly selected when considered as part of holistic modelling approach to the simulation settings.

A thorough literature review has failed to identify enough data to establish a value for $\boldsymbol{\kappa}$ in metal AM powders. Hence, the information found formed the basis of the calibration process as opposed to a direct reference for the material sample. Of the sources available, Lampitella et al [180] tested the AoR formed by Inconel 718 powder both experimentally and within LIGGGHTS®, at a PSD comparable to that used in LBPF systems (15-45μm). They tested CED at a range of $\boldsymbol{\kappa} = 10\,\frac{kJ}{m^3}$ to $\boldsymbol{\kappa} = 100\,\frac{kJ}{m^3}$ and sliding friction values of $\mu_{Sliding} = 0.1$ to $\mu_{Sliding} = 1$. Their value of E was set to three orders of magnitude below the real value for Inconel 718 at 0.2 GPa. The authors found the optimum values to replicate the practical AoR of 28.7° were at $\boldsymbol{\kappa} = 90\,\frac{kJ}{m^3}$ and $\mu_{Sliding} = 0.7$.

According to ***Subsection 2.1.2***, the cohesive force depends on the contact area between the particles. Thus, although it was theorised that the AoR formed was not sensitive to the Young's Modulus of the material, it was likely that calibrating the models with the correct value of $\boldsymbol{\kappa}$ depended on the value of E chosen, which then had implications for the AoR. This further complicated calibrating the value of $\boldsymbol{\kappa}$, because as previously mentioned E is often set to multiple orders of magnitude below reality to induce computational savings.

Commentary from the developers of LIGGGHTS® suggests that establishing the value of $\boldsymbol{\kappa}$ for a given material can only be done empirically [213]. Thus, it is reasonable to suggest that establishing the value ranges of $\boldsymbol{\kappa}$ for the SS316l powder in these simulations has provided a significant data contribution to the wider research sphere. As stated, the vast majority of cohesive contact models in DEM-AM analysis use the surface energy property, $\gamma_{Surface}$, instead of the CED. The work of Lee et al [175] attempted to relate the two properties mathematically:

$$\boldsymbol{\kappa} = \sqrt[3]{\frac{8 \times E_*^2}{3 \times R_* \times \pi^2}} \times \sqrt[3]{\gamma_{Surface}} \tag{72}$$

Or equivalently:

$$\gamma_{Surface} = \frac{3}{8} \times \frac{r_*}{E_*^2} \times \boldsymbol{\kappa}^3 \tag{73}$$

Where:

r_* = The effective particle radius from the contact of two particles.

E_* = The effective elastic contact modulus.

The values of r_* & E_* are given by:

$$\frac{1}{r_*} = \frac{1}{r_i} + \frac{1}{r_j} \tag{74}$$

&

$$\frac{1}{E_*} = \frac{1-\nu_1^2}{E_1} + \frac{1-\nu_2^2}{E_2} \tag{75}$$

Where, as in ***Subsection 2.1.2***:

r_i = The radius of the particle of type i.

r_j = The radius of the particle of type j.

E_1 = The Young's Modulus of the particle of material type 1.

E_2 = The Young's Modulus of the particle of material type 2.

ν_1 = The Poisson's ratio of the particle of material type 1.

ν_2 = The Poisson's ratio of the particle of material type 2.

In the work of Han et al [20], a similar PSD and properties to the SS316l samples in these simulations were used. The data in ***Table 6 (Subsection 3.6)*** showed that $\gamma_{Surface}$ values in the range of 0.097 – 2 $\frac{\mathrm{mJ}}{\mathrm{m}^2}$ are assigned to metallic powders processed in PBF. Hence, based on these values and the known properties, a range of $\boldsymbol{\kappa}$ values were established prior to testing by the relations calculated in ***Equation 72*** and ***Equation 73***. In agreement with Lampitella et al [180], Chen et al [181] noted that the coefficient of $\mu_{Rolling}$ used in DEM-AM modelling is often very small or neglected altogether for SS316l. As preliminary testing showed pile formation to be independent of $\mu_{Rolling}$, an initial coefficient of $\mu_{Rolling}$ value of 0.01 was used for consistency with Chen et al [181] and to ensure the particles did not roll more than 10-15 times their own diameter.

Stating the properties used for SS316l powder in the simulation when the Young's Modulus was three orders of magnitude smaller than reality:

Table 12 - Properties of Stainless Steel 316l for Calibration Models.

Material Property	Symbol	Value	Units
Young's Modulus of Elasticity	E	0.193	GPa
Poisson's ratio	ν	0.27	Dimensionless
Particle Size Distribution	PSD	20-40	µm
Density	ρ_{SS316l}	8000	$\frac{\text{kg}}{\text{m}^3}$
Rolling Friction	$\mu_{Rolling}$	0.01	Dimensionless

With the values for $\mu_{Sliding}$ and $\boldsymbol{\kappa}$ established through the calibration process.

Thus, the effective particle radius is found as below:

$$\frac{1}{r_*} = \left(\frac{1}{20\times10^{-6}} + \frac{1}{40\times10^{-6}}\right) \text{ µm}$$

$$\therefore$$

$$\frac{1}{r_*} = (50{,}000 + 25{,}000) \text{ µm}$$

$$\therefore$$

$$\frac{1}{r_*} = 75{,}000 \text{ µm}$$

$$\therefore$$

$$r_* = \frac{1}{75{,}000} = 13.33 \text{ µm}$$

As only a single powder material is used, the values for E and Poisson's ratio are uniform. Hence, when E is three orders of magnitude below reality, E_* can be found using:

$$\frac{1}{E_*} = \frac{1-\nu_1^2}{E_1} + \frac{1-\nu_2^2}{E_2}$$

$$\therefore$$

$$\frac{1}{E_*} = \left(\frac{1-0.27^2}{1.93\times10^8} + \frac{1-0.27^2}{1.93\times10^8}\right) \text{ Pa}$$

$$\therefore$$

$$\frac{1}{E_*} = 2 \times 4.803626943 \times 10^{-9}\ \text{Pa}$$

$$\therefore$$

$$\frac{1}{E_*} = 9.607253886 \times 10^{-9}\ \text{Pa}$$

$$\therefore$$

$$E_* = \frac{1}{9.607253886 \times 9} = 1.040880164\ \times 10^{8}\ \text{Pa} = 104.09\ \text{MPa}$$

Thus, for $\gamma_{Surface}$ = 0.097 $\frac{\text{mJ}}{\text{m}^2}$:

$$\boldsymbol{\kappa} = \sqrt[3]{\frac{8 \times (1.040880164\ \times 10^{8})^2}{3 \times (13.33 \times 10^{-6}) \times \pi^2}} \times \sqrt[3]{0.097 \times 10^{-3}}\ \frac{J}{m^3}$$

$$\therefore$$

$$\boldsymbol{\kappa} = 6.033186717\ \times 10^{6} \times \sqrt[3]{0.097 \times 10^{-3}}\ \frac{J}{m^3}$$

$$\therefore$$

$$\boldsymbol{\kappa} = 227{,}206.9\ \frac{J}{m^3} = 227.2\ \frac{kJ}{m^3}$$

And for $\gamma_{Surface}$ = 2$\frac{\text{mJ}}{\text{m}^2}$:

$$\boldsymbol{\kappa} = 6.033186717 \times 10^{6} \times \sqrt[3]{2 \times 10^{-3}}\ \frac{J}{m^3}$$

$$\therefore$$

$$\boldsymbol{\kappa} = 760{,}133.9\ \frac{J}{m^3} = 760.1\ \frac{kJ}{m^3}$$

Thus, for the models where E is three orders of magnitude below the real value, the baseline range of $\boldsymbol{\kappa}$ values can be approximated to between $\boldsymbol{\kappa} = 227.2\ \frac{kJ}{m^3}$ to $\boldsymbol{\kappa} = 760.1\ \frac{kJ}{m^3}$.

For the simulations in which E is two orders of magnitude smaller than the real value, r_* and ν are unchanged. Thus, the value of E_* is given by:

$$\frac{1}{E_*} = \left(\frac{1 - 0.27^2}{1.93 \times 10^9} + \frac{1 - 0.27^2}{1.93 \times 10^9}\right)\ \text{Pa}$$

$$\therefore$$

$$\frac{1}{E_*} = \ 9.607253886\ \times 10^{-10}\ \text{Pa}$$

$$\therefore$$

$$E_* = 1.040880164 \times 10^9 \text{ Pa} = 1.04 \text{ GPa}$$

Thus, inserting this value for E_* to ***Equation 72***:

$$\boldsymbol{\kappa} = \sqrt[3]{\frac{8 \times (1.040880164 \times 10^9)^2}{3 \times (13.33 \times 10^{-6}) \times \pi^2}} \times \sqrt[3]{\gamma_{Surface}} \frac{J}{m^3}$$

Thus:

$$\boldsymbol{\kappa} = 28.00357217 \times 10^6 \times \sqrt[3]{\gamma_{Surface}} \frac{J}{m^3}$$

Hence, when $\gamma_{Surface} = 0.097 \times 10^{-3} \frac{J}{m^2}$:

$$\boldsymbol{\kappa} = 28.00147169 \times 10^6 \times \sqrt[3]{0.097 \times 10^{-3}} \frac{J}{m^3}$$

$$\therefore$$

$$\boldsymbol{\kappa} = 1.28668 \times 10^6 \frac{J}{m^3} = 1.29 \frac{\text{M}J}{m^3}$$

When $\gamma_{Surface} = 2 \times 10^{-3} \frac{J}{m^2}$:

$$\boldsymbol{\kappa} = 28.00147169 \times 10^6 \times \sqrt[3]{2 \times 10^{-3}} \frac{J}{m^3}$$

$$\therefore$$

$$\boldsymbol{\kappa} = 3.52823 \times 10^6 \frac{J}{m^3} = 3.53 \frac{\text{M}J}{m^3}$$

Hence, ***Table 13*** compiles the proposed benchmark range of values for $\boldsymbol{\kappa}$ and $\gamma_{Surface}$ at scaled values of E.

Table 13 - Benchmark Values for Energy Parameters with Scaled Young's Modulus.

Scaling	E_*	κ	$\gamma_{Surface}$
Young's Modulus at two orders of magnitude below reality.	1.040880164×10^9 Pa	$1.29 \frac{\text{MJ}}{m^3}$	$0.097 \times 10^{-3} \frac{J}{m^2}$
	1.040880164×10^9 Pa	$3.53 \frac{\text{MJ}}{m^3}$	$2 \times 10^{-3} \frac{J}{m^2}$
Young's Modulus at three orders of magnitude below reality.	1.040880164×10^8 Pa	$227.2 \frac{kJ}{m^3}$	$0.097 \times 10^{-3} \frac{J}{m^2}$
	1.040880164×10^8 Pa	$760.1 \frac{kJ}{m^3}$	$2 \times 10^{-3} \frac{J}{m^2}$

Note that as the CGS units style is implemented for accuracy in the LIGGGHTS® model, κ has units of $\frac{\text{Dynes}}{cm^2}$. 1 $\frac{\text{Dyne}}{cm^2}$ is equal to 0.1 $\frac{J}{m^3}$. Hence, the value for κ when Young's Modulus is three orders of magnitude below reality would be in the range of $2.272 \times 10^6 \frac{\text{Dynes}}{cm^3}$ to $7.601 \times 10^6 \frac{\text{Dynes}}{cm^3}$.

5.3.2 Practical Experimental Method

Practical angle of repose testing was required to create a benchmark for the simulation results. To achieve this, a calibrated funnel, in the form of a HFM device, was used to contain the powder before it was allowed to discharge a set distance to the plate below. The discharge distance was set to 25mm in accordance with powder analysis literature and frameworks and the set-up instructions issued with the HFM [22, 120, 200]. The orifice of the funnel was recessed approximately 2mm above the funnel base. Thus, a 23mm spatula is provided such that the 25mm gap can be set by fitting the spatula in the space between the funnel and plate.

To nullify the effect of the plate friction on the pile formed, a very thin layer of powder was applied to the top of the plate before commencing powder flow. Despite its widespread use for calibrating DEM models, the amount of powder required to form an AoR can make the simulations extremely computationally intensive, rendering a 1:1 scale model of the device and powder quantity impossible. Hence, it was necessary to firstly ascertain the point at which a measurable AoR was formed, and then establish when the AoR became independent of powder mass.

Prior to loading the powder samples to the HFM, the device was levelled to the flat work surface to ensure angulations did not affect the results. A very thin rod was used to align the orifice of the funnel and the centre of the receiver plate, such that the peak of the pile was along the same axis as the orifice. As in the powder discharge analysis described in ***Subsection 5.2***, the powder mass was measured with electronic weighing scales before being poured into the funnel of the HFM. The vessel containing the powder was firstly weighed, and the weight of the vessel was then subtracted from the combined weight of both the vessel and powder to reduce the measurement errors.

After setting up the HFM, the weighed powder samples were slowly poured into the funnel and allowed to settle under gravity. The flow of powder was constrained by a mechanical shutter over the funnel orifice. After settling, the shutter was removed to discharge powder to the receiver plate. In the event of blockages, the funnel was tapped with the spatula to restart flow as permitted in the framework established by BS EN ISO 4490 [200].

Precautions were taken to nullify the impact of environmental factors on the results when possible. For example, the powder was sealed in a waterproof container prior to the practical analysis to minimise the moisture effects. Furthermore, the AoR formed by the real powder samples were measured three times for each given powder mass set, with the average AoR of this data set taken for comparison with the model.

Finally, in accordance with published literature [75] and to account for the assumptions stated, a margin of error of ± 3° was considered acceptable between the experimental and simulated AoR. This was to ensure that the model authentically reflected the dynamic behaviour of powder in both the deposition and spreading operations.

5.3.3 Results of Practical Angle of Repose Testing

The AoR was found by measuring the powder pile diameter, $\boldsymbol{d_{Pile}}$, and the height of the peak point, $\boldsymbol{h_{Pile}}$. The value of $\boldsymbol{d_{Pile}}$ was measured by reference to the graduations marked out on the receiver plate, and a depth gauge board was used to find the powder level at $\boldsymbol{h_{Pile}}$. The AoR is given by ***Equation 76*** [180]:

$$AoR = \tan^{-1}\left(\frac{\boldsymbol{h_{Pile}}}{0.5 \times \boldsymbol{d_{Pile}}}\right) \tag{76}$$

Four different powder quantities were tested. As in the discharge time analysis (***Subsection 5.2***), the mass samples used were 50g, 25g, 12.5g, and 6.25g. An interest was held as to how the decrease in mass influenced the AoR formed, and whether a limit existed as to how small a quantity of powder produced a pile with a discernible AoR. All four powder samples created a noticeable AoR. A graphical depiction of the AoR formed by the 50g powder sample is provided in ***Figure 35***. For brevity, images of the AoR formed by the other three sample sets and the full set of results have been included in ***Appendix E***.

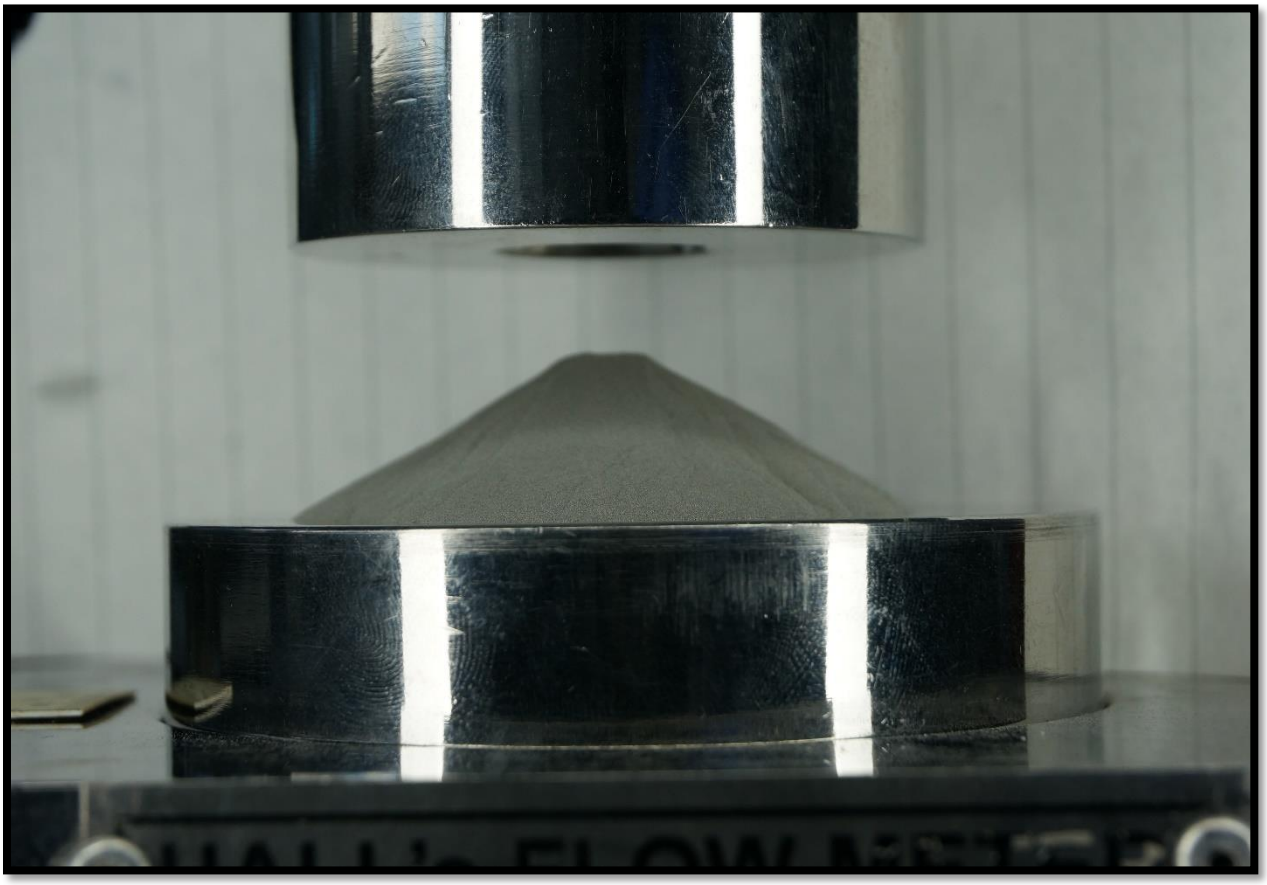

Figure 35 - Angle of Repose of 50g Sample of SS316l.

As expected, the pile size diminished when less powder was used. ***Table 14*** demonstrates the height and depth of each powder pile formed for three tests of the four mass sets, generating 24 data values in all. The average AoR is taken from the three test values for that mass set.

Table 14 - Results of Practical Angle of Repose Testing.

	Mass (g)							
Test	**50**		**25**		**12.5**		**6.25**	
	h_{Pile} (mm)	d_{Pile} (mm)	h_{Pile} (mm)	d_{Pile} (mm)	h_{Pile} (mm)	d_{Pile} (mm)	h_{Pile} (mm)	d_{Pile} (mm)
1	15	47	12	35	9	27.5	7	20
2	15	40	13	35	7	24	8	22.5
3	18	45	10	35	10	25	6	22
Average Angle of Repose (°)	36.03		33.60		34.04		33.01	

As shown, the AoR was generally stable and had a range of approximately 3° between the smallest and largest sample sets. The AoR formed by the 50g sample showed strong agreement with values for the AoR in published literature. Notably, static AoR testing approximated at 36° for SS316l powder [214], and the same value was quoted for the heap in front of the recoater during dynamic powder spreading [215]. Based on these results, and to account for the assumptions induced to the digital twin model, an AoR value between 33° and 36° was considered to constitute a successful calibration of the material properties.

5.3.4 Simulation Method

As stated previously, limitations existed in developing an accurate model reflective of the practical AoR analysis set up. For example, a 1:1 scale domain in the digital twin system was computationally unviable for these experiments. The stable range of AoR values between the different mass sets allowed for fewer particles to be inserted to manage the computational costs, and to expedite the process with respect to the large range of CED and friction parameters that were required to calibrate the model. Preliminary testing showed that a discernible AoR was achieved when more than 40,000 particles were inserted and allowed to pile, and a negligible difference in powder behaviour was observed when the assigned Young's Modulus was two or three orders of magnitude below reality, as also observed numerous times in literature [176, 177, 178]. Hence, for further computational savings, a Young's Modulus value three orders of magnitude below reality was used.

Despite efforts to create a digital model that matched the practical conditions, an exact replica of the environmental and parametric properties was unreasonable to expect. Hence, the digital twin induced assumptions to better manage the time and computational costs. For example, the presence of moisture in the environment was omitted, and the modelling was simplified by the assumption that all constituent particles were spherical, as regularly observed in DEM-AM studies [20, 21]. A further limitation was reflected by the inability to assign friction parameters for a given material (as observed in other analytical software, such as SolidWorks® [216]. This was accounted for in the calibration process by assigning particle-plane friction values in accordance with the contact models selected.

Another assumption induced to simplify the model was to neglect the influence of air resistance on powder flow, which would have required CFD-DEM coupling to achieve. Neglecting air resistance was considered to have a minimal impact on the accuracy of modelling, as research shows that van der Waals, capillary and electrostatic forces dominate air interactions at the size range of powder modelled (15-45 µm). Thus, the contact models implemented to replicate these forces, in conjunction with friction coefficients, provided a sufficient model of interparticle cohesion to accurately portray the AoR. Numerous researchers have limited their studies to cohesion and friction modelling and neglected air resistance, and observed a minimal deviation between digital and practical AoR results, with it theorised that the high density of the SS316l nullifies the influence of air resistance in piling behaviour [217, 218, 219].

Two simulation processes were used to validate the model. The first was based on the works of Shenouda and Hoff [220], where the powder was allowed to freefall into the simulation domain in a cylindrical insertion region at an equal diameter to the HFM outlet. To ensure the model was robust to the practical testing process, the distance from the bottom of the insertion region to the fixed plane where the particles pile up was set to 25mm. In the second approach, the powder was inserted to a cone representing the HFM and allowed to settle before being discharged. Note that, to reduce the computational intensity incurred by including the full geometry in the system, the cone was sliced in the z axis to house only the required number of particles.

As in ***Subsection 5.2***, powder pouring was constrained by a fixed plane situated at the cone orifice which was removed to initiate flow. In both techniques, another fixed plane accounted for the receiver plate and thus the cohesive and friction coefficients were also calibrated for the particle-plane interactions to ensure realistic piling behaviour. The initial input properties of the powder, fixed planes, and cone geometry were uniform across simulations (outlined in ***Table 12***) such that the effect of friction and cohesion settings could be isolated. Both model set ups used an orthogonal simulation domain with lengths of 0.5cm × 0.5cm × 1.25cm in the x, y, and z planes, respectively. A visual comparison of the two simulation processes is provided in ***Figure 36***.

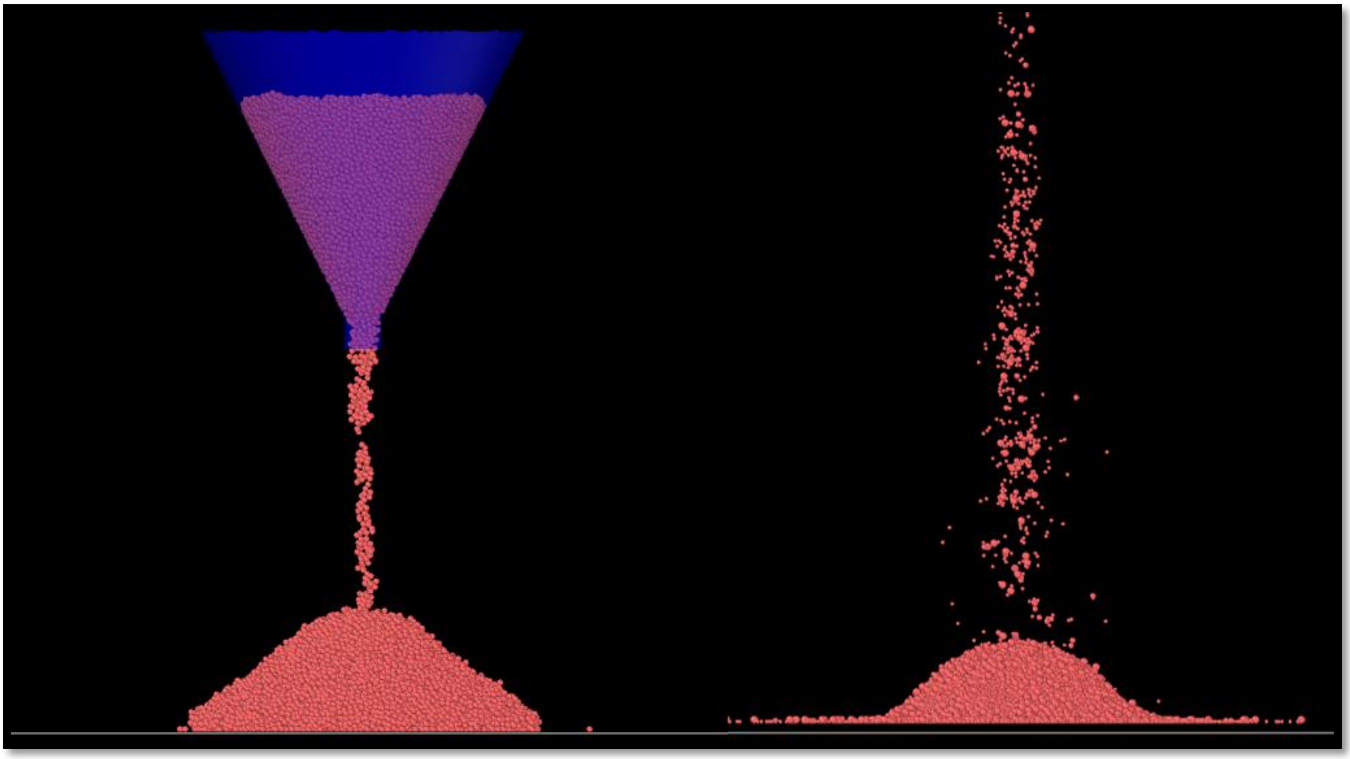

Figure 36 - Comparison of the HFM Digital Twin and Freefall Simulations.

5.3.5 Results of Angle of Repose Simulations

As outlined in ***Subsection 5.3.1***, the expected range for the CED values was between $\boldsymbol{\kappa} = 227.2 \frac{kJ}{m^3}$ and $\boldsymbol{\kappa} = 760.1 \frac{kJ}{m^3}$ when E was three orders of magnitude below reality. From literature, the range for the sliding friction coefficients was between 0 and 1 (***Table 6***). A wide range of values were tested for both cohesion and sliding friction particle-wall and particle-particle relationships. The complete data set for all tested values is recorded in ***Appendix F***. Preliminary testing highlighted that the coefficient of restitution should be set to a universal value of 0.1. Calibration of the digital twin parameters was achieved at the values outlined in **Table *15***, which has been combined with ***Table 12*** to state all the input properties for the simulation.

Table 15 - Complete Properties of SS316l for Digital Twin Calibration.

Material Property	Symbol	Value	Units
Young's Modulus of Elasticity	E	0.193	GPa
Poisson's ratio	N	0.27	Dimensionless
Particle Size Distribution	PSD	20-40	µm
Density	ρ_{SS316l}	8000	$\frac{\text{kg}}{\text{m}^3}$
Coefficient of Rolling Friction	$\mu_{Rolling}$	0.01	Dimensionless
Cohesive Energy Density (Particle-Particle)	$\boldsymbol{\kappa}$	550	$\frac{kJ}{m^3}$.
Cohesive Energy Density (Particle-Wall)	$\boldsymbol{\kappa}$	100	$\frac{kJ}{m^3}$.
Coefficient of Sliding Friction (Particle-Particle)	$\mu_{Sliding}$	0.7	Dimensionless
Coefficient of Sliding Friction (Particle-Wall)	$\mu_{Sliding}$	0.7	Dimensionless
Coefficient of Restitution	$\boldsymbol{e}$	0.1	Dimensionless

The assigned value for the particle-particle CED showed a good agreement with the expected range calculated in ***Subsection 5.3.1***. The same input parameters were assigned to both the free-falling and HFM-poured models and in both cases, the particle-particle interactions had a more pronounced effect on piling behaviour than the particle-wall relationships. After establishing the calibrated values, the simulation with the parameters outlined in ***Table 15*** was executed again with different seed numbers assigned to the particle insertions to evaluate the repeatability of the results. Seed numbers are values coded into the simulation to randomise the location of the particle insertions, ensuring that variability is accounted for between simulations. A negligible deviation (33.06° in the second test of the HFM-poured model compared to 33.45° in the first test, a less than 1.25% discrepancy) confirmed the repeatability of the results.

The comparison between the AoR formed in practical analysis and the digital models of freefalling and HFM-poured powder is outlined in ***Table 16***.

Table 16 - Angle of Repose Results for Practical and Simulation Tests.

Model Set Up	Angle of Repose (º)
Practical Test.	33.01-36.03
Sim: Freefalling Powder.	33.68
Sim: HFM-Poured Powder.	33.06-33.45

The results showed a strong agreement between the practically formed powder pile and the digital twin in the experiments from both pouring types. A visual comparison between each powder pile is provided in ***Figure 37***.

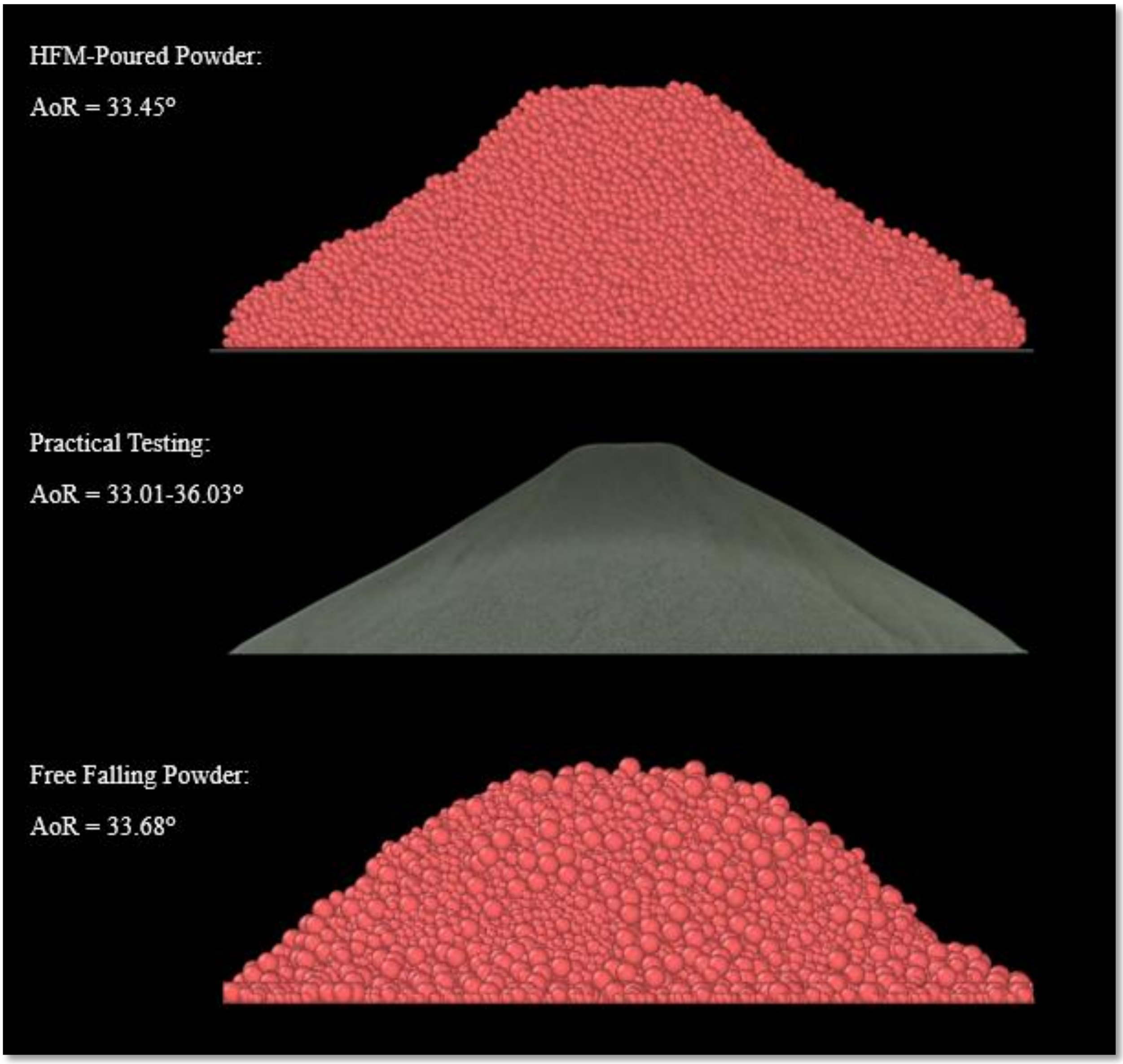

Figure 37 - Comparison between Practical and Digital Angles of Repose.

As ***Figure 37*** shows, although a minimal difference was observed between the AoR in both digital twin models, the HFM-Poured powder gave a significantly closer reflection of the real piling behaviour. A significant slope is noticed on the sides of the HFM-Poured model compared to the pile formed by allowing powder to free-fall into the simulation domain. Post-processing of the two models showed that the free-falling powder had a proclivity to fan out and disperse over a wider zone onto the receiver plate. In contrast, the outlet of the HFM model constrained the powder flow and engendered the formation of a taller powder pile. A depiction of this phenomena is provided in ***Figure 36***.

Various reasons are proposed for the differences in the piles formed in LIGGGHTS®. For example, particles allowed to rain into the domain in the digital model would not be subjected to the same friction forces that constrain movement when the powder was discharged from the cone outlet practically. Furthermore, the randomised position of the particle centroids when inserted in a cylinder is the possible cause of the fanning phenomena, as particles inserted via the HFM geometry are more liable to agglomerate in the cone during settling and thus, discharge as a continuous mass.

The differences in the digitally modelled piles have interesting implications for the validation of DEM models, and the analysis of powder flow in this project. It is obvious from the results that configuring the material properties and parameters is only a partial aspect of model calibration, and that an accurate representation of the full system is required to produce a model reflecting the real powder behaviour. This raises further questions about the mechanical perturbations of powder during processing and presents another area for further exploration.

With respect to the observed differences between the simulations and the physical results, the AoR showed a good agreement between each testing method. However, a more sophisticated and intensive analysis may have highlighted disparities between experimental and modelled flow behaviour. For example, research shows that gas atomised SS316l powder in the 15-45 μm range, as used in this study, can comprise irregular elements consisting of satellites and inconsistent morphology [53]. This can have ramifications for interparticle cohesion and the piling behaviour and contradicts the assumed spherical particles modelled with the DEM.

Whilst the purpose of the exercise was to calibrate properties to produce a model with a strong fidelity to real powder flow, it is imperative to rationalise the research by recognising that all simulation and modelling-based work, regardless of the approach used, is only ever a best approximation of real-world engineering processes. Certain external factors not accounted for within the contact models, such as temperature, may also influence the piling behaviour but could not be accounted for within the limitations of the modelling process.

For the purposes of validation in this project, the results shown have fallen within the stated tolerance for the AoR and thus a successful calibration of the properties implemented to the digital twin has been achieved. This, in conjunction with the results of the experiments across ***Section 5***, provide the grounds to justify the use of LIGGGHTS® and the implemented properties for powder flow analysis in subsequent simulations.

5.4 Practical Analysis using a Powder Test Rig

5.4.1 Experimental Method

To evaluate the fidelity of the DEM powder spreading models (***Section 6*** and ***Section 7***), it was essential to validate the data against a practical powder spreading operation. To achieve this, a simple powder spreading system was developed as part of the practical analysis. As a proxy for the substrate and powder bed, a block of mild steel was cut to dimensions of $50\text{mm} \times 25\text{mm} \times 15\text{mm}$. Within this block, a channel was machined of dimensions $30\text{mm} \times 12\text{mm} \times 5\text{mm}$. to analyse the profile of the spread layer. A graphical depiction of the mild steel block and machined channel is provided in ***Figure 38***.

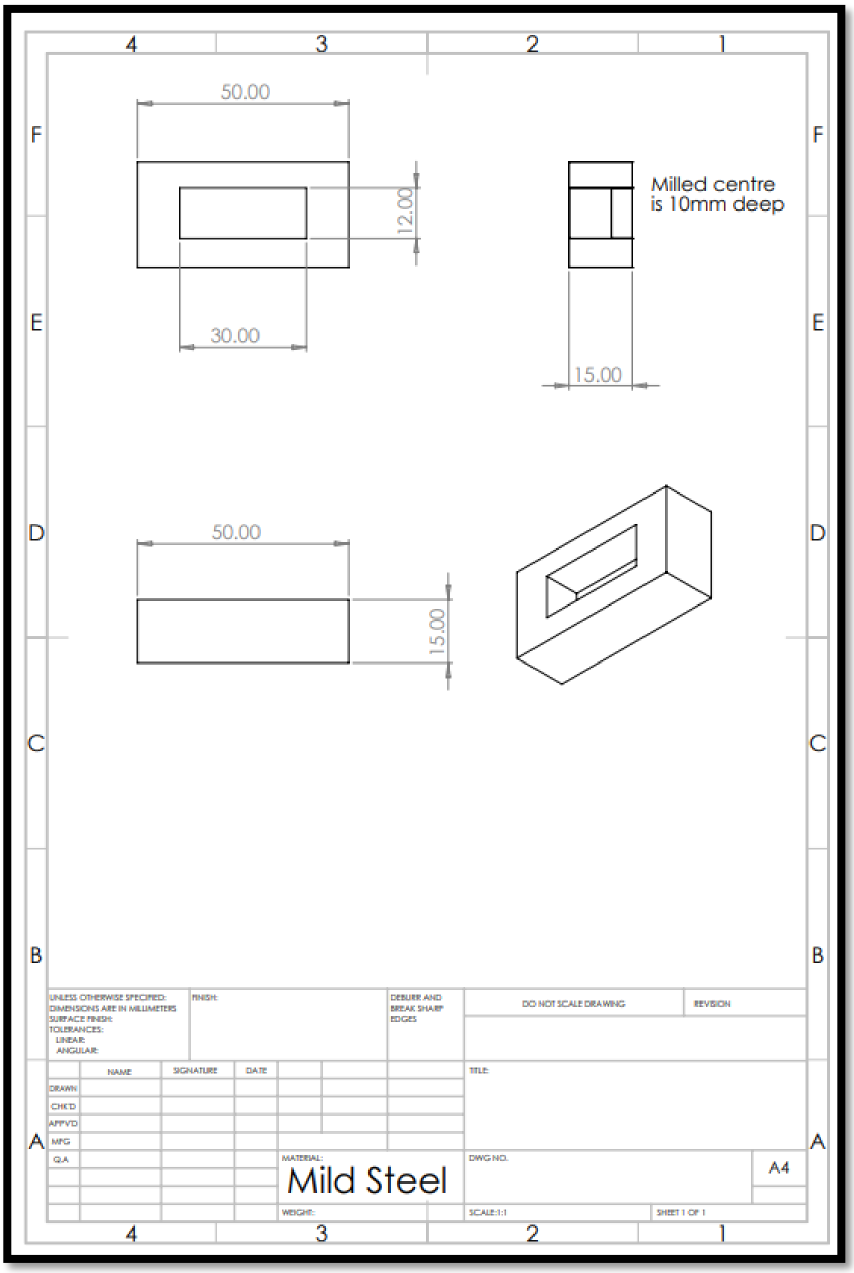

Figure 38 - Technical Engineering Drawing of Steel Block used for Powder Spreading Operation.

To disperse the powder, a 5 axis CNC machining centre was adapted to incorporate a fixture capable of holding a Stainless Steel precision ground machining parallel to the machine spindle. Hence, allowing a recoater to be fixed to the machine and spread the powder under various controlled speeds, allowing for a parametric approach to the analysis. A graphical depiction of the adapted 5 Axis CNC machining centre, configured to incorporate the recoater blade, is depicted in ***Figure 39.***

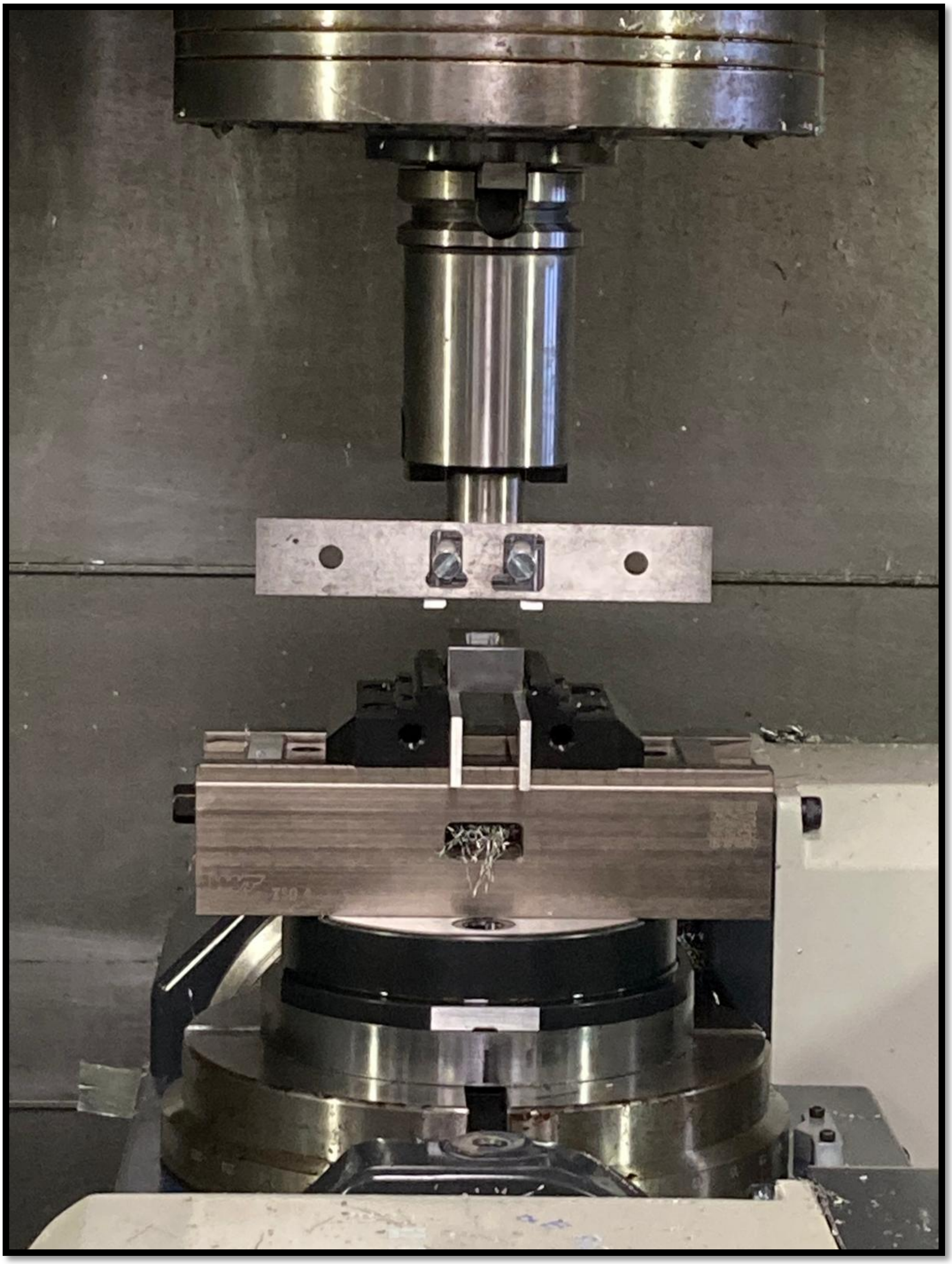

Figure 39 - 5 Axis CNC Hardware Configured to Incorporate Recoater Blade.

Prior to commencing the spreading operation. A thin layer of SS316l powder was randomly distributed over the surface within the valley to more closely mimic AM spreading conditions. Subsequently, SS316l powder was delivered under gravity to form a pile in front of the recoater face, to model the rainfall insertion process observed in DEM-AM modelling as closely as reasonably practicable.

Following a brief pause to allow the powder to settle, the SS316l was dispersed across the top of the machine valley by the spreader to analyse the spread layer profile. The mild steel block was then carefully transported to the Bruker device at which measurements were taken of the spread layer surface roughness. Given the powder size range of 15-45 μm, the Bruker measured a powder bed region of $0.5\text{mm} \times 0.6\text{mm}$ (approximately 20 times greater than the median average particle size). The Bruker Contour GT device is a 3D optical profilometer used for measuring the surface topography of a range of engineering materials. The hardware is capable of creating surface maps and quantifying surface roughness parameters at nano and micron-scale accuracy, underpinning its use for evaluating AM powder beds. An image of the Bruker machine is provided in ***Figure 40***.

Figure 40 - Bruker Hardware used for Surface Profile Roughness Analysis.

The spreading operation was conducted five times at increasing recoater speed intervals of $2\ \frac{cm}{s}$. Each recoater speed was trialled three times with the roughness value produced taken to evaluate the repeatability of the spreading operation. The surface roughness of the spread layer for a given recoater speed was taken as the average of these three values. In an effort to minimise experimental variability, and therefore decrease the prospect of producing erroneous results, the tests of each recoater speed were not performed in any order of speed. Instead, the trials were conducted as such that, whilst the three trials per speed setting were performed and yielded the 15 data readings overall, the order of speed was non-sequential. The aim of this experimental choice was to alleviate the possible sources of experimental error, such as by ensuring that any recoater blade wear did not diminish the accuracy of results over time with successive experiments. Whilst every precaution was taken to reduce all sources of experimental error so far as reasonably practicable, there were, as with every engineering experiment, potential error sources that should be acknowledged:

- The loading of the machined block, containing the valley in which the powder was spread, was performed by manual handling. This was the case both into the CNC machining centre and Bruker hardware. The same was true for the removal of the block from both devices. To minimise the impact of vibrations when transporting the sample from the CNC machining centre to the Bruker, the sample was housed in a sealed container, within a sponge cradle to dampen the influence of disturbances.

- Whilst the operators were adequately trained and experienced on the machinery used to perform the experiments, prospective experimental errors could feasibly arise due to the repetitive nature of the experiments.

- As the powder was rained in to fill and overflow the valley within the machined block, it is highly likely that inconsistent powder quantities were used. Thus, discrepancies in the powder quantity between samples are likely to have engendered some deviations in the surface roughness values measured. This is a noteworthy oversight and a justified critique of the experiment, and instead, using measured quantities of powder (similar as to how the testing was performed in the AoR analysis in ***Subsection 5.3***, would afford more veracity to the results.

Prior to commencing the surface roughness analysis, a stitching operation was performed. Stitching describes the process of combining various adjacent image fields into a single, larger composite image by taking multiple overlapping scans of the surface being measured. The hardware then combines these images to present a continuous depiction of the powder bed surface topography. The stitching process incurred a minimal increase in accuracy compared to the non-stitched measurement when tested with an initial sample inspection of the surface topography. An arithmetic roughness value of 4.131 μm was observed prior to stitching, compared to 4.153 μm in the stitched sample. The negligible difference (of approximately 0.53%)

in results, in consideration with the stitching process quadrupling the measuring time for each sample, justified the use of the original unstitched values in the subsequent surface roughness analysis.

5.4.2 Results and Discussion

The complete set of results from the practical analysis using a powder test rig is presented in ***Table 17***.

Table 17 - Data from Practical Powder Spreading Analysis.

	Trial and Roughness Values (μm)			
Recoater Speed ($\frac{cm}{s}$)	**1**	**2**	**3**	**Mean Roughness (μm)**
2	5.859	1.458	1.409	2.909
4	3.021	1.495	1.519	2.012
6	1.456	6.257	2.405	3.373
8	7.444	6.594	7.46	7.166
10	8.368	7.675	7.513	7.852

For brevity, samples of the surface roughness profiles at selected speeds from various trials have been recorded subsequently. The surface roughness profile formed by the recoater at 2 $\frac{cm}{s}$ is shown in ***Figure 41***.

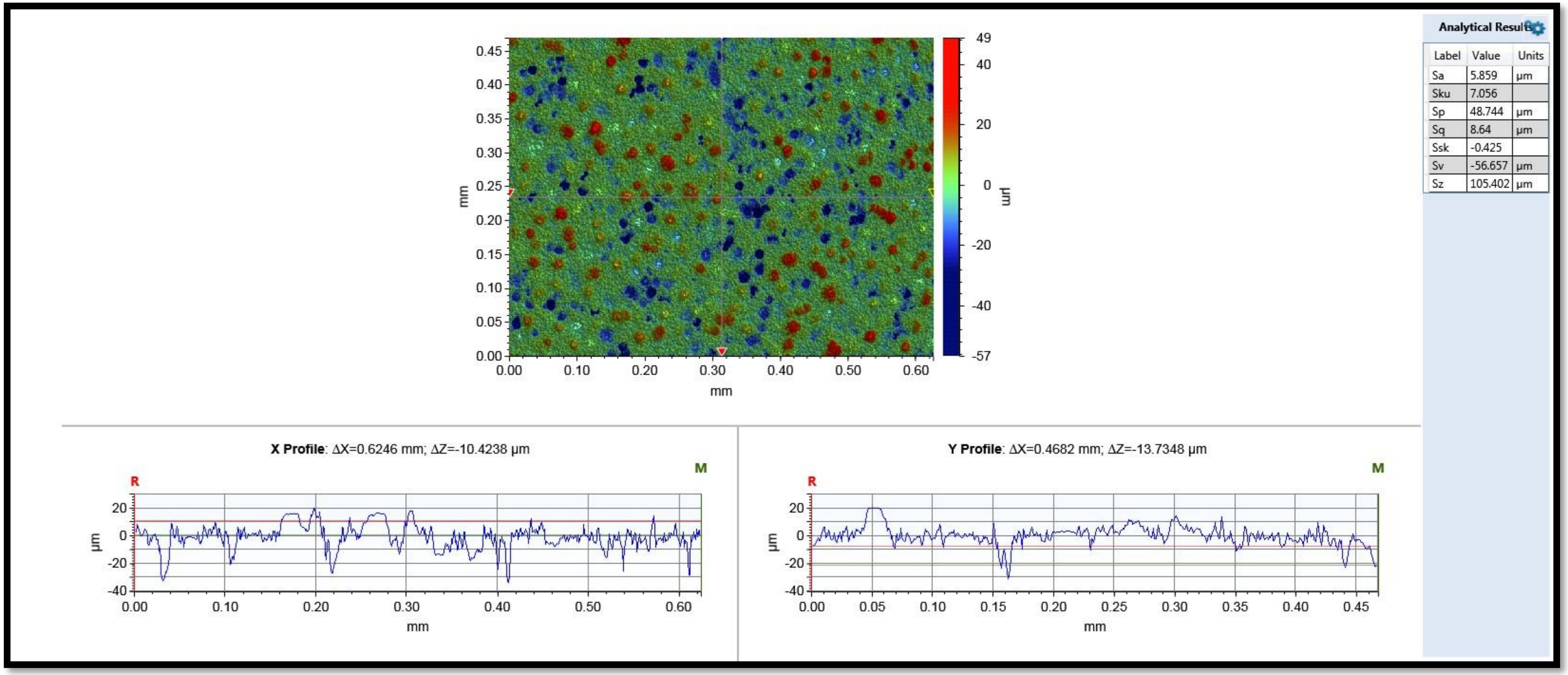

Figure 41 - Surface Roughness Profile formed by Recoating Speed of 2 cm/s.

The surface roughness profile formed by the recoater at 4 $\frac{cm}{s}$ is demonstrated in ***Figure 42***.

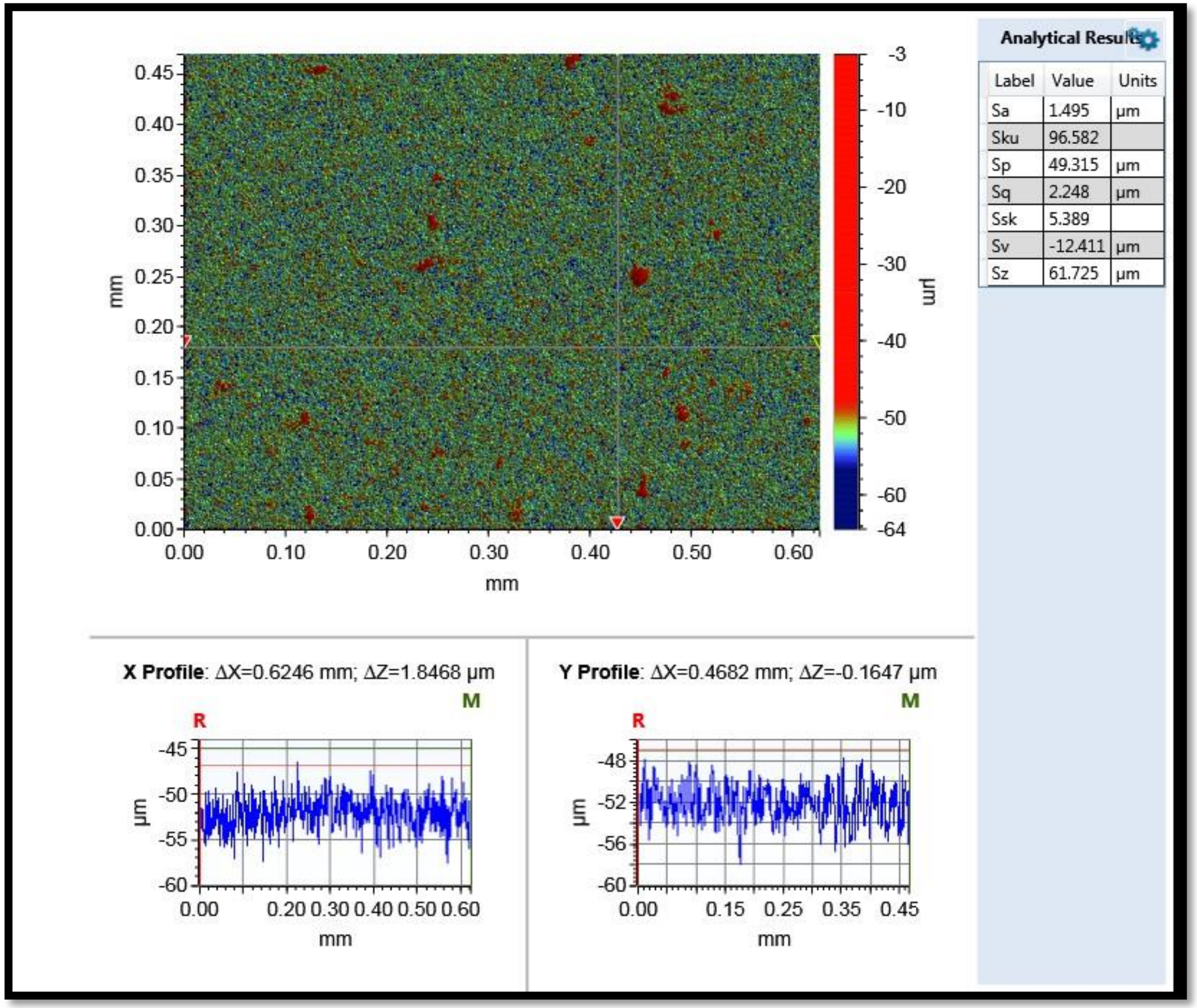

Figure 42 - Surface Roughness Profile formed by Recoating Speed of 4 cm/s.

The surface roughness profile incurred by the recoater at 8 $\frac{cm}{s}$ is demonstrated in ***Figure 43***.

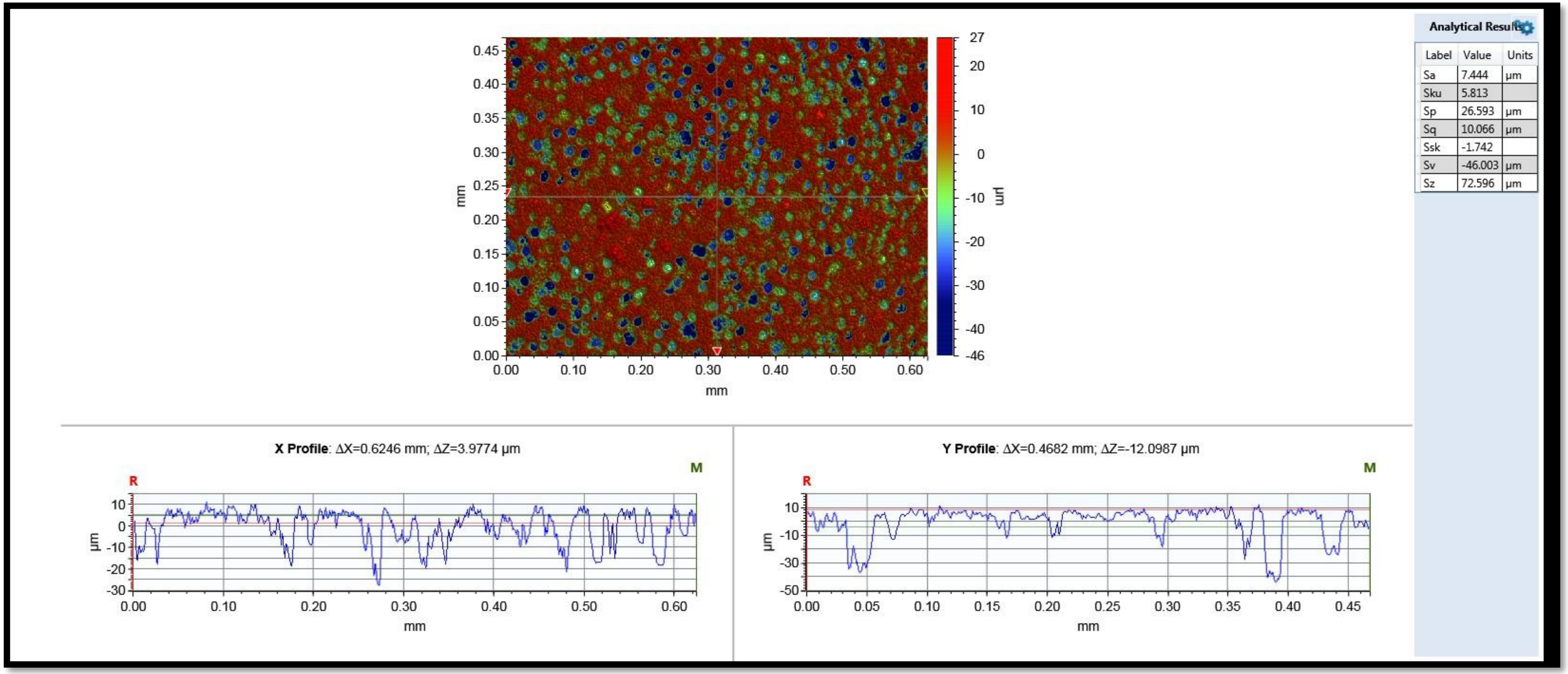

Figure 43 - Surface Roughness Profile formed by Recoating Speed of 8 cm/s.

The surface roughness profile incurred by the recoater at 10 $\frac{cm}{s}$ is shown in ***Figure 44***.

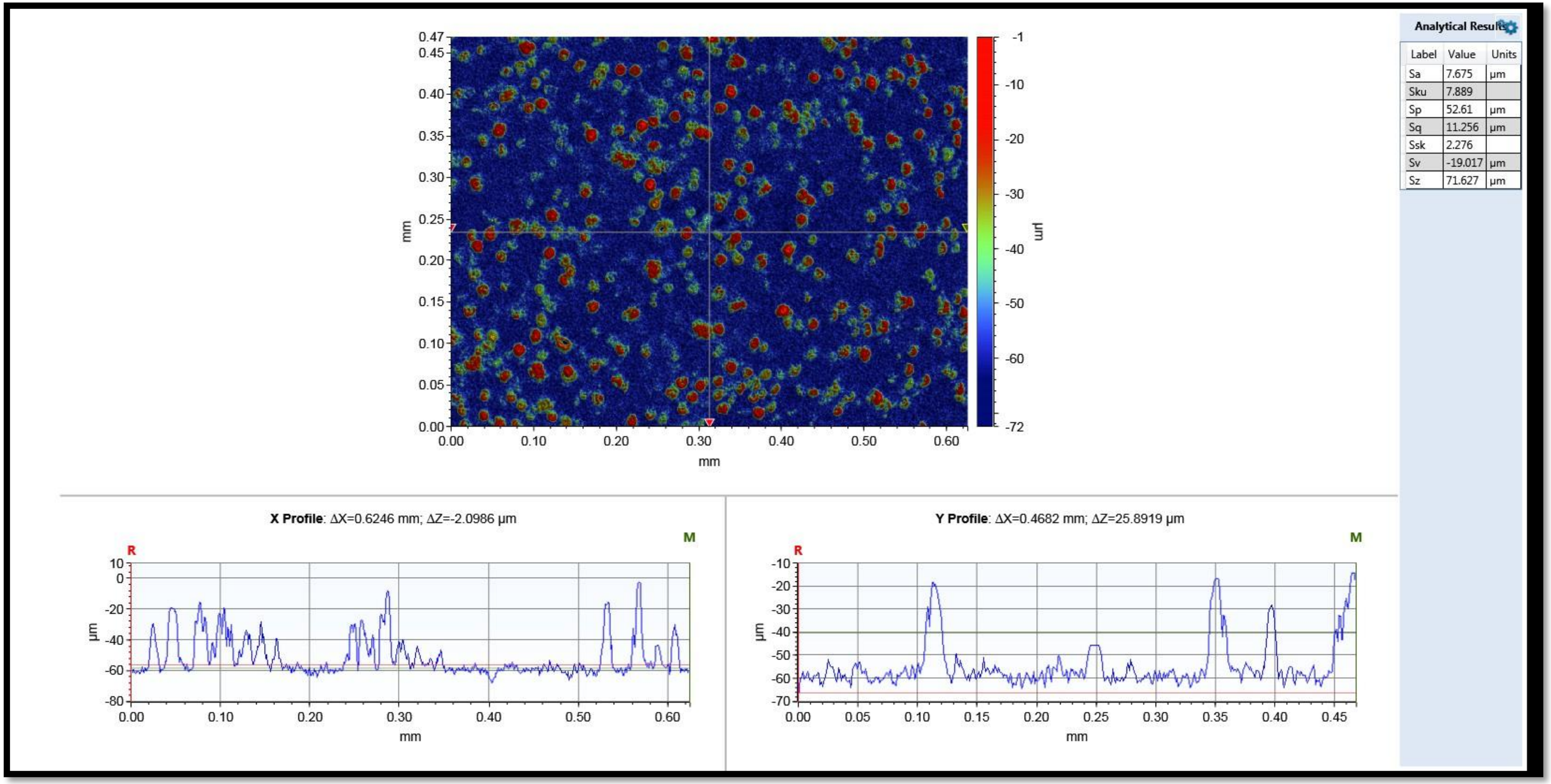

Figure 44 - Surface Roughness Profile formed by Recoating Speed of 10 cm/s.

A graph of the surface roughness results from the practical experiments is presented in ***Figure 45***. The data markers reflect the mean values, with error bars used to reflect the minimum and maximum values from the analysis (***Table 17***).

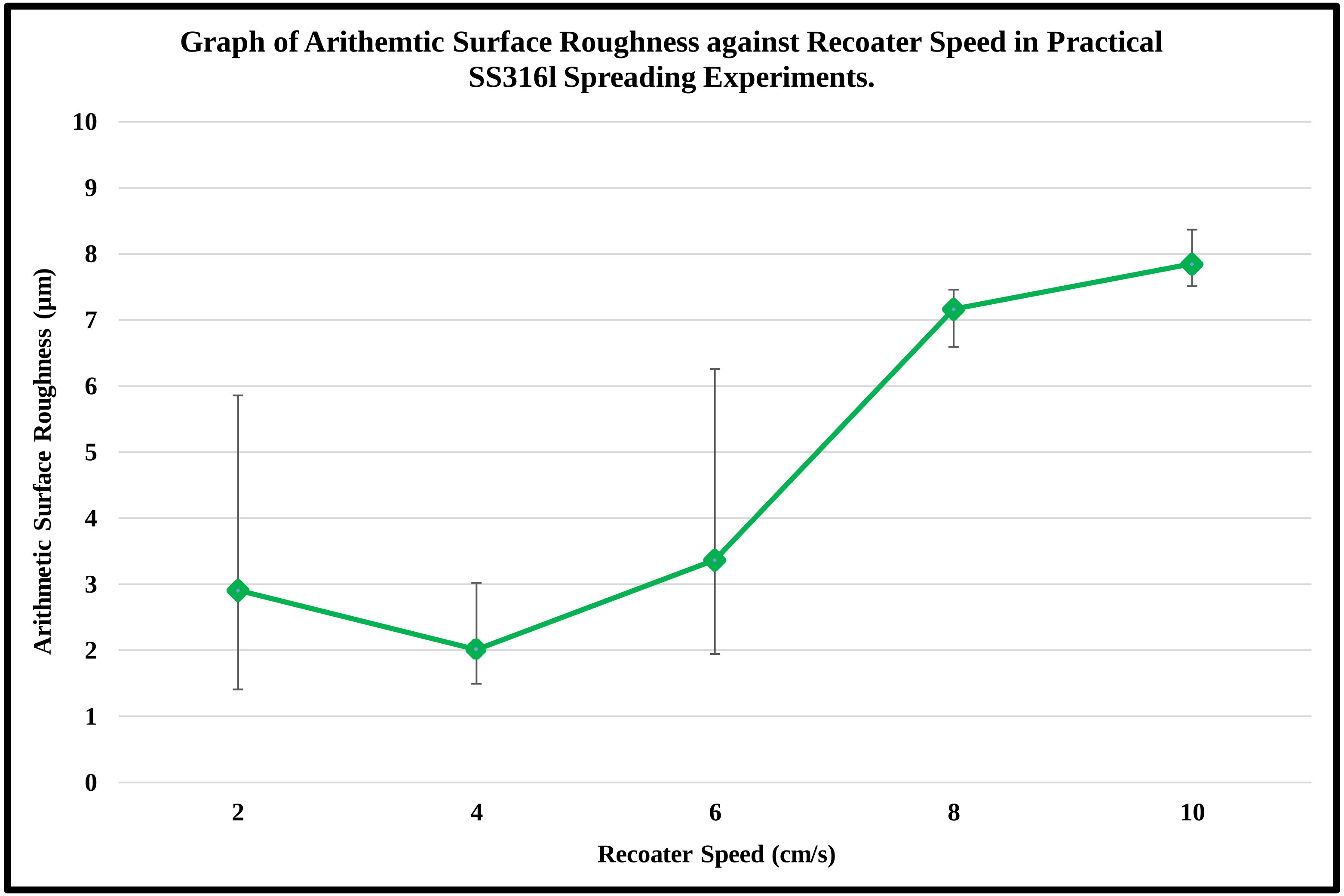

Figure 45 – Results of Surface Roughness Analysis in Practical Powder Spreading Experiments.

Analysis of the surface roughness results from the testing of the practical powder bed set up, broadly, conformed to literature, by showing generally that surface roughness increased with recoater velocities. Thus, showing agreement with the theories of Haeri et al [12], that increased recoater speeds generally diminished the quality of the spread layer by reducing the uniformity of the surface profile. It is noteworthy, however, that the roughness did not consistently increase with the spreader speed, as the average roughness for the bed produced with a recoater speed at 4 $\frac{cm}{s}$ was smoother than the average roughness observed when the spread layer was formed by the recoater at 2 $\frac{cm}{s}$ (2.01 μm to 2.91 μm). However, a viable explanation for this can be proposed by a closer inspection of the results record in ***Table 17*** which showed a wider range of values and in particular the significantly higher roughness for the first trial at 2 $\frac{cm}{s}$. It is plausible this can be attributed to an experimental error, as Trial 1 at 2 $\frac{cm}{s}$ was the first trial performed overall for the experiments. In respect of the rest of the data established, a rougher surface topography was incurred at increasing recoater speeds.

A reasonable criticism of the analysis, and how reflective it is of the DEM modelling processes implemented in the rainfall analysis of both ***Section 6*** and ***Section 7***, is based on the variable parameters. In ***Section 6*** the PSD was varied, and in ***Section 7*** the deposition method and the PSD were both varied. Conversely, in these experiments, constraints in sieving equipment meant that the only variable was the recoater speed. Thus, it is clear that some elements of the efforts to optimise the powder bed will remain unexplored by this testing method. The remaining results (testing at 6 $\frac{cm}{s}$, 8 $\frac{cm}{s}$, and 10 $\frac{cm}{s}$) showed a consistent increase of the surface roughness at higher recoater speeds. Thus, it is feasible that elevated speeds culminate in a diminished surface and that this influence is exacerbated at increasing velocities, which would in part explain (along with possible sources of experimental error discussed previously) the anomalous results between 2 $\frac{cm}{s}$ and 4 $\frac{cm}{s}$.

Considering the data established holistically, it is clear the experiment could be further refined and that limitations exist in respect of the wide range of values for certain speed settings (***Table 17***) which have caused potential disparities in the expectations of results. Nevertheless, in general terms an agreement is observed between the findings of the experiment and the consensus of authors in the DEM-AM research landscape, that increasing recoater speeds diminish surface layer uniformity and thereby impede the quality of the formed powder bed. Arguably the most significant finding, in reflection of the implications of the practical testing for the digital modelling methods pursued in ***Section 6*** and ***Section 7*** of this report, is that the powder surface roughness values are generally in agreement with respect to the order of magnitude and range of results. The roughness values approximated between 4.10μm and 10.07μm for the various PSD sets in ***Section 6***, 5.87μm and 12.83μm for the differently weighted rainfall PSD sets in ***Section 7***, and ranging from 2.01μm and 7.85μm for the 15-45μm SS316l powder tested at various recoater speeds in the practical analysis of this subsection.

6. Effect of the Particle Size Distribution on the Surface Roughness, Solid Volume Fraction, and Segregation in the Powder Bed

This section contains all relevant information pertaining to investigating the effect of the PSD on powder bed spread layer quality against three discrete metrics: the surface roughness, SVF, and presence of segregation between polydisperse elements. ***Subsection 6.1*** introduces the analysis by contextualising the PSD and establishing the aims and assumptions applied to the simulation processes. The simulation method, which explains how the models were set up, parametric and powder configurations, and how different cases of PSD powder sets were inserted and spread across the powder bed, is provided in ***Subsection 6.2***. ***Subsections 6.2.1***, ***6.2.2***, and ***6.2.3*** explain how the surface roughness, SVF, and segregation analysis techniques were performed, respectively.

Subsection 6.3 and the subsections within document the results of all three metrics of powder bed quality inspections, and contains a brief check of the inserted quantity of particles to each simulation case to ensure the powder insertion process was performed correctly. A discussion of the results and the implications of the inserted PSD sets, and a summary of the key findings of the research in this section, is performed in ***Subsections 6.4*** and ***6.5*** respectively.

6.1 Introduction

As alluded to throughout ***Section 3***, the characteristics of the AM powder bed significantly affects the quality of the build process and the components generated. The work in this chapter explores the influence of the PSD on three discrete metrics of quality: the surface roughness, the SVF, and the segregation between particles in the spread layer. The PSD has been widely shown in literature to influence the formation of the powder bed and is reviewed at length in ***Subsection 3.2.3***.

It was of interest to this research if a coarser PSD, in which the concentration is skewed to a higher insertion of coarse elements, generally produced a smoother powder profile with controlled spherical particle size fractions. The aim therefore is to generate data that ascertains the merits of inducing a wider, or otherwise, distribution of fine or coarse particles to the bed. Thus, this chapter investigates the influence of the PSD by using three sets of uniform particles, and four polydisperse powder sets comprised of the majority fine (20 µm in diameter), the majority coarse (40 µm in diameter), the majority median-sized particles (30 µm in diameter), and an even distribution of the finest, median, and coarsest elements by mass. The selection criteria for this powder size range is discussed more thoroughly in ***Subsection 6.2***.

In AM literature, the term "surface roughness" often refers to the surface profile of the built components. In this project, a distinction is made that the term surface roughness describes a measure of the 2D projection of the powder bed profile onto the xz plane, after the powder has been spread. A comprehensive explanation of how the surface roughness is measured in this project is provided in ***Subsection 6.2.1***.

The following assumptions were made prior to simulation.

- In accordance with random uniform sphere packing randomly packed in Euclidean space [125, 221, 222]. A slight difference is likely to be observed depending on if the spheres are in a poured or close-packed state (for example, due to vibration or compaction). Thus, 64% was considered to be the maximum possible packing limit in these models. However, due to the nuances and stochasticity of the spreading process this value is unlikely to be achievable in an AM powder bed. Hence, the critical volume fraction proposed by Haeri et al [12] of 58.5% provided an expected upper boundary for these models.

- In metal AM, it is desirable for the humidity in the building chamber to be minimised. Owing to the vacuum environment of the EBM process and the inherent vacuum in the LIGGGHTS® model, the moisture content and thus capillary effects of the SS316l powder has been neglected in these simulations.

- The gap between the recoater and the spread layer in the z plane will also influence the quality of the powder bed, by determining the mass flow of powder in the spreading regime.

As the aim was to determine the PSD which maximised the SVF, the recoater velocity was set at 20 $\frac{mm}{s}$ across all seven cases. This value was considered typical of AM spreading processes and isolated the PSD as the dominant factor in the SVF formed [49]. The approach used in this research project to find the SVF is explained in ***Subsection 6.2.2***.

Segregation was the third metric of powder bed quality used in these tests in conjunction with the surface roughness and SVF, and was measured in three discrete segments across the three planes of the powder bed to give nine segments in total. An explanation as to how segregation is quantified is provided in ***Subsection 6.2.4***. With respect to the three quality indicators chosen an optimised powder bed would possess a homogenous, smooth surface profile at the spread layer, a high packing density, and an even distribution of polydisperse particles in each axis.

6.2 Simulation Method

Design of the Model

Attempts to model a full powder spreading operation scaled to a real AM machine are currently unviable, as filling a volume of 30cm $\times$ 30cm $\times$ 10cm (the approximate dimensions of an EBM powder bed) would require several billion particles to derive meaningful data. This was obviously far beyond the computational and time resources available in this project, necessitating a scaled approach in which information could be derived from smaller powder bed areas reflective of the larger domain. To achieve this, only a segment of the bed was tested, with periodic boundaries in the y plane to model the wider span of the bed.

To perform the simulations, LIGGGHTS® uses coded input scripts from which all features of the simulation are defined and executed. In this simulation, two discrete scripts were used. The first was the "set-up" script, which defined the material properties of both the powder particles and geometries in the model, established the domain sizes and timestep, and then specified the stereolithographic (STL) files that were imported to the model. The set-up script also inserted the particles to the simulation. The second input file was the "run" script, which governed the position and motion of the recoater as it spread powder across the substrate.

To connect the "set-up" and "run" scripts, a "write-restart" command was coded to generate a restart file after a given number of steps during the set-up phase of the simulation. This provided a form of checkpoint, from which a simulation could be recommenced and progress made from the timestep at which the restart file was written. This aided in adapting the parameters of the model as it enabled configurations to be made without having to restart the simulation. An example in which this may be applied would be to run simulations with two different recoater velocities to ascertain the influence on powder bed quality, without the time-consuming and computationally intensive process of rerunning the initial particle insertions. An example of a complete copy of the scripts used to set up and run the model is included in ***Appendix G***.

The same system domain was used across all simulations and seven cases were built with each having a different PSD set. Three sets consisted entirely of uniform particles of diameter 40 µm, 30 µm, and 20 µm, and four polydisperse sets with particle fractions of the three diameters stated. The percentage of each particle diameter used in the simulations is outlined in ***Table 18***.

Table 18 - Particle Size Distribution for each Case in Powder Spreading Analysis.

Case Number	**Particle Size Distribution**		
	40 µm	**30 µm**	**20 µm**
1	100%	0%	0%
2	33.33%	33.33%	33.33%
3	60%	25%	15%
4	15%	25%	60%
5	25%	50%	25%
6	0%	0%	100%
7	0%	100%	0%

Concerning the powder size distribution, research into the use of finer powders for EBM systems is limited, but multiple authors have investigated their use and highlighted various areas of interest. The size range of powder chosen and outlined in ***Table 18***. is in response to the literature reviewed in ***Subsection 3.7***, and is intended to account for the breakdown of particles into finer elements over the course of multiple recoating cycles, which will have a pronounced influence on flow characteristics and the formed layer uniformity. Wider reading [184, 185, 187], and in particular the work performed by Karlsson et al [186], has elucidated a noticeable research gap in the potential for powder size refinements in EBM systems and the possibility for advantages in the built components.

Furthermore, the analysis of relatively fine particles of the range 20-40 µm will demonstrate a more detailed depiction of interparticle forces than the coarse size range typically quoted as observed in commercial EBM hardware, and determine the robustness of the contact models, calibration processes, and cohesion conditions assigned to the particles in the digital system. A considerably more detailed review of the literature which underpins the methods investigated is provided in ***Subsection 3.7***.

Within the size range selected, varying concentrations of elements of uniform and polydisperse compositions have been inserted to evaluate the relative influence on powder bed formation. This, in part, is informed by the theorised "critical fraction" of fines, the point beyond which the concentration of finer particles serves to diminish bed quality. To investigate the effect of the PSD, the inserted particle fractions comprise relatively fine (20 µm diameter), relatively median-sized (30 µm diameter), and relatively coarse elements (40 µm diameter). Note, the "relatively" refers to the context of the simulations and not observed EBM values in literature. These were inserted within controlled distributions to better determine whether the proposed critical point exists, by ascertaining the influence of the PSD on layer quality.

To evaluate the repeatability of the results, three models of each of the seven case sets were run and denoted alphabetically from A-C. A feature of the LIGGGHTS® software in which a random prime number greater than 10,000, known as a "seed number", was inputted into the particle insertion code which randomises the position of the particle centroids within the insertion volume [223]. Identical seed numbers would result in identical particle insertions and therefore identical simulations. Thus, this number was adapted for each run to ensure stochasticity was achieved across all models.

To distinguish between the simulation terminology, "cases" refers to the simulation set with a discrete PSD from one to seven, and from this point onwards the term "models" refers to the simulations within that case set that are identical apart from different seed numbers. For example, the second iteration of the simulation set comprised entirely of 40 µm particles would be denoted: ***Case 1, Model B***. A 3D rectangular domain was used across all seven cases and the dimensions of the domain are outlined in ***Table 19***.

Table 19 - Dimensions of the Simulation Domain for Particle Size Distribution Cases.

Plane	Distance (cm)
x	1.2
y	0.2
z	0.35

To reduce the computational intensity of the simulations, a periodic boundary was used in the y plane as such that particles exiting one side of the domain entered at the corresponding point in the opposite side. To control the flow, and prevent excess particles from leaving the domain, a buffer was situated at either end of the powder bed. Each of these buffers were of dimensions 1mm × 2mm × 7.5mm in x, y, and z respectively. Hence, the total spread region of powder across the substrate was 1cm long.

In the z axis, the recoater originated directly on top of the buffer and had dimensions of 1mm × 2mm × 25mm in x, y, and z respectively. Thus, allowing for clearance between the top of the recoater and the ceiling of the domain and space to increase the powder insertion volume in subsequent simulations. The dimensions of the simulation domain are outlined in ***Figure 46***.

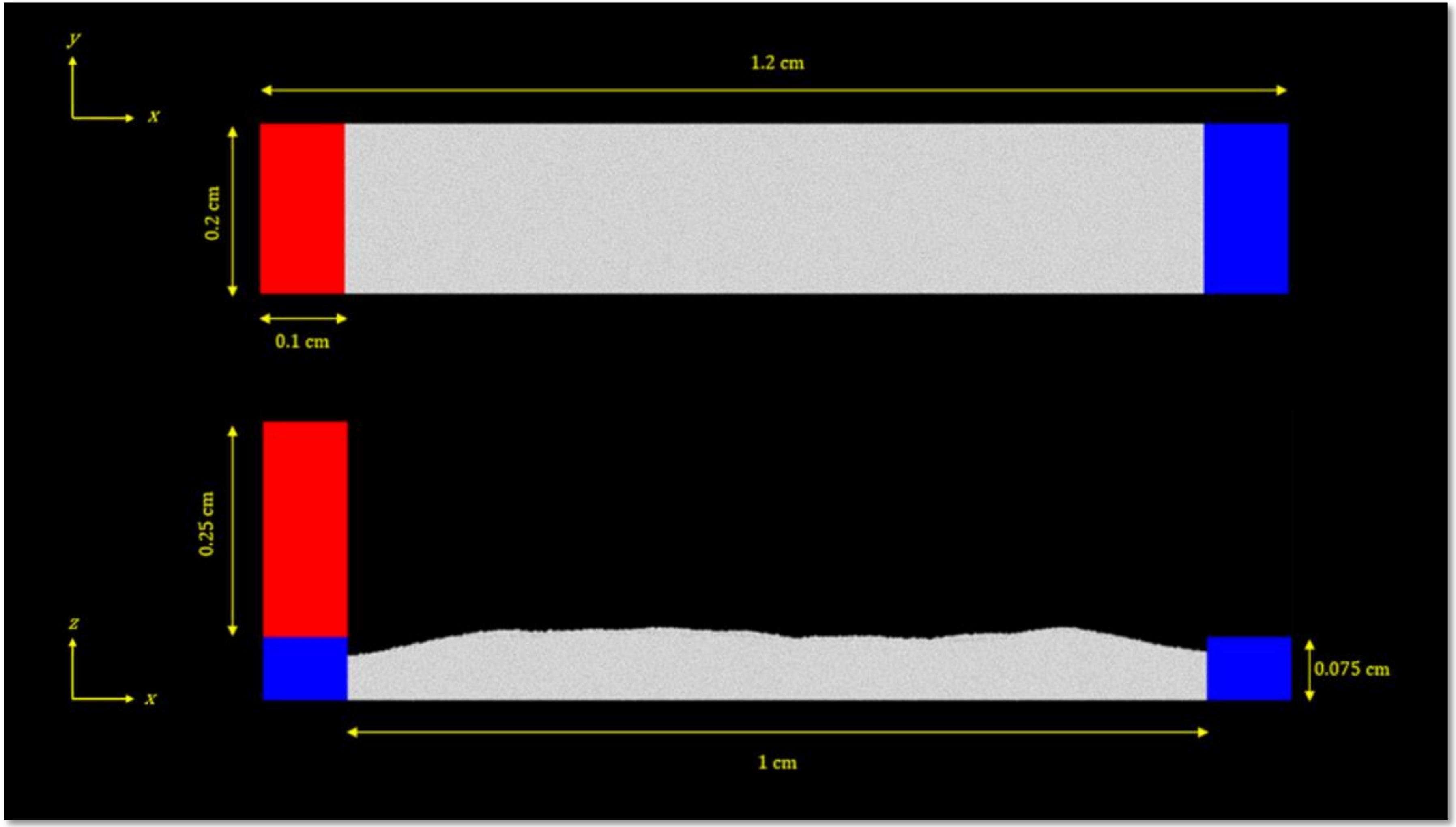

Figure 46 - Simulation Domain Dimensions for Effect of Particle Size Distribution Analysis.

All seven cases simulated the spreading of SS316l, and the properties of this metal powder were replicated as closely as reasonably practicable within the LIGGGHTS® software interface in an effort to ensure fidelity with practical testing. The same properties were applied to the recoater and buffer geometries as such that the powder bed frame could be considered to be constructed from SS316l. The material properties for SS316l as defined in the LIGGGHTS® scripts are recorded in ***Table 20***, and repeated from ***Table 15***.

Table 20 - Properties of SS316l Assigned to the Powder and Geometries in Particle Size Distribution Analysis.

Material Property	Symbol	Value	Units
Young's Modulus of Elasticity	E	0.193	GPa
Poisson's ratio	ν	0.27	Dimensionless
Particle Size Distribution	PSD	20-40	μm
Density	ρ_{SS316l}	8000	$\frac{\mathrm{kg}}{\mathrm{m}^3}$
Coefficient of Rolling Friction	$\mu_{Rolling}$	0.01	Dimensionless
Cohesive Energy Density (Particle-Particle)	$\boldsymbol{\kappa}$	550	$\frac{kJ}{m^3}$.
Cohesive Energy Density (Particle-Wall)	$\boldsymbol{\kappa}$	100	$\frac{kJ}{m^3}$.
Coefficient of Sliding Friction (Particle-Particle)	$\mu_{Sliding}$	0.7	Dimensionless
Coefficient of Sliding Friction (Particle-Wall)	$\mu_{Sliding}$	0.7	Dimensionless
Coefficient of Restitution	$\boldsymbol{e}$	0.1	Dimensionless

*Note that due to instabilities with the rheological powder behaviour, Young's Modulus of Elasticity was set to two orders of magnitude below the actual value. This approach has been implemented multiple times in DEM literature with no adverse effects on the model output reported [98, 165].

The timestep which governed the simulations had a significant influence on the powder flow behaviour. Preliminary tests with a timestep of 1×10^{-7} s resulted in instabilities whereby particles exploded at the contact points due to an overload of pressure and velocity. The timestep was iteratively tested based on the values in literature with similar PSD values [32, 48, 49, 98]. A more mathematical approach would have been to calculate the appropriate timestep based on the Rayleigh timestep criterion [202]. The equation for the Rayleigh timestep criterion reproduced here from ***Subsection 5.3.1***.

$$t_c = \frac{\pi r}{0.8766 + (0.163\nu)} \times \sqrt{\frac{\rho}{G}}$$

Where:

$r = Particle\ Radius.$

ν = Poisson ratio.

$\rho = Particle\ Density.$

$G = Shear\ Modulus.$

When determining the timestep based on the Rayleigh time, standard practice is to use approximately 20% of the value found for t_c, and then further refine the timestep chosen in accordance with the optimal performance of the simulation against the computational load [207]. However, as noted by Burns et al [202], this approach induces further complications to the process when polydisperse particle types are used, as was the case in these models. Based on the conservative estimates of the variables, the results of preliminary testing, and the timestep values in literature for modelling similar particle sizes, a timestep of 1×10^{-8} s was chosen for each case powder set.

Particles were inserted via the rainfall method across the bed and allowed to settle under gravity. To prevent an overlap with the geometries in the computational domain, the minimum and maximum x values of the insertion volume are set 0.25 mm away from the internal face of the buffers. Due to the periodic boundary in the y plane, particles were inserted 20 µm away from either side of the border to prevent fractions of the particles from appearing in both domain boundaries simultaneously.

Finally, the populated fraction of the powder insertion volume was specified. As previously stated, random sphere packing cannot exceed about 64% for a volume under consideration, and using high values would have destabilised the simulation by causing particles to overlap and thus, exit the domain at extremely high velocities. A trial-and-error approach found that a fill volume of 0.3 produced a stable powder bed at the required height for powder spreading. Due to the computational intensity of the simulations, all of the simulations were performed on Prospero: LJMU HPC Facility [224].

In LIGGGHTS®, a simulation can be scripted to run for a given length of time, a number of run steps, or until certain criterions are met such as until the energy falls below a given value. As previously outlined, the timestep can be used with the number of run steps to convert the simulation time to real time:

$$Timestep\ Value\ (s) \times Number\ of\ Time\ Steps = Real\ Time\ (s)$$

To analyse the results of each simulation, output files which stated the x, y, and z coordinate of each particle at a given timestep were post-processed in OVITO® to visualise the powder dynamics and system behaviour. Due to the small timestep used in the simulations, the frequency at which each output file was written was set as to provide an accurate representation of the powder flow, whilst not producing so many files that were prohibitively large with respect to storage and the simulation run time.

Prior to executing the simulation, the run duration had to be specified in terms of the number of steps or by converting to real time. Initial tests showed that all particles were inserted to the powder bed after running for 5×10^6 timesteps (0.05 seconds). The particles were allowed to settle under gravity for four times longer than their insertion cycle until a time instance of 25×10^6 (0.25 seconds) was reached. From the recoater velocity of $20\frac{mm}{s}$ and the known 1cm powder bed span, the total amount of real time it would take for the recoater to reach the end of the bed was calculated at $0.5\ s$. At a timestep equal to $1 \times 10^{-8}\ s$, it was established that this would require 50×10^6 steps from spreader initiation. Hence, the insertion, settling, and spreading phases of the process was coded to run for 75×10^6 steps. A final 5×10^6 timesteps ran for the recoater to pass over the buffer and out of the domain, giving a total of 80×10^6 timesteps in the simulation.

In conjunction with the run cycle, the domain size, recoater velocity, and timestep value were all considered to determine the frequency of the output files. In-situ monitoring of the simulation was constrained by the large output file sizes and the remote running of the simulations on the HPC, as no post-processing interface exists within Prospero. Therefore, correct management of the output frequency expedites the monitoring of the digital experiments, as the simulation terminating prior to the final timestep is indicative of an error in the model.

Given the 1cm spreading distance, an output frequency was required that showed the small incremental changes in the position of the recoater. Post-processing of the simulation with 100 output files of the spreading operation demonstrated the recoater moving at 0.1mm increments, providing a good reflection of the continuous recoater trajectory. To generate 100 output files of the spreading process from the 50×10^6 spreading steps, an output frequency of one file every 5×10^5 timesteps was implemented. At this output frequency, the simulation generated 160 output frames in total.

6.2.1 Analysing the Surface Roughness

Various methods can be used to measure the surface roughness of the powder bed. A simple technique would be to take the arithmetic average roughness, R_a, by measuring the deviation from the mean powder height across the length of the spread layer. A similar approach was used by Haeri et al [12, 17], where the standard deviation of the profile height data points were normalised by the diameter of the particles.

$$\epsilon = \frac{\sqrt{((h - \langle h \rangle)^2}}{D_{Sphere}}$$

The other approach quantifies the Root Mean Square (RMS) average of the height deviations from the mean line in the length of interest chosen. More specifically, the RMS roughness is found by squaring each height value point in the powder bed, then taking the square root of the mean [225]. Both approaches use the same discrete measurements of the peaks and troughs in the powder bed, but these values are applied in different formulas [226, 227]. The RMS roughness types is shown in ***Equation 77***:

$$RMS\ Roughess = \sqrt{\frac{1}{n}\sum_{i=1}^{n}(z_i - \bar{z})^2} \tag{77}$$

Where:

$n =$ Number of surface points analysed.

$z_i =$ Height of the best-fit plane in the z axis.

$\bar{z} =$ Average position of the surface point group data.

The above equations that the RMS roughness is more sensitive to deviations from the mean line than the R_a roughness. In commercial AM powder beds, the presence of deep valleys would induce porosity to the melted powder and diminish the mechanical properties of the component. Hence, detection of these defects in the models would be desirable to avoid defective powder beds. Furthermore, the RMS formula takes the same form as the standard deviation of a data set, allowing for a more accurate benchmark to be established in this research against the work of contemporary authors [19, 168]. Notably, both approaches measure only 2D surfaces [225, 226, 227]. Hence, to evaluate the total powder surface topography the measurements must be taken in segments across the powder bed width.

In the context of this project, the surface roughness of the AM powder bed has been judged by the homogeneity of the top layer of the surface profile with respect to deviations across the horizontal. Thus, as practiced by Parteli and Pöschel, the surface roughness was measured as a 2D projection of the powder bed onto the xz plane, after being spread by the recoater [49]. Thus, a more heterogenous surface pattern characterised by larger undulations between the peaks and troughs of the powder profile presented a higher surface roughness, and thus lower powder bed quality.

To commence the surface roughness analysis, the output files for a given simulation were firstly post-processed in OVITO®. The contact area between the recoater and powder was determined by the start and end points in the x axis of the powder bed where particle-blade interactions occurred. Due to the settling characteristics of the powder the full span of the powder bed could not be used for the surface roughness analysis, as approximately the first quarter of the bed span housed powder lower than the recoater face in the *z* plane. Hence, including this segment in the surface roughness evaluation would have skewed the overall roughness observed, as the slope of the powder deviated significantly from the rest of the region of interest.

Similarly, a small area at the end segment of the powder bed was obviated from the surface profile assessment to minimise any wall effects arising due to the buffer geometry. Furthermore, instabilities due to the overlap between the particles, the buffer, and the recoater at the end of the spreading process caused a surge of particles to exit the domain, further reducing the section available for analysis. To illustrate the region of interest selected to measure the surface roughness, ***Figure 47*** highlights the initial spreader interaction with the powder bed, the sloped region at the onset of recoater travel and the region of interest chosen for the analysis.

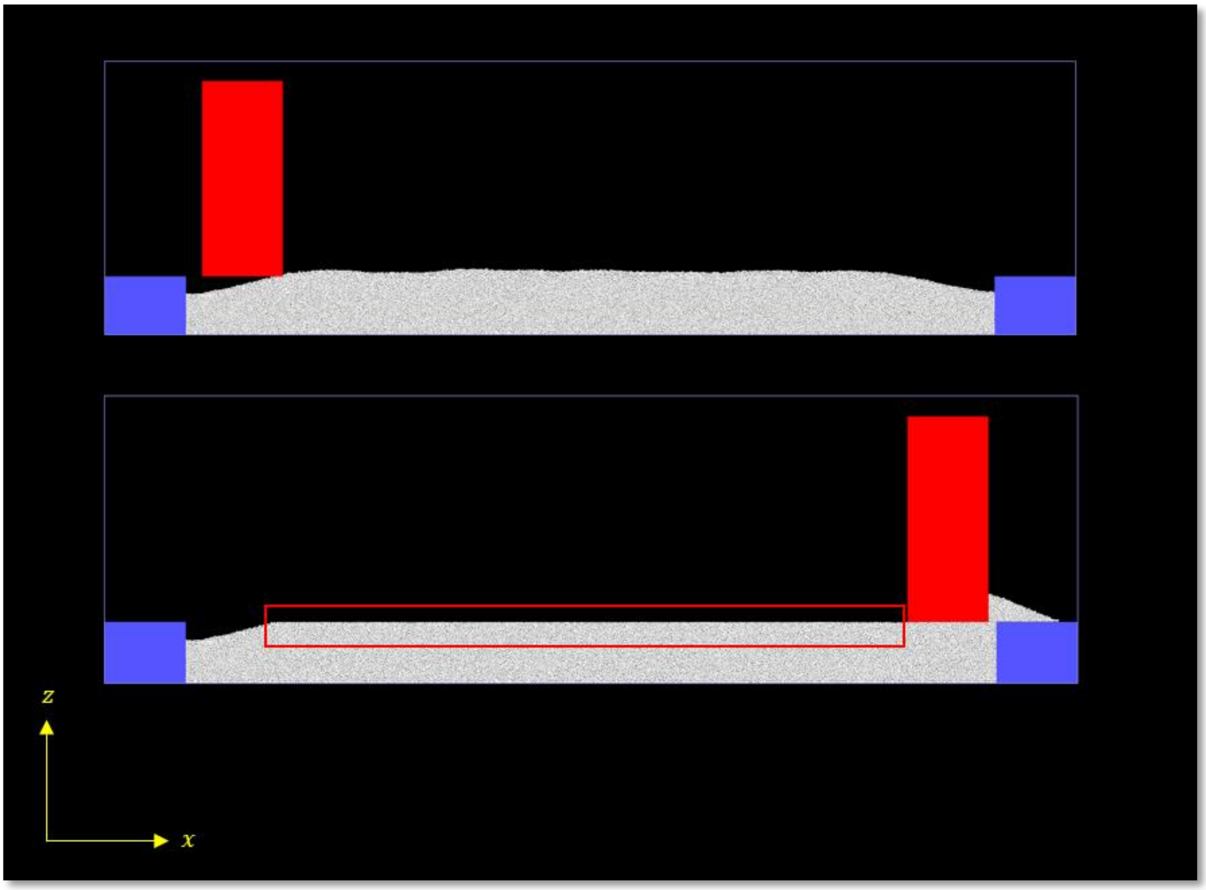

Figure 47 - Recoater and Powder Bed Interactions Highlighting the Region of Interest for Surface Roughness Analysis.

Figure 48 highlights the isolated region of interest for the surface roughness evaluation and the SVF analysis.

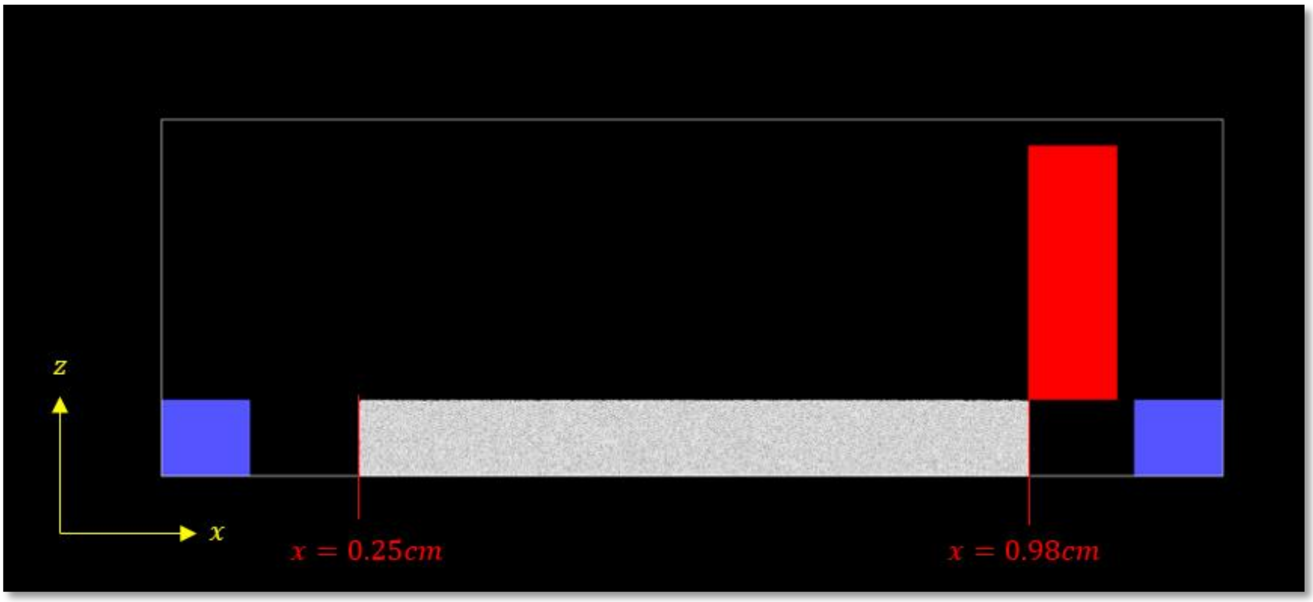

Figure 48 - Isolated Region of Interest in the Powder Bed for Surface Roughness Analysis.

In all simulations the onset of particle-blade interactions occurred between $x = 0.2$cm and $x = 0.25$cm. Thus, for consistency in the analysis the initial point of contact was assumed to be at the maximum value of $x = 0.25$cm. Only the x coordinate was used as the recoater did not move in the other two dimensions. The maximum value for the area of interest was at $x = 0.98$cm due to the instabilities at the end of the powder bed and to neglect wall effects.

Figure 49 shows the top view of two different surface roughness profiles, one with a slab thickness equal to twice the diameter of the largest particle in the system at 40 µm, and one with a slab thickness ten times this diameter at 400 µm. Note that the recoater has been suppressed to demonstrate the full span of the powder bed segment chosen, and that the slab thickness describes the width of the powder strip across the y plane selected for evaluation.

Figure 49 - Top View of the Powder Bed Line Segment Thicknesses considered for Surface Roughness Analysis at 40 µm (Top) and 400 µm (Bottom).

Figure 50 presents the side view of the powder bed slabs depicted in ***Figure 49***, and illustrates the line projections onto the *xz* plane. It can be observed that a narrow slab thickness presents a more irregularly packed profile at the top of the powder bed, compared to the more homogenous, smoother profile of the wider slab chosen.

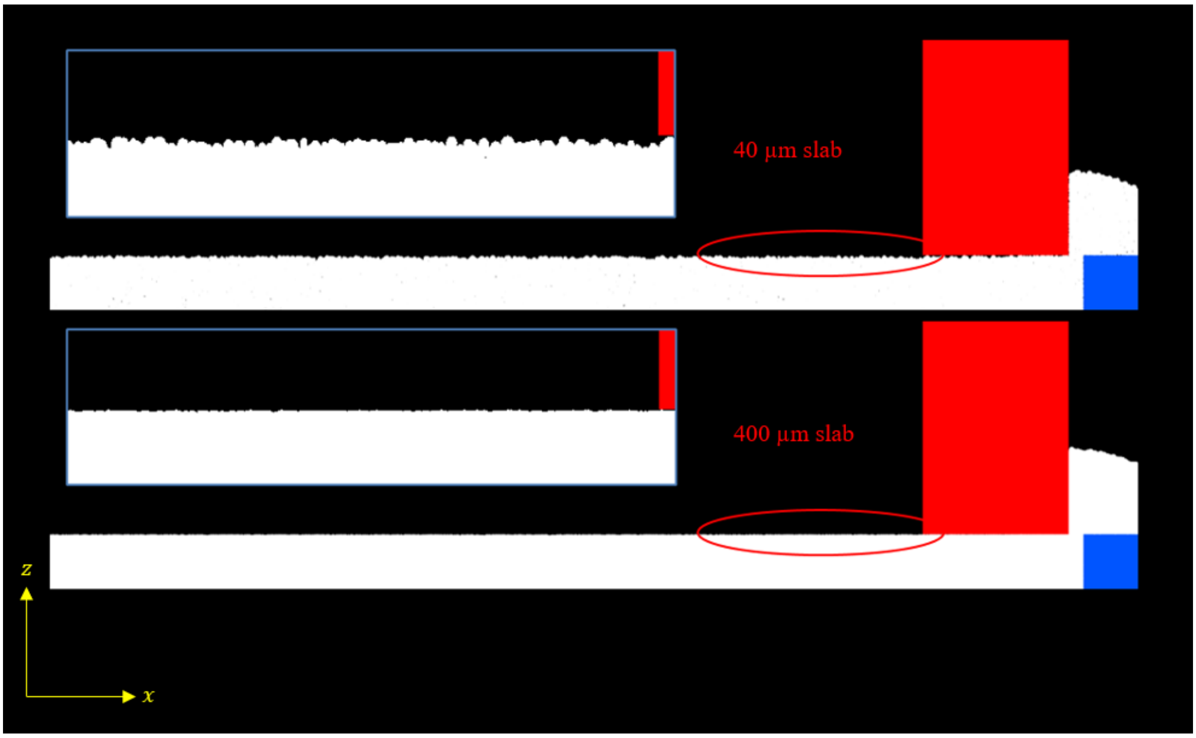

Figure 50 - Surface Roughness Profiles formed at 40 µm and 400 µm Slab Thicknesses.

Note that in ***Figure 50*** the particles have been rendered out in 2D circles to better demonstrate the surface roughness profile. The difference between the powder profiles at the narrower and wider slab thicknesses is expected, as when the profile is viewed from the xz plane a wider slab of powder will populate more the interstices across the y axis. Thus, making the profile appear smoother. It follows that the slab thickness chosen presents another influential parameter on the measured surface roughness and must represent the profile across the full width of the bed. Preliminary testing showed a discernible surface roughness in the profile of the powder at two times the maximum particle diameter, with the roughness decreasing at higher slab widths and thus compromising the analysis. Hence, the slab thickness of twice the maximum particle diameter was used in all simulations.

To monitor the effect of the slab thickness on the surface roughness, simulations with a bed comprised of uniform smaller particles used a slab thickness of both twice the largest particle diameter across all simulations (80 µm slabs), and twice the diameter of the particles in that given set (60 µm and 40 µm slabs for the uniform 30 µm and 20 µm sets respectively).

To quantify the surface roughness across the whole powder bed, three discrete segments were proposed. One through the centre of the powder bed, and one either side set an equal distance between the centre line and bed edges. As the total width of the powder bed was 2mm, these slabs were at 0.5mm, 1mm, 1.5mm in the y axis. A graphical depiction of the three slab segments is provided in ***Figure 51***.

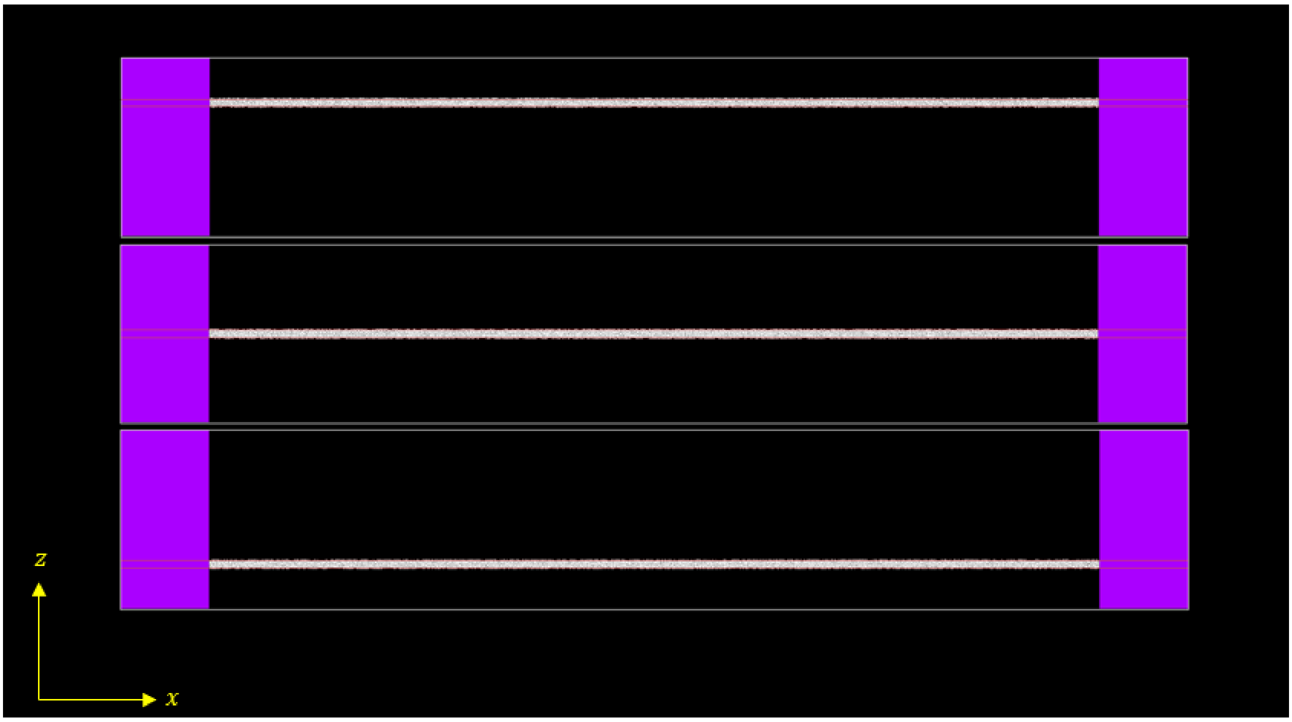

Figure 51 - Three Line Profiles across the Powder Bed Width for Surface Roughness Analysis.

Images of each slice were rendered out in OVITO®, generating three images per powder bed. As the surface roughness depends on the quality of the image, a high-resolution Portable Network Graphics (PNG) output of dimensions 5000 × 480 pixels was chosen in favour of a Joint Photographic Experts Group (JPEG) format, to remove the influence of JPEG artefacting.

The surface roughness was quantified by processing the images of each slab through the ImageJ application (https://imagej.net/ij/). Firstly, each image was imported and scaled to derive the correct units and dimensions for the analysis. Following which, a region of interest was defined by selecting the segment of the bed encompassing the top layer of the powder. As described previously, the region of interest was selected where stable particle-blade interactions occurred in the x direction from $x = 0.25$cm to $x = 0.98$cm.

After segmenting the image, a thresholding process determined the pixels that constituted the top layer of the powder bed and ensured that a continuous layer was achieved in the span of the x axis. In ***Figure 52***, the random pixels below the edge in the top powder bed graphic represent voids in the bed when a narrow slab thickness has been selected. In the bottom picture, noise manifested by the porosity has been manually painted out in ImageJ to prevent it from interfering with the roughness calculations.

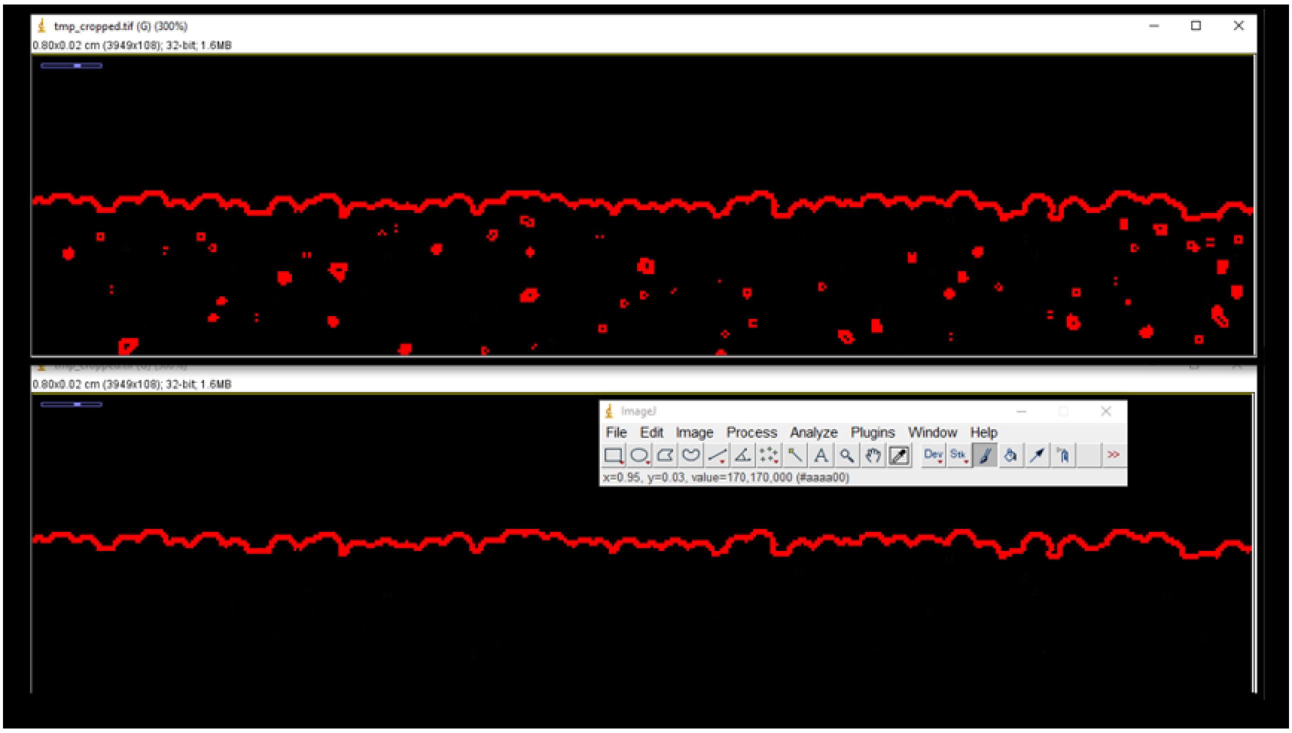

Figure 52 - Thresholding of the Surface Roughness Profile in ImageJ.

After processing the powder graphics in ImageJ, the software calculated the RMS value of the region of interest (denoted as R_q in the application). To find the R_q values, a macro was installed to measure stripes with two approximately parallel edges. In the case of the powder surface roughness, the macro measured the continuous profile of the top layer projected onto the xz plane parallel to the recoating direction. This provided an initial check of the veracity of the results, as the software generated an error report if the second parallel distinct edge failed to be identified. Thus, it could be established by reference to the results log in ImageJ as to whether a surface roughness measurement had failed.

To further ensure the accuracy of the results, two samples of the same image were tested for each of the three slabs across the y plane, with the disparity in R_q values recorded. Provided a minimal variance was found (± 10% of the largest particle diameter), the average of the two R_q values were taken as in ***Equation 78***. In the event of significant variance between R_q values, further testing was performed until the result fell within 0.5 µm of a previous sample.

$$R_q = \frac{R_{q1} + R_{q2}}{2} \tag{78}$$

Where:

R_q = The average RMS surface roughness of a given slab (µm).

R_{q1} = The first tested RMS surface roughness of a given slab (µm).

R_{q2} = The second tested RMS surface roughness of a given slab (µm).

Table 21 demonstrates how the equation for R_q was applied to the slab measurement for each region in the powder bed.

Table 21 - Calculation of the Average RMS Surface Roughness for each Slab in Models A, B, and C.

Region	Model		
	A	B	C
$y_{0.5\mathrm{mm}}$	$y_{0.5\mathrm{mm}}R_{q_{A_1}} + y_{0.5\mathrm{mm}}R_{q_{A_2}}$	$y_{0.5\mathrm{mm}}R_{q_{B_1}} + y_{0.5\mathrm{mm}}R_{q_{B_2}}$	$y_{0.5\mathrm{mm}}R_{q_{C_1}} + y_{0.5\mathrm{mm}}R_{q_{C_2}}$
$y_{1\mathrm{mm}}$	$y_{1\mathrm{mm}}R_{q_{A_1}} + y_{1\mathrm{mm}}R_{q_{A_2}}$	$y_{1\mathrm{mm}}R_{q_{B_1}} + y_{1\mathrm{mm}}R_{q_{B_2}}$	$y_{1\mathrm{mm}}R_{q_{C_1}} + y_{1\mathrm{mm}}R_{q_{C_2}}$
$y_{1.5\mathrm{mm}}$	$y_{1.5\mathrm{mm}}R_{q_{A_1}} + y_{1.5\mathrm{mm}}R_{q_{A_2}}$	$y_{1.5\mathrm{mm}}R_{q_{B_1}} + y_{1.5\mathrm{mm}}R_{q_{B_2}}$	$y_{1.5\mathrm{mm}}R_{q_{C_1}} + y_{1.5\mathrm{mm}}R_{q_{C_2}}$

Where:

$y_{0.5\mathrm{mm}}R_{q_{A_1}}$ = The first tested RMS surface roughness in Model A for the slab at $y = 0.5$mm (µm).

$y_{0.5\mathrm{mm}}R_{q_{A_2}}$ = The second tested RMS surface roughness in Model A for the slab at $y = 0.5$mm (µm).

$y_{0.5\mathrm{mm}}R_{q_{B_1}}$ = The first tested RMS surface roughness in Model B for the slab at $y = 0.5$mm (µm).

$y_{0.5\mathrm{mm}}R_{q_{B_2}}$ = The second tested RMS surface roughness in Model B for the slab at $y = 0.5$mm (µm).

$y_{0.5\text{mm}}R_{q_{c_1}}$ = The first tested RMS surface roughness in Model C for the slab at $y = 0.5\text{mm}$ (µm).

$y_{0.5\text{mm}}R_{q_{c_2}}$ = The second tested RMS surface roughness in Model C for the slab at $y = 0.5\text{mm}$ (µm).

$y_{1\text{mm}}R_{q_{\text{A}_1}}$ = The first tested RMS surface roughness in Model A for the slab at $y = 1\text{mm}$ (µm).

$y_{1\text{mm}}R_{q_{\text{A}_2}}$ = The second tested RMS surface roughness in Model A for the slab at $y = 1\text{mm}$ (µm).

$y_{1\text{mm}}R_{q_{B_1}}$ = The first tested RMS surface roughness in Model B for the slab at $y = 1\text{mm}$ (µm).

$y_{1\text{mm}}R_{q_{B_2}}$ = The second tested RMS surface roughness in Model B for the slab at $y = 1\text{mm}$ (µm).

$y_{1\text{mm}}R_{q_{c_1}}$ = The first tested RMS surface roughness in Model C for the slab at $y = 1\text{mm}$ (µm).

$y_{1\text{mm}}R_{q_{c_2}}$ = The second tested RMS surface roughness in Model C for the slab at $y = 1\text{mm}$ (µm).

$y_{1.5\text{mm}}R_{q_{\text{A}_1}}$ = The first tested RMS surface roughness in Model A for the slab at $y = 1.5\text{mm}$ (µm).

$y_{1.5\text{mm}}R_{q_{\text{A}_2}}$ = The second tested RMS surface roughness in Model A for the slab at $y = 1.5\text{mm}$ (µm).

$y_{1.5\text{mm}}R_{q_{B_1}}$ = The first tested RMS surface roughness in Model B for the slab at $y = 1.5\text{mm}$ (µm).

$y_{1.5\text{mm}}R_{q_{B_2}}$ = The second tested RMS surface roughness in Model B for the slab at $y = 1.5\text{mm}$ (µm).

$y_{1.5\text{mm}}R_{q_{c_1}}$ = The first tested RMS surface roughness in Model C for the slab at $y = 1.5\text{mm}$ (µm).

$y_{1.5\text{mm}}R_{q_{c_2}}$ = The second tested RMS surface roughness in Model C for the slab at $y = 1.5\text{mm}$ (µm).

R_q values for each of the three slabs in three models per case produced nine different roughness values per powder bed. The average roughness for each slab in the y plane was found by taking the sum of the roughness measurements for that slab across all models and dividing by the number of models analysed. Following which, the overall surface roughness for the powder bed was found by dividing the total roughness of each segment by the number of segment averages analysed. The process was then repeated for each set of cases to derive the total powder bed surface roughness values for comparison. A clear explanation of the process is given in ***Table 22***.

Table 22 - Calculation of the Total Surface Roughness of a Powder Bed from each Segment of Models A, B, and C.

Region	Model A	Model B	Model C	Segment Average	Overall Average
$y_{0.5\mathrm{mm}}$	$y_{0.5\mathrm{mm}}\colon {R_q}_{\mathrm{A}}$	$y_{0.5\mathrm{mm}}\colon {R_q}_{\mathrm{B}}$	$y_{0.5\mathrm{mm}}\colon {R_q}_{\mathrm{C}}$	$\frac{\Sigma_{y_{0.5mm}}}{Number\ of\ Models}$	$\frac{\Sigma_{Segment\ Average}}{Number\ of\ Segment\ Averages}$
$y_{1\mathrm{mm}}$	$y_{1\mathrm{mm}}\colon {R_q}_{\mathrm{A}}$	$y_{1\mathrm{mm}}\colon {R_q}_{\mathrm{B}}$	$y_{1\mathrm{mm}}\colon {R_q}_{\mathrm{C}}$	$\frac{\Sigma_{y_{1mm}}}{Number\ of\ Models}$	
$y_{1.5\mathrm{mm}}$	$y_{1.5\mathrm{mm}}\colon {R_q}_{\mathrm{A}}$	$y_{1.5\mathrm{mm}}\colon {R_q}_{\mathrm{B}}$	$y_{1.5\mathrm{mm}}\colon {R_q}_{\mathrm{C}}$	$\frac{\Sigma_{y_{1.5mm}}}{Number\ of\ Models}$	

Where:

$y_{0.5\mathrm{mm}}\colon {R_q}_{\mathrm{A}}$ = The surface roughness at $y = 0.5$mm from the Model A analysis (μm).

$y_{0.5\mathrm{mm}}\colon {R_q}_{\mathrm{B}}$ = The surface roughness at $y = 0.5$mm from the Model B analysis (μm).

$y_{0.5\mathrm{mm}}\colon {R_q}_{\mathrm{C}}$ = The surface roughness at $y = 0.5$mm from the Model C analysis (μm).

$y_{1\mathrm{mm}}\colon {R_q}_{\mathrm{A}}$ = The surface roughness at $y = 1$mm from the Model A analysis (μm).

$y_{1\mathrm{mm}}\colon {R_q}_{\mathrm{B}}$ = The surface roughness at $y = 1$mm from the Model B analysis (μm).

$y_{1\mathrm{mm}}\colon {R_q}_{\mathrm{C}}$ = The surface roughness at $y = 1$mm from the Model C analysis (μm).

$y_{1.5\mathrm{mm}}\colon {R_q}_{\mathrm{A}}$ = The surface roughness at $y = 1.5$mm from the Model A analysis (μm).

$y_{1.5\mathrm{mm}}\colon {R_q}_{\mathrm{B}}$ = The surface roughness at $y = 1.5$mm from the Model B analysis (μm).

$y_{1.5\mathrm{mm}}\colon {R_q}_{\mathrm{C}}$ = The surface roughness at $y = 1.5$mm from the Model C analysis (μm).

$\Sigma_{Y_{0.5mm}}$ = The sum of the roughness values at $y = 0.5$mm from Models A, B, and C (μm).

$\Sigma_{Y_{1mm}}$ = The sum of the roughness values at $y = 1$mm from Models A, B, and C (μm).

$\Sigma_{Y_{1.5mm}}$ = The sum of the roughness values at $y = 1.5$mm from Models A, B, and C (μm).

$\Sigma_{Segment\ Averages}$ = The average roughness of a slab in a given powder bed segment Models A, B, and C combined (μm).

6.2.2 The Solid Volume Fraction

Solid Volume Fraction Methodology

Measurement of the SVF was performed in OVITO®. The expression selection command was used to isolate a given volume of the powder bed and quantify the number of particles in the chosen segment. Three segments were selected for analysis across the x plane. The top view of the powder bed with the segments chosen is illustrated in ***Figure 53***.

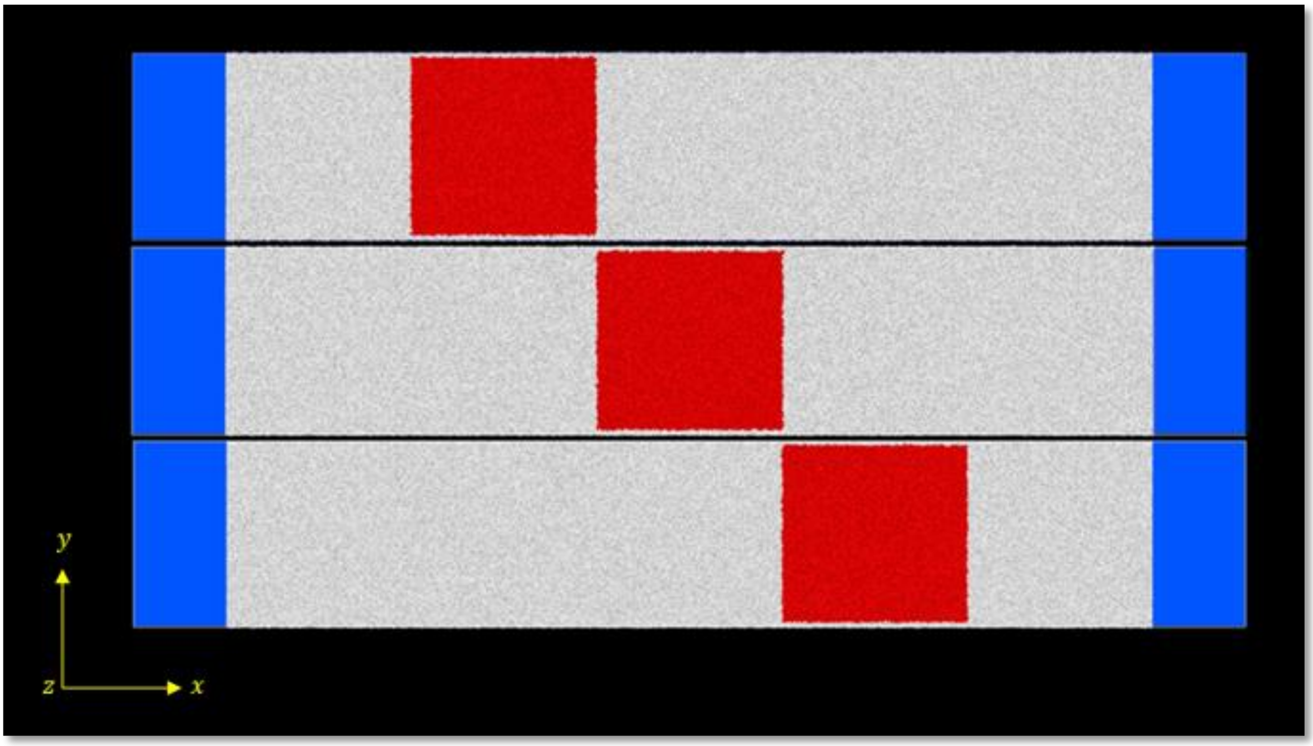

Figure 53 - Top View of the Powder Bed Showing the Regions chosen (denoted by the red particles) for Solid Volume Fraction Analysis.

A full explanation of the process used to calculate the SVF is provided as follows:

The volume of a single particle was found from the radius of said particle. As in all simulation cases all of the particles were spherical in morphology, the volume was found by ***Equation 79***:

$$V_{Particle} = V_{Sphere} = \frac{4}{3}\pi r_{Sphere}{}^{3}\ (\mathrm{m}^3) \tag{79}$$

Equation 79 was then used to find the volume of all particle types present in the system. The total occupied volume was found by multiplying the volume of one particle by the number of particles in the selection. As controlled fractions of set particle diameters were inserted in the polydisperse cases, ***Equation 79*** could be repeated for each particle size and summated together to calculate the total occupied volume, yielding ***Equation 80***.

$$Total\ Occupied\ Volume = V_{Particle}\ \times \text{Number of Particles (m}^3\text{)} \tag{80}$$

The volume region describes the full segment of powder chosen with the expression selection tool in OVITO®, as demonstrated in ***Figure 54***.

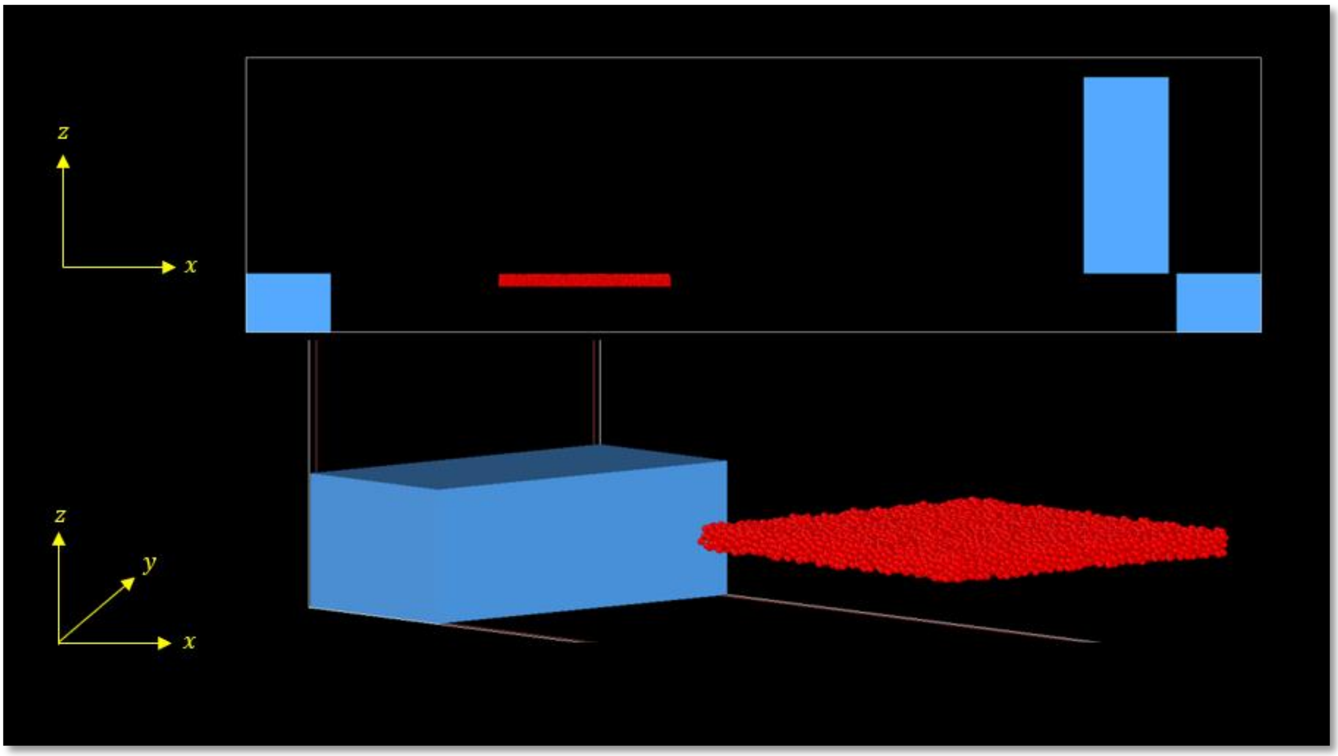

Figure 54 - Isolated Volume Region for Solid Volume Fraction Analysis.

In ***Figure 54***, the powder in Volume Region 1 has been isolated from the rest of the powder bed for demonstrative purposes. As ***Table 23*** shows, the volume region changed only across the length of the bed (in the x plane) and was consistent with respect to the total volume. Note that, to ensure homogeneity with the areas of interest used in the surface roughness analysis, the first 0.25cm of the powder bed span was neglected due to the slope formed in front of the recoater where no particle-blade interaction occurred (***Figure 48***).

Furthermore, the periodic boundary effects were neglected from the volume in the y plane by trimming the volume region by a single particle diameter (of the largest particle) in from either side of the domain, to prevent particles appearing partially in or out of either side. This is best shown by ***Figure 53***.

Table 23 - Dimensions of the Volume Regions used for Solid Volume Fraction Analysis.

Volume Region	Range in x (cm)	Range in y (cm)	Range in z (cm)	Total Volume (mm^3)
1	0.3-0.5	0.004-0.196	0.06-0.075	0.576

2	0.5-0.7	0.004-0.196	0.06-0.075	0.576
3	0.7-0.9	0.004-0.196	0.06-0.075	0.576

The range selected in the z axis for the SVF analysis was based on layer thicknesses in literature for DEM-AM analysis [228, 229, 230, 231] and conversations with AM specialists regarding the influence that heat dissipation from the melting medium has on neighbouring particles. It is noted here that compared to practical PBF layer thicknesses, the values used in DEM-AM may be artificially increased [56, 232].

To further justify the volume range in the z axis, ***Figure 55*** shows the magnitude of the particle displacements through the powder bed after spreading. In the image, the recoater is represented by the blue block which spreads powder in the x plane. Warmer colours (red, orange) depict higher magnitudes and cooler colours show less pronounced particle displacements. For these reasons, a layer thickness of 150 µm in the z plane was used. A comprehensive test of how the SVF changes with both segment depth, and the location of the segment taken in the powder bed, has been performed in ***Subsection 6.2.3***.

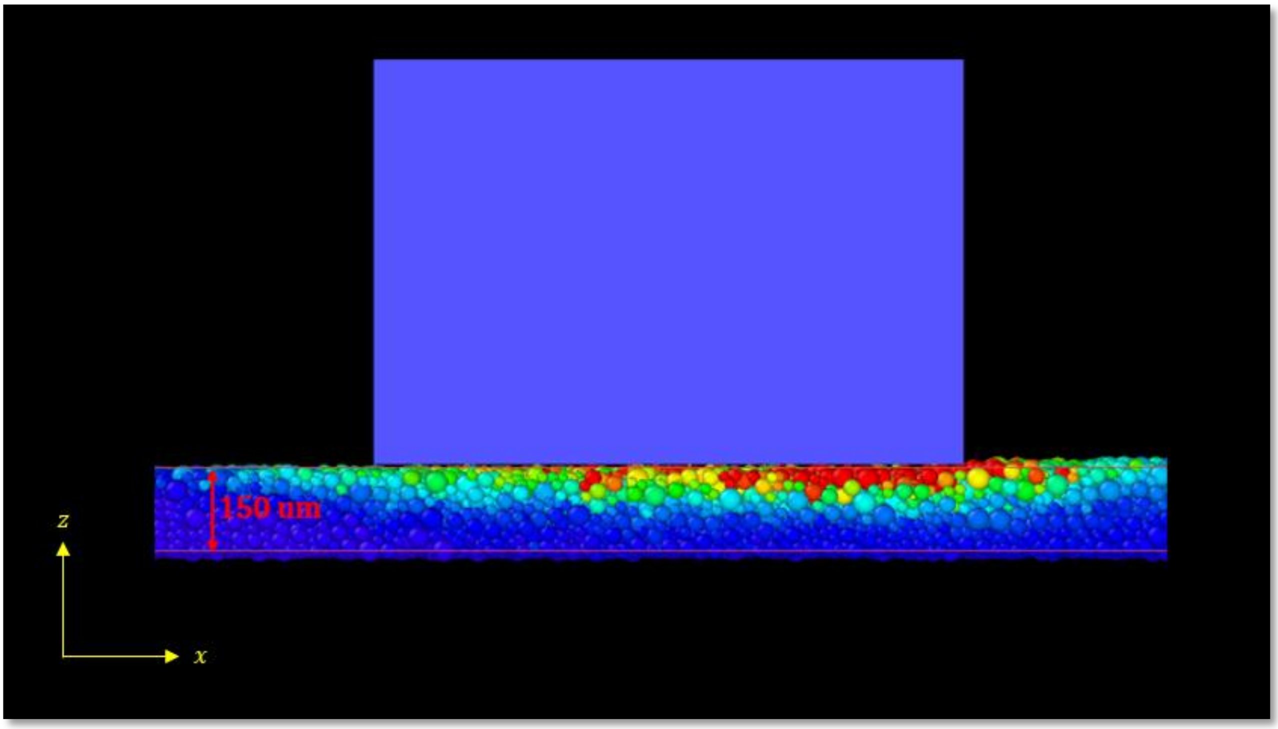

Figure 55 - Magnitude of Particle Displacements through the Powder Bed Depth.

The underside of the powder segment was also evaluated to ensure that the magnitude of particle displacements was consistent throughout the segment. As shown in ***Figure 56***, a stable volume region was selected save for some minor particle velocities.

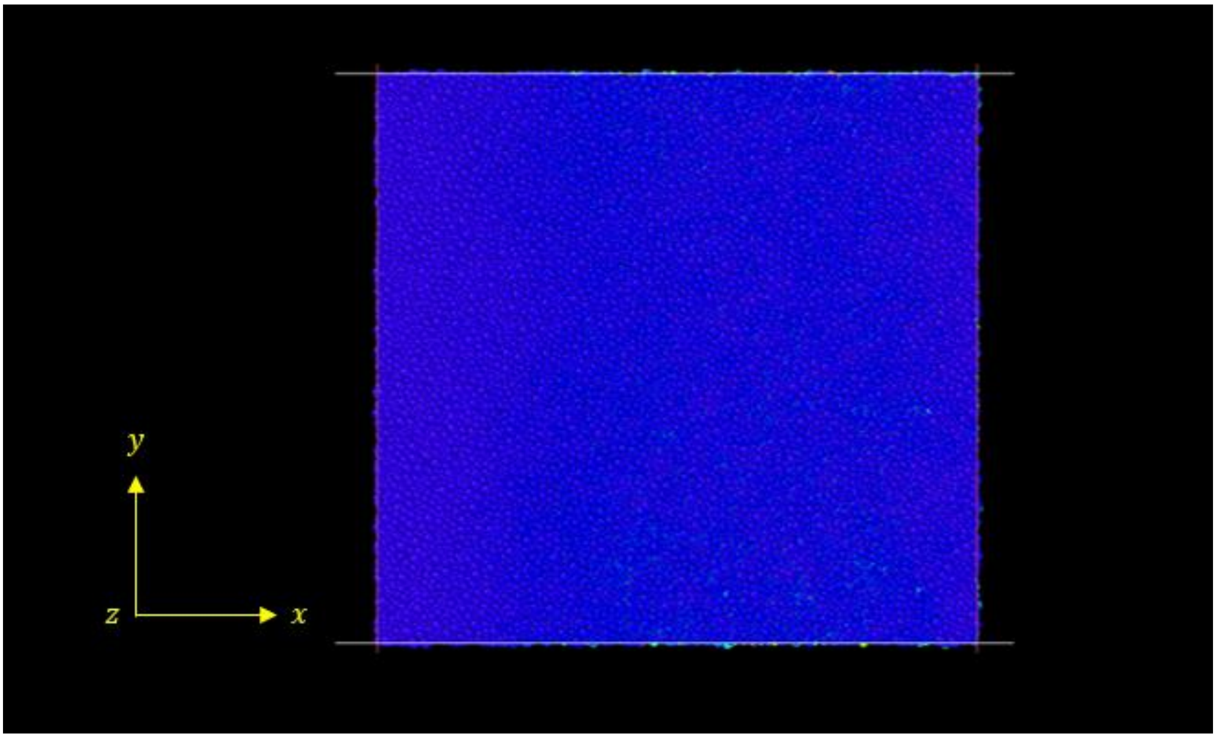

Figure 56 - Underside of Powder Bed Segment to show Stability in the Magnitude of Particle Displacements.

Finally, the SVF was calculated by dividing the volume occupied by the powder by the total volume analysed, and multiplying by 100 to convert to the percentage SVF, yielding ***Equation 81***:

$$\%\, SVF = \frac{Occupied\ Volume}{Total\ Volume} \times 100 \tag{81}$$

6.2.3 Inspection of the Solid Volume Fraction Measurement

As noted previously in ***Subsection 6.2.2***, an analysis was performed to determine the effect that the depth of the segment had on the SVF and the location in the powder bed at which the SVF was taken.

Solid Volume Fraction at Increasing Slab Thicknesses

The first validity check performed was to take SVF measurements at increasing depths through the powder bed. The SVF was tested at increasing 75 µm increments down from the top layer of the powder, with the top layer defined as the coordinate of the highest particle centroid in the z axis. A 75 µm increment was chosen as the magnitude of displacements appeared to become negligible beyond this point (***Figure 55***). The same process was repeated for four slab thicknesses in the z axis in the three volume regions across the x plane of the bed, giving 12 readings per case. The average SVF for each of the four slab thicknesses was taken from the three volume regions in x. This process was performed for all seven case sets with differing PSD values, yielding 84 data points in total.

Intuitively, it was expected that the SVF would increase with the slab thickness measured. There will naturally be voids present in the very top of the powder bed due to the lack of a succeeding layer, and thus increasing the thickness of the slab diminishes how pronounced an effect this had on solidity by increasing the overall volume measured. Furthermore, including more powder material increased the weight of the succeeding layers at increasing powder depths, compacting the powder below and pushing the particles to occupy interstices. The powder bed image in ***Figure 57*** outlines the increasing thicknesses at which the SVF is measured.

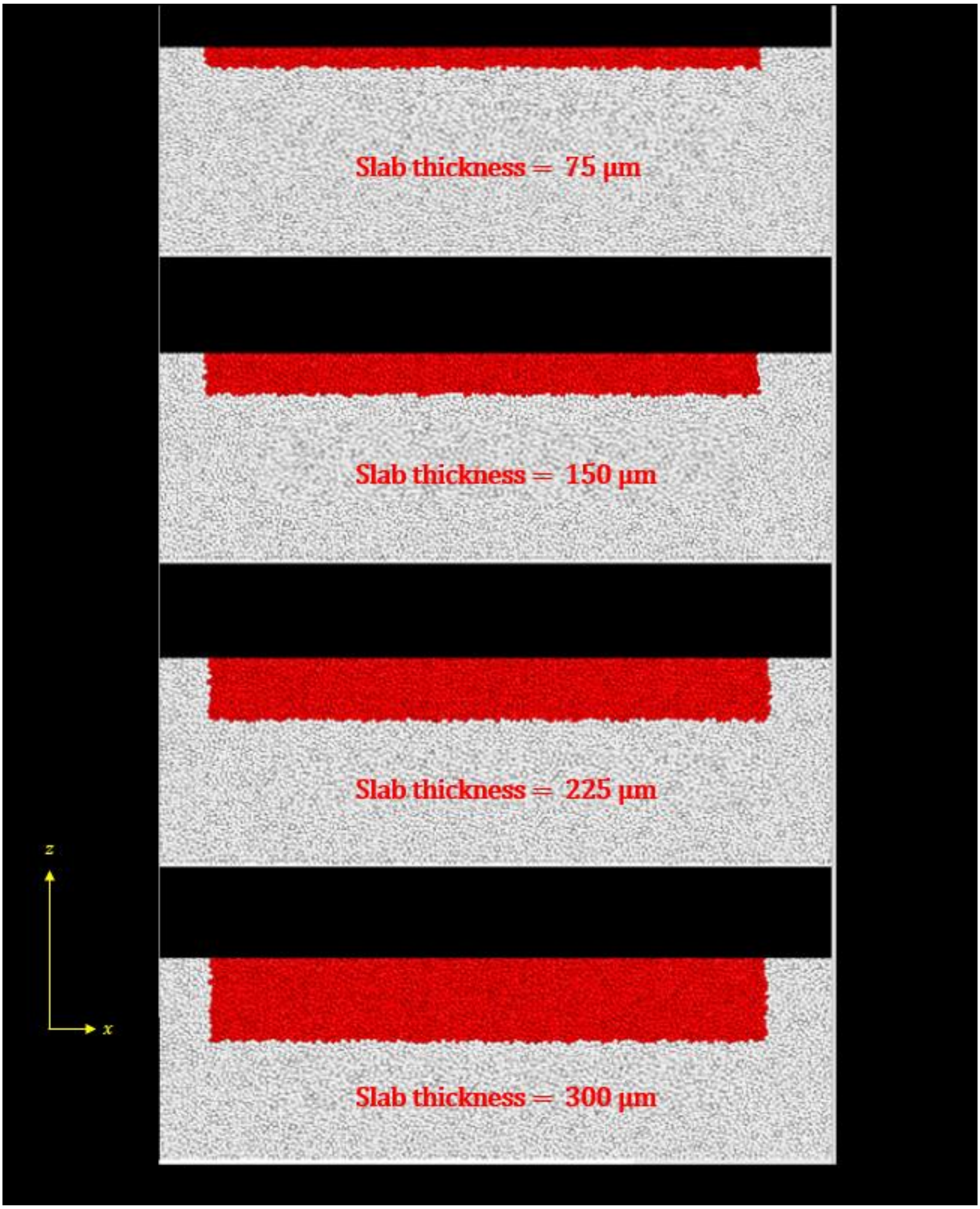

Figure 57 - Increasing Slab Thicknesses through the Depth of the Powder Bed.

The influence of increasing the slab thicknesses against the SVF for all cases is shown in ***Figure 58***.

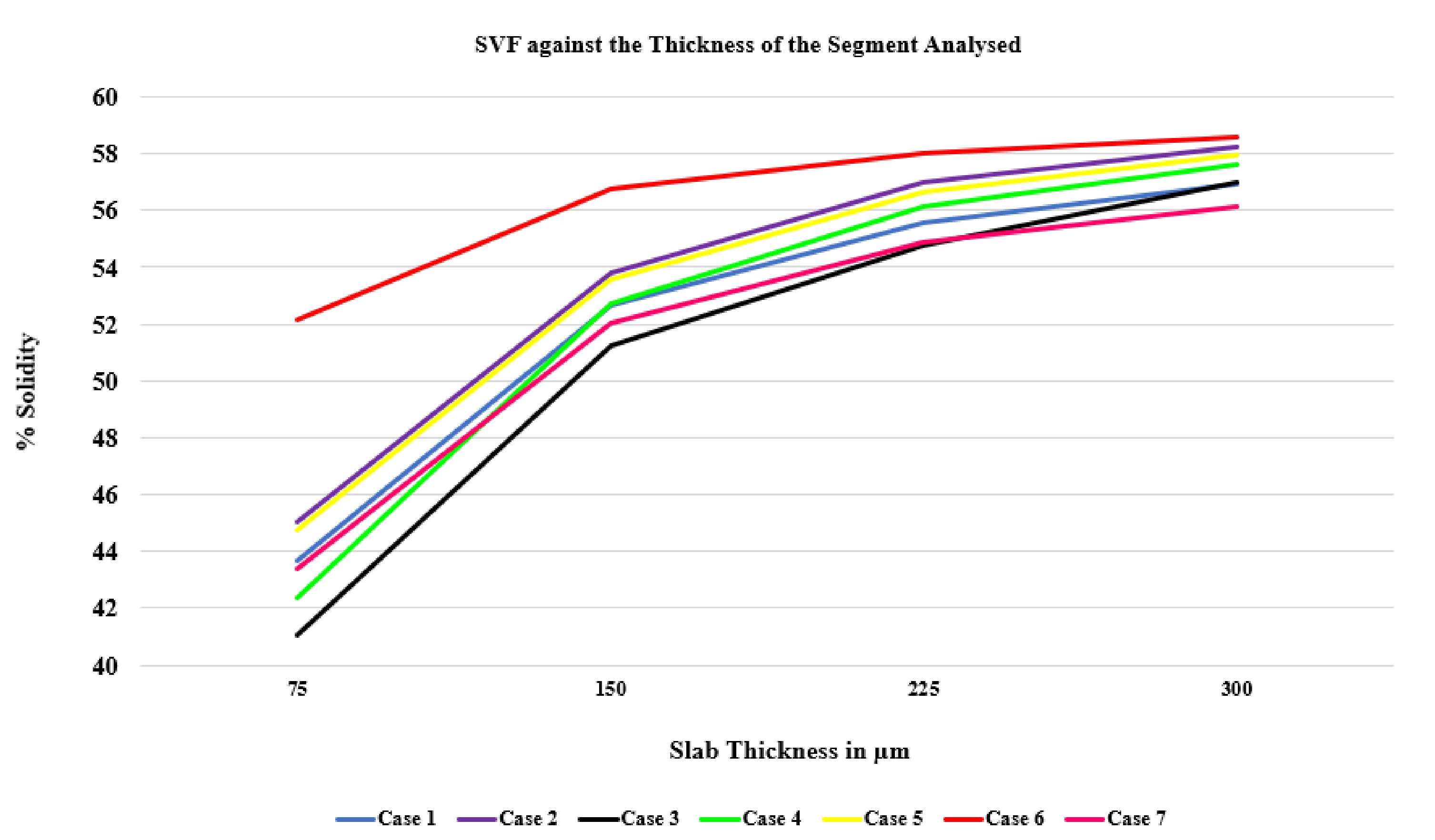

Particle sizes in each case:

Case 1: All 40 µm Particles

Case 2:
33.3% of 20 µm Particles
33.3% of 30 µm Particles
33.3% of 40 µm Particles

Case 3:
15% of 20 µm Particles
25% of 30 µm Particles
60% of 40 µm Particles

Case 4:
60% of 20 µm Particles
25% of 30 µm Particles
15% of 40 µm Particles

Case 5:
25% of 20 µm Particles
50% of 30 µm Particles
25% of 40 µm Particles

Case 6:
All 20 µm Particles

Case 7:
All 30 µm Particles

Figure 58 - Chart of Solid Volume Fraction against the Thickness of the Segment Analysed.

Evaluation of the SVF at varying thicknesses has highlighted the following conclusions. For brevity, the full set of results has been included in ***Appendix H***.

- The SVF increased with the thickness of the slab taken in all cases.
- The segment chosen along the length of the powder bed (relative to recoating direction) had a negligible influence on the SVF value, allowing an average to be taken for each slab thickness from the three segments in the x plane without skewing the results.
- A 150 µm slab thickness was chosen, as the increase in SVF becomes less pronounced after this value and for consistency with the layer thicknesses used in DEM-AM literature [228, 229, 230, 231]. It is remarked once more that 150 µm is an artificially increased layer thickness compared to real EBM processes [56, 232], but this is intended to account for heat dissipation from the melting process.
- It would be difficult lower than a depth of 150 µm to determine what is a higher SVF due to particles being compressed by the weight of the above layer, and what the effect of the recoating operation is on the packing density at lower bed depths. Thus, based on: the values of layer thickness observed in literature, empirical evidence, consideration of the melting strategy applied in PBF, consultation with industry, and the confines of the digital model, 150 µm was the slab thickness chosen for these cases.

Solid Volume Fraction at Decreasing Layer Location

In conjunction with analysing the slab thickness effect, an inspection was performed to ascertain the effect of measuring a consistent slab thickness at various depths throughout the bed (in z) on the SVF. Three measurements were chosen in the z axis. The first slab ranged from 0 µm to 75 µm depth, where 0 µm is the top layer of powder again defined by the centroid point of the highest particle in that plane. The subsequent measurements ranged from powder bed depths at z = 75 µm to 150 µm, and from z = 150 µm to 225 µm. As previously the 75 µm increments were chosen after analysing the magnitude of the particle displacements after spreading (***Figure 55***). Due to the increasing distance away from the recoating process, further depths were neglected.

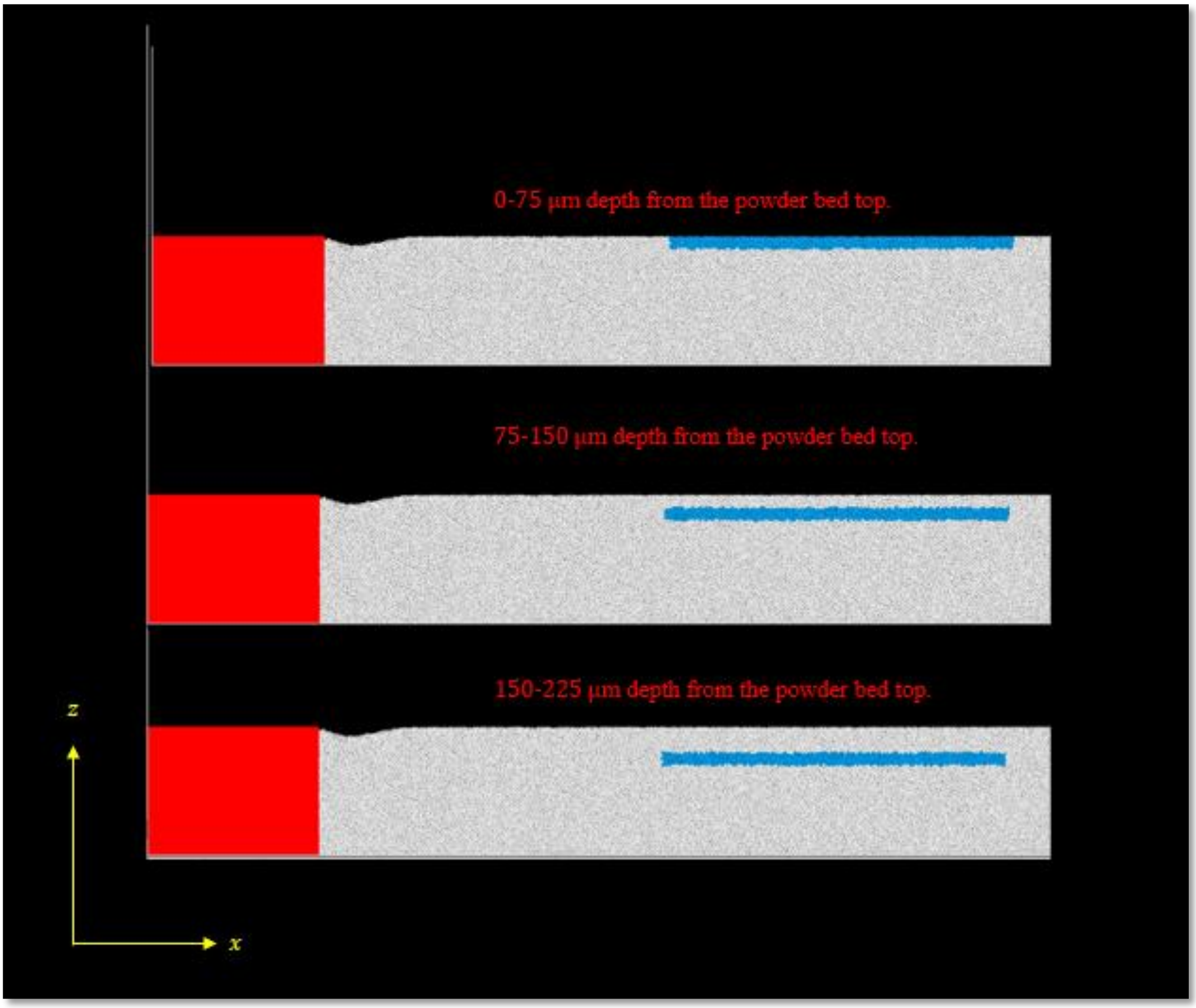

Figure 59 - Solid Volume Fraction at Decreasing Layer Location in the Powder Bed Depth.

Figure 59 shows the increasing depths at which the SVF was measured. The segments at each depth of the bed were evaluated at three discrete increments across the length (x plane) of the bed, at a constant width of 0.192mm in the y plane. Hence, nine data points were determined for each of the seven powder sets yielding 63 data points overall.

The three sections at which measurements were taken in the x axis were denoted x_-, x_0, and x_+ where:

x_- = The initial segment measured in the x plane relative to recoater velocity at x = 0.3cm to x = 0.5cm.

x_0 = The middle segment measured in the x plane relative to recoater velocity at x = 0.5cm to x = 0.7cm.

x_+ = The last segment measured in the x plane relative to recoater velocity at x = 0.7cm to x = 0.9cm.

The average value of the SVF at points x_-, x_0, and x_+ was taken for each of the three depth segments to establish the SVF for that powder set. As in the slab thickness analysis, the width of the slabs in y was set one maximum particle diameter in from either boundary to neglect the periodicity effect on neighbouring particles. The bar chart in ***Figure 60*** shows the SVF against the depth of the segment measured for all experiments.

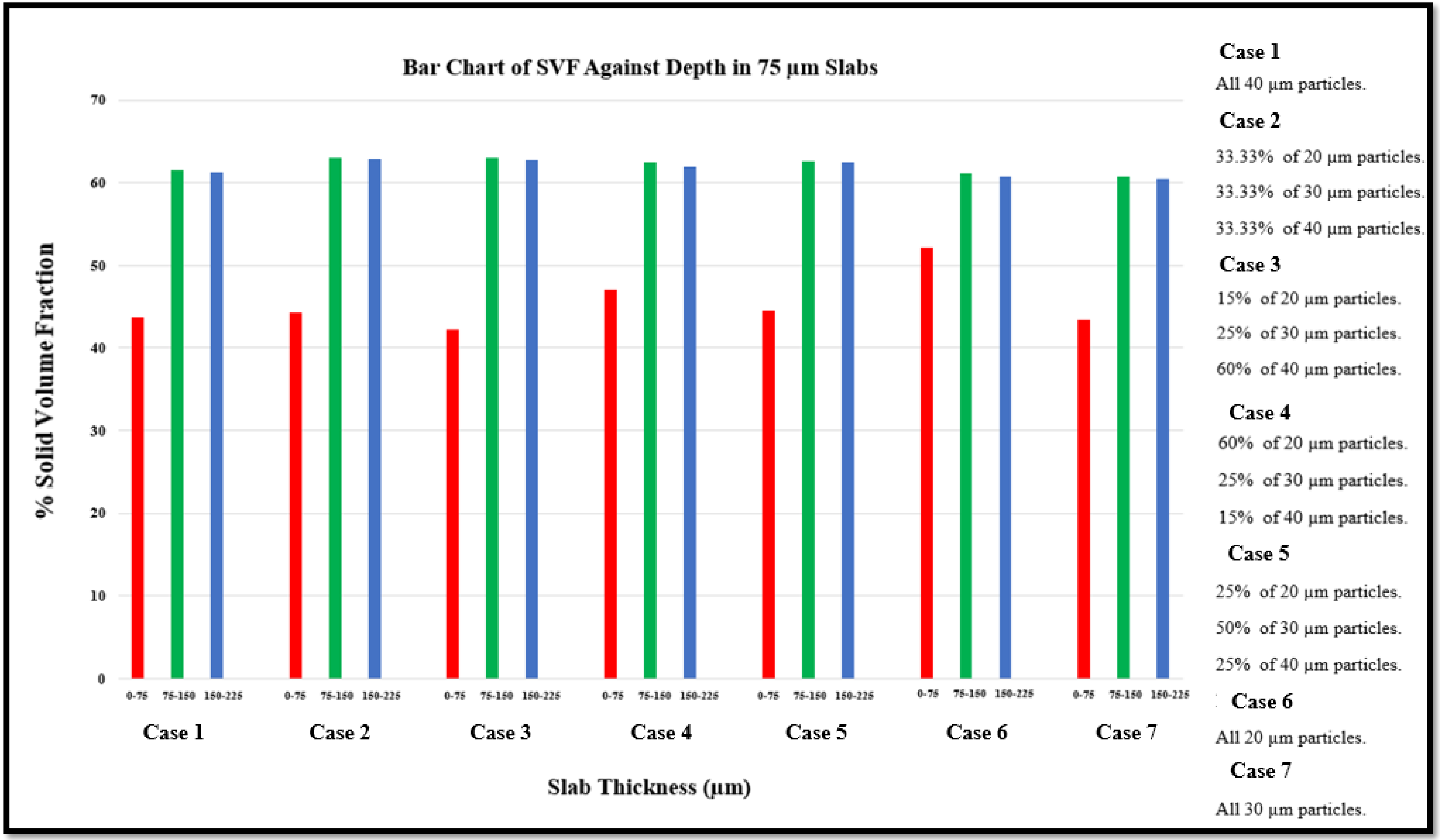

Figure 60 - Chart of Solid Volume Fraction Measured against Depth in the Powder Bed.

Figure 60 shows a significant increase in SVF occurred when the segment depth was increased to between 75 µm to 150 µm, and the same effect was observed in all simulations. Notably, the highest SVF was taken at this depth and was very slightly higher than at 150-225 µm, suggesting that, whilst ***Figure 58*** shows that the packing density increased with the thickness of the slab chosen, it did not necessarily increase with bed depth at uniform slab sizes. It is feasible that the spreading operation induced a sorting motion and caused interstices to be occupied by smaller particles, and that this effect did not extend to the deeper regions of the powder bed. However, this fails to explain why the same result was observed for both uniform and polydisperse powder beds, or what the effect would be if aspherical elements were added to the mixture. These results, in conjunction with the findings of the slab thickness analysis and the approaches used in DEM-AM literature, provided the rationale to measure the SVF from the top of the bed to a depth of 150 µm for all powder sets. A complete record of the SVF depth results has been included in ***Appendix I***.

6.2.4 Quantifying Powder Bed Segregation

As detailed in ***Subsection 3.2.4***, various methods exist in literature to quantify the segregation in AM powder beds. As particles were inserted by mass in these models, segregation could not be measured by quantity. Instead, the percentage population of a given particle diameter in each axis of the powder bed was used. For example, an even distribution of the coarsest particles across a given number of divisions would suggest negligible segregation. Conversely, an accumulation of most of the coarse particles in the initial phases of recoating would imply a strong segregation effect. To the best of the author's knowledge, this was a novel technique as no previous examples of this approach have been found in literature. Thus, it was not possible to benchmark the results against existing data.

Based on this approach, the domain was divided into three discrete segments in each plane: x, y, and z. A segment spanned approximately one-third between the minimum and maximum coordinates of the axis and was denoted by the subscript symbol -, 0, or $+$. For example, the segment x_- defined the first one-third of the powder bed length with respect to the direction of the recoater travel. Hence, x_0 defined the middle region of the bed, and x_+ described the final third of the powder bed in line with the spreading direction. ***Table 24*** outlines all of the axis segments used for the segregation analysis. A graphical depiction of each powder segment is provided in ***Appendix J***.

Table 24 - Definition of Each Segment in the Powder Bed for Segregation Analysis.

Segment	Location
x_-	The first 1/3rd length of the spread region nearest to the recoater starting point.
x_0	The middle segment of the spread region in the length of powder bed.
x_+	The segment of the spread region at the "far" end of the length of the bed, relative to the recoater starting position.
y_-	The first 1/3rd of the bed width.
y_0	The middle segment of the powder bed width.
y_+	The far end of the bed powder width.
z_-	The bottom 50 µm in the depth of the powder bed (z = 0 µm to z = 50 µm).
z_0	The 50 µm segment in the vertical middle of the powder bed (z = 50 µm 0 to z = 100 µm).
z_+	The top 50 µm in the height of the bed (z = 100 µm to z = 150 µm).

6.3 Results

6.3.1 Confirmation of Inserted Powder Sets

As the particles were inserted by mass, the expected mass of each particle size was found and multiplied by the insertion fraction. Firstly, the volume of a single particle of a given radius was calculated as previously:

$$V_{Particle} = V_{Sphere} = \frac{4}{3}\pi {r_{Sphere}}^3 \ (\mathrm{m}^3)$$

As the density of the material was known, it was multiplied by the volume to calculate the mass of a single particle. Following which, this value was multiplied by the number of particles in the system to find the total mass of particles of the diameter concerned.

$$m_{Particle\ Set} = V_{Particle} \times \rho_{Particle} \times Number\ of\ Particles\ (kg) \tag{82}$$

In a polydisperse powder mix, the mass of each set was then added together to give the total mass of the system. This was then multiplied by the insertion fraction of a given particle set to find the expected mass of particles of a given diameter.

$$m_{Particle\ Set\ 1} + m_{Particle\ Set\ 2} + m_{Particle\ Set\ 3} = \Sigma_{m_{System}}\ (kg) \tag{83}$$

$$\Sigma_{m_{System}} \times m_{Fraction} = m_{Expected}\ (kg) \tag{84}$$

Finally, the discrepancy between the observed and expected values were found, and expressed as a percentage to determine the accuracy of the PSD inserted compared to the requested value in the LIGGGHTS® script.

$$(\frac{m_{Expected} - m_{Particle\ Set}}{m_{Particle\ Set}}) \times 100 = m_{Error} \tag{85}$$

The average errors between the expected and observed masses is shown in ***Table 25***. A comprehensive record of all deviations in mass values, and a graphical demonstration of the PSD in each simulation set, is given in ***Appendix K***. Note that, as uniform particles have been used in ***Cases***, ***1***, ***6***, and ***7***, no discrepancy was expected or observed.

Table 25 - Average Mass Errors for Each Powder Set.

Case	**Particle Size Distribution (% particle diameter)**			**Average Mass Error (%)**
	40 µm	**30 µm**	**20 µm**	
1	100	0	0	0
2	33.33	33.33	33.33	0.033
3	60	25	15	0.024
4	15	25	60	0.695
5	25	50	25	0.001
6	0	0	100	0
7	0	100	0	0

As shown in ***Table 25***, a negligible disparity in mass values (<1%) was observed in all sets. An interesting anomaly is presented in ***Case 4***, where the average error was more than an order of magnitude greater than the next largest discrepancy in ***Case 2***, motivating a closer inspection of the mass errors in this set as shown in ***Table 26***.

Table 26 - Average Mass Errors for Case 4.

Case	Particle Size Distribution (% particle diameter)			Mass Error in 40 µm particles (g)	Mass Error in 30 µm particles (g)	Mass Error in 20 µm particles (g)
	40 µm	30 µm	20 µm			
4	15	25	60	0.00022	0.00013	0.00009

By reference to ***Table 26***, it can be observed that even in the case of the relatively large percentage error, a negligible difference in mass was presented for the each particle size in the system.

6.3.2 Surface Roughness Results

Based on the processes described in ***Subsection 6.2.1*** and ***Subsection 6.2.2*** the average surface roughness and SVF were identified for all digital experimental powder sets. Recapping the technique to find the surface roughness: firstly, the roughness value was taken of the three slabs across the y plane as in ***Equation 72*** and repeated for each model in the simulation (A, B, and C), giving nine values in total. After which, the three values for each slab were averaged across the models to generate an R_q value for the y axis segment. Finally, the total surface roughness across the powder bed for the simulation was determined by averaging these three y data readings, leaving one final overall average surface roughness per case.

Table 27 records the results of the surface roughness analysis. As shown, two values were taken for the total average surface roughness observed in ***Cases 6*** and ***7***. The first average roughness was at slab widths equal to twice the diameter of the largest particle across all cases (2D). The second average roughness was taken at slab widths equal to twice the diameter of the largest particle present in the bed ($2D_{Max}$). For ***Cases 6*** and ***7***, these slab widths were 40 µm and 60 µm respectively. In ***Figure 61***, an average value has been taken from the slab widths of 2D and $2D_{Max}$ to find the final average surface roughness.

Table 27 - Results showing the Effect of the Particle Size Distribution on the Powder Bed Surface Roughness.

Case	Particle Size Distribution (% particle diameter)			Overall Average Surface Roughness (µm)
	40 µm	30 µm	20 µm	
1	100	0	0	10.07
2	33.33	33.33	33.33	7.35
3	60	25	15	9.10
4	15	25	60	6.00
5	25	50	25	7.29
6 (Slab Width = 2D)	0	0	100	4.91
6 (Slab Width = 2D_{Max})	0	0	100	3.28
7 (Slab Width = 2D)	0	100	0	8.51
7 (Slab Width = 2D_{Max})	0	100	0	7.26

Unless stated otherwise, all error bars in the thesis were calculated based on a 2% percentage error to account for mathematical errors in the handling of data.

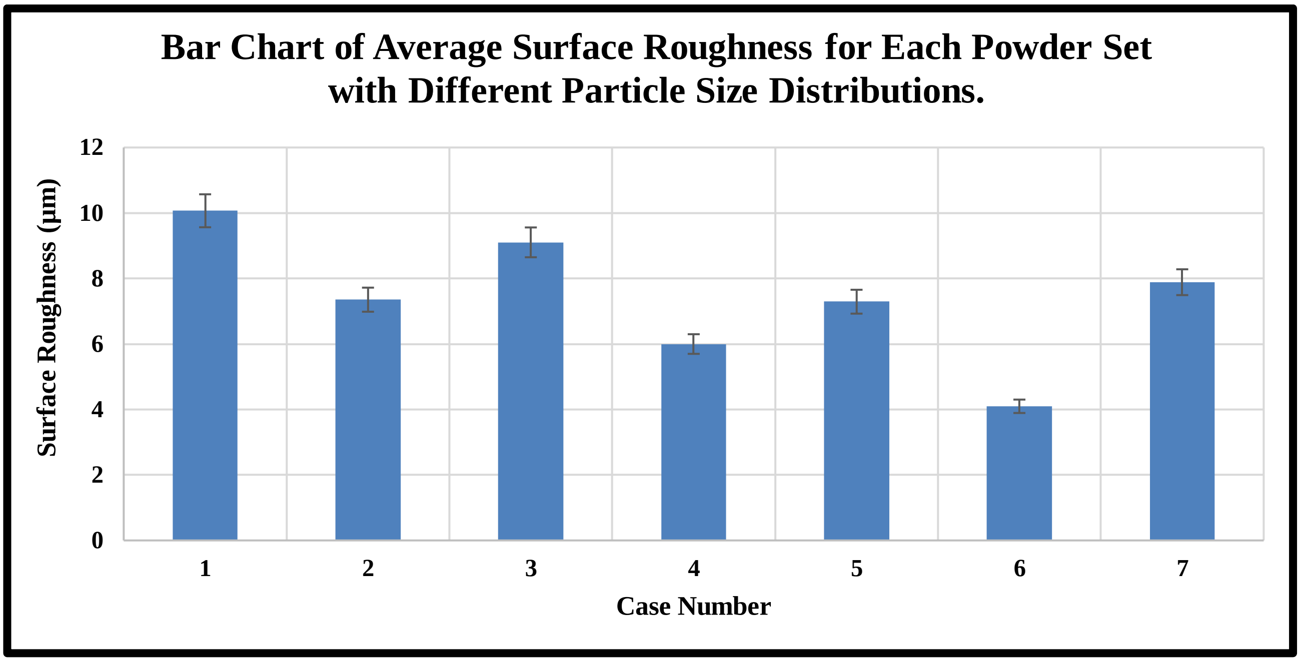

Figure 61 - Chart of Average Surface Roughness against the Different Particle Size Distributions.

Figure 61 shows that the lowest surface roughness occurred when the bed was uniformly populated by the finest particles, followed by the polydisperse mix with the largest population of fines. The roughest powder bed was comprised entirely of the coarsest particles, followed by the polydisperse set with a majority of 40 µm elements. The effect of the PSD on bed quality can more critically evaluated by comparing the surface roughness against the percentage of a given particle size. For example, ***Figure 62***, ***Figure 63***, and ***Figure 64*** demonstrate the roughness against the percentage concentration of 40 µm, 30 µm, and 20 µm particles. Note that in each case the two uniform PSD sets not under analysis have been excluded from the chart.

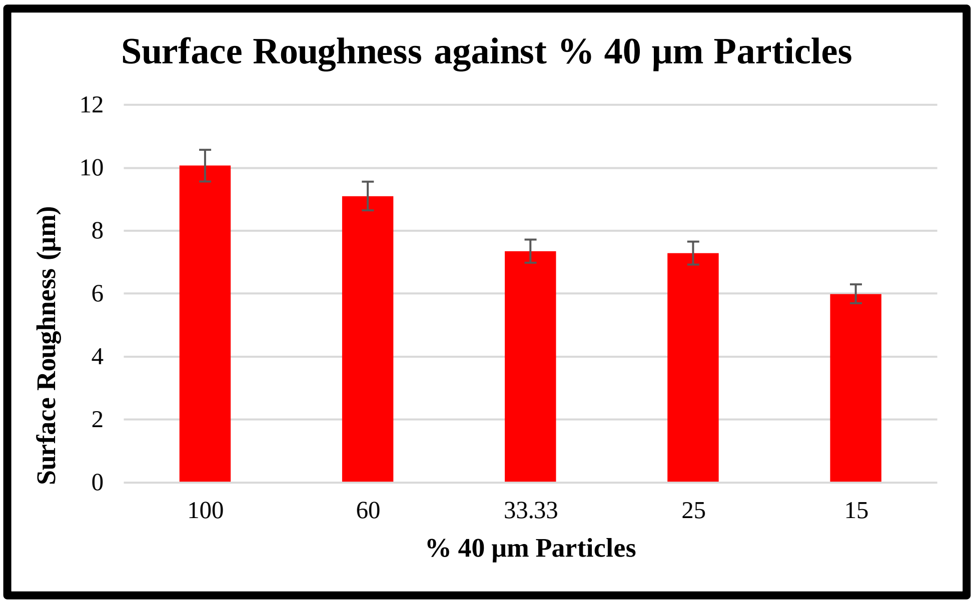

Figure 62 - Chart of Surface Roughness against the Percentage of 40 µm Particles in Different Particle Size Distribution Sets.

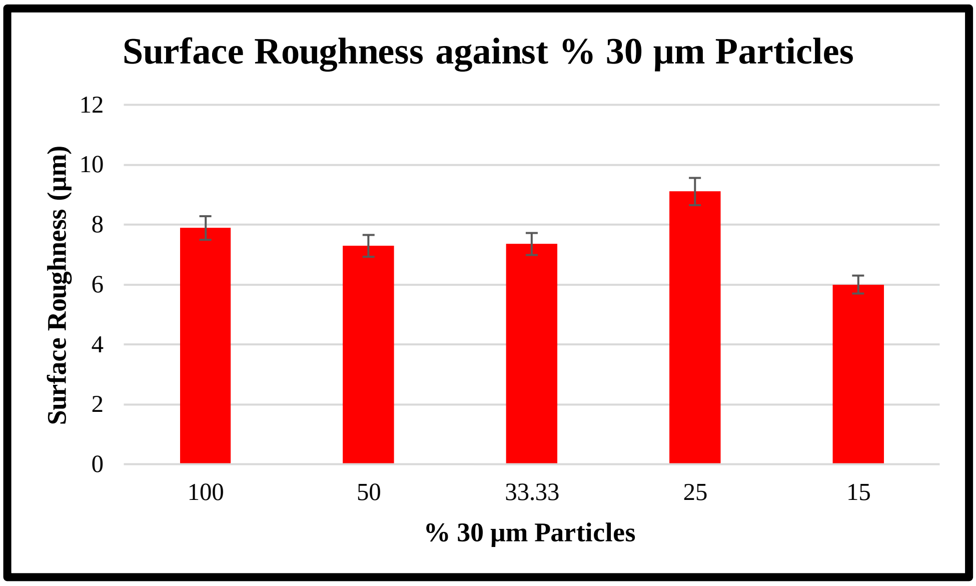

Figure 63 - Chart of Surface Roughness against the Percentage of 30 µm Particles in Different Particle Size Distribution Sets.

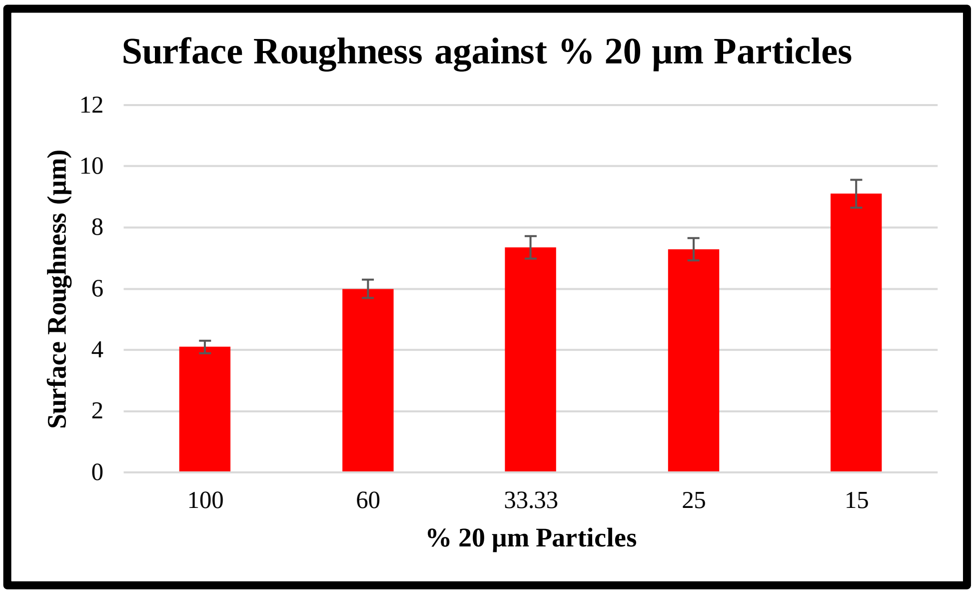

Figure 64 - Chart of Surface Roughness against the Percentage of 20 μm Particles in Different Particle Size Distribution Sets.

Analysis of ***Figure 62***, ***Figure 63***, and ***Figure 64*** suggests that PSD sets with a higher concentration of finer particles generally culminated in a smoother surface profile. ***Figure 62*** and ***Figure 63*** show that the lowest surface roughness occurred when the lowest fraction of 40 μm and 30 μm particles were inserted respectively. ***Figure 64*** corroborates ***Figure 61*** by showing that a uniform bed comprised entirely of the finest particles yielded the lowest surface roughness. The implications for powder bed optimisation and proposed reasons for these findings are discussed in ***Subsection 6.4***.

The complete surface roughness data set for all cases is provided in ***Appendix L***.

6.3.3 Solid Volume Fraction Results

The SVF calculations were performed in OVITO® from three discrete powder segments across the length of the recoating path. The SVF was taken at points x_-, x_0, and x_+ for three models in each case. The SVF of each segment was summated and then averaged by the three models to determine the SVF in that region of the bed. Once the average SVF of each segment was found, the total SVF across the bed was found by averaging the three segments. The results of the SVF analysis are provided in ***Table 28***.

Table 28 - Results showing the Effect of the Particle Size Distribution on the Powder Bed Solid Volume Fraction.

Case	Particle Size Distribution (% particle diameter)			Solid Volume Fraction (%)
	40 µm	30 µm	20 µm	
1	100	0	0	52.659
2	33.33	33.33	33.33	53.801
3	60	25	15	52.690
4	15	25	60	55.102
5	25	50	25	53.600
6	0	0	100	56.783
7	0	100	0	52.069

The results recorded in ***Table 28*** are graphically depicted in ***Figure 65***.

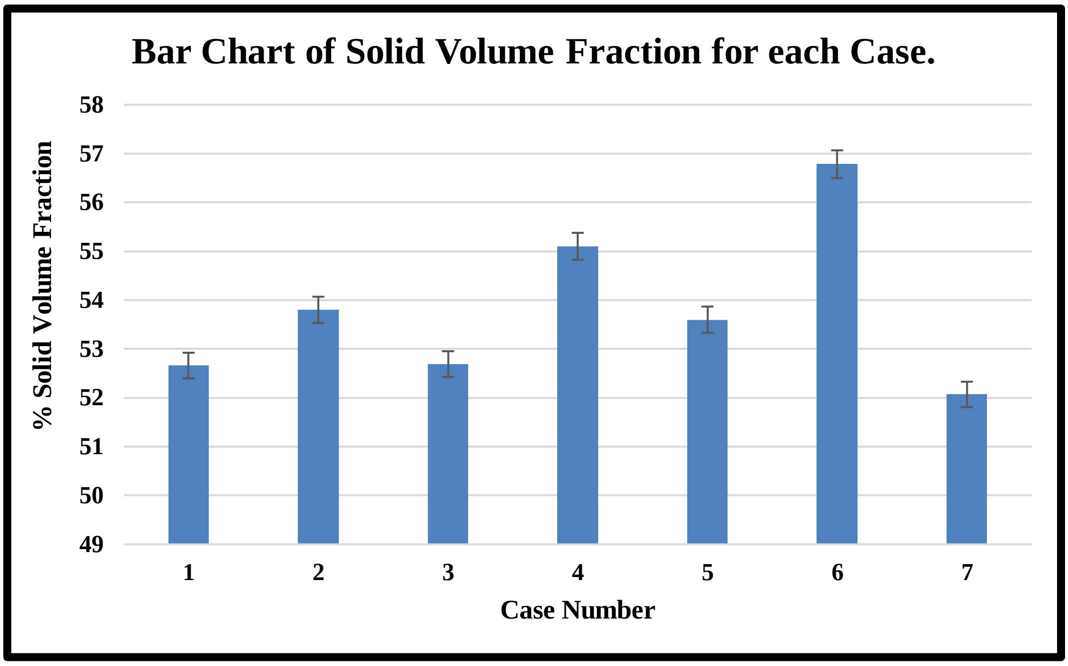

Figure 65 - Chart of Solid Volume Fraction against the Different Particle Size Distributions.

Table 28 and ***Figure 65*** show that the highest SVF was achieved in ***Case 6***, which was comprised entirely of the uniform 20 µm particles. The next most densely packed powder bed was in ***Case 4***, where the majority of the polydisperse powder set was made up of the finest particles. This suggests that a saturation of the coarsest particle size engenders the most porous powder bed. Interestingly, only a slightly more porous powder bed (by about 0.6%) was observed when the bed consisted of uniform 20 µm particles compared to a bed with only uniform 40 µm particles. These findings afford credence to the theory that a polydisperse PSD raised the SVF by populating the interstices between particles.

To better understand the influence of particle sizes on packing density, ***Figure 66***, ***Figure 67***, and ***Figure 68*** depict the solidity against the percentage population of given particle sizes.

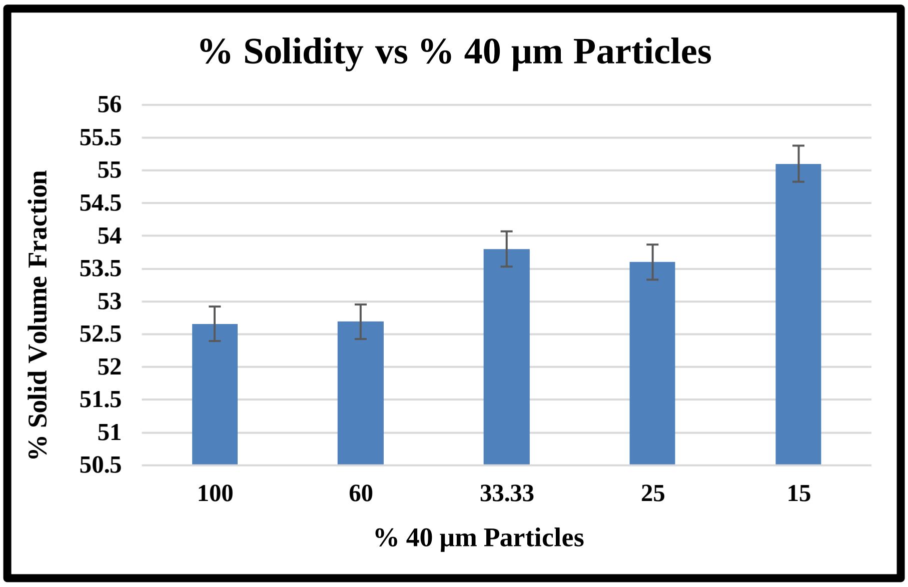

Figure 66 - Chart of Solid Volume Fraction against the Percentage of 40 μm Particles in Different Particle Size Distribution Sets.

Figure 66 shows that the SVF generally decreased at higher fractions of the coarsest particles. Interestingly, a slightly more solid bed was created in ***Case 2*** where one-third of each particle size was inserted, than in ***Case 5*** which inserted 25% of the coarsest particles. ***Case 2***, however, also inserted a greater percentage of the finest particle size than ***Case 5***, suggesting the inclusion of the 20 μm particles had a more pronounced influence on raising the packing density than the 30 μm particles.

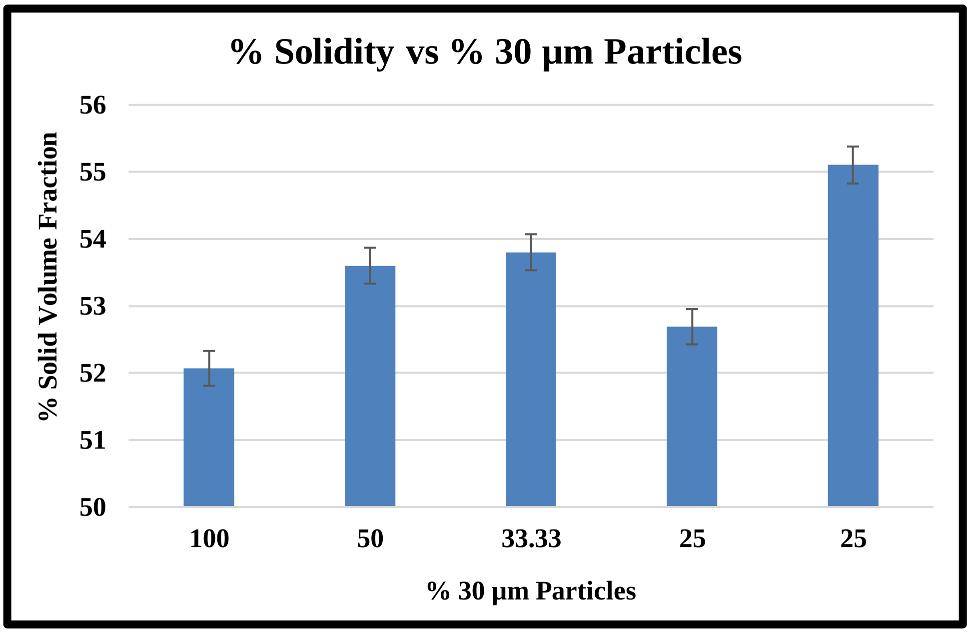

Figure 67 - Chart of Solid Volume Fraction against the Percentage of 30 μm Particles in Different Particle Size Distribution Sets.

Figure 67 shows that the lowest packing density occurred when the bed was comprised entirely of 30 µm particles, with the next lowest occurring in ***Case 3*** when the PSD contained a majority of coarse particles. Notably, the highest SVF of any bed housing 30 µm particles was observed when the majority of the bed contained the finest elements. A significant difference in packing density was observed in the polydisperse sets depending on what size particles constituted the majority, with a solidity of 52.69% for a majority of coarse particles increasing to 55.1% for a majority of fines.

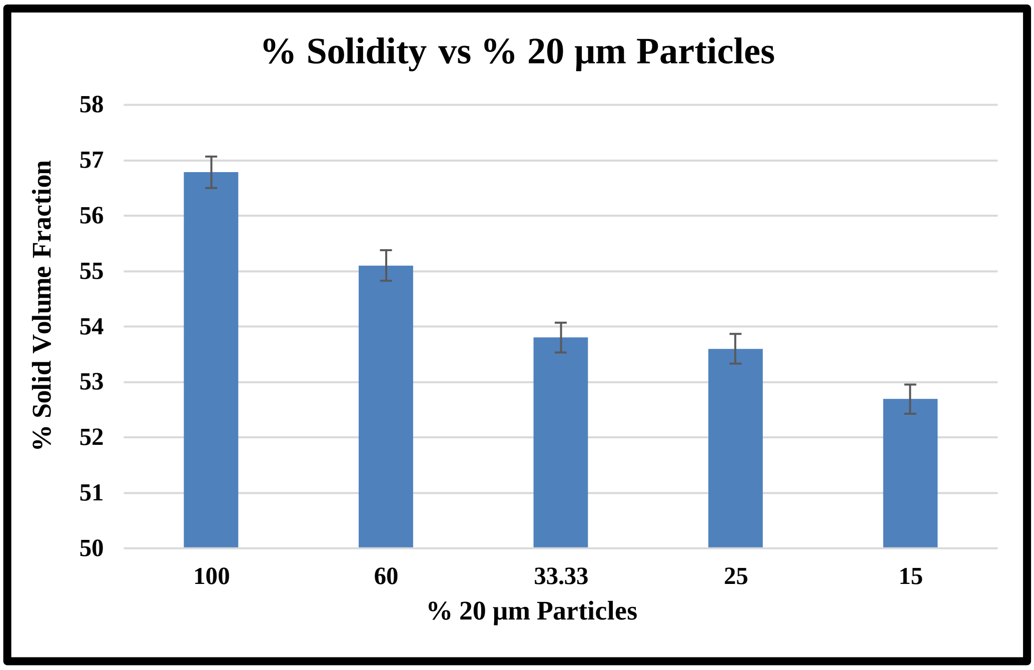

Figure 68 - Chart of Solid Volume Fraction against the Percentage of 20 µm Particles in Different Particle Size Distribution Sets.

The clearest depiction of the effect of the PSD is found in ***Figure 68***. Both this chart and ***Table 28*** show that the most densely packed powder bed occurred when only uniform 20 µm particles were used. This finding merits further discussion as it contradicts the widely-held belief that a polydisperse PSD is required to produce a more stable powder bed, by allowing finer elements to occupy interstices and thereby increase the packing density [13, 14, 15, 17]. Interestingly, the polydisperse set with the highest concentration of fines was still marginally less dense than the uniform finest set. A thorough discussion of the results is given in ***Subsection 6.4*** and the complete set of results is provided in ***Appendix M***.

6.3.4 Segregation Results in Full Polydisperse Powder Beds

This section shows the segregation results between particles in the polydisperse powder sets from ***Case 2*** to ***Case 5***. As the particles are uniform in ***Case 1***, ***6***, and ***7***, no segregation analysis was performed. ***Table 29*** outlines the results of ***Case 2***.

Table 29 - Results showing the Effect of the Particle Size Distribution on Segregation in Case 2.

Case 2 (33% of 20 µm, 33% of 30 µm, 33% of 40 µm)				
Region		**Average Segregation**		
		20 µm	**30 µm**	**40 µm**
x	-	34.111	33.337	33.308
	0	34.135	33.308	33.043
	+	31.633	33.356	33.650
y	-	32.677	33.481	33.572
	0	34.070	33.098	33.010
	+	33.253	33.423	33.418
z	-	39.545	38.793	38.972
	0	40.730	38.212	37.535
	+	19.706	22.995	23.493

The results of the segregation analysis in ***Table 29*** are charted in ***Figure 69***. Note that, as a negligible segregation was observed in either the x or y planes, only the segregation in the z axis is shown.

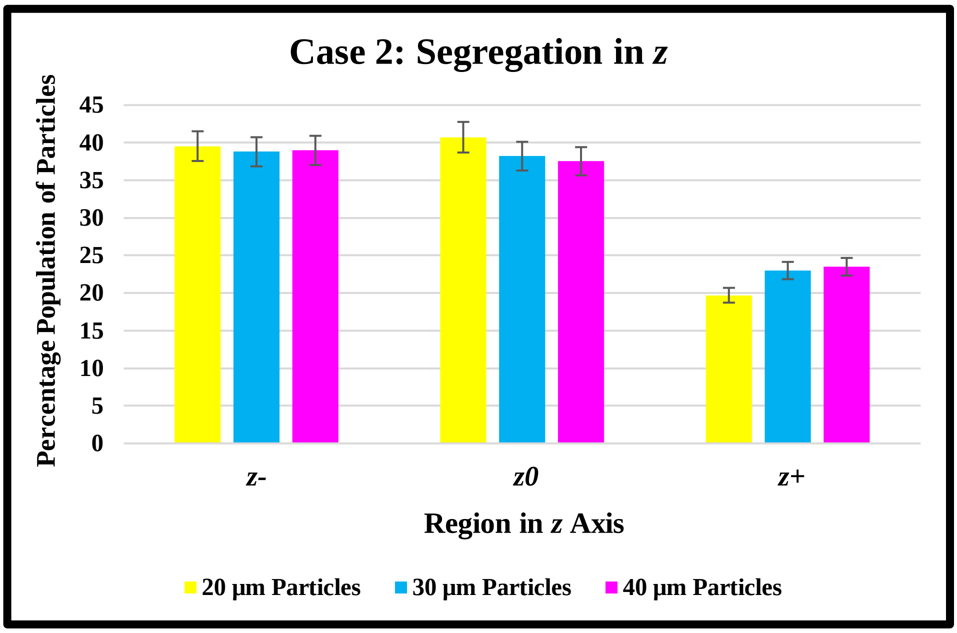

Figure 69 - Chart showing the Effect of the Particle Size Distribution on Segregation in Case 2.

Segregation was clearly observed in z when the PSD contained one-third of each particle size. The lowest concentration of all sizes was observed in the top 50 µm layer of the powder bed (z_+). A fairly similar segregation was observed for all particle sizes in the subsequent layers. A slightly more pronounced segregation was found in the finest particle size with respect to the range of the particle population percentage, compared to the 30 µm and 40 µm elements.

Table 30 - Results showing the Effect of the Particle Size Distribution on Segregation in Case 3.

Case 3 (15% of 20 µm, 25% of 30 µm, 60% of 40 µm)				
Region		**Average Segregation**		
		20 µm	**30 µm**	**40 µm**
x	**-**	33.515	33.415	33.376
	0	33.910	33.325	33.420
	+	32.575	33.260	33.204
y	**-**	32.622	33.499	33.360
	0	33.970	33.621	33.143
	+	33.408	32.880	33.498
z	**-**	40.472	39.920	39.812
	0	44.193	39.934	38.378
	+	15.335	20.146	21.811

Table 30 records the segregation in each axis of ***Case 3***. As found in ***Case 2***, no segregation was found in the x and y planes. ***Figure 70*** shows the segregation effect in z for ***Case 3***.

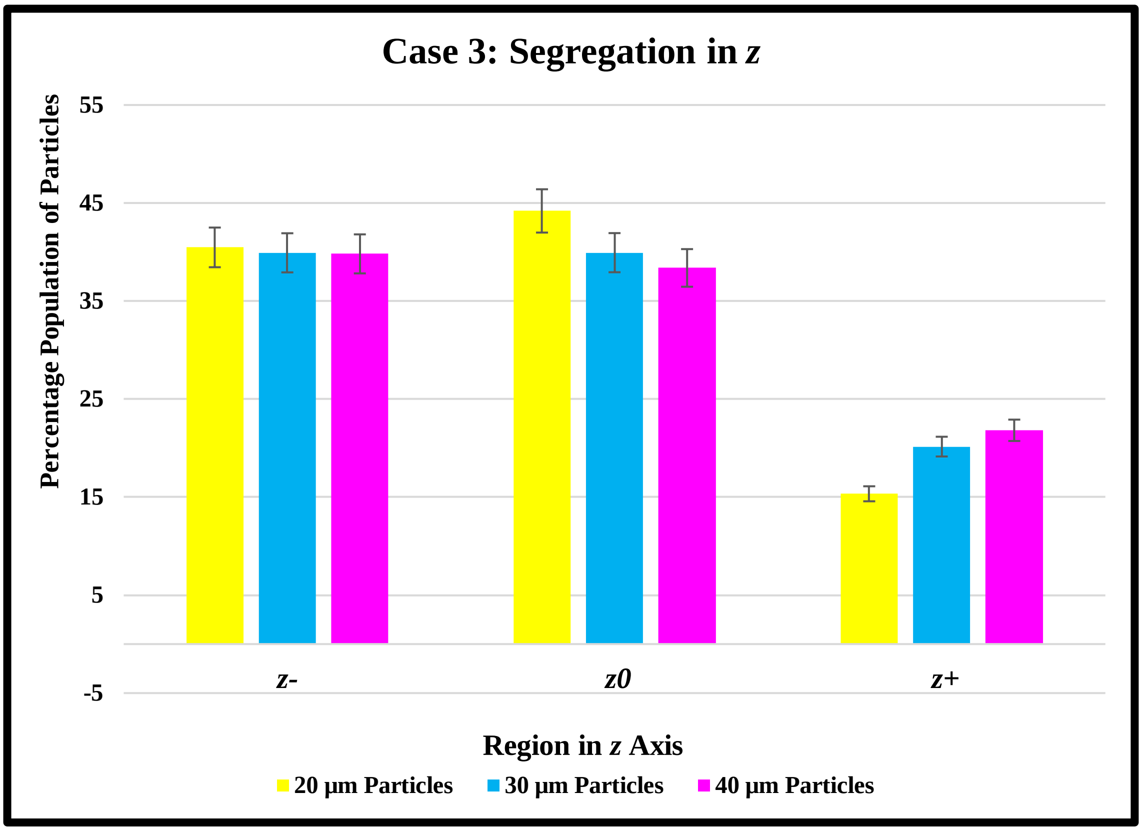

Figure 70 - Chart showing the Effect of the Particle Size Distribution on Segregation in Case 3.

A significant segregation effect was observed in the finest particle size, which was approximately 5-6% less likely to accumulate in the top layer of the bed compared to the 30 µm and 40 µm elements. A greater presence of fines was also likely to accumulate in the middle segment of the bed, suggesting there was a point at which the migration effect through the interstitial layers ceased. This finding indicated that higher concentrations of coarser particles are liable to increase the segregation effect observed, as was the case in this simulation.

Table 31 - Results showing the Effect of the Particle Size Distribution on Segregation in Case 4.

Case 4 (60% of 20 μm, 25% of 30 μm, 15% of 40 μm)				
Region		**Average Segregation**		
		20 μm	**30 μm**	**40 μm**
x	**-**	33.592	33.200	32.246
	0	33.072	33.432	33.875
	+	33.336	33.369	33.880
y	**-**	33.459	33.127	33.488
	0	33.550	33.282	33.328
	+	32.990	33.591	33.184
z	**-**	37.890	38.254	37.766
	0	38.718	36.638	36.502
	+	23.392	25.108	25.731

Once more, the results of ***Case 4*** show no segregation in the x or y planes. Thus, ***Figure 71*** demonstrates the segegation in z.

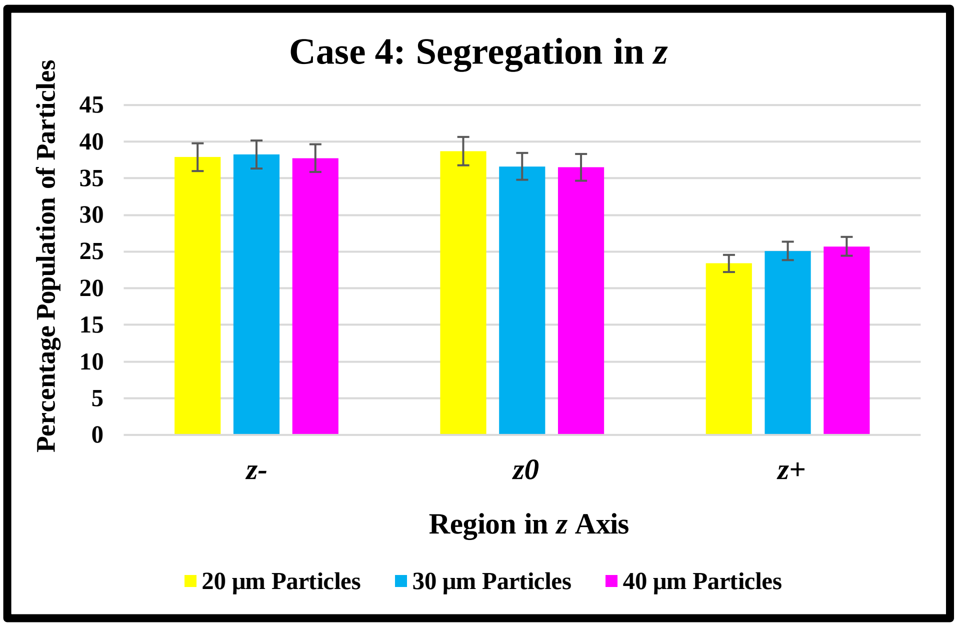

Figure 71 - Chart showing the Effect of the Particle Size Distribution on Segregation in Case 4.

Figure 71 shows minimal segregation between the particles in z_{-} and z_0. The smallest concentration of particles, irrespective of size, was observed in z_{+}. A similar segregation range was observed for all particles with appoximately a quarter of each size accumulating in the top layer. The reduced segregation effects between ***Case 3*** and ***Case 4*** suggests that a powder bed consisting of a majority of fine particles will yield a superior bed for AM processing, judged on segregation alone.

Table 32 - Results showing the Effect of the Particle Size Distribution on Segregation in Case 5.

Case 5 (25% of 20 µm, 50% of 30 µm, 25% of 40 µm)				
Region		**Average Segregation**		
		20 µm	**30 µm**	**40 µm**
x	**-**	33.331	33.364	33.426
	0	33.552	33.299	33.047
	+	33.118	33.337	33.527
y	**-**	33.095	33.330	33.683
	0	33.971	33.647	32.556
	+	32.935	33.023	33.761
z	**-**	38.749	39.046	39.154
	0	41.651	38.106	37.229
	+	19.600	22.849	23.616

As in all previous cases, no segregation was found in either the x or y plane. Segregation in the z axis is shown in ***Figure 72***.

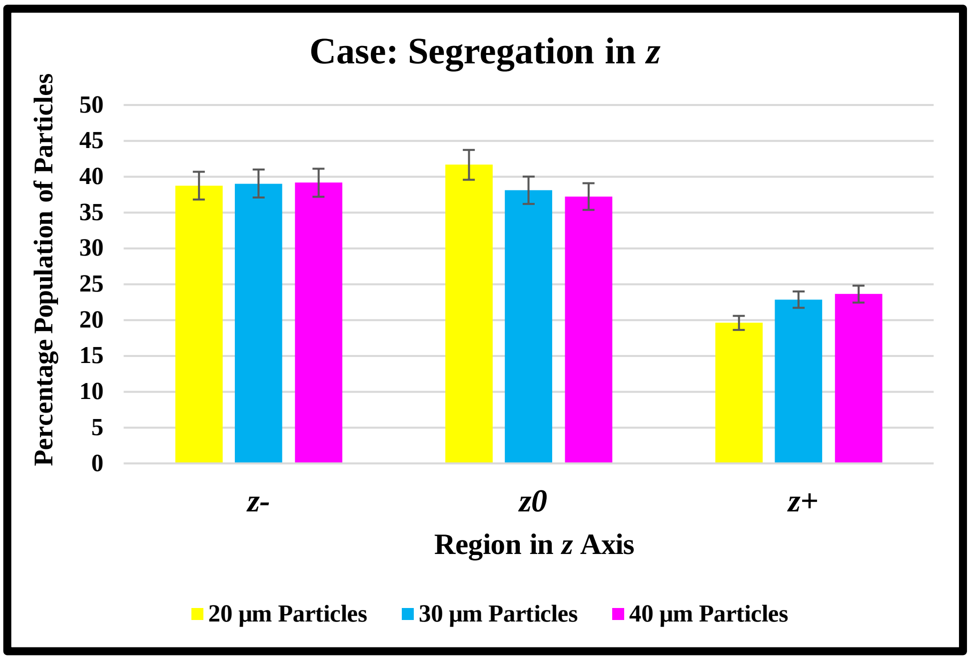

Figure 72 - Chart showing the Effect of the Particle Size Distribution on Segregation in Case 5.

In ***Case 5***, the finest particles appeared to show a slight proclivity to accumulate in the middle of the powder bed depth (z_0), as also found in ***Case 3***. These results appear to closely corrospond to the results of ***Case 2***, which follows as these two powder sets shared the most similarly weighted PSD. ***Case 5*** conformed to the findings of all polydisperse simulations that the lowest percentage of all particles sizes were found in the top 50 µm of the powder bed. In all cases, this was most clearly shown by the finest particles, as approximately half the number of fines were present in z_+ compared to z_- and z_0.

6.4 Discussion

The surface roughness results in ***Subsection 6.3.2*** suggest that, in polydisperse beds, a more homogeneous layer is formed when comprised of a majority of the finest particles. A uniform bed containing only the finest particle size yielded the most optimised surface across all cases. However, the ramifications of using this PSD in practical PBF builds are severalfold. Notably, the PSD in commercial AM is governed by the material from the powder supplier, so refining the powder would require intensive sieving that adds steps to the manufacturing process. Furthermore, a smaller powder size per particle would increase the quantity of powder required to realise a design, increasing the cost of production due to necessitating more raw material per part built. For economic and logistical reasons, there are strong grounds to argue that creating a powder bed comprised entirely of uniform 20 µm particles is commercially unviable.

Multiple reasons can be proposed for the above observations. For example, the powder profile from a PSD of entirely uniform fines is likely to be more continuous due to the greater number of particles populating the region of interest. Similarly, as the particles are assumed to be spherical in morphology, two fine elements adjacent to one another will have a smaller radius and therefore a shorter distance between their poles than larger particles. This has significant implications for the surface roughness measurements when the cutout of the powder bed projected onto the xz plane (parallel to the recoating direction) is used [49], as particles are more likely to be aligned along the horizontal axis, reducing the surface roughness observed. In this case, the results found can be more likely attributed to the method of evaluation as opposed to the characteristics of the powder bed.

With respect to existing literature, the finding that a majority of fines contributes to a smoother profile of the spread layer contradicts the work of Parteli and Pöschel [49], who found that a concentration of finer particles would be more prone to localised agglomerations and thus diminish the homogeneity of the surface profile. The reason for the disparities in findings are clear however, so far as different powder materials were analysed with different morphologies (spheres in this research, irregular multi-sphere approximations in their work), different contact models were implemented, and Parteli and Pöschel removed all elements below 60 µm from their study [49]. Thus, whilst general DEM-AM observations such as simulation domains and processing characteristics were informative, drawing like-for-like comparisons between the inserted PSD would be misleading to the research agenda.

A more comparable study to the work in this research was performed by Mussatto et al [101], who analysed three different PSD sets of SS316l for PBF processing using the DEM and practical experiments. Of these powder sets, a majority coarse (approximating 100µm), Gaussian distributed, and majority fine set (with about half of the particles below 30 µm) were investigated and a clear improvement, measured by the powder bed topography and thus surface roughness profile, was incurred by the majority fine set compared to the coarser powder sample. Thus, corresponding to the data in this research, a polydisperse powder mix with a majority of fines (***Case 4***) incurs a generally smoother surface profile, and highlights an alignment with existing literature.

The disparities between publications in existing literature (refer to ***Subsection 3.2.3***), in conjunction with the overall finding that a higher concentration of fines yields a superior powder bed in terms of surface roughness (***Cases 4*** and ***6*** in this section), demonstrates that the effect of the PSD on spread layer profile homogeneity is dependent on numerous other variables and that accurate contact modelling, in particular with respect to cohesive and friction based properties, is a prerequisite to achieving robust powder flow models.

Results showed that the packing density increased with the percentage of the finest particles used. The highest SVF was recorded in ***Case 6*** where the bed is comprised entirely of the finest (20 µm) particles. These results have interesting implications for AM processing, as maximum sphere packing theory suggests a polydisperse powder bed will be more prone to occupying interstitial spaces compared to uniform sphere packing [233, 234].

Multiple reasons are proposed as to why the highest SVF was found in the finest uniform bed. As particles are inserted by mass, ***Case 6*** contained the highest quantity of particles of all simulations. It is hypothesised that the significant increase in the number of particles increased the weight of the powder layers, and thereby induced compressive forces to the layers below. Thus, it is possible the sheer amount of powder inserted was the driving force behind raising the SVF.

The range of SVF values (52.07% to 56.78%) were in agreement with expected values observed in literature, such as the work of Haeri [17] and conforms to the theorised expected maximum packing density of approximately 58% (***Subsection 3.2.2***). As similarly observed when comparing the surface roughness analysis to existing literature, Mussatto et al [101] indicated that a higher presence of fines reduced inter-particle spacing and thus raised the packing density of the formed powder bed. The work of Lee et al [235], who also studied the PBF processing of SS316l with the DEM, observed that increasing the quantity of fines (below 25 μm) also culminated in a more densely packed powder bed. Thus, corroborating the findings of this work (***Case 4***). In contrast to the results of this research, Brika et al [14] also measured the three different Ti-6Al-4V sets for PBF processing, all broadly in the same size region as the DEM modelling in this section, and observed that the inclusion of fines generally diminished packing density due to the increased incidence of particle interactions.

A possible hypothesis is that the contact models and parameters used failed to account for all of the interparticle physics that will influence the cohesive behaviour fundamental to the packing density, such as the moisture content, the phase of processing and composition of recycled and virgin powder, and the temperature of the powder in the build chamber [161, 94, 236, 197]. Whilst the inherent material properties have been calibrated against practical powder flow (***Section 5***), it is a truism that all real-world processes will be subject to variables that cannot be accounted for by the digital counterpart. Thus, inducing a bounded rationality to the simulation design.

In the context of commercial AM, it is reasonable to argue that such intricate control of the PSD to raise the SVF, by including only the finest particles, would incur the same economic and logistical constraints as also discussed in reference to the surface roughness results.

Literature has shown that there is generally an inverse relationship between the surface homogeneity of the spread powder layer and the packing density [17, 32]. This finding was also present in the simulations performed in this section. This finding is logical as a smoothly spread layer and densely packed region analysed are both indicative of suitable conditions that engender an optimised powder bed for AM. In terms of qualitative inspections, it also follows that a more densely packed powder bed will improve the surface profile, by populating more interstices within the top layer of the powder bed and thus reducing spacing between neighbouring particles. A mathematical inspection highlights further quantitative depth to the relationship between the two metrics of bed quality, with a Pearson Correlation Coefficient of -0.9, showing clearly that as one variable increases, the other decreases proportionally. Thus, exemplifying a strong negative linear relationship between surface roughness and packing density. The full calculation process to find the Pearson Correlation Coefficient has been performed in ***Appendix N***.

Considering the manufacturing constraints with the SVF of each simulation, the most suitable powder bed would comprise a polydisperse mix with a majority of particles near to the finest size of the PSD. An approximate value for SS316l under these conditions would be 15-25 µm particles at a population of 60%, 25% of the population between 25-40 µm, and no more than 15% of the particles ≥ 40 µm in diameter.

Current industrial practice suggests that the average PSD weightings for SS316l in SLM approximate d_{10} = 18-24 µm and d_{50} = 32.2-34.4 µm, with presumably the rest of the powder between 34.4 µm to 45 µm [237, 238]. These percentile values are statistical parameters used when measuring the constituents of a cumulative PSD and indicate the size range at which the percentage value in the subscript is found.

Minimal segregation occurred in either the x or y plane for any of the PSD sets. However, a significant segregation by particle population percentage occurred in the z plane. All powder sets showed a larger portion of all particle sizes populating the middle and lower segments in z compared to the top 50 µm segment. A proposed reason for this finding is that the lack of a successive layer above the top 50 µm segment likely affords the particles the freedom to disperse in both the x and y directions, thereby occupying more interstices. Furthermore, the movement of particles in the middle segment of the powder bed (z_0) is likely to be constrained by the above and below layers of powder. Similarly, the bottom segment of the powder bed depth measured, z_-, is likely to house particles with movement constrained by both the above layer and the substrate.

As observed in literature, a more densely packed powder bed is often recorded when subjected to the compressive forces of a roller type recoater. It is plausible that the weight of the powder layers exert minor compressions to the underlying layers, which would explain the broadly stable particle population percentages observed in all simulation sets for z_- and z_0.

All results in the z axis, with varying segregation severity, show that the finest particles comprise the smallest percentage population in the top 50 µm segment of the powder bed. This result conforms to the theory in literature that the finest elements have a proclivity to migrate under gravity through the interstices of the bed and accumulate in the lower layer depths. A hypothesis as to how this occurs is that larger particles are pushed along by the recoater when a heap is formed in front of the spreader, and that the finer particles migrate to the bottom of the heap and thus have an advanced motion to descend into the lower layers. Furthermore, as the segments are populated by the particles with centroids falling in defined boundaries, it is likely that the lack of a successive layer above z_+ results in fewer particles of all types being accounted for, explaining the pronounced segregation effect and the smallest population of all particle sizes in that region.

6.5 Summary

Analysis of the results for the surface roughness, SVF, and segregation tests have yielded the following conclusions, with respect to the effect of inserting controlled PSD fractions on the powder bed quality:

- The lowest surface roughness, and thus smoothest powder bed, was found in ***Case 6*** where all particles were uniform spheres and 20 µm in diameter.

- The highest SVF, and thus the most densely packed powder bed, was also observed in ***Case 6***, suggesting that based on these two metrics alone a powder bed populated by only 20 µm particles engenders the most suitable manufacturing conditions. However, as discussed in ***Subsection 6.4*** this is unviable in reality.

- A negligible segregation occurred for any particle size in the x and y planes, with almost exactly one-third of each particle population dispersed across the y segments in each simulation.

- The least pronounced segregation in any polydisperse bed occurred when the PSD consisted of a majority of fine particles, judged by the range of the percentage particle population in the z axis. Although a degree of segregation was observed, the fines were less dispersed than in the other digital experimental sets.

- Lower surface roughness values, higher packing densities, and a reduced segregation were found when the PSD consisted of a majority of fine particles. Considering the economic and logistical limitations of populating a powder bed with only uniform 20 µm particles, a real polydisperse powder bed should contain a majority of fines. Under the conditions of these simulations and accounting for the constraints of powder size sorting, an approximate value for SS316l would be 15-25 µm particles at a population of 60%, 25% of the population being between 25-40 µm, and no more than 15% of the particles ≥ 40 µm in diameter.

7. Influence of Deposition Mechanism on Powder Bed Quality

Section 7 records all of the information relating to the investigation of dynamic powder deposition, when compared to the rainfall-formed spread layer, on powder bed quality. The subject is briefly introduced in ***Subsection 7.1*** to provide context for the subsequent investigations. The simulation method is explained fully in the following subsection, encompassing all aspects of setting up the models, including particle size insertions, domain sizes, parametric configurations, and general conditions of the simulations performed. ***Subsection 7.3*** contains all of the results of the metrics of powder bed quality tested, including the surface roughness and packing density, and three separate segregation inspections at different regions and stages of the powder insertion and spreading process. The discussion of the results and the key findings of the investigations are performed in ***Subsection 7.4***, and the concluding section summarising the main findings of the analysis is provided in ***Subsection 7.5***.

7.1 Introduction to Dynamic Powder Deposition

This chapter investigates the effect that a dynamic powder deposition has on the resulting powder bed. To the best of the author's knowledge, no previous research into using the DEM to model powder deposition with a moving funnel exists. Almost exclusively in the DEM analysis of AM powder, a "rainfall technique" is used to populate the beds. This approach describes powder being inserted in a set volume or region of space to fall under gravity and occupy the powder substrate. In a dynamic deposition, a moving funnel delivers the powder directly in front of the recoater to form a heap which is then spread by the recoater. In commercial PBF machines, powder is often delivered in front of the recoater using a hopper or fed by the action of piston [59, 60, 163, 195]. However, a small amount of contemporary AM machines use a moving funnel [56].

As in ***Section 6***, the quality of the spread layer has been judged against the metrics of surface roughness, SVF, and segregation for powder beds filled by both rainfall and dynamic deposition. Thus, modelling the influence of the powder delivery technique to determine its quality on the powder bed.

As in the PSD sets used in ***Section 6***, a mix of uniform and polydisperse powders have been inserted by both techniques, to see if the effect of deposition on the quality of the formed layer was consistent across various PSD sets. The full simulation method is outlined subsequently in ***Subsection 7.2***.

7.2 Simulation Set Up of Dynamic Powder Deposition Modelling

Prior to commencing the modelling of the dynamic deposition process, it was essential to define the assumptions which governed the model set up, and manage expectations by establishing the limitations of what can be expected from the research and modelling process. As in the calibration of model parameters against practical powder flow, and the analysis into the effect of the PSD on powder bed quality performed in the previous section, the presence of moisture was omitted in the study owing to the vacuum environment of EBM processes, and the inherent vacuum within the LIGGGHTS® system. The influence these omissions would have had on particle flow behaviour is, however, accounted for by the extensive calibration process performed in ***Subsection 5.3.1***. Furthermore, neglecting air resistance and moisture is not uncommon in DEM-AM investigations [217, 219], with it theorised that van der Waals forces, electrostatics, and capillary interactions are the dominant factors behind powder cohesion at the size range of SS316l modelled.

All particles were, once more, assumed to be perfectly spherical in composition. This reflects a limitation of the study, with the powder processed likely to contain satellites and irregularities. These would, however, be less pronounced depending on the refinement of the atomisation process (as shown in the literature, plasma-atomised powders, which are often observed in EBM processing, generally possess a more spherical morphology than their gas-atomised counterparts [14]). Thus, potentially limiting how much this diminishes the robustness of the model. As also implemented in the previous work, the value of Young's Modulus was scaled to three orders of magnitude below the sourced value for SS316l. As noted previously, this is a common technique in DEM analysis of PBF powders to incur computational savings, with minimal influence on results observed [176, 177, 178, 179].

Arguably the most significant limitation of the study is that the travelling funnel set up modelled is not necessarily reflective of all commercial EBM systems, some of which, as outlined in ***Figure 25***, provide powder to the build plate using a hopper or piston-operated table. As highlighted in ***Subsection 1.1.1***, the literature showed that the quality of the built components is subject to more than 130 different processing variables [31]. Thus, producing multiple powder deposition models would increase the number of interdependent variables analysed, both intentionally and inadvertently. Similarly, parametric variables, such as the speed of the moving funnel and the recoater, were kept constant to ascertain the influence of realistic deposition methods and isolate variables to the delivery technique.

Prior to analysing the influence of the deposition method, all cases had a preliminary powder layer approximately 2-3 particles thick inserted by the rainfall technique across the length of the substrate. Thus, accounting for preceding layers and making the model more reflective of a real PBF process. As in ***Subsection 6.2***, the test bed was comprised of a substrate with buffers at either end to constrain powder flow. To prevent the particles piling up at the periodic boundary in the y plane, small walls were added to restrict powder movement to the substrate. ***Figure 73*** shows the powder bed set up with the preliminary powder layer. Note, all geometries except the spreader have been set to 50% transparency to illustrate the powder.

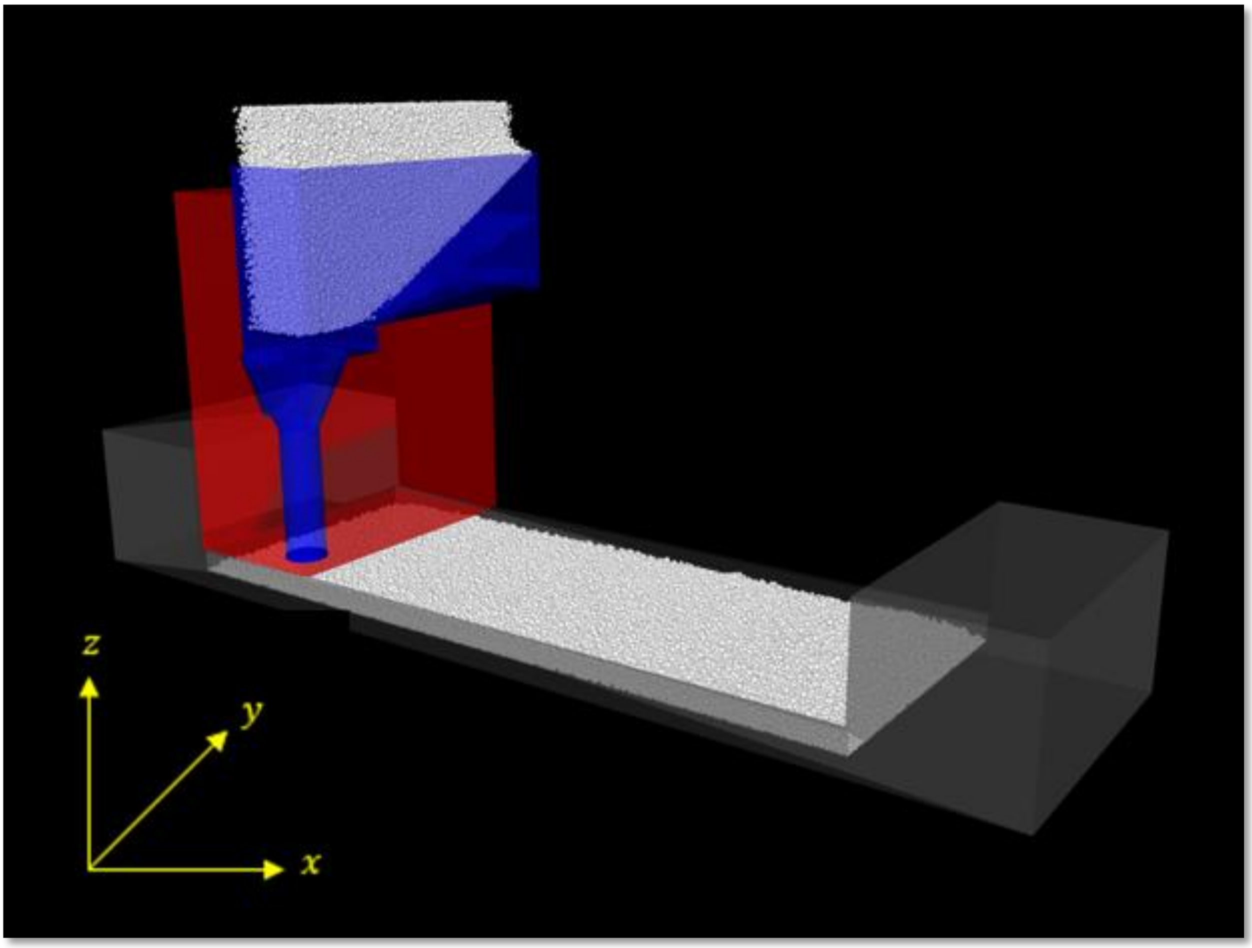

Figure 73 - Powder Bed System with Moving Funnel Deposition Method.

To determine the effect of deposition, two approaches have been used. In the dynamic technique, a funnel was positioned in front of the recoater at a standoff distance from the substrate to allow the powder to discharge. Powder was supplied to the funnel through the open top of the geometry and allowed to settle under gravity. The flow was constrained by a lid under the funnel. To commence powder deposition, the lid is removed in sequence with the onset of funnel motion in the y plane and powder flowed out of the funnel nozzle to generate a powder heap in front of the spreader. The funnel moved at a constant speed of 4 $\frac{mm}{s}$ in the y axis. This slow deposition speed was due to the scaling of the model and the narrow diameter of the funnel orifice (0.3mm). In practicality, such a deposition speed would adversely influence the production throughput. The internal volume of the funnel powder chamber included a steel plate inclined at 45° to encourage powder flow.

After the powder deposition, the heap was allowed to settle under gravity and then spread by the recoater across the length of the substrate. To isolate the effect of deposition, a relatively slow constant spreading speed of 20 $\frac{mm}{s}$ was applied to the blade in all simulations. The idealised spreading speed was selected to reduce the impact of recoater velocity on packing density, surface roughness, and segregation.

Preliminary testing showed that stable model behaviour occurred at a timestep value of 1×10^{-8} s, so this value was implemented for all simulations. Two scripts were executed in LIGGGHTS®. In the first script, the preliminary powder layer was inserted to the powder bed for a total of 5×10^{6} timesteps (0.05 seconds), the simulation domain was also established and all of the required geometries were inserted. The powder supply for the spread layer was then inserted to the funnel or by the rainfall technique over another 5×10^{6} timesteps (0.05 seconds). In either case, the powder was then allowed to settle for 10×10^{6} timesteps (0.1 second).

The second script was coded according to the deposition mechanism. In the rainfall model, the powder was simply spread by the recoater for the required number of steps to reach the end of the bed. At a recoater speed of 20 $\frac{mm}{s}$ and a spreading distance of 5mm, the recoating process was scripted to run for 25×10^{6} timesteps (0.25s).

When the powder was delivered by the moving funnel, an extra phase was included for the model to deposit the powder. To clear the 2mm width of the powder bed and deliver one sequential layer at 4 $\frac{mm}{s}$, the funnel was in motion across the y plane for 62.5×10^{6} timesteps (0.625 seconds). After which, the formed heap was allowed to settle for a further 10×10^{6} timesteps (0.1 second) and the recoater then spread the powder for the required 25×10^{6} timesteps (0.25 seconds). Hence, the total number of timesteps in the rainfall models was 45×10^{6} timesteps (0.45 seconds), compared to the 177.5×10^{6} timesteps (1.175 seconds) required for the dynamic deposition approach.

Multiple parameters are theorised to influence the quality of the spread layer, including:

- The size of the pile formed in front of the recoater.
- The distance between the spreader and the funnel during the powder discharge, and thus the proximity of the pile to the recoater face.
- The shape and diameter of the funnel nozzle.
- The velocity of the funnel and thus the deposition speed.
- The spreader gap that the powder flows under.
- The standoff distance between the funnel aperture and the substrate.

Figure 74 provides a visual explanation of these parameters.

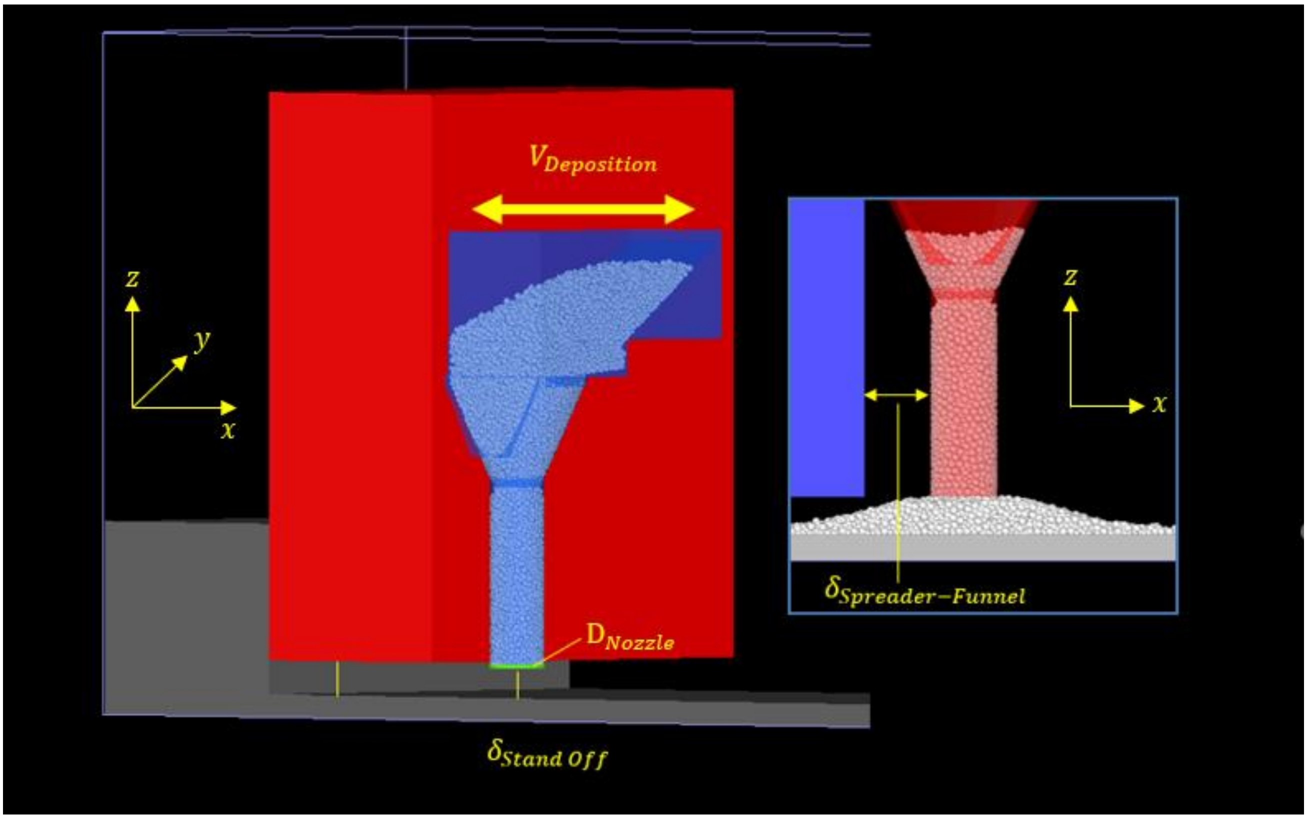

Figure 74 - Proposed Parameters to Influence the Spread Layer Quality in the Moving Funnel Deposition Method.

The rainfall technique inserted the particles in the same volume as when they were inserted to fill the funnel. Thus, ensuring the quantity of the particles and deposition location was consistent across the simulation sets. To ensure that different velocities and forces on impact did not influence the formation of the powder heap, the height of both the funnel and the insertion point of the rainfall powder in the z axis was kept constant in the respective simulations. The PSD and experiment denotations were identical to those in ***Subsection 6.2***. These values are outlined in ***Table 33***.

Table 33 - Particle Size Distribution for each Case into the Influence of Deposition Mechanism on Powder Bed Quality.

Case Number	**Particle Size Distribution**		
	40 µm	**30 µm**	**20 µm**
1	100%	0%	0%
2	33.33%	33.33%	33.33%
3	60%	25%	15%
4	15%	25%	60%
5	25%	50%	25%
6	0%	0%	100%
7	0%	100%	0%

To the best of the author's knowledge, no previous research has used the DEM to analyse how the deposition approach effects the formation of the powder bed. Due to the propriety nature of such data in industry, this subject is unlikely to receive significant research in near future. For this reason, the simulations were constrained by the limited existing data pertaining to the parameters governing the system. Furthermore, due to the computationally intense nature of the simulations, it was not feasible to digitally reproduce the powder bed at a 1:1 scale.

The dimensions of the system are outlined in ***Figure 75***. As shown, the spread region of powder was situated between the internal faces of the buffers. Note that to prevent multiple layers of powder being deposited, and thereby model an unrealistic deposition method, 1mm of clearance was inserted to the domain either side of the substrate walls in y. Particles which were discharged in this region evaded the deposited pile and thus were allowed to freefall out of the simulation.

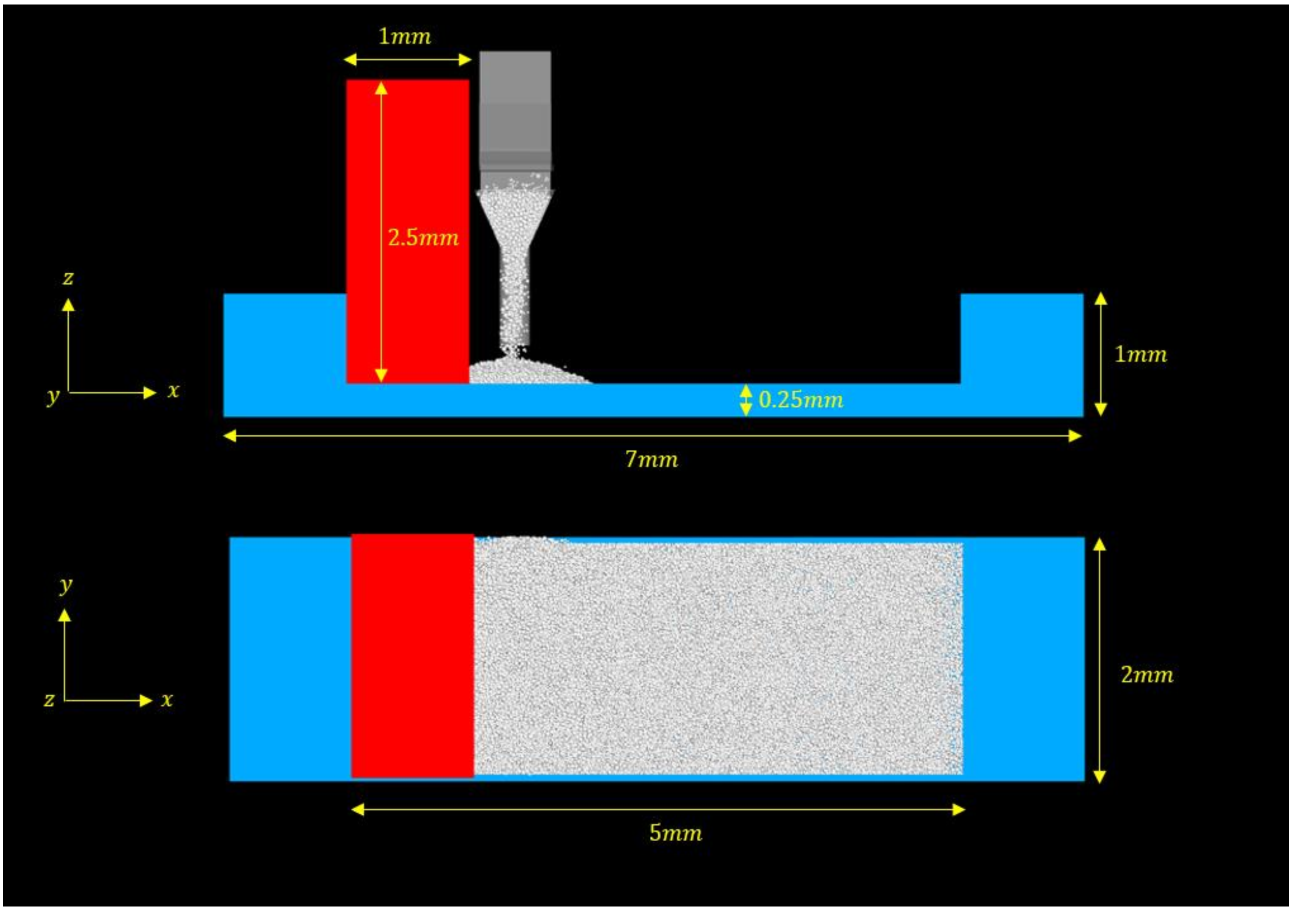

Figure 75 - Dimensions of the Powder Bed System with the Moving Funnel Deposition Method (top) and with the Funnel Suppressed (bottom).

The dimensions of the simulation domain were significantly smaller than in a full-sized commercial AM system. This approach has been observed many times in DEM literature to reduce computational costs [21, 32, 49, 98]. Often, periodic boundaries are used in a given axis to increase the fidelity of the model. As described, applying periodic boundaries in the y axis of these models would have created a multi-layering scenario which contradicts the setup observed in commercial EBM machines [56]. Hence, the setup was intended to reflect a microcosm of the spreading process across the powder bed. Homogeneity was assumed with respect to the powder characteristics across the digital model as a proxy for the full bed as the powder properties were consistent, and the system was based on the nuances of an industrial AM spreading process.

To aid a qualitative analysis of the segregation in each model, the particles are coloured by their diameter as shown in ***Table 34***.

Table 34 - Particles as Coloured by their Diameter for Segregation Analysis.

Particle Diameter	Colour
20 µm	
30 µm	
40 µm	

Figure 76 shows particles inserted both via rainfall and to the funnel and coloured by their diameter. Note that the funnel geometry has been suppressed to illustrate the segregation phenomena. The image suggests that the coarser particles preferentially migrated to the top of funnel prior to deposition, and therefore were likely to be discharged later in the pouring regime.

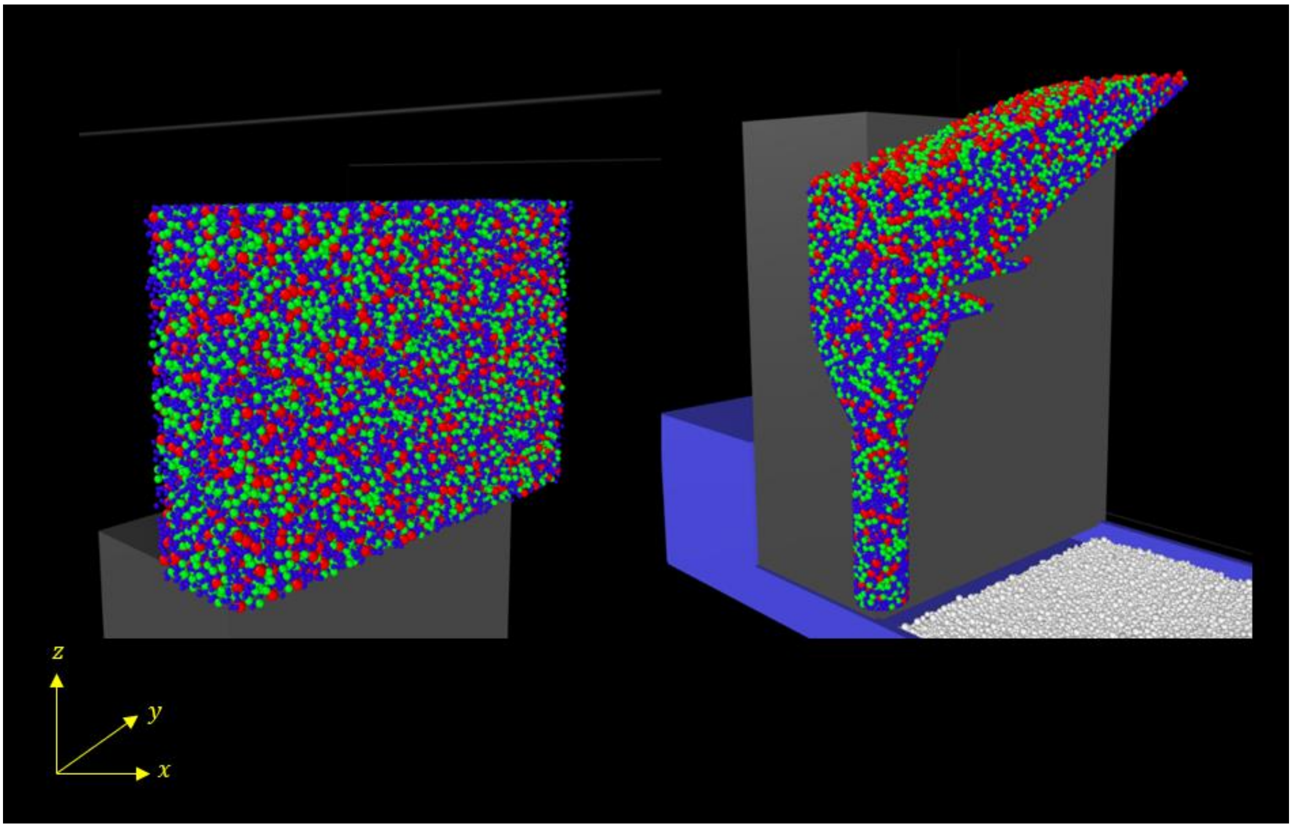

Figure 76 - Particles Coloured by their Diameter in Rainfall and Funnel Deposition Techniques.

To isolate the deposition influence, the parameters and properties of the powder and system were uniform across each case. Thus, the only variables were the deposition technique and the PSD. As in ***Section 6***, the powder and substrate were modelled as being SS316l in all cases. ***Table 35*** outlines these assigned properties, and repeats ***Table 15*** and ***Table 20***.

Table 35 - Properties of SS316l Assigned to the Powder and Geometries in the Influence of Deposition Mechanism Analysis.

Material Property	Symbol	Value	Units
Young's Modulus of Elasticity	E	0.193	GPa
Poisson's ratio	ν	0.27	Dimensionless
Particle Size Distribution	PSD	20-40	μm
Density	ρ_{SS316l}	8000	$\frac{\text{kg}}{\text{m}^3}$
Coefficient of Rolling Friction	$\mu_{Rolling}$	0.01	Dimensionless
Cohesive Energy Density (Particle-Particle)	$\boldsymbol{\kappa}$	550	$\frac{kJ}{m^3}$.
Cohesive Energy Density (Particle-Wall)	$\boldsymbol{\kappa}$	100	$\frac{kJ}{m^3}$.
Coefficient of Sliding Friction (Particle-Particle)	$\mu_{Sliding}$	0.7	Dimensionless
Coefficient of Sliding Friction (Particle-Wall)	$\mu_{Sliding}$	0.7	Dimensionless
Coefficient of Restitution	$\boldsymbol{e}$	0.1	Dimensionless

Once again, the metrics used to judge the quality of the powder bed were the surface roughness, the SVF, and the segregation. The techniques used to analyse these metrics were functionally identical to those used in ***Section 6***, and adapted according to the dimensions of the powder bed in these simulations. A comprehensive explanation of how each of these powder bed measurements were performed was provided previously in ***Subsection 6.2.1*** (the surface roughness), ***Subsection 6.2.2*** (the SVF), and ***Subsection 6.2.4*** (the segregation).

7.3 Results

7.3.1 Solid Volume Fraction Results

To comprehensively analyse the packing densities for both deposition methods, two approaches were used. Firstly, a bed segment consisting of the pre-spread layer described in ***Subsection 7.2*** was analysed to more closely mimic the spreading process in commercial PBF machinery. In the second method, the pre-spread layer was abnegated by filtering out all particles below the highest particle centroid in the z axis before the main powder insertion. Thus, in this technique the SVF values could be taken as a measurement of only the spread layer of the heap and isolated the influence of the deposition method.

In all simulations, powder parcel segments were taken at a distance away from the buffers at x values of 0.2cm-0.3cm, 0.3cm-0.4cm, and 0.4cm-0.5cm. The parcel dimensions in the other axes were consistent with the segments used for the SVF analysis performed in ***Section 6*** at 0.192cm in y (the full span, minus the largest particle diameter in from either side to negate the periodic boundary effects) and at a depth of 0.015cm or 150μm from the powder bed surface in the z plane.

Note the assumption that, as only the top layer of powder is inspected for profile homogeneity, the surface roughness was not influenced by the removal of the pre-spread layer later on. This assumption was made in accordance with the analysis of the particle displacements through the depth of the spread layer performed in ***Subsection 6.2.2*** (see ***Figure 55***).

The results for each case with and without the pre-spread layers are provided in ***Figure 77*** and ***Figure 78***.

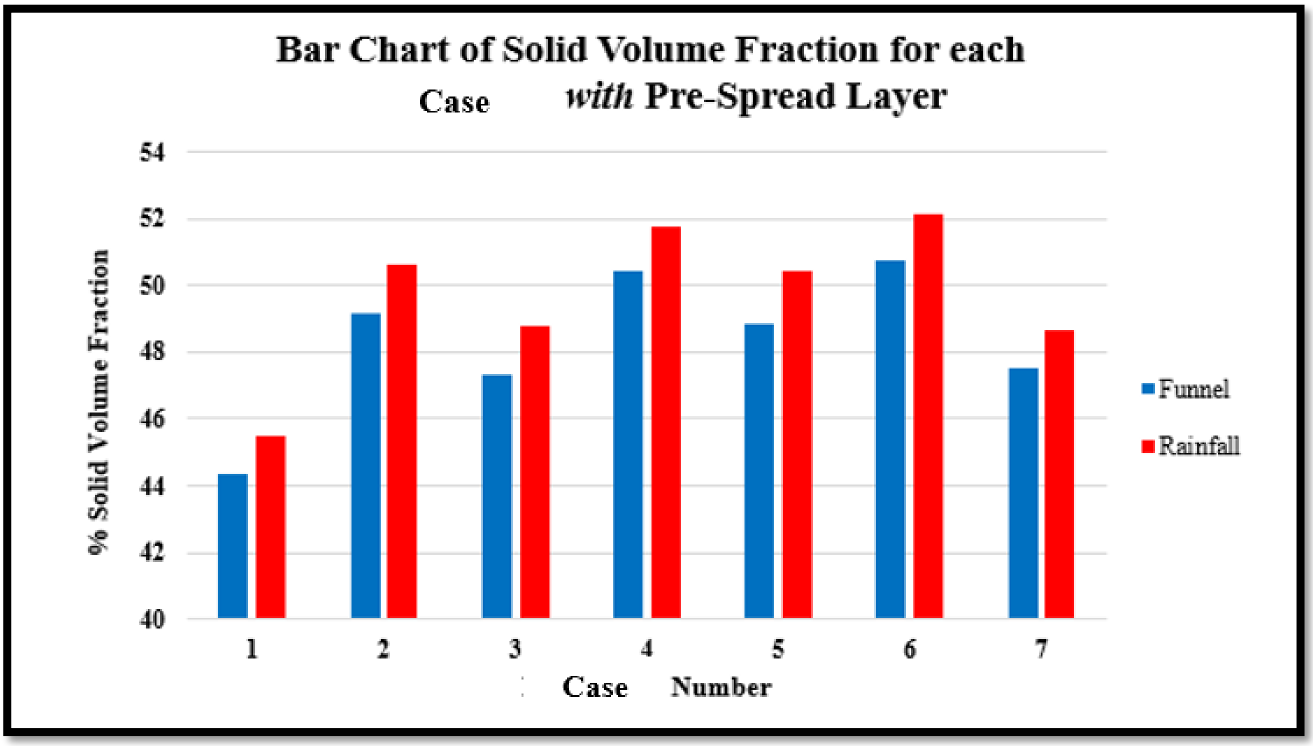

Figure 77 - Chart of Solid Volume Fraction Results for each Case including the Pre-Spread Layer in the Effect of Deposition Mechanism Analysis.

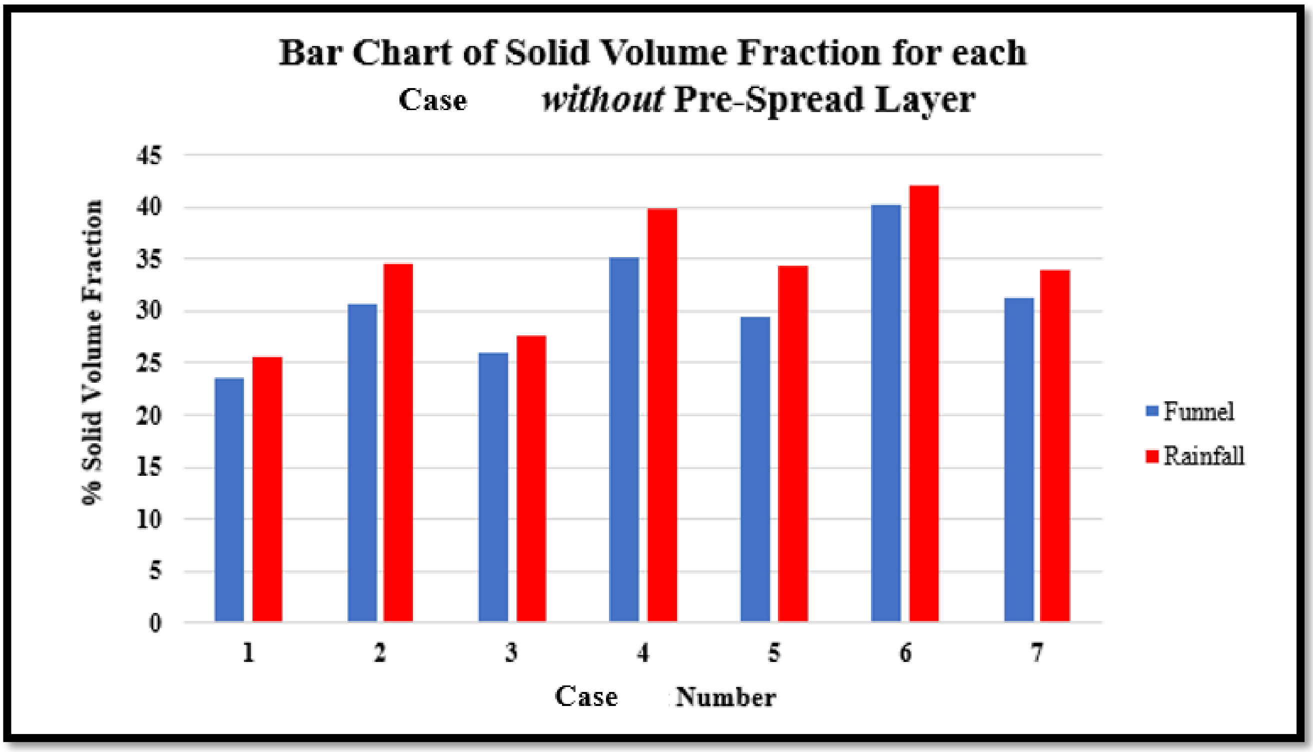

Figure 78 - Chart of Solid Volume Fraction Results for each Case excluding the Pre-Spread Layer in the Effect of Deposition Mechanism Analysis.

As expected, a higher SVF was achieved in all simulations with the pre-spread layer. This is likely attributable to the presence of the pre-spread particles filling the interstices on the substrate, and the cohesion between the main powder insertion and the pre-spread layer. Regarding deposition, higher SVF values were achieved in all simulations for the rainfall method, suggesting that the funnel approach had a detrimental effect on powder bed formation irrespective of the pre-layering condition for this metric.

By measuring the SVF against the percentage of particle sizes in a given PSD set, the influence of the PSD can be estimated for each deposition approach. The results of this analysis for the simulations including the pre-spread layer are demonstrated in ***Figure 79***, ***Figure 80***, and ***Figure 81***.

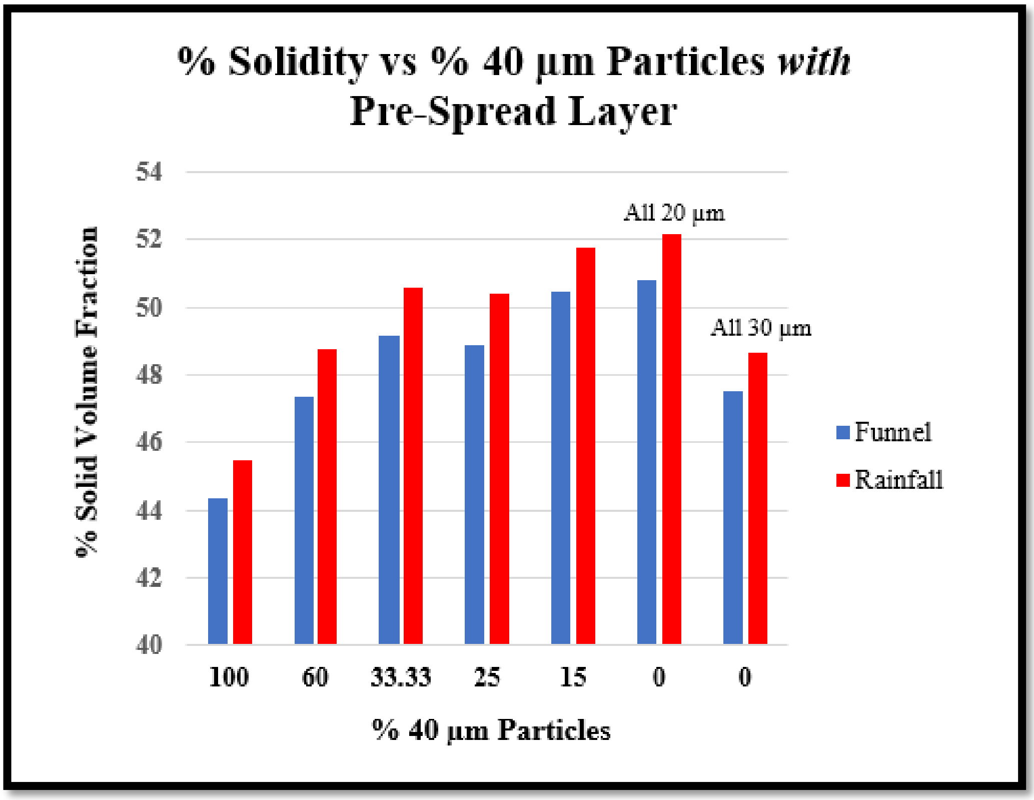

Figure 79 - Chart of Solid Volume Fraction against the Percentage of 40 µm Particles with the Pre-Spread Layer.

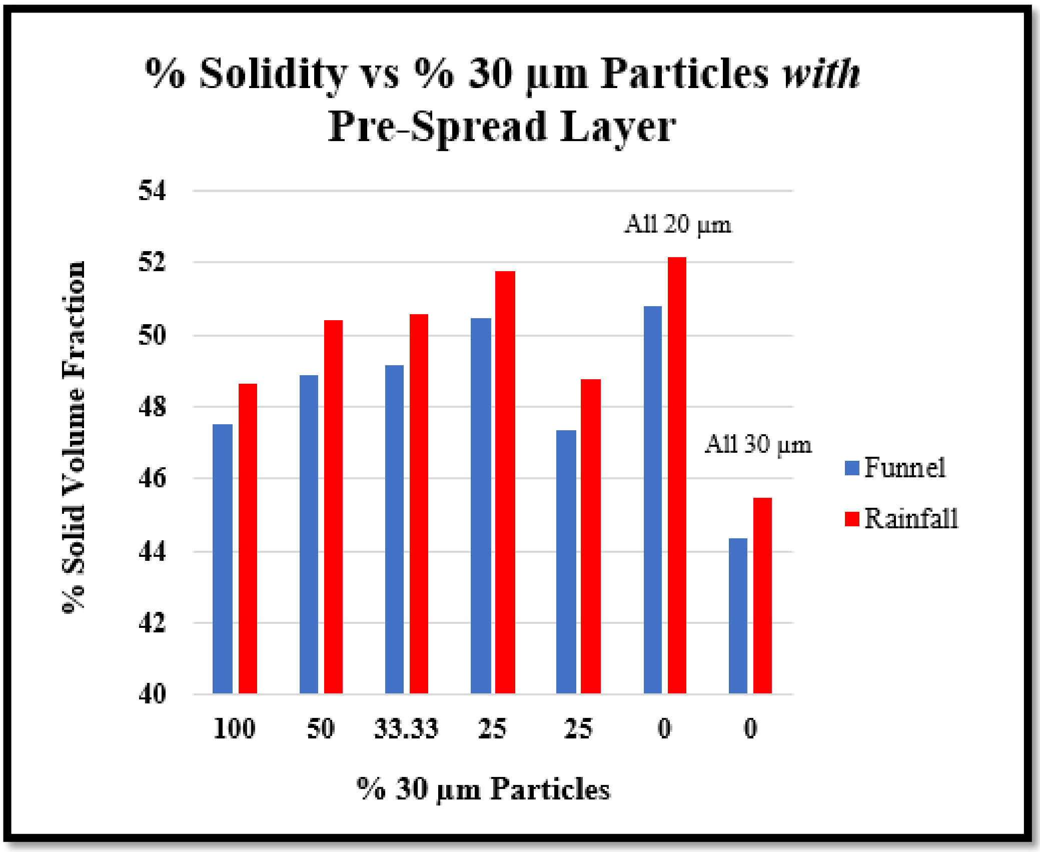

Figure 80 - Chart of Solid Volume Fraction against the Percentage of 30 µm Particles with the Pre-Spread Layer.

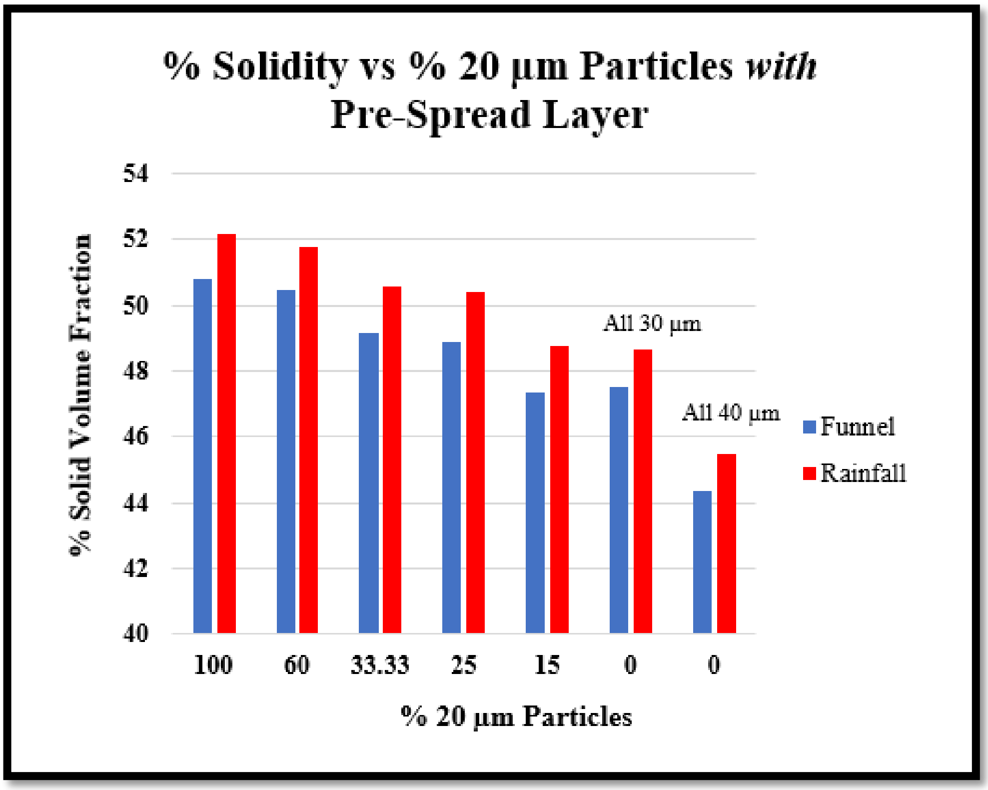

Figure 81 - Chart of Solid Volume Fraction against the Percentage of 20 µm Particles with the Pre-Spread Layer.

The SVF increased with the concentration of fines for both the funnel and rainfall depositions when the pre-spread layer was included. Therefore, to maximise the SVF it is desirable to decrease the quantity of the coarsest particles. The highest packing density was observed for both deposition techniques when uniform 20 µm particles were used. As stated frequently throughout the analysis of the results in ***Subsection 6.3***, and the discussion of those results in ***Subsection 6.4***, this could not be feasibly achieved in a commercial AM system.

The results of the SVF analysis against the percentage of particle sizes for the simulations which abnegated the pre-spread layer are provided in ***Figure 82***, ***Figure 83***, and ***Figure 84***.

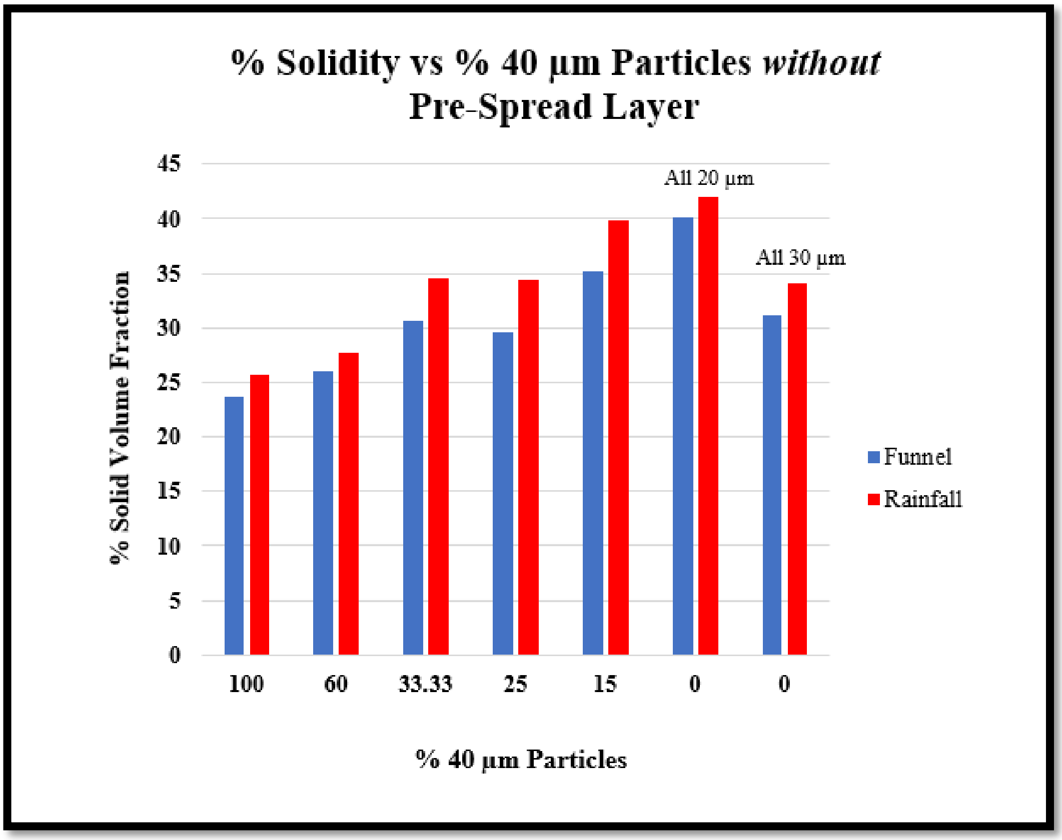

Figure 82 - Chart of Solid Volume Fraction against the Percentage of 40 µm Particles without the Pre-Spread Layer.

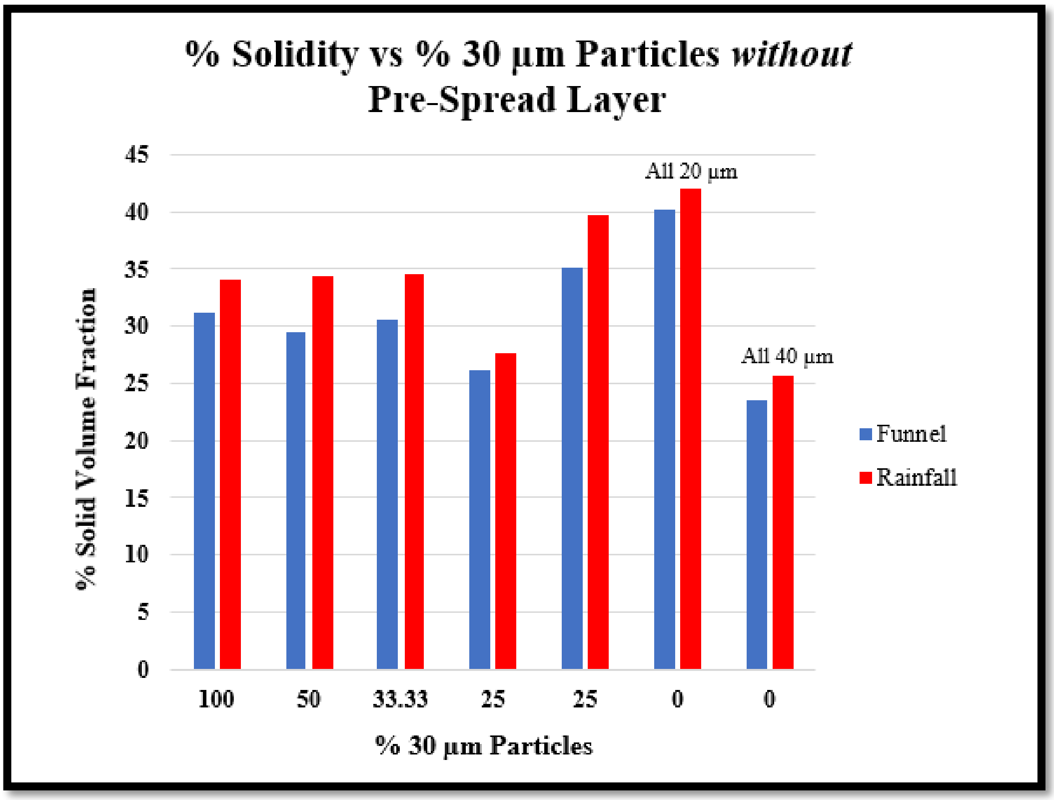

Figure 83 - Chart of Solid Volume Fraction against the Percentage of 30 µm Particles without the Pre-Spread Layer.

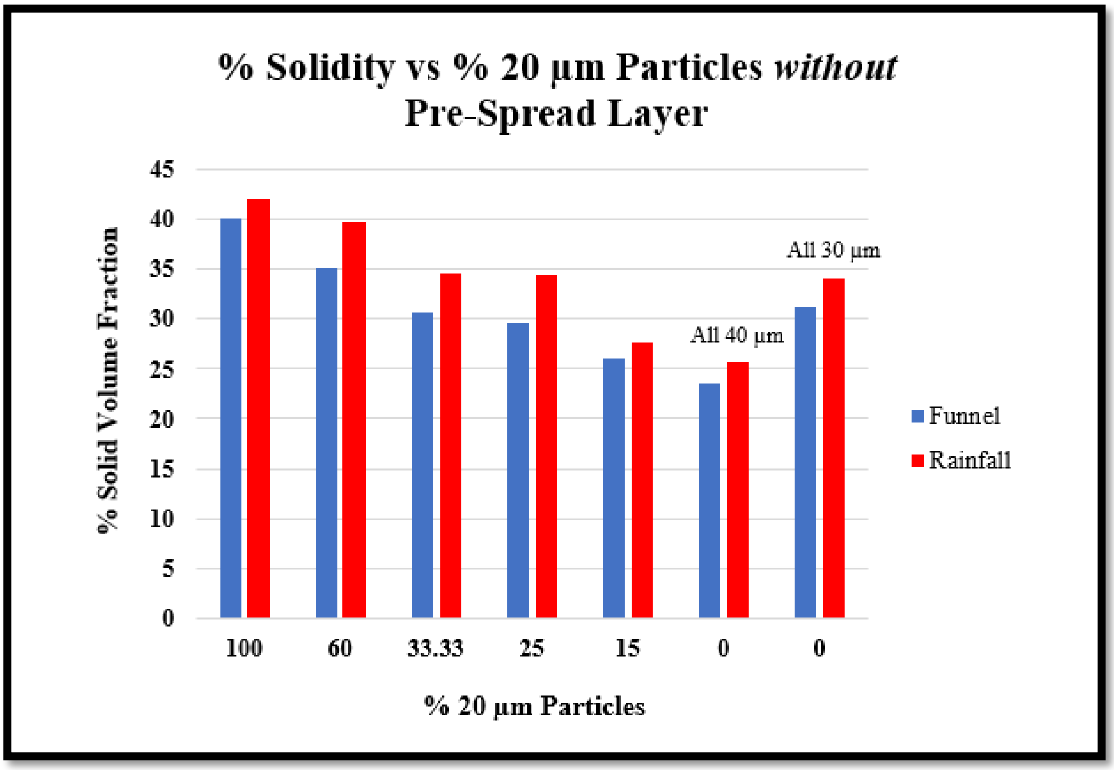

Figure 84 - Chart of Solid Volume Fraction against the Percentage of 20 µm Particles without the Pre-Spread Layer.

As also found in the powder sets including the pre-spread layer, the packing density increased with the population of fines. The SVF was higher in all simulations where the pre-spread layer was accounted for. ***Table 36*** shows that, by the metric of packing density, the rainfall deposition outperformed the moving funnel in all simulations. The values recorded for both deposition methods are from the models including the pre-spread layer.

Table 36 - Solid Volume Fraction Results for all Cases of the Rainfall and Moving Funnel Deposition Methods including the Pre-Spread Layer.

Case	Particle Size Distribution			Solid Volume Fraction (%)	
	% 40 µm	% 30 µm	% 20 µm	Travelling Funnel	Rainfall
1	100	0	0	44.33	45.5
2	33.33	33.33	33.33	49.17	50.6
3	60	25	15	47.35	48.76
4	15	25	60	50.44	51.76
5	25	50	25	48.87	50.41
6	0	0	100	50.77	52.13
7	0	100	0	47.52	48.66

The complete set of SVF results for this chapter have been recorded in ***Appendix O***.

7.3.2 Surface Roughness Results

Surface Roughness Results for all Case Sets.

As in ***Section 6***, the line profiles were taken at y plane values equal to 0.5mm (y_-), 1mm (y_0), and 1.5mm (y_+). In these simulations, the surface roughness was measured twice for each line profile and performed for Models A and B for the moving funnel technique, and Models C and D for the rainfall approach. Note that, due to the high repeatability of the simulation results in ***Section 6***, only two models were used to find the averages in this chapter. ***Equation 86*** is adapted here from earlier work for the average line profile at y_-:

$$y_- = \frac{y_{-_1} + y_{-_2}}{2} \tag{86}$$

Where y_{-_1} and y_{-_2} are the first and second tested RMS roughness values in the y_- segment line profile, respectively.

Thus, the average y_- for a given model was found by the average of that line profile from the two models tested. Once the average surface roughness was established for all line profiles in y, the roughness values were summated and divided by the number of line profiles to find the total average surface roughness for the deposition approach in that simulation set. As in the surface roughness results in ***Subsection 6.3.2***, the total average surface roughness values in ***Case 6*** and ***Case 7*** have been found from line profile slab widths of two times the diameter of the largest particle across all cases (80 µm slab width), and two times the diameter of the largest particle in that specific cases (60 µm and 40 µm for the uniform 30 µm and 20 µm powder sets respectively). The full surface roughness results for the travelling funnel and rainfall deposition methods are recorded in ***Table 37***.

Table 37 - Surface Roughness of Powder Beds created with Travelling Funnel and Rainfall Deposition Techniques.

Case	Particle Size Distribution			Surface Roughness (µm)	
	% 40 µm	% 30 µm	% 20 µm	Travelling Funnel	Rainfall
1	100	0	0	14.91	12.83
2	33.33	33.33	33.33	15.39	8.93
3	60	25	15	13.49	11.15
4	15	25	60	7.13	6.08
5	25	50	25	8.97	8.59
6	0	0	100	6.15	5.87
7	0	100	0	8.967	9.358

Surface Roughness Analysis by Percentage Particles in PSD

The effect of the PSD on both deposition techniques was also evaluated by measuring the surface roughness against the percentage of a given particle size. The results of this inspection for the population of each particle size is presented in ***Figure 85***, ***Figure 86***, and ***Figure 87***.

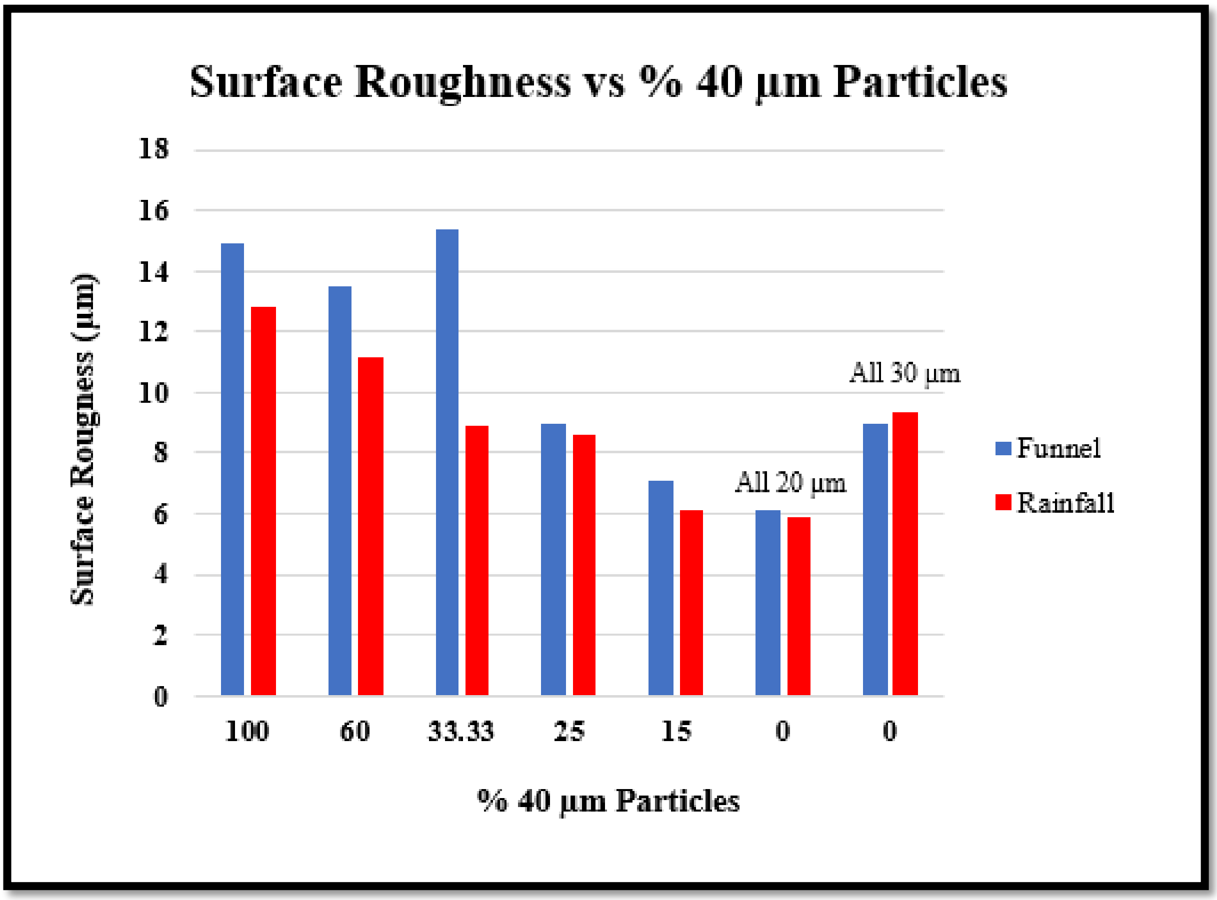

Figure 85 - Chart of Surface Roughness against the Percentage 40 µm Particles in the Effect of Deposition Method Analysis.

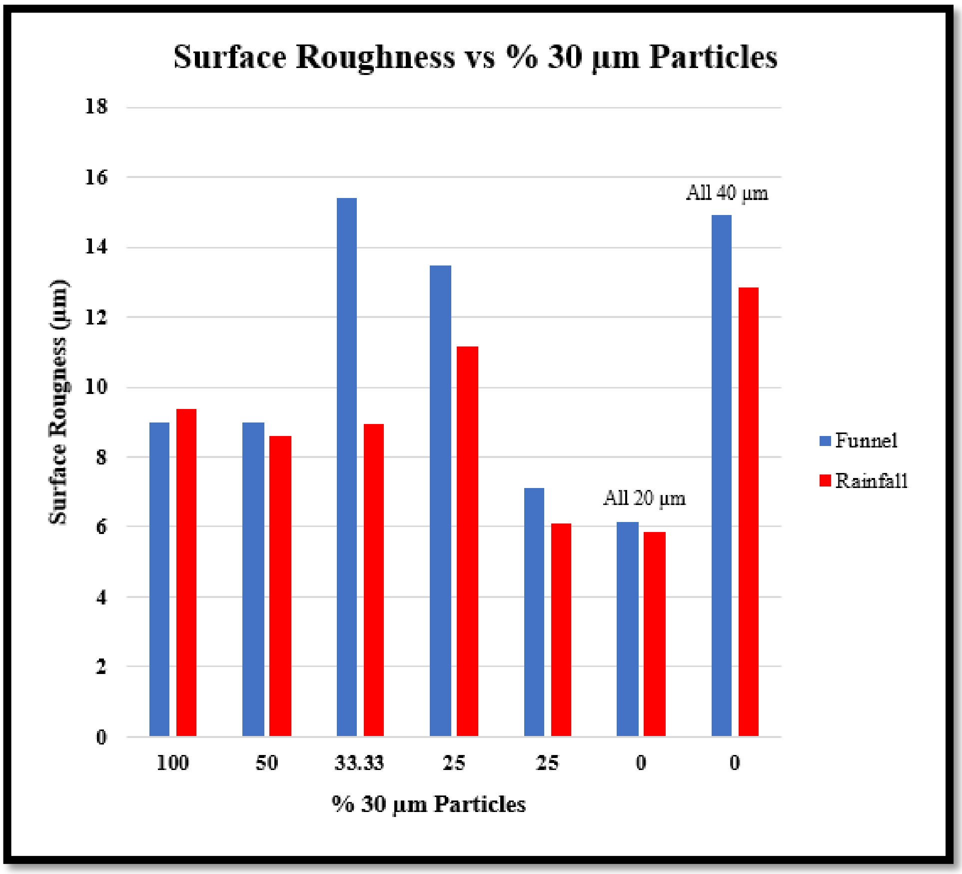

Figure 86 - Chart of Surface Roughness against the Percentage 30 µm Particles in the Effect of Deposition Method Analysis.

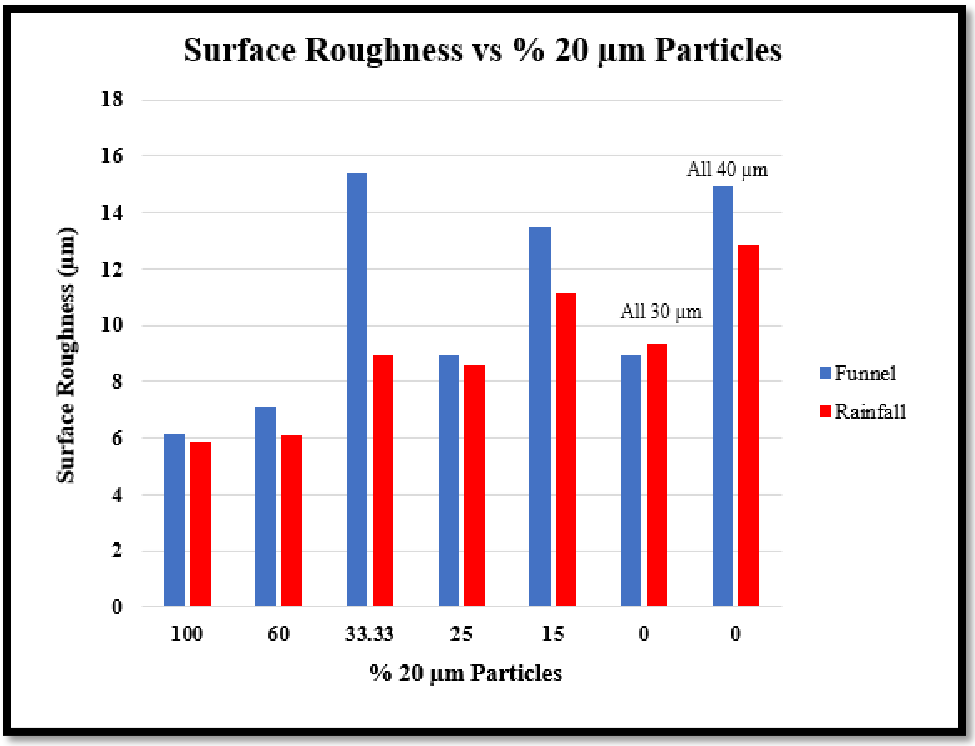

Figure 87 - Chart of Surface Roughness against the Percentage 20 µm Particles in the Effect of Deposition Method Analysis.

As shown, the surface roughness was slightly more stochastic across the different PSD sets than the SVF. It can, however, be generally remarked that the surface roughness appeared to increase with higher concentrations of coarse particles. This finding appears to be consistent for both deposition types and suggests that a higher percentage of fines increases the homogeneity of the spread layer profile. Interestingly, ***Case 2*** which inserts one-third of each particle diameter recorded the highest surface roughness of all funnel-based depositions, and was almost twice as rough as the profile formed by rainfall insertion for the same powder set. This is by some margin the largest disparity between the funnel and rainfall deliveries in the same case. The reasons for this finding are as yet inconclusive.

Effect of the Pouring Stage on the Quality of the Spread Powder Layer.

Due to the novelty of the moving funnel approach, the analysis was extended to determine what, if any, effect the technique had on the powder layers in the axis where the funnel had a transverse motion. Thus, the surface roughness values at y_{-}, y_0, and y_{+} were compared to evaluate the effect of early, mid, and late-stage pouring from the funnel. The same test was performed at these points in powder beds formed by the rainfall insertion approach for comparison. ***Figure 88*** recaps the location of y_{-}, y_0, and y_{+} from ***Subsection 6.2.1***.

Figure 88 - Location of the Three Line Profiles in the y Plane for the Effect of Deposition Mechanism on Surface Roughness Analysis.

Three profile layer tests per deposition method generated six different values per case for all 7 of the PSD sets, producing 42 data points in total. A sample chart comparing the roughness of each line in y from ***Case 2*** has been provided in ***Figure 89***. For brevity, the bar charts for all case sets are available in ***Appendix P***.

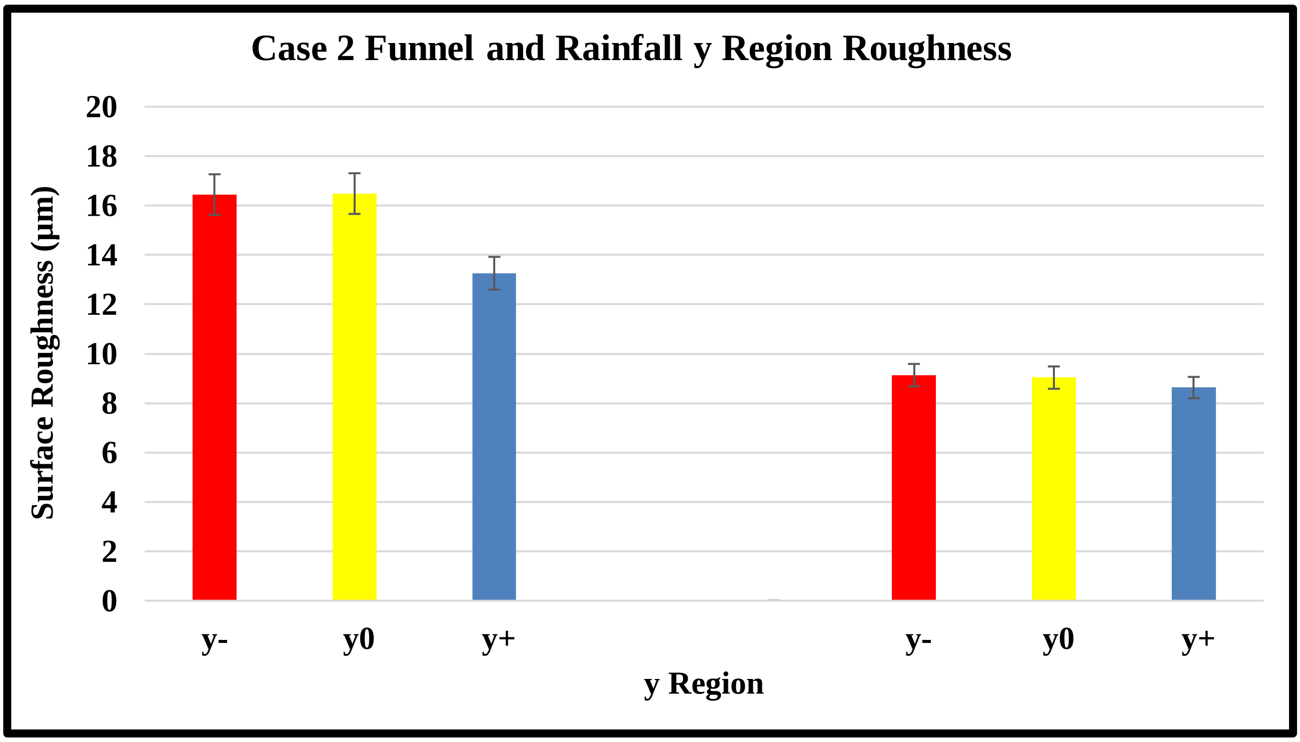

Figure 89 - Chart of the Average Roughness of Each Line Profile in the y Axis of Case 2.

In the travelling funnel simulations, the profile of the line taken from the late-pouring phase (y_+) was generally slightly smoother than the other profiles. y_+ had the smoothest line profile in ***Cases 2***, ***4***, ***5***, ***6***, & ***7***. The rainfall method produced a smoother profile line at all tested regions in the polydisperse powder sets.

It is theorised that a slight avalanche occurs from the centre of the deposited heap whilst the powder is still being dispersed over that area, and that these particles in conjunction with the deposition trajectory raise the packing and culminate in a more uniform line profile in y_+. It is of significant interest if this engenders a segregation effect during the recoating process.

Solid Volume Fraction and Surface Roughness Results for all Case Sets

Table 38 combines the SVF and surface roughness results for both deposition methods in all cases. As shown, the green data points demonstrate a positive influence with regards to powder bed quality (lower roughness and higher packing solidity) and a red value presents a negative effect.

Table 38 - Combined Solid Volume Fraction and Surface Roughness Results for the Rainfall and Travelling Funnel Deposition Methods.

Case	Particle Size Distribution			Surface Roughness (µm)		Solid Volume Fraction (%)	
	% 40 µm	% 30 µm	% 20 µm	Travelling Funnel	Rainfall	Travelling Funnel	Rainfall
1	100	0	0	14.91	12.83	44.33	45.5
2	33.33	33.33	33.33	15.39	8.93	49.17	50.6
3	60	25	15	13.49	11.15	47.35	48.76
4	15	25	60	7.13	6.08	50.44	51.76
5	25	50	25	8.97	8.59	48.87	50.41
6	0	0	100	6.15	5.87	50.77	52.13
7	0	100	0	8.967	9.358	47.52	48.66

The data demonstrated in ***Table 38*** is graphically depicted in ***Figure 90*** and ***Figure 91***. These figures are presented next to each other to provide a more comprehensive representation of the effect of the deposition mechanism on powder quality.

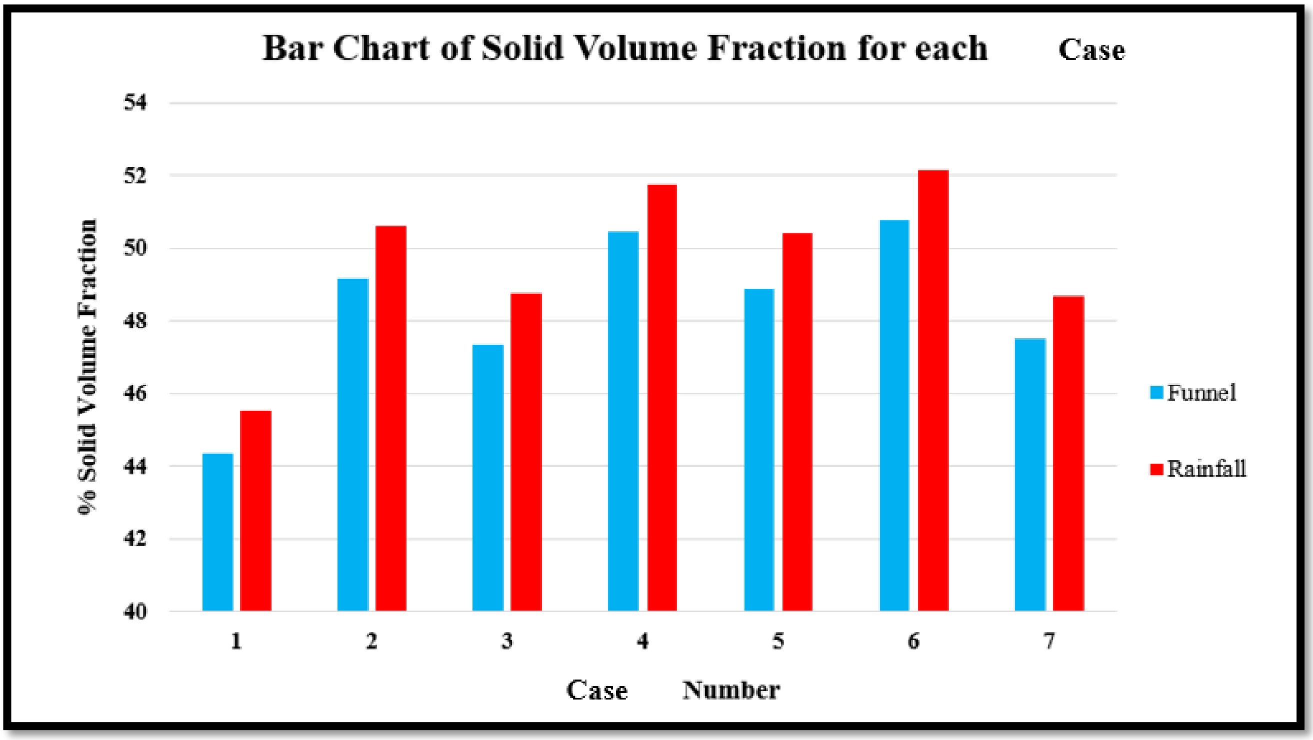

Figure 90 - Chart of the Solid Volume Fraction for Each Case in Testing the Effect of the Deposition Methods.

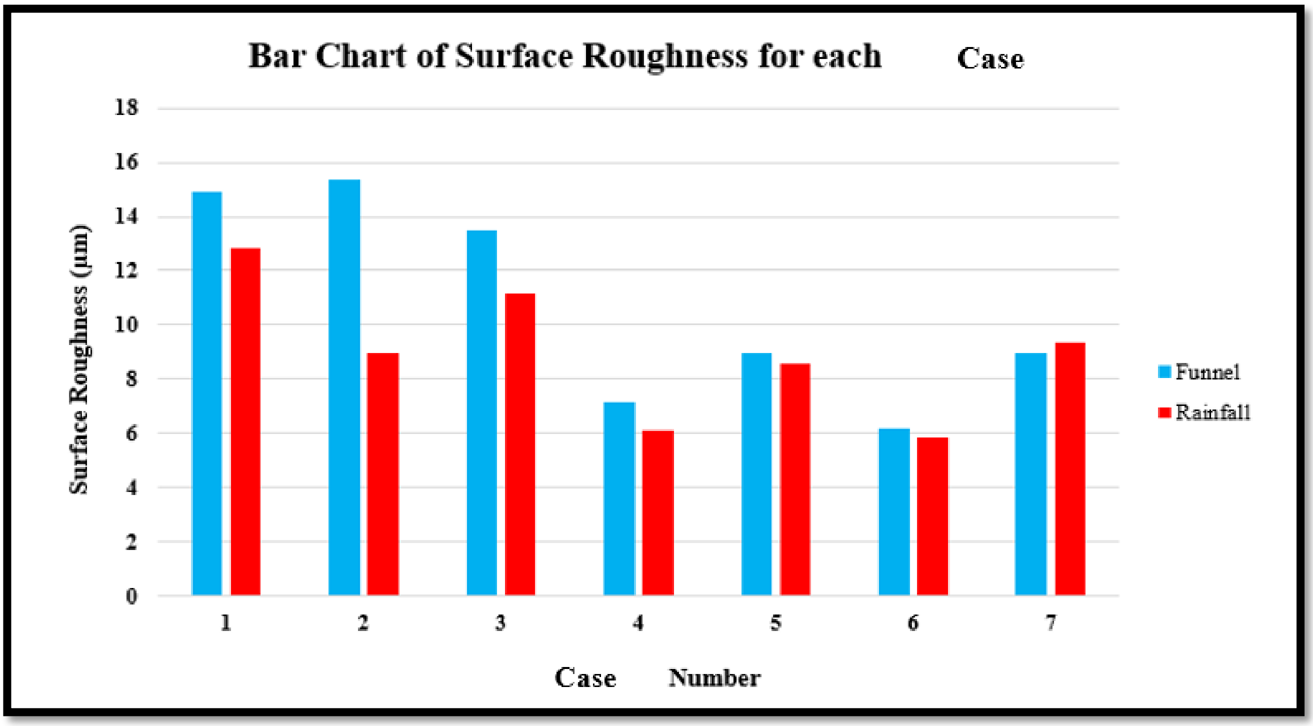

Figure 91 - Chart of the Surface Roughness for Each Case in Testing the Effect of the Deposition Methods.

The data shows that in all metrics of bed quality except the surface roughness measurement for ***Case 7***, the rainfall technique outperformed the travelling funnel, it can therefore be proposed that the funnel approach is generally detrimental to the bed quality.

The full set of surface roughness results for the dynamic and rainfall deposition methods have been recorded in ***Appendix Q.***

7.3.3 Segregation Results in Full Polydisperse Powder Sets with Dynamic and Rainfall Deposition Techniques

As discussed in ***Subsection 3.2.4***, segregation between the particles has been shown to degrade the quality of polydisperse powder beds in AM. As explained in ***Subsection 6.2.4***, segregation cannot be measured by the quantity of particles in a given bed segment as the PSD is controlled by mass. For this reason, the same approach as used previously was taken in which segregation was judged by the percentage population of a given particle size in a measured segment of the powder bed. Once more, the bed was divided into three discrete regions for each of the three axes, giving nine segments in total. As previously (see ***Table 24*** in ***Subsection 6.2.4***), each segment within a given axis was defined by **-**, 0, or **+** segment relative to the movement of the funnel and recoater depending on the axis considered. For example, x_{-}, x_0, and x_{+} represents the initial, middle, and late phases of spreading respectively.

The sum of the particle percentages of a given diameter in the measured axis of the powder bed is equal to 100%, and the concentration of that sized powder in each segment was determined to establish segregation.

Furthermore, the average position of each particle size in each axis was found to underpin the segregation analysis. The simulation method applied to this investigation was explained in ***Subsection 6.2.4***.

Segregation by Percentage Particle Population for Travelling Funnel and Rainfall Deposition Methods.

Segregation cannot occur in uniform powder beds and thus only polydisperse case sets have been analysed for both deposition approaches. As noted in ***Subsection 7.2***, the particles have been coloured by diameter as in ***Table 39***.

Table 39 - Particle Coloured by their Diameter in Travelling Funnel against Rainfall Deposition Analysis.

Particle Diameter	Colour
20 µm	
30 µm	
40 µm	

A depiction of segregation in the top and bottom views of the powder bed is given as an example in ***Figure 92***. Note that this sample is from ***Case 2*** in which approximately one-third of each powder size was inserted by mass, and that the recoater and funnel geometries have been suppressed to fully demonstrate the segregation phenomena. The top graphic presents segregation in the powder bed as viewed from above, and the graphic underneath presents segregation as viewed looking up through the bottom of the powder bed.

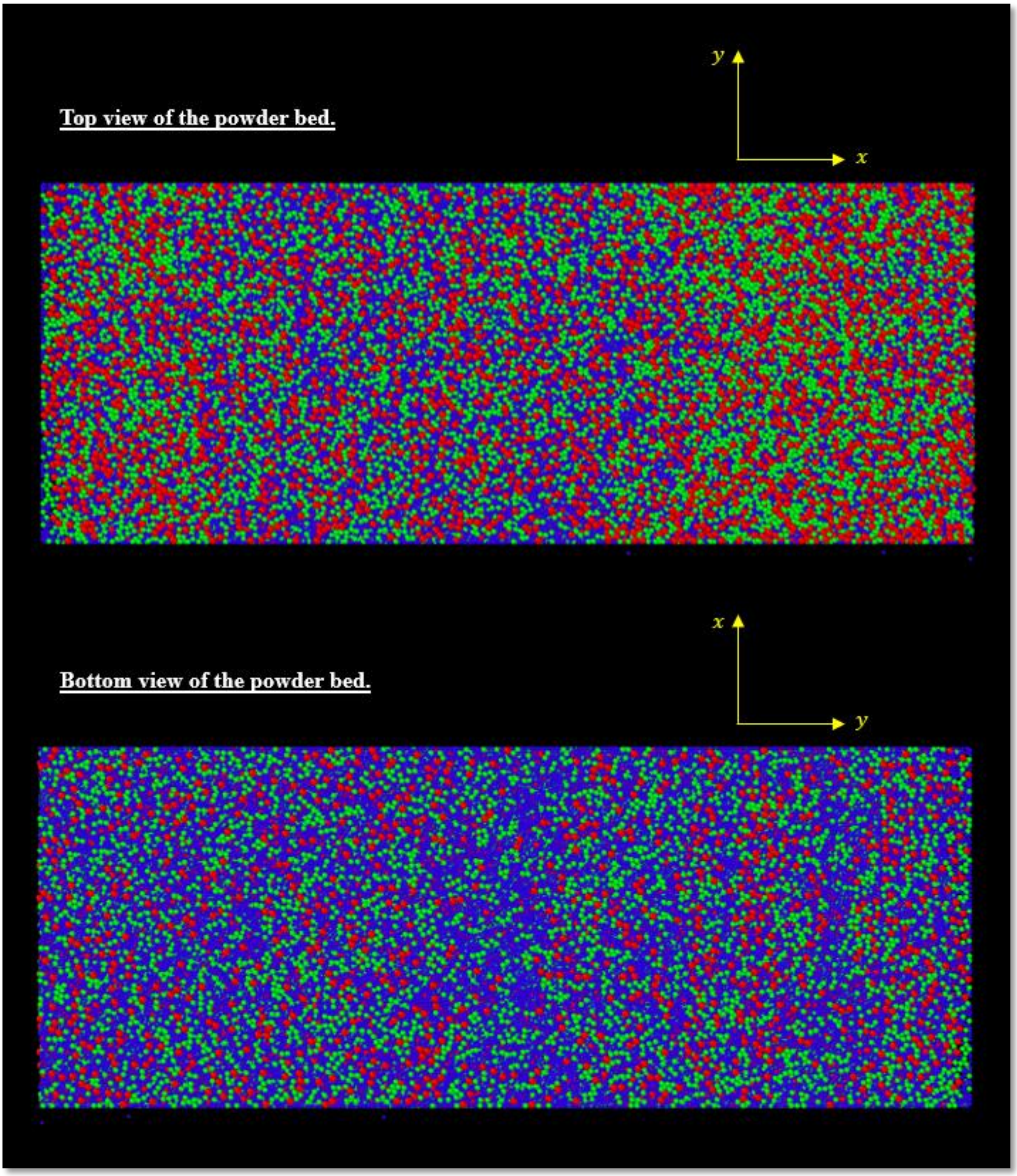

Figure 92 - Segregation in the Top and Bottom Views of the Powder Bed (From *Case 2, Model A*, using the Funnel Deposition Technique).

Processing and refining of ***Figure 92*** with ImageJ (https://imagej.net/ij/), and analysing the plot by colour, shows that, in the top view of the powder bed, the finest particles accounted for 27.45% of the population, 34.12% were 30 µm, and 38.43% of the coarsest elements were observed. In the bottom view of the bed 53.75% of the particles were 20 µm, 29.23% were 30 µm, and 17.02 were 40 µm. Thus, clearly demonstrating a proclivity for fines to migrate through the powder layers.

The full results of segregation for each polydisperse case is given in ***Table 40*** to ***Table 43***, where the percentage population for each particle size is shown.

Table 40 - Segregation Results for the Travelling Funnel and Rainfall Deposition Methods in Case 2.

Case 2 (33% of 20 µm, 33% of 30 µm, 33% of 40 µm)								
Region		Average Funnel Segregation			Average Rainfall Segregation			
		20 µm	30 µm	40 µm	20 µm	30 µm	40 µm
	-	38.867	33.149	30.813	36.178	33.849	33.979
x	0	33.119	33.831	32.938	36.101	33.286	31.005
	+	27.014	33.020	36.248	27.721	32.865	35.016
	-	33.100	33.271	33.202	33.054	33.610	33.741
y	0	33.380	33.159	32.719	33.321	32.570	32.800
	+	33.520	33.569	34.079	33.626	33.821	33.459
	-	49.511	38.000	33.086	46.022	37.597	33.396
z	0	36.711	42.698	43.841	37.271	41.094	42.958
	+	13.777	19.302	23.073	16.707	21.300	23.646

Segregation in ***Case 2*** was manifested primarily by the separation of the finest and coarsest particles (20 µm and 40 µm respectively). Notably, fines were preferentially deposited for both powder supply methods in the early stages of spreading (x_{-}), and the concentration of fines decreased with the recoater trajectory in this plane. ***Table 40*** shows that 38.87% of the finest particles measured in x were deposited in the first one-third of the recoater travel in the moving funnel models, compared to 36.18% when dropped by a rainfall technique.

Minimal segregation of the 30 µm particles was observed in line with recoater trajectory for either deposition set up. A minor segregation was induced by the funnel for the 40 µm particles whereby a slight majority were pushed along in x and came to rest in the final third of the substrate. A smaller range of the percentage population of the finest and coarsest elements was generally observed by the rainfall approach in the x plane, suggesting the funnel gave rise to segregation.

A negligible segregation effect was observed in the y plane irrespective of deposition method. In z, smaller particles were clearly preferentially deposited in the lowest one-third of the bed structure depth. Almost half of all the finest particles (49.51% for the funnel and 46.02% for the rainfall approaches respectively) were situated in the lowest third of the spread layer. This suggests that the finer particles were migrating under gravity through the bed structure and accumulating at lower bed levels, which corroborates the findings from similar powder bed set ups in literature [52, 53, 54]. The most pronounced segregation of the 30 μm particles were observed in the z axis, where the largest concentration was in the middle segment for both deposition types. A similar effect was observed for the coarsest particle type.

Table 41 - Segregation Results for the Travelling Funnel and Rainfall Deposition Methods in Case 3.

Case 3 (15% of 20 μm, 25% of 30 μm, 60% of 40 μm)							
Region		Average Funnel Segregation			Average Rainfall Segregation		
		20 μm	30 μm	40 μm	20 μm	30 μm	40 μm
	-	43.227	35.398	32.244	38.080	34.594	34.229
x	0	30.418	33.471	32.840	36.858	34.646	31.905
	+	26.354	31.131	34.916	25.062	30.760	33.866
	-	33.398	33.423	33.447	33.302	33.577	33.555
y	0	32.672	33.065	32.821	32.493	33.192	32.734
	+	33.930	33.511	33.732	34.205	33.231	33.711
	-	61.085	43.539	35.682	54.286	41.733	36.030
z	0	30.884	42.215	44.904	34.454	40.946	43.711
	+	8.030	14.246	19.413	11.260	17.320	20.260

Table 41 shows the results of the segregation analysis in ***Case 3***. A pronounced segregation was observed in the x and z planes for the finest particles, with the 20 μm particles preferentially deposited in x_{-} for both deposition methods. The funnel powder delivery induced a slightly greater segregation in x_{-} than the rainfall method (43.23% of the finest particle population compared to 38.08% respectively).

A very minor segregation was observed for the coarsest particles in the x plane, which were slightly more likely to accumulate in x_{+} when deposited by a funnel. Conversely, the 40 μm particles had a mild tendency to preferentially populate x_{-} when inserted by rainfall. In either case, the segregation was so small that it could feasibly be changed by running the model again with the positions of the particle centroids randomised in the insertion volume. Thus, the segregation can be neglected. A negligible segregation is again observed for all particle sizes in y.

The most significant segregation in ***Case 3*** was observed in the z plane. In both deposition approaches more than half of the finest particles situated in the top one-third of the powder bed, at percentages of 61.09% for the funnel method and 54.29% in the rainfall insertion. Once more, the segregation effect was more pronounced in the funnel models. A similar, but less dramatic, effect emerged for the 30 µm particles, with the population decreasing slightly between the top and middle vertical segments of the bed, and then dropping to less than half in the bottom third.

Almost half of the 40 µm population in z accumulated in the middle of the powder bed depth for both techniques, at 42.22% in the dynamic deposition models and 40.95% for the rainfall approach. Interestingly, the percentage population of the coarsest particles in z did not decrease with powder bed depth, as was the case for the 20 µm and 40 µm elements. Little difference was observed in the segregation of 40 µm particles between the deposition methods applied, with less than a 2% deviation between corresponding segments in each method.

Table 42 - Segregation Results for the Travelling Funnel and Rainfall Deposition Methods in Case 4.

Case 4 (60% of 20µm, 25% of 30 µm, 15% of 40 µm)							
Region		**Average Funnel Segregation**			**Average Rainfall Segregation**		
		20 µm	**30 µm**	**40 µm**	**20 µm**	**30 µm**	**40 µm**
	-	36.945	31.373	30.756	35.096	33.150	32.584
x	**0**	34.037	33.621	32.697	34.778	32.486	30.677
	+	29.018	35.006	36.547	30.126	34.364	36.740
	-	32.950	33.044	33.596	33.694	33.176	33.333
y	**0**	33.631	33.130	31.612	33.177	33.448	32.152
	+	33.418	33.826	34.792	33.129	33.376	34.515
	-	42.968	36.000	29.270	40.988	35.142	29.700
z	**0**	38.725	40.960	42.992	37.984	40.165	42.325
	+	18.307	23.039	27.737	21.028	24.693	27.975

The results of ***Case 4*** suggest that the segregation effect was less significant when the majority of the powder bed was comprised of fine particles, compared to the majority of coarse particles populating ***Case 3***. Fine particles in x appeared to situate in the initial regions of spreading but less dramatically than those observed in ***Case 3***. A similar population pattern in the x plane was observed when compared to ***Case 2***. The percentage population of 20 µm particles decreased slightly with recoating direction in x for both deposition methods. Negligible segregation occurred in the population of 30 µm particles in either the x or y plane. A similar trend was observed in both deposition methods for the coarsest particle size, so far as a slight majority of the population was observed at the far end of the powder bed spreading regimes. No segregation was recorded for any powder size in the y plane.

For the finest particles in z, the percentage population once more decreased with bed depth, maintaining the trend observed in ***Cases 2*** and ***3***. However, this effect was less significant compared to the previous cases, as the range in population was smaller for ***Case 4*** than for ***Cases 2*** and ***3***. For the 30 µm particles in the z plane, the highest percentage population was in the middle of the powder bed, with approximately 13% more of the population in the lower depths than the highest layer.

The majority of the coarsest particles in the z axis populated z_0. However, there was less of a disparity between the percentage population of these particles in the top and bottom regions than observed previously in ***Case 2*** and ***Case 3*** for both deposition methods, showing a reduced general segregation effect. The population values were very close for both deposition techniques implying that, in this case, the PSD had a more pronounced effect on segregation than the deposition method.

Table 43 - Segregation Results for the Travelling Funnel and Rainfall Deposition Methods in Case 5.

Case 5 (25% of 20 µm, 50% of 30 µm, 25% of 40 µm)							
Region		**Average Funnel Segregation**			**Average Rainfall Segregation**		
		20 µm	**30 µm**	**40 µm**	**20 µm**	**30 µm**	**40 µm**
	-	38.401	31.280	28.818	36.444	34.249	33.585
x	**0**	33.814	34.856	33.517	36.389	33.042	31.450
	+	27.785	33.865	37.665	27.168	32.710	34.965
	-	33.237	33.395	33.370	33.636	33.403	33.864
y	**0**	33.333	32.726	32.898	33.319	33.082	32.090
	+	33.430	33.878	33.732	33.045	33.515	34.047
	-	50.515	38.348	34.052	46.174	38.189	33.779
z	**0**	36.380	42.403	42.324	37.164	40.612	41.967
	+	13.105	19.249	23.624	16.662	21.199	24.254

The trends observed previously continued in ***Case 5*** for the finer particles in x, so far as the 20 µm elements were preferentially deposited in x_{-} and the percentage population of these particles diminished with the recoater trajectory. As also observed previously, this effect was slightly greater when particles were inserted by a funnel, implying the funnel technique mildly exacerbates the segregation in the spreading direction. As in most other PSD sets analysed, larger particles had a tendency to accumulate at the far end of the powder bed relative to the recoater direction, and the range of the coarse particle population percentage was increased by the funnel deposition. A negligible segregation was observed for the 30 µm particles in the x plane regardless of deposition methods and, as found in all previous cases, a negligible segregation occurred for any particle size in the y axis.

In the z plane, the percentage populations were similar for all three particle diameters to those in ***Case 2***, which is logical as these two PSD sets were the most similar between all cases. In both ***Case 2*** and ***Case 5***, the majority of fine particles (approximately half) accumulated in the bottom third of the z axis for each deposition approach, and the presence of fines diminished at increasing bed heights. In the case of the 30 µm particles the percentage population was similar for both deposition approaches, with approximately half as many 30 µm particles in the bottom segment as in the top and middle segments of the bed. The deposition method did not appear to dramatically influence the population of the coarsest particles in the z axis. In both techniques, the middle segment had the highest concentration of these particles and the lowest population was in the top one-third of the powder bed.

Case 3 showed the most dramatic segregation in the x and z planes with respect to the range in populations, and thus has been charted in ***Figure 93*** and ***Figure 94*** respectively. A bar chart of segregation for ***Cases 2***, ***4***, and ***5*** is provided in ***Appendix R***.

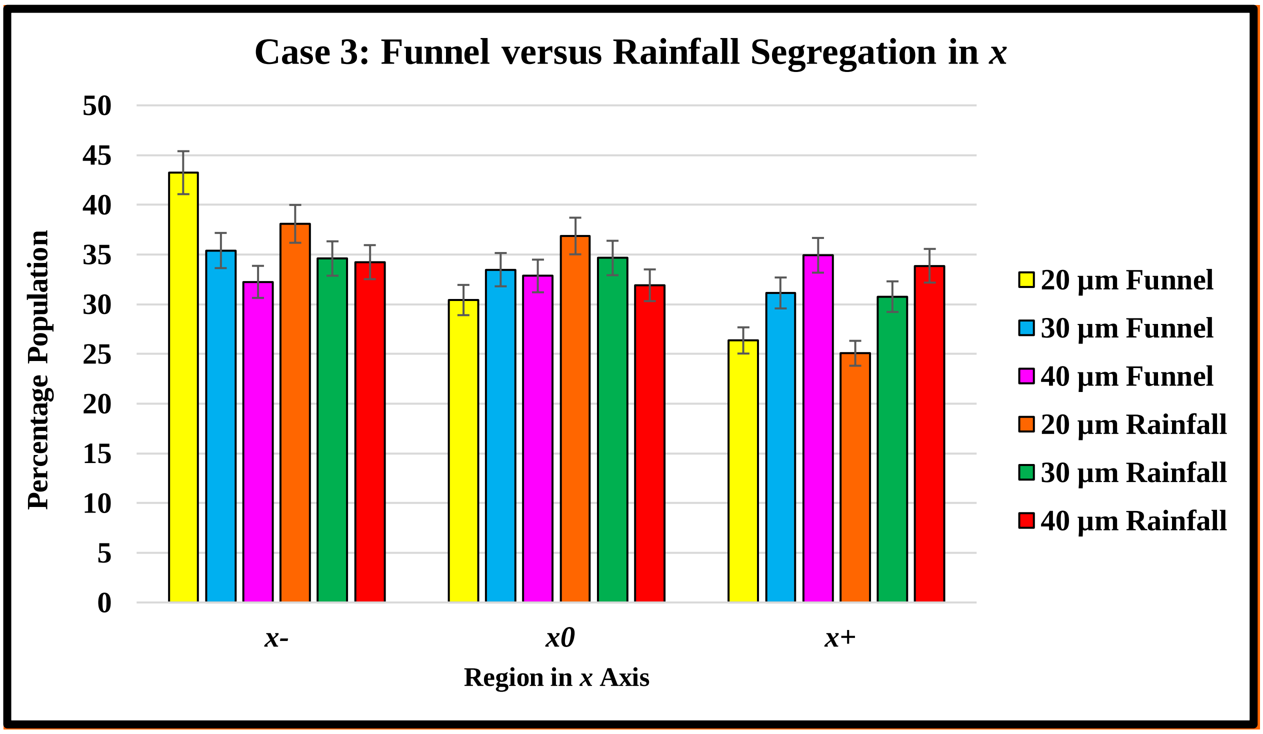

Figure 93 - Funnel versus Rainfall Segregation in the *x* Plane of Case 3.

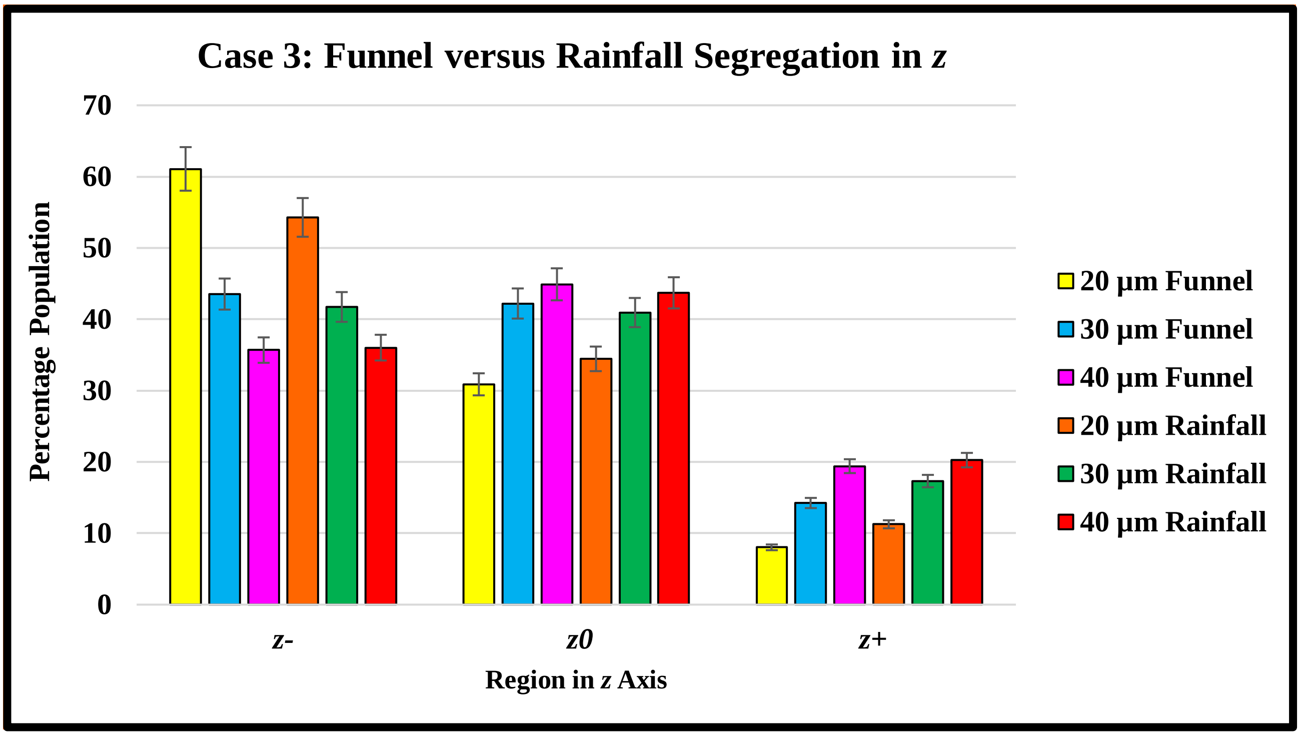

Figure 94 - Funnel versus Rainfall Segregation in the *z* Plane of Case 3.

Differences in Percentage Particle Populations for Travelling Funnel and Rainfall Deposition Methods.

The differences in percentage population between the funnel and rainfall powder supplies is depicted in ***Table 44*** to ***Table 47***. The values have been established by subtracting the rainfall percentage population from the funnel percentage population. Thus, a positive value suggests a greater percentage population for that particle size in the funnel method, and a negative recording suggests a higher percentage population for the corresponding particle diameter in the rainfall technique.

Table 44 - The Differences in Percentage Particle Populations for each Particle Size in Case 2.

Region		Case 2		
		20 µm	**30 µm**	**40 µm**
x	**-**	2.690	-0.700	-3.166
	0	-2.982	0.545	1.934
	+	-0.708	0.155	1.232
y	**-**	0.047	-0.338	-0.538
	0	0.059	0.590	-0.081
	+	-0.106	-0.251	0.620
z	**-**	3.490	0.403	-0.310
	0	-0.560	1.604	0.883
	+	-2.930	-2.007	-0.573

Table 44 suggests that the deposition technique had the most pronounced segregation effect on the 20 µm particles in the z plane at the lowest one-third of the powder bed depth. The largest particles were slightly more likely to populate the initial spreading region in x when delivered by the moving funnel, with slightly over 3% more of the particle population compared to rainfall method. This provides further evidence to suggest that the funnel deposition incurred a slightly more pronounced segregation effect than the rainfall technique. The minimal difference for any particle size in the y plane reinforces the finding that negligible segregation occurs in this axis.

Table 45 - The Differences in Percentage Particle Populations for each Particle Size in Case 3.

Region		Case 3		
		20 μm	**30 μm**	**40 μm**
x	**-**	5.147	0.803	-1.985
	0	-6.440	-1.174	0.934
	+	1.292	0.371	1.050
y	**-**	0.096	-0.154	-0.108
	0	0.179	-0.127	0.087
	+	-0.275	0.280	0.021
z	**-**	6.800	1.806	-0.348
	0	-3.570	1.269	1.193
	+	-3.230	-3.075	-0.845

Case 3 generally showed the most pronounced segregation for the moving funnel technique. Slightly over 5% more of the 20 μm particle population were likely to situate in the initial spreading region in the x plane compared to the rainfall method. This is consistent with, albeit more pronounced, the ***Case 2*** data set. This underpins the hypothesis that the funnel deposition engenders the migration of smaller particles to the lower layers of the heap in front of the spreader. Thus, allowing them to pass through the powder layers under gravity and form higher concentration of fines at lower bed depths. This is further evidenced by the fact that the finest elements saw a near 7% increase in their percentage population in the lowest one-third of the powder bed for the funnel deposition, compared to their rainfall counterparts. Negligible deviations are noted in the average particle positions in y, confirming that negligible segregation occurs in this plane.

Table 46 - The Differences in Percentage Particle Populations for each Particle Size in Case 4.

Region		Case 4		
		20 µm	**30 µm**	**40 µm**
x	**-**	1.849	-1.778	-1.828
	0	-0.741	1.136	2.020
	+	-1.108	0.642	-0.192
y	**-**	-0.744	-0.132	0.263
	0	0.455	-0.318	-0.540
	+	0.290	0.450	0.277
z	**-**	1.980	0.859	-0.430
	0	0.741	0.794	0.667
	+	-2.721	-1.653	-0.238

The largest discrepancy in the ***Case 4*** average particle positions was observed in the finest particles situated in the top one-third of the powder bed height, with an almost 3% increase in the percentage population in this segment for the rainfall method. This slightly reduced the segregation effect, lowering the range of particle population values and making the powder bed slightly more homogenous. Once more, this conforms to the ongoing theory that the particle bed is slightly more segregated in the funnel technique. As found previously, there was little difference across the y plane and thus a negligible segregation.

Table 47 - The Differences in Percentage Particle Populations for each Particle Size in Case 5.

Region		Case 5		
		20 µm	**30 µm**	**40 µm**
x	**-**	1.958	-2.969	-4.767
	0	-2.575	1.814	2.067
	+	0.617	1.155	2.700
y	**-**	-0.399	-0.007	-0.494
	0	0.014	-0.355	0.808
	+	0.385	0.363	-0.314
z	**-**	4.341	0.159	0.273
	0	-0.784	1.791	0.357
	+	-3.557	-1.951	-0.630

A small discrepancy was observed in ***Case 5*** for the average particle populations of the coarsest elements in x_{-}, and the finest particles in the top and bottom one-thirds of the powder bed depth. A similar trend emerged for ***Case 2***, which follows as these two cases had the most similarly weighted PSD sets. Once more, the coarsest particle population was smallest in the initial region of the spreading regime in the x plane when delivered by a funnel.

The smallest presence of coarse particles in x_{-} for all polydisperse cases gives credence to the hypothesis that the funnel technique appears to, with varying degrees of severity depending on the PSD, increase segregation by increasing the range of the particle populations in the x plane. As in all previous cases, a negligible segregation in y was confirmed by a minimal difference in particle population regardless of deposition methods.

Finally, a disparity was recorded in the top and bottom layers of the z plane between the deposition methods for the finest particle sizes. Again, a wider range of the population percentages and thus a more severe segregation effect was engendered by the funnel deposition. A less significant difference was noted for the 30 µm particles in this axis and a minimal difference between deposition techniques for the coarsest particles was observed.

Segregation by Average Particle Position for Travelling Funnel and Rainfall Deposition Methods.

Another technique used to measure the powder layer segregation was to find the average position of each particle size in the bed structure. To achieve this, the x, y, and z coordinate of all particles of a given diameter was imported to a spreadsheet from OVITO®. The particles were then organised by their position in each axis and the average position was taken from the complete data set to identify the most populated location. The average particle positions were then taken for each deposition technique and the disparity between each size evaluated to ascertain whether one approach engendered a more pronounced segregation effect than the other.

Using this technique, a numerical value could be established to indicate the proclivity of particles to accumulate in a given bed segment relative to the dimensions of the simulation domain. Selected coordinates in the powder bed have been specified in ***Figure 95*** for reference.

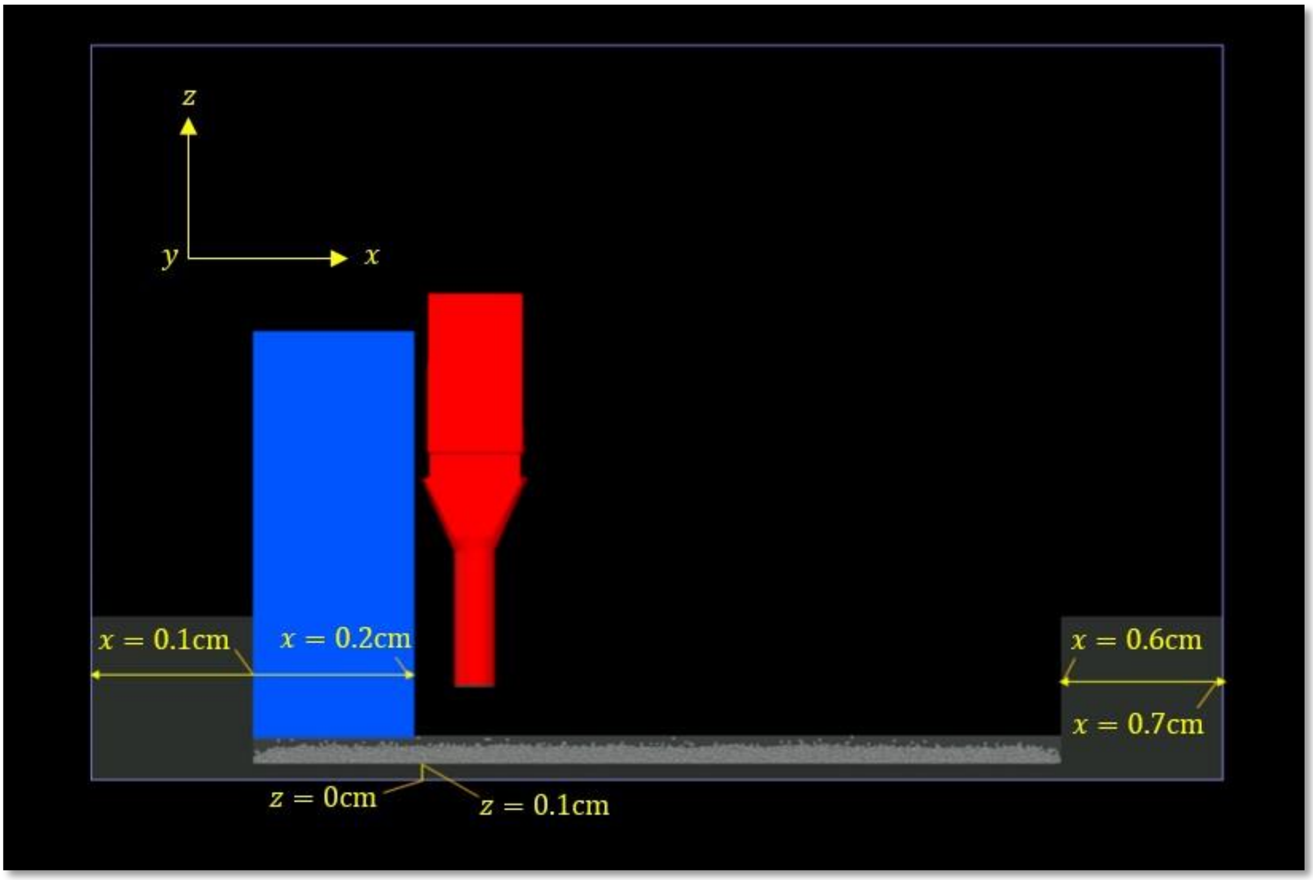

Figure 95 - Selected Powder Bed Coordinates in the *x* and *z* planes for Average Particle Position Segregation Analysis.

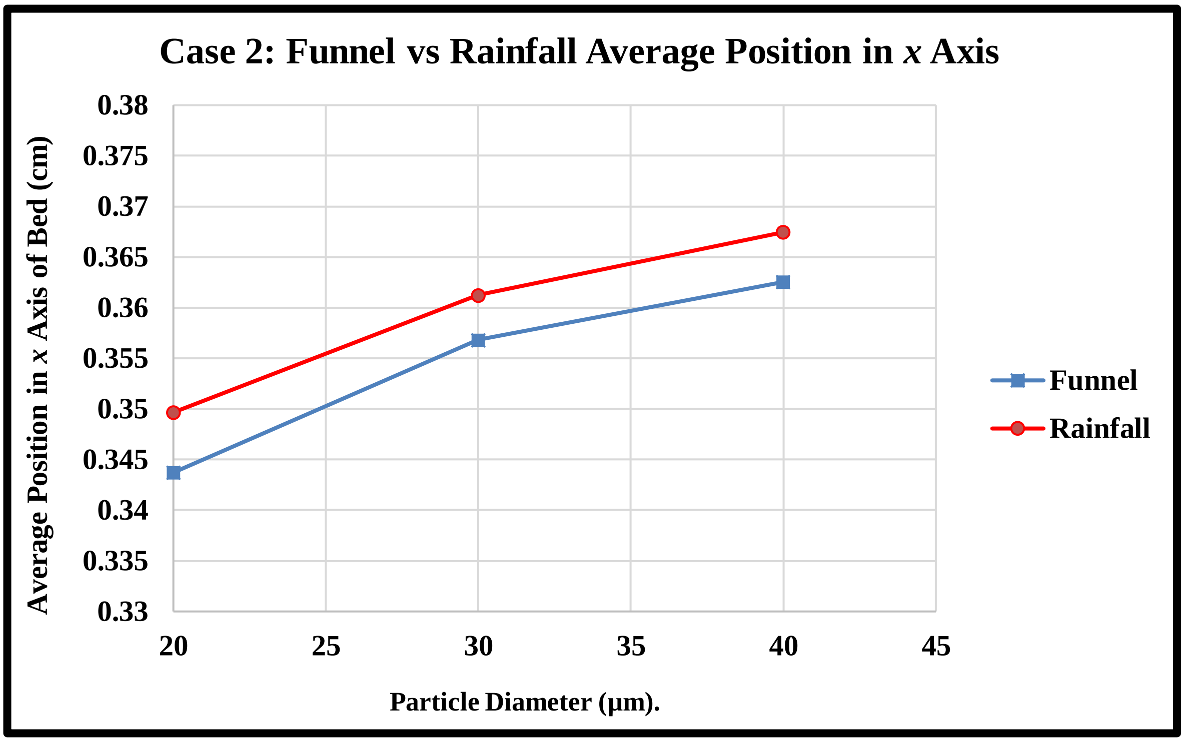

Figure 96 - Average Particle Positions in the *x* axis of Case 2 for the Influence of Deposition Mechanism Analysis.

As no segregation has been found for any powder size in the y axis, the average position of each particle size has been neglected for that plane. ***Figure 96*** shows the average particle positions in ***Case 2***.

The average particle positions in ***Case 2*** agree with the findings of the percentage population analysis, and suggest that coarser particles were pushed along in the recoating direction and accumulated further down the bed compared to the finer particles. The average position of the finest particles were about 188 µm nearer the recoater origin point (at the start of spreading) compared to the coarsest elements in the x axis (refer to ***Figure 95*** for coordinates).

For all particle sizes, the average position was slightly further down the substrate for the rainfall insertion compared to its funnel deposited counterpart.

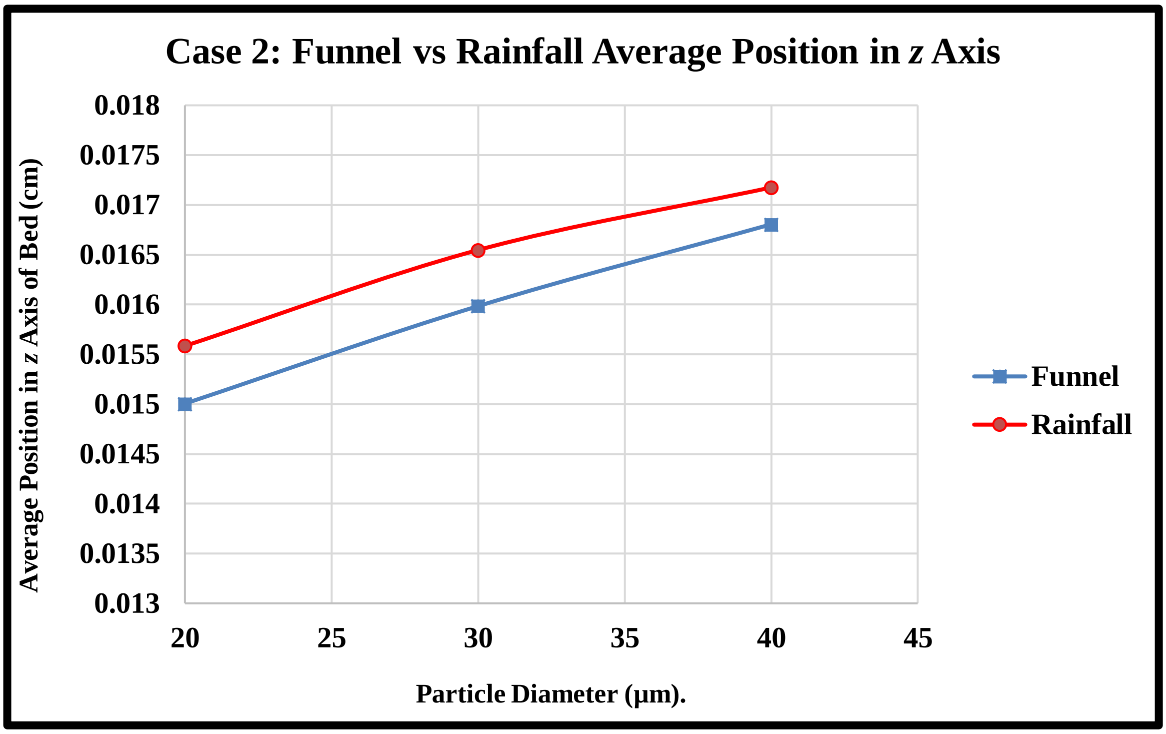

Figure 97 - Average Particle Positions in the *z* axis of Case 2 for the Influence of Deposition Mechanism Analysis.

Analysis of the average particle positions in the powder bed depth for ***Case 2*** also corroborated the findings of percentage population testing, in that finer particles generally situated at lower regions of the spread layer for both deposition techniques. Thus, implying the finer particles settled more readily, as the average position of the 20 µm particles in *z* was about 18 µm deeper in the powder bed than the average position of the 40 µm particles when delivered by a moving funnel. The average positions of each particles size were slightly higher in the bed for the rainfall method compared to the funnel.

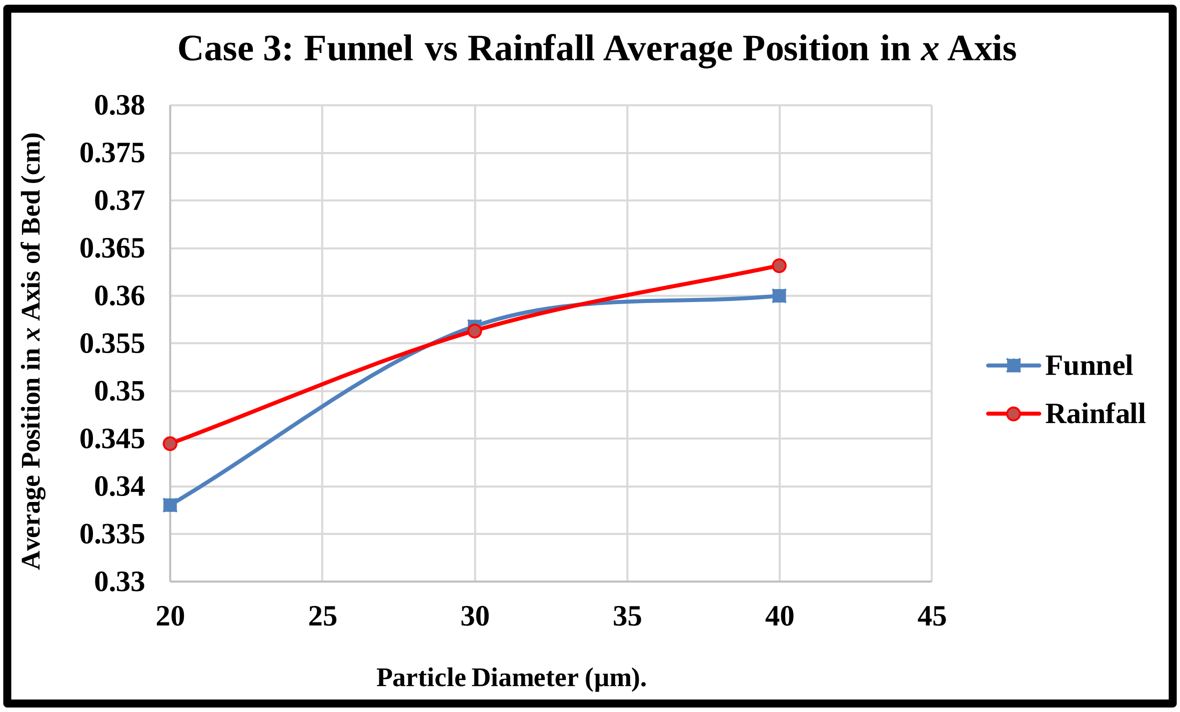

Figure 98 - Average Particle Positions in the *x* axis of Case 3 for the Influence of Deposition Mechanism Analysis.

Case 3 shows that in both deposition cases the average particle position increased with the particle size along the x plane. This relationship was more linear for the rainfall technique. Analysis of the powder bed created with the moving funnel deposition suggested a plateau in the distance between average particle positions at coarser particle sizes. Once more, fine particles showed a greater proclivity to settle earlier on in the spreading regime, with the average position of the 20 µm elements around 220 µm nearer the recoater original point than that of the coarsest particles in the spread layer.

Interestingly, the average positions were similar for the 30 µm particles in both techniques. This underpins the hypothesis that the segregation effect could be feasibly reduced, if the majority of particles approximated the mid-range of the size of SS316l used in PBF processes.

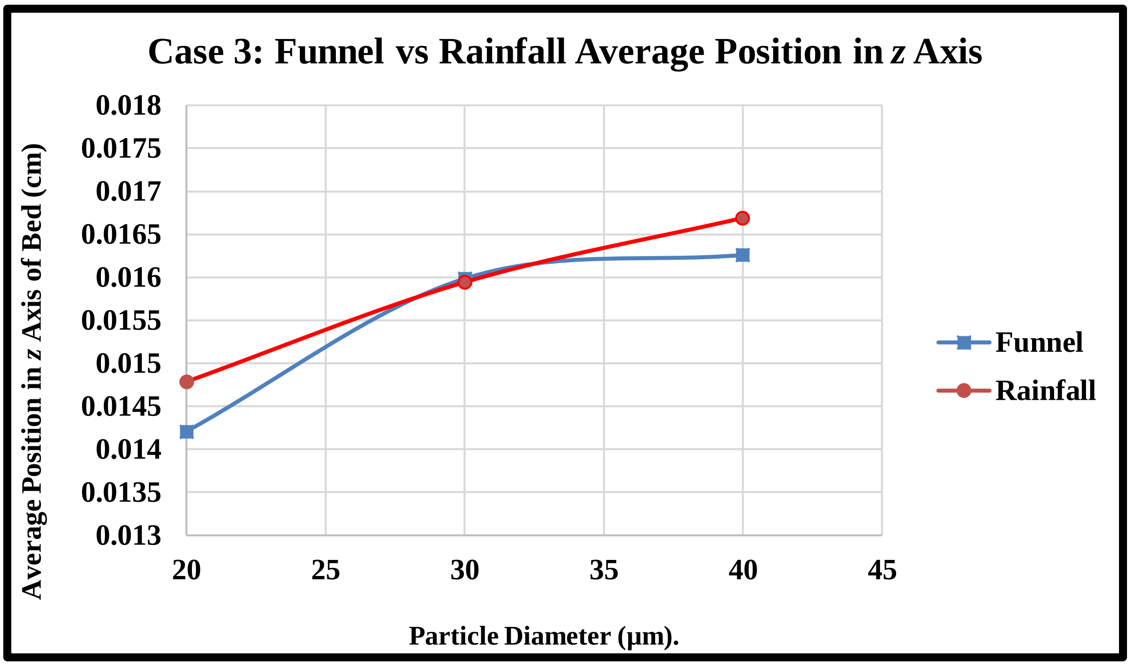

Figure 99 - Average Particle Positions in the *z* axis of Case 3 for the Influence of Deposition Mechanism Analysis.

Figure 99 shows the average positions for funnel delivered particles were generally lower in the bed depth compared to the rainfall technique in ***Case 3***. Hence, as in the percentage population analysis, finer particles tended to accumulate in lower layers. As in the analysis of the x plane, a similar average position was observed for the 30 µm particles irrespective of the delivery method, suggesting the segregation effect may be mitigated for both the length and depth of the spread layer if a majority of particles approximating the median size are used. Using the rainfall method as the example data set, the average position of the finest elements was about 8 µm deeper than the median sized particles and about 19 µm deeper than the coarsest particles.

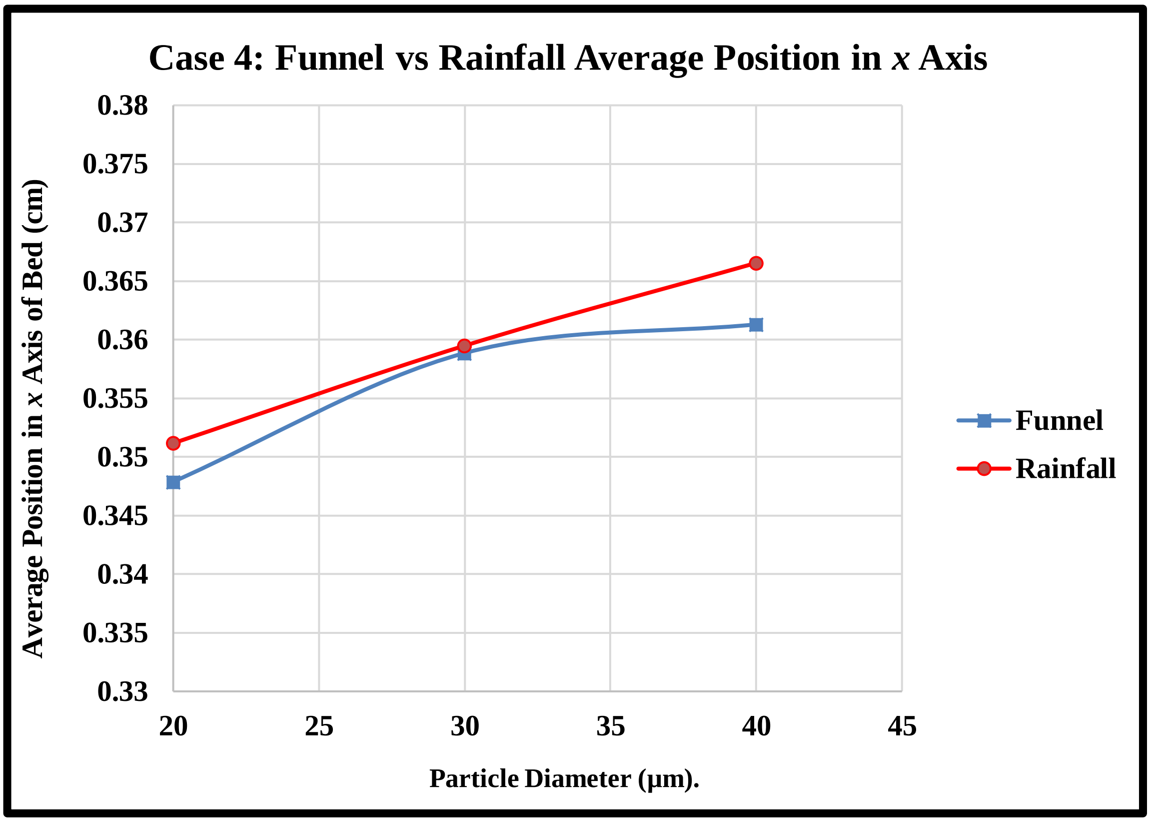

Figure 100 - Average Particle Positions in the *x* axis of Case 4 for the Influence of Deposition Mechanism Analysis.

Analysis of the average particle positions in the x plane of ***Case 4*** indicates that the same plateauing of coarser particle sizes may have occurred as in ***Case 3***, when the powder was supplied by the moving funnel. The data also suggests a more linear relationship existed between the particle diameters and their average positions in the rainfall method, as in the previous cases. The average particle position of all sizes was slightly earlier in the spreading process (nearer the recoater origin point) when powder was supplied by the travelling funnel technique, and once more this effect is consistent across the cases so far. As seen previously in ***Case 3***, the average positions were very similar for the 30 µm elements in x. The average position of the finest particles in x was about 60 µm nearer the origin of the spreading process than the median sized particles and about 144 µm nearer than the coarsest elements, when the powder was inserted by a rainfall technique.

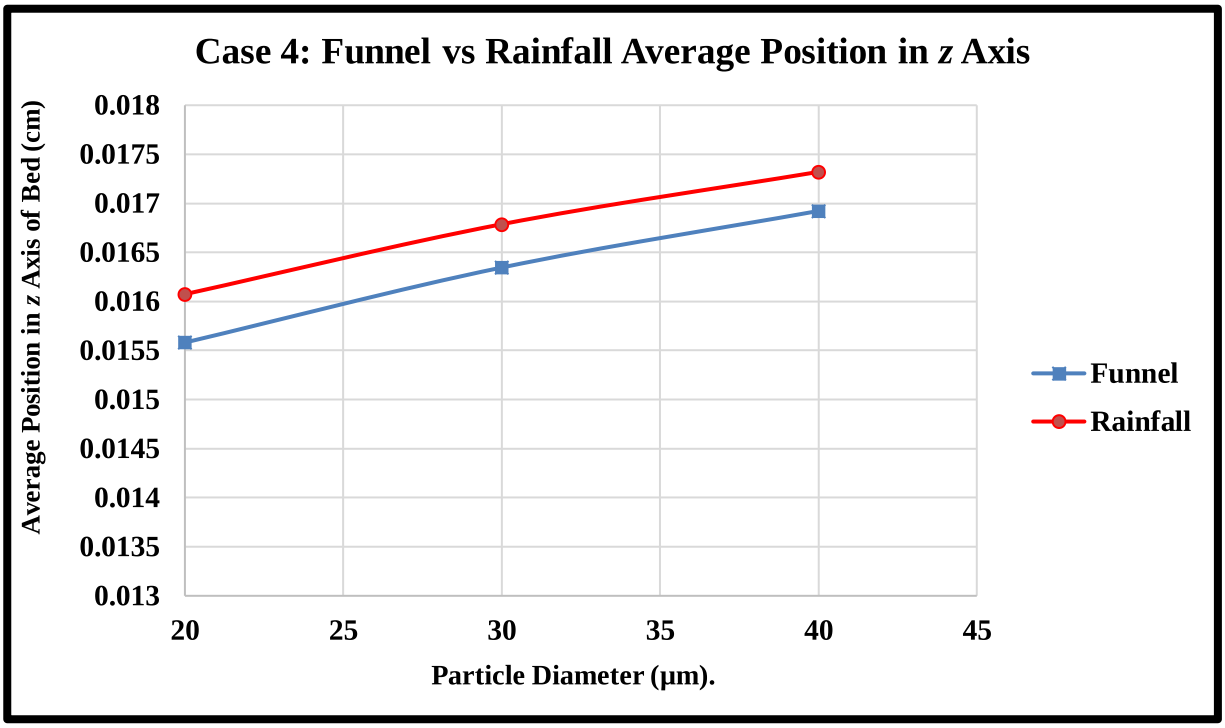

Figure 101 - Average Particle Positions in the *z* axis of Case 4 for the Influence of Deposition Mechanism Analysis.

The average position analysis of the *z* axis in ***Case 4*** shows that all particle sizes were generally situated slightly lower in the bed depth when deposited by a funnel, compared to their same sized counterparts in the rainfall method. As also observed in the percentage population analysis, coarser particles had a general predilection to situate at higher positions in the spread layer. The average position of the 20 µm particles was about 13 µm deeper in the powder bed than the 40 µm particles using the rainfall method. A greater discrepancy in the average particle position of the 30 µm elements was observed in this PSD set compared to the previous data for the *z* axis of ***Case 3***, and was more similar to the data set observed for the same plane in ***Case 2***.

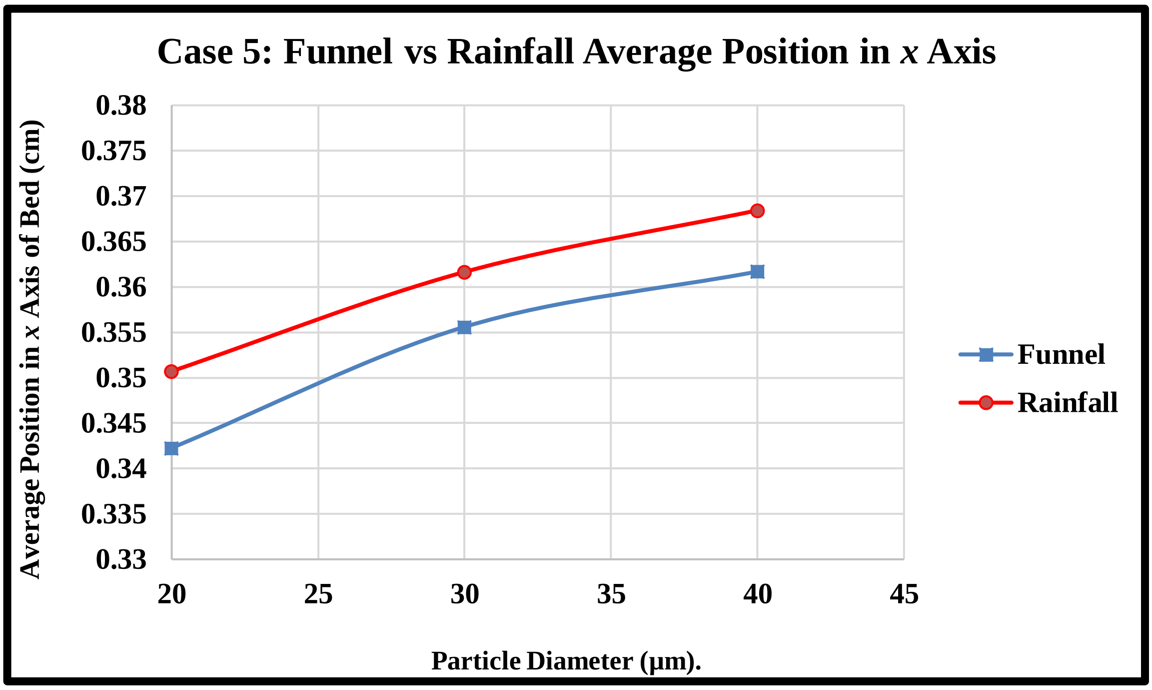

Figure 102 - Average Particle Positions in the *x* axis of Case 5 for the Influence of Deposition Mechanism Analysis.

Average particle locations in the x plane of ***Case 5*** maintained the consistent observation that the average particle positions for all particle sizes were located further down the spreading regime when inserted by a rainfall approach, compared to the funnel deposition. The results generated were broadly similar to those observed in ***Case 2***, which is logical as these two data sets have the most similarly weighted PSD. For all particle sizes, an almost linear relationship exists between the diameter of the particles and their position in x. In the moving funnel method, the average position of the coarsest particles was around 195 µm later in the spreading direction (nearer the end of the recoater travel) than the finest elements. This was more than twice the gap between the average positions of the finest elements and the median sized particles (a distance of 61 µm), implying in this case the increase in particle size engendered a more pronounced segregation effect.

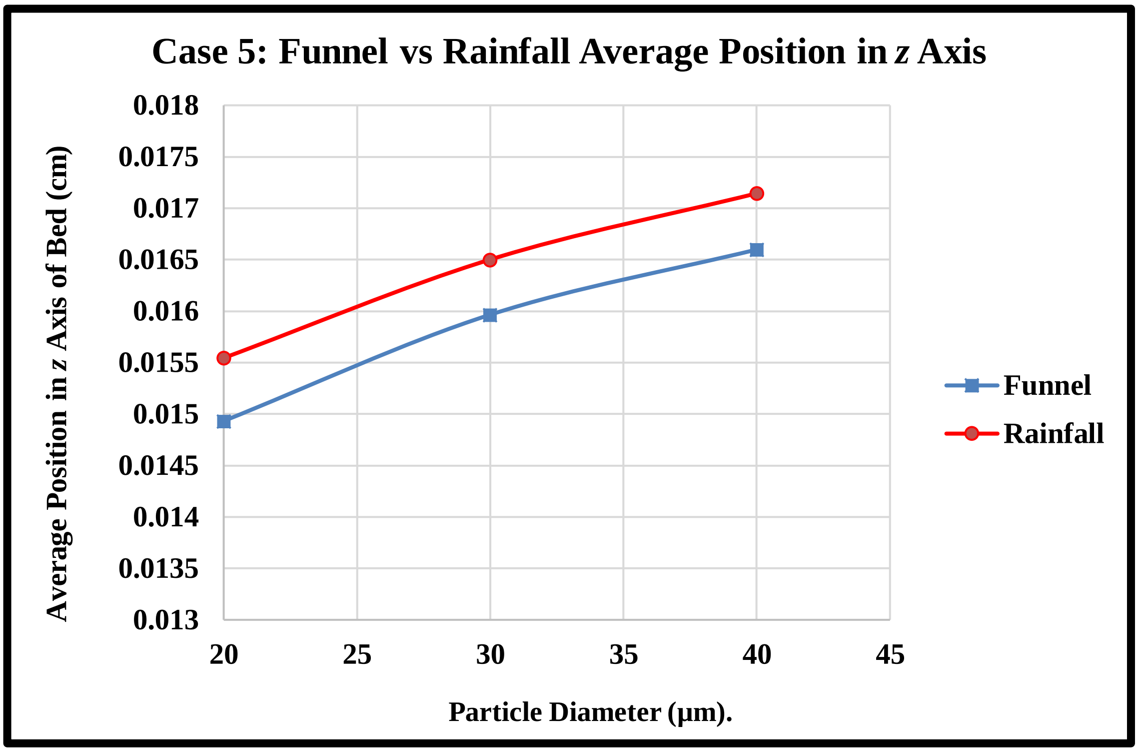

Figure 103 - Average Particle Positions in the *z* axis of Case 5 for the Influence of Deposition Mechanism Analysis.

Case 5 confirms that all of the funnel deposited particles had a lower average position in the powder bed depth across almost all cases. The exceptions were in both the x and z planes of ***Case 3*** where the 30 µm particles had almost the same average position. The average location of particles in the z axis of ***Case 5*** was broadly consistent with ***Cases 2*** and ***4***, which are all slightly higher in the powder bed depth than in ***Case 3***. The average position of all particles in the z axis of ***Case 5*** was almost identical to the average positions in ***Case 2***. As stated previously, this can likely be attributed to these powder sets having the most similar PSD across all cases.

The finest particles in the rainfall method for this powder set had an average position approximately 6 µm deeper in the powder bed than the median sized particles, and about 16 µm deeper than the coarsest elements. This confirms that throughout the average position analysis the difference in the average locations of the finest and coarsest elements was generally considerably more pronounced for the spreading of the powder in the x direction (ranging from 144 µm - 220 µm) compared to the z direction (ranging from 13 µm - 19 µm).

7.3.4 Segregation in the Heap in Front of the Spreader

To understand how the funnel deposition segregated the powder, an isolated analysis of both the heap formed prior to spreading and the layer formed by dispersing this heap was required. To perform this analysis, the funnel-delivered layer was isolated in OVITO® by neglecting all particles from the preliminary layer occupying the bed, and errant particles that fell outside of the formed heap were excluded as not to dramatically skew the average segregation for each particle size.

As the insertion volume and seed numbers of the preliminary layer was uniform across all cases, it could be assumed that all of the particle centroids were in the same position. Thus, the height of the powder underneath the delivered heap was constant across all measurements. As the preliminary layer was constrained by the walls of the substrate, the minimum and maximum values of the particle centroids in the y plane is also uniform across each model, and taken at the position of the wall plus the value of the smallest particle radius. Similarly, the minimum value at x_h was governed by the origin point of the recoater which contacted the heap. The preliminary visual inspection has showed that the heap formed was slightly shorter in the x axis when delivered by the rainfall method.

Based on the system dimensions and the recoater and walls constraining the heap dispersion, the only variable heap coordinates were in x_{h+}, the maximum point of the heap in the recoating direction, and z_{h+}, the highest particle centroid position in the heap. To ensure an accurate measurement of the heap was made, the values of x_{h+} and z_{h+} were inspected for each model and adjusted as required. Only very minor variations were detected at these points across each case set, suggesting that funnel characteristics including the shape of the nozzle and deposition speed had a more pronounced effect on the formed heap than the PSD of the inserted powder. As in all previous segregation analysis, the powder was allowed to settle under gravity and the segregation in the heap was then measured by the percentage particle population in three segments as outlined by ***Table 48***.

Table 48 - Segment Labelling and Location of the Analysed Segments in the Heap Formed by both Deposition Methods.

Segment	Location
x_h	The axis in length of the heap in line with the recoater trajectory.
x_{h-}	The first one-third in the length of the heap.
x_{h0}	The middle segment of the heap.
x_{h+}	The final one-third segment of the heap at the “far” end of the bed.
y_h	The plane measured as the width of the heap in line with the funnel trajectory.
y_{h-}	The first 1/3rd of the heap width nearest to the funnel starting point (early pouring).
y_{h0}	The middle segment of the heap width between the start and end of the funnel trajectory (mid pouring).
y_{h+}	The far end of the heap width relative to the funnel trajectory (late pouring).
z_h	The axis representing the depth and therefore vertical measurements of the heap.
z_{h-}	The bottom 50 µm in the depth of the heap.
z_{h0}	The 50 µm segment in the vertical middle of the heap.
z_{h+}	The top 50 µm of the heap.

As in the previous segregation analysis, the percentage particle population measured the concentration of each particle size in each one-third segment of the axis evaluated in both deposition methods. For example, the sum of the values found for the finest particles in x_{h-}, x_{0-}, and x_{h+} equates to 100% of the 20 µm particle in that plane, and segregation was determined by the population of fines in a given segment. Thus, a percentage population of 33.3% in each segment of the measured axis would suggest an even distribution of that powder size and negligible segregation.

Case 2

Table 49 - Segregation Results for the Heap Formed by the Travelling Funnel and Rainfall Deposition Methods in Case 2.

Case 2 (33% of 20 µm, 33% of 30 µm, 33% of 40 µm)							
Region		Average Funnel Segregation			Average Rainfall Segregation		
		20 µm	30 µm	40 µm	20 µm	30 µm	40 µm
x_h	-	43.133	41.826	39.812	46.408	45.863	44.549
	0	42.059	39.935	40.654	34.732	32.654	32.392
	+	14.807	18.239	19.534	18.860	21.483	23.059
y_h	-	26.573	26.625	26.780	32.708	33.495	32.690
	0	34.949	37.559	36.849	34.998	35.046	35.338
	+	38.477	35.816	36.371	32.294	31.459	31.972
z_h	-	62.048	51.364	49.993	55.808	53.684	53.537
	0	33.844	38.735	38.770	34.806	35.231	34.100
	+	4.108	9.902	11.238	9.386	11.084	12.363

The segregation in the x plane of the heap in ***Case 2*** showed that the smallest percentage population of all particle sizes generally accumulated further away from the recoater in x_{h+}. A visual inspection of the heap corroborated this finding, as the powder sloped away into the rest of the bed in this region. A higher range was observed in the finest particle sets for both deposition methods than for the other two sizes, indicating a more pronounced segregation of fines.

In the y axis, the funnel deposition engendered a more pronounced segregation in the heap, with the smallest population percentage of all sizes present in the early phase of pouring. Minimal segregation was observed in the y plane of the heap when powder was inserted via rainfall.

The most notable segregation was in the z axis. Only slightly over 4% of the finest particles accumulated in the z_{h+} segment of the heap. The majority of fines situated in the lower regions of the bed depth for both deposition methods. As proposed previously in the analysis of the full powder bed, this may have been due to the effect of the lack of a successive layer of powder above this point. A similar segregation was observed for all particle sizes in each deposition technique, so far as the percentage particle population increased at lower bed depths.

A bar chart showing the segregation in each axis of the heap formed by both deposition techniques is shown in ***Figure 104*** to ***Figure 106***.

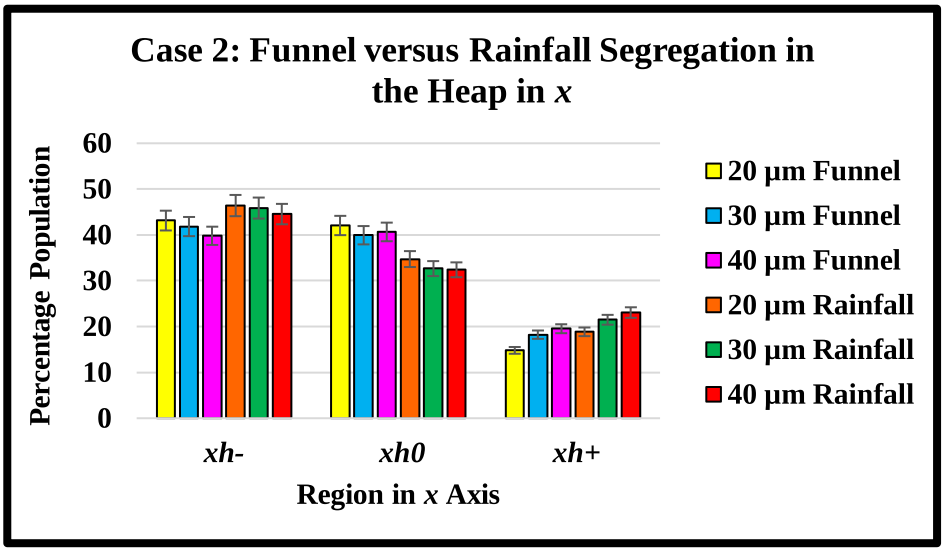

Figure 104 - Funnel versus Rainfall Segregation in the x Plane of the Heap in Case 2.

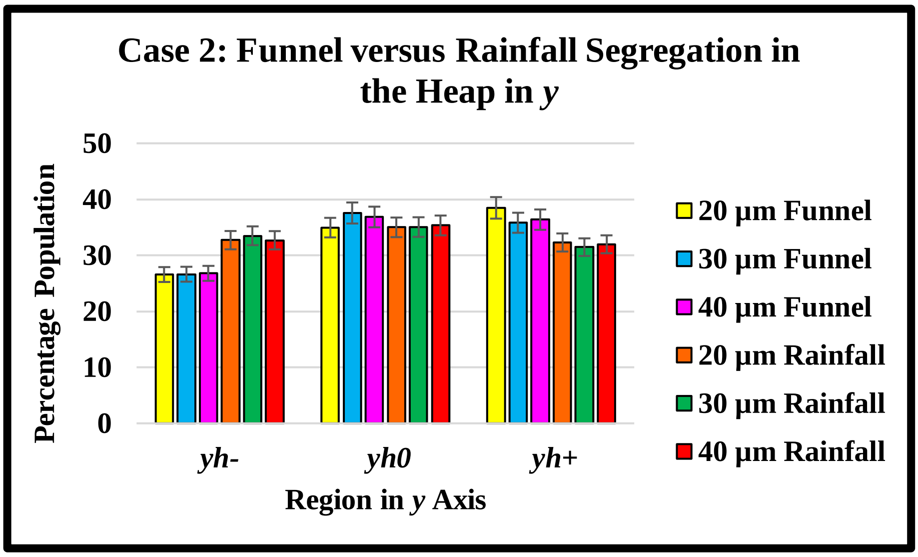

Figure 105 - Funnel versus Rainfall Segregation in the *y* Plane of the Heap in Case 2.

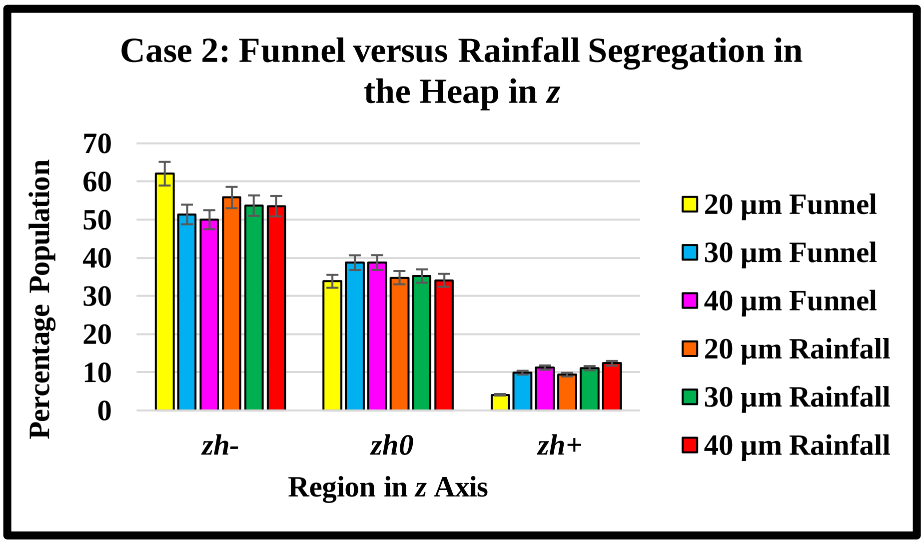

Figure 106 - Funnel versus Rainfall Segregation in the *z* Plane of the Heap in Case 2.

Table 50 shows the difference in percentage particle populations in the segment of the heap formed by both deposition methods. As in ***Subsection 7.3.3***, the difference between each method was found by subtracting the percentage population of a given particle size in a heap segment in the rainfall technique, from the corresponding segment in the heap created by the moving funnel. Thus, a negative value suggests a larger percentage population for that segment occurred in the rainfall approach.

Table 50 - The Differences in Percentage Particle Populations for each Particle Size in the Heap in Case 2.

Region		Case 2		
		20 µm	**30 µm**	**40 µm**
x_h	**-**	-3.275	-4.037	-4.738
	0	7.328	7.281	8.262
	+	-4.053	-3.244	-3.524
y_h	**-**	-6.135	-6.870	-5.911
	0	-0.049	2.513	1.511
	+	6.184	4.357	4.399
z_h	**-**	-3.544	-2.321	-3.544
	0	4.669	3.503	4.669
	+	-1.125	-1.183	-1.125

The results recorded in ***Table 50*** show that the deposition approach had a significantly more pronounced effect on the heap formed than the full powder bed analysed in ***Subsection 7.3.3***. This supports the hypothesis that the spreading operation induced a self-sorting effect and reduced the overall segregation. It would be interesting to observe how this would influence the overall segregation if a larger powder bed was modelled. The most pronounced difference in the population percentages was observed in the x_{h0} segment for the coarsest particles, with more than 8% more of this population deposited in this segment by the funnel.

Case 3

Table 51 - Segregation Results for the Heap Formed by the Travelling Funnel and Rainfall Deposition Methods in Case 3.

Case 3 (15% of 20 µm, 25% of 30 µm, 60% of 40 µm)							
Region		Average Funnel Segregation			Average Rainfall Segregation		
		20 µm	30 µm	40 µm	20 µm	30 µm	40 µm
x_h	-	42.013	40.289	49.993	46.281	44.778	43.789
	0	43.641	40.768	38.770	34.946	34.097	32.416
	+	14.346	18.943	11.238	18.773	21.125	23.795
y_h	-	26.973	27.400	26.209	33.162	32.489	33.485
	0	31.746	35.680	36.860	34.433	35.093	34.527
	+	41.280	36.920	36.932	32.405	32.418	31.988
z_h	-	67.971	56.792	52.959	56.692	53.113	51.904
	0	29.428	36.869	38.633	35.572	36.414	36.576
	+	2.601	6.339	8.408	7.736	10.473	11.521

The ***Case 3*** results show a similar pattern to the ***Case 2*** data, so far as the percentage concentration of all particle sizes was lowest in x_{h+}. The range in the percentage population of the coarsest particles deposited in the length of the heap suggested that the funnel engendered a more pronounced segregation, at 38.76% for the dynamic deposition compared to 19.99% for the rainfall.

As in ***Case 2***, a negligible segregation was found in the rainfall deposition in the y axis, with all particles only marginally more likely to situate at y_{h0}. Interestingly, the percentage population increased with deposition trajectory for all powder sizes in the moving funnel approach, showing that the funnel technique had a pronounced influence on heap segregation.

In the z_h axis, the highest percentage population of fines was found in the lowest regions of the heap, suggesting that either the fine particles migrated to the bottom of the funnel during the filling stage and thus discharged first onto the preliminary powder layer, or that the fines migrated through the heap layers during the deposition and settling of powder prior to spreading. The segregation effect in z_h was slightly less pronounced for the rainfall deposition method, and the results were consistent across powder sizes so far as more than half of the particles accumulated in the lower regions of the bed, slightly over one-third situated in the middle of the bed depth, and the remainder were found in z_{h+} for all powder diameter sets.

Figure 107 to ***Figure 109*** records the data for all particle sizes in each segment for both deposition techniques from the PSD used in ***Case 3***.

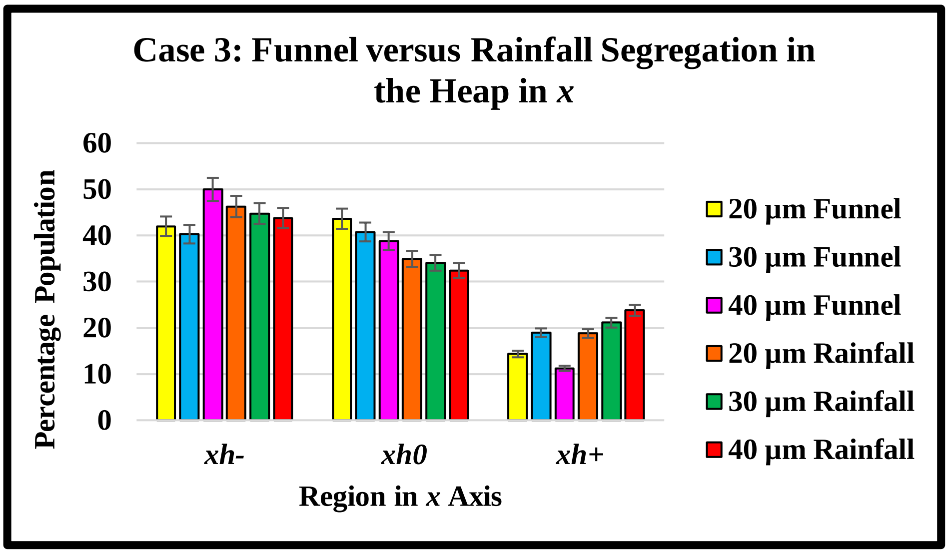

Figure 107 - Funnel versus Rainfall Segregation in the *x* Plane of the Heap in Case 3.

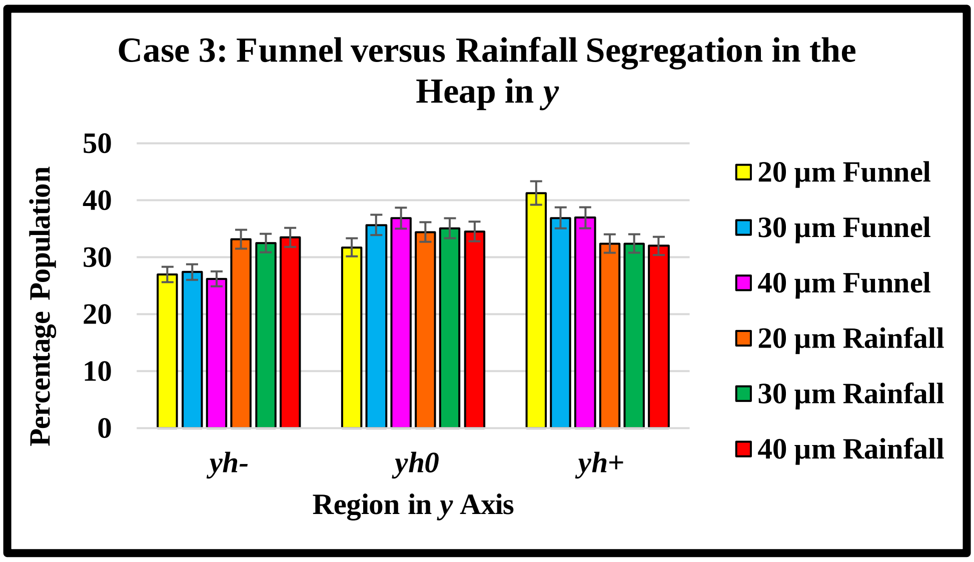

Figure 108 - Funnel versus Rainfall Segregation in the *y* Plane of the Heap in Case 3.

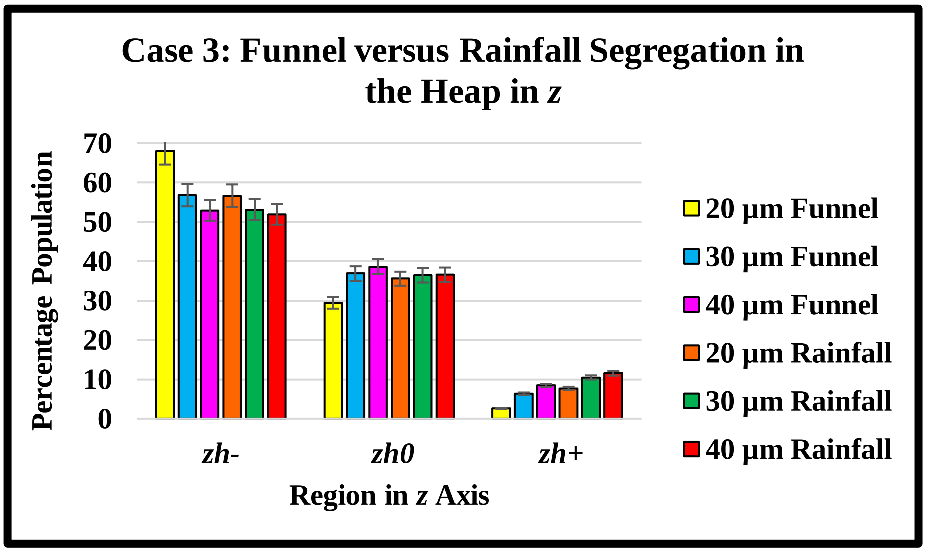

Figure 109 - Funnel versus Rainfall Segregation in the *z* Plane of the Heap in Case 3.

Table 52 shows the difference in percentage particle population for each segment of the heap formed by both deposition methods in ***Case 3***.

Table 52 - The Differences in Percentage Particle Populations for each Particle Size in the Heap in Case 3.

Region		Case 3		
		20 µm	30 µm	40 µm
x_h	-	-4.268	-4.489	6.204
	0	8.695	6.670	6.354
	+	-4.428	-2.181	-12.557
y_h	-	-6.189	-5.089	-7.276
	0	-2.687	0.587	2.333
	+	8.875	4.502	4.944
z_h	-	11.279	3.679	1.056
	0	-6.144	0.455	2.058
	+	-5.136	-4.134	-3.113

The significant disparity between the percentage particle populations in x_{h+} further emphasises the segregation effect caused by the funnel. A similar disparity was found between the concentration of the finest particles in z_{h-}, with just over 11% more of the fines accumulating in this region in the funnel-fed heap. Thus, significantly increasing the range in particle size concentrations to suggest a more pronounced segregation.

Case 4

Table 53 - Segregation Results for the Heap Formed by the Travelling Funnel and Rainfall Deposition Methods in Case 4.

Case 4 (60% of 20 µm, 25% of 30 µm, 15% of 40 µm)							
Region		Average Funnel Segregation			Average Rainfall Segregation		
		20 µm	30 µm	40 µm	20 µm	30 µm	40 µm
x_h	-	38.911	37.996	36.878	46.905	47.425	47.422
	0	38.978	38.839	40.380	34.138	32.457	29.771
	+	22.111	23.166	22.742	18.956	20.118	22.807
y_h	-	26.723	26.598	27.767	33.204	32.828	33.016
	0	36.534	37.838	36.303	33.995	35.517	32.343
	+	36.743	35.564	35.929	31.625	31.654	34.640
z_h	-	54.624	46.003	47.673	59.137	57.915	55.915
	0	36.807	37.682	37.597	32.569	32.521	34.642
	+	8.569	16.316	14.730	8.294	9.564	9.443

A smaller range was observed in the concentration of funnel-delivered fines for each segment in the x plane of this data set when judged against ***Case 2*** and ***Case 3***. As previously, little difference was found between the percentage populations in the x plane for the 30 µm and 40 µm particles, and results were fairly consistent across deposition types so far as the smallest concentration of all particle sizes was located in x_{h+}.

As found in both previous cases, the funnel approach segregated more powder in the y plane compared to the rainfall deposition, with all tested sizes showing a tendency to accumulate in the early pouring regions compared to later in the deposition.

A slightly lower segregation of fines in the heap depth was observed in this PSD set compared to ***Case 2*** and ***Case 3***. Interestingly, the range of particle populations, indicative of a general segregation effect, was lower for all three particle sizes measured in the x_h and z_h planes for the moving funnel approach, but the same was not true for the rainfall method. As found in both previous cases, the percentage population of all particle sizes increased with the powder heap depth.

Once more, the bar charts presented in ***Figure 110*** to ***Figure 112*** record all of the particle size concentrations in each axis for both powder delivery techniques.

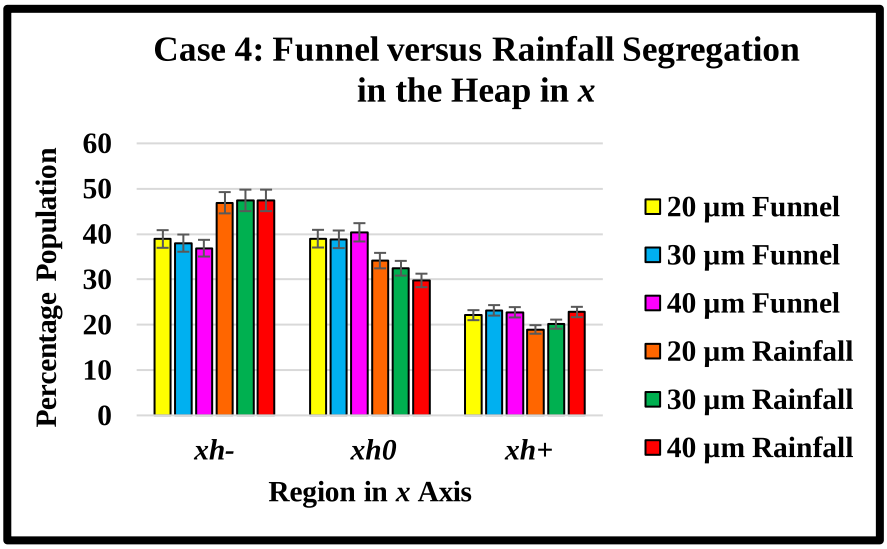

Figure 110 - Funnel versus Rainfall Segregation in the *x* Plane of the Heap in Case 4.

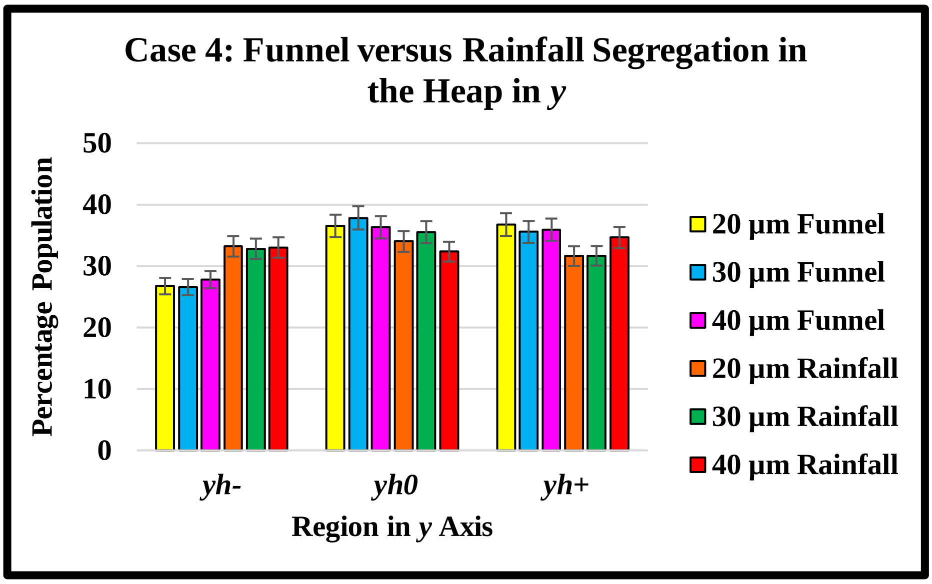

Figure 111 - Funnel versus Rainfall Segregation in the *y* Plane of the Heap in Case 4.

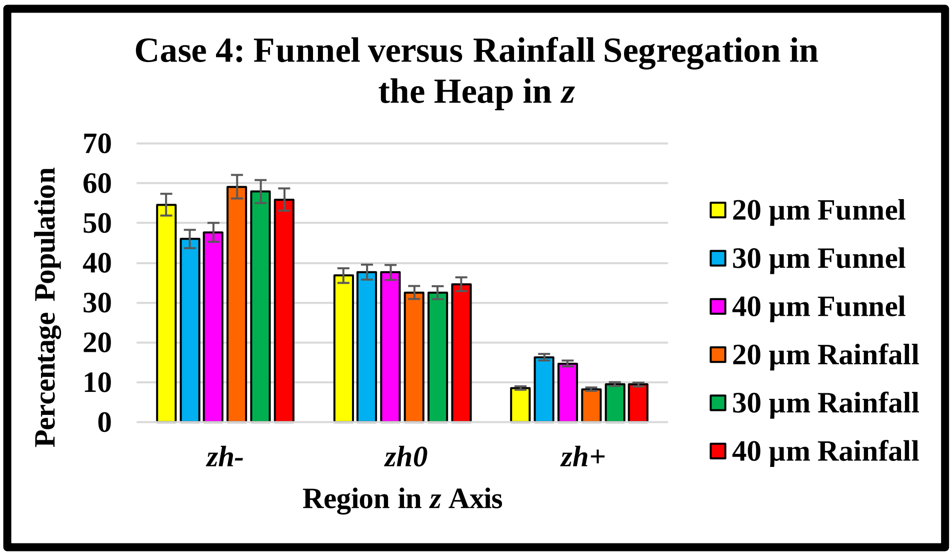

Figure 112 - Funnel versus Rainfall Segregation in the *z* Plane of the Heap in Case 4.

The data in ***Table 54*** records the discrepancy between the funnel and rainfall delivered powder heaps for each segment and deposition method in ***Case 4***.

Table 54 - The Differences in Percentage Particle Populations for each Particle Size in the Heap in Case 4.

Region		Case 4		
		20 µm	30 µm	40 µm
x_h	-	-7.994	-9.429	-10.545
	0	4.839	6.381	10.609
	+	3.155	3.048	-0.064
y_h	-	-6.481	-6.230	-5.249
	0	2.539	2.320	3.960
	+	5.118	3.910	1.289
z_h	-	-4.513	-11.912	-8.242
	0	4.238	5.160	2.954
	+	0.275	6.752	5.287

The data in ***Table 54*** shows that the most significant disparities between the deposition methods were found in segments x_{h-}, x_{h0}, and z_{h-}. Interestingly, almost 12% more of the 30 µm particles were likely to situate in the bottom segment of the heap if delivered by a rainfall method. Another notable data point was shown by the coarsest particles at x_{h-} and x_{h0}, with these particles more likely to occupy the initial region of spreading when delivered by the rainfall method, and more likely to be pushed along to the centre of the bed span if inserted by a moving funnel.

<u>Case 5</u>

Table 55 - Segregation Results for the Heap Formed by the Travelling Funnel and Rainfall Deposition Methods in Case 5.

Case 5 (25% of 20 µm, 50% of 30 µm, 25% of 40 µm)							
Region		Average Funnel Segregation			Average Rainfall Segregation		
		20 µm	30 µm	40 µm	20 µm	30 µm	40 µm
x_h	-	42.212	40.935	41.029	45.603	45.351	45.416
	0	43.088	40.514	40.648	34.584	33.365	30.234
	+	14.700	18.551	18.323	19.813	21.284	24.350
y_h	-	26.696	26.970	26.543	34.077	33.144	33.127
	0	34.711	36.681	36.777	34.316	35.425	33.014
	+	38.593	36.349	36.680	31.606	31.431	33.860
z_h	-	61.122	49.690	48.171	55.721	54.631	53.736
	0	33.513	38.252	37.362	35.741	35.280	34.653
	+	5.365	12.057	14.467	8.538	10.090	11.611

Analysis of the x_h axis in ***Case 5*** conformed to all previous cases so far as the concentration of all particle sizes was lowest at the furthest heap segment from the recoater. A similar percentage concentration was found for the coarsest and median sized particles in each segment of the x axis of the heap when delivered via a moving funnel. In the rainfall created heap, the concentration of each particle size decreased with distance from the recoater face. In both deposition methods, the range in percentage populations was greatest for the finest particles.

As seen in all previous cases, the funnel deposition approach induced a more pronounced segregation in y_h, with all particle sizes showing the lowest population percentage at the early stages of pouring. A negligible segregation occurred in the y_h plane when powder was delivered via rainfall.

A significant segregation was observed for all particle sizes in the depth of the heap. The most pronounced segregation with respect to the range in size concentrations was found for the fines delivered by the moving funnel, with only 5.37% of the fine particle population in this axis situated at the top of the heap in z_{h+}, compared to 61.12% in z_{h-}. As found in all previous cases, the percentage population of all particle sizes increased with heap depth.

The heaps formed by each deposition effect in ***Case 5*** generally showed a segregation effect in line with ***Case 2*** and ***Case 3***, all of which showed a generally higher segregation in the funnel-fed heap than ***Case 4***. Results for ***Case 5*** were similar to those observed in ***Case 2*** which, as in the previous analysis of segregation throughout the whole powder bed, was expected as these two sets had the most similar PSD.

Figure 113 to ***Figure 115*** are bar charts of the funnel versus rainfall segregation for all particle sizes in each axis of the heap formed in ***Case 5***.

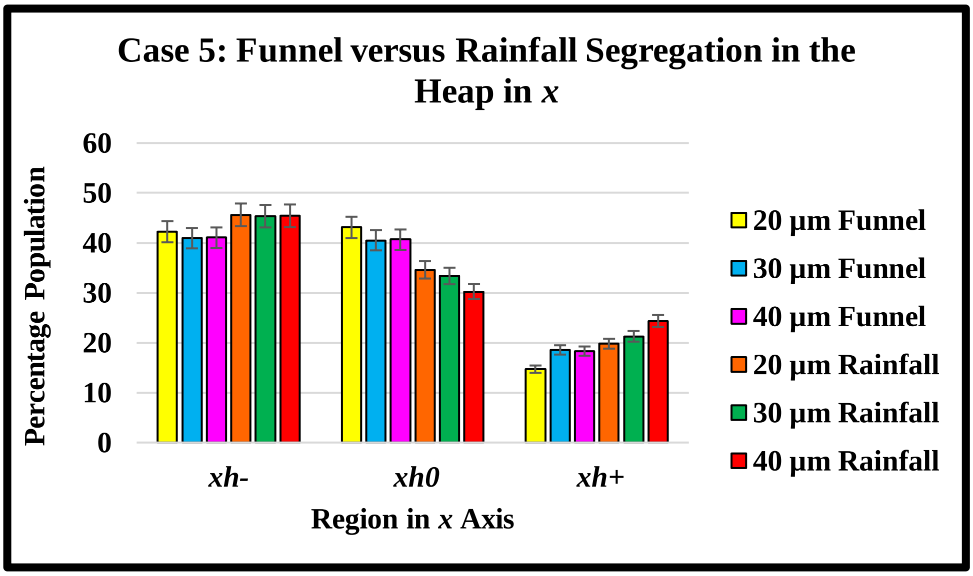

Figure 113 - Funnel versus Rainfall Segregation in the *x* Plane of the Heap in Case 5.

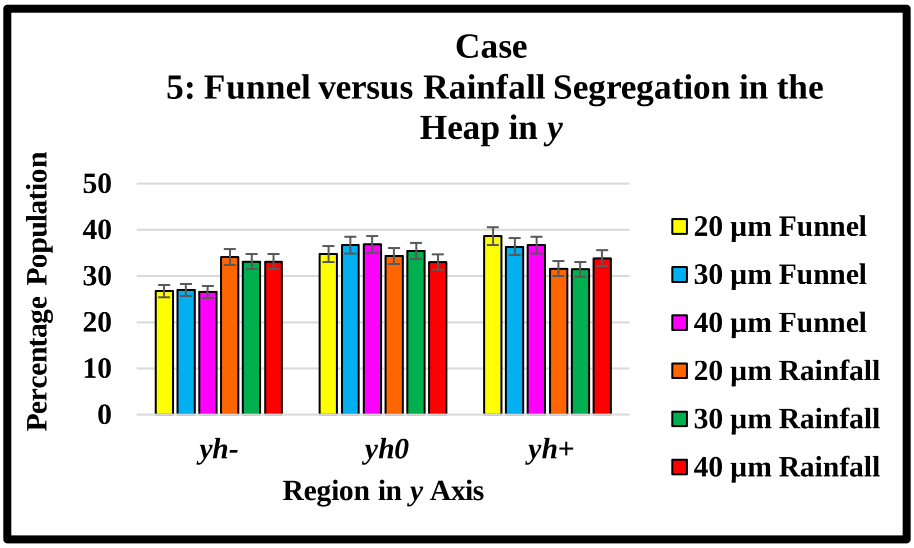

Figure 114 - Funnel versus Rainfall Segregation in the *y* Plane of the Heap in Case 5.

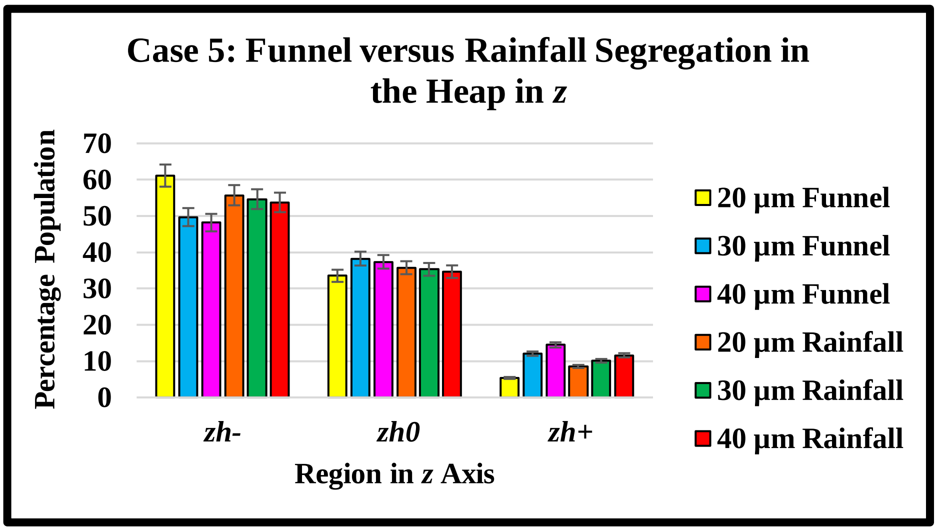

Figure 115 - Funnel versus Rainfall Segregation in the *z* Plane of the Heap in Case 5.

Table 56 - The Differences in Percentage Particle Populations for each Particle Size in the Heap in Case 5.

Region		Case 5		
		20 µm	**30 µm**	**40 µm**
x_h	**-**	-3.391	-4.416	-4.387
	0	8.504	7.149	10.413
	+	-5.113	-2.733	-6.027
y_h	**-**	-7.381	-6.174	-6.584
	0	0.394	1.256	3.764
	+	6.987	4.918	2.820
z_h	**-**	5.401	-4.940	-5.565
	0	-2.228	2.972	2.709
	+	-3.173	1.968	2.856

Table 56 shows that the most significant disparity in the deposition methods occurred between the coarsest particles in x_{h0}, with a 10.4% increase in the population accumulating in this segment when delivered by a funnel compared to the rainfall approach. This segment in the x_h plane generally had the highest difference in percentage particle concentrations between both powder delivery techniques. Significant differences between particle populations were also observed in the bottom segment of the heap depth, and the initial region in the heap width where early pouring from the funnel occurred.

7.3.5 Segregation in the Spread Layer Formed by Dispersing the Heap

The content of this subsection describes the segregation analysis of the layer formed by dispersing the heap analysed in ***Subsection 7.3.4***. To achieve this, the same process was applied to isolate the powder inserted via the moving funnel and the rainfall techniques from the preliminary layer as performed previously, and the segregation was measured at the end of the recoater trajectory when all dispersed particles had settled in the powder bed. The example in ***Figure 116*** shows a top view of the powder bed rendered in OVITO®, with the layer formed by dispersing the heap coloured in white against all other constituent particles of the bed in red.

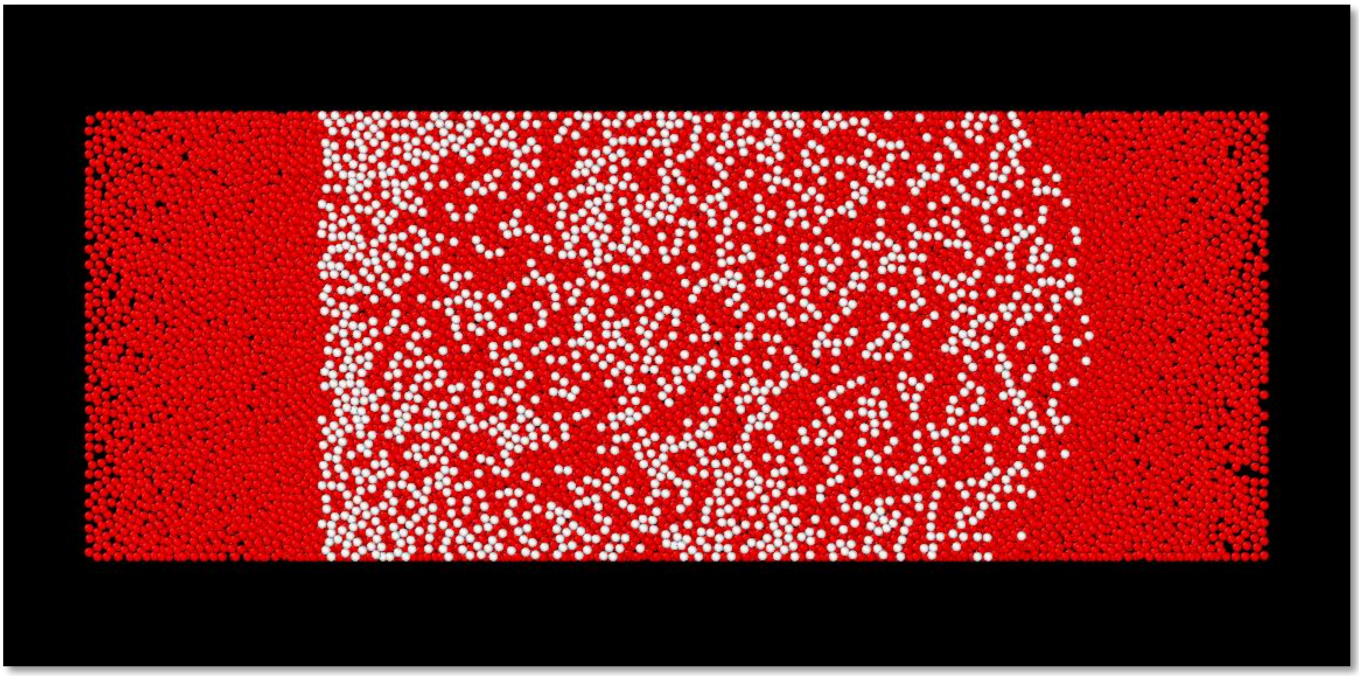

Figure 116 - Example of the Spread Layer Formed by Dispersing the Heap Isolated from the Rest of the Powder Bed (Top View).

As in all previous segregation tests, the analysis measured the percentage particle population across each segment in the powder bed comprising one-third of the evaluated axis. Hence, the concentration of a given particle size demonstrated the segregation effect in the powder delivered by each deposition method, to provide a clearer insight of the effect of each technique on segregation. Note that, as the same segments were used in this analysis as in ***Subsection 7.3.3***, the nomenclature is retained here.

Case 2

Table 57 - Segregation Results for the Spread Layer formed by Dispersing the Heap created by both Deposition Methods in Case 2.

Case 2 (33% of 20 µm, 33% of 30 µm, 33% of 40 µm)								
Region		Average Funnel Segregation			Average Rainfall Segregation			
		20 µm	30 µm	40 µm	20 µm	30 µm	40 µm	
x	-	61.348	45.365	40.277	60.311	58.106	59.948	
	0	28.014	31.974	30.345	23.993	18.644	15.385	
	+	10.638	22.661	29.379	15.696	23.250	24.667	
y	-	32.089	32.200	32.702	31.377	31.493	32.391	
	0	36.641	36.784	34.969	36.323	36.153	36.056	
	+	31.270	31.016	32.329	32.300	32.354	31.553	
z	-	7.928	2.431	1.090	17.802	13.578	12.502	
	0	57.098	50.267	43.666	49.533	45.975	43.916	
	+	34.974	47.303	55.244	32.665	40.447	43.582	

Analysis of the spread layer in ***Case 2*** showed that the finest particles had a proclivity to accumulate in the first one-third of the powder bed span, with almost two-thirds of the particles accumulating at x_{-} and only slightly over 10% being pushed along to the final third. Interestingly, less than 8% of these particles migrated to the bottom depths of the powder bed. For all particle sizes delivered by a funnel in the x plane, the percentage population decreased with spreading distance. The same effect was not observed in the spread layer of the dispersed heap created by the rainfall method. The range of coarse particle population in the x plane was much lower for the travelling funnel deposition at 10.9% compared to 44.6% for the rainfall technique. Similarly, the median sized particles in the funnel deposition showed a lower range of segregation (22.7%) than the rainfall (39.46%).

Only minor segregation was observed in the y plane with a negligible difference between deposition methods. In both deposition techniques, the majority of particles situated in the middle of the powder bed depth except the coarsest particles delivered by the funnel. A significant segregation was observed by these particles, with only around 1% of the 40 µm elements migrating to the bottom one-third of the powder bed. A similar but less dramatically segregated effect was observed in the rainfall technique.

The bar charts in ***Figure 117*** to ***Figure 119*** show the percentage particle population in each axis for both deposition methods.

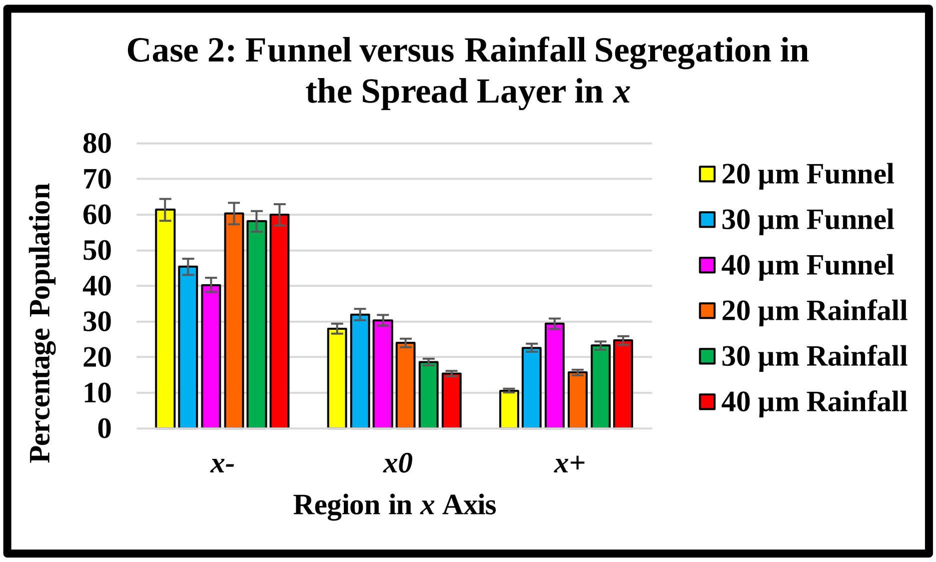

Figure 117 - Funnel versus Rainfall Segregation in the *x* Plane of the Spread Layer in Case 2.

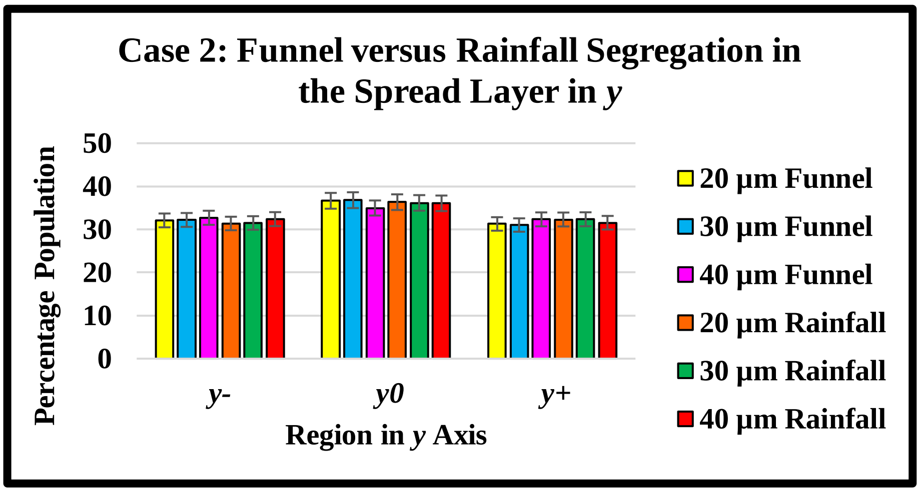

Figure 118 - Funnel versus Rainfall Segregation in the *y* Plane of the Spread Layer in Case 2.

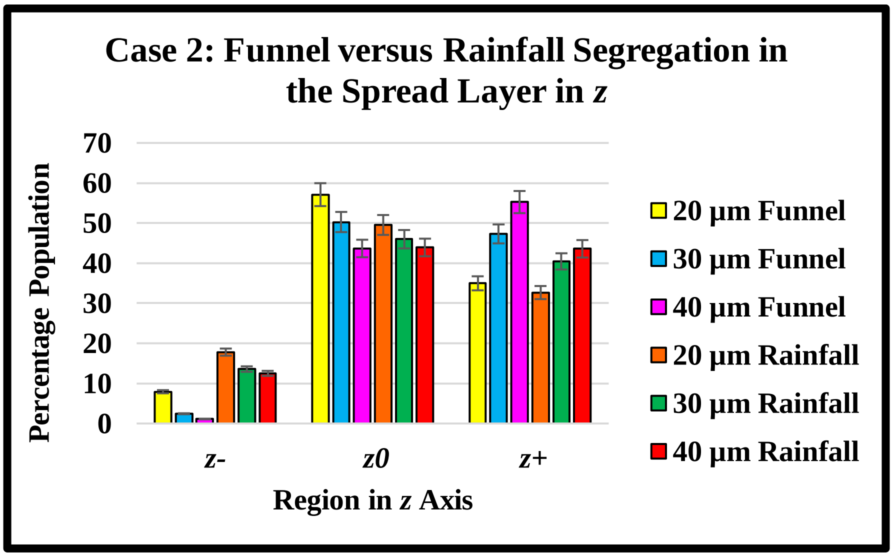

Figure 119 - Funnel versus Rainfall Segregation in the *z* Plane of the Spread Layer in Case 2.

Table 58 shows the significant difference in percentage particle populations in the x and z planes between the funnel and rainfall methods. The coarsest particles were significantly more likely to accumulate in the initial region of spreading relative to recoater direction when delivered via rainfall, as also implied by ***Table 57*** and ***Figure 117***. A similar effect was observed in the median sized particles in this axis. The disparity between both deposition methods, for all particle sizes in the z axis, further reinforces the segregation effect engendered by the moving funnel in this plane.

Table 58 - The Differences in Percentage Particle Populations for each Particle Size in the Spread Layer between the Funnel and Rainfall Methods in Case 2.

Region		Case 2		
		20 µm	**30 µm**	**40 µm**
x	**-**	1.037	-12.741	-19.671
	0	4.020	13.329	14.959
	+	-5.058	-0.588	4.712
y	**-**	0.712	0.707	0.311
	0	0.318	0.632	-1.087
	+	-1.030	-1.339	0.776
z	**-**	-9.874	-11.147	-11.413
	0	7.565	4.292	-0.250
	+	2.309	6.855	11.663

__Case 3__

Table 59 - Segregation Results for the Spread Layer formed by Dispersing the Heap created by both Deposition Methods in Case 3.

Case 3 (15% of 20 µm, 25% of 30 µm, 60% of 40 µm)							
Region		Average Funnel Segregation			Average Rainfall Segregation		
		20 µm	**30 µm**	**40 µm**	**20 µm**	**30 µm**	**40 µm**
x	**-**	71.903	52.778	45.256	62.213	58.202	60.562
	0	21.553	30.435	30.594	26.809	22.969	17.456
	+	6.544	16.787	24.150	10.978	18.829	21.982
y	**-**	32.728	32.198	32.711	31.961	32.015	31.471
	0	34.925	36.344	35.653	35.501	36.144	36.669
	+	32.347	31.458	31.636	32.538	31.841	31.860
z	**-**	18.107	4.608	2.159	24.197	15.759	13.144
	0	60.649	58.883	50.144	53.562	49.861	47.929
	+	21.244	36.510	47.697	22.241	34.379	38.927

A strong segregation in the spread layer along the length of the powder bed is again observed in ***Table 59***, with almost 72% of the fines accumulating at x_{-} and approximately 6.5% reaching the final one-third of the bed. As previously, for all powder sizes the percentage population decreased with powder bed length when inserted by the funnel. Once again, the funnel deposition induced a greater range in percentage particle population of the fine particles than the rainfall, whereas the rainfall method created a higher range in concentrations for the 30 µm and 40 µm particles. A negligible segregation was observed in the y plane for either deposition method.

The funnel technique generally created a more pronounced segregation effect than the rainfall method in the powder bed depth, and the smallest concentration of all particle sizes delivered by the funnel was in the bottom one-third of the bed. As in ***Case 2***, the majority of all particle sizes accumulated in z_0 and only a small amount of the coarsest particles, just over 2%, migrated to z_{-} in the funnel method. In both deposition techniques, significantly more of the fine particle percentage migrated to the bottom one-third of the powder bed compared to the median and coarse particles.

A bar chart of the percentage population in each spread layer, formed by both deposition methods, is shown for each axis in ***Figure 120*** to ***Figure 122***.

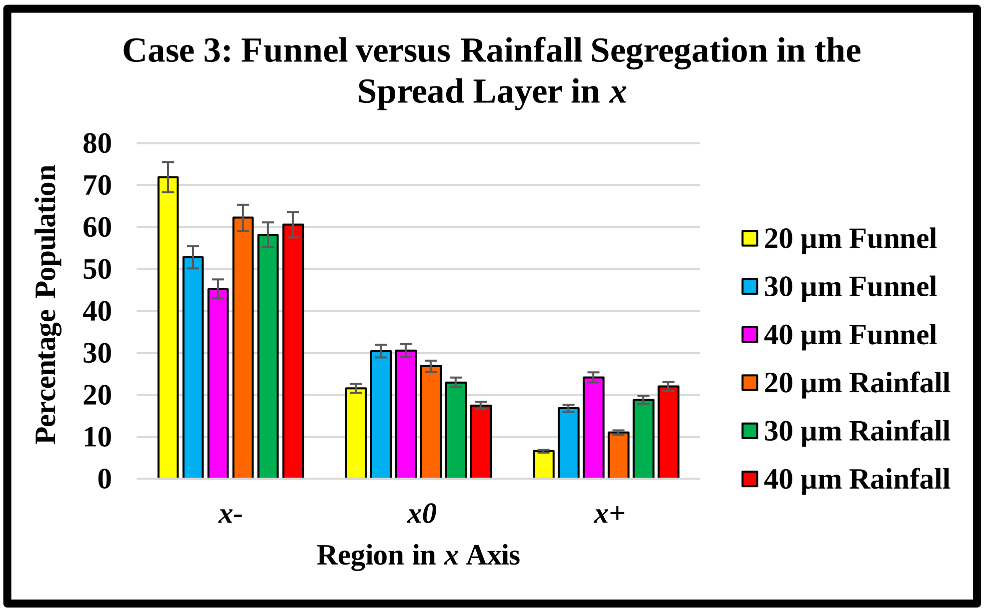

Figure 120 - Funnel versus Rainfall Segregation in the *x* Plane of the Spread Layer in Case 3.

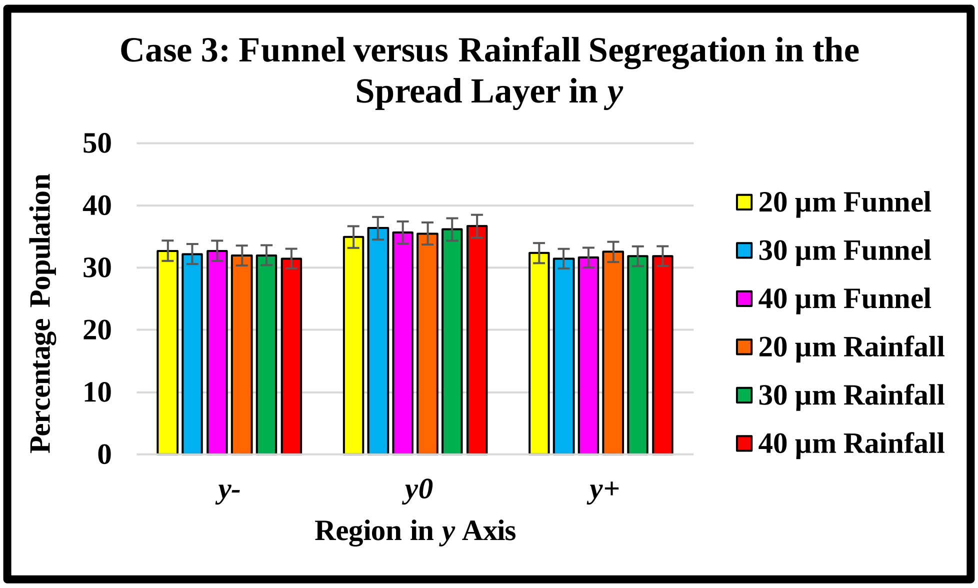

Figure 121 - Funnel versus Rainfall Segregation in the *y* Plane of the Spread Layer in Case 3.

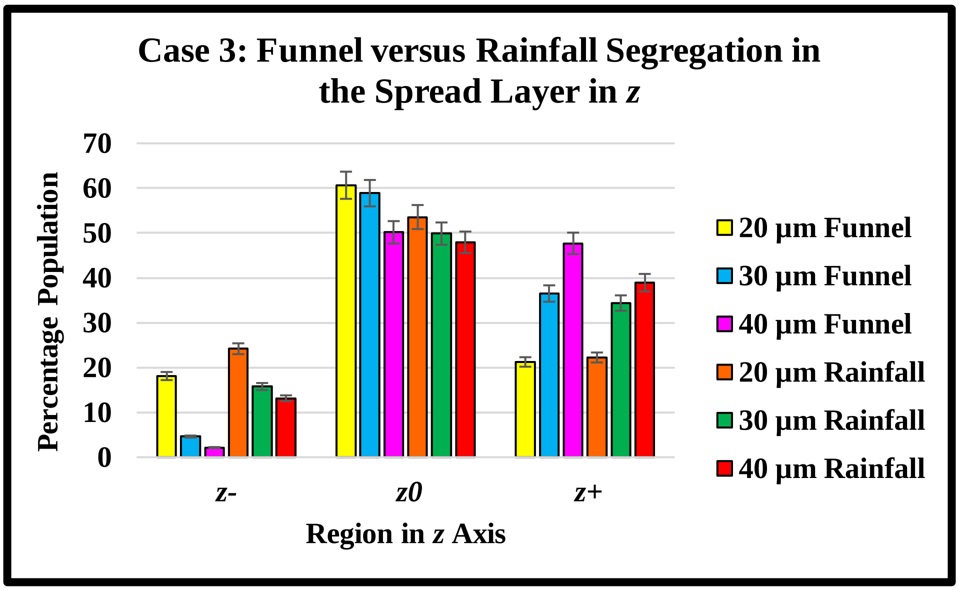

Figure 122 - Funnel versus Rainfall Segregation in the *z* Plane of the Spread Layer in Case 3.

Table 60 shows that the most significant disparity in the percentage populations occurred in the 40 µm particles at the initial region of spreading, with less than half of these particles in this segment in the moving funnel method, compared to more than 60% in the rainfall approach. Analysis of the difference in percentage particle populations in the *y* plane showed only a minor discrepancy and affirmed the negligible segregation in this axis. More deviations were observed in the *z* plane and highlighted the more pronounced segregation observed in the spread layer created with the moving funnel.

Table 60 - The Differences in Percentage Particle Populations for each Particle Size in the Spread Layer between the Funnel and Rainfall Methods in Case 3.

Region		Case 3		
		20 µm	30 µm	40 µm
x	-	9.690	-5.424	-15.306
	0	-5.256	7.466	13.138
	+	-4.434	-2.042	2.168
y	-	0.766	0.183	1.240
	0	-0.575	0.200	-1.016
	+	-0.191	-0.383	-0.224
z	-	-6.090	-11.152	-10.985
	0	7.087	9.022	2.216
	+	-0.997	2.130	8.769

Case 4

Table 61 - Segregation Results for the Spread Layer formed by Dispersing the Heap created by both Deposition Methods in Case 4.

Case 4 (60% of 20 µm, 25% of 30 µm, 15% of 40 µm)							
Region		Average Funnel Segregation			Average Rainfall Segregation		
		20 µm	30 µm	40 µm	20 µm	30 µm	40 µm
x	-	53.901	41.293	41.228	58.387	56.965	56.492
	0	31.883	32.432	29.587	21.862	17.626	16.239
	+	14.215	26.276	29.185	19.751	25.409	27.269
y	-	32.142	32.305	32.833	32.263	32.131	32.761
	0	37.325	34.438	33.710	35.814	36.116	33.184
	+	30.533	32.333	32.120	31.923	31.753	34.055
z	-	5.377	2.145	0.993	15.498	12.409	10.829
	0	49.913	43.088	36.102	44.846	42.535	40.207
	+	44.709	54.767	62.905	39.656	45.056	48.964

Case 4 showed a less pronounced segregation of fines in the x plane for both deposition methods than previously observed, potentially due to the PSD in this case set being comprised of mostly fine particles. Once more, the coarsest particles delivered by the funnel had a reduced segregation compared to the rainfall method with respect to the range in population concentration. The percentage populations were similar in the length of the bed for the median and coarsest particles when delivered by travelling funnel, but about 11% more of the 40 µm elements accumulated in the final one-third of the bed than the middle in the rainfall

approach. As also found in ***Case 2*** and ***Case 3***, the percentage concentration of each particle size generally decreased with the spreading distance in the funnel deposited layer. The same was not observed for the rainfall method.

As previously, a negligible segregation was observed in the y plane regardless of deposition method. The percentage populations had a greater range in the funnel deposition for all powder sizes measured in the bed depth, and fewer than 1% of the 40 µm elements migrated to the bottom one-third of the bed when delivered by the funnel. Significantly more of all particle sizes reached z_{-} when supplied to the bed by the rainfall approach. Almost half of the fines measured in the z plane were in the middle segment of the bed depth when deposited by the moving funnel, and in all cases the larger the particle size the more likely it was to be situated higher in the z axis.

Figure 123 to ***Figure 125*** shows the data for the spread layer formed by both deposition methods in each axis, for the PSD set inserted in ***Case 4***.

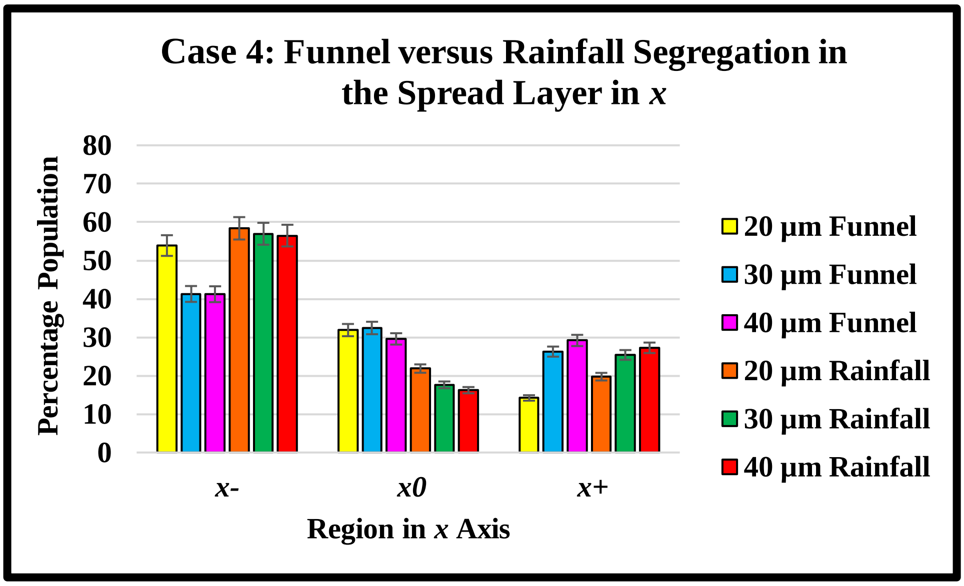

Figure 123 - Funnel versus Rainfall Segregation in the *x* Plane of the Spread Layer in Case 4.

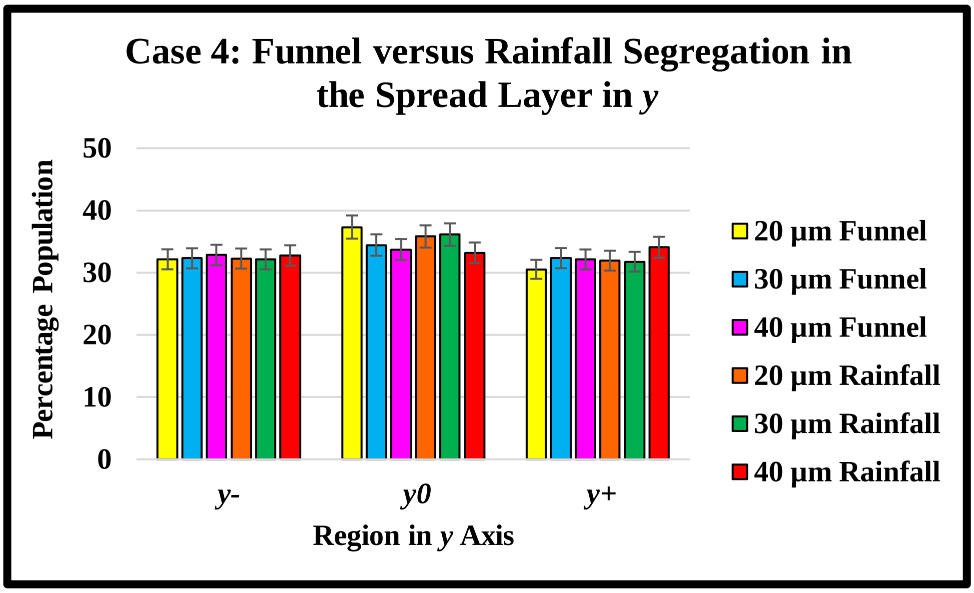

Figure 124 - Funnel versus Rainfall Segregation in the *y* Plane of the Spread Layer in Case 4.

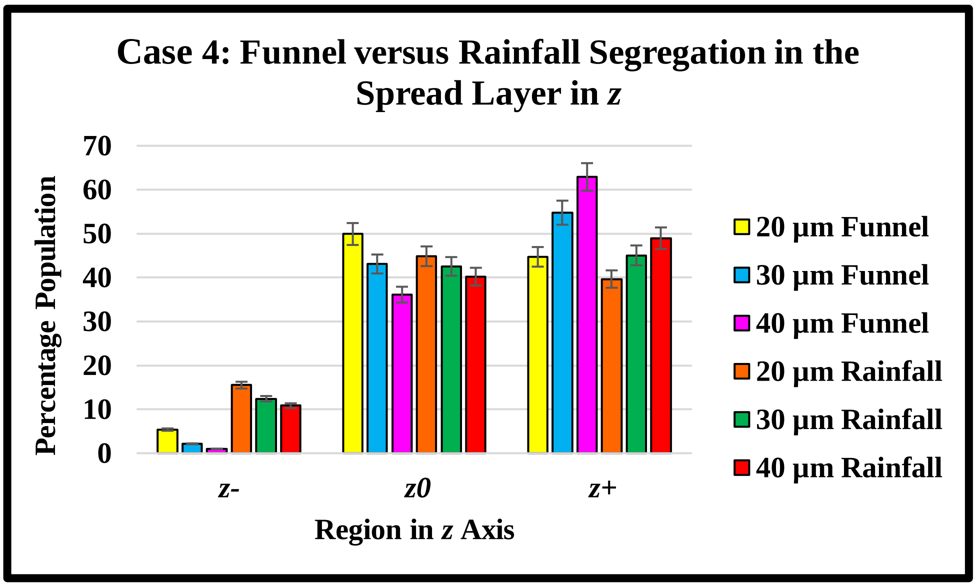

Figure 125 - Funnel versus Rainfall Segregation in the *z* Plane of the Spread Layer in Case 4.

Significant discrepancies between the percentage populations in ***Case 4*** are shown in ***Table 62***. Notably, about 15% more of the 30 µm and 40 µm particles percentage accumulated in the initial one-third of the powder bed length when delivered by the rainfall technique, compared to the travelling funnel. In the funnel method, the median and coarsest particles were more likely to accumulate in the longitudinal middle of the powder bed (x_0) than the rainfall approach. As in ***Case 2*** and ***Case 3***, ***Table 62*** reinforces the point that a more pronounced segregation is engendered by the moving funnel technique in the powder bed depth than the rainfall method, and the minor difference between percentage concentrations in y yields further evidence of minimal segregation in both deposition techniques for this axis.

Table 62 - The Differences in Percentage Particle Populations for each Particle Size in the Spread Layer between the Funnel and Rainfall Methods in Case 4.

Region		Case 4		
		20 µm	30 µm	40 µm
x	-	-4.485	-15.672	-15.264
	0	10.021	14.806	13.348
	+	-5.535	0.866	1.916
y	-	-0.121	0.173	0.072
	0	1.512	-1.678	0.526
	+	-1.390	0.580	-1.935
z	-	-10.120	-10.263	-9.836
	0	5.067	0.553	-4.105
	+	5.054	9.710	13.941

Case 5

Table 63 - Segregation Results for the Spread Layer formed by Dispersing the Heap created by both Deposition Methods in Case 5.

Case 5 (25% of 20 µm, 50% of 30 µm, 25% of 40 µm)							
Region		Average Funnel Segregation			Average Rainfall Segregation		
		20 µm	30 µm	40 µm	20 µm	30 µm	40 µm
x	-	62.233	45.343	40.124	61.071	59.225	61.623
	0	27.536	31.686	29.647	24.271	17.757	14.471
	+	10.231	22.971	30.229	14.658	23.018	23.906
y	-	32.045	32.768	32.156	31.992	32.116	32.510
	0	36.830	35.639	35.469	36.115	36.307	34.567
	+	31.125	31.593	32.374	31.893	31.578	32.923
z	-	7.952	2.080	1.310	18.561	14.168	12.853
	0	57.458	49.231	41.174	48.655	45.454	43.177
	+	34.590	48.689	57.516	32.784	40.379	43.970

A less pronounced segregation was generally observed in the x plane of ***Case 5*** than ***Case 3***, but compared unfavourably with the range of segregation in ***Case 4*** except for the coarsest particles. In both deposition techniques, the results were similar to those found in ***Case 2***. This was expected as ***Cases 2*** and ***5*** had the most similar PSD of all tested sets. As in all cases a slightly greater segregation, as measured by the range in fine concentrations, was given by the funnel deposition method but a smaller range was observed for the median sized and coarsest particles. In all particle sizes in the x axis, the majority of the particle percentages were situated in the first one-third of the spreading direction. The y plane analysis confirms that, once the heap had been dispersed across the powder bed, a minimal segregation was observed regardless of the PSD.

Analysis of the z plane showed that all particles were less likely to accumulate in the lower regions of the powder bed depth when delivered by a funnel. About 10.6% more of the 20 µm particles supplied by the rainfall method reached z_- than when delivered by the moving funnel, and similar values were observed for the other percentage particle populations. As observed consistently across each case, the funnel method impeded the migration of coarse particles to the bottom one-third of the powder bed depth, as no case had a higher percentage concentration of 40 µm particles than 2.16% in z_-, which was found in ***Case 3*** when the PSD was comprised of a majority of coarse elements. A similar but less dramatic segregation effect was observed in the powder beds delivered by the rainfall method.

Figure 126 to ***Figure 128*** present the bar charts for all particle sizes across each axis and deposition method in ***Case 5***.

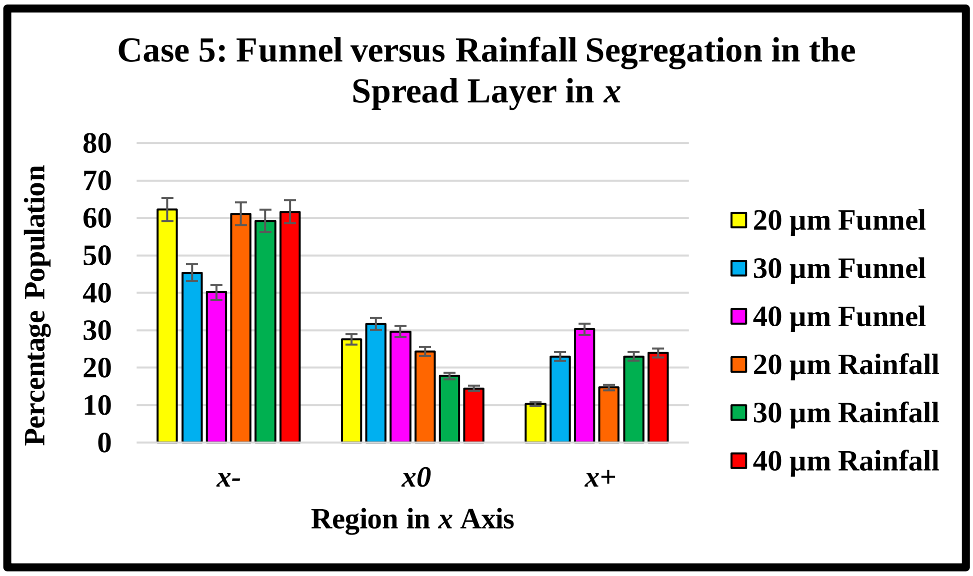

Figure 126 - Funnel versus Rainfall Segregation in the x Plane of the Spread Layer in Case 5.

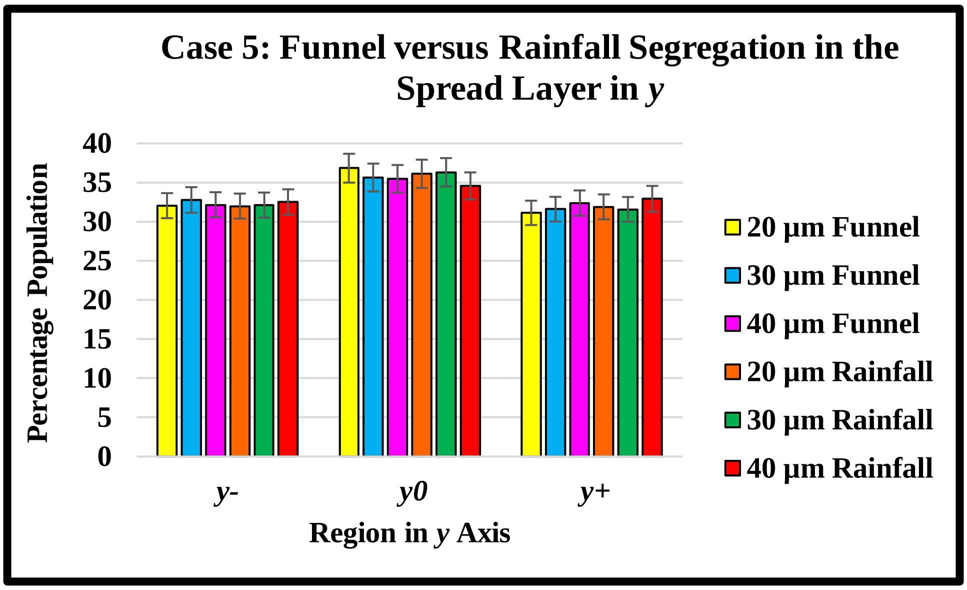

Figure 127 - Funnel versus Rainfall Segregation in the *y* Plane of the Spread Layer in Case 5.

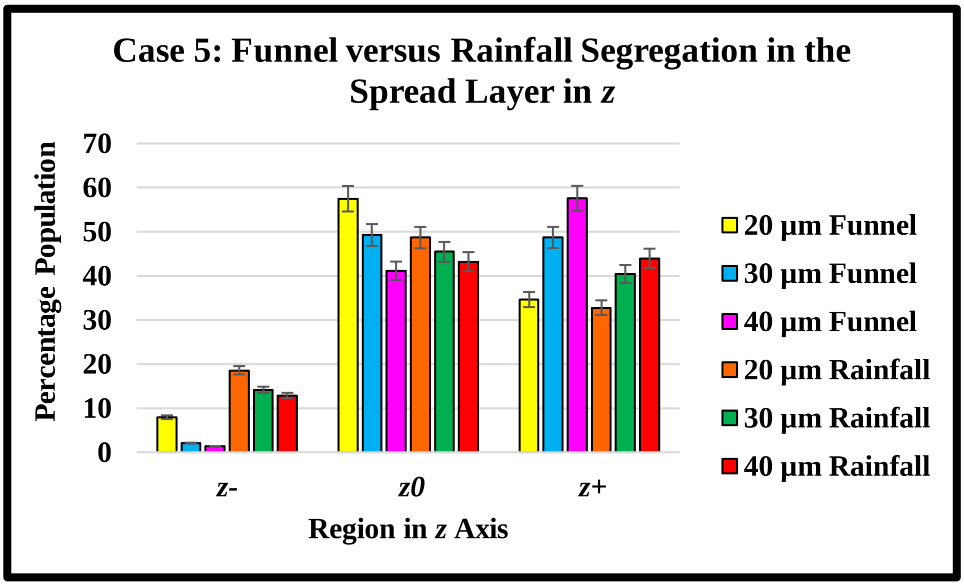

Figure 128 - Funnel versus Rainfall Segregation in the *z* Plane of the Spread Layer in Case 5.

Table 64 shows the difference in percentage particle populations in each segment between the deposition methods. Notably, the 40 µm particles were more prevalent in the initial region of spreading when delivered via rainfall across all cases as confirmed here. Conversely, the 30 µm particles were more likely to situate in x_0 when delivered by a moving funnel, as was consistently observed in all PSD sets.

More discrepancies were observed in the comparisons made for the z axis, with coarser particles more capable of migrating through the powder layers if delivered by the rainfall technique. The funnel engendered a more pronounced segregation in the powder bed depth across all cases, with respect to the range in percentage particle populations.

Table 64 - The Differences in Percentage Particle Populations for each Particle Size in the Spread Layer between the Funnel and Rainfall Methods in Case 5.

Region		Case 5		
		20 µm	**30 µm**	**40 µm**
x	**-**	1.162	-13.882	-21.499
	0	3.265	13.928	15.176
	+	-4.427	-0.047	6.323
y	**-**	0.053	0.653	-0.354
	0	0.715	-0.668	0.902
	+	-0.768	0.015	-0.549
z	**-**	-10.609	-12.088	-11.544
	0	8.803	3.778	-2.003
	+	1.806	8.310	13.547

7.4 Discussion

7.4.1 Discussion of the Solid Volume Fraction Results for the Investigation of the Deposition Technique

As also observed in ***Subsection 6.3.3***, the highest packing density was found in ***Case 6*** for both powder beds with and without the preliminary spread layer. As the inclusion of the preliminary layer gave the models a greater fidelity to commercial PBF processes, the average SVF value taken for each case encompassed the pre-spread layer.

In all cases, the rainfall deposition outperformed the travelling funnel. Notably, the packing density was only 1-2% higher for the rainfall depositions in each case, suggesting that testing a different range of parameters and conditions in the travelling funnel models may overcome this deficit, and aid the development of further DEM-AM research by presenting a more realistic model of the initial spreading conditions.

As only a minor discrepancy was observed between the funnel and rainfall techniques, there are grounds to argue that the PSD had a more pronounced effect on solidity than the deposition method. This argument is further underpinned by the fact that some of the travelling funnel models outperformed the rainfall techniques in separate cases. For example, the polydisperse layer created with the funnel approach in ***Case 4*** was more densely packed than the uniform layer of 30 µm particles inserted by rainfall in ***Case 7***.

As in ***Subsection 6.3.3***, reducing the population of coarse particles appeared to be advantageous to the packing density. The highest SVF overall was in ***Case 6***, comprised entirely of 20 µm particles. The highest packing density in the polydisperse powder sets was observed in ***Case 4***, which had a majority of fine particles. As noted multiple times in ***Subsection 6.3*** and ***Subsection 6.4***, generating a powder bed comprised entirely of uniform fine particles is both logistically and economically unviable in an PBF process.

Considering the PSD sets used in this investigation, the minimal discrepancy between the packing density found in each case, and the manufacturing constraints of controlling the inserted size fractions of the powder, the same PSD is proposed for SS316l under these spreading conditions as in ***Subsection 6.4***. Thus, the most suitable polydisperse powder bed for either a moving funnel or rainfall approach would approximately consist of fine particles (15-25 µm in diameter) at a population of 60%, with 25% of the population between 25-40 µm, and no more than 15% of the particles ≥ 40 µm in diameter.

7.4.2 Discussion of the Surface Roughness Results for the Investigation of the Deposition Technique

The surface roughness results showed that the travelling funnel deposition generally created a less homogenous spread layer profile. A smoother spread layer was formed in all cases when powder was delivered by the rainfall method except ***Case 7***, where the moving funnel produced a slightly smoother layer for the uniform 30 µm elements. Interestingly, the disparity in the surface roughness between each deposition technique appeared to increase with the particle size in the uniform models: 0.28 µm for the finest uniform set of 20 µm particles, 0.39 µm in the uniform 30 µm set, and up to 2.08 µm for the powder bed comprised entirely of 40 µm particles. As in the findings of ***Subsection 6.3.2***, the most homogeneous powder layer was formed by a uniform set of fine powders for both deposition techniques. The smoothest layer profile from the polydisperse PSD sets was found in ***Case 4***, where the majority of fines and the fewest coarse particles were inserted.

It is not obvious why the moving funnel produced a superior powder bed in ***Case 7***. However, analysis of the average particle positions in the x axis of ***Cases 3*** and ***4*** showed a minimal disparity between the average position of the 30 µm elements compared to other models. It is feasible, and ultimately logical, that this particle size may be less prone to segregation than the coarsest and finest particles, which may extend to having implications on the surface roughness.

As in ***Subsection 6.3.2***, the range of the roughness values vary with the PSD. In most cases, the PSD appears to have a more pronounced effect on surface roughness than the deposition mechanism (as also recorded for the SVF analysis). For example, the surface roughness of the travelling funnel model in ***Case 5*** (8.97 µm) is lower than the roughness created by the rainfall model in ***Case 3*** (11.15 µm). Nonetheless, the difference in surface roughness values, between the deposition mechanisms in the same case, yields promise that refining the travelling funnel parameters is a potential route to optimising the powder bed by using a model with a greater fidelity to commercial PBF processes.

Surface roughness measurements were also taken at each line segment in the formed powder bed at y_{-}, y_0, and y_{+}. The results showed that in the travelling funnel models the profile of the line taken from the late-pouring phase (y_+) was generally slightly smoother than the other profiles. The y_+ segment had the smoothest line profile in ***Cases 2***, ***4***, ***5***, ***6***, & ***7***. It is proposed that this was due to the direction of the funnel trajectory, in conjunction with powder avalanching from the heap formed in front of the recoater. The deposition of powder over the avalanching layer was likely to have raised the quantity of powder being spread in that segment and thus, occupied more of the interstices in the projected powder profile when measured in the xz plane. The rainfall method produced a smoother profile at all tested line segments in the polydisperse PSD sets than the funnel technique.

7.4.3 Discussion of the Segregation Results for the Investigation of the Deposition Technique

All samples saw the 20 µm particles preferentially deposited in the x_- and z_- segments. Qualitative analysis of the funnel deposition technique suggested that the larger particles (30 µm and 40 µm in diameter) seemed to accumulate at the top of the funnel and thus were discharged later in the deposition process. The consequence being a greater population of the coarsest particles generally accumulated in the lower bed depth when delivered by the rainfall than the funnel method. In theory, this is because as they were discharged later in the deposition phase of the funnel than their fine counterparts. Thus, causing the fines to deposit earlier and migrate to the bottom of the powder heap which was pushed by the recoater to form the spread layer. These particles then migrated under gravity through the interstices of the powder bed and situated in the bottom of the spread powder layer.

As the finer elements slipped through the recoater gap, it left the coarser elements to be pushed along by the spreader and accumulate at the far end of the spread layer. For all cases using the funnel deposition, the percentage population of the largest particles increased with spreading distance in x, giving further credence to the above point. This conformed to the consensus in literature that larger particles are pushed along with the recoater trajectory, and the results suggested that the funnel deposition exacerbated the segregation effect in the x and z planes, as the same effects were not observed for the rainfall approach. This has interesting implications for the cohesive properties of the powder coded in the digital model, as it is logical to suggest that large particles would separate into finer particles when subjected to the forces of the recoater face.

Both the percentage population analysis and the average particle positions showed that a negligible segregation occurred in the y plane, irrespective of the powder size or deposition method used in all samples. Observations of the models during post-processing suggested that the recoating operation engendered a self-sorting process between the elements in this axis, creating a homogenous distribution in the powder bed width.

With respect to segregation in the depth of the powder bed, in all cases the highest percentage of the coarsest particle type was found in the middle segment, z_0. A negligible difference was observed in the percentages between deposition methods. It is feasible these particles also migrated under gravity through the powder bed layers but were too large to penetrate interstices when surrounded by the finest particles, which had their greatest population percentage in z_{-} for both deposition techniques in all cases. As discussed in ***Subsection 6.4***, the lack of a succeeding layer on the top of the powder bed likely also influenced the percentage populations, as particles will have had more freedom to disperse in both the x and y directions.

Segregation by the average particle positions corroborated the findings of segregation by the percentage particle population, so far as both cases showed that the finest particles were preferentially deposited in the x_{-} and z_{-} segments. A greater segregation effect, manifested by the range in the concentrations of a given particle size, was also generally observed for the funnel deposition technique than the rainfall insertion in the length (x) and depth (z) of the powder bed. The working hypothesis for this is that, in comparison to the rainfall method, analysis of the funnel deposition illustrated that the finer particles were deposited first to the heap, which was then spread by the recoater. Thus, they naturally situated lower in the heap and deposited to the powder bed earlier in the spreading regime. In the case of the funnel deposition, it is feasible that the advanced deposition of fines culminated in them migrating under gravity through the interstices in the depths of the powder bed. Thus, explaining the accumulation of fines at lower bed depths.

The average particle position analysis in ***Subsection 7.3.3*** also showed that the segregation in the length of the powder bed (in line with the spreading direction) was significantly more pronounced than in the depths of the powder bed, when judged by the disparity in the average position of the finest and coarsest particles. It is highly likely this was attributable to the design of the simulation, as the spread length of powder was approximately 16 times the distance of the powder bed depth. Nonetheless, this still yields useful information for the segregation analysis, due to the small layer thicknesses and comparatively long spreading distances observed in commercial PBF systems.

An interesting observation is made by comparison to the segregation results in ***Subsection 6.3.4***. The total layer depth from the substrate to the top of the powder bed was much larger in the simulations of ***Section 6*** compared to the deposition method analysis in ***Section 7***. Thus, there was a greater number of particles present overall and it follows these layers will have a greater packing, which conformed to the effect observed.

In comparison to the x plane analysis of the powder sets in ***Subsection 6.3.4***, a more pronounced segregation effect was generally observed in the rainfall approach of the current chapter. A possible explanation for this is due to the length of the substrate which the powder was spread over, as the spreading region was approximately half as long in the deposition investigation cases as the set up used in ***Section 6***. It is feasible a self-sorting effect was induced to the spread layer in ***Section 6*** as has also been hypothesised for the results of the y plane segregation. However, a much more likely scenario is that the initial deposition location determined the degree of segregation in this chapter. In ***Section 6***, the particles were inserted in a volume across the span of the substrate. Conversely, in the simulations of the rainfall method of ***Section 7***, the particles are inserted in a smaller volume near the recoater origin point to create a powder mound, which was then distributed over the powder bed by the blade.

It is highly likely the rainfall technique of ***Section 7*** presents a more robust model of the segregation in the spread layer due to its closer fidelity to commercial AM spreading. This reinforces the motivation of investigating the effect of the deposition method on the spread layer, and highlights the limitations of the rainfall technique used in contemporary DEM-AM research.

7.4.4 Discussion of the Segregation Results for the Heap and Spread Layer Formed by Dispersing the Heap in All Cases

To provide a comprehensive assessment of the segregation effect engendered by each deposition approach, three different analyses have been performed. The first measured segregation in the overall powder bed was recorded in ***Subsection 7.3.3***, the second test measured segregation in the heap formed in front of the recoater by each deposition method in ***Subsection 7.3.4***, and the third evaluated the segregation of particles in the spread layer formed by the recoater dispersing the heap across the powder bed, as documented in ***Subsection 7.3.5***.

All cases investigating segregation in the heap showed that the lowest concentration of fines was at the furthest distance from the recoater. The same effect was observed but to a lesser extent for all particle sizes. The fact that this was the case for all particle sizes suggests that the slope of the heap had a pronounced effect on the particle size concentrations, and a visual inspection of the heaps formed by both deposition methods suggested that the slope was greater when the particles were inserted by the travelling funnel. Thus, there are grounds to suggest that in this case the deposition method had a more significant effect on segregation than the PSD.

Analysis of all cases showed that the percentage particle population decreased for all sizes in the height of the heap, regardless of deposition method. No particle size across either delivery technique had more than 16% of the percentage particle population in z_{h+}, which was observed in ***Case 4***. It is proposed that this was also due to the lack of a successive layer applying compressive forces to the particles situated in z_{h+}, as previously theorised for the segregation analysis of the complete powder bed in ***Subsection 7.3.3***.

As the fine particles showed a proclivity to accumulate in z_{h-}, it is feasible that the recoater spread the powder in the heap in the successive layers above this segment and left the fines undisturbed. This finding is supported by the majority of fines accumulating in the x_{-} segment of the spread layer formed from the heap. The range of powder sizes in the depth of the heap was greater for the fine particles delivered by the funnel than the rainfall, and the range was larger for the rainfall method in the median and coarsest particle sizes. This was the case in all PSD sets except ***Case 4***, where the range was greater for all particle sizes.

In the analysis of the spread layer formed from the heap (***Subsection 7.3.5***), the range of particle populations was lower for all three particle sizes measured in the x and z planes for ***Case 4*** than for all other cases. This could be of significant importance as this PSD was comprised of a majority of fines, considering that the previous analysis in ***Section 6*** found that inserting more fines to the PSD optimised the powder bed, with regards to the SVF and surface roughness.

In the x axis of all spread layers formed, a slightly greater segregation measured by the range in fine concentrations was given by the funnel deposition method, and a smaller range was observed for the median sized and coarsest particles. This suggested that the funnel method was more prone to segregating the fine particles, but favourable for the 30 µm and 40 µm elements. Notably, the smallest difference in range for the fine particles in the spreading length direction of the bed was in ***Case 4***, at 39.69% for the funnel method and 38.64% for the rainfall technique, showing a difference of only 1.05%. This finding, in conjunction with the previous point regarding the same effect being observed in the heap formed prior to spreading, provides further evidence that using a larger concentration of fines in the PSD benefits the composition of the overall powder bed.

A consistent observation across each case was that the funnel method impeded the migration of coarse particles in the layer formed by spreading the pile in front of the recoater to the lower regions of the powder bed depth; no case had a higher percentage concentration of 40 µm particles than the 2.16% in found in the z_{-} segment of ***Case 3***. A similar but less dramatic effect was observed in the layers created by the rainfall method. This corroborated the qualitative analysis of the particles in the funnel, which appeared to show that finer particles migrated to the bottom of the funnel outlet and thus discharged first onto the preliminary layer, with the median and coarse particles accumulating at the top of the powder reservoir and thus were discharged later in the pouring regime. Hence, advancing the migration of fines through the powder bed depths. This also explains the propensity for higher populations of 30 µm and 40 µm elements in yh_{-}, but does not provide a satisfactory explanation as to why the same effect was observed for the finest particles.

An unexpected result found that the coarsest particles did not appear to be pushed along to the end of the powder bed by the recoater, which contradicts literature [52, 101]. In all cases and delivery techniques, the majority of 40 µm elements accumulated in x_{-}. However, a rational explanation is provided by reference to ***Figure 116***, which shows that the spread layer was discontinuous with large interstices between neighbouring particles. Thus, coarse elements would occupy these interstices and be deposited to the powder bed during spreading. It is therefore proposed that either depositing a larger pile to deliver more powder to the bed, or reducing the recoater gap, would result in a greater percentage population of coarse elements in the final segment of spreading. This hypothesis is supported by the generally higher percentage population of 40 µm particles in x_{+} when the whole powder bed was analysed for segregation in ***Subsection 7.3.3***.

A negligible segregation was observed in the y plane of the heap when the powder was delivered via rainfall in all cases. The moving funnel approach induced a minor segregation effect in the heap, with about a quarter of all particle sizes accumulating early in the pouring phase in y_{h-}. Analysis of the segregation in the y axis after the heap had been spread, and the virtually equal dispersion of powder sizes across the width of the powder bed when all constituent particles were considered, confirmed the hypothesised self-sorting motion incurred by the spreading operation.

The travelling funnel method used in ***Case 4*** outperforming its rainfall counterpart underpins the argument that a dynamic deposition approach, with a PSD comprised of a majority of fines, may be a novel technique to optimise the AM powder bed formed. This statement is made with consideration afforded to the previous findings, that populating a polydisperse powder bed with a majority of fine particles is advantageous with respect to the highest packing density, lower surface roughnesses, and minimised segregation.

7.4.5 Discussion of All Results

With respect to the fidelity of the moving funnel, and its scalability for larger systems, it is clear this presents an area of further research to ascertain whether some of the key findings hold true across larger powder bed regions. For example, the self-sorting of powders to alleviate segregation in the transverse motion across the face of the recoater (the y plane in this analysis). The primary challenge to scalability currently is the number of particles required to generate a complete powder bed, and the extreme computational intensity this would incur. For example, research in ***Subsection 5.2.1*** showed that modelling only 50g of SS316l powder required the inclusion of over 442 million elements. It is feasible to suggest that, barring significant advancements in simulation and modelling capabilities such as through quantum computing, the scalability of the moving funnel technique for larger systems will still be dependent on the use of techniques intended to mimic a larger powder bed, such as the use of periodic boundary conditions.

A possible criticism of the analysis is that the rainfall method is not representative of powder delivery in contemporary AM methods, limiting the usefulness of its comparison to the dynamic deposition approach. It is acknowledged that direct comparisons between the rainfall and moving funnel deposition approaches may not have like-for-like comparisons in commercial PBF machinery. In fact, no commercial hardware can be sourced that inserts powder by raining the powder onto the substrate in front of the spreader under gravity. This is, however, arguably the key motivating factor in the research agenda, that existing DEM-AM investigations misrepresent the powder delivery method by using rainfall. For this reason, the rainfall approach has provided a benchmark due to its ubiquity in DEM-AM investigations and justifies the research methods of this section to examine the difference between existing methods in the research landscape, and the models with a closer fidelity to real powder delivery techniques generated in this project.

A further criticism of the analysis is that the influence of certain environmental conditions, such as the temperature inside the build chamber, is not accounted for in the modelling processes. It would be beneficial to investigate whether changing temperatures to be consistent with the build chamber environment of the EBM process had a pronounced influence on flow behaviour and deposition quality.

Similarly, humidity is not modelled as part of the input parameters as the assumption is induced that the moisture content is negligible owing to vacuum environment of LIGGGHTS® and the EBM build chamber. A suitable step to building on this study would be to implement CFD-DEM techniques to more realistically depict the controlled vacuum environment typical of EBM (2×10^{-3} mbar) [152]. However, with respect to powder calibration, the modelling of interparticle forces, manifested by cohesion and friction settings

(Subsection 5.3.1) and the amendment of properties in the run script, provided sufficient data to underpin the modelling processes in this research and is consistent with existing DEM-AM calibration methods in literature ***(Subsection 3.6)***.

The analysis of both the travelling funnel and rainfall deposition methods, against the powder bed quality metrics of the SVF, surface roughness, and segregation, has elucidated numerous interrelated findings that both align with and extend existing knowledge in the DEM-AM research sphere.

As observed by the results in ***Section 7***, the rainfall deposition method consistently outperformed the moving funnel deposition in respect of achieving a higher packing density. Notably, however, only by a narrow margin (a 1-2% general increase in SVF values). This corresponds to the theory of Chen et al [92], who suggest that random deposition mechanisms can reduce the formation of void space and thereby increasing the packing density by promoting more closely packed powder beds. The relatively small differences between SVF values provides scope for optimising the moving funnel method. For example, by adapting parameters including outlet size and deposition speed, to generate an optimised and more industry-representative depiction of powder deposition.

As reflected in the results, the PSD generally had a more pronounced influence on packing density than the deposition method. The finest uniform powder set (***Case 6***) produced the most densely packed powder bed, supporting the findings of Brika et al [14] that a concentrated insertion of fines improves the solidity of the bed by occupying interstices between elements in the overall powder bulk mix. The most fine-heavy polydisperse powder set inserted, ***Case 4***, further supports this conclusion and conforms to the findings of Averardi [13]. The similarity in results between ***Case 4*** and ***Case 6*** highlights the potential for an economic compromise, as a means of maximising the SVF without relying on excessively refined powder elements.

The PSD proposed to optimise the powder bed, a 60% population of 15-25 µm particles, 25% of the population between 25-40 µm, and no more than 15% of the particles ≥ 40 µm in diameter, provides an optimal compromise, and aligns with existing literature such as commercially available technical data sheets [237, 238], which show that SS316l powder insertions in the size range tested in these models tend to have a distribution skewed toward fines to enhance the layer homogeneity.

The surface roughness analysis underpins the findings of the SVF inspections, so far as the rainfall deposited powder layers generally incurred smoother and more homogenous layers in most cases tested. The exception, ***Case 7*** in which the PSD was comprised of entirely 30 µm particles, highlights the nuances and influence of the individual particle sizes. Thus, implying in accordance with the work of Kiani et al [126], that elements in this approximate size generally promote flowability and thus reduce segregation.
Notably, the surface roughness of the spread layer showed a more pronounced variation in the uniform inserted PSD sets than in polydisperse powder mixes. It is plausible this is due to the particle interactions recorded by Chen et al [92], who noted that a polydisperse mix populated with a majority of fine elements

can result in mechanical interlocking, nullifying segregation and promoting the formation of a more homogenous surface profile.

The moving funnel approached consistently incurred a more pronounced segregation than the rainfall method. The dispersal of fines and coarse elements was consistent with observations in literature, including from Mindt et al [54], who found coarser particles preferentially are pushed along to the end of the spreading process, and finer particles generally situate nearer to the recoater origin point in line with the direction of spreading. Contrastingly, a less pronounced segregation was generally observed in the rainfall models. There was, however, still some notable segregation in the vertical axis through the powder layers. Thus, implying that finer particles migrated through interstices under gravitational forces, conforming to observed behaviour in particulate systems as also stated by Jacob et al [52].

Case 4 yielded particularly intriguing insights and supports the analysis that an optimised PSD with adapted parameters applied to the dynamic deposition technique is a viable route to powder bed optimisation. This conforms to the point raised by Haeri [12], who reflected that accurate layering in the DEM must consider both the deposition mechanics and a suitable PSD to engender conditions that promote optimised AM powder beds.

The full portfolio of results show that the PSD had a more profound and consistent influence on the powder bed quality than the deposition method. However, the deposition method used still had a pronounced effect on the layer characteristics in terms of profile homogeneity, packing density, and segregation. This is consistent with the consensus in literature, that the layer uniformity, driven by spreading parameters and powder deposition and settling mechanics, are critically influences on the suitability of the powder bed to support conditions which enable successful AM builds to be achieved [12, 17, 22].

The rainfall method, though commonly used in DEM-AM publications, fundamentally misrepresents the delivery of powder in industrial AM applications. Thus, there is a reasonable doubt to the veracity of data in the current research landscape, as the initial state of the powder, as clearly evidenced in this research project, is noticeably different between methods prior to the commencement of spreading. The moving funnel approach, although outperformed by rainfall generally, more closely resembles existing commercial delivery methods. The relatively minor differences in quality against the three measured metrics (SVF, surface roughness, and segregation), provide sufficient grounds to propose that further refinement of the moving funnel method, by adapting operating parameters, provides a viable route to powder bed optimisation and outperforming existing rainfall techniques.

In conclusion, the results reinforce established knowledge regarding powder behaviour in the DEM-AM research sphere, and lays the foundations for further exploration and opportunities. The sensitivity of all three metrics to changing the PSD, in particular by increasing the concentration of fines, heavily suggests that refining the PSD is amongst the most viable methods of engineering optimised powder beds for AM processing. Furthermore, the travelling funnel, previously not seen in DEM-AM modelling, has yielded promise as a technique to improve the fidelity of DEM models to industrial AM practices, and therefore bridge the knowledge gaps that exist between simulations and reality.

7.5 Summary

The following conclusions have been drawn from the analysis of the full powder bed:

- The rainfall approach produced a more densely packed powder bed than the travelling funnel in all cases. However, only a minor disparity (1-2% in all cases) was noted.

- With respect to the SVF, the moving funnel method in certain powder sets outperformed the rainfall technique in separate cases. This suggests that the PSD had a more pronounced effect on powder bed solidity than the deposition method. As in ***Subsection 6.3.3***, the uniform powder bed comprised of the finest elements had the highest packing density overall, and the highest SVF in the polydisperse sets was found in the PSD with the highest fraction of fines for both deposition methods.

- In terms of the surface roughness, the rainfall models formed a smoother spread layer than the travelling funnel in all cases except ***Case 7***. As also observed in ***Subsection 6.3.2***, the smoothest powder profile was formed when the highest fraction of uniform fine particles were used in both deposition techniques, and the smoothest layer in the polydisperse powder sets was found in the PSD with the majority of fines.

- Inserting particles by the moving funnel generally engendered a more pronounced segregation across cases than the rainfall technique. In particular, fine particles showed a proclivity to migrate through the powder layers and accumulate in lower bed depths, and coarse particles tended to travel along the recoating direction and situate at the far end of the spread layer. The range of the particle population percentage appeared to increase when inserted by a funnel, manifesting the segregation effect.

- Based on the above points, it can be remarked that the travelling funnel deposition method generally degraded the powder bed with respect to the SVF, surface roughness, and segregation. As the findings of the SVF and surface roughness analysis were consistent with the results in ***Section 6***, it is feasible that the segregation analysis is more informative for optimising the powder bed with dynamic deposition methods.

- The evidence generated in this section underpins the belief that control of the powder delivery method, by refining the parameters of the simulations, presents a clear opportunity to engender conditions which benefit the formation of the spread layer. Due to the extremely limited availability of proprietary commercial data pertaining to the travelling funnel deposition, the set of parameters chosen were implemented with respect to the requirements of the digital model, and not explicitly commercial practice. Further investigations of the model would elucidate how the parameters can be configured to optimise the AM powder bed, and thus yield results with practical implications for industry and the wider DEM-AM sphere.

- The finding that the moving funnel has a clear influence on the quality of the spread powder layer is significant. It proves that there is a knowledge gap in existing DEM-AM research by showing that the influence is not negligible. There are strong grounds to argue that a novel contribution has been made to the DEM-AM research landscape with respect to the investigation of the moving funnel powder delivery technique against the widely used rainfall insertion approach.

- By extension of the above point, it is reasonable to state that the models used in this project have provided a more accurate depiction of powder deposition than what is, to the best of the author's knowledge, currently available in DEM-AM literature. This statement is made in reflection of the differences of the initial state of the powder prior to spreading, after being deposited by a moving funnel as observed in commercial PBF systems [56].

The following conclusions have been reached from the heap and spread layer segregation analysis:

- The lowest population of all particle sizes measured in the x axis of the heap was found in the segment furthest away from the recoater. This segregation was generally more pronounced in all PSD sets delivered by the moving funnel except in ***Case 4***, implying the segregation effect in the initial delivered powder state can be reduced by using a higher concentration of fines.

- A qualitative inspection of the heap formed implied a higher gradient on the slope when delivered by the moving funnel, explaining the relative deficiency of all particle sizes in x_{h+}. Thus, it is proposed that the deposition technique had a more significant influence on the segregation in the deposited heap than the PSD. This may extend to increasing the deposition of fine particles in the initial regions of spreading, as they could have feasibly migrated to lower layers of the heap and thus not have been pushed along by the recoater as the coarser elements were theorised to have been.

- All percentage particle populations decreased in depth of the deposited heap, regardless of PSD or deposition approach.

- In all PSD sets except ***Case 4***, the range of powder sizes in the depth of the heap was greater for the funnel deposited fines than the rainfall. A larger range was generally observed in the rainfall method for the median and coarsest particle sizes, with the exception being in ***Case 3*** where a 60% majority of particles were coarse. Thus, providing yet further evidence to suggest that populating the bed with a majority of fine particles is a viable means of optimisation.

- In the x axis analysis of all spread layers formed by dispersing the heap, the funnel method induced a slightly greater segregation than the rainfall in terms of the range of fine particle concentrations. Conversely, the funnel produced a smaller range in segregation for the 30 µm and 40 µm elements. ***Case 4*** had the smallest disparity in the range of fines in x, at only 1.05% between the rainfall and funnel depositions. Suggesting, once again, that a dynamic deposition of powder with a PSD consisting of a majority of fines benefits the formed powder bed.

- Investigation of the y_h axis in all cases showed a segregation in the heap that was not present in the spread layer formed by dispersing the same heap. The negligible segregation observed in the y axis of the full powder bed and the spread layer proves the existence of the self-sorting motion in this plane incurred by recoating. It would be of interest to ascertain whether the same effect is observed at variable recoating speeds and spreader shapes, and over wider powder beds.

- The finding which contradicts literature relating to the trajectory of coarser particles in the spreading direction has been attributed to the design of the simulation. The spread layer formed by dispersing the heap is too small a powder sample to observe a trend of coarse particles situating late in the recoating operation. Investigations of the complete powder bed showed a higher percentage population of 40 µm particles in the x_+ segment, supporting this conclusion.

- In all cases, investigations of the heap deposited by both the moving funnel and rainfall deposition methods, and the spread layer formed by dispersing the heap, corroborated the proposed theory that a polydisperse PSD with a majority of fine particles is advantageous with respect to segregation. This follows the previous hypothesis that this powder bed composition is also advantageous in terms of attaining a higher packing density and generally reduced surface profile roughness.

8. Project Conclusions

This project used DEM-AM investigations to analyse the effect of different parameters, such as varying PSD sets and deposition methods, on the quality of the formed spread layers. Firstly, AM, powder flow behaviour, and the principles of the DEM were introduced, followed by a review of contemporary literature to establish the state of the art and existing knowledge gaps in the current DEM-AM landscape. The mathematical framework of the DEM was outlined to support its use in modelling dynamic powder flow, and various areas of further exploration were identified. Although not all of these areas could viably be investigated in this project, several of them have been proposed as recommendations for future work to contribute to DEM-AM knowledge. Modelling processes comprised assessing the influence of the PSD and deposition method on powder bed quality with three discrete metrics: the SVF, surface roughness, and segregation between polydisperse particles.

A novel deposition technique, not previously observed in DEM models for PBF analysis, was built in the simulations using dynamic funnel deposition. Differences were revealed in powder discharge behaviour. Coarser particles accumulated higher in the funnel and discharged later in the deposition, proposed to be the mechanism of increasing segregation. This effect, absent in rainfall-deposition, highlights a limitation in existing DEM-AM methods. The project successfully presents a higher-fidelity digital twin of commercial PBF systems that employ a moving funnel, and the results present an interesting finding that the spread layers formed after funnel-deposition were generally inferior to the rainfall beds. Thus, suggesting the quality of powder beds in existing DEM-AM may be overestimated. An improvement to the powder beds (denser packing, smoother layer topography, and reduced segregation) with the moving funnel was observed when a PSD rich in fines was inserted.

The most pertinent project conclusions are:

- The project has achieved its aim to examine suitable processing conditions for the spreading and delivery of an AM powder set. It introduced a novel, more realistic powder deposition approach using a moving funnel, addressing a critical oversight in the rainfall approach used in contemporary DEM-AM modelling.

- The funnel method revealed powder element sorting effects not captured in existing models, offering insights into segregation behaviour. Existing rainfall methods do not capture powder flow behaviour and may artificially increase the quality depicted in the results of the spread layer.

- A direct conversion between Surface Energy and the CED properties has been established which is likely to be highly informative to other researchers in the DEM community. Quantitative information pertaining the exact conversion process is given in ***Subsection 5.3.1***.

- The results supported the adoption of dynamic deposition with fine-dominated PSD sets. Specifically, a powder bed comprised of SS316l, delivered by the moving funnel in the spreading conditions tested, would be a 60% population of 15-25 µm particles, 25% of the population between 25-40 µm, and no more than 15% of the particles ≥ 40 µm in diameter. Further refinement may yield further improvements to the realised powder bed, and thus the results have generated knowledge for the optimisation of commercial AM powder beds in industry by suggesting appropriate PSD weightings.

9. Recommended Future Research Areas

This final section of the report records the recommendations for future research to build on the work and findings of this project. ***Subsection 9.1*** outlines all future research areas in DEM-AM analysis including, but not limited to, considerations as to optimise the use of computational resources in future DEM-AM work, how simulations can be set up to more closely resemble commercial AM systems and thus, increase the accuracy of future DEM-AM investigations, and how practical analysis can be improved to provide better calibration processes for digital powder flow models. ***Subsection 9.2*** outlines the baseline of a potential future powder flow research agenda by identifying the variables of powder flowability, that could inform the future development of a mathematical model with the ultimate aim of developing flow regimes that quantify the flowability of AM powder materials in application.

9.1 Future Research in Discrete Element Methods for AM Powder Beds

The future of research in DEM modelling of PBF powder beds should concentrate on several key areas. For example, by optimising the use of computational resources, and by increasing the fidelity of the digital models to commercial PBF systems. As outlined previously, parametric analysis of the travelling funnel technique is a possible extension of this work, in order to identify parameters which serve to optimise the powder bed. Various aspects of the dynamic deposition that may inform optimisation strategies were identified in ***Subsection 7.2*** and ***Subsection 7.5***. With sufficient time and resources, it would be advantageous to compare the travelling funnel method to other powder deposition models, including DEM set ups of hopper-supplied EBM powder systems, and by modelling powder delivery with a DEM model of a reciprocating powder supply table.

Furthermore, evaluation of the forces the powder exerts on the recoater and an AoR analysis of the heap formed in front of the spreader could explain segregation mechanisms through force chain behaviour.

To optimise the use of computational resources in future DEM-AM work, and thereby better manage the computational intensity of the simulations, the author recommends that load-balancing techniques are investigated when simulations necessitating very fine particles (≤ 30 μm) are performed. Load-balancing alleviates the computational costs by reducing the number of idle cores during the simulation, and thereby aids in reducing the overall run time.

A key approach to improving the future research of this project would be to optimise the validation processes, which would afford more veracity to the contact models and properties implemented to mimic cohesive powder behaviour. A recommendation would be to perform a HFM analysis of the formed AoR of the powder sample in a vacuum chamber to reduce experimental variability, and depending on the accuracy of the results, extend the modelling in a practical vacuum environment to a powder spreading test rig.

DEM-AM research has almost exclusively investigated facets of the process in isolation (inserted PSD, substrate topography, powder morphology, and in the case of this project the powder deposition mechanism, and many others). The most complete depiction, and the most accurate reflection of PBF spreading operations applicable to real world scenarios, would encompass a combination of all these conditions, with isolated parameters adapted thereafter to ascertain the influence of changing variables on the condition of the spread layer. Thus, the most accurate model of a DEM-AM powder bed investigation would consist of:

- Powder flow modelled in both an inert gas and vacuum environment to ascertain the effect of atmospheric conditions on powder flow.

- The use of irregular, realistic substrate surfaces, comparable to previously melted layers of the AM component.

- Powder elements that are irregular in morphology and modelled to represent the shape of constituent AM powder particles more accurately.

- Realistic deposition methods, such as by building on the work in this project to optimise the moving funnel technique, and exploring alternative deposition methods to expand the scope of the research and its applicability to commercial methods for practical implementation.

9.2 Future Research in the Dimensional Analysis of Powder Flowability

Based on the findings of the project, an area of further research is to characterise the flow behaviour of metal AM powders with dimensional analysis. To achieve this, all of the variables which are thought to influence the flow have been stated and grouped into those which can and cannot be controlled. Adaptable variables include operational parameters such as the recoater spreading speed, and powder characteristics such as the PSD. Variables which cannot be controlled include inherent material properties, morphology, and the chemical composition of the powder as influenced by the atomisation method. A limit is introduced to the analysis such that the flowability is only evaluated from the delivery of the powder to the build chamber, until the point when the powder has been spread and settled immediately prior to melting. Thus, neglecting the changes in powder composition engendered by thermodynamic processes. The variables which influence flowability are listed in ***Table 65*** and are based on extensive research during this project.

Table 65 - Variables of Powder Flowability Before, During, and After the Spreading Operation.

Pre-Spreading	During Spreading	Post-Spreading
Young's Modulus: An inherent property of the powder material.	PSD inserted to the bed.	Melting methods.
Density: An inherent property of the powder material.	Phase of powder processed (recycled/fresh).	Melting pattern.
Morphology: Depends on the atomisation process used to produce the powder.	Spreading speed.	Optical properties.
Porosity: Depends on the atomisation process used to produce the powder.	Spreader shape.	Thermo-Physical properties.
Chemical composition and surface texture: Depends on the powder production process and the material selected.	Chamber environment.	
Time of storage at rest.	Moisture.	
Permeability: An inherent property of the powder material.	Electrostatic charge and interparticle forces.	
Delivery technique (immediately prior to spreading).		

To characterise the powder flow behaviour, a dimensional analysis is proposed to identify the variables which are likely to effect a change in the spread layer formed. Considering the previously identified metrics to quantify a suitable powder bed for AM processing, the changes may constitute an improvement in the packing density, surface roughness, or segregation effect of polydisperse powders. An alternative inspection would be to compare the surface roughness profiles of the spread layers against a combination of input variables, such as the PSD of the powder set and the recoater velocity used to spread the powder, and then analyse the data to determine if proposed spreading regimes exist which either give rise to a smoother surface engendering favourable AM conditions, or a heterogeneous profile liable to induce an inconsistent melting pattern and thus porosity in the built component.

It is proposed that through further development of the dimensional analysis, regimes can be defined from the considered variables to mathematically quantify the spreading parameters that form a smooth, transitional, and rough layer. This is analogous to other analytical engineering techniques, such as by using the properties of fluid flow to determine a Reynold's Number which characterises laminar, transitional, and turbulent regimes. The suggested method of developing these proposed powder flow regimes would require the use of sophisticated statistical modelling techniques, such as Gaussian process emulation, in conjunction with more advanced digital models of the AM powder spreading systems.

Table 66 to ***Table 68*** assigns dimensions to the units most commonly associated with each variable of the process outlined in ***Table 65***.

Table 66 - Units and Dimensions Associated with Powder Flow Variables Prior to the Commencement of Spreading.

Variable	Associated units	Dimensions
Young's Modulus.	GPa	$m\,\mathrm{L}^{-1}\,\mathrm{T}^{-2}$
Density.	$\frac{\mathrm{kg}}{\mathrm{m}^3}$	$m\,\mathrm{L}^{-3}$
Morphology: Depends on the atomisation process used to produce the powder.	µm	L
Porosity: Depends on the atomisation process used to produce the powder.	No units.	None
Chemical composition and surface texture: Depends on the powder production process and the material selected.	Chemical composition will vary depending on alloying elements. Surface texture: nm	Chemical composition will vary depending on alloying elements. Surface texture: L
Time of storage at rest.	Seconds	T
Permeability: An inherent property of the powder material.	Darcy (d)	$m\,\mathrm{L}\,\mathrm{T}^{-2}\ \mathrm{I}^{-2}$
Delivery technique (immediately prior to spreading).	Either rainfall (acceleration due to gravity) or funnel deposition (the speed of the funnel in $\frac{m}{s}$).	Rainfall: $m^{-1}\,\mathrm{L}^3\,\mathrm{T}^{-2}$ Moving Funnel: $\mathrm{L}\,\mathrm{T}^{-1}$

Table 67 - Units and Dimensions Associated with Powder Flow Variables During Spreading.

Variable	Associated units	Dimensions
PSD inserted to the bed.	Percentile of sizes (%) or a diameter or length dimension (m).	L
Phase of powder processed (recycled/fresh).	Either cycle number, or inserted percentage of fresh powder (%).	None.
Spreading speed.	$\frac{\mathrm{m}}{\mathrm{s}}$	$\mathrm{L}\ \mathrm{T}^{-1}$
Spreader shape.	Width, length, and height.	L
Chamber environment.	Pa	$m\ \mathrm{L}^{-1}\ \mathrm{T}^{-2}$
Moisture.	Relative Humidity (%)	None.
Electrostatic charge and interparticle forces.	C or N	Coulomb: $m^0\ \mathrm{L}^0\ \mathrm{T}\ \mathrm{I}$ Newtons: $m\mathrm{L}^{-1}\ \mathrm{T}^{-2}$

Table 68 - Units and Dimensions Associated with Powder Flow Variables After Spreading.

Variable	Associated units	Dimensions
Melting methods.	Laser or electron beam.	Line Energy: $m\,\mathrm{L}\,\mathrm{T}^{-2}$ Energy Density: $m\,\mathrm{L}^{-1}\,\mathrm{T}^{-2}$
Melting pattern.	Various	Various
Thermo-Physical properties.	Various	Various
Optical properties.	Various	Various

The following assumptions should be made prior to the commencement of any dimensional analysis:

- More spherical powder particles are generally more flowable [14, 239, 240].
- Significant research of powder flowability characterisation has been done in the field of pharmaceuticals [130, 133, 94].
- A wide PSD is beneficial for occupying interstices in the powder bed, but a narrow PSD contributes to a greater flowability [13, 49, 197, 241].
- The recycling effect is mainly manifested by the changes to the PSD, and the more recycled the powder is the better the flowability. Recycling can almost certainly be accounted for by moisture content and the PSD of the recycled sample set [161, 197].
- With respect to the surface texture of the particles, elements with rougher surfaces are likely to have a propensity for mechanical interlocking and higher frictional forces, and thus behave more cohesively [240].
- The van der Waals forces appear to be the dominant cohesive force at finer particle sizes, and for coarser particles gravitational forces are dominant. A high moisture content engenders capillary interactions and causes particles to bridge, thereby raising agglomerations [242].

- Denser and less porous particles are more flowable [243].

- Reducing electrostatic charges can improve powder flowability [244].

- Young's Modulus appears to influence particle flow at the millimetre scale but it is unknown if the same effect is observed at the micrometre level [245].

- It is assumed that the spreader shape and speed can be mathematically correlated to reduce bed degradation at higher recoater speeds, by adapting the shape of the recoater [17].

- Empirical evidence suggests that powder is about twice as flowable in a vacuum. It is feasible that this is due to the lack of friction forces and reduced moisture content.

Table 69 is adapted from ***Table 27*** in ***Subsection 6.3.2*** and records the surface roughness results from the cases in that section.

Table 69 - Surface Roughness Results for Powder Flow Regimes.

Case	Particle Size Distribution (% particle diameter)			Overall Average Surface Roughness (µm)
	40 µm	30 µm	20 µm	
1	100	0	0	10.07
2	33.33	33.33	33.33	7.35
3	60	25	15	9.10
4	15	25	60	6.00
5	25	50	25	7.29
6	0	0	100	4.09
7	0	100	0	7.89

Based on the average surface roughness values generated, an example regime may resemble:

$$Smooth\ < 7.08\ \mu\text{m}\ > Rough$$

The powder profiles projected onto the xz plane of the bed for these cases were too similar to be compared visually. Because the particles were so small, and there were so many of them in the powder bed spreading length, taking a segment sample (such as from ***Case 1*** and ***Case 6***, the roughest and smoothest layers as shown in ***Table 69*** respectively) was unlikely to be representative of the full powder span. For this reason, a numerical value (7.08 µm) has been proposed as the transition point in this instance between the smooth and rough powder layers. Note that because the data population is small, this is fairly arbitrary and has been selected as the mid-point between the lowest and highest surface roughness values. An alternative would have been to use the mean average value of a larger data set. The boundary of the regime is given here simply as an example. Applying this logic as a base concept, it could therefore be proposed that the powders generated by the PSD in each case can be classified as in ***Table 70***.

Table 70 - Example Flow Regime Classifications based on Surface Roughness Values.

Case	Overall Average Surface Roughness (µm)	Regime Classification
1	10.07	Rough
2	7.35	Slightly Rough (transitional)
3	9.10	Rough
4	6.00	Smooth
5	7.29	Slightly Rough (transitional)
6	4.09	Smooth
7	7.89	Slightly Rough (transitional)

Based on the proposed spreading regimes defined in ***Table 70***, the dimensional analysis could be extended to plot the influence of a range of variables on the dynamic behaviour of powder. Other key performance indicators, such as the segregation in the spread layer or the packing density, could also be used as well as or instead of the surface roughness.

By deriving the relationships mathematically, the multifaceted variables which serve to influence the quality of the formed powder bed could be discretised into multiple groups, with the input properties (such as recoater speeds and PSD ranges) calibrated to optimise the powder bed for a given manufacturing operation. Thus, a comprehensive dimensional analysis is proposed as being a feasible route for improving the efficiency of commercial AM operations and contemporary powder-based AM research projects.

References

[1] International Standards for Organisation, *Additive Manufacturing - General Principles - Terminology,* London: British Standards Institution Limited, 2015.

[2] UK Government, "https://www.gov.uk/government/publications," UK Government, 11 June 2019. [Online]. Available: https://www.gov.uk/government/publications/regulation-for-the-fourth-industrial-revolution. [Accessed 1 December 2020].

[3] J. Gardan, "Additive Manufacturing Technologies: State of the Art and Trends.," *International Journal of Production Research,* vol. 54, no. 10, 2016.

[4] S. Ford and M. Despeisse, "Additive Manufacturing and Sustainability: An Exploratory Study of the Advantages and Challenges," *Journal of Cleaner Production,* vol. 137, no. 1, 2016.

[5] G. Sossou, F. Demoly, G. Montavon and S. Gomes, "An Additive Manufacturing Oriented Design Approach to Mechanical Assemblies," *Journal of Computational Design and Engineering,* vol. 5, no. 1, pp. 3-18, 2018.

[6] I. Gibson, D. Rosen and B. Stucker, Additive Manufacturing Technologies: 3D Printing, Rapid Prototyping, and Direct Digital Manufacuring., 2nd ed., New York: Springer, 2015.

[7] R. Liu, Z. Wang, T. Sparks, F. Liou and J. Newkirk, "Aerospace Applications of Laser Additive Manufacture," in *Laser Additive Manufacturing: Materials, Design, Technologies, and Applications*, 2nd ed., Rolla, Missouri: Woodhead Publishing, 2016, pp. pp 351-371.

[8] E. Dimla, M. Camilotto and F. Miani, "Design and Optimisation of Conformal Cooling Channels in Injection Moulding Tools," *Journal of Materials Processing Technology,* Vols. 164-165, no. 1, pp. 1294-1300, 2005.

[9] S. Broginia, M. Sartoria, G. Giavaresia, P. Cremascolib, F. Alemanib, D. Bellinic, L. Martinia, M. Maglioa, S. Pagania and M. Finia, "Osseointegration of Additive Manufacturing Ti–6Al–4V and Co–Cr–Mo Alloys, With and Without Surface Functionalization with Hydroxyapatite and Type I Collagen," *Journal of the Mechanical Behavior of Biomedical Materials,* vol. 115, no. 1, pp. 104262 - 104271, 2021.

[10] H. Chen, Y. Sun, W. Yuan, S. Pang, W. Yan and Y. Shi, "A Review on Discrete Element Method Simulation in Laser Powder Bed Fusion Additive Manufacturing," *Chinese Journal of Mechanical Engineering: Additive Manufacturing Frontiers,* vol. 1, no. 1, pp. 1-13, 2022.

[11] E. Li, Z. Zhou, L. Wang, R. Zou and A. Yu, "Particle Scale Modelling of Powder Recoating and Melt Pool Dynamics in Laser Powder Bed Fusion Additive Manufacturing: A Review," *Powder Technology,* vol. 409, no. 1, pp. 1-15, 2022.

[12] S. Haeri, Y. Wang, O. Ghita and Y. Sun, “Discrete Element Simulation and Experimental Study of Powder Spreading Process in Additive Manufacturing,” *Powder Technology,* vol. 306, no. 1, pp. 45-54, 2016.

[13] A. Averardi, C. Cola, S. Zeltmann and N. Gupta, “Effect of Particle Size Distribution on the Packing of Powder Beds: A Critical Discussion Relevant to Additive Manufacturing,” *Materials Today Communications,* vol. 24, pp. 1-14, 2020.

[14] S. Brika, M. Letenneur, C. Dion and V. Brailovski, “Influence of Particle Morphology and Size Distribution on the Powder Flowability and Laser Powder Bed Fusion Manufacturability of Ti-6Al-4V Alloy,” *Additive Manufacturing,* vol. 31, no. 1, pp. 100929-100945, 2020.

[15] M. Lutter-Günther, M. Horn, C. Seidel and G. Reinhart, “Influence of Particle Size Distribution on Powder Flowability and Part Properties in Laser Beam Melting,” in *Proceedings of the 14th Rapid.Tech Conference Erfurt*, Erfurt, 2017.

[16] P. Wang, W. Sin, M. Nai and J. Wei, “Effects of Processing Parameters on Surface Roughness of Additive Manufactured Ti-6Al-4V via Electron Beam Melting,” *Materials,* vol. 10, no. 10, 2017.

[17] S. Haeri, “Optimisation of Blade Type Spreaders for Powder Bed Preparation in AM using DEM Simulations,” *Powder Technology,* vol. 321, no. 1, pp. 94-104, 2017.

[18] E. Espiritu, A. Kumar, A. Nommeots-Nomm, J. Muñiz Lerma and M. Brochu, “Investigation of the Rotating Drum Technique to Characterise Powder Flow in Controlled and Low Pressure Environments,” *Powder Technology,* vol. 366, no. 1, pp. 925-937, 2020.

[19] A. Phua, C. Doblin, P. Owen, C. Davies and G. Delaney, “The Effect of Recoater Geometry and Speed on Granular Convection and Size Segregation in Powder Bed Fusion,” *Powder Technology,* vol. 391, no. 1, pp. 632-644, 2021.

[20] Q. Han, H. Gu and R. Setchi, “Discrete Element Simulation of Powder Layer Thickness in Laser Additive Manufacturing,” *Powder Technology,* vol. 352, no. 1, pp. 91-102, 2019.

[21] Y. Fouda and A. Bayly, “A DEM Study of Powder Spreading in Additive Layer Manufacturing,” *Granular Matter,* vol. 22, no. 10, pp. 1-18, 2020.

[22] C. Meier, R. Weissbach, J. Weinberg, A. Wall and A. Hart, “Modeling and Characterisation of Cohesion in Fine Metal Powders with a Focus on Additive Manufacturing Process Simulations,” *Powder Technology,* vol. 343, no. 1, pp. 855-866, 2019.

[23] S. Haeri, D. Bailey, M. Calder, B. Clark, A. Rogalsky and E. Toyserkani, “On the Impact of Powder Cohesion on the Bulk Properties of a Powder Bed in Additive Manufacturing using Discrete Element Method Simulations,” in *Proceedings of the 6th European Conference on Computational Mechanics and 7th European Conference on Computational Fluid Dynamics 2018*, Glasgow, 2018.

[24] Y. He, A. Hassanpour and A. Bayly, “Linking Particle Properties to Layer Characteristics: Discrete Element Modelling of Cohesive Fine Powder Spreading in Additive Manufacturing,” *Additive Manufacturing,* vol. 36, no. 1, pp. 101685-101680, 2020.

[25] A. Burgess, R. Dodd, M. Radwani, T. T. Opoz and S. Tammas-Williams, "The Effect of Surface Finish and Post-Processing on Mechanical Properties of 17-4 PH Stainless Steel Produced by the Atomic Diffusion Additive Manufacturing Process," *The International Journal of Advanced Manufacturing Technology ,* vol. 130, no. 1, p. 4053–4066, 2024.

[26] N. Béraud, F. Vignat, F. Villeneuve and R. Dendievel, "Improving Dimensional Accuracy in EBM using Beam Characterisation and Trajectory Optimisation," *Additive Manufacturing,* vol. 14, no. 1, pp. 1-6, 2017.

[27] S. Tammas-Williams, H. L. F. Zhao, F. Derguti, I. Todd and P. P.B, "XCT Analysis of the Influence of Melt Strategies on Defect Population in Ti–6Al–4V Components Manufactured by Selective Electron Beam Melting," *Materials Characterization,* vol. 102, no. 1, pp. 47-61, 2015.

[28] Q. Guo, C. Zhao, M. Qu, L. Xiong, L. Escano, S. Mohammad, H. Hojjatzadeh, N. Parab, K. Fezzaa, W. Everhart, T. Sun and L. Chen, "In-situ Characterization and Quantification of Melt Pool Variation under Constant Input Energy Density in Laser Powder Bed Fusion Additive Manufacturing Process," *Additive Manufacturing,* vol. 28, no. 1, pp. 600-609, 2019.

[29] X. Peng, L. Kong, J. Fuh and H. Wang, "A Review of Post-Processing Technologies in Additive Manufacturing," *Journal of Manufacturing and Materials Processes,* vol. 5, no. 2, pp. 1-23, 2021.

[30] A. Diniță, A. Neacșa, P. A.I, M. Tănase, C. Ilinca and I. and Ramadan, "Additive Manufacturing Post-Processing Treatments, a Review with Emphasis on Mechanical Characteristics," *Materials,* vol. 16, no. 13, pp. 4610-4701.

[31] I. Yadroitsev, Selective Laser Melting: Direct Manufacturing of 3D-Objects by Selective Laser Melting of Metal Powders, 2nd ed., Bloemfontein: LAP LAMBERT Academic Publishing, 2009.

[32] W. Nan and M. Ghadiri, "Numerical Simulation of Powder Flow during Spreading in Additive Manufacturing," *Powder Technology,* vol. 342, no. 1, pp. 801-807, 2019.

[33] P. Cundall and O. Strack, "Discrete Numerical Model for Granular Assemblies," *Géotechnique,* vol. 29, no. 1, pp. 47-65, 1979.

[34] G. de Josselin de Jong and A. Verruijt, "(Translated: French to English) Photo-Elastic Study of a Stack of Disks.," in *Soil Mechanics and Transport in Porous Media: Selected Works of G. De Josselin De Jong*, R. Schotting, C. Hans van Duijn and A. Verruijt, Eds., Utrecht, Springer, 2006.

[35] R. Kačianauskas, R. Balevičius, D. Markauskas and A. Maknickas, "Discrete Element Method in Simulation of Granular Materials," in *IUTAM Symposium on Multiscale Problems in Multibody System Contacts*, Stuttgart, 2007.

[36] P. Bhalode and M. Ierapetritou, "Multi-zonal Compartmentalization Methodology for Surrogate Modelling in Continuous Pharmaceutical Manufacturing," *Computer Aided Chemical Engineering,* vol. 50, no. 1, pp. 725-731, 2021.

[37] C. Wood, D. Sagzhanov and X. Li, "Distinct/Discrete Element Method," The University of Texas at Dallas, Dallas, 2011.

[38] H. Matuttis and J. Chen, Understanding the Discrete Element Method: Simulation of Non-Spherical Particles for Granular and Multi-Body Systems, 1st ed., Tokyo: John Wiley & Sons, 2014.

[39] A. López Marrero, “A New Simulation Tool For The Predictive Assessment of Fluidized and Circulatory Granular Flow Behaviour,” Liverpool John Moores University, Liverpool, 2020.

[40] J. Ahuir-Torres, X. Chen, Y. Akar, P. Bingham, F. Jackson, H. Li, L. Mason, R. Mishra, D. Walker and G. Yu, “Influence of the Grain Chemical Composition on the Fused Silica Polishing at Atomic Scale using Molecular Dynamic Simulations,” *Ceramics International,* vol. 51, no. 7, pp. 9278-9291, 2025.

[41] R. Berger, C. Kloss, A. Kohlmeyer and S. Pirker, “Hybrid Parallelisation of the LIGGGHTS Open-Source DEM Code,” *Powder Technology,* vol. 278, no. 1, pp. 234-247, 2015.

[42] P. Prokopovich and S. Perni, “Comparison of JKR- and DMT-based Multi-Asperity Adhesion Model: Theory and Experiment,” *Colloids and Surfaces A: Physicochemical and Engineering Aspects,* vol. 383, no. 1, pp. 95-101, 2011.

[43] S. Yim, J. Sun, K. Minowa, H. Wang, K. Aoyagi, Y. Yamanaka and A. Chiba, “In-situ Observation of Powder Spreading in Powder Bed Fusion Metal Additive Manufacturing Process using Particle Image Velocimetry,” *Additive Manufacturing,* vol. 78, no. 1, pp. 103823-103845, 2023.

[44] “https://www.ansys.com/en-gb/products,” Ansys, 2022 July 2022. [Online]. Available: https://www.ansys.com/en-gb/products/fluids/ansys-rocky. [Accessed 14 March 2025].

[45] V. Vidyapati and S. Subramaniam, “Granular Flow in Silo Discharge: Discrete Element Method Simulations and Model Assessment,” *Industrial & Engineering Chemistry Research,* vol. 52, no. 36, pp. 13171-13182 , 2013.

[46] S. Gatesy and P. Falkingham, “Hitchcock's Leptodactyli, Penetrative Tracks, and Dinosaur Footprint Diversity,” *Journal of Vertebrate Paleontology,* vol. 40, no. 3, pp. 1-18, 2020.

[47] D. C. GmbH, J. Linz and a. S. Corporation, “https://www.cfdem.com/media/DEM/docu/dump.html?highlight=dump,” DCS Computing GmbH; JKU Linz; and Sandia Corporation;, 15 January 2016. [Online]. Available: https://www.cfdem.com/media/DEM/docu/dump.html?highlight=dump. [Accessed 27 March 2023].

[48] Q. Wu, C. Qiao, J. Wang, D. Yao, Y. Wu, W. Fan, M. Li, An and X., “Adaptability Investigations on Bottom Modified Blade in Powder Spreading Process of Additive Manufacturing,” *Additive Manufacturing,* vol. 49, no. 1, pp. 1-13, 2021.

[49] E. Parteli and T. Pöschel, “Particle-Based Simulation of Powder Application in Additive Manufacturing,” *Powder Technology,* vol. 288, no. 1, pp. 96-102, 2016.

[50] H. Chen, T. Cheng, Q. Wei and W. Yan, “Dynamics of Short Fiber/Polymer Composite Particles in Paving Process of Additive Manufacturing,” *Additive Manufacturing,* vol. 47, no. 1, pp. 102246-102257, 2021.

[51] M. Markl and C. Körner, "Powder Layer Deposition Algorithm for Additive Manufacturing Simulations," *Powder Technology,* vol. 330, no. 1, pp. 125-136, 2018.

[52] G. Jacob, C. Brown and A. Donmez, "The Influence of Spreading Metal Powders with Different Particle Size Distributions on the Powder Bed Density in Laser-Based Powder Bed Fusion Processes," National Institution of Standards & Technology, Gaithersburg, 2018.

[53] D. Yao, J. Wang, M. Li, T. Zhao, Y. Cai, X. An, R. Zou, H. Zhang, H. Fu, X. Yang and Q. Zou, "Segregation of 316L Stainless Steel Powder during Spreading in Selective Laser Melting Based Additive Manufacturing," *Powder Technology,* vol. 397, no. 1, pp. 117096-117111, 2022.

[54] H. W. Mindt, M. Megahed, N. P. Lavery, M. Holmes and S. G. R. Brown, "Powder Bed Layer Characteristics: The Overseen First-Order Process Input," *Metallurgical and Materials Transactions A,* vol. 47, no. 1, p. 3811–3822, 2016.

[55] M. Sousani and S. Pantaleev, "Understanding Powder Behavior in an Additive Manufacturing Process Using DEM," *Processes,* vol. 10, no. 9, pp. 1-11, 2022.

[56] W. Richardson, *Neubeam: Metal AM without Compromise,* Huddersfield: Wayland Additive Ltd, 2021.

[57] C. Pirozzi, S. Franchitti, R. Borrelli, G. Diodati and G. Vattasso, "Experimental Study on the Porosity of Electron Beam Melting-Manufactured Ti6Al4V," *Journal of Materials Engineering and Performance,* vol. 28, no. 5, pp. 2649-2660, 2019.

[58] S. Sun, M. Brandt and M. Easton, Laser Additive Manufacturing: Materials, Design, Technologies, and Applications, Melbourne: Woodhead Publishing, 2017.

[59] J. Walker, J. Middendorf, C. Lesko and G. J, "Multi-material Laser Powder Bed Fusion Additive Manufacturing in 3-Dimensions," *Manufacturing Letters,* vol. 31, no. 1, pp. 74-77, 2022.

[60] A. Mussatto, "Research Progress in Multi-Material Laser-Powder Bed Fusion Additive Manufacturing: A Review of the State-of-the-Art Techniques for Depositing," *Results in Engineering,* vol. 16, no. 1, pp. 100769-100780, 2022.

[61] G. Liu, W. Xu, Q. Zhou and X. Zhang, "Contact Overlap Calculation Algorithms and Benchmarks Based on Blocky Discrete-Element Method," *International Journal of Geomechanics,* vol. 22, no. 12, pp. pp 1-14, 2022.

[62] F. Wu, Y. Fan, J. Chen and J. Wang, "Contrastive Study on the Granular Avalanche Dynamic Process Using the Depth-Integrated Continuum and Discrete Element Methods," *Bulletin of Engineering Geology and the Environment,* vol. 79, no. 1, p. 2815–2831, 2020.

[63] J. Zhang, Y. Tan, T. Bao, Y. Xu, X. Xiao and S. Jiang, "Discrete Element Simulation of the Effect of Roller-Spreading Parameters on Powder-Bed Density in Additive Manufacturing," *Materials,* vol. 13, no. 10, pp. 2285-2300, 2020.

[64] L. Del Cid, “https://lizidelcidphd.com/2016/09/12/the-hertzian-contact-stress-theory/,” 12 September 2016. [Online]. Available: https://lizidelcidphd.com/2016/09/12/the-hertzian-contact-stress-theory/. [Accessed 13 March 2023].

[65] Wikipedia, “https://en.wikipedia.org/wiki/Contact_mechanics,” 18 February 2023. [Online]. Available: https://en.wikipedia.org/wiki/Contact_mechanics. [Accessed 13 March 2023].

[66] Wikipedia, “https://en.wikipedia.org/wiki,” Wikipedia, 1 September 2023. [Online]. Available: https://en.wikipedia.org/wiki/Contact_mechanics. [Accessed 13 October 2023].

[67] L. Del Cid, “https://lizidelcidphd.com/2016/06/08/contact-area-of-particle-plane-impact/,” 8 June 2016. [Online]. Available: https://lizidelcidphd.com/2016/06/08/contact-area-of-particle-plane-impact/. [Accessed 15 March 2023].

[68] L. Del Cid, “https://lizidelcidphd.com/2016/11/21/the-johnson-kendall-roberts-model-for-cohesion/,” 21 November 2016. [Online]. Available: https://lizidelcidphd.com/2016/11/21/the-johnson-kendall-roberts-model-for-cohesion/. [Accessed 15 March 2023].

[69] K. Johnson, K. Kendall and R. A.D, “Surface Energy and the Contact of Elastic Solids,” *Proceedings of the Royal Society A,* vol. 324, no. 1558, pp. 301-313, 1971.

[70] L. Del Cid, “https://lizidelcidphd.com/2017/07/07/the-simplified-johnson-kendall-roberts-model/,” 7 July 2017. [Online]. Available: https://lizidelcidphd.com/2017/07/07/the-simplified-johnson-kendall-roberts-model/. [Accessed 21 March 2023].

[71] DCS Computing GmbH, JKU Linz and Sandia Corporation., “https://www.cfdem.com/media/DEM/docu,” DCS Computing GmbH, JKU Linz and Sandia Corporation., 17 January 2016. [Online]. Available: https://www.cfdem.com/media/DEM/docu/gran_cohesion_sjkr.html. [Accessed 22 March 2023].

[72] E. Weisstein, “https://mathworld.wolfram.com/Sphere-SphereIntersection.html,” Wolfram Alpha, 11 August 2007. [Online]. Available: https://mathworld.wolfram.com/Sphere-SphereIntersection.html. [Accessed 25 March 2023].

[73] C. Ramírez-Aragón, J. Ordieres-Meré, F. Alba-Elías and A. González-Marcos, “Comparison of Cohesive Models in EDEM and LIGGGHTS for Simulating Powder Compaction,” *Materials,* vol. 11, no. 11, pp. 1-17, 2018.

[74] Wayland Additive, “https://www.waylandadditive.com/wp-content,” 12 July 2021. [Online]. Available: https://www.waylandadditive.com/wp-content/uploads/2021/07/Technical-Specifications-FINAL-AW.pdf. [Accessed 24 October 2024].

[75] S. Geer, M. L. Bernhardt-Barry, E. Garboczi J, J. Whiting and A. Donmez, “A More Efficient Method for Calibrating Discrete Element Method Parameters for Simulations of Metallic Powder used in Additive Manufacturing,” *Granular Matter,* vol. 20, no. 4, pp. 1-17, 2018.

[76] Renishaw, “https://www.renishaw.com/en/,” 19 November 2023. [Online]. Available: https://www.renishaw.com/en/metal-additive-manufactured-parts-for-aircraft-assembly--44235. [Accessed 17 March 2025].

[77] Stratasys, “Flying High: BAE Systems Reduces Costs and Lead Times for Prototyping, Aircraft Tooling and Part Production with FDM Additive Manufacturing,” Stratasys, Eden Prairie, 2020.

[78] T. Stoll, P. S. S. Trautnitz, J. Franke and N. Travitzky, “Process Development for Laser Powder Bed Fusion of Pure Copper,” in *Proceedings Volume 11271, Laser 3D Manufacturing VII;* , San Francisco, 2020.

[79] E. Bojestig, Y. Cao and L. Nyborg, “Surface Chemical Analysis of Copper Powder Used in Additive Manufacturing,” *Surface and Interface Analysis,* vol. 52, no. 12, pp. 1104-1110, 2020.

[80] H. Wang, L. Chen, B. Dovgyy, W. Xu, A. Sha, X. Li, H. Tang, Y. Liu, H. Wu and P. M. , “Micro-cracking, Microstructure and Mechanical Properties of Hastelloy-X Alloy Printed by Laser Powder Bed Fusion: As-Built, Annealed and Hot-Isostatic Pressed,” *Additive Manufacturing,* vol. 39, no. 1, pp. 101853-101867, 2021.

[81] A. Lee, M. Wynn, L. Quigley, M. Salviato and N. Zobeiry, “Effect of Temperature History During Additive Manufacturing on Crystalline Morphology of Polyether Ether Ketone,” *Advances in Industrial and Manufacturing Engineering ,* vol. 4, no. 1, pp. 100085-100094, 2022.

[82] S. Singh, S. Ramakrishna, Singh and R, “Material Issues in Additive Manufacturing: A Review,” *Journal of Manufacturing Processes,* vol. 25, no. 1, pp. 185-200, 2017.

[83] H. Kalami and J. Urbanic, “Exploration of Surface Roughness Measurement Solutions for Additive Manufactured Components Built by Multi-Axis Tool Paths,” *Additive Manufacturing,* vol. 38, no. 1, pp. 101822-101842, 2021.

[84] A. Drégelyi-Kiss and A. Horváth, “Investigations on the Accuracy of Additive and Conventional Manufacturing,” in *IOP Conference Series: Materials Science and Engineering*, Budapest, 2018.

[85] M. Islam, B. Boswell and A. Pramanik, “An Investigation of Dimensional Accuracy of Parts Produced by Three-Dimensional Printing,” in *Proceedings of the World Congress on Engineering 2*, London, 2013.

[86] S. Roy, Weinhart and T, “The Role of Granular Matter in Additive Manufacturing,” *Granular Matter,* vol. 26, no. 102, pp. 1-4, 2024.

[87] M. Trovato, F. Perquoti and P. Cicconi, “Topological Optimization for the Redesigning of Components in Additive Manufacturing: The Case Study of the Connecting Rod,” in *Proceedings of The 4th International Electronic Conference on Applied Sciences*, Rome, 2023.

[88] T. Vialiva, “https://3dprintingindustry.com/news,” 18 October 2018. [Online]. Available: https://3dprintingindustry.com/news/criq-uses-ge-additive-arcam-ebm-machine-to-develop-3d-printed-maxillofacial-implants-142053/. [Accessed 21 January 2025].

[89] J. Kowen, "https://www.metal-am.com/articles," 15 July 2020. [Online]. Available: https://www.metal-am.com/articles/unrealised-potential-the-story-and-status-of-electron-beam-powder-bed-fusion-3d-printing/. [Accessed 21 January 2025].

[90] GE Aviation, *The GE9X Engine: Explore The World's Largest Jet Engine,* GE Aviation.

[91] C. Amin, O. Talukder and S. M. G. Mostafa, "Analysis of Performance and Environmental Impact of Hydrogen Fuel in Aviation: A Case Study of the Ge9x Engine," Social Science Research Network, Chittagong, 2025.

[92] H. Chen, Q. Wei, Y. Zhang, F. Chen, Y. Shi and W. Yan, "Powder-Spreading Mechanisms in Powder-Bed-based Additive Manufacturing: Experiments and Computational Modeling," *Acta Materialia,* vol. 179, no. 1, pp. 158-171, 2019.

[93] C. Meier, R. Weissbach, J. Weinberg, W. Wall and A. Hart, "Critical Influences of Particle Size and Adhesion on The Powder Layer Uniformity in Metal Additive Manufacturing," *Journal of Materials Processing Technology,* vol. 266, no. 1, pp. 484-501, 2019.

[94] A. Crouter and L. Briens, "The Effect of Moisture on the Flowability of Pharmaceutical Excipients," *AAPS PharmSciTech,* vol. 15, no. 1, pp. 65-74, 2014.

[95] S. Negi, A. Nambolan, S. Kapil, P. Joshi, R. Manivannan, K. Karunakaran and P. Bhargava, "Review On Electron Beam Melting Additive Manufacturing," *Rapid Prototyping Journal,* vol. 26, no. 3, pp. 485-498, 2020.

[96] J. Zhang, Y. Tan, X. Xiao and S. Jiang, "Comparison of Roller-Spreading and Blade-Spreading Processes in Powder-Bed Additive Manufacturing by DEM Simulations," *Particuology,* vol. 66, no. 1, pp. 48-58, 2022.

[97] S. Tammas-Williams, *Powder Bed Fusion,* Liverpool: Liverpool John Moores University, 2019.

[98] W. Nan, P. M, T. Bonakdar, A. Lopez, U. Zafar, S. Nadimi and M. Ghadiri, "Jamming During Particle Spreading in Additive Manufacturing," *Powder Technology,* vol. 338, no. 1, pp. 253-262, 2018.

[99] I. Gibson and D. Shi, "Material Properties and Fabrication Parameters in Selective Laser Sintering Process," *Rapid Prototyping Journal,* vol. 3, no. 4, pp. 129-136, 1997.

[100] R. Goodridge, K. Dalgarno and D. Wood, "Indirect Selective Laser Sintering of an Apatite-Mullite Glass-Ceramic for potential Use in Bone Replacement Applications," *Proceedings of the Institution of Mechanical Engineers, Part H: Journal of Engineering in Medicine,* vol. 220, no. 1, pp. 57-68, 2006.

[101] A. Mussatto, R. Groarke, A. O'Neill, M. Obeidi, Y. Delaure and D. Brabazon, "Influences of Powder Morphology and Spreading Parameters on the Powder Bed Topography Uniformity in Powder Bed Fusion Metal Additive Manufacturing," *Additive Manufacturing,* vol. 38, no. 1, pp. 101807-101818, 2021.

[102] S. Ziegelmeier, P. Christou, F. Wöllecke, C. Tuck, R. Goodridge, R. Hague, E. Krampe and E. Wintermantel, "An Experimental Study into the Effects of Bulk and Flow Behaviour of Laser Sintering

Polymer Powders on Resulting Part Properties," *Journal of Materials Processing Technology,* vol. 215, no. 1, pp. 239-250, 2015.

[103] M. Ahmed, M. Pasha, W. Nan and M. Ghadiri, "A Simple Method for Assessing Powder Spreadability for Additive Manufacturing," *Powder Technology,* vol. 367, no. 1, pp. 671-679, 2020.

[104] A. Boschetto, L. Bottini and S. Vatanparast, "Summary of Powder Bed Monitoring via Digital Image Analysis in Additive Manufacturing," *Journal of Intelligent Manufacturing ,* vol. 35, no. 1, p. 991–1011, 2024.

[105] British Standards Institution, *BS ISO 9276-1:1998,* London: British Standards Institution, 1998.

[106] A. Shaji Karapuzha, D. Fraser, D. Schliephake, S. Dietrich, Y. Zhu, X. Wu and A. Huang, "Microstructure, Mechanical Behaviour and Strengthening Mechanisms in Hastelloy X Manufactured by Electron Beam and Laser Beam Powder Bed Fusion," *Journal of Alloys and Compounds,* vol. 862, no. 1, 2021.

[107] Q. Nguyen, M. Nai, Z. Zhu, C. Sun, J. Wei and W. Zhou, "Characteristics of Inconel Powders for Powder-Bed Additive Manufacturing," *Engineering,* vol. 3, no. 5, pp. 695-700, 2017.

[108] C. Woodcock and J. Mason, Bulk Solids Handling: An Introduction to the Practice and Technology, 1st ed., Glasgow: Springer, 1987.

[109] X. Sun, Y. Zhiang, J. Li, N. Aslam, H. Sun, J. Zhao, Z. Wu and S. He, "Effects of Particle Size on Physicochemical and Functional Properties of Superfine Black Kidney Bean (Phaseolus vulgaris. L) Powder," *PeerJ,* vol. 7, no. 1, pp. e6369-6390, 2019.

[110] E. Bassoli and L. Denti, "Assay of Secondary Anisotropy in Additively Manufactured Alloys for Dental Applications," *Materials,* vol. 11, no. 10, pp. 1831-1846, 2018.

[111] J. He, D. Li, W. Jiang, L. Ke, G. Qin, Y. Ye, Q. Qin and D. Qiu, "The Martensitic Transformation and Mechanical Properties of Ti6Al4V Prepared via Selective Laser Melting," *Materials,* vol. 12, no. 2, pp. 321-335, 2019.

[112] A. Agrawal and A. Satapathy, "Effects of Aluminium Nitride Inclusions on Thermal and Electrical Properties of Epoxy and Polypropylene: An Experimental Investigation," *Composites Part A: Applied Science and Manufacturing,* vol. 63, no. 1, pp. 51-58, 2014.

[113] N. Ural, "The Importance of Clay in Geotechnical Engineering," in *Current Topics in the Utilization of Clay in Industrial and Medical Applications*, Bilecik, IntechOpen, 2018.

[114] Health and Safety Executive, "https://www.hse.gov.uk/asbestos/," Health and Safety Executive, 22 May 2020. [Online]. Available: https://www.hse.gov.uk/asbestos/. [Accessed 25 March 2021].

[115] Themofisher Scientific, "https://www.thermofisher.com/uk/en/home," 13 March 2022. [Online]. Available: https://www.thermofisher.com/uk/en/home/materials-science/learning-center/applications/sem-resolution.html. [Accessed 28 March 2025].

[116] Y. Lee, A. Kate Gurnon, D. Bodner and S. Simunovic, “Effect of Particle Spreading Dynamics on Powder Bed Quality in Metal Additive Manufacturing,” *Integrating Materials and Manufacturing Innovation,* vol. 9, no. 1, pp. 410-422, 2020.

[117] U. Habiba and R. Herbert, “Powder Spreading Mechanism in Laser Powder Bed Fusion Additive Manufacturing: Experiments and Computational Approach using Discrete Element Method,” *Materials,* vol. 16, no. 1, pp. 2824-2844, 2023.

[118] O. Kovalev, A. Gusarov and V. Belyaev, “Morphology of Random Packing of Micro-Particles and its Effect on the Absorption of Laser Radiation during Selective Melting of Powders,” *International Journal of Engineering Science,* vol. 157, no. 1, pp. 103378-103396, 2020.

[119] L. Cao, “Numerical Simulation of the Impact of Laying Powder on Selective Laser Melting Single-Pass Formation,” *International Journal of Heat and Mass Transfer,* vol. 141, pp. 1036-1048, 2019.

[120] L. Wang, E. Li, H. Shen, R. Zou, A. Yu and Z. Zhou, “Adhesion Effects on Spreading of Metal Powders in Selective Laser Melting,” *Powder Technology,* vol. 363, no. 1, pp. 602-610, 2020.

[121] J. Muñiz-Lerma, A. Nommeots-Nomm, K. Waters and M. Brochu, “A Comprehensive Approach to Powder Feedstock Characterization for Powder Bed Fusion Additive Manufacturing: A Case Study on AlSi7Mg,” *Materials,* vol. 11, no. 12, pp. 2386-2401, 2018.

[122] B. Liu, R. Wildman, C. Tuck, I. Ashcroft and R. Hague, “Investigation the Effect of Particle Size Distribution on Processing Parameters Optimisation in Selective Laser Melting Process,” Loughborough University, Loughborough, 2011.

[123] V. Seyda, D. Herzog and C. Emmelman, “Relationship between Powder Characteristics and Part Properties in Laser Beam Melting of Ti–6Al–4V, and Implications on Quality,” *Journal of Laser Applications,* vol. 29, no. 2, p. 022311, 2017.

[124] R. Baitimerov, P. Lykov, D. Zherebtsov, L. Radionova, A. Shultc and K. Gokuldoss-Prashanth, “Influence of Powder Characteristics on Processability of AlSi12 Alloy Fabricated by Selective Laser Melting,” *Materials,* vol. 11, no. 5, pp. 742-756, 2018.

[125] H. Jaeger and S. Nagel, “Physics of the Granular State,” *Science,* vol. 255, no. 5051, pp. 1523-1531, 1992.

[126] P. Kiani, U. Bertoli, A. Dupuy, K. Ma and J. Schoenung, “A Statistical Analysis of Powder Flowability in Metal Additive Manufacturing,” *Advanced Engineering Materials,* vol. 22, no. 10, pp. 1-6, 2020.

[127] A. Amado, M. Schmid, L. G. and L. Wegener, “Advances in SLS Powder Characterization,” in *Proceedings of the International Solid Freeform Fabrication Symposium*, Austin, 2011.

[128] A. Spierings, M. Voegtlin, T. Bauer and K. Wegener, “Powder Flowability Characterisation Methodology for Powder-Bed-Based Metal Additive Manufacturing,” *Progress in Additive Manufacturing,* vol. 1, no. 1, pp. 9-20, 2016.

[129] Mercury Scientific Inc., "http://www.mercuryscientific.com," Mercury Scientific Inc., 1 March 2008. [Online]. Available: http://www.mercuryscientific.com/instruments/revolution-powder-analyzer. [Accessed 12 April 2021].

[130] Z. Zatloukal, "Effect of Fractal Dimensions of Powdered Pharmaceutical Aids on their Flow Rate," *Ceska a Slovenska Farmacie,* vol. 51, no. 5, pp. 236-239, 12107816 2002.

[131] A. Mihranyan and M. Strømme, "Fractal Aspects of Powder Flow and Densification," *Particle and Particle Systems Characterisation,* vol. 24, no. 3, pp. 223-228, 1521-4117 2007.

[132] D. Schulze, Powders and Bulk Solids: Behavior, Characterization, Storage and Flow, 1st ed., Berlin: Springer, 2008.

[133] Y. Qiu, Developing Solid Oral Dosage Forms: Pharmaceutical Theory and Practice, 1st ed., Y. Chen, G. Zhang, L. Yu and R. Mantri, Eds., Chicago: Academic Press, 2016.

[134] T. Hao, "Understanding Empirical Powder Flowability Criteria Scaled by Hausner Ratio or Carr Index with the Analogous Viscosity Concept," *RSC Advances,* vol. 5, no. 70, pp. 57212-57215, 2015.

[135] J. Cain, "An Alternative Technique for Determining ANSI/CEMA Standard 550 Flowability Ratings for Granular Materials," *Powder Handling and Processing,* vol. 14, no. 3, pp. 218-220, 2002.

[136] PowderProcess.Net, "https://powderprocess.net/Powder_Flow," Powder Process, 30 June 2021. [Online]. Available: https://powderprocess.net/Powder_Flow/Carr_Index_Hausner_Ratio.html. [Accessed 19 July 2021].

[137] E. Abdullah and D. Geldart, "The Use of Bulk Density Measurements as Flowability Indicators," *Powder Technology,* vol. 102, no. 2, pp. 151-165, 1999.

[138] J. Soh, C. Liew and P. Heng, "New Indices to Characterize Powder Flow Based on Their Avalanching Behaviour," *Pharmaceutical Development and Technology,* vol. 11, no. 1, pp. 93-102, 2006.

[139] D. Sharma and A. Lanjewar, "Optimization and Evaluation of Ibuprofen Tablets by MADG Method," *PharmaTutor,* vol. 6, no. 1, pp. 56-71, 2018.

[140] G. Lumay, F. Boschini, K. Traina, S. Bontempi, J. Remy, R. Cloots and N. Vandewalle, "Measuring the Flowing Properties of Powders and Grains," *Powder Technology,* vol. 224, no. 1, pp. 19-27, 2012.

[141] M. Šimek, V. Grünwaldová and B. Kratochvíl, "Comparison of Compression and Material Properties of Differently Shaped and Sized Paracetamols," *KONA Powder and Particle,* vol. 34, no. 1, pp. 197-206, 2017.

[142] J. Clayton, D. Millington-Smith and B. Armstrong, "The Application of Powder Rheology in Additive Manufacturing," *The Journal of The Minerals, Metals & Materials Society,* vol. 67, no. 1, p. 544–548, 2015.

[143] ASTM International, *F3049-14: Standard Guide for Characterizing Properties of Metal Powders used for Additive Manufacturing Processes.,* vol. 1, West Conshohocken: ASTM Recommended: ASTM_International (2014) ASTM F3049-14, 2014.

[144] G. Shanbhag and M. Vlasea, "Powder Reuse Cycles in Electron Beam Powder Bed Fusion - Variation of Powder Characteristics," *Materials,* vol. 14, no. 16, pp. 4602-4621, 2021.

[145] Carpenter Additive, "https://www.carpenteradditive.com/news-events," Carpenter Additive, 11 January 2016. [Online]. Available: https://www.carpenteradditive.com/news-events/news/lpw-launches-new-product-line-powderflow. [Accessed 8 June 2021].

[146] L. Murr, E. Martinez, K. Amato, S. Gaytan, J. Hernandez, D. Ramirez, P. Shindo, F. Medina and R. Wicker, "Fabrication of Metal and Alloy Components by Additive Manufacturing: Examples of 3D Materials Science," *Journal of Materials Research and Technology,* vol. 1, no. 1, pp. 42-54, 2012.

[147] X. Gong, T. Anderson and K. Chou, "Review on Powder-Based Electron Beam Additive Manufacturing.," *Manufacturing Review,* vol. 1, no. 2, pp. 1-12, 2014.

[148] C. Leung, R. Tosi, E. Muzangaza, S. Nonni, P. Withers and P. Lee, "Effect of Preheating on the Thermal, Microstructural and Mechanical Properties of Selective Electron Beam Melted Ti-6Al-4V Components.," *Materials & Design,* vol. 174, no. 107792, pp. 1-10, 2019.

[149] E. Landau, E. Tiferet, Y. Ganor, R. Ganeriwala, M. Matthews, D. Braun, M. Chonin and G. Ziskind, "Thermal Characterization of the Build Chamber in Electron Beam Melting," *Additive Manufacturing,* vol. 36, no. 101535, 2020.

[150] C. Smith, F. Derguti, E. Hernandez Nava, M. Thomas, S. Tammas-Williams, S. Gulizia, D. Fraser and I. Todd, "Dimensional Accuracy of Electron Beam Melting (EBM) Additive Manufacture with Regard to Weight Optimized Truss Structures," *Journal of Materials Processing Technology,* vol. 229, no. 1, pp. 128-138, 2016.

[151] L. Murr and S. Gaytan, "Comprehensive Materials Processing," in *978-0-08-096533-8*, 1st ed., vol. 10, El Paso, Elsevier, 2014, pp. 135-161.

[152] GE Additive, *Arcam EBM A2X,* Mölndal: GE Additive, 2017.

[153] B. Wysocki, P. Maj, R. Sitek, J. Buhagiar, K. Kurzydłowsk and W. Swieszkowski, "Laser and Electron Beam Additive Manufacturing Methods of Fabricating Titanium Bone Implants," *Applied Sciences,* vol. 7, no. 7, pp. 657-677, 2017.

[154] M. Galati and L. Iuliano, "A Literature Review of Powder-Based Electron Beam Melting Focusing on Numerical Simulations," *Additive Manufacturing,* vol. 19, no. 1, pp. 1-20, 2018.

[155] J. Bruno, A. Rochman and G. Cassar, "Effect of Build Orientation of Electron Beam Melting on Microstructure and Mechanical Properties of Ti-6Al-4V," *Journal of Materials Engineering and Performance,* vol. 26, no. 2, pp. 692-703, 2017.

[156] G. del Sorbio, "GranuDrum: The New Powder Flow Rheometer. Cohesion, Dynamic Angle of Repose, Aeration, and Thixotropy.," Granutools, Awans, 2022.

[157] W. Yuan, H. Chen, S. Ruan, R. Lupoi, S. Qin, E. Guo, J. Wang and S. Yin, "Oscillatory Nature in Melt-Gas-Powder Interactions during Laser Powder Bed Fusion Process Revealed by CFD-DEM Coupled Modelling," *Virtual and Physical Prototyping,* vol. 20, no. 1, pp. 1-24, 2024.

[158] G. Parivendhan, P. Cardiff, T. Flint, Z. Tuković, M. Obeidi, D. Brabazon and A. Ivanković, "A Numerical Study of Processing Parameters and their Effect on the Melt-Track Profile in Laser Powder Bed Fusion Processes," *Additive Manufacturing,* vol. 67, no. 1, pp. 103482-103495, 2023.

[159] N. Aminnia, B. Peters and A. Donoso, "Multi-Scale Modeling of Melt Pool Formation and Solidification in Powder Bed Fusion: A Fully Coupled Computational Fluid Dynamics-Extended Discrete Element Method Approach," University of Luxembourg, Esch-sur-Alzette, 2023.

[160] A. Nouri and A. Sola, "Electron Beam Melting in Biomedical Manufacturing," in *Metallic Biomaterials Processing and Medical Device Manufacturing*, 1st ed., Tehran, Woodhead Publishing, 2020, pp. 271-314.

[161] D. Powell, A. Rennie, L. Geekie and N. Burns, "Understanding Powder Degradation in Metal Additive Manufacturing to Allow the Upcycling of Recycled Powders," *Journal of Cleaner Production,* vol. 268, no. 1, pp. 122077-122092, 2020.

[162] J. Dawes, R. Bowerman and R. Trepleton, "Introduction to the Additive Manufacturing Powder Metallurgy Supply Chain," *Johnson Matthey Technology Review,* vol. 59, no. 3, pp. 243-256, 2015.

[163] Q. Chen, G. Guillemot, C. Gandin and M. Bellet, "Three-Dimensional Finite Element Thermomechanical Modeling of Additive Manufacturing by Selective Laser Melting for Ceramic Materials," *Additive Manufacturing,* vol. 16, no. 1, pp. 124-137, 2017.

[164] A. Kumar Mishra and A. Kumar, "Effect of Surface Morphology on the Melt Pool Geometry in Single Track Selective Laser Melting," *Materials Today: Proceedings,* vol. 27, no. 2, pp. 816-823, 2020.

[165] Z. Xiang, M. Zhang, R. Yan, Q. Yin and K. Zhang, "Powder-Spreading Dynamics and Packing Quality Improvement for Laser Powder Bed Fusion Additive Manufacturing," *Powder Technology,* vol. 389, no. 1, pp. 278-291, 2021.

[166] G. Strano, L. Hao, R. Everson and K. Evans, "Surface Roughness Analysis, Modelling and Prediction in Selective Laser Melting.," *Journal of Materials Processing Technology,* vol. 213, no. 4, pp. 589-597, 2013.

[167] K. Alrbaey, D. Wimpenny, R. Tosi, W. Manning and A. Moroz, "On Optimization of Surface Roughness of Selective Laser Melted Stainless Steel Parts: A Statistical Study," *Journal of Materials Engineering and Performance,* vol. 23, no. 1, pp. 2139-2148, 2014.

[168] A. Phua, P. Cook, C. Davies and G. Delaney, "Powder Spreading over Realistic Laser Melted Surfaces in Metal Additive Manufacturing," *Additive Manufacturing Letters,* vol. 3, no. 1, pp. 100039-100047, 2022.

[169] A. Townsend, N. Senin, L. Blunt, R. Leach and J. Taylor, “Surface Texture Metrology for Additive Manufacturing: A Review,” *Precision Engineering,* vol. 46, no. 1, pp. 34-47, 2016.

[170] P. Wang, M. Nai, X. Tan, G. Vastola, S. Raghavan, W. Sin, Q. Pei and J. Wei, “Recent Progress of Additive Manufactured Ti-6Al-4V by Electron Beam Melting,” *Solid Freeform Fabrication 2016: Proceedings of the 26th Annual International Solid Freeform Fabrication Symposium – An Additive Manufacturing Conference,* vol. 1, no. 1, pp. 691-705, 08-10 August 2016.

[171] L. Spitaels, E. Rivière-Lorphèvre, M. Cantero Díaz, J. Duquesnoy and F. Ducobu, “Surface Finishing of EBM Parts by (Electro-)Chemical Etching,” *Procedia CIRP,* vol. 108, no. 1, pp. 112-117, 2022.

[172] B. Vayssette, N. Saintier, C. Brugger, M. Elmay and P. Etienne, “Surface Roughness of Ti-6Al-4V Parts Obtained by SLM and EBM: Effect on the High Cycle Fatigue Life,” *Procedia Engineering,* vol. 213, no. 1, pp. 89-97, 2018.

[173] K. Chan, M. Koike, R. Mason and T. Okabe, “Fatigue Life of Titanium Alloys Fabricated by Additive Layer Manufacturing Techniques for Dental Implants,” *Metallurgical and Materials Transactions A,* vol. 44, no. 1, p. 1010–1022, 2013.

[174] Y. Ma, T. Evans, N. Phillips and N. Cunningham, “Numerical Simulation of the Effect of Fine Fraction on the Flowability of Powders in Additive Manufacturing,” *Powder Technology,* vol. 360, no. 1, pp. 608-621, 2020.

[175] Y. Lee, A. Gurnon, D. Bodner and S. Simunovic, “Effect of Particle Spreading Dynamics on Powder Bed Quality in Metal Additive Manufacturing,” *Integrating Materials and Manufacturing Innovation,* vol. 9, no. 1, pp. 1-25, 2020.

[176] E. Alizadeh, F. Bertrand and J. Chaouki, “Comparison of DEM results and Lagrangian Experimental Data for the Flow and Mixing of Granules in a Rotating Drum,” *AlCHe Journal,* vol. 60, no. 1, pp. 60-75, 2013.

[177] F. Gilabert, J. Roux and A. Castallanos, “Computer Simulation of Model Cohesive Powders: Influence of Assembling Procedure and Contact Laws on Low Consolidation States.,” *Physical Review E,* vol. 75, no. 1, pp. 011303-011334, 2007.

[178] K. Hanley and C. O'Sullivan, “Analytical Study of the Accuracy of Discrete Element Simulations,” *International Journal for Numerical Methods in Engineering,* vol. 109, no. 1, pp. 29-51, 2017.

[179] P. Cleary, “DEM Prediction of Industrial and Geophysical Particle Flows,” *Particuology,* vol. 8, no. 2, pp. 106-118, 2010.

[180] V. Lampitella, M. Trofa, A. Astarita and G. D'Avino, “Discrete Element Method Analysis of the Spreading Mechanism and Its Influence on Powder Bed Characteristics in Additive Manufacturing,” *Micromachines,* vol. 12, no. 4, pp. 392-406, 2021.

[181] H. Chen, Q. Wei, S. Wen, Z. Li and Y. Shi, “Flow Behaviour of Powder Particles in Layering Process of Selective Laser Melting: Numerical Modelling and Experimental Verification Based on Discrete

Element Method," *International Journal of Machine Tools and Manufacture ,* vol. 123, no. 1, pp. 146-159, 2017.

[182] D. Yao, J. Wang, M. Li, T. Zhao, Y. Cai, X. An, R. Zou, H. Zhang, H. Fu, X. Yang and Q. Zou, "Segregation of 316l Stainless Steel Powder during Spreading in Selective Laser Melting based Additive Manufacturing," *Powder Technology,* vol. 397, no. 1, pp. 117096-117111, 2022.

[183] Haynes International, "https://haynesintl.com/docs/default-source/pdfs/new-alloy-brochures/high-temperature-alloys/brochures," Haynes International, 22 April 2022. [Online]. Available: https://haynesintl.com/docs/default-source/pdfs/new-alloy-brochures/high-temperature-alloys/brochures/x-brochure.pdf?sfvrsn=15b829d4_40. [Accessed 7 May 2023].

[184] E. Sullivan, S. Hedås, M. Engström and G. Lindwall, "Effect of powder particle size distribution and contouring on build quality in electron beam powder bed fusion of a medium-C hot-work tool steel," *The International Journal of Advanced Manufacturing Technology,* vol. 128, no. 1, p. 2953–2967, 2023.

[185] G. Wang, C. Wang, M. Cai, X. Lin and J. Ye, "Influence of Scanning Speed on Spheroidisation Effect in Electron Beam Selective Melting," *Materials Today Communications,* vol. 41, no. 1, pp. 111004-111019, 2024.

[186] J. Karlsson, A. Snis, H. Engqvist and J. Lausmaa, "Characterisation and Comparison of Materials Produced by Electron Beam Melting (EBM) of Two Different Ti–6Al–4V Powder Fractions," *Journal of Materials Processing Technology,* vol. 213, no. 12, pp. 2109-2118, 2013.

[187] A. Strondl, L. O, B. H. and U. Ackelid, "Characterisation and Control of Powder Properties for Additive Manufacturing," *The Journal of The Minerals, Metals & Materials Society,* vol. 67, no. 3, p. 549–554, 2015.

[188] S. Yim, H. Bian, K. Aoyagi, K. Yamanaka and A. Chiba, "Spreading behavior of Ti-48Al-2Cr-2Nb Powders in Powder Bed Fusion Additive Manufacturing Process. Experimental and Discrete Element Method Study," *Additive Manufacturing,* vol. 49, no. 1, pp. 102489-102503, 2022.

[189] R. Lakraimi, H. Abouchadi, M. Taha Janan, M. Bounouib and H. Benakrach, "Thermal Modeling of Powder-Based Additive Manufacturing Processes Using the Discrete Element Method," in *Smart Mobility and Industrial Technologies: The Quality of Life in Sustainable Cities*, Salerno, 2024.

[190] Y. Zhao and J. Chew, "Effect of Lognormal Particle Size Distributions on Particle Spreading in Additive Manufacturing," *Advanced Powder Technology,* vol. 32, no. 4, pp. 1127-1144, 2021.

[191] A. Yu and J. Hall, "Packing of Fine Powders Subjected to Tapping," *Powder Technology,* vol. 78, no. 3, pp. 247-256, 1994.

[192] J. Visser, "Van der Waals and Other Cohesive Forces Affecting Powder Fluidization," *Powder Technology,* vol. 58, no. 1, pp. 1-10, 1989.

[193] M. Shaneen, A. Thornton, S. Luding and T. Weinhart, "The Influence of Material and Process Parameters on Powder Spreading in Additive Manufacturing," *Powder Technology,* vol. 383, no. 1, pp. 564-583, 2021.

[194] M. Rangapuram, S. Babalola, J. Newkirk, L. Bartlett, F. Liou, K. Chandrashekhara and S. Cluff, "Multiphysics Modeling and Experimental Validation of High-Strength Steel in Laser Powder Bed Fusion Process," *Progress in Additive Manufacturing,* vol. 9, no. 2, pp. 1-17, 2023.

[195] I. Yadroitsev, I. Yadroitsava, A. Du Plessis and E. MacDonald, Fundamentals of Laser Powder Bed Fusion of Metals, Bloemfontein: Elsevier, 2021.

[196] R. Baserinia, I. Sinka and P. Rajniak, "Vacuum Assisted Flow Initiation in Arching Powders," *Powder Technology,* vol. 301, no. 1, pp. 493-502, 2016.

[197] P. Carrion, A. Soltani-Tehrani, S. Thompson and N. Shamsaei, "Effect of Powder Degradation on the Fatigue Behavior of Additively Manufactured As-Built Ti-6Al-4V," in *Solid Freeform Fabrication 2018: Proceedings of the 29th Annual International Solid Freeform Fabrication Symposium*, Auburn, 2018.

[198] W. Yan, Y. Qian, W. Ma, B. S. Y. Zhou and F. Lin, "Modeling and Experimental Validation of the Electron Beam Selective Melting Process," *Engineering,* vol. 3, no. 5, pp. 701-707, 2017.

[199] T. Roessler and A. Katterfeld, "Scaling of the Angle of Repose Test and its Influence on the Calibration of DEM Parameters using Upscaled Particles," *Powder Technology,* vol. 330, no. 1, pp. 58-66, 2018.

[200] British Standards Institution, *Metallic powders – Determination of flow,* vol. 1, London: British Standards Institution, 2018, pp. 1-32.

[201] Thyssenkrupp Materials, "https://www.thyssenkrupp-materials.co.uk/stainless-steel-316l," Thyssenkrupp Materials, 15 11 2017. [Online]. Available: https://www.thyssenkrupp-materials.co.uk/stainless-steel-316l-14404.html. [Accessed 8 June 2022].

[202] S. Burns, P. Piiroinen and K. Hanley, "Critical Time Step for DEM Simulations of Dynamic Systems using a Hertzian Contact Model," *International Journal for Numerical Methods in Engineering,* vol. 119, no. 5, pp. 432-451, 2019.

[203] A. Grima and P. Wypych, "Investigation into Calibration of Discrete Element Model Parameters for Scale-Up and Validation of Particle–Structure Interactions under Impact Conditions," *Powder Technology,* vol. 212, no. 1, pp. 198-209, 2011.

[204] S. Karkala, N. Davis, C. Wassgren, Y. Shi, X. Liu, C. Riemann, G. Yacobian and R. Ramachandran, "Calibration of Discrete-Element-Method Parameters for Cohesive Materials Using Dynamic-Yield-Strength and Shear-Cell Experiments," *Processes,* vol. 7, no. 5, pp. 1-16, 2019.

[205] M. Marigo, "Discrete Element Method Modelling of Complex Granular Motion in Mixing Vessels: Evaluation and Validation," University of Birmingham, Birmingham, 2012.

[206] A. Materials, "https://www.azom.com/properties," AZO Materials, 13 September 2001. [Online]. Available: https://www.azom.com/article.aspx?ArticleID=863. [Accessed 22 August 2023].

[207] A. Jensen, K. Fraser and G. Laird, "Improving the Precision of Discrete Element Simulations through Calibration Models," in *Proceedings of the 13th International LS-DYNA Users Conference*, Detroit, 2014.

[208] Aspheryx, "https://www.cfdem.com/media," Aspheryx, 3 March 2016. [Online]. Available: https://www.cfdem.com/media/DEM/docu/units.html. [Accessed 24 August 2023].

[209] Y. Zhou, B. Wright, R. Wang, B. Xu and A. Yu, "Rolling Friction in the Dynamic Simulation of Sandpile Formation," *Physica A: Statistical Mechanics and its Applications,* vol. 269, no. 2-4, pp. 536-553, 1999.

[210] E. J. R. Parteli, J. Schmidt, B. C, W. K. W. Peukert and T. & Pöschel, "Attractive Particle Interaction Forces and Packing Density of Fine Glass Powders," *Scientific Reports,* vol. 4, no. 1, pp. 1-7, 2014.

[211] Aspheryx, "https://www.cfdem.com/forums," Aspheryx, 27 May 2019. [Online]. Available: https://www.cfdem.com/forums/cohesive-energy-density-0. [Accessed 9 May 2023].

[212] Aspheryx, "https://www.cfdem.com/forums," Aspheryx, 28 August 2012. [Online]. Available: https://www.cfdem.com/forums/references-values-cohesive-energy-density. [Accessed 9 May 2023].

[213] C. Kloss, "https://www.cfdem.com/forums," Aspheryx, 04 September 2013. [Online]. Available: https://www.cfdem.com/forums/cohesion-energy-density. [Accessed 23 August 2023].

[214] Granutools, "Correlations Between the Angle of Repose & Vertical Flow," Medical & Life Sciences, Awans, 2019.

[215] L. Escano, N. Parab, L. Xiong, Q. Guo, C. Zhao, K. Fezzaa, W. Everhart, T. Sun and L. Chen, "Revealing Particle-Scale Powder Spreading Dynamics in Powder-Bed-Based Additive Manufacturing Process by High-Speed X-Ray Imaging," *Scientific Reports,* vol. 8, no. 1, pp. 1-11, 2018.

[216] Dassault Systemes, "https://help.solidworks.com/2021/english/SolidWorks," 2015 November 2024. [Online]. Available: https://help.solidworks.com/2021/english/SolidWorks/sldworks/c_materials_overview.htm. [Accessed 26 April 2025].

[217] S. Derakhshani, D. Schitt and G. Lodewijks, "Calibrating the Microscopic Properties of Quartz Sand with Coupled CFD-DEM Framework," *Engineering Computations,* vol. 33, no. 4, pp. 1141-1160, 2016.

[218] H. Al-Hashemi and O. Al-Amoudi, "A Review on the Angle of Repose of Granular Materials," *Powder Technology,* vol. 330, no. 1, pp. 397-417, 2018.

[219] B. Abdelkrim and S. & Vaudreuil, "An Open-Source Discrete Element Model for SS316L Alloy Powder Characterisation Using a Virtual Hall-Flow Metre to Study the Flowability in Powder Bed Fusion Additive Manufacturing," in *Proceedings of CASICAM 2022*, Casablanca, 2023.

[220] S. Shenouda and A. Hoff, “Discrete Element Method Analysis for Metal Powders Used in Additive Manufacturing, and DEM Simulation Tutorial Using LIGGGHTS-PUBLIC.,” United States Department of Energy, Oak Ridge, 2020.

[221] G. Scott and D. Kilgour, “The Density of Random Close Packing of Spheres,” *Journal of Physics D: Applied Physics,* vol. 2, no. 6, pp. 863-866, 1969.

[222] P. Jalali and M. Li, “An Estimate of Random Close Packing Density in Monodisperse Hard Spheres,” *The Journal of Chemical Physics ,* vol. 120, no. 2, p. 1138–1139, 2004.

[223] DCS Computing GmbH; JKU Linz; and Sandia Corporation, “https://www.cfdem.com/media/DEM/,” DCS Computing GmbH, JKU Linz and Sandia Corporation, 2016. [Online]. Available: DCS Computing GmbH, JKU Linz and Sandia Corporation. [Accessed 10 January 2023].

[224] R. Crain, “https://www.astro.ljmu.ac.uk/prospero/docs,” Liverpool John Moores University, 12 February 2021. [Online]. Available: https://www.astro.ljmu.ac.uk/prospero/docs/prospero/welcome/. [Accessed 16 January 2023].

[225] The American Society of Mechanical Engineers, *Surface Texture (Surface Roughness, Waviness, and Lay),* New York: The American Society of Mechanical Engineers, 2019.

[226] K. Yuasa, M. Tagmami, M. Yonehara, T. Ikeshoji, K. Takeshita, H. Aoki and K. Kyogoku, “Influences of Powder Characteristics and Recoating Conditions on Surface Morphology of Powder Bed in Metal Additive Manufacturing,” *The International Journal of Advanced Manufacturing Technology,* vol. 115, no. 1, pp. 3919-3932, 2021.

[227] D. Nasato, M. Heinl, T. Hausotte and T. Pöschel, “Numerical and Experimental Study of the Powder Bed Characteristics in the Recoated Bed of the Additive Manufacturing Process,” in *International Conference on Particle-Based Methods*, Hannover, 2017.

[228] Z. Li and M. Miztuani, “Influence of Layer Thickness and Substrate Bed on the Void Fraction of Powder Layers for Laser Powder Bed Fusion,” *Powder Technology,* vol. 418, no. 1, pp. 118293 - 118304, 2023.

[229] P. Cook, A. Phua, C. Davies and G. Delaney, “Modelling the Influences of Powder Layer Depth and Particle Morphology on Powder Bed Fusion using a Coupled DEM-CFD Approach,” *Powder Technology,* vol. 429, no. 1, pp. 118927-118945, 2023.

[230] Y. Zhao, K. Aoyagi, K. Yamanaka and A. Chiba, “Processing Condition Dependency of Increased Layer Thickness on Surface Quality during Electron Beam Powder Bed Fusion,” *Journal of Materials Research and Technology,* vol. 26, no. 1, pp. 5264-5279, 2023.

[231] Y. Zhao, Y. Koizumi, K. Aoyagi, K. Yamanaka, Chibal and A, “Characterization of Powder Bed Generation in Electron Beam Additive Manufacturing by Discrete Element Method.,” in *Materials Today: Proceedings*, Novosibirsk, 2017.

[232] M. Thomas, G. Baxter and I. Todd, “Normalised Model-Based Processing Diagrams for Additive Layer Manufacture of Engineering Alloys,” *Acta Materialia,* vol. 108, no. 1, pp. 26-35, 2016.

[233] Y. Shi and Y. Zhang, "Simulation of Random Packing of Spherical Particles with Different Size Distributions," *Applied Physics A,* vol. 92, no. 1, pp. 621-626, 2008.

[234] L. Burtseva, B. Valdez Salas, R. Romero and F. Werner, "Multi-Sized Sphere Packings : Models and Recent Approaches," Autonomous University of Baja California, Tijuana, 2015.

[235] Y. Lee, P. Nandwana and W. & Zhang, "Dynamic Simulation of Powder Packing Structure for Powder Bed Additive Manufacturing," *International Journal of Advanced Manufacturing Technology ,* vol. 96, no. 1, p. 1507–1520, 2018.

[236] A. Stavrou, C. Hare, A. Hassanpour and C. Wu, "Investigation of Powder Flowability at Low Stresses by DEM Modelling," *Chemical Engineering Science,* vol. 211, no. 1, pp. 115307-115318, 2020.

[237] Croft Filters Ltd, *Gas Atomised 316L Stainless Steel LPBF Technical Data Sheet,* Warrington: Croft Filters Ltd, 2021.

[238] Carpenter Additive Ltd, *CT Powderrange SS 316L Technical Data Sheet,* Liverpool, 2020.

[239] M. Mehrabi, J. Gardy, F. Talebi, A. Farshchi, A. Hassanpour and A. Bayly, "An Investigation of the Effect of Powder Flowability on the Powder Spreading in Additive Manufacturing," *Powder Technology,* vol. 413, no. 1, pp. 117997-118010, 2023.

[240] Y. Zhao, Y. Cui, Y. Hasebe, H. Bian, K. Yamanaka, K. Aoyagi, T. Hagisawa and A. Chiba, "Controlling Factors Determining Flowability of Powders for Additive Manufacturing: A Combined Experimental and Simulation Study," *Powder Technology,* vol. 393, no. 1, pp. 482-493, 2021.

[241] S. Vock, B. Klöden, A. Kirchner, T. Weißgärber and B. Kieback, "Powders for Powder Bed Fusion: A Review," *Progress in Additive Manufacturing,* vol. 4, no. 4, p. 383–397, 2019.

[242] N. Sandler, K. Reiche, J. Heinämäki and J. Yliruusi, "Effect of Moisture on Powder Flow Properties of Theophylline," *Pharmaceutics,* vol. 2, no. 3, p. 275–290, 2010.

[243] D. Shah, K. Moravkar, D. Jha, V. Lonkar, P. Amin and S. Chalikwar, "A Concise Summary of Powder Processing Methodologies for Flow Enhancement," *Heliyon,* vol. 9, no. 6, pp. 1-17, 2023.

[244] Z. Liu, F. Muzzio and G. Callegari, "Powder Property Change after Passing through a Feeder: The Effect of Electrostatics on Powder Flow," *Powder Technology,* vol. 425, no. 1, pp. 118532-118543, 2023.

[245] T. Pongó, V. Stiga, J. Török, S. Lévay, B. Szabó, R. Stannarius, R. Hidalgo and T. Börzsönyi, "Flow in an Hourglass: Particle Friction and Stiffness Matter," *New Journal of Physics,* vol. 23, no. 1, pp. 1-17, 2021.

[246] L. Geekie, *Additive Manufacturing: Identifying and Gaining Value,* Liverpool: Croft Filters Ltd, 2019..

[247] L. Zhang, Y. Liu, S. Li and Y. Hao, "Additive Manufacturing of Titanium Alloys by Electron Beam Melting: A Review," *Advanced Engineering Materials,* vol. 20, no. 5, pp. 1-16, 2018.

[248] C. Li, Z. Liu, X. Fang and Y. Guo, "Residual Stress in Metal Additive Manufacturing," in *4th CIRP Conference on Surface Integrity (CSI 2018)*, Jaipur, 2018.

[249] I. Bij-Corral, A. Tejo-Otero and F. Fenollosa-Arté, "Development of AM Technologies for Metals in the Sector of Medical Implants," *Metals,* vol. 10, no. 5, pp. 1-31, 2020.

[250] S. Sing, J. An, W. Yeong and F. Wiria, "Laser and Electron-Beam Powder-Bed Additive Manufacturing of Metallic Implants: A Review on Processes, Materials and Designs," *Journal of Orthopaedic Research ,* vol. 34, no. 3, pp. 369-385, 2015.

[251] T. Ngo, A. Kashani, G. Imbalzano, K. Nguyen and D. Hui, "Additive Manufacturing (3D Printing): A Review of Materials, Methods, Applications and Challenges.," *Composites Part B: Engineering,* vol. 143, no. 1, pp. 172-196, 2018.

[252] P. Gokuldoss, S. Kolla and J. Eckert, "Additive Manufacturing Processes: Selective Laser Melting, Electron Beam Melting and Binder Jetting—Selection Guidelines," *Materials,* vol. 10, no. 6, 2017.

[253] M. Qian and F. Froes, Titanium Powder Metallurgy: Science, Technology and Applications, 1st ed., Melbourne: Elsevier, 2015.

[254] M. F. Zäh and S. Lutzmann, "Modelling and Simulation of Electron Beam Melting," *Production Engineering,* vol. 4, no. 1, 2010.

[255] L. Wang, A. Yu, E. Li, H. Shen and Z. Zhou, "Effects of Spreader Geometry on Powder Spreading Process in Powder Bed Additive Manufacturing," *Powder Technology,* vol. 384, no. 1, pp. 211-222, 2021.

Appendices

Appendix A: Advantages & Limitations of EBM

To identify what constitutes an improvement to EBM powder spreading, it is necessary to firstly identify the current advantages of an EBM approach that can be leveraged to support further optimisation, and the constraints for which solutions can be developed.

Advantages of EBM

Compared to traditional or subtractive manufacturing, a staple and key pitch of AM marketing strategies argues that EBM offers ‘complexity for free’ design solutions, implying that more sophisticated designs do not necessitate specialist tooling systems. Another advantage of generating parts using an EBM approach, and one that appears to be often overlooked in literature but has been identified by industrial consultation, is the ability to streamline assemblies by consolidating multiple components serving integrated functions to a single geometric structure. Thus, reducing the processing costs of the design build [246].

When considering the advantages of EBM in the context of AM, Zhang et al [247] and Li et al [248] note that the high temperatures within the powder bed reduces the residual stresses in the component. As Li et al suggest that residual stresses in metal AM components occur on account of the high temperature gradients and rapid subsequent cooling [248]. Consequently, this reduces the post-processing steps required as EBM parts can, theoretically, be installed without heat treatment methods [154]. This has the added advantage of reducing the likelihood of the part shrinking [249].

In addition to alleviating the residual stresses in the part, the previous benefits of the vacuum environment described in ***Subsection 3.4.1*** incurs an oxidation reduction compared to SLM processes, and thus provides a better protection against contamination. The dense powder packing of the components during the sintering phase is also proposed to reduce the number of structural supports required, enabling a greater freedom of design [249].

Limitations of EBM

The primary limitation of EBM, and the one which underpins the motivations of this study, is that it remains a developing technology along with other AM techniques. As the process is highly reliant on the charges of the electrons used as the melting medium, only conductive metals, such as Inconel® 718, SS316l, titanium alloys and alloys of cobalt and chrome, can be used. Processing non-conductive metals powders would repel the electron beam and give rise to the smoking effect described in ***Subsection 3.4.1***. A further limitation of EBM is in the acquisition of machinery. For SLM or FDM techniques, AM hardware can be procured from several manufacturers. Conversely, EBM machines have until recently only been available from ARCAM AB, highlighting that EBM is not an open process [250].

Compared to SLM, optimising EBM parameters is more difficult to achieve, further limiting the number of materials that can be used. Difficulty in introducing new materials is a common constraint in many categories of AM. This inhibits the adoption of the technique in various industries, and the further development of the process overall [251]. Additionally, EBM is a complex and comparatively slow process, increasing the cost of the produced parts for the end user [252]. One of the most expensive costs is in the powder material, providing yet further motivation to optimise flowability.

The economic impact of this work highlights the prospective financial benefits for industry. A key consideration for an AM enterprise, in their efforts to foster a strong customer base and attain a sustainable market share, is the ability to offer higher quality products and services to their clients at a lower price than competitors. Qian and Froes [253] discussed how the high cost of titanium powders in AM constrains the wider use of the material, and thus more efficient powder processing to lower this cost is one such avenue for the optimisation of EBM.

Theoretically, optimising powder flow and bed formation can generate significant savings for the manufacturing firm that may be passed on to the end user. For example, by reducing the amount of powder required for a given production run, decreasing the waste generated by improving the design builds, and reducing the auxiliary processing costs by optimising the AM system.

As Leung et al found [148], dimensional discrepancies between the CAD drawing and real part present another constraint of EBM. Gong et al [147] notes that these errors are usually far greater than for parts created with traditional manufacturing. This was corroborated by Negi et al [95], who remarked that the accuracy of EBM components is generally inferior to that of their conventionally manufactured counterparts, and that these disparities are exacerbated at decreasing design sizes.

Overall, literature suggests EBM is constrained by defects and inconsistent quality in the parts generated, dimensional inaccuracies, and a lack of understanding of the multi-physics powder flow behaviour due to the previous ‘black box’ nature of the process [254]. A clear area of research is presented by the latter topic.

Appendix B: Communications of Commercial Interests in the Project

RE: LIGGGHTS - Powder Characterisation

DB Declan Bourke <declan_bourke@fwmetals.com>
To Burgess, Andrew; Paul Healy

Start your reply all with: Sounds good. Sounds good, thanks! You're welcome. Feedback

Hi Andy,

Thanks for the very detailed follow up. It is definitely an area where there is gap in the research.

The LIGGGHTS model looks very interesting – we will take closer look and get back if we've any questions.

Thanks again

Best Regards,

Declan

From: Burgess, Andrew <A.Burgess@2016.ljmu.ac.uk>
Sent: Monday 25 July 2022 14:31
To: Paul Healy <Paul_Healy@fwmetals.com>; Declan Bourke <declan_bourke@fwmetals.com>
Subject: LIGGGHTS - Powder Characterisation

Hi Declan and Paul,

Apologies for the slight delay in sending this over, I have been gathering materials together and ran out of time last week.

Excellent to meet you both in Dublin, thank you for your kind welcome! I will return the favour should you find yourselves in Liverpool.

As promised, I have put together a handful of media demonstrating LIGGGHTS work and a brief presentation (6/7 slides) that I use to introduce my PhD project.

Figure 129 - Evidence of Commercial Interest in the Project from Fort Wayne Metals.

Re: Introduction - Smart Factory Expo

AA Anas Achouri <anas@donaa.ai>
To Burgess, Andrew

Reply Reply All Forward
Sun 21/11/2021 17:04

You replied to this message on 24/11/2021 14:15.
Click here to download pictures. To help protect your privacy, Outlook prevented automatic download of some pictures in this message.

Action Items Suggested Meetings Get more add-ins

Dear Andrew,

It was a pleasure to meet you too at the Smart Factory Expo, and thank you for the presentation.
Your PhD project is really interesting to me, and it seems to be aligned with our aim to enable error-free 3D printing.

Would you be available Friday 26th Nov at 10 am to discuss potential collaborations over Teams? I am also available on Wednesday 24th at 5.30 pm if that works.
Otherwise, feel free to let me know what time is best for you.

Kind regards,
Anas
--
Dr. Anas Achouri
Founder and CEO
Mobile: +447930524655
Email: anas@donaa.ai

On Mon, 15 Nov 2021 at 12:01, Burgess, Andrew <A.Burgess@2016.ljmu.ac.uk> wrote:

> Dear Anas,
>
> It was a pleasure to meet you at the Smart Factory Expo last week, I hope you enjoyed the event, and your time in Liverpool. I trust the city treated you well.
>
> I was very enthused to hear about your work at DONAA toward achieving error-free 3D printing, and would be eager to explore any opportunity for collaboration or further networking, possibly through an expo at my institution: Liverpool John Moores University, or in the work of my PhD project, should such an opportunity arise.
>
> To this end, I considered it correct to follow up with an email. As I provided a brief introduction to my field of research at the expo, I thought it would be a good idea to supplement this with the brief presentation attached, outlining the key points of my PhD.

Figure 130 - Evidence of Commercial Interest in the Project From DONAA.

RE: New Lead - Liverpool John Moores University

Giuseppe Del Sorbo <Giuseppe.DelSorbo@granutools.com>
To Burgess, Andrew

Reply Reply All Forward
Mon 22/08/2022 07:53

You replied to this message on 22/08/2022 13:11.

Hi Andy,
Sorry for the late reply but I took my time to go through your slides and have a look at the papers you sent.
I think your PhD is a super interesting project, which for sure will open many possibilities to you in the future.
From my side, I really hope we will find a way to collaborate together 😊
Next step I think is to check if your supervisor is interested.
In the meantime, we will keep in touch.

Have a nice day,
Giuseppe

Giuseppe Rosario Del Sorbo, Ph.D.
Sales Manager

GRANUTOOLS™
Rue Jean-Lambert Defrêne 107/3, 4340 AWANS, BELGIUM
Phone: +32 470 93 55 47
Giuseppe.DelSorbo@granutools.com

This email and any attachments are intended solely for the addressee(s) and may contain confidential and/or privileged information and may be legally protected from disclosure. If you are not the intended recipient of this message or their agent, or if this message has been addressed to you in error, please immediately alert the sender by reply email and then delete this message and any attachments. If you are not the intended recipient, you are hereby notified that any use, dissemination, copying, or storage of this message or its attachments is strictly prohibited.

From: Burgess, Andrew <A.Burgess@2016.ljmu.ac.uk>
Sent: Monday, 15 August 2022 17:52
To: Giuseppe Del Sorbo <Giuseppe.DelSorbo@granutools.com>
Subject: RE: New Lead - Liverpool John Moores University

Hi Giuseppe,

Many thanks for returning my email.

I would be delighted to share more about my PhD project with you! Thank you for your interest! If you would please see the attached (brief, 6-7 slides) presentation this should provide an insight to my project.

In terms of where the GranuDrum device and the associated experiments would fit into my research, the first chapter of my PhD thesis is likely to be on the topic of "Validation of the DEM approach for Powder Analysis", whereby (with your approval if all goes to plan, Non-Disclosure Agreements would not be a problem), a digital twin would be created within the LIGGGHTS system and the results compared to those generated in the GranuDrum.

Figure 131 - Evidence of Commercial Interest in the Project from Granutools.

Appendix C: Poppy Seeds Discharging from Cell

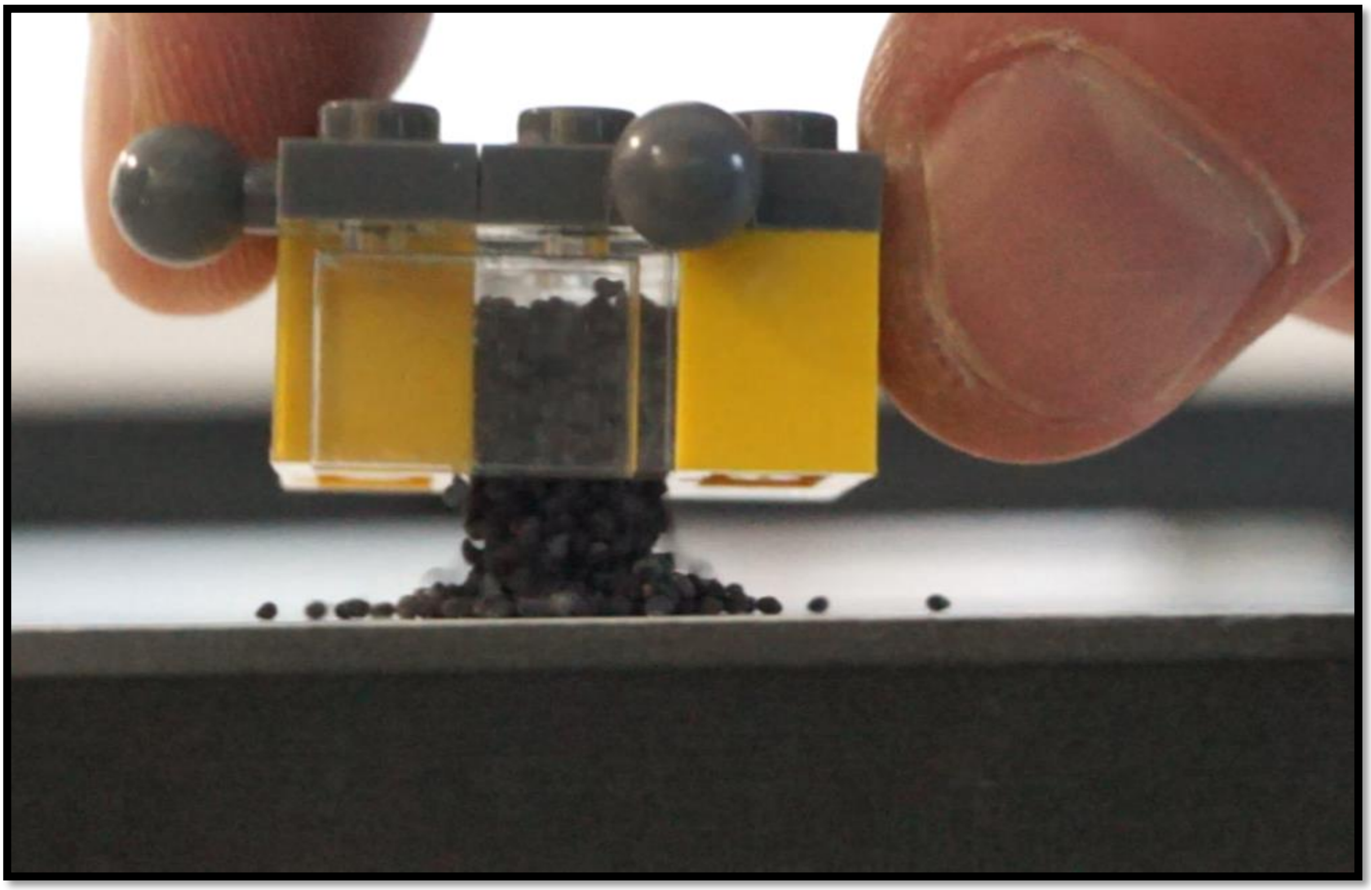

Figure 132 - Still Image of Poppy Seeds Discharging from a Cell in the Preliminary Testing of Granular Media.

Appendix D: Complete Results of Powder Discharge Time Testing with Hall Flow Meter

Table 71 to ***Table 74*** show the full results of the powder discharge time test with the HFM. In all cases, the discharge time is calculated as in ***Equation 62*** with 240 frames per second captured by the camera recording powder flow.

$$Powder\ Flow\ Rate = \frac{Final\ Frame\ of\ Flow - Start\ Frame\ of\ Flow}{Number\ of\ Frames\ per\ Second} = \frac{\Delta_{Frame}}{240}$$

Table 71 - Powder Discharge Time Test Results of 50g Mass Sample through the Hall Flow Meter.

Test	Required Tapping	Start Frame	End Frame	Δ_{Frame}	Discharge Time
1	N	10657	15362	4705	19.60416667
2	N	935	5651	4716	19.65
3	Y	5140	10020	4880	20.33333333
4	N	1070	5686	4616	19.23333333
5	N	820	5503	4683	19.5125

Table 72 - Powder Discharge Time Test Results of 25g Mass Sample through the Hall Flow Meter.

Test	Required Tapping	Start Frame	End Frame	Δ_{Frame}	Discharge Time
1	N	1620	3892	2272	9.466666667
2	N	1150	3412	2262	9.425
3	N	670	2928	2258	9.408333333
4	N	1130	3410	2280	9.5
5	N	1025	3347	2322	9.675

Table 73 - Powder Discharge Time Test Results of 12.5g Mass Sample through the Hall Flow Meter.

Test	Required Tapping	Start Frame	End Frame	Δ_{Frame}	Discharge Time
1	N	840	1945	1105	4.604166667
2	N	725	1860	1135	4.729166667
3	N	978	2082	1104	4.6
4	N	1059	2144	1085	4.520833333
5	Y	4926	6044	1118	4.658333333

Table 74 - Powder Discharge Time Test Results of 6.25g Mass Sample through the Hall Flow Meter.

Test	Required Tapping	Start Frame	End Frame	Δ_{Frame}	Discharge Time
1	N	794	1318	524	2.183333333
2	N	849	1373	524	2.183333333
3	N	1009	1557	548	2.283333333
4	N	781	1297	516	2.15
5	N	1111	1619	508	2.116666667

Appendix E: Angle of Repose Results for Powder Piles

Table 75 - Complete Angle of Repose Results for each Powder Pile in the Validation of LIGGGHTS®.

Stainless Steel 316l					
Mass	**Pile Height (mm)**	**Pile Diameter (mm)**	**Angle of Repose (rad)**	**Angle of Repose (º)**	**Average Angle of Repose (º)**
50 g					
1	15	47	0.568104732	32.55000349	
2	15	40	0.643501109	36.86989765	
3	18	45	0.674740942	38.65980825	36.0265698
25 g					
1	12	35	0.601073754	34.43898931	
2	13	35	0.638913985	36.60707481	
3	10	35	0.519146114	29.7448813	33.59698181
12.5 g					
1	9	27.5	0.579563985	33.20657032	
2	7	24	0.528074448	30.25643716	
3	10	25	0.674740942	38.65980825	34.04093858
6.25 g					
1	7	20	0.610725964	34.9920202	
2	8	22.5	0.618144226	35.41705528	
3	6	22	0.499346722	28.61045967	33.00651171

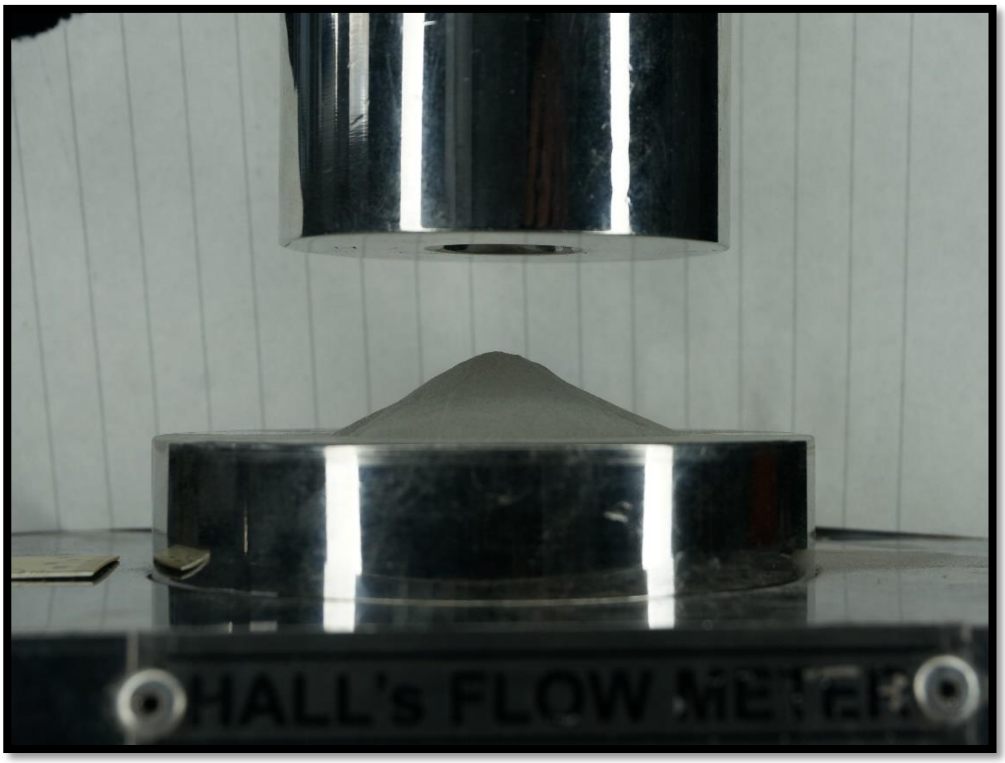

Figure 133 - Angle of Repose of 25g Sample of SS316l.

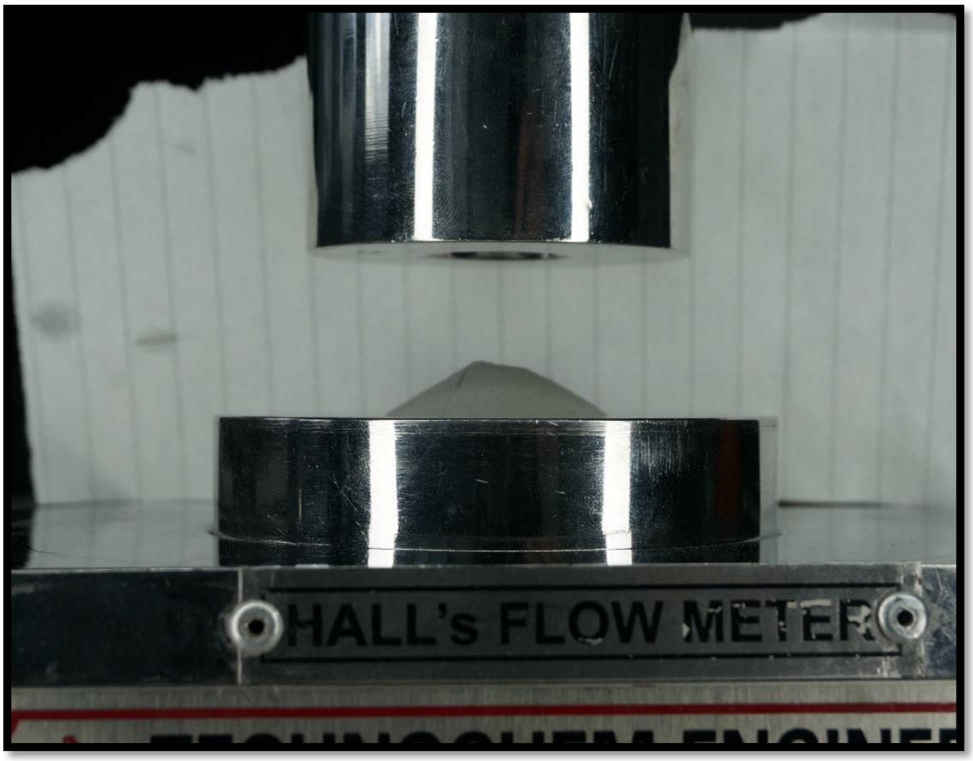

Figure 134 - Angle of Repose of 12.5g Sample of SS316l.

Figure 135 - Angle of Repose of 6.25g Sample of SS316l.

Appendix F: Complete Simulation Results Set for the Validation of LIGGGHTS®

Table 76 outlines the complete set of results for the AoR analysis of the models in LIGGGHTS®.

Table 76 - Complete Data Set for Calibrating Simulation Properties and Parameters to Validate LIGGGHTS.

Parameter Changed	Test (Number of particles)	Cohesion (P-W) ($\frac{\text{Dynes}}{cm^2}$)	Cohesion (P-P) ($\frac{\text{Dynes}}{cm^2}$)	Sliding Friction (P-W)	Sliding Friction (P-P)	Rolling Friction (Global)	Coefficient of Restitution	Platform	Angle of Repose	Commentary
Identical to source script provided (1).	0 (6500)	1×10^6	1×10^6	0.75	0.75	0.01	0.6	DESKTOP	6500 particles not enough.	Appears too cohesive.
Particle-Particle Cohesion.	1 (15000)	1×10^6	1×10^5	0.75	0.75	0.01	0.6	DESKTOP	Melted.	Does not pile up, not cohesive enough.
Particle-Particle Cohesion.	2 (15000)	1×10^6	5×10^5	0.75	0.75	0.01	0.6	DESKTOP	Did not stabilise.	Piles up then melts. Better, but probably still not cohesive enough.
Particle-Particle Cohesion.	3(15000)	1×10^6	7.5×10^5	0.75	0.75	0.01	0.6	DESKTOP	Too cohesive.	Still too cohesive, Piles up.
All the subsequent models use the properties of SS316l										
This model and the models after it now have the properties of SS316l as in the real-world experiments.	4 (2000)	1×10^6	1×10^6	0.75	0.75		0.2	DESKTOP	2000 particles not enough.	Real PSD. Timestep = 1 E-7. Seems to behave quite stable.
Particle-Particle Cohesion & Timestep.	5 (2000)	1×10^6	1×10^6	0.75	0.75		0.2	DESKTOP	Failed.	Real PSD. Timestep = 1 E-6. Catastrophic Failure. Timestep way too large.

All the subsequent models use the timestep of 1 E-7										
Particle-Particle Cohesion & Timestep.	6 (2000)	1×10^6	6×10^6	0.75	0.75	0.01	0.2	DESKTOP	2000 particles not enough.	Real PSD. Timestep = 1 E-7. Stable. All the following models have Timestep = 1 E-7.
Number of particles.	7 (20k)	1×10^6	6×10^6	0.75	0.75	0.01	0.2	DESKTOP	50.44º	Angle of Repose too high. 6 million is probably too cohesive.
Particle-Particle Cohesion.	8 (20k)	1×10^6	3×10^6	0.75	0.75	0.01	0.2	DESKTOP	22º	Angle of Repose is too low, perhaps between 3 million and 6 million is the correct value.
Particle-Particle Cohesion.	9 (20k)	1×10^6	5×10^5	0.75	0.75	0.01	0.2	DESKTOP	20.76º	Very little difference (less than 1.5º) is found between an Angle of Repose at CED = 500k and CED = 3 million.
Particle-Particle Cohesion.	10 (20k)	1×10^6	1.5×10^6	0.75	0.75	0.01	0.2	DESKTOP	20.49º	It seems there is a lower limit of the CED whereby the piling behaviour is unaffected.
Particle-Particle Cohesion.	11 (20k)	1×10^6	4×10^6	0.75	0.75	0.01	0.2	PROSPERO	25.11º	Piles up higher than at P-P CED = 3m.
Version 6 with periodic boundary and narrow domain.	12 (2k)	1×10^6	6×10^6	0.75	0.75	0.01	0.2	PROSPERO	2000 particles not enough. More inserted and modelled in V25	The periodic boundary seems to work and the particles do not disperse at a slice thickness of 1mm. The model was rerun with a slice thickness of 0.5mm and seemed to work also. The narrower domain reduced the insertion quantity.

Particle-Particle Cohesion Processor distribution.	13 (20k)	1×10^6	4.5×10^6	0.75	0.75	0.01	0.2	PROSPERO	28.29º	Piles up slightly higher than at P-P CED = 4m.
Particle-Particle Cohesion.	14 (20k)	1×10^6	5×10^6	0.75	0.75	0.01	0.2	PROSPERO	30.32º	Piles up slightly higher than at P-P CED = 4.5m.
Since there is seemingly no difference between the angle of repose formed at P-P CED = 0.5m to 3m, try CED P-P 3m with CED P-W = 6m (V15) and 3m (V16).										
V8 but with six times the P-W cohesion.	15 (20k)	6×10^6	3×10^6	0.75	0.75	0.01	0.2	PROSPERO	16.16º	Disperses out wider and does not pile up as high. It has a lower angle of repose than V8. On this evidence raising P-W CED lowers the angle of repose.
V8 but with three times the P-W cohesion.	16 (20k)	3×10^6	3×10^6	0.75	0.75	0.01	0.2	PROSPERO	23.2º	Lowering the P-W CED raises the angle of repose, confirming the above theory.
The following models use base cohesion values of 3m for both P-P and P-W and have P-P sliding friction at double (V17) and 10x (V18) the original values.										
V16 but with double the P-P sliding friction.	17 (20k)	3×10^6	3×10^6	0.75	1.5	0.01	0.2	PROSPERO	21.7º	Doubling the P-P sliding friction seems to make the pile slightly wider and slightly shorter.
V16 but with 10x the P-P sliding friction.	18 (20k)	3×10^6	3×10^6	0.75	7.5	0.01	0.2	PROSPERO	21.7º	The angle of repose is about the same, changing P-P sliding friction between 0.75 to 7.5 seems to make no difference. Make it dramatically bigger in V24.

The next model is V8 again but with P-W sliding friction changed to 10x higher.										
V8 but with 10 times the P-W Sliding Friction.	19 (20k)	1×10^6	3×10^6	7.5	0.75	0.01	0.2	PROSPERO	22.67º	The angle of repose is only marginally higher (0.67º) when the P-W friction is made 10 times greater.
The next model is V8 once more, but now with the P-P rolling friction set 10x higher.										
V8 but with 10 times the P-P Rolling Friction.	20 (20k)	1×10^6	3×10^6	0.75	0.75	0.01	0.2	PROSPERO	22.16º	Making the rolling friction 10x higher made no difference.
V7 had a known angle of repose but was too stumpy to establish whether this would pile up into a peak rather than a mound. The next model is V7 with 200k particles.										
V7 but with 10 times the number of particles.	21 (90k)	1×10^6	6×10^6	0.75	0.75	0.01	0.2	PROSPERO	Multiple scripts required.	Second Settle script queued on 2 nodes of Prospero.
V14 but with a slightly higher cohesion.	22 (20k)	1×10^6	5.5×10^6	0.75	0.75	0.01	0.2	PROSPERO	33.8º	Does not look unlike reality. Test this model with a cone geometry.
V22 but with 10k as many particles.	23 (200k)	1×10^6	5.5×10^6	0.75	0.75	0.01	0.2	PROSPERO	Still melting.	Melting effect when allowed to settle to account for the smaller timestep compared to micro models. Allow model 21 to run with a continuous settle script.
V18 but with very high P-P sliding friction = 50.	24 (20k)	3×10^6	3×10^6	0.75	50	0.01	0.2	PROSPERO	20.06º	3.5k particles disappeared at one stage. When the powder piled up it was smaller. Rebuild this into V26 with P-P sliding friction = 25.

The following simulation (V25) is V12 with 10x as many particles inserted and a slightly lower particle-particle CED.										
Version 12 with periodic boundary and narrow domain.	25 (20k)	1×10^6	5.5×10^6	0.75	0.75	0.01	0.2	PROSPERO	N/A	Local sliding causes it to disperse as in Phase 3 models.
The following simulation (V26) is V24 with P-P sliding friction halved.										
V24 but with half the P-P sliding friction = 25.	26 (20k)	3×10^6	3×10^6	0.75	25	0.01	0.2	PROSPERO	N/A	Unstable as in V24. 8000 particles inserted the model explodes and jettisons particles out.
The following simulation (V27) is V8 with P-W sliding friction set much higher.										
V25 but with sliding friction P-W = 25.	27 (20k)	1×10^6	3×10^6	25	0.75	0.01	0.2	PROSPERO	20.06º	Interestingly, this model does not explode. It seems to pile up so far then no higher. It is likely this is due to P-P CED rather than the sliding friction settings. The angle of repose is about the same regardless of what value is assigned to sliding friction.
V7 but set to run for longer.	28 (20k)	1×10^6	6×10^6	0.75	0.75	0.01	0.2	DESKTOP	50.44º	Angle of Repose too high. 6 million is probably too cohesive.

Appendix G: Scripts for Simulations

The text script below is a sample set-up script for the "***Effect of the Particle Size Distribution on the Surface Roughness, Solid Volume Fraction, and Segregation in the Powder Bed***" simulations. The sample script has been taken from Case Set 1, Model A. This was the first case to run on Prospero. All text that follows a hash symbol (#) is considered commentary and is not read as a command by LIGGGHTS®. Note that, due to the ability to set units in LIGGGHTS®, the units system may differ from the nomenclature of this report and thus they are stated in the script.

Set-up script.

```
#Case 1 - Model A - Uniform 40 µm Particles - set-up script.

#----------SET UP THE FOLDER FOR OUTPUT & PROCESSOR DISTRIBUTION----------#

shell mkdir output #Creates a folder for post-processing of the output files, named "output".

processors 64 2 2 #Defines the division of processors for the simulation domain.



#----------SYSTEM VARIABLES----------#

#These variables are adapted to define the properties of the particles/system.

variable    r equal 0.002       # 1st Radius of the particles (cm) #40 µm.

#variable   a equal 0.001       # 2nd Radius of the particles (cm) #20 µm.

#variable   b equal 0.0015      # 3rd Radius of the particles (cm) #30 µm.

####################################Properties to Control the Powder, Floor, and Angle of Repose##########################################
variable natoms equal 2 #1 -> particle #2->Inserted Geometries.
####variable for material properties####
####Young Modulus####
variable youngmodulus1 equal 1930000000 #Barye (=0.193 GPa, 3 orders lower than reality for SS316l).
variable youngmodulus2 equal 1930000000 #Barye (=0.193 GPa, 3 orders lower than reality for SS316l).

####Poission ratio####
variable poission1 equal 0.27
variable poission2 equal 0.27


####variable for contact properties####
####coefficient of restitution####
variable CoR11 equal 0.1
variable CoR12 equal 0.1
```

```
variable CoR21 equal 0.1
variable CoR22 equal 0.1
####sliding friction coefficient####
variable sf11 equal 0.75
variable sf12 equal 0.75
variable sf21 equal 0.75
variable sf22 equal 0.75

####rolling friction coefficient####
variable rf11 equal 0.01
variable rf12 equal 0.01
variable rf21 equal 0.01
variable rf22 equal 0.01


####Cohesion ####
variable coh11 equal 6000000
variable coh12 equal 1000000
variable coh21 equal 1000000
variable coh22 equal 1000000


#----------SIMULATION SETTINGS----------#
units      cgs        #CGS units enable smaller particles of the same size range used in an Electron Beam Melting system to be used.

atom_style granular

newton     off

boundary   f p f      #Fixed boundaries, this means the particles will be deleted if they leave the simulation box.

communicate single vel yes

############ Create Simulation Domain ############

region     simdomain block -0.0001 1.2001 -0.001 0.2001 0 0.35   units box #Block dimension arguments are given in the form of: xlo xhi ylo yhi zlo zhi.

create_box 1 simdomain

print "stop 1" #Print commands are written to isolate any errors in the script.

neighbor   $r bin #Governs neighbouring dynamic relationships between particles. Describes how the list of neighbouring particle interactions is compiled. The “rule of thumb” is that the neighbour should equal particle diameter.
```

```
neigh_modify every 1 delay 0 check yes #Determines how often the neighbouring lists are compiled, for example, delay 100 means "compile the list after the 100th time step". #Delay 0 means start instantly.

#----------MATERIAL PROPERTIES----------#

# These determine the behaviour of the simulation.

###################################Definition of Material properties#################################################
fix m1 all property/global youngsModulus peratomtype ${youngmodulus1} ${youngmodulus2}
fix m2 all property/global poissonsRatio peratomtype ${poission1} ${poission2}
fix m3 all property/global coefficientRestitution peratomtypepair ${natoms} 0.1 0.1 0.1 0.1
fix m4 all property/global coefficientFriction peratomtypepair ${natoms} ${sf11} ${sf12} ${sf21} ${sf22}
fix m5 all property/global coefficientRollingFriction peratomtypepair ${natoms} ${rf11} ${rf12} ${rf21} ${rf22}
fix m6 all property/global cohesionEnergyDensity peratomtypepair ${natoms} ${coh11} ${coh12} ${coh21} ${coh22}
#fix m7 all property/global characteristicVelocity scalar 24 #this property is only used with the hooke model, it does nothing in the hertz model.


#hard_particles yes #Command used to enable high values of Young's Modulus if required.

print "stop 2"

#----------FORCE MODEL----------#

#Takes the given material properties and applies them to all particles.

pair_style gran model hertz tangential history cohesion sjkr # hertzian with cohesion.

#Atom style is granular thus pair style is gran, model is the definer prior to hertz stiffness, hooke stiffness etc.

#Tangential means measure tangential forces, and history means retain the tangential forces measured.

pair_coeff * *          # applies this interaction to all particle pairs.

print "stop 3"

#----------PHYSICS SETTINGS----------#

fix    nparticles all nve/sphere #Fixes the ID chosen, nparticles. All means all spheres, nve means integrate the velocity and energy in the particle pack, and /sphere is the particle type.

#Initialise time integration.

fix    gravi all gravity 981 vector 0.0 0.0 -1.0   #Gravity as on Earth at 9.81 m/s^2 in negative Z.

timestep 1e-7
```

group nvegroup region simdomain #nvegroup is the ID (arbitrary), which should be set to region and the region ID.

print "stop 4"

#----------WALLS----------#

#Bounds the model with surfaces in the specified walls plane.

fix floor all wall/gran model hertz tangential history primitive type 1 zplane 0 #Adding a floor to the simulation to prevent particles falling out.

print "stop 5"

#----------GEOMETRY INSERTION----------#

#Imports all the STL files needed to create the geometries within the system.

fix Recoater1 all mesh/surface file Recoater.STL type 1 scale 1 move 0 0 0.075 curvature_tolerant yes

fix Buffers1 all mesh/surface file Buffers.STL type 1 scale 1 curvature_tolerant yes

fix cont1 all wall/gran model hertz tangential history mesh n_meshes 2 meshes Buffers1 Recoater1

print "stop 6"

#----------PARTICLE INSERTION----------#

insertdomain block 0.125 1.075 0.002 0.198 0.01 0.17

#Insert particles in this volume within the domain block.

#First 1/3rd of particles.

fix parttemp1 all particletemplate/sphere 290039 atom_type 1 density constant $d radius constant $r

#Second 1/3rd of particles – Input in a Polydisperse PSD only.

#fix parttemp2 all particletemplate/sphere 290021 atom_type 1 density constant 8 radius constant $a.

#Third 1/3rd – Input in a Polydisperse PSD only.

#fix parttemp3 all particletemplate/sphere 290023 atom_type 1 density constant 8 radius constant $b.

fix partdist all particledistribution/discrete 290041 1 parttemp1 1

#Final number is then_temp or the number of particle templates, “parttemp” is defined as the template the particles distribution is pulling it from.

```
print "stop 7"

fix particleinsert1 nvegroup insert/pack seed 290047 distributiontemplate partdist maxattempt 500
insert_every once overlapcheck yes all_in yes region insertdomain volumefraction_region 0.3 ntry_mc 5000

#Governs the insertion volume of the particles.

print "stop 8"

#----------RUNNING THE SIMULATION----------#

############ Dump Files and Run Command ############

dump        dmp all custom 500000 output/particles_*.txt id x y z radius

dump        dumpstl1 all mesh/vtk 500000 output/buffers_*.vtk id Buffers1

dump        dumpstl2 all mesh/vtk 500000 output/recoater_*.vtk id Recoater1

#Execute the script to run until particles are full and settled.

run 25000000

write_restart restart1.res

#End of Simulation.
```

Run script.

#Case 1 - Model A - Uniform 40 µm Particles - Run Script.

#----------SET UP THE FOLDER FOR OUTPUT & PROCESSOR DISTRIBUTION----------#

shell mkdir output #Adds the output files generated to the “output” folder created earlier.

processors 64 2 2 #Defines the division of processors for the simulation.

#----------SYSTEM VARIABLES----------#

#These variables are adapted to define the properties of the particles/system.

variable r equal 0.002 # 1st RADIUS of the particles (cm) #40 µm.

#variable a equal 0.001 # 2nd RADIUS of the particles (cm) #20 µm.

#variable b equal 0.0015 # 3rd RADIUS of the particles (cm) #30 µm.

###################################Definition of Material Properties##
fix m1 all property/global youngsModulus peratomtype ${youngmodulus1} ${youngmodulus2}
fix m2 all property/global poissonsRatio peratomtype ${poission1} ${poission2}
fix m3 all property/global coefficientRestitution peratomtypepair ${natoms} 0.1 0.1 0.1 0.1
fix m4 all property/global coefficientFriction peratomtypepair ${natoms} ${sf11} ${sf12} ${sf21} ${sf22}
fix m5 all property/global coefficientRollingFriction peratomtypepair ${natoms} ${rf11} ${rf12} ${rf21} ${rf22}
fix m6 all property/global cohesionEnergyDensity peratomtypepair ${natoms} ${coh11} ${coh12} ${coh21} ${coh22}
#fix m7 all property/global characteristicVelocity scalar 24 #this property is only used with the hooke model, it does nothing in the hertz model.

#----------SIMULATION SETTINGS----------#

units cgs #CGS units enable smaller particles of the same size range used in an Electron Beam Melting system to be used.

atom_style granular

newton off

boundary f p f #Fixed boundaries, particles will be deleted if they leave the simulation box.

communicate single vel yes

neighbor $r bin #Governs neighbouring dynamic relationships between particles. This describes how the list of neighbouring particle interactions is compiled. Rule of thumb is neighbour=particle diameter.

```
neigh_modify   every 1 delay 0 check yes #Determines how often the neighbouring lists are compiled, for example, delay 100 means "compile the list after the 100th time step". Delay 0 means start instantly.

############ Read the Restart File ############
read_restart restart1.res          # Reads the restart file to recommence the simulation from "set-up".

print "stop 1"

hard_particles yes #Enables high Young's Modulus values to be used.

print "stop 2"

#----------FORCE MODEL----------#
# Takes the given material properties and applies them to all particles.

pair_style gran model hertz tangential history cohesion sjkr #hertzian with cohesion.

#Atom style is granular thus pair style is gran, model is the definer prior to hertz stiffness, hooke stiffness.
#Tangential means measure tangential forces, and history means retain the tangential forces measured.
pair_coeff  * *           # applies this interaction to all particle pairs.
print "stop 3"


#----------PHYSICS SETTINGS----------#
fix     nparticles all nve/sphere #Fixes the ID chosen, nparticles, all means all spheres, nve means integrate the velocity and energy in the particle pack, and /sphere is the particle type.
#Initialises time integration.
fix     gravi all gravity 981 vector 0.0 0.0 -1.0   #Gravity as on Earth at 9.81 m/s^2 in negative Z.
timestep    1e-7

print "stop 4"


#----------WALLS----------#
#Bounds the model with surfaces in the specified walls plane.

fix    floor all wall/gran model hertz tangential history primitive type 1 zplane 0     #Adding a floor to the simulation.
print "stop 5"
```

```
#----------GEOMETRY INSERTION----------#

fix   Recoater1 all mesh/surface file Recoater.STL type 1 scale 1 curvature_tolerant yes
fix   Buffers1 all mesh/surface file buffers.STL type 1 scale 1 curvature_tolerant yes
fix   cont1 all wall/gran model hertz tangential history mesh n_meshes 2 meshes Buffers1 Recoater1

print "stop 6"

#----------PARTICLE INSERTION----------#
#Not required in this script because the particles are already inserted, so this is for powder spreading only.

#----------RUNNING THE SIMULATION----------#
############ Dump Files, Run Command, Unfixed the Particle Insertions ############

dump      dmp all custom 500000 output/particles_*.txt id x y z radius
dump      dumpstl1 all mesh/vtk 500000 output/buffers_*.vtk id Buffers1
dump      dumpstl2 all mesh/vtk 500000 output/recoater_*.vtk id Recoater1

#Recoater moves in x to spread the powder.
fix    MoveRecoater1   all move/mesh mesh Recoater1 linear 2 0.0 0.0

run 10000000 #Execute the script. 10 million steps is 20 outputs.
160 outputs are needed in total. Thus, 80 million steps.

#Write a restart file after several particle runs to provide a checkpoint if the maximum real-
world simulation run allocation times out (limited by the computer cluster).
#Subsequent restart files with duplicated names will overwrite the previous restart file.

write_restart restart2.res

#70 million steps required. Do this in 10 million step increments
to avoid data loss.

run 10000000

write_restart restart2.res

run 10000000
```

```
write_restart restart2.res

run 10000000

write_restart restart2.res

run 10000000

#30 million steps required.

write_restart restart2.res

run 10000000

write_restart restart2.res

run 10000000

write_restart restart2.res

run 10000000

#End of Simulation.
```

Appendix H: Effect of Slab Size on Solid Volume Fraction

Table 77 - Effect of Slab Size on Solid Volume Fraction for All Simulation Sets.

Case	Particle Size Distribution	Region	75 µm slab	150 µm slab	225 µm Slab	300 µm Slab
		X_-	42.88855749	52.14655954	55.24161008	56.6242987
E1	All 40 µm particles	X_0	43.60996024	52.69730788	55.44329257	56.83955597
		X_+	44.43608276	53.13557945	55.96689135	57.24679947
E2	33.3% of 20, 30, 40	X_-	45.13821417	54.04160532	56.86276643	58.09428408
	µm particles	X_0	44.99531534	53.90064574	57.04099606	58.29749677
		X_+	44.99549714	53.46170755	57.05148015	58.39739868
E3	15% (20), 25% (30),	X_-	40.46937419	50.12832892	54.38271912	56.98843236
	60% (40) µm	X_0	40.82154097	51.72361911	55.17281012	57.03643728
	particles	X_+	41.81295431	51.82715268	54.82647623	56.90582308
E4	60% (20), 25% (30),	X_-	42.66021024	52.81669325	56.26117325	57.58213903

	15% (40) µm	X_0	42.76474819	52.91080771	56.17663387	57.78430633
	particles	X_+	41.60574049	52.34472713	55.91707674	57.50528091
E5	25% (20), 50% (30),	X_-	45.16966646	53.66002665	56.70974711	57.94506752
	25% (40) µm	X_0	44.88841392	53.55161019	56.726958	58.08051234
	particles	X_+	44.20046331	53.58930445	56.53297192	57.9195239
		X_-	51.64720145	56.41073827	57.79512374	58.34090274
E6	All 20 µm particles	X_0	52.13589364	56.86209981	58.06080164	58.66124338
		X_+	52.59840589	57.07735708	58.22806236	58.80850554
		X_-	44.12465057	52.15616491	54.92551156	56.06515702
E7	All 30 µm particles	X_0	43.23126016	51.99254029	54.89605913	56.18051238
		X_+	42.87292224	52.05880826	54.78970313	56.15105994

Appendix I: Effect of Bed Depth on Solid Volume Fraction

Table 78 - Effect of Bed Depth on Solid Volume Fraction for All Case Sets.

Case	Particle Size Distribution	Region in Depth (µm)	X_{-}	X_0	X_{+}
E1	All 40 µm particles	0-75 (powder bed top)	42.94091736	43.74958658	44.48844263
		75-150	61.20869687	61.66830024	61.66248247
		150-225	61.4472252	61.03416394	61.56939825
E2	33.3% of 20, 30, 40 µm particles	0-75 (powder bed top)	44.89168641	44.72224403	43.41933756
		75-150	63.16019314	62.92339195	62.98084238
		150-225	62.46533393	62.97866071	63.10446986

E3	**15% (20), 25% (30),**	**0-75 (powder bed top)**	42.276056	42.85037841	41.61437623
	60% (40) µm	**75-150**	63.05292811	62.93839088	63.14683046
	particles	**150-225**	62.53332905	62.84594297	62.86357807
E4	**60% (20), 25% (30),**	**0-75 (powder bed top)**	46.61938057	47.11752662	47.6765774
	15% (40) µm	**75-150**	62.40115672	62.50569467	62.60923269
	particles	**150-225**	61.63993864	62.07354387	62.25380366
E5	**25% (20), 50% (30),**	**0-75 (powder bed top)**	44.60916124	44.45426327	44.49653296
	25% (40) µm	**75-150**	62.58941593	62.68259106	62.81839949
	particles	**150-225**	62.11190476	62.53987403	62.84457943

		0-75 (powder bed top)	51.44139804	52.31842599	52.72494226
E6	All 20 µm particles	75-150	61.12870261	61.21015131	61.19778856
		150-225	60.58401444	60.78909063	60.80436226
		0-75 (powder bed top)	43.94548161	43.3711592	43.21653394
E7	All 30 µm particles	75-150	60.62292074	60.81927028	60.81190717
		150-225	60.0829595	60.55174403	60.73827609

Appendix J: Segmentation of the Powder Bed for Surface Roughness and Segregation Analysis

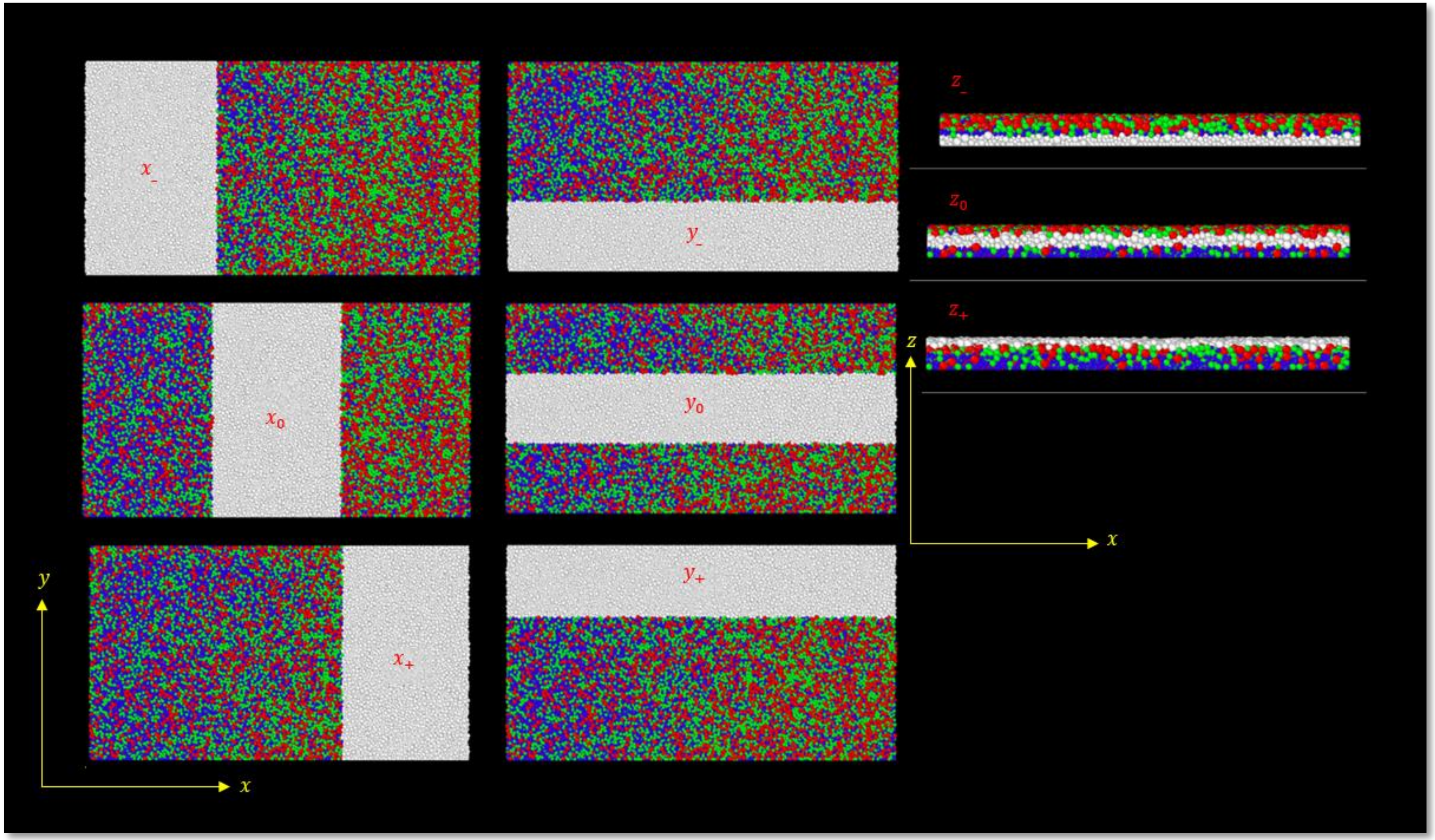

Figure 136 - Definition of Each Segment of the Powder Bed for Surface Roughness & Segregation Analysis.

Appendix K: Particle Size Distribution check for the Effect of the Particle Size Distribution on the Powder Bed

Table 79 - Particle Size Distribution check for the Effect of the Particle Size Distribution on the Surface Roughness, Solid Volume Fraction, and Segregation in the Powder Bed.

Case	Particle Size Distribution (% particle diameter)			Error in 40 µm particles		Error in 30 µm particles		Error in 20 µm particles	
	40 µm	30 µm	20 µm	g	%	g	%	g	%
1	100	0	0	0	0	0	0	0	0
2	33.33	33.33	33.33	0.0000043	0.018	-0.000012	0.050	0.0000075	0.031
3	60	25	15	-0.0000080	0.019	0.0000059	0.033	0.0000022	0.021
4	15	25	60	-0.000090	0.84	-0.00013	0.72	0.00022	0.52
5	25	50	25	0.0000013	0.0071	0.0000011	0.0032	0.0000024	0.013
6	0	100	0	0	0	0	0	0	0
7	0	0	100	0	0	0	0	0	0

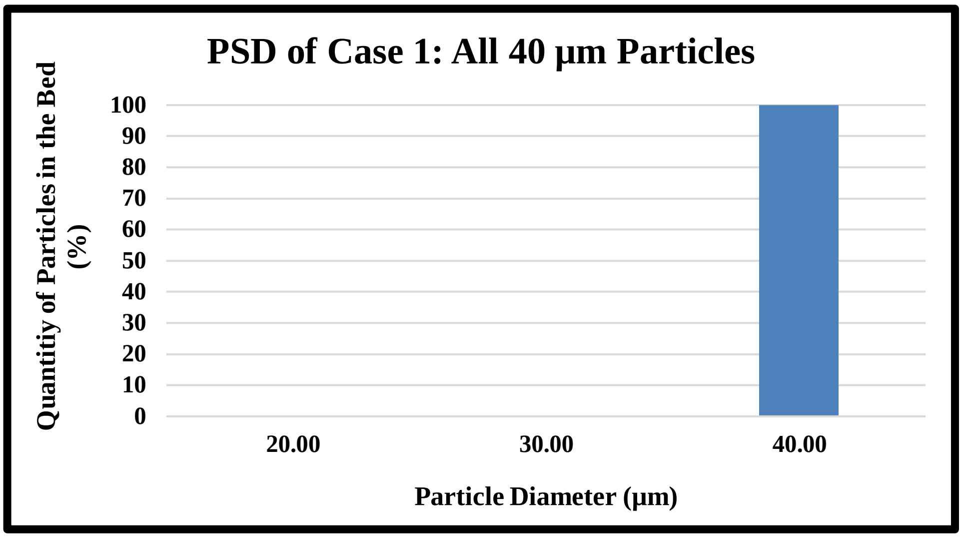

Figure 137 - Chart of the Particle Size Distribution check for Case 1 in the Effect of the Particle Size Distribution on the Powder Bed.

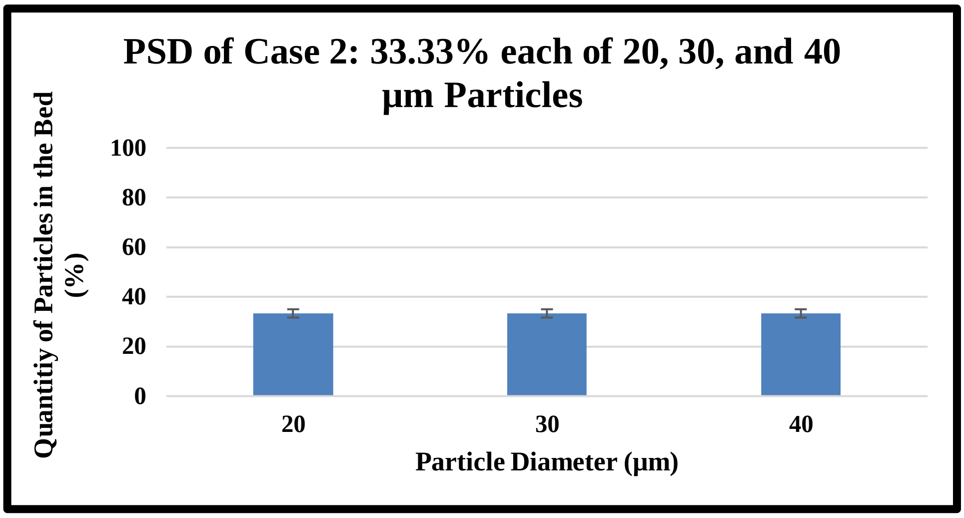

Figure 138 - Chart of the Particle Size Distribution check for Case 2 in the Effect of the Particle Size Distribution on the Powder Bed.

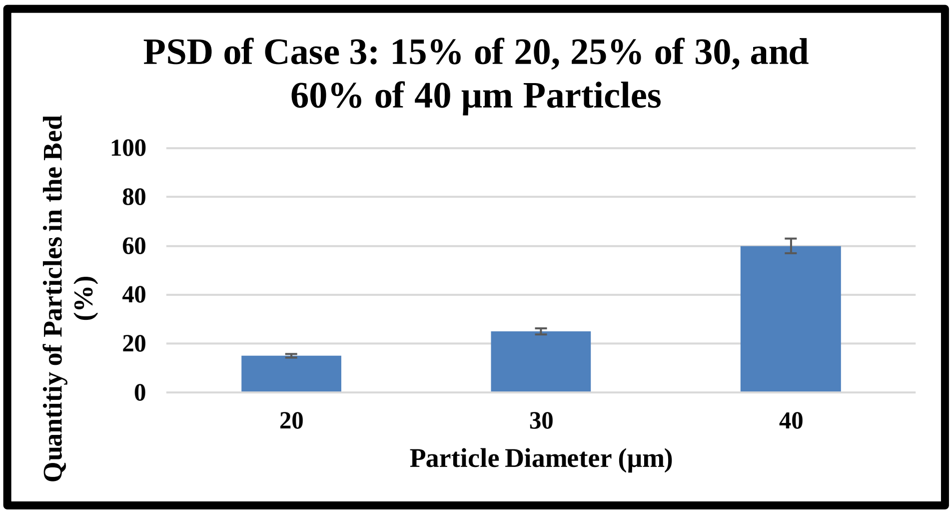

Figure 139 - Chart of the Particle Size Distribution check for Case 3 in the Effect of the Particle Size Distribution on the Powder Bed.

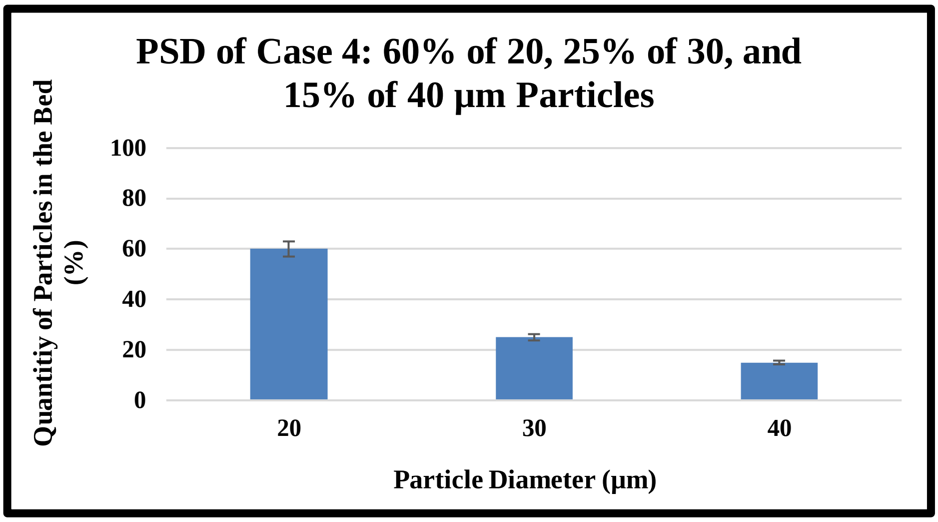

Figure 140 - Chart of the Particle Size Distribution check for Case 4 in the Effect of the Particle Size Distribution on the Powder Bed.

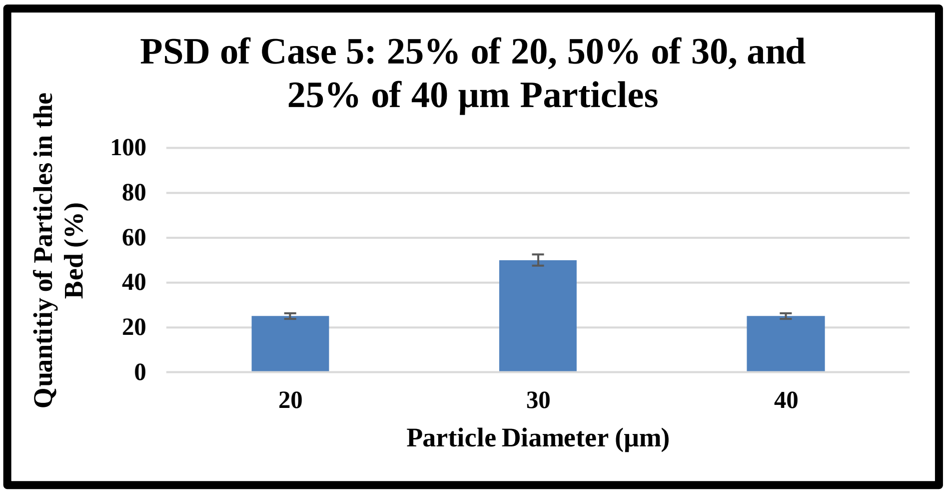

Figure 141 - Chart of the Particle Size Distribution check for Case 5 in the Effect of the Particle Size Distribution on the Powder Bed.

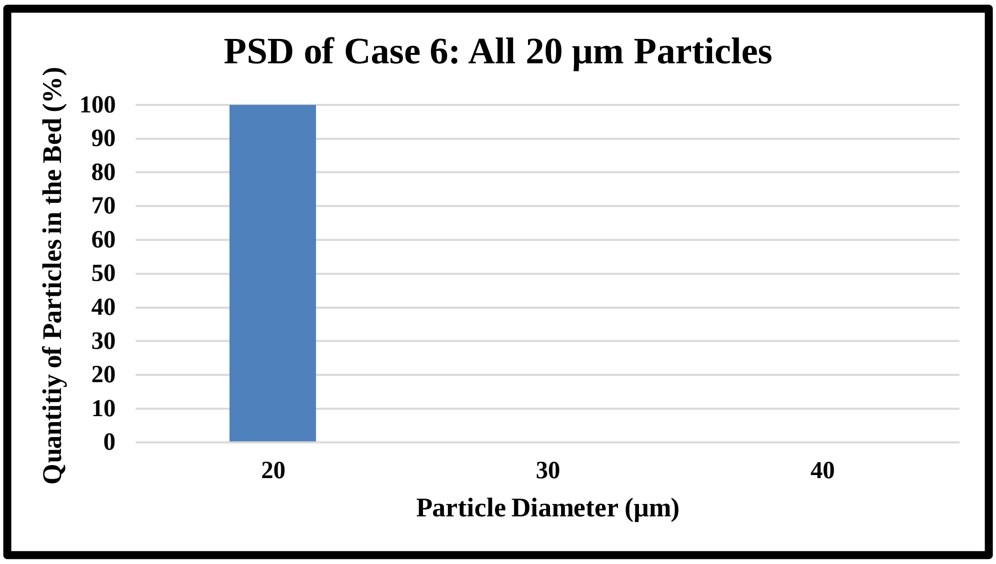

Figure 142 - Chart of the Particle Size Distribution check for Case 6 in the Effect of the Particle Size Distribution on the Powder Bed.

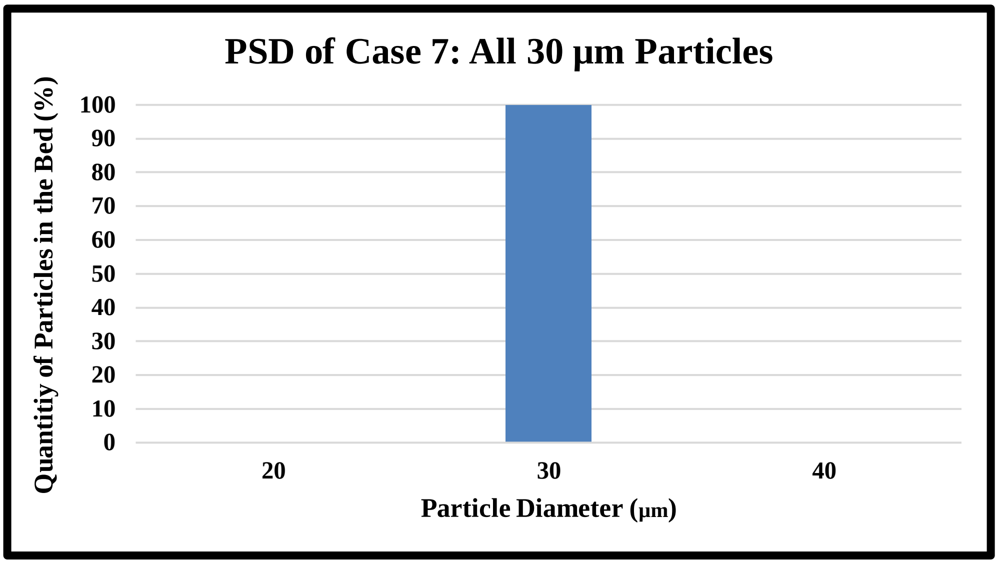

Figure 143 - Chart of the Particle Size Distribution check for Case 7 in the Effect of the Particle Size Distribution on the Powder Bed.

Appendix L: Data Tables of Complete Surface Roughness Results for the Effect of the Particle Size Distribution Analysis

Table 80 - Data Tables of Complete Surface Roughness Results for the Effect of the Particle Size Distribution in Cases 1 & 2.

Case 1: All 40 µm particles.				Case 2: 33% of 40 µm, 30 µm, and 20 µm particles.		
Model A – Test 1				**Model A – Test 1**		
Segment measured	**R_q (µm)**	**Peak to Trough Distance (µm)**		**Segment measured**	**R_q (µm)**	**Peak to Trough Distance (µm)**
y_-	9.425	45.49		y_-	6.827	35.51
y_0	10.19	55.1		y_0	7.567	45.89
y_+	10.23	60.19		y_+	7.714	45.27
Model A – Test 2				**Model A – Test 2**		
y_-	9.417	44.85		y_-	6.813	35.23
y_0	10.18	55.03		y_0	7.527	45.87
y_+	10.31	60.17		y_+	7.701	45.56
Model B – Test 1				**Model B – Test 1**		
Segment measured	**R_q (µm)**	**Peak to Trough Distance (µm)**		**Segment measured**	**R_q (µm)**	**Peak to Trough Distance (µm)**
y_-	10.59	71.59		y_-	7.159	39.37
y_0	9.707	63.06		y_0	7.53	41.34
y_+	10.68	68.89		y_+	7.366	43.21
Model B – Test 2				**Model B – Test 2**		
y_-	10.58	71.16		y_-	7.138	38
y_0	10.11	63.44		y_0	7.378	38.76
y_+	10.66	68.86		y_+	7.36	43.21
Model C – Test 1				**Model C – Test 1**		
Segment measured	**R_q (µm)**	**Peak to Trough Distance (µm)**		**Segment measured**	**R_q (µm)**	**Peak to Trough Distance (µm)**
y_-	10	52.1		y_-	7.38	40.07
y_0	9.41	51.84		y_0	7.341	40.96
y_+	10.31	59.99		y_+	7.475	43.14
Model C – Test 2				**Model C – Test 2**		
y_-	9.905	52.35		y_-	7.319	40.09
y_0	9.47	51.8		y_0	7.325	40.86
y_+	10.04	60.39		y_+	7.418	41.15

Table 81 - Data Tables of Complete Surface Roughness Results for the Effect of the Particle Size Distribution in Cases 3 & 4.

Case 3: 60% of 40 μm, 25% of 30 μm, and 15% of 20 μm particles.		
Model A – Test 1		
Segment measured	**R_q (μm)**	**Peak to Trough Distance (μm)**
y_-	8.933	56.09
y_0	9.057	49.94
y_+	8.935	51.21
Model A – Test 2		
y_-	8.977	55.8
y_0	9.239	55.74
y_+	8.928	53.19
Model B – Test 1		
Segment measured	**R_q (μm)**	**Peak to Trough Distance (μm)**
y_-	9.268	49.99
y_0	9.36	51.99
y_+	8.792	50.61
Model B – Test 2		
y_-	9.325	52.02
y_0	9.315	51.82
y_+	9.08	54.18
Model C – Test 1		
Segment measured	**R_q (μm)**	**Peak to Trough Distance (μm)**
y_-	9.274	50.84
y_0	8.442	46.59
y_+	9.572	48.96
Model C – Test 2		
y_-	9.226	52.83
y_0	8.521	46.57
y_+	9.614	48.95

Case 4: 15% of 40 μm, 25% of 30 μm, and 60% of 20 μm particles.		
Model A – Test 1		
Segment measured	**R_q (μm)**	**Peak to Trough Distance (μm)**
y_-	5.943	34.55
y_0	5.786	34.16
y_+	6.708	38.36
Model A – Test 2		
y_-	6.018	34.52
y_0	5.787	34.15
y_+	6.711	38.16
Model B – Test 1		
Segment measured	**R_q (μm)**	**Peak to Trough Distance (μm)**
y_-	5.273	32.85
y_0	5.953	33.25
y_+	5.655	35.32
Model B – Test 2		
y_-	5.396	32.8
y_0	5.929	33.31
y_+	5.36	35.07
Model C – Test 1		
Segment measured	**R_q (μm)**	**Peak to Trough Distance (μm)**
y_-	6.206	33.03
y_0	5.914	33.51
y_+	6.703	43
Model C – Test 2		
y_-	6.155	33.21
y_0	5.924	33.5
y_+	6.546	41.86

Table 82 - Data Tables of Complete Surface Roughness Results for the Effect of the Particle Size Distribution in Case 5.

Case 5: 25% of 40 µm, 50% of 30 µm, and 25% of 20 µm particles.		
Model A – Test 1		
Segment measured	R_q (µm)	**Peak to Trough Distance (µm)**
y_-	7.27	43.96
y_0	7.349	43.09
y_+	7.51	40.78
Model A – Test 2		
y_-	7.353	44.02
y_0	7.31	43.09
y_+	7.355	41.39
Model B – Test 1		
Segment measured	**R_q (µm)**	**Peak to Trough Distance (µm)**
y_-	7.038	40.55
y_0	7.48	40.53
y_+	7.54	40.74
Model B – Test 2		
y_-	6.977	40.54
y_0	7.446	38.1
y_+	7.547	40.73
Model C – Test 1		
Segment measured	**R_q (µm)**	**Peak to Trough Distance (µm)**
y_-	7.066	50.1
y_0	7.55	43.79
y_+	7.117	41.32
Model C – Test 2		
y_-	7.063	50.29
y_0	7.546	45.95
y_+	7.067	41.31

Table 83 - Data Tables of Complete Surface Roughness Results for the Effect of the Particle Size Distribution for both Slab Widths in Case 6.

Case 6: All 20 µm particles at slab width = 2D$_{Max}$.		
Model A – Test 1		
Segment measured	**R_q (µm)**	**Peak to Trough Distance (µm)**
y_-	3.055	16.75
y_0	3.245	20.14
y_+	3.257	21.84
Model A – Test 2		
y_-	3.043	16.76
y_0	3.2	20.13
y_+	3.275	21.9
Model B – Test 1		
Segment measured	**R_q (µm)**	**Peak to Trough Distance (µm)**
y_-	3.318	18.23
y_0	3.322	20.52
y_+	3.4	19.73
Model B – Test 2		
y_-	3.355	18.16
y_0	3.277	20.21
y_+	3.34	20.68
Model C – Test 1		
Segment measured	**R_q (µm)**	**Peak to Trough Distance (µm)**
y_-	3.277	18.56
y_0	3.365	20.51
y_+	3.363	20.26
Model C – Test 2		
y_-	3.221	18.52
y_0	3.368	20.5
y_+	3.379	20.11

Case 6: All 20 µm particles at slab width = D$_{Max}$.		
Model A – Test 1		
Segment measured	**R_q (µm)**	**Peak to Trough Distance (µm)**
y_-	4.673	27.41
y_0	4.793	28.66
y_+	4.996	30.9
Model A – Test 2		
y_-	4.734	27.39
y_0	4.755	28.54
y_+	4.941	28.88
Model B – Test 1		
Segment measured	**R_q (µm)**	**Peak to Trough Distance (µm)**
y_-	4.975	29.53
y_0	4.995	33.02
y_+	5.091	40.34
Model B – Test 2		
y_-	4.954	29.44
y_0	4.947	33.05
y_+	5.039	40.48
Model C – Test 1		
Segment measured	**R_q (µm)**	**Peak to Trough Distance (µm)**
y_-	5.12	31.21
y_0	4.818	30.59
y_+	4.84	31.01
Model C – Test 2		
y_-	5.141	31.35
y_0	4.826	30.55
y_+	4.781	30.42

Table 84 - Data Tables of Complete Surface Roughness Results for the Effect of the Particle Size Distribution for both Slab Widths in Case 7.

Case 7: All 30 µm particles at slab width = 2D$_{Max}$.				Case 7: All 30 µm particles at slab width = D$_{Max}$.		
Model A – Test 1				**Model A – Test 1**		
Segment measured	**R_q (µm)**	**Peak to Trough Distance (µm)**		**Segment measured**	**R_q (µm)**	**Peak to Trough Distance (µm)**
y_-	7.376	43.99		y_-	8.814	57.48
y_0	6.873	40.01		y_0	7.988	45.91
y_+	7.09	44.69		y_+	8.331	52.15
Model A – Test 2				**Model A – Test 2**		
y_-	7.392	44.19		y_-	8.863	57.52
y_0	6.988	41.49		y_0	8.018	47.78
y_+	7.091	45.18		y_+	8.351	52.15
Model B – Test 1				**Model B – Test 1**		
Segment measured	**R_q (µm)**	**Peak to Trough Distance (µm)**		**Segment measured**	**R_q (µm)**	**Peak to Trough Distance (µm)**
y_-	7.582	54.49		y_-	8.97	58.8
y_0	7.603	46.29		y_0	8.816	50.19
y_+	7.054	39.26		y_+	8.886	59.51
Model B – Test 2				**Model B – Test 2**		
y_-	7.523	52.48		y_-	9.085	54.82
y_0	7.598	46.29		y_0	8.803	50.15
y_+	7.283	46.28		y_+	8.375	58.68
Model C – Test 1				**Model C – Test 1**		
Segment measured	**R_q (µm)**	**Peak to Trough Distance (µm)**		**Segment measured**	**R_q (µm)**	**Peak to Trough Distance (µm)**
y_-	7.118	44.09		y_-	8.458	52.63
y_0	7.044	42.98		y_0	8.034	52.06
y_+	7.205	42.78		y_+	8.413	49.97
Model C – Test 2				**Model C – Test 2**		
y_-	7.177	44.18		y_-	8.358	50.93
y_0	7.163	47.11		y_0	8.144	54.99
y_+	7.46	43.62		y_+	8.561	51.73

Appendix M: Data Tables of Complete Solid Volume Fraction Results for the Effect of the Particle Size Distribution Analysis

Table 85 - Data Tables of Complete Solid Volume Fraction Results for the Effect of the Particle Size Distribution in Case 1.

Case 1: All 40 µm particles.						
Model A						
Segment measured	**Particle Radius (cm)**	**Volume of One Particle**	**Number of Particles in the Selection**	**Volume of Region (cm^3)**	**Total Occupied Volume (cm^3)**	**Percentage Solid Volume Fraction**
x_-	0.002	3.35103E-08	8976	0.000576	0.000300789	52.22025122
x_0	0.002	3.35103E-08	9041	0.000576	0.000302967	52.59840589
x_+	0.002	3.35103E-08	9131	0.000576	0.000305983	53.12200467
Model B						
Segment measured	**Particle Radius (cm)**	**Volume of One Particle**	**Number of Particles in the Selection**	**Volume of Region (cm^3)**	**Total Occupied Volume (cm^3)**	**Percentage Solid Volume Fraction**
x_-	0.002	3.35103E-08	8926	0.000576	0.000299113	51.92936301
x_0	0.002	3.35103E-08	9079	0.000576	0.00030424	52.81948093
x_+	0.002	3.35103E-08	9115	0.000576	0.000305447	53.02892044
Model C						
Segment measured	**Particle Radius (cm)**	**Volume of One Particle**	**Number of Particles in the Selection**	**Volume of Region (cm^3)**	**Total Occupied Volume (cm^3)**	**Percentage Solid Volume Fraction**
x_-	0.002	3.35103E-08	8988	0.000576	0.000301191	52.29006439
x_0	0.002	3.35103E-08	9054	0.000576	0.000303402	52.67403683
x_+	0.002	3.35103E-08	9154	0.000576	0.000306753	53.25581324
Averages across the powder bed from Models A, B, and C						
x_-	52.14655954					
x_0	52.69730788					
x_+	53.13557945					

Table 86 - Data Tables of Complete Solid Volume Fraction Results for the Effect of the Particle Size Distribution in Case 2.

Case 2: 33% of 40 µm, 30 µm, and 20 µm particles.						
Model A						
Segment measured	**Particle Radius (cm)**	**Volume of One Particle**	**Number of Particles in the Selection**	**Volume of Region (cm^3)**	**Total Occupied Volume (cm^3)**	**Percentage Solid Volume Fraction**
x_-	0.002	3.35103E-08	2967	0.000576	9.94251E-05	53.218725
	0.0015	1.41372E-08	7256	0.000576	0.000102579	
	0.001	4.18879E-09	24956	0.000576	0.000104535	
x_0	0.002	3.35103E-08	3045	0.000576	0.000102039	54.41054853
	0.0015	1.41372E-08	7341	0.000576	0.000103781	
	0.001	4.18879E-09	25684	0.000576	0.000107585	
x_+	0.002	3.35103E-08	3024	0.000576	0.000101335	53.56170037
	0.0015	1.41372E-08	7063	0.000576	9.98508E-05	
	0.001	4.18879E-09	25623	0.000576	0.000107329	
Model B						
Segment measured	**Particle Radius (cm)**	**Volume of One Particle**	**Number of Particles in the Selection**	**Volume of Region (cm^3)**	**Total Occupied Volume (cm^3)**	**Percentage Solid Volume Fraction**
x_-	0.002	3.35103E-08	3101	0.000576	0.000103916	54.83388177
	0.0015	1.41372E-08	7280	0.000576	0.000102919	
	0.001	4.18879E-09	26024	0.000576	0.000109009	
x_0	0.002	3.35103E-08	2947	0.000576	9.87549E-05	53.23508746
	0.0015	1.41372E-08	7220	0.000576	0.00010207	
	0.001	4.18879E-09	25260	0.000576	0.000105809	
x_+	0.002	3.35103E-08	3113	0.000576	0.000104318	52.83847957
	0.0015	1.41372E-08	7371	0.000576	0.000104205	
	0.001	4.18879E-09	22877	0.000576	9.5827E-05	
Model C						
Segment measured	**Particle Radius (cm)**	**Volume of One Particle**	**Number of Particles in the Selection**	**Volume of Region (cm^3)**	**Total Occupied Volume (cm^3)**	**Percentage Solid Volume Fraction**
x_-	0.002	3.35103E-08	3032	0.000576	0.000101603	54.07220918
	0.0015	1.41372E-08	7255	0.000576	0.000102565	
	0.001	4.18879E-09	25613	0.000576	0.000107287	
x_0	0.002	3.35103E-08	3034	0.000576	0.00010167	54.05630123
	0.0015	1.41372E-08	7210	0.000576	0.000101929	
	0.001	4.18879E-09	25727	0.000576	0.000107765	
x_+	0.002	3.35103E-08	3056	0.000576	0.000102408	53.98494272
	0.0015	1.41372E-08	7207	0.000576	0.000101887	
	0.001	4.18879E-09	25463	0.000576	0.000106659	
Averages across the powder bed from Models A, B, and C						
x_-	54.04160532					
x_0	53.90064574					
x_+	53.46170755					

Table 87 - Data Tables of Complete Solid Volume Fraction Results for the Effect of the Particle Size Distribution in Case 3.

Case 3: 60% of 40 µm, 25% of 30 µm, and 15% of 20 µm particles.						
Model A						
Segment measured	**Particle Radius (cm)**	**Volume of One Particle**	**Number of Particles in the Selection**	**Volume of Region (cm^3)**	**Total Occupied Volume (cm^3)**	**Percentage Solid Volume Fraction**
x_-	0.002	3.35103E-08	5323	0.000576	0.000178375	52.68276347
	0.0015	1.41372E-08	5344	0.000576	7.5549E-05	
	0.001	4.18879E-09	11824	0.000576	4.95283E-05	
x_0	0.002	3.35103E-08	5313	0.000576	0.00017804	52.95410763
	0.0015	1.41372E-08	5403	0.000576	7.63831E-05	
	0.001	4.18879E-09	12078	0.000576	5.05922E-05	
x_+	0.002	3.35103E-08	5358	0.000576	0.000179548	52.65031126
	0.0015	1.41372E-08	5289	0.000576	7.47715E-05	
	0.001	4.18879E-09	11685	0.000576	4.8946E-05	
Model B						
Segment measured	**Particle Radius (cm)**	**Volume of One Particle**	**Number of Particles in the Selection**	**Volume of Region (cm^3)**	**Total Occupied Volume (cm^3)**	**Percentage Solid Volume Fraction**
x_-	0.002	3.35103E-08	5323	0.000576	0.000178375	52.68276347
	0.0015	1.41372E-08	5344	0.000576	7.5549E-05	
	0.001	4.18879E-09	11824	0.000576	4.95283E-05	
x_0	0.002	3.35103E-08	5326	0.000576	0.000178476	52.83466166
	0.0015	1.41372E-08	5349	0.000576	7.56197E-05	
	0.001	4.18879E-09	11992	0.000576	5.0232E-05	
x_+	0.002	3.35103E-08	5299	0.000576	0.000177571	52.11162265
	0.0015	1.41372E-08	5351	0.000576	7.5648E-05	
	0.001	4.18879E-09	11207	0.000576	4.69438E-05	
Model C						
Segment measured	**Particle Radius (cm)**	**Volume of One Particle.**	**Number of Particles in the Selection.**	**Volume of Region (cm^3)**	**Total Occupied Volume (cm^3)**	**Percentage Solid Volume Fraction**
x_-	0.002	3.35103E-08	5363	0.000576	0.000179716	53.08455281
	0.0015	1.41372E-08	5396	0.000576	7.62842E-05	
	0.001	4.18879E-09	11881	0.000576	4.9767E-05	
x_0	0.002	3.35103E-08	5388	0.000576	0.000180554	52.94365383
	0.0015	1.41372E-08	5306	0.000576	7.50118E-05	
	0.001	4.18879E-09	11791	0.000576	4.939E-05	
x_+	0.002	3.35103E-08	5267	0.000576	0.000176499	52.27224749
	0.0015	1.41372E-08	5388	0.000576	7.61711E-05	
	0.001	4.18879E-09	11559	0.000576	4.84182E-05	
Averages across the powder bed from Models A, B, and C						
x_-	52.81669325					
x_0	52.91080771					
x_+	52.34472713					

Table 88 - Data Tables of Complete Solid Volume Fraction Results for the Effect of the Particle Size Distribution in Case 4.

Case 4: 15% of 40 μm, 25% of 30 μm, and 60% of 20 μm particles.						
Model A						
Segment measured	**Particle Radius (cm)**	**Volume of One Particle**	**Number of Particles in the Selection**	**Volume of Region (cm^3)**	**Total Occupied Volume (cm^3)**	**Percentage Solid Volume Fraction**
x_-	0.002	3.35103E-08	1323	0.000576	4.43342E-05	53.9701256
	0.0015	1.41372E-08	5486	0.000576	7.75565E-05	
	0.001	4.18879E-09	45115	0.000576	0.000188977	
x_0	0.002	3.35103E-08	1393	0.000576	4.66799E-05	54.64125924
	0.0015	1.41372E-08	5475	0.000576	7.7401E-05	
	0.001	4.18879E-09	45515	0.000576	0.000190653	
x_+	0.002	3.35103E-08	1404	0.000576	4.70485E-05	54.87669688
	0.0015	1.41372E-08	5533	0.000576	7.82209E-05	
	0.001	4.18879E-09	45555	0.000576	0.00019082	
Model B						
Segment measured	**Particle Radius (cm)**	**Volume of One Particle**	**Number of Particles in the Selection**	**Volume of Region (cm^3)**	**Total Occupied Volume (cm^3)**	**Percentage Solid Volume Fraction**
x_-	0.002	3.35103E-08	1432	0.000576	4.79868E-05	55.05286605
	0.0015	1.41372E-08	5539	0.000576	7.83058E-05	
	0.001	4.18879E-09	45553	0.000576	0.000190812	
x_0	0.002	3.35103E-08	1402	0.000576	4.69815E-05	54.98414371
	0.0015	1.41372E-08	5583	0.000576	7.89278E-05	
	0.001	4.18879E-09	45550	0.000576	0.000190799	
x_+	0.002	3.35103E-08	1429	0.000576	4.78862E-05	55.40811328
	0.0015	1.41372E-08	5519	0.000576	7.8023E-05	
	0.001	4.18879E-09	46133	0.000576	0.000193241	
Model C						
Segment measured	**Particle Radius (cm)**	**Volume of One Particle**	**Number of Particles in the Selection**	**Volume of Region (cm^3)**	**Total Occupied Volume (cm^3)**	**Percentage Solid Volume Fraction**
x_-	0.002	3.35103E-08	1858	0.000576	6.22622E-05	55.58682772
	0.0015	1.41372E-08	7305	0.000576	0.000103272	
	0.001	4.18879E-09	36919	0.000576	0.000154646	
x_0	0.002	3.35103E-08	2091	0.000576	7.00701E-05	55.77099632
	0.0015	1.41372E-08	7415	0.000576	0.000104827	
	0.001	4.18879E-09	34937	0.000576	0.000146344	
x_+	0.002	3.35103E-08	2038	0.000576	6.8294E-05	55.63264262
	0.0015	1.41372E-08	7377	0.000576	0.00010429	
	0.001	4.18879E-09	35299	0.000576	0.00014786	
Averages across the powder bed from Models A, B, and C						
x_-	54.86993979					
x_0	55.13213309					
x_+	55.30581759					

Table 89 - Data Tables of Complete Solid Volume Fraction Results for the Effect of the Particle Size Distribution in Case 5.

Case 5: 25% of 40 µm, 50% of 30 µm, and 25% of 20 µm particles.						
Model A						
Segment measured	**Particle Radius (cm)**	**Volume of One Particle**	**Number of Particles in the Selection**	**Volume of Region (cm^3)**	**Total Occupied Volume (cm^3)**	**Percentage Solid Volume Fraction**
x_-	0.002	3.35103E-08	2345	0.000576	7.85817E-05	53.96812574
	0.0015	1.41372E-08	10764	0.000576	0.000152172	
	0.001	4.18879E-09	19123	0.000576	8.01022E-05	
x_0	0.002	3.35103E-08	2225	0.000576	7.45605E-05	53.77741216
	0.0015	1.41372E-08	10854	0.000576	0.000153445	
	0.001	4.18879E-09	19517	0.000576	8.17526E-05	
x_+	0.002	3.35103E-08	2258	0.000576	7.56663E-05	53.60578812
	0.0015	1.41372E-08	10806	0.000576	0.000152766	
	0.001	4.18879E-09	19179	0.000576	8.03368E-05	
Model B						
Segment measured	**Particle Radius (cm)**	**Volume of One Particle**	**Number of Particles in the Selection**	**Volume of Region (cm^3)**	**Total Occupied Volume (cm^3)**	**Percentage Solid Volume Fraction**
x_-	0.002	3.35103E-08	2252	0.000576	7.54652E-05	53.23190587
	0.0015	1.41372E-08	10683	0.000576	0.000151027	
	0.001	4.18879E-09	19128	0.000576	8.01232E-05	
x_0	0.002	3.35103E-08	2234	0.000576	7.48621E-05	53.36016939
	0.0015	1.41372E-08	10756	0.000576	0.000152059	
	0.001	4.18879E-09	19202	0.000576	8.04331E-05	
x_+	0.002	3.35103E-08	2316	0.000576	7.76099E-05	53.70914434
	0.0015	1.41372E-08	10729	0.000576	0.000151678	
	0.001	4.18879E-09	19117	0.000576	8.00771E-05	
Model C						
Segment measured	**Particle Radius (cm)**	**Volume of One Particle**	**Number of Particles in the Selection**	**Volume of Region (cm^3)**	**Total Occupied Volume (cm^3)**	**Percentage Solid Volume Fraction**
x_-	0.002	3.35103E-08	2228	0.000576	7.4661E-05	53.78004834
	0.0015	1.41372E-08	10917	0.000576	0.000154335	
	0.001	4.18879E-09	19284	0.000576	8.07766E-05	
x_0	0.002	3.35103E-08	2288	0.000576	7.66716E-05	53.51724902
	0.0015	1.41372E-08	10692	0.000576	0.000151155	
	0.001	4.18879E-09	19202	0.000576	8.04331E-05	
x_+	0.002	3.35103E-08	2271	0.000576	7.61019E-05	53.45298091
	0.0015	1.41372E-08	10803	0.000576	0.000152724	
	0.001	4.18879E-09	18875	0.000576	7.90634E-05	
Averages across the powder bed from Models A, B, and C						
x_-	53.66002665					
x_0	53.55161019					
x_+	53.58930445					

Table 90 - Data Tables of Complete Solid Volume Fraction Results for the Effect of the Particle Size Distribution in Case 6.

Case 6: All 20 µm particles						
Model A						
Segment measured	**Particle Radius (cm)**	**Volume of One Particle**	**Number of Particles in the Selection**	**Volume of Region (cm^3)**	**Total Occupied Volume (cm^3)**	**Percentage Solid Volume Fraction**
x_-	0.001	4.18879E-09	77916	0.000576	0.000326374	56.66211417
x_0	0.001	4.18879E-09	78465	0.000576	0.000328673	57.06135823
x_+	0.001	4.18879E-09	78672	0.000576	0.000329541	57.21189288
Model B						
Segment measured	**Particle Radius (cm)**	**Volume of One Particle**	**Number of Particles in the Selection**	**Volume of Region (cm^3)**	**Total Occupied Volume (cm^3)**	**Percentage Solid Volume Fraction**
x_-	0.001	4.18879E-09	77518	0.000576	0.000324707	56.3726804
x_0	0.001	4.18879E-09	77973	0.000576	0.000326613	56.70356574
x_+	0.001	4.18879E-09	78260	0.000576	0.000327815	56.91227803
Model C						
Segment measured	**Particle Radius (cm)**	**Volume of One Particle**	**Number of Particles in the Selection**	**Volume of Region (cm^3)**	**Total Occupied Volume (cm^3)**	**Percentage Solid Volume Fraction**
x_-	0.001	4.18879E-09	77277	0.000576	0.000323697	56.19742025
x_0	0.001	4.18879E-09	78135	0.000576	0.000327291	56.82137546
x_+	0.001	4.18879E-09	78529	0.000576	0.000328942	57.10790035
Averages across the powder bed from Models A, B, and C						
x_-	56.41073827					
x_0	56.86209981					
x_+	57.07735708					

Table 91 - Data Tables of Complete Solid Volume Fraction Results for the Effect of the Particle Size Distribution in Case 7.

Case 7: All 30 µm particles						
Model A						
Segment measured	**Particle Radius (cm)**	**Volume of One Particle**	**Number of Particles in the Selection**	**Volume of Region (cm^3)**	**Total Occupied Volume (cm^3)**	**Percentage Solid Volume Fraction**
x_-	0.0015	1.41372E-08	21268	0.000576	0.000300669	52.19952543
x_0	0.0015	1.41372E-08	21230	0.000576	0.000300132	52.1062594
x_+	0.0015	1.41372E-08	21280	0.000576	0.000300839	52.22897787
Model B						
Segment measured	**Particle Radius (cm)**	**Volume of One Particle**	**Number of Particles in the Selection**	**Volume of Region (cm^3)**	**Total Occupied Volume (cm^3)**	**Percentage Solid Volume Fraction**
x_-	0.0015	1.41372E-08	21337	0.000576	0.000301645	52.36887691
x_0	0.0015	1.41372E-08	21221	0.000576	0.000300005	52.08417008
x_+	0.0015	1.41372E-08	21105	0.000576	0.000298365	51.79946325
Model C						
Segment measured	**Particle Radius (cm)**	**Volume of One Particle**	**Number of Particles in the Selection**	**Volume of Region (cm^3)**	**Total Occupied Volume (cm^3)**	**Percentage Solid Volume Fraction**
x_-	0.0015	1.41372E-08	21146	0.000576	0.000298945	51.90009239
x_0	0.0015	1.41372E-08	21100	0.000576	0.000298294	51.7871914
x_+	0.0015	1.41372E-08	21247	0.000576	0.000300372	52.14798368
Averages across the powder bed from Models A, B, and C						
x_-	52.15616491					
x_0	51.99254029					
x_+	52.05880826					

Appendix N: The Pearson Correlation Coefficient

The Pearson Correlation Coefficient is a statistical measure that describes the direction and strength of a relationship between two analysed variables. ***Equation 87*** demonstrates the quantification of the measure:

$$\boldsymbol{r} = \frac{\sum(\mathrm{x}_i - \bar{\mathrm{x}})\ (\mathrm{y}_i - \bar{\mathrm{y}})}{\sqrt{\sum(\mathrm{x}_i - \bar{\mathrm{x}})^2\ \sum(\mathrm{y}_i - \bar{\mathrm{y}})^2}} \tag{87}$$

Where:

$\boldsymbol{r}$ = The Pearson Correlation Coefficient.

x_i = Values of the Surface Roughness.

$\bar{\mathrm{x}}$ = Mean average of the Surface Roughness.

y_i = Values of the Solid Volume Fraction.

$\bar{\mathrm{y}}$ = Mean average of the Solid Volume Fraction.

Hence, from the data in ***Subsection 6.3.2*** and ***Subsection 6.3.3***.

$$\bar{\mathrm{x}} = \frac{10.07+7.35+9.10+6.00+7.29+4.09+7.89}{7} = \frac{51.79}{7} = 7.4\ \mu\mathrm{m}$$

$$\bar{\mathrm{y}}\ = \frac{52.659+53.801+52.690+55.102+53.600+56.783+52.069}{7} = \frac{376.704}{7} = 53.8\%$$

Finding the constituents of $\boldsymbol{r}$:

Table 92 - Data for Pearson Correlation Coefficient.

Case	x_i	y_i	$x_i - \bar{x}$	$y_i - \bar{y}$	$(x_i - \bar{x})(y_i - \bar{y})$	$(x_i - \bar{x})^2$	$(y_i - \bar{y})^2$
1	10.07	52.659	2.67	-1.141	-3.04647	7.1289	1.301881
2	7.35	53.801	-0.05	0.001	-0.00005	0.0025	0.000001
3	9.10	52.690	1.7	-1.11	-1.887	2.89	1.2321
4	6.00	55.102	-1.4	1.302	-1.8228	1.96	1.695204
5	7.29	53.600	-0.11	-0.2	0.022	0.0121	0.04
6	4.09	56.783	-3.31	2.983	-9.87373	10.9561	8.898289
7	7.89	52.069	0.49	-1.731	-0.84819	0.2401	2.996361
$\sum$	*Data not required.*				-17.4562	23.1897	16.16384

Thus, inserting the knowns into ***Equation 87***:

$$\boldsymbol{r} = \frac{-17.4562}{\sqrt{23.1897 \times 16.16384}} = \frac{-17.4562}{\sqrt{374.8346}} = \frac{-17.4562}{19.360645662} = -0.902$$

Appendix O: Data Tables of Complete Solid Volume Fraction Results for the Influence of Deposition Mechanism on Powder Bed Quality

Table 93 to ***Table 99*** records the complete SVF results in the investigations of what effects the deposition approach had on powder bed quality. In each data set, the number of particles and occupied volume in each segment measured have been summated to find the total values used for the analysis.

Table 93 - Complete Solid Volume Fraction Results for Case 1 in the Influence of Deposition Mechanism on Powder Bed Quality Analysis.

Case 1: All 40 µm particles						
Travelling Funnel						
Model A						
Segment measured	**Particle Radius (cm)**	**Volume of One Particle**	**Number of Particles in the Selection**	**Volume of Region (cm^3)**	**Total Occupied Volume (cm^3)**	**Percentage Solid Volume Fraction**
x_-	0.002	3.35103E-08	3905	0.000288	0.000130858	45.43673819
x_0	0.002	3.35103E-08	3764	0.000288	0.000126133	43.7961287
x_+	0.002	3.35103E-08	3774	0.000288	0.000126468	43.91248398
Model B						
Travelling Funnel						
Segment measured	**Particle Radius (cm)**	**Volume of One Particle**	**Number of Particles in the Selection**	**Volume of Region (cm^3)**	**Total Occupied Volume (cm^3)**	**Percentage Solid Volume Fraction**
x_-	0.002	3.35103E-08	3891	0.000288	0.000130389	45.2738408
x_0	0.002	3.35103E-08	3801	0.000288	0.000127373	44.22664325
x_+	0.002	3.35103E-08	3724	0.000288	0.000124792	43.33070756
Averages across the powder bed from Models A and B						
x_-	45.3552895					
x_0	44.01138597					
x_+	43.62159577					
Model C						
Rainfall						
Segment measured	**Particle Radius (cm)**	**Volume of One Particle**	**Number of Particles in the Selection**	**Volume of Region (cm^3)**	**Total Occupied Volume (cm^3)**	**Percentage Solid Volume Fraction**
x_-	0.002	3.35103E-08	4033	0.000288	0.000135147	46.92608582
x_0	0.002	3.35103E-08	3963	0.000288	0.000132801	46.11159884
x_+	0.002	3.35103E-08	3740	0.000288	0.000125329	43.51687602
Model D						
Rainfall						
Segment measured	**Particle Radius (cm)**	**Volume of One Particle**	**Number of Particles in the Selection**	**Volume of Region (cm^3)**	**Total Occupied Volume (cm^3)**	**Percentage Solid Volume Fraction**
x_-	0.002	3.35103E-08	4030	0.000288	0.000135047	46.89117924
x_0	0.002	3.35103E-08	3940	0.000288	0.000132031	45.84398169
x_+	0.002	3.35103E-08	3757	0.000288	0.000125898	43.71468
Averages across the powder bed from Models D and C						
x_-	46.90863253					
x_0	45.97779026					
x_+	43.61577801					

Table 94 - Complete Solid Volume Fraction Results for Case 2 in the Influence of Deposition Mechanism on Powder Bed Quality Analysis.

Case 2: 33% of 40 μm, 30 μm, and 20 μm particles						
Travelling Funnel						
Model A						
Segment measured	**Particle Radius (cm)**	**Volume of One Particle**	**Number of Particles in the Selection**	**Volume of Region (cm^3)**	**Total Occupied Volume (cm^3)**	**Percentage Solid Volume Fraction**
x_-	0.002	3.35103E-08	1266	0.000288	4.24241E-05	50.60654888
	0.0015	1.41372E-08	3316	0.000288	4.68788E-05	
	0.001	4.18879E-09	13475	0.000288	5.64439E-05	
x_0	0.002	3.35103E-08	1334	0.000288	4.47028E-05	48.75995417
	0.0015	1.41372E-08	3317	0.000288	4.6893E-05	
	0.001	4.18879E-09	11658	0.000288	4.88329E-05	
x_+	0.002	3.35103E-08	1478	0.000288	4.95283E-05	48.12890856
	0.0015	1.41372E-08	3424	0.000288	4.84057E-05	
	0.001	4.18879E-09	9711	0.000288	4.06773E-05	
Model B						
Travelling Funnel						
Segment measured	**Particle Radius (cm)**	**Volume of One Particle**	**Number of Particles in the Selection**	**Volume of Region (cm^3)**	**Total Occupied Volume (cm^3)**	**Percentage Solid Volume Fraction**
x_-	0.002	3.35103E-08	1276	0.000288	4.27592E-05	50.78944484
	0.0015	1.41372E-08	3310	0.000288	4.6794E-05	
	0.001	4.18879E-09	13541	0.000288	5.67204E-05	
x_0	0.002	3.35103E-08	1340	0.000288	4.49038E-05	48.85067493
	0.0015	1.41372E-08	3318	0.000288	4.69071E-05	
	0.001	4.18879E-09	11669	0.000288	4.8879E-05	
x_+	0.002	3.35103E-08	1492	0.000288	4.99974E-05	47.87619943
	0.0015	1.41372E-08	3374	0.000288	4.76988E-05	
	0.001	4.18879E-09	9594	0.000288	4.01873E-05	
Averages across the powder bed from Models A and B						
x_-	50.69799686					
x_0	48.80531455					
x_+	48.002554					
Model C						
Rainfall						
Segment measured	**Particle Radius (cm)**	**Volume of One Particle**	**Number of Particles in the Selection**	**Volume of Region (cm^3)**	**Total Occupied Volume (cm^3)**	**Percentage Solid Volume Fraction**
x_-	0.002	3.35103E-08	1383	0.000288	4.63448E-05	51.99735813
	0.0015	1.41372E-08	3450	0.000288	4.87732E-05	

	0.001	4.18879E-09	13043	0.000288	5.46344E-05	
x_0	0.002	3.35103E-08	1306	0.000288	4.37645E-05	51.55902596
	0.0015	1.41372E-08	3369	0.000288	4.76281E-05	
	0.001	4.18879E-09	13631	0.000288	5.70974E-05	
x_+	0.002	3.35103E-08	1333	0.000288	0.002	48.27471628
	0.0015	1.41372E-08	3454	0.000288	0.0015	
	0.001	4.18879E-09	10870	0.000288	0.001	
Model D						
Rainfall						
Segment measured	**Particle Radius (cm)**	**Volume of One Particle**	**Number of Particles in the Selection**	**Volume of Region (cm^3)**	**Total Occupied Volume (cm^3)**	**Percentage Solid Volume Fraction**
x_-	0.002	3.35103E-08	1382	0.000288	4.63113E-05	52.13662086
	0.0015	1.41372E-08	3436	0.000288	4.85753E-05	
	0.001	4.18879E-09	13194	0.000288	5.52669E-05	
x_0	0.002	3.35103E-08	1343	0.000288	4.50044E-05	51.43503486
	0.0015	1.41372E-08	3339	0.000288	4.7204E-05	
	0.001	4.18879E-09	13351	0.000288	5.59245E-05	
x_+	0.002	3.35103E-08	1361	0.000288	0.002	48.17654151
	0.0015	1.41372E-08	3402	0.000288	0.0015	
	0.001	4.18879E-09	10754	0.000288	0.001	
Averages across the powder bed from Models D and C						
x_-	52.06698949					
x_0	51.49703041					
x_+	48.22562889					

Table 95 - Complete Solid Volume Fraction Results for Case 3 in the Influence of Deposition Mechanism on Powder Bed Quality Analysis.

Case 3: 60% of 40 µm, 25% of 30 µm, and 15% 20 µm particles						
Travelling Funnel						
Model A						
Segment measured	**Particle Radius (cm)**	**Volume of One Particle**	**Number of Particles in the Selection**	**Volume of Region (cm^3)**	**Total Occupied Volume (cm^3)**	**Percentage Solid Volume Fraction**
x_-	0.002	3.35103E-08	2331	0.000288	7.81126E-05	49.33191311
	0.0015	1.41372E-08	2627	0.000288	3.71383E-05	
	0.001	4.18879E-09	6404	0.000288	2.6825E-05	
x_0	0.002	3.35103E-08	2320	0.000288	7.77439E-05	45.9047046
	0.0015	1.41372E-08	2426	0.000288	3.42968E-05	
	0.001	4.18879E-09	4814	0.000288	2.01648E-05	
x_+	0.002	3.35103E-08	2492	0.000288	8.35077E-05	46.22595426
	0.0015	1.41372E-08	2327	0.000288	3.28972E-05	
	0.001	4.18879E-09	3993	0.000288	1.67258E-05	
Model B						
Travelling Funnel						
Segment measured	**Particle Radius (cm)**	**Volume of One Particle**	**Number of Particles in the Selection**	**Volume of Region (cm^3)**	**Total Occupied Volume (cm^3)**	**Percentage Solid Volume Fraction**
x_-	0.002	3.35103E-08	2364	0.000288	7.92184E-05	49.23301112
	0.0015	1.41372E-08	2523	0.000288	3.56681E-05	
	0.001	4.18879E-09	6423	0.000288	2.69046E-05	
x_0	0.002	3.35103E-08	2356	0.000288	7.89503E-05	46.37739794
	0.0015	1.41372E-08	2442	0.000288	3.4523E-05	
	0.001	4.18879E-09	4797	0.000288	2.00936E-05	
x_+	0.002	3.35103E-08	2549	0.000288	8.54178E-05	47.01098882
	0.0015	1.41372E-08	2329	0.000288	3.29255E-05	
	0.001	4.18879E-09	4070	0.000288	1.70484E-05	
Averages across the powder bed from Models A and B						
x_-	49.28246212					
x_0	46.14105127					
x_+	46.61847154					
Model C						
Rainfall						
Segment measured	**Particle Radius (cm)**	**Volume of One Particle**	**Number of Particles in the Selection**	**Volume of Region (cm^3)**	**Total Occupied Volume (cm^3)**	**Percentage Solid Volume Fraction**
x_-	0.002	3.35103E-08	2500	0.000288	8.37758E-05	50.65436363
	0.0015	1.41372E-08	2561	0.000288	3.62053E-05	

	0.001	4.18879E-09	6184	0.000288	2.59035E-05	
x_0	0.002	3.35103E-08	2315	0.000288	7.75764E-05	49.42572456
	0.0015	1.41372E-08	2647	0.000288	3.74211E-05	
	0.001	4.18879E-09	6529	0.000288	2.73486E-05	
x_+	0.002	3.35103E-08	2398	0.000288	8.03578E-05	46.71682812
	0.0015	1.41372E-08	2499	0.000288	3.53288E-05	
	0.001	4.18879E-09	4502	0.000288	1.88579E-05	
Model D						
Rainfall						
Segment measured	**Particle Radius (cm)**	**Volume of One Particle**	**Number of Particles in the Selection**	**Volume of Region (cm^3)**	**Total Occupied Volume (cm^3)**	**Percentage Solid Volume Fraction**
x_-	0.002	3.35103E-08	2448	0.000288	8.20333E-05	50.49092082
	0.0015	1.41372E-08	2632	0.000288	3.7209E-05	
	0.001	4.18879E-09	6248	0.000288	2.61716E-05	
x_0	0.002	3.35103E-08	2290	0.000288	7.67386E-05	49.35772944
	0.0015	1.41372E-08	2669	0.000288	3.77321E-05	
	0.001	4.18879E-09	6608	0.000288	2.76795E-05	
x_+	0.002	3.35103E-08	2381	0.000288	7.97881E-05	45.91652193
	0.0015	1.41372E-08	2405	0.000288	3.39999E-05	
	0.001	4.18879E-09	4405	0.000288	1.84516E-05	
Averages across the powder bed from Models D and C						
x_-	50.57264223					
x_0	49.391727					
x_+	46.31667502					

Table 96 - Complete Solid Volume Fraction Results for Case 4 in the Influence of Deposition Mechanism on Powder Bed Quality Analysis.

Case 4: 15% of 40 µm, 25% of 30 µm, and 60% 20 µm particles						
Travelling Funnel						
Model A						
Segment measured	**Particle Radius (cm)**	**Volume of One Particle**	**Number of Particles in the Selection**	**Volume of Region (cm^3)**	**Total Occupied Volume (cm^3)**	**Percentage Solid Volume Fraction**
x_-	0.002	3.35103E-08	562	0.000288	1.88328E-05	
	0.0015	1.41372E-08	2396	0.000288	3.38727E-05	
	0.001	4.18879E-09	22908	0.000288	9.59568E-05	51.61883985
x_0	0.002	3.35103E-08	635	0.000288	2.12791E-05	
	0.0015	1.41372E-08	2443	0.000288	3.45371E-05	
	0.001	4.18879E-09	21256	0.000288	8.90369E-05	50.29620752
x_+	0.002	3.35103E-08	694	0.000288	2.32562E-05	
	0.0015	1.41372E-08	2753	0.000288	3.89196E-05	
	0.001	4.18879E-09	19186	0.000288	8.03661E-05	49.49371968
Model B						
Travelling Funnel						
Segment measured	**Particle Radius (cm)**	**Volume of One Particle**	**Number of Particles in the Selection**	**Volume of Region (cm^3)**	**Total Occupied Volume (cm^3)**	**Percentage Solid Volume Fraction**
x_-	0.002	3.35103E-08	590	0.000288	1.97711E-05	
	0.0015	1.41372E-08	2341	0.000288	3.30951E-05	
	0.001	4.18879E-09	22743	0.000288	9.52657E-05	51.43467125
x_0	0.002	3.35103E-08	585	0.000288	1.96035E-05	
	0.0015	1.41372E-08	2543	0.000288	3.59508E-05	
	0.001	4.18879E-09	21300	0.000288	8.92212E-05	50.26930037
x_+	0.002	3.35103E-08	716	0.000288	2.39934E-05	
	0.0015	1.41372E-08	2716	0.000288	3.83965E-05	
	0.001	4.18879E-09	19158	0.000288	8.02488E-05	49.52735363
Averages across the powder bed from Models A and B						

x_-	51.52675555					
x_0	50.28275394					
x_+	49.51053665					
Model C						
Rainfall						
Segment measured	**Particle Radius (cm)**	**Volume of One Particle**	**Number of Particles in the Selection**	**Volume of Region (cm^3)**	**Total Occupied Volume (cm^3)**	**Percentage Solid Volume Fraction**
x_-	0.002	3.35103E-08	624	0.000288	2.09104E-05	52.73821404
	0.0015	1.41372E-08	2523	0.000288	3.56681E-05	
	0.001	4.18879E-09	22753	0.000288	9.53075E-05	
x_0	0.002	3.35103E-08	596	0.000288	1.99722E-05	52.29570035
	0.0015	1.41372E-08	2533	0.000288	3.58094E-05	
	0.001	4.18879E-09	22639	0.000288	9.483E-05	
x_+	0.002	3.35103E-08	613	0.000288	2.05418E-05	50.13349193
	0.0015	1.41372E-08	2598	0.000288	3.67284E-05	
	0.001	4.18879E-09	20797	0.000288	8.71143E-05	
Model D						
Rainfall						
Segment measured	**Particle Radius (cm)**	**Volume of One Particle**	**Number of Particles in the Selection**	**Volume of Region (cm^3)**	**Total Occupied Volume (cm^3)**	**Percentage Solid Volume Fraction**
x_-	0.002	3.35103E-08	597	0.000288	2.00057E-05	52.83947949
	0.0015	1.41372E-08	2586	0.000288	3.65587E-05	
	0.001	4.18879E-09	22826	0.000288	9.56133E-05	
x_0	0.002	3.35103E-08	610	0.000288	2.04413E-05	52.50895777
	0.0015	1.41372E-08	2556	0.000288	3.61346E-05	
	0.001	4.18879E-09	22596	0.000288	9.46499E-05	
x_+	0.002	3.35103E-08	625	0.000288	2.0944E-05	50.04931616

	0.0015	1.41372E-08	2577	0.000288	3.64315E-05	
	0.001	4.18879E-09	20714	0.000288	8.67666E-05	
Averages across the powder bed from Models D and C						
x_-	52.78884677					
x_0	52.40232906					
x_+	50.09140405					

Table 97 - Complete Solid Volume Fraction Results for Case 5 in the Influence of Deposition Mechanism on Powder Bed Quality Analysis.

Case 5: 25% of 40 µm, 50% of 30 µm, and 25% 20 µm particles						
Travelling Funnel						
Model A						
Segment measured	**Particle Radius (cm)**	**Volume of One Particle**	**Number of Particles in the Selection**	**Volume of Region (cm^3)**	**Total Occupied Volume (cm^3)**	**Percentage Solid Volume Fraction**
x_-	0.002	3.35103E-08	946	0.000288	3.17008E-05	50.44928744
	0.0015	1.41372E-08	4993	0.000288	7.05869E-05	
	0.001	4.18879E-09	10267	0.000288	4.30063E-05	
x_0	0.002	3.35103E-08	994	0.000288	3.33093E-05	48.23744623
	0.0015	1.41372E-08	4919	0.000288	6.95407E-05	
	0.001	4.18879E-09	8612	0.000288	3.60739E-05	
x_+	0.002	3.35103E-08	1090	0.000288	3.65263E-05	47.9705563
	0.0015	1.41372E-08	5091	0.000288	7.19723E-05	
	0.001	4.18879E-09	7080	0.000288	2.96566E-05	
Model B						
Travelling Funnel						
Segment measured	**Particle Radius (cm)**	**Volume of One Particle**	**Number of Particles in the Selection**	**Volume of Region (cm^3)**	**Total Occupied Volume (cm^3)**	**Percentage Solid Volume Fraction**
x_-	0.002	3.35103E-08	973	0.000288	3.26055E-05	50.51891881
	0.0015	1.41372E-08	4950	0.000288	6.9979E-05	
	0.001	4.18879E-09	10244	0.000288	4.291E-05	
x_0	0.002	3.35103E-08	975	0.000288	3.26726E-05	48.40725222
	0.0015	1.41372E-08	4969	0.000288	7.02476E-05	
	0.001	4.18879E-09	8712	0.000288	3.64927E-05	
x_+	0.002	3.35103E-08	1084	0.000288	3.63252E-05	47.65039746
	0.0015	1.41372E-08	5056	0.000288	7.14775E-05	
	0.001	4.18879E-09	7026	0.000288	2.94304E-05	
Averages across the powder bed from Models A and B						

x_-	50.48410313					
x_0	48.32234922					
x_+	47.81047688					
Model C						
Rainfall						
Segment measured	**Particle Radius (cm)**	**Volume of One Particle**	**Number of Particles in the Selection**	**Volume of Region (cm^3)**	**Total Occupied Volume (cm^3)**	**Percentage Solid Volume Fraction**
x_-	0.002	3.35103E-08	1049	0.000288	3.51523E-05	51.86918551
	0.0015	1.41372E-08	5191	0.000288	7.3386E-05	
	0.001	4.18879E-09	9751	0.000288	4.08449E-05	
x_0	0.002	3.35103E-08	959	0.000288	3.21364E-05	51.20486957
	0.0015	1.41372E-08	5101	0.000288	7.21137E-05	
	0.001	4.18879E-09	10318	0.000288	4.32199E-05	
x_+	0.002	3.35103E-08	1010	0.000288	3.38454E-05	48.31834951
	0.0015	1.41372E-08	5046	0.000288	7.13361E-05	
	0.001	4.18879E-09	8111	0.000288	3.39753E-05	
Model D						
Rainfall						
Segment measured	**Particle Radius (cm)**	**Volume of One Particle**	**Number of Particles in the Selection**	**Volume of Region (cm^3)**	**Total Occupied Volume (cm^3)**	**Percentage Solid Volume Fraction**
x_-	0.002	3.35103E-08	1022	0.000288	3.42475E-05	51.91663665
	0.0015	1.41372E-08	5246	0.000288	7.41636E-05	
	0.001	4.18879E-09	9814	0.000288	4.11088E-05	
x_0	0.002	3.35103E-08	959	0.000288	3.21364E-05	50.77599126
	0.0015	1.41372E-08	5016	0.000288	7.0912E-05	
	0.001	4.18879E-09	10310	0.000288	4.31864E-05	
x_+	0.002	3.35103E-08	1005	0.000288	3.36779E-05	48.35307429

	0.0015	1.41372E-08	5115	0.000288	7.23116E-05	
	0.001	4.18879E-09	7942	0.000288	3.32674E-05	
Averages across the powder bed from Models D and C						
x_-	51.89291108					
x_0	50.99043041					
x_+	48.3357119					

Table 98 - Complete Solid Volume Fraction Results for Case 6 in the Influence of Deposition Mechanism on Powder Bed Quality Analysis.

Case 6: All 20 µm particles						
Travelling Funnel						
Model A						
Segment measured	**Particle Radius (cm)**	**Volume of One Particle**	**Number of Particles in the Selection**	**Volume of Region (cm^3)**	**Total Occupied Volume (cm^3)**	**Percentage Solid Volume Fraction**
x_-	0.001	4.18879E-09	35671	0.000288	0.000149418	51.88136646
x_0	0.001	4.18879E-09	34928	0.000288	0.000146306	50.80071676
x_+	0.001	4.18879E-09	34227	0.000288	0.00014337	49.78115359
Model B						
Travelling Funnel						
Segment measured	**Particle Radius (cm)**	**Volume of One Particle**	**Number of Particles in the Selection**	**Volume of Region (cm^3)**	**Total Occupied Volume (cm^3)**	**Percentage Solid Volume Fraction**
x_-	0.001	4.18879E-09	35564	0.000288	0.00014897	51.72574126
x_0	0.001	4.18879E-09	34854	0.000288	0.000145996	50.69308812
x_+	0.001	4.18879E-09	34217	0.000288	0.000143328	49.76660918
Averages across the powder bed from Models A and B						
x_-	51.80355386					
x_0	50.74690244					
x_+	49.77388138					
Model C						
Rainfall						
Segment measured	**Particle Radius (cm)**	**Volume of One Particle**	**Number of Particles in the Selection**	**Volume of Region (cm^3)**	**Total Occupied Volume (cm^3)**	**Percentage Solid Volume Fraction**
x_-	0.001	4.18879E-09	36300	0.000288	0.000152053	52.79620987
x_0	0.001	4.18879E-09	36272	0.000288	0.000151936	52.75548552
x_+	0.001	4.18879E-09	34950	0.000288	0.000146398	50.83271446
Model D						
Rainfall						
Segment measured	**Particle Radius (cm)**	**Volume of One Particle**	**Number of Particles in the Selection**	**Volume of Region (cm^3)**	**Total Occupied Volume (cm^3)**	**Percentage Solid Volume Fraction**
x_-	0.001	4.18879E-09	36198	0.000288	0.000151626	52.64785689
x_0	0.001	4.18879E-09	36388	0.000288	0.000152422	52.92420068
x_+	0.001	4.18879E-09	34948	0.000288	0.00014639	50.82980558
Averages across the powder bed from Models D and C						
x_-	52.72203338					
x_0	52.8398431					
x_+	50.83126002					

Table 99 - Complete Solid Volume Fraction Results for Case 7 in the Influence of Deposition Mechanism on Powder Bed Quality Analysis.

Case 7: All 30 µm particles						
Travelling Funnel						
Model A						
Segment measured	**Particle Radius (cm)**	**Volume of One Particle**	**Number of Particles in the Selection**	**Volume of Region (cm^3)**	**Total Occupied Volume (cm^3)**	**Percentage Solid Volume Fraction**
x_-	0.0015	1.41372E-08	9889	0.000288	0.000139802	48.54251524
x_0	0.0015	1.41372E-08	9713	0.000288	0.000137314	47.67857726
x_+	0.0015	1.41372E-08	9477	0.000288	0.000133978	46.52011497
Model B						
Travelling Funnel						
Segment measured	**Particle Radius (cm)**	**Volume of One Particle**	**Number of Particles in the Selection**	**Volume of Region (cm^3)**	**Total Occupied Volume (cm^3)**	**Percentage Solid Volume Fraction**
x_-	0.0015	1.41372E-08	9889	0.000288	0.000139802	48.54251524
x_0	0.0015	1.41372E-08	9557	0.000288	0.000135109	46.91281405
x_+	0.0015	1.41372E-08	9555	0.000288	0.000135081	46.90299657
Averages across the powder bed from Models A and B						
x_-	48.54251524					
x_0	47.29569565					
x_+	46.71155577					
Model C						
Rainfall						
Segment measured	**Particle Radius (cm)**	**Volume of One Particle**	**Number of Particles in the Selection**	**Volume of Region (cm^3)**	**Total Occupied Volume (cm^3)**	**Percentage Solid Volume Fraction**
x_-	0.0015	1.41372E-08	10120	0.000288	0.000143068	49.67643383
x_0	0.0015	1.41372E-08	10044	0.000288	0.000141994	49.30336971
x_+	0.0015	1.41372E-08	9536	0.000288	0.000134812	46.80973054
Model D						
Rainfall						
Segment measured	**Particle Radius (cm)**	**Volume of One Particle**	**Number of Particles in the Selection**	**Volume of Region (cm^3)**	**Total Occupied Volume (cm^3)**	**Percentage Solid Volume Fraction**
x_-	0.0015	1.41372E-08	10176	0.000288	0.00014386	49.95132319
x_0	0.0015	1.41372E-08	10027	0.000288	0.000141753	49.21992115
x_+	0.0015	1.41372E-08	9579	0.000288	0.00013542	47.02080629
Averages across the powder bed from Models D and C						
x_-	49.81387851					
x_0	49.26164543					
x_+	46.91526842					

Appendix P: Data Tables of Complete Surface Roughness Results for the Influence of Deposition Mechanism on Powder Bed

Table 100 - Complete Surface Roughness Results in Deposition Mechanism Analysis for Cases 1 & 2.

Case 1: All 40 µm particles.			**Case 2: 33% of 40 µm, 30 µm, and 20 µm particles.**		
Travelling Funnel			**Travelling Funnel**		
Model A – Test 1			**Model A – Test 1**		
Segment measured	**R_q (µm)**	**Peak to Trough Distance (µm)**	**Segment measured**	**R_q (µm)**	**Peak to Trough Distance (µm)**
y_-	15.52	86.14	y_-	17.45	90.91
y_0	16.38	84.37	y_0	16.99	86.54
y_+	18.94	104.2	y_+	12.24	83.9
Model A – Test 2			**Model A – Test 2**		
y_-	16.29	90.92	y_-	17.07	88.99
y_0	15.53	81.75	y_0	15.14	77.63
y_+	17.69	110.7	y_+	13.8	77.66
Model B – Test 1			**Model B – Test 1**		
Segment measured	**R_q (µm)**	**Peak to Trough Distance (µm)**	**Segment measured**	**R_q (µm)**	**Peak to Trough Distance (µm)**
y_-	13.34	70.69	y_-	16.17	85.76
y_0	15.28	89.53	y_0	17.58	86.69
y_+	11.95	58.3	y_+	13.49	73.73
Model B – Test 2			**Model B – Test 2**		
y_-	12.06	68.79	y_-	15.09	87.09
y_0	13.98	88.84	y_0	16.23	82.22
y_+	11.96	58.3	y_+	13.51	73.94
Model C – Test 1			**Model C – Test 1**		
Rainfall			**Rainfall**		
Segment measured	**R_q (µm)**	**Peak to Trough Distance (µm)**	**Segment measured**	**R_q (µm)**	**Peak to Trough Distance (µm)**
y_-	12.33	87.55	y_-	8.466	64.42
y_0	13.17	70.81	y_0	8.872	56.4
y_+	12.26	72.82	y_+	8.682	53.19
Model C – Test 2			**Model C – Test 2**		
y_-	11.87	74.21	y_-	8.068	52.36
y_0	12.73	68.43	y_0	8.969	56.37
y_+	12.96	73.1	y_+	8.086	47.19
Model D – Test 1			**Model D – Test 1**		
Rainfall			**Rainfall**		
Segment measured	**R_q (µm)**	**Peak to Trough Distance (µm)**	**Segment measured**	**R_q (µm)**	**Peak to Trough Distance (µm)**
y_-	12.22	81.12	y_-	9.835	59.07
y_0	12.36	73.11	y_0	8.756	57.45
y_+	14.81	74.15	y_+	8.662	54.5
Model D – Test 2			**Model D – Test 2**		
y_-	14.4	78.56	y_-	10.14	73.51
y_0	12.23	75.15	y_0	9.544	67.37
y_+	12.64	75.22	y_+	9.095	59.12

Table 101 - Complete Surface Roughness Results in Deposition Mechanism Analysis for Cases 3 & 4.

Case 3: 60% of 40 µm, 25% of 30 µm, and 15% of 20 µm particles.				Case 4: 15% of 40 µm, 25% of 30 µm, and 60% of 20 µm particles.		
Travelling Funnel				**Travelling Funnel**		
Model A – Test 1				**Model A – Test 1**		
Segment measured	**R_q (µm)**	**Peak to Trough Distance (µm)**		**Segment measured**	**R_q (µm)**	**Peak to Trough Distance (µm)**
y_-	14.37	89.94		y_-	7.287	37.75
y_0	13.94	77.22		y_0	7.897	54.55
y_+	13.8	90.37		y_+	6.356	32.99
Model A – Test 2				**Model A – Test 2**		
y_-	12.28	74.95		y_-	7.473	49.33
y_0	14.37	80.02		y_0	6.92	41.51
y_+	14.33	91.82		y_+	6.332	33.17
Travelling Funnel				**Travelling Funnel**		
Model B – Test 1				**Model B – Test 1**		
Segment measured	**R_q (µm)**	**Peak to Trough Distance (µm)**		**Segment measured**	**R_q (µm)**	**Peak to Trough Distance (µm)**
y_-	12.34	74.31		y_-	6.578	44.55
y_0	14.79	93.63		y_0	8.325	62.36
y_+	11.8	70.2		y_+	6.782	47.96
Model B – Test 2				**Model B – Test 2**		
y_-	12.5	77.83		y_-	6.614	44.57
y_0	13.43	87.11		y_0	8.453	62.36
y_+	13.89	87.59		y_+	6.576	37.04
Rainfall				**Rainfall**		
Model C – Test 1				**Model C – Test 1**		
Segment measured	**R_q (µm)**	**Peak to Trough Distance (µm)**		**Segment measured**	**R_q (µm)**	**Peak to Trough Distance (µm)**
y_-	11.59	72.86		y_-	6.033	38.51
y_0	10.05	61.25		y_0	5.715	34.98
y_+	12.86	76.26		y_+	6.347	39.86
Model C – Test 2				**Model C – Test 2**		
y_-	11.66	77.28		y_-	6.132	43.25
y_0	9.927	62.08		y_0	5.875	35.77
y_+	11.8	68.49		y_+	6.594	40.58
Rainfall				**Rainfall**		
Model D – Test 1				**Model D – Test 1**		
Segment measured	**R_q (µm)**	**Peak to Trough Distance (µm)**		**Segment measured**	**R_q (µm)**	**Peak to Trough Distance (µm)**
y_-	9.97	59.07		y_-	6.348	35.9
y_0	13.65	82.68		y_0	5.494	30.52
y_+	10.6	75.22		y_+	6.348	-0.1248
Model D – Test 2				**Model D – Test 2**		
y_-	10.05	60.29		y_-	6.598	35.67
y_0	12.3	77.45		y_0	5.558	33.82
y_+	9.344	55.5		y_+	6.155	34.94

Table 102 - Complete Surface Roughness Results in Deposition Mechanism Analysis for Case 5.

Case 5: 25% of 40 µm, 50% of 30 µm, and 25% of 20 µm particles.		
Travelling Funnel		
Model A – Test 1		
Segment measured	**R_q (µm)**	**Peak to Trough Distance (µm)**
y_-	9.566	58.53
y_0	9.647	54.16
y_+	8.223	42.36
Model A – Test 2		
y_-	9.682	59.14
y_0	9.639	54.2
y_+	8.217	42.31
Travelling Funnel		
Model B – Test 1		
Segment measured	**R_q (µm)**	**Peak to Trough Distance (µm)**
y_-	8.618	46.51
y_0	8.154	59.14
y_+	8.967	49.7
Model B – Test 2		
y_-	8.575	46.62
y_0	8.86	58.76
y_+	9.567	55.37
Rainfall		
Model C – Test 1		
Segment measured	**R_q (µm)**	**Peak to Trough Distance (µm)**
y_-	8.618	61.05
y_0	8.239	50
y_+	9.447	65.83
Model C – Test 2		
y_-	9.15	60.82
y_0	8.279	47.77
y_+	10.12	70.59
Rainfall		
Model D – Test 1		
Segment measured	**R_q (µm)**	**Peak to Trough Distance (µm)**
y_-	8.088	61.21
y_0	8.106	52.06
y_+	8.64	56.51
Model D – Test 2		
y_-	8.354	60.62
y_0	8.118	53.37
y_+	7.945	47.34

Table 103 - Complete Surface Roughness Results in Deposition Mechanism Analysis for both Slab Widths in Case 6.

Case 6: All 20 μm particles at slab width = 2D.				**Case 6: All 20 μm particles at slab width = 2D$_{Max}$.**		
Travelling Funnel				**Travelling Funnel**		
Model A – Test 1				**Model A – Test 1**		
Segment measured	**R_q (μm)**	**Peak to Trough Distance (μm)**		**Segment measured**	**R_q (μm)**	**Peak to Trough Distance (μm)**
y_-	7.5	52.21		y_-	5.045	32.77
y_0	7.142	44.46		y_0	6.128	44.56
y_+	6.12	50.68		y_+	5.767	49.98
Model A – Test 2				**Model A – Test 2**		
y_-	7.569	52.24		y_-	5.039	32.7
y_0	7.132	48.46		y_0	6.304	47.66
y_+	6.293	44.64		y_+	4.781	34.02
Travelling Funnel				**Travelling Funnel**		
Model B – Test 1				**Model B – Test 1**		
Segment measured	**R_q (μm)**	**Peak to Trough Distance (μm)**		**Segment measured**	**R_q (μm)**	**Peak to Trough Distance (μm)**
y_-	6.376	37.52		y_-	5.437	44.69
y_0	7.423	48.22		y_0	6.584	48.89
y_+	6.058	35.74		y_+	5.239	52.39
Model B – Test 2				**Model B – Test 2**		
y_-	6.299	38.99		y_-	5.226	43.9
y_0	6.488	38.97		y_0	6.444	46.99
y_+	6.463	46.87		y_+	4.76	28.8
Rainfall				**Rainfall**		
Model C – Test 1				**Model C – Test 1**		
Segment measured	**R_q (μm)**	**Peak to Trough Distance (μm)**		**Segment measured**	**R_q (μm)**	**Peak to Trough Distance (μm)**
y_-	6.44	40.07		y_-	4.853	35.6
y_0	6.39	44.94		y_0	4.985	33.66
y_+	7.742	57.08		y_+	5.227	29.07
Model C – Test 2				**Model C – Test 2**		
y_-	6.291	38.96		y_-	4.767	35.27
y_0	6.43	44.77		y_0	4.858	32.94
y_+	6.625	44.9		y_+	4.871	27.57
Rainfall				**Rainfall**		
Model D – Test 1				**Model D – Test 1**		
Segment measured	**R_q (μm)**	**Peak to Trough Distance (μm)**		**Segment measured**	**R_q (μm)**	**Peak to Trough Distance (μm)**
y_-	5.151	34.22		y_-	5.409	41.16
y_0	7.059	47.21		y_0	6.602	47.85
y_+	5.569	36.54		y_+	6.433	48.48
Model D – Test 2				**Model D – Test 2**		
y_-	5.253	34.18		y_-	4.909	30.48
y_0	6.573	47.33		y_0	6.581	47.98
y_+	5.513	36.52		y_+	6.252	49.9

Table 104 - Complete Surface Roughness Results in Deposition Mechanism Analysis for both Slab Widths in Case 7.

Case 7: All 30 µm particles at slab width = 2D.		
Travelling Funnel		
Model A – Test 1		
Segment measured	**R_q (µm)**	**Peak to Trough Distance (µm)**
y_-	8.375	50.11
y_0	8.763	51
y_+	8.048	42.15
Model A – Test 2		
y_-	8.491	54.93
y_0	8.655	51.33
y_+	8.388	42.74
Travelling Funnel		
Model B – Test 1		
Segment measured	**R_q (µm)**	**Peak to Trough Distance (µm)**
y_-	8.405	53.65
y_0	8.446	47.22
y_+	7.199	44.04
Model B – Test 2		
y_-	8.836	51.8
y_0	8.388	47.37
y_+	7.067	41.53
Rainfall		
Model C – Test 1		
Segment measured	**R_q (µm)**	**Peak to Trough Distance (µm)**
y_-	8.06	50.95
y_0	9.835	63.41
y_+	8.114	52.91
Model C – Test 2		
y_-	8.4	55.62
y_0	8.649	56.3
y_+	8.934	64.22
Rainfall		
Model D – Test 1		
Segment measured	**R_q (µm)**	**Peak to Trough Distance (µm)**
y_-	8.829	49.74
y_0	9.231	59.54
y_+	9.279	77.15
Model D – Test 2		
y_-	8.363	46.9
y_0	8.016	46.99
y_+	10.21	72.97

Case 7: All 30 µm particles at slab width = 2D$_{Max}$.		
Travelling Funnel		
Model A – Test 1		
Segment measured	**R_q (µm)**	**Peak to Trough Distance (µm)**
y_-	9.315	55.71
y_0	10.12	63.5
y_+	8.995	48.33
Model A – Test 2		
y_-	9.115	47.93
y_0	11.24	64.6
y_+	9.587	57.14
Travelling Funnel		
Model B – Test 1		
Segment measured	**R_q (µm)**	**Peak to Trough Distance (µm)**
y_-	9.71	53.56
y_0	10.21	66.94
y_+	9.204	54.31
Model B – Test 2		
y_-	10.01	54.27
y_0	9.169	55.62
y_+	9.474	64.82
Rainfall		
Model C – Test 1		
Segment measured	**R_q (µm)**	**Peak to Trough Distance (µm)**
y_-	9.059	45.27
y_0	9.18	56.37
y_+	10.54	68.57
Model C – Test 2		
y_-	9.074	46.8
y_0	8.714	50.29
y_+	10.38	65.23
Rainfall		
Model D – Test 1		
Segment measured	**R_q (µm)**	**Peak to Trough Distance (µm)**
y_-	10.77	64.99
y_0	11.1	68.88
y_+	9.657	71.03
Model D – Test 2		
y_-	10.12	59.54
y_0	11.19	70.43
y_+	8.892	50.11

Appendix Q: Charts of Surface Roughness at Different Regions in the y Plane

Case 1: All 40 μm Particles.

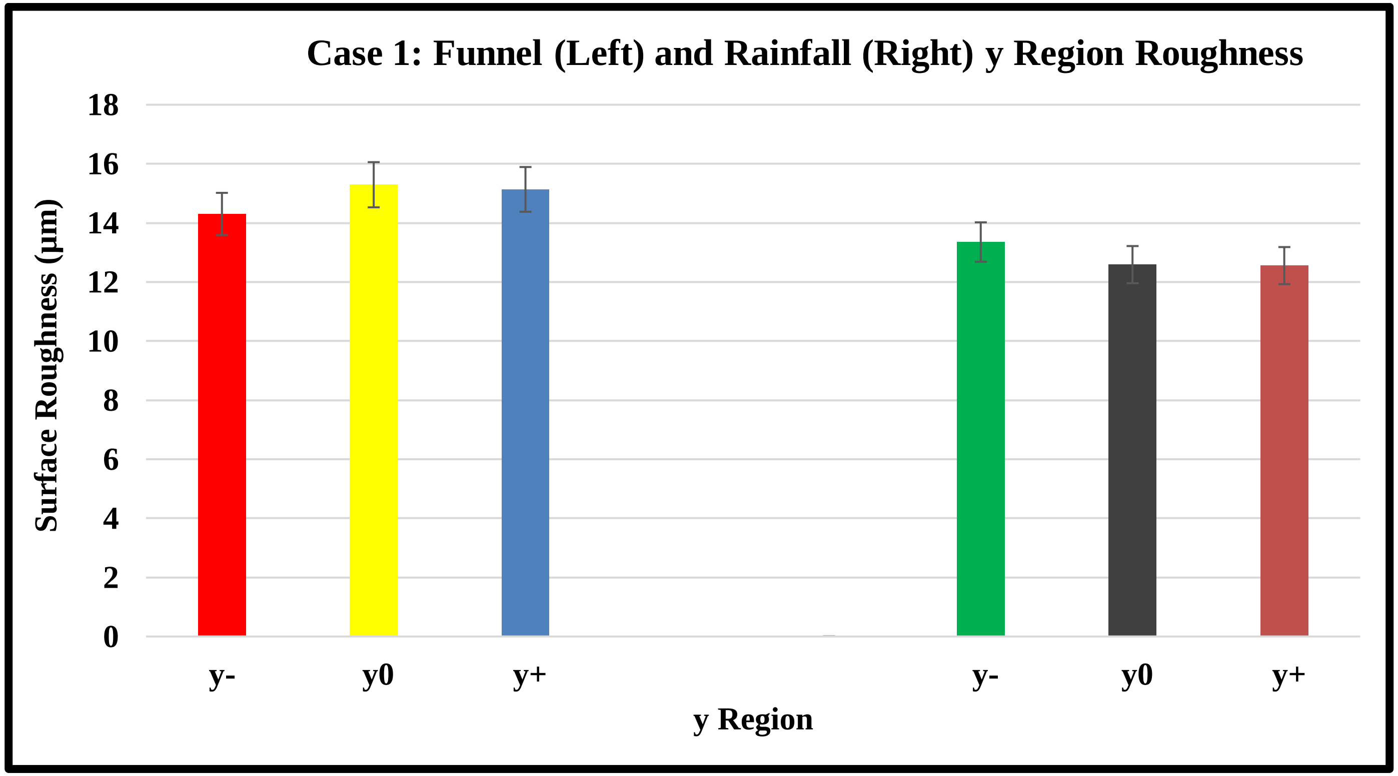

Figure 144 - y Region Roughness in Case 1.

Case 2: One-Third of 20 µm, 30 µm, and 40 µm Particles.

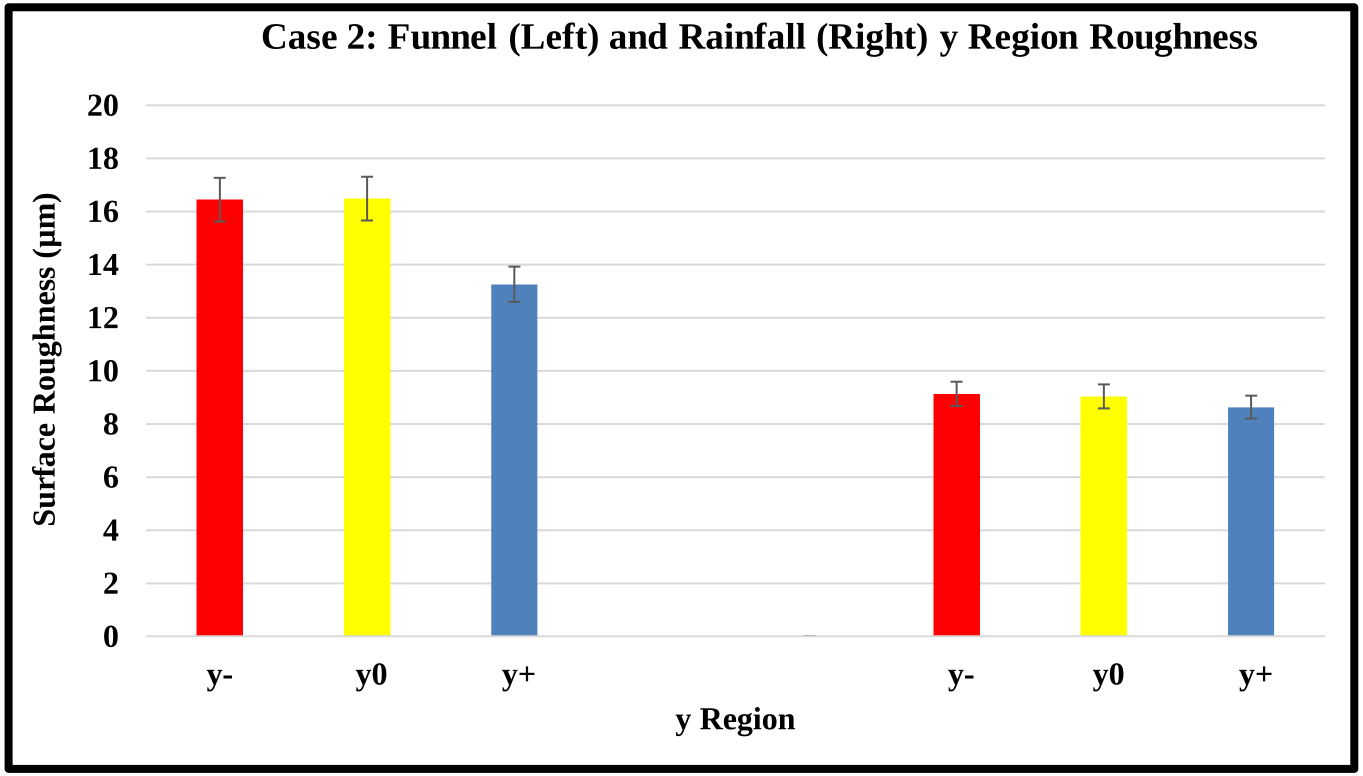

Figure 145 - y Region Roughness in Case 2.

Case 3: 15% of 20 µm, 25% of 30 µm, and 60% of 40 µm Particles.

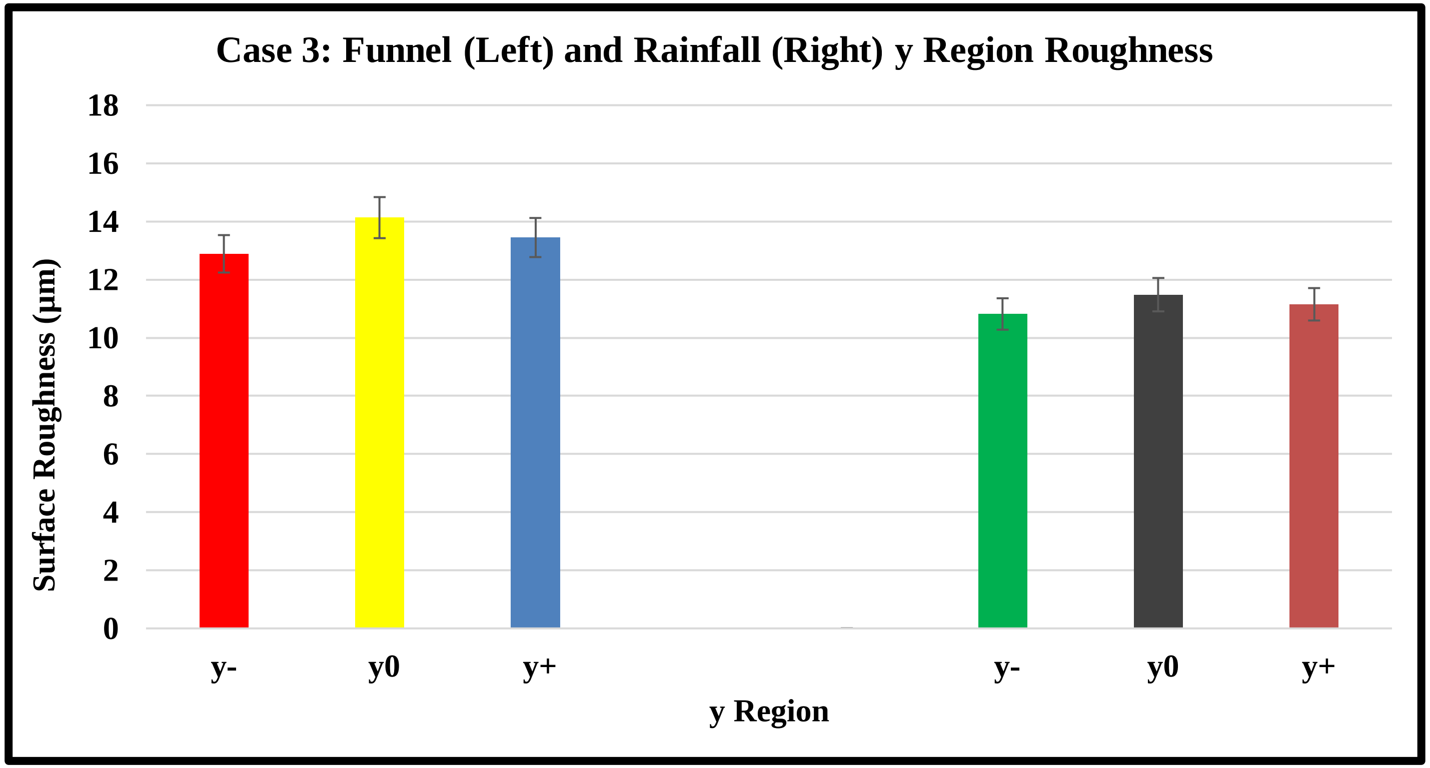

Figure 146 - y Region Roughness in Case 3.

Case 4: 60% of 20 µm, 25% of 30 µm, and 15% of 40 µm Particles.

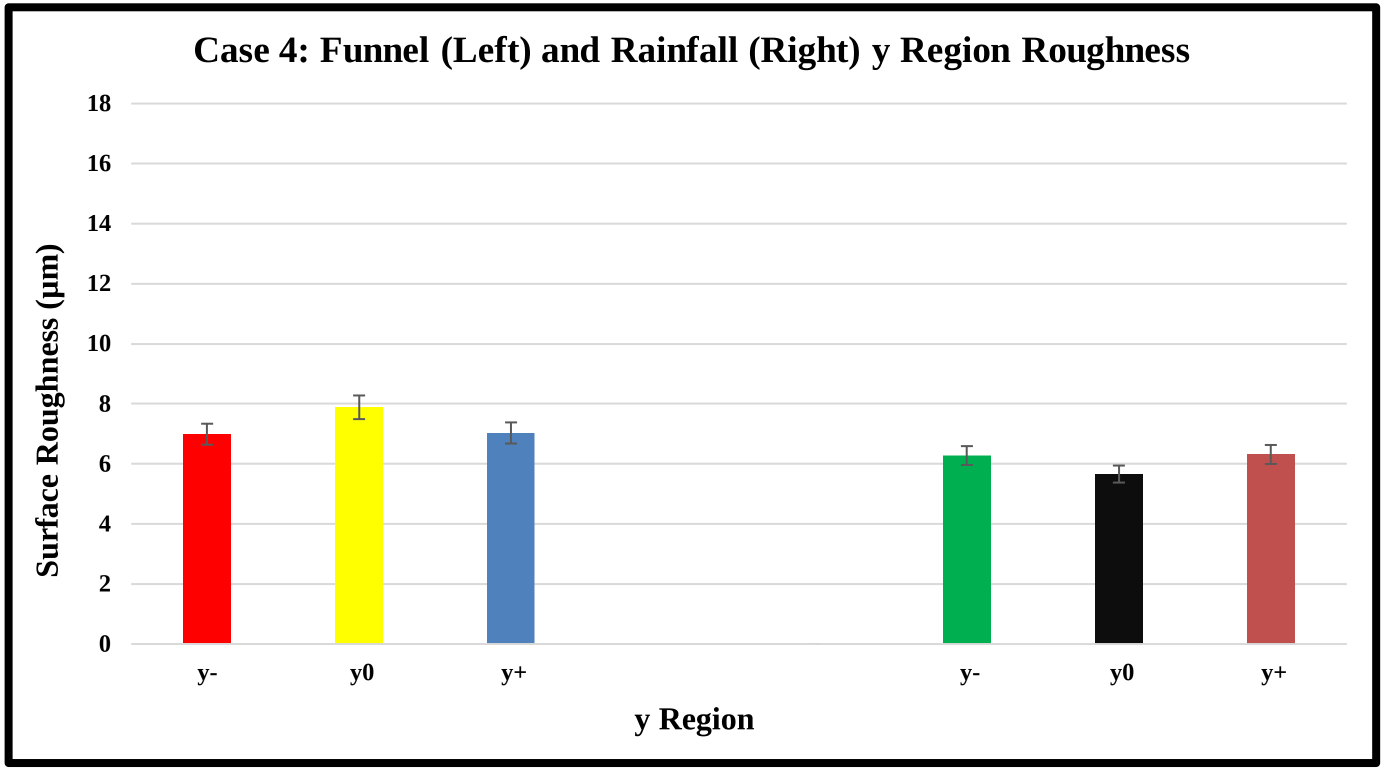

Figure 147 – y Region Roughness in Case 4.

Case 5: 25% of 20 μm, 50% of 30 μm and 25% of 40 μm Particles.

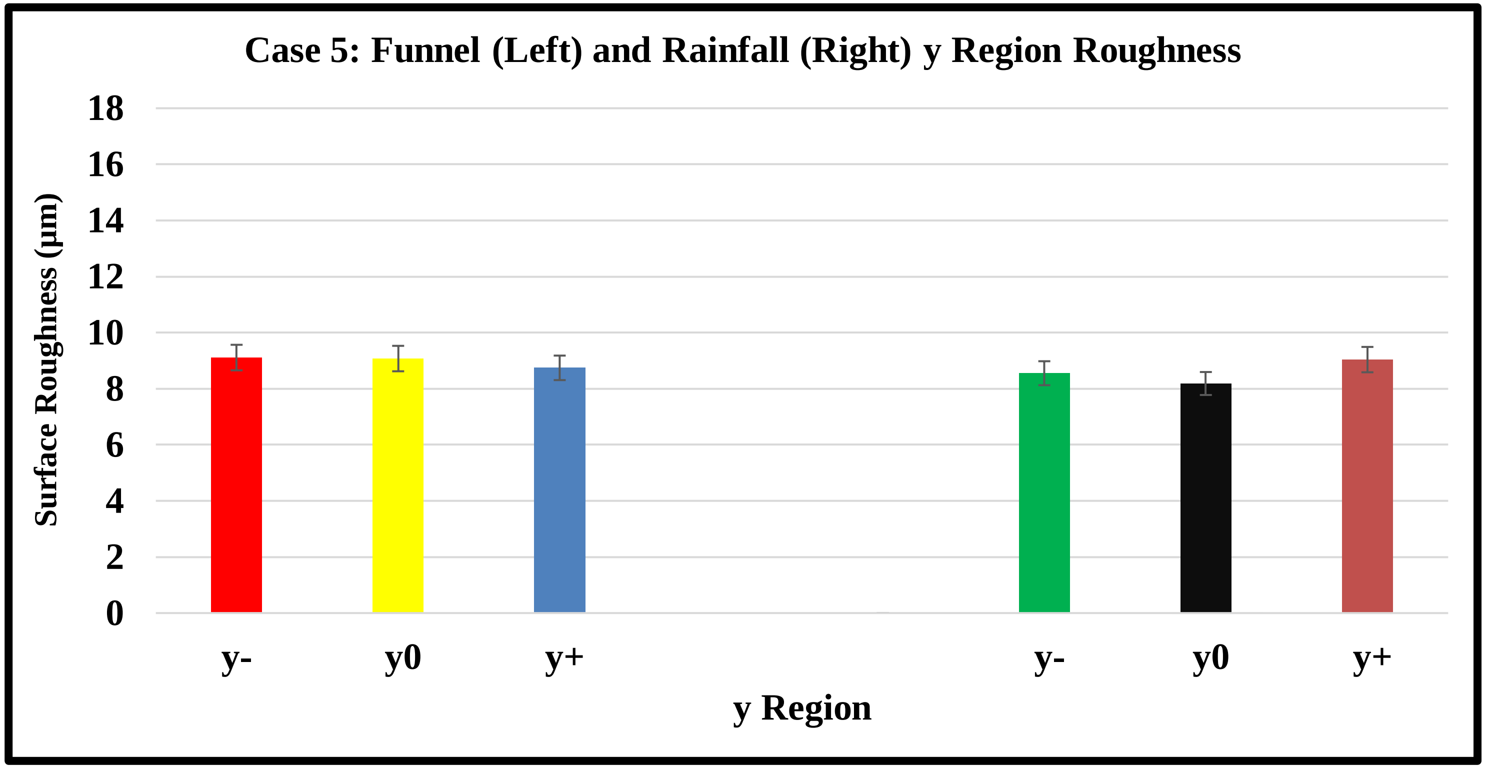

Figure 148 - y Region Roughness in Case 5.

Case 6: All 20 µm Particles.

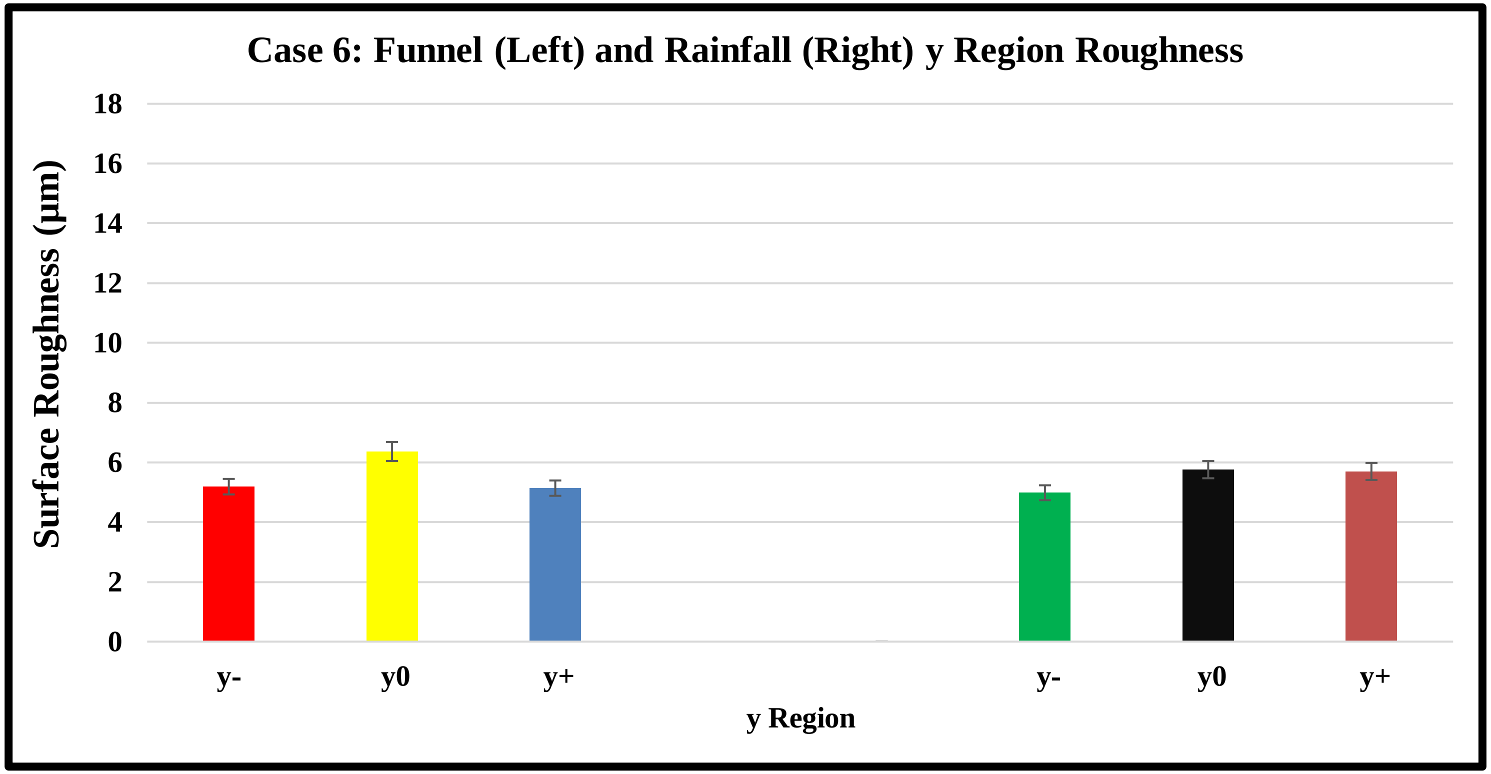

Figure 149 – y Region Roughness in Case 6.

Case 7: All 30 µm Particles.

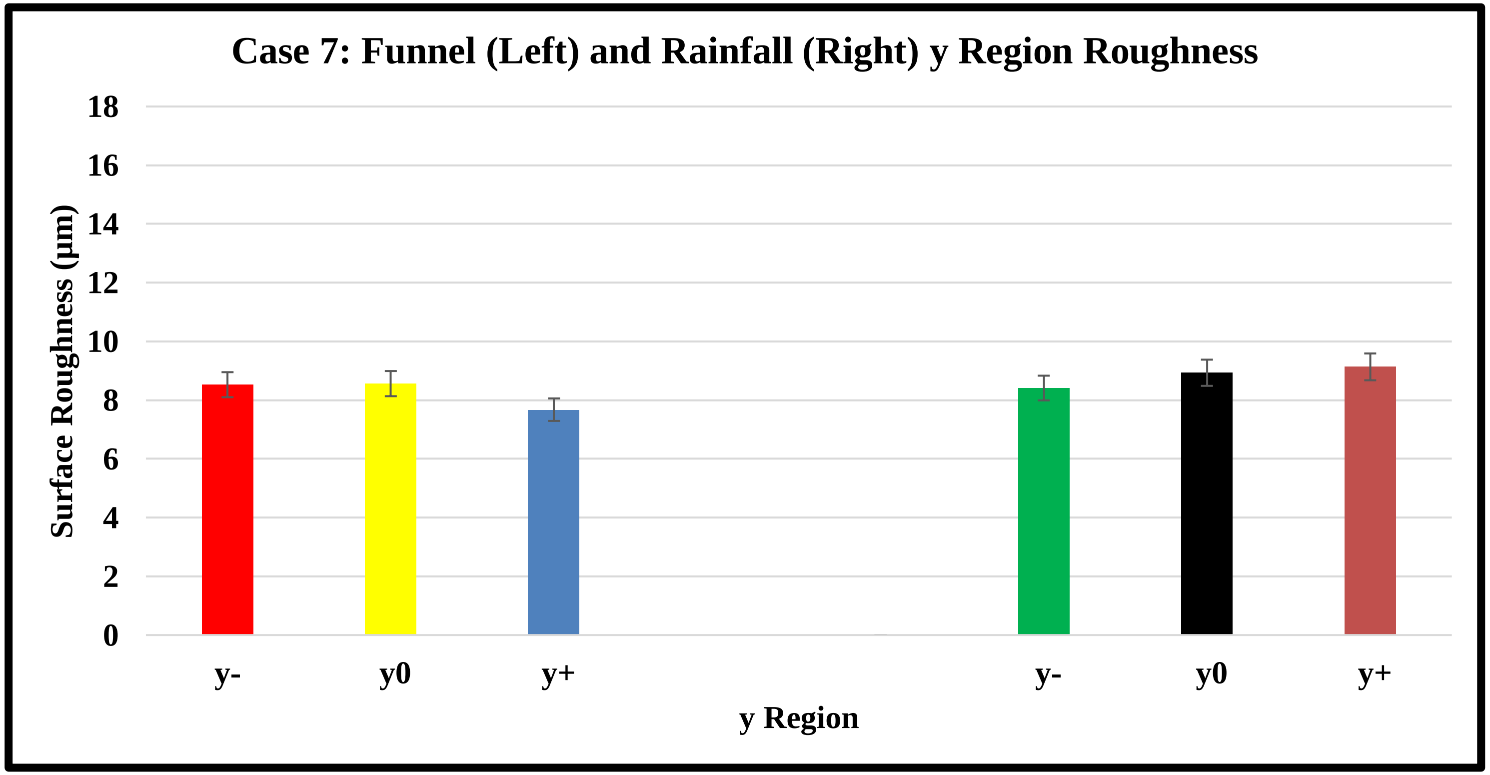

Figure 150 – y Region Roughness in Case 7.

Appendix R: Bar Chart of Funnel versus Rainfall Segregation Results

Case 2: One-Third of 20 µm, 30 µm, and 40 µm Particles.

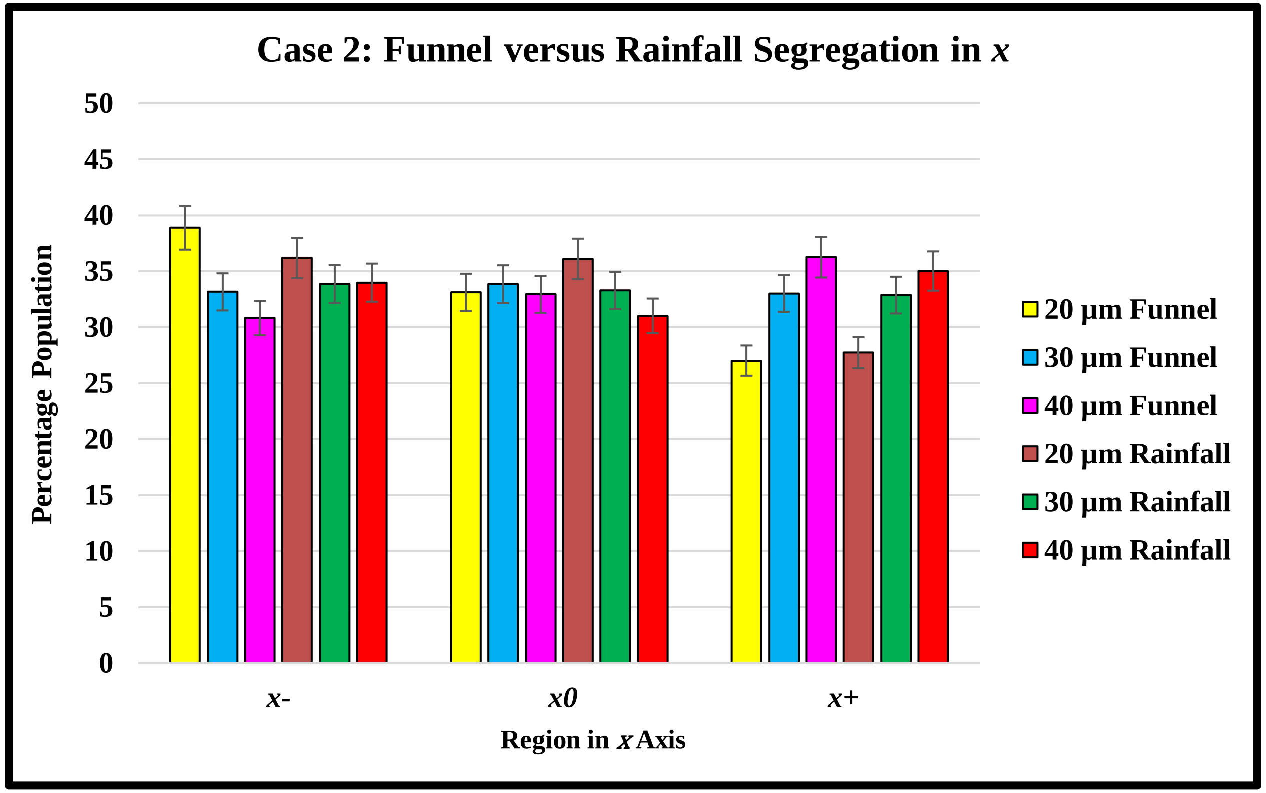

Figure 151 - Funnel versus Rainfall Segregation in the *x* Plane of Case 2.

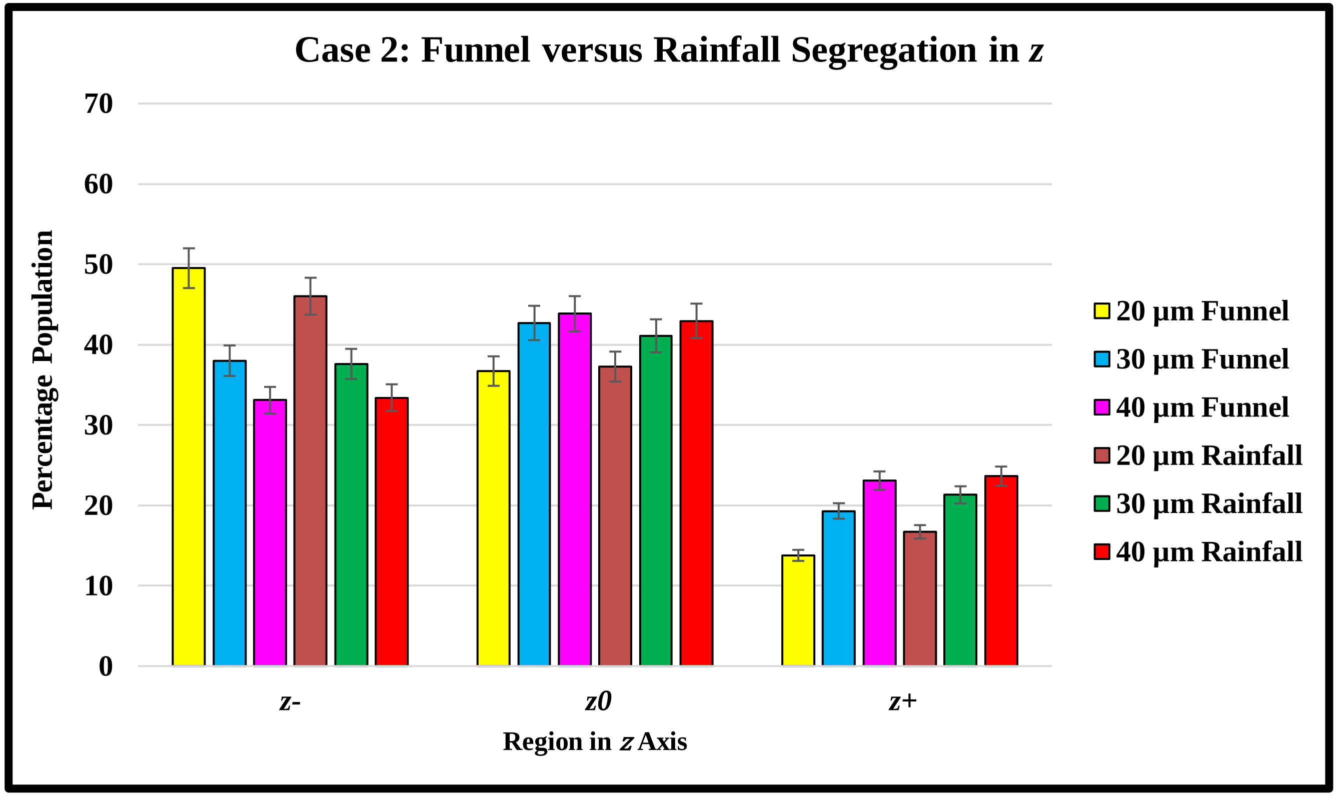

Figure 152 - Funnel versus Rainfall Segregation in the *z* Plane of Case 2.

Case 4: 60% of 20 µm, 25% of 30 µm, and 15% of 40 µm Particles.

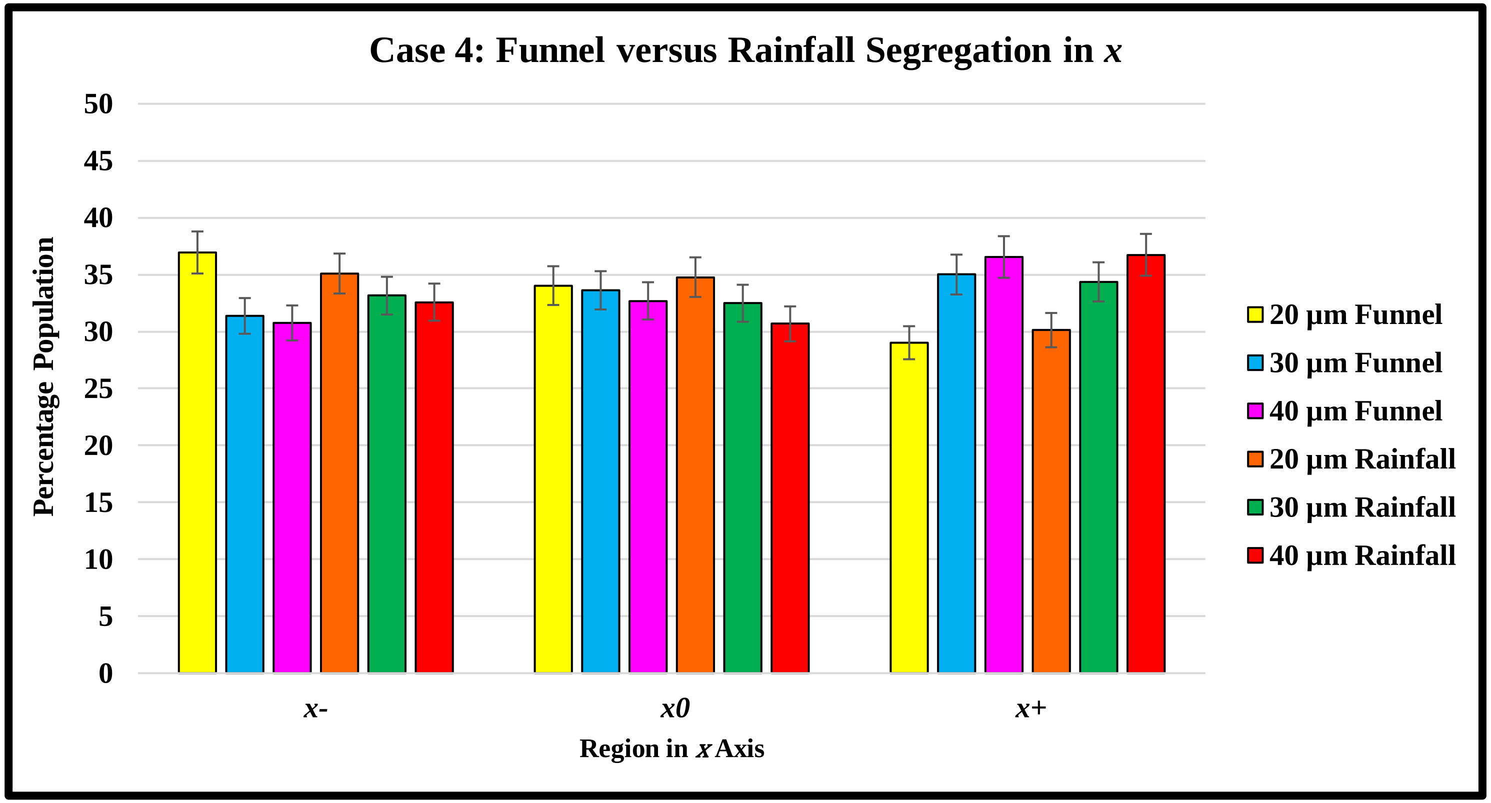

Figure 153 - Funnel versus Rainfall Segregation in the *x* Plane of Case 4.

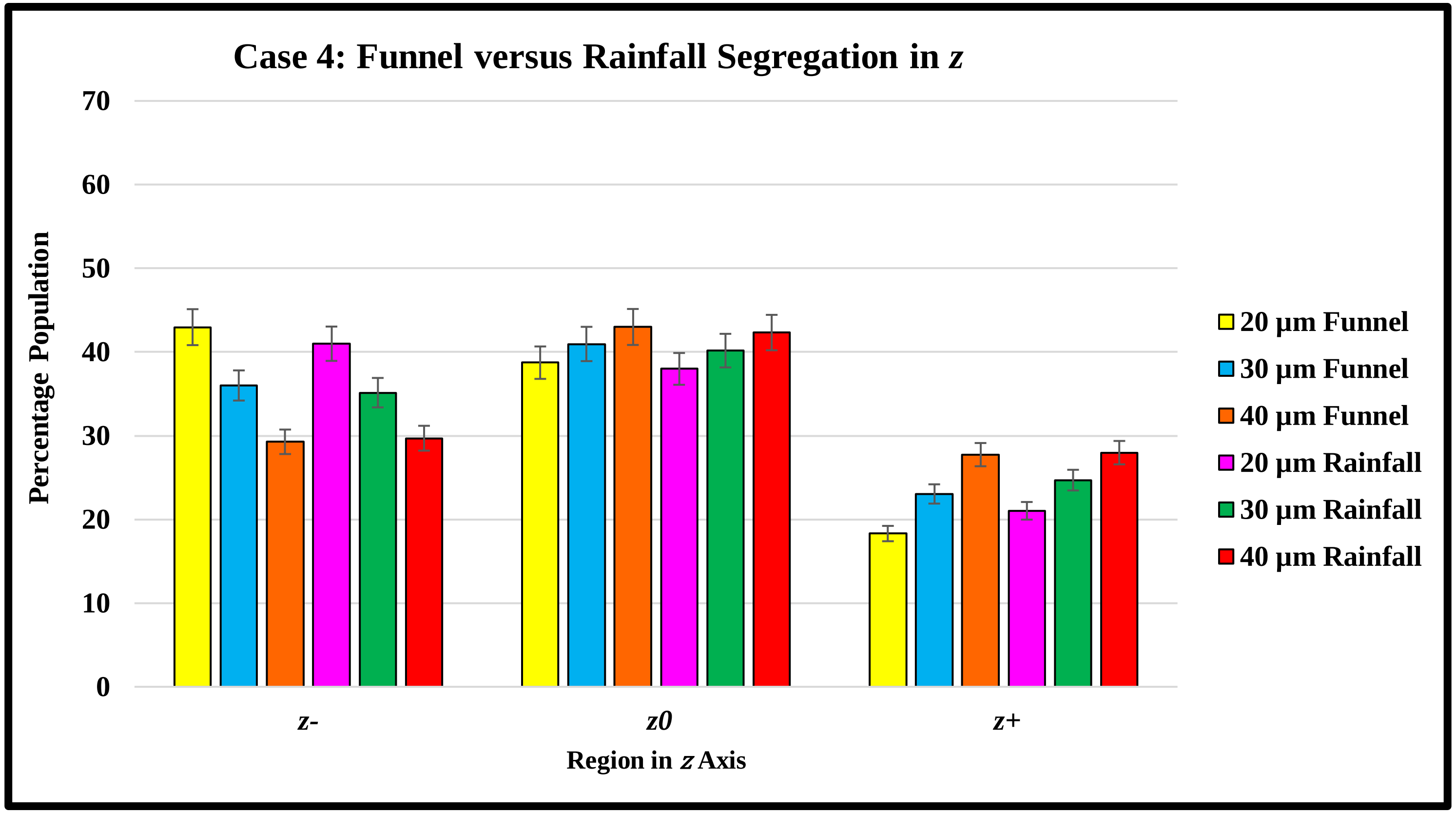

Figure 154 - Funnel versus Rainfall Segregation in the *z* Plane of Case 4.

Case 5: 25% of 20 μm, 50% of 30 μm and 25% of 40 μm Particles.

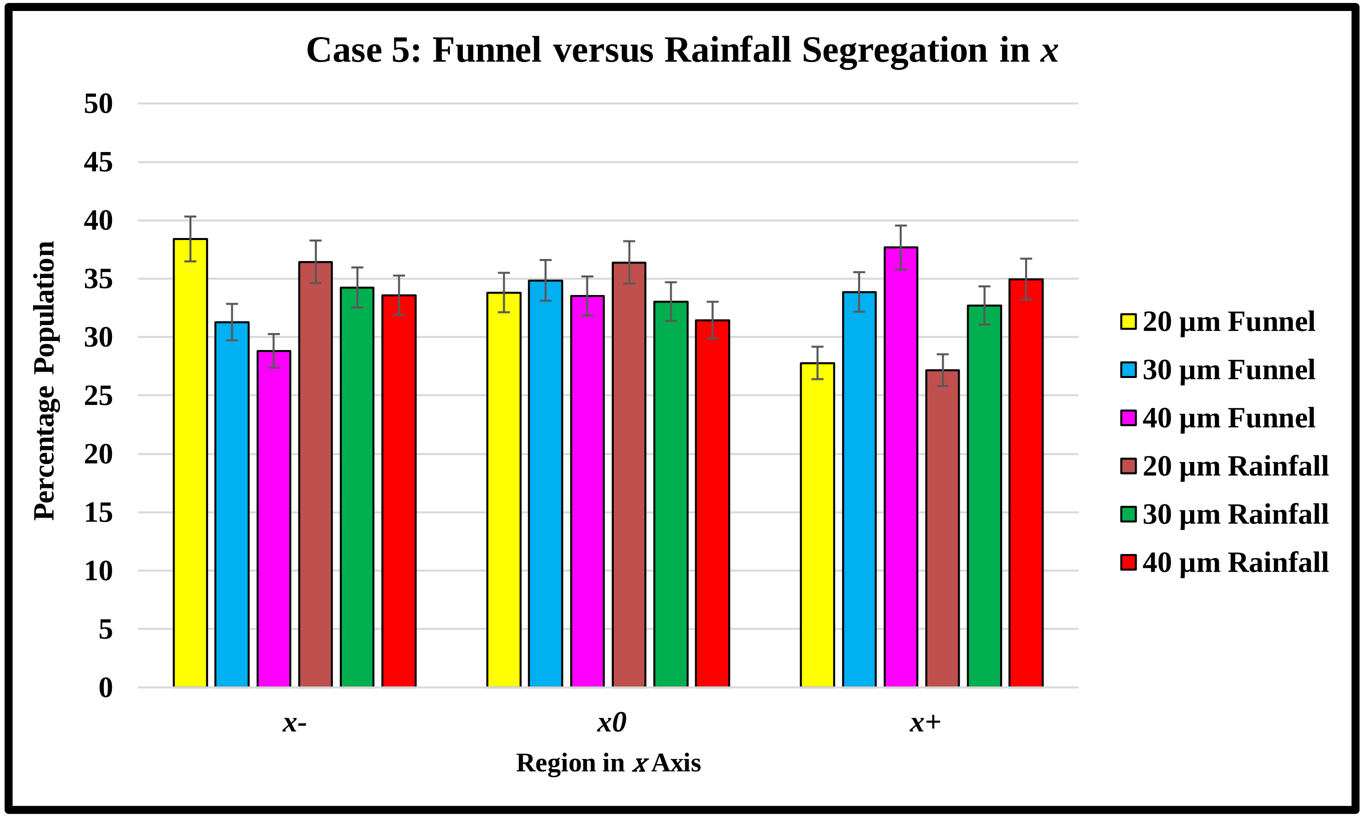

Figure 155 - Funnel versus Rainfall Segregation in the *x* Plane of Case 5.

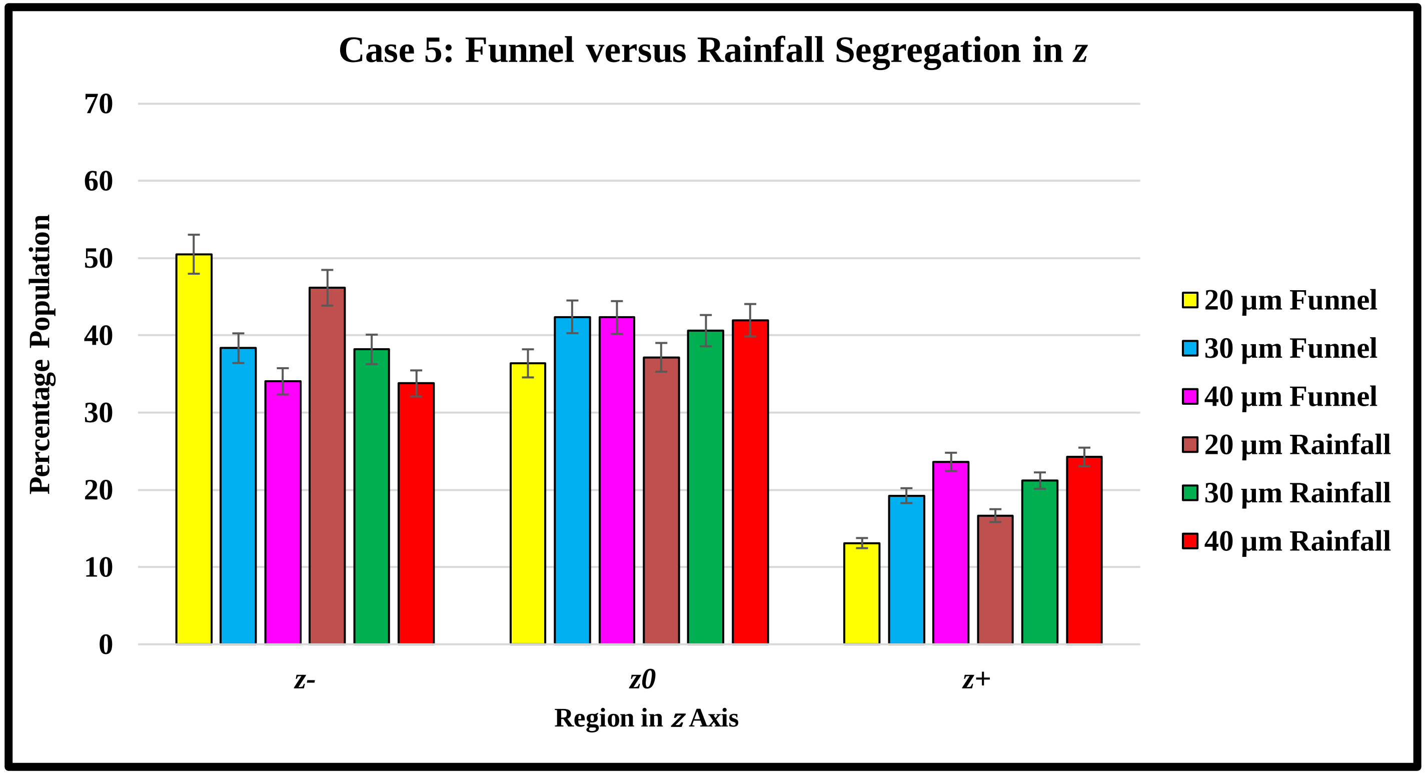

Figure 156 - Funnel versus Rainfall Segregation in the *z* Plane of Case 5.